Lawrence
Livermore
National
Laboratory

UCRL-LR-113717-98

Laboratory Directed Research and Development

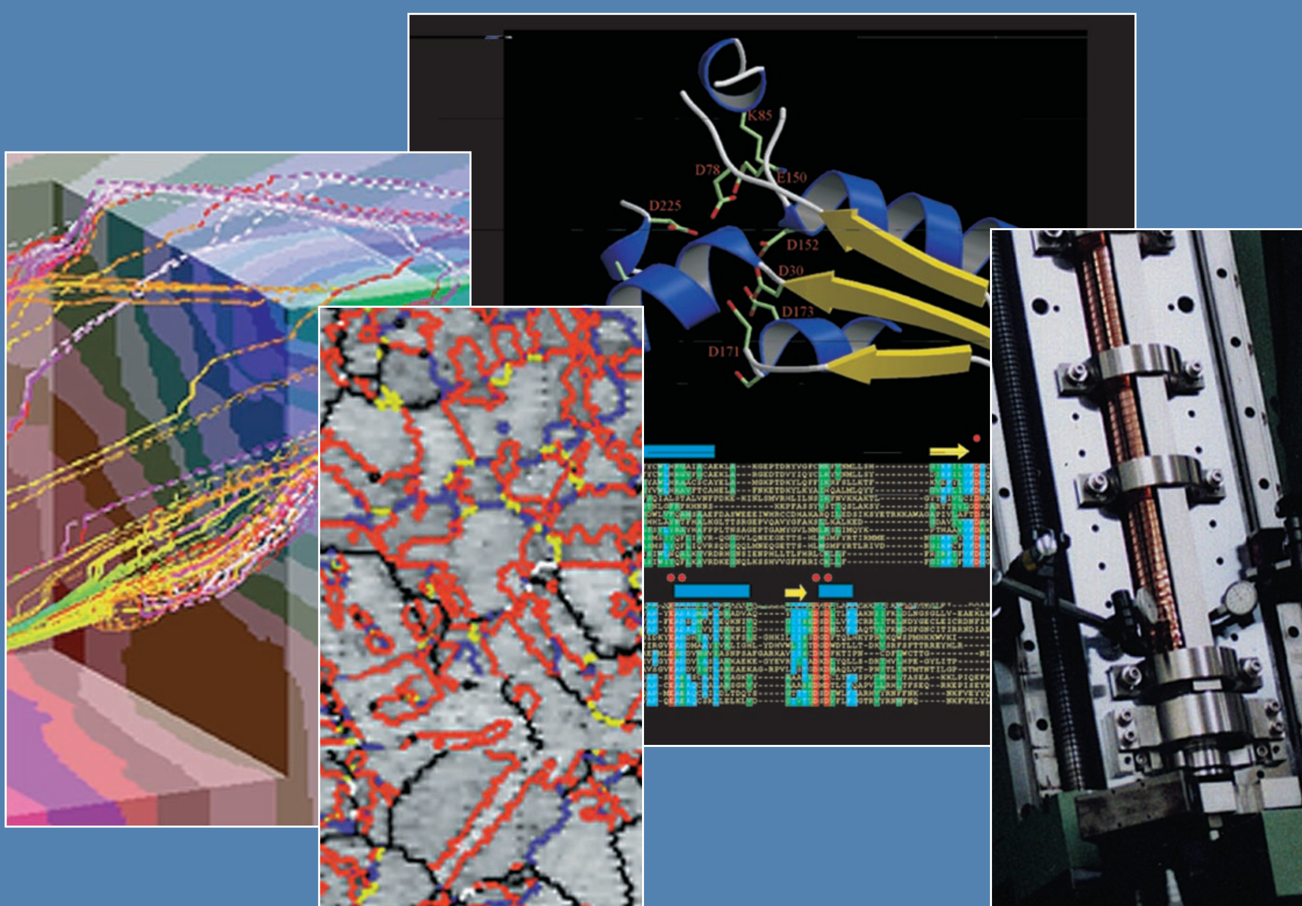

FY98 Annual Report

Work performed under the auspices of the U.S. Department of Energy by Lawrence Livermore National Laboratory under Contract W-7405-ENG-48.

Laboratory Directed Research and Development

FY98 Annual Report

Lawrence Livermore National Laboratory

UCRL-LR-113717-98

University of California

Lawrence Livermore National Laboratory

Director
C. Bruce Tarter

Deputy Director of Science and Technology
Jeffrey Wadsworth

Director of the Laboratory Science and Technology Office,
Laboratory Directed Research and Development Program
John F. Holzrichter

Deputy Director of the Laboratory Directed Research and Development Program
Rokaya A. Al-Ayat

Acknowledgements

This Annual Report provides an overview of the the Laboratory Directed Research and Development (LDRD) Program at Lawrence Livermore National Laboratory. It presents a summary of progress achieved by the LDRD projects funded in FY98. We send our sincere appreciation to the principal investigators of these projects for providing the technical content of this report. Also, a special thank you to TID editors Alane Alchorn (CASC) and Jason Carpenter (Lasers) for their efforts in providing quality input from their programs, to Jane Staehle for her review of the final draft, to the support of the Laboratory Science and Technology Office staff, and to the dedicated publications team listed below.

Scientific Editor
Rokaya A. Al-Ayat

Publication Editor
Tim Peck

Publication Designer
Lee Dravidzius

Publications Staff
Sherry Emmons (art and composition)
Coralyn McGregor (editorial)
Janet Tanaka (art and composition)

Database Management
Nancy A. Campos
Pamela R. Harris

Contents

Section 2 Atmospheric and Geosciences

Section 3 Biotechnology and Health Care Technologies

Section 4 Computing/Modeling/Simulation

Section 10 Space Science and Technology

Appendix

Introduction

In 1984, Congress and the Department of Energy (DOE) established the Laboratory Directed Research and Development (LDRD) Program to enable the director of a national laboratory to foster and expedite innovative research and development (R&D) in mission areas. The Lawrence Livermore National Laboratory (LLNL) continually examines these mission areas through strategic planning and shapes the LDRD Program to meet its long-term vision.

The goal of the LDRD Program is to spur development of new scientific and technical capabilities that enable LLNL to respond to the challenges within its evolving mission areas. In addition, the LDRD Program provides LLNL with the flexibility to nurture and enrich essential scientific and technical competencies and enables the Laboratory to attract the most qualified scientists and engineers.

The FY98 LDRD portfolio described in this annual report has been carefully structured to continue the tradition of vigorously supporting DOE and LLNL strategic vision and evolving mission areas. The projects selected for LDRD funding undergo stringent review and selection processes, which emphasize strategic relevance and require technical peer reviews of proposals by external and internal experts. These FY98 projects emphasize the Laboratory's national security needs: stewardship of the U.S. nuclear weapons stockpile, responsibility for the counter- and nonproliferation of weapons of mass destruction, development of high-performance computing, and support of DOE environmental research and waste management programs.

Components of the LDRD Program

The Laboratory's LDRD Program consists of three major components: Strategic Initiatives (SI), Exploratory Research (ER), and the Laboratory-Wide (LW) Competition.

The *Strategic Initiative* (SI) component focuses on innovative research and development activities that are likely to set new directions for existing programs, will help develop new programmatic areas within LLNL mission responsibilities, and can enhance the Laboratory's science and technology base. Projects in this category are usually larger and more technically challenging than projects funded in the other categories. An SI project must be aligned with the articulated strategic R&D priorities of at least one of the four Laboratory strategic councils: (1) the Council on Bioscience and Biotechnology, (2) the Council on Energy and Environmental Systems, (3) the Council on National Security, and (4) the Council on Strategic Science and Technology. Typically many deserving proposals are considered, and less than a third of the proposals are funded.

The *Exploratory Research* (ER) component, on the other hand, is aligned with the Laboratory directorates' strategic R&D requirements. Each directorate develops a strategic R&D "needs statement" for its technical staff and for members of the ER Oversight Committee responsible for reviewing the proposals. Typically, fewer than half the proposals submitted to a directorate are forwarded to the ER Oversight Committee for further review and selection.

Projects in the third LDRD component, the *Laboratory-Wide* (LW) competition, are chosen to emphasize innovative research concepts and ideas, which are subject to limited management filtering so as to encourage the creativity of individual researchers. The competition is open to all LLNL staff in programmatic, scientific, engineering, technical, support, or administrative areas.

We also fund, throughout the year, a few projects in a fourth category—*Definition/Feasibility* projects (D/F). This special category of LDRD projects provides flexibility to develop better definition of and feasibility for potential projects in any category. In FY98, we funded three projects in this D/F category.

LDRD Funding for FY98

In FY98, LDRD funding totaled $55.6 million to projects in all categories. Figure 1 shows the distribution of the FY98 budget: roughly 69% for ER, 26% for SI, and 5% for LW.

The LDRD projects vary in size: about 60% of the projects are funded at less than $250,000, while seven projects exceeded the $1M funding level. The average size of an LDRD project for FY98 was $322,000. Figure 2 shows the distribution of funds for the FY98 portfolio of projects.

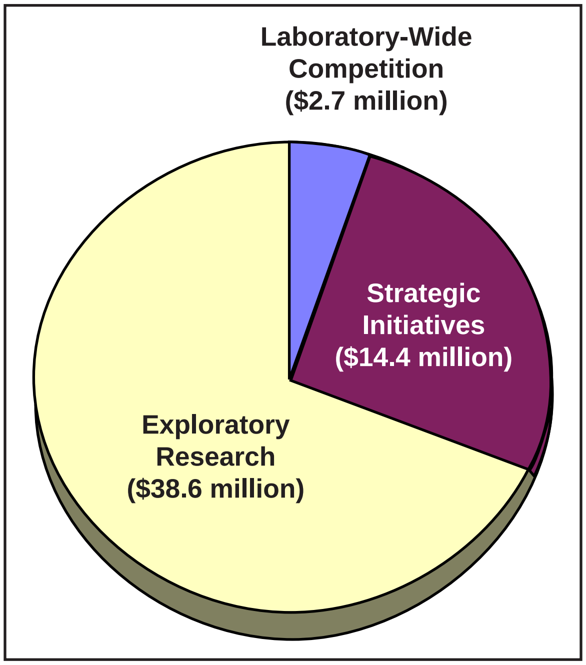

Figure 1. Distribution of FY98 funding dollars among the three categories in the Laboratory's LDRD Program

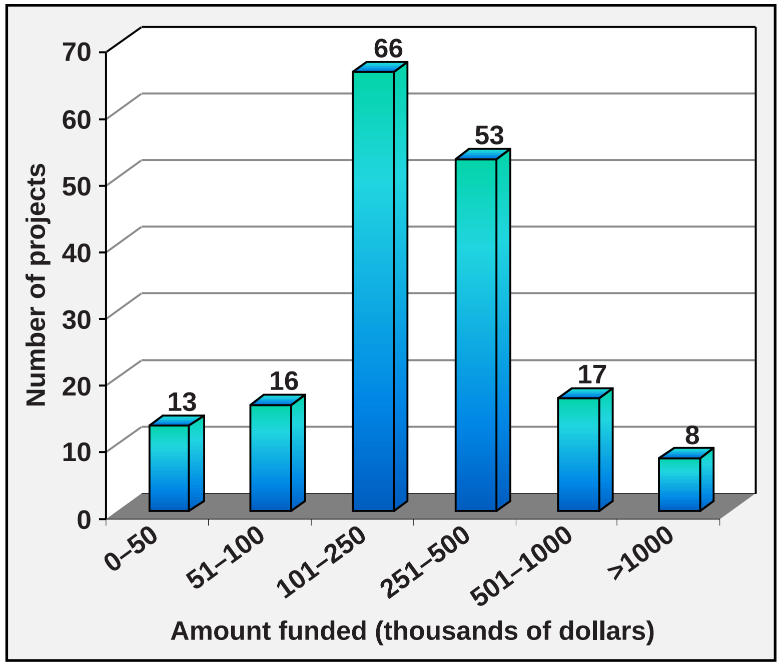

Figure 2. Distribution of FY98 funding dollars among the Laboratory's LDRD projects (in thousands of dollars).

Projects are categorized into 10 competency areas. Although projects often address more than one competency area, the report classifies each project in the most appropriate category. Figure 3 shows the FY98 funding distribution among these competency areas.

Highlights of LDRD FY98 Program Accomplishments

The Laboratory's FY98 LDRD Program continues to provide many far-reaching scientific and technical accomplishments. Livermore's LDRD Program has been well managed and very productive since its inception in FY85, with an outstanding record of scientific and technical output. In fact, in compiling statistics on publications, patents, staff-member hires, and national awards, we find the LDRD Program is far more productive than other programmatic areas of the Laboratory. For example in FY96, 35 of 83 patents issued for LLNL research were based on LDRD-funded research. Similarly, in FY97, 29 of LLNL's 64 patents were LDRD-based.

In addition, Laboratory scientists and their research funded by LDRD have continued to garner national recognition. Three are worth highlighting here: Dr. Steve Payne received the *1998 Excellence in Fusion Engineering Award*; Dr. Charles Alcock was named as one of the *Top 50 R&D Stars* by *Industry Week* magazine; and recently, the American Physical Society (APS) selected the LLNL results on Petawatt and Falcon lasers as two "dramatic advances in laser/matter interactions" to be highlighted at the APS centennial meeting.

In recent years, many *R&D 100 Awards* from *R&D Magazine* have been earned for innovative technologies developed through LDRD-funded research. In FY98, four of the seven *R&D 100 Awards* received by LLNL scientists were based on their LDRD research:

- A computer-aided-software simulation tool was developed for optimizing plasma-assisted manufacturing and could find uses in the semiconductor industry.
- The High-performance Electromagnetic Roadway Mapping and Evaluation System, or HERMES, is a high-resolution, radar-based mobile inspection system for detecting and mapping structural defects.
- A new optical dental imaging system has been created to non-invasively image internal tooth and soft tissue microstructure for dental applications.
- A two-color fiber-optic infrared sensor measures temperature and emissions for medical and industrial applications.

By its nature, an R&D project often takes many years before realizing its the full impact. Several previously funded LDRD activities achieved major successes during FY98; they have been broadly reported in the scientific communities as major scientific accomplishments that have significant implications for the Laboratory's role in support of DOE's national security missions. Below we highlight three examples where earlier LDRD research played a major role in terms of spin-off technologies.

Research leading to the Extreme Ultraviolet Lithography (EUV) Cooperative Research and Development Agreement (CRADA). The earliest work sponsored by LDRD in FY85–86 was in the development of multilayer mirrors for soft x-ray reflectors. Between 1988 and 1989, LDRD sponsored early conceptual studies for a soft x-ray projection lithography system, using reflection masks. In the 1990s, this work was funded by DoD's Defense Advanced Research Projects Agency (DARPA). The LDRD-funded research provided much of the basic capability to enable the Laboratory to be a major player in a $250-million CRADA with the leaders in semiconductor manufacturing.

Biological Weapon Agent Detection and Identification. In the case of a terrorist attack or on the battlefield, it is important to determine quickly if a biological agent has been used. LDRD-funded research has developed two highly portable and extremely sensitive technologies. One uses polymerase chain reaction and the other the fluorescent tagging of cells. These technologies were tested by the Army at Dugway Proving Ground in Utah (along with several competing technologies) and found to be in all ways superior. They are presently being developed under programmatic sponsorship.

Environmental Clean-Up Technologies. For many years, LDRD has funded research projects to identify better methods to clean up soil and groundwater contamination. Most contaminants at the LLNL sites are either petroleum distillates or chlorinated hydrocarbons used as solvents. Traditional pump-and-treat cleanup methods are inefficient and could take decades to complete. In early 1990s, in collaboration with the University of California at Berkeley, LLNL developed the dynamic underground stripping process. LLNL scientists also developed hydrous pyrolysis/oxidation, a process that converts contaminants in the ground to such benign products as carbon dioxide, chloride ions, and water. During the summer of 1997, both processes were used to clean up a four-acre site in Visalia, California. During the first six weeks of operations, over 300,000

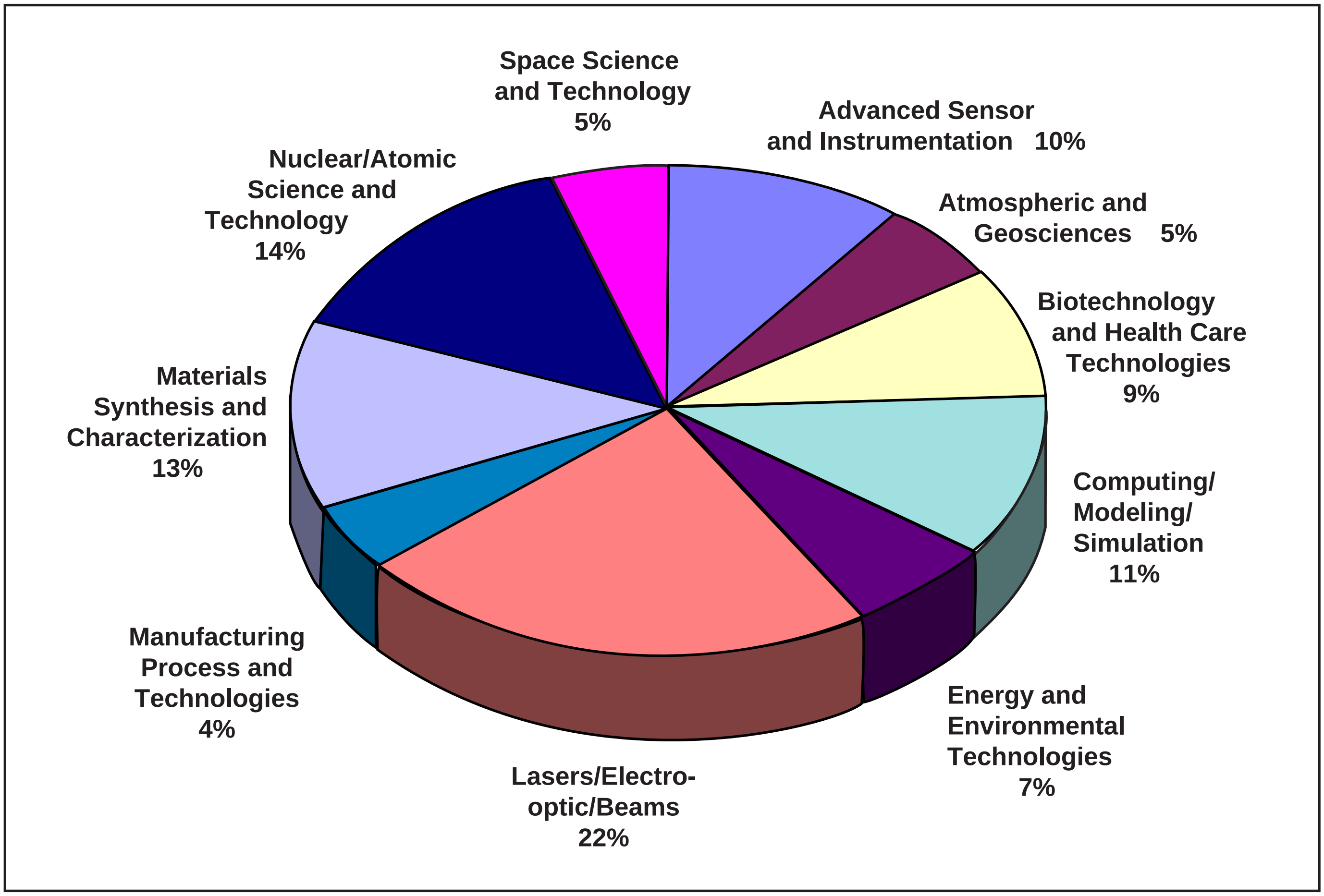

Figure 3. Distribution of FY98 funding among the 10 competency areas.

pounds of contaminants were removed or destroyed (estimated to be equivalent to 600 years of pump-and-treat). The Visalia cleanup, using the underground stripping process plus hydrous pyrolysis/oxidation, has been considered an unprecedented success. Currently, these technologies are being used for site cleanup at two major DOE facilities, at the Portsmouth Gaseous Diffusion Plant in Ohio and the Savannah River site in South Carolina.

Some FY98 LDRD Project Highlights

Synthesis, Characterization, and Formulation of New Insensitive High-Performance Explosive Molecules. Using LDRD funding, LLNL is accelerating the development of new high-performance, enhanced safety explosive molecules. By combining advanced quantum-chemistry calculations with aggressive synthesis of promising candidate molecules, LLNL is significantly enhancing explosives research, including shaped-charge development, formulation, synthesis, and theory. A high-explosive performance prediction code has been developed by linking a thermomechanical code with an *ab initio* electronic structure and a molecular packing code. Stability prediction is performed on the basis of first-principles electronic structure calculation and neutron scattering measurements. Through an extensive computational search using the linked codes, two target molecules have been synthesized. A third target molecule is in the final stages of synthesis, with a predicted performance nearly equal to that of high melting explosives, but with much better thermal and impact stability. The system used in synthesizing all three molecules and in predicting stability and safety is unique and represents a major advance in the development of insensitive high explosives, which could improve the safety of the weapons stockpile. (See page 8-6).

Proton Radiography Research. This LDRD investment has supported research to investigate the use of protons to image nuclear explosives. The Laboratory has been exploring the fundamental science underlying the use of high-energy protons as radiographic probes. In addition, ideas have been explored to reduce the costs of a proton radiography facility and to examine the technique's potential for advanced hydrodynamic testing as part of the Stockpile Stewardship Program (SSP). Much of this work has been carried out in collaboration with groups at LANL (also supported by LDRD funds). (See page 9-2).

The Laboratory's LDRD has also supported a study to explore the use of available accelerator resources at other DOE Laboratories (such as Brookhaven National Laboratory and Fermilab) to construct a proton radiography accelerator facility at a site that could support a hydrotest experimental program. This program would provide the experience of using high-energy protons as radiographic probes and provide additional experimental data not available from existing facilities. The DOE DP Program has been supportive of the findings of this study, and efforts are under way to develop the ideas further within the SSP. (See page 9-11).

Radiation Opacity Experiments. LDRD at LLNL has funded experiments in laboratory astrophysics, performed in collaboration with Sandia National Laboratories on their 500-kJ Saturn Z-pinch pulsed power facility. The experiments created stellar conditions in the laboratory and measured the radiative opacities needed for a detailed understanding of stars that serve as extragalactic distance indicators. The experimental techniques and spectroscopic diagnostics developed in this project are also important for the SSP. They enable the capability for precision opacity experiments of interest to SSP to multi-megajoule DOE plasma generation facilities and for prototype diagnostics and techniques important for the National Ignition Facility (NIF). Techniques developed here are being extended to model LLNL production codes and supernovae simulations. (See page 10-6).

Report Organization

This annual report presents a one-page summary of each unclassified FY98 LDRD-funded project. The project summaries discuss the motivation, scope, and progress of all FY98 LDRD-funded projects, grouped according to the 10 competency areas shown in Fig. 3. Each of the projects is given a unique designation or a tracking code, which consists of three elements (e.g., 97-SI-004). The first element is the year the project began, the second is the LDRD component in which the project is funded (i.e., SI, ER, LW, or FS), and the third identifies the order in which the proposal was received. The report also includes a list of LDRD-funded publications, a principal investigators index, and an index of the projects according to their tracking codes.

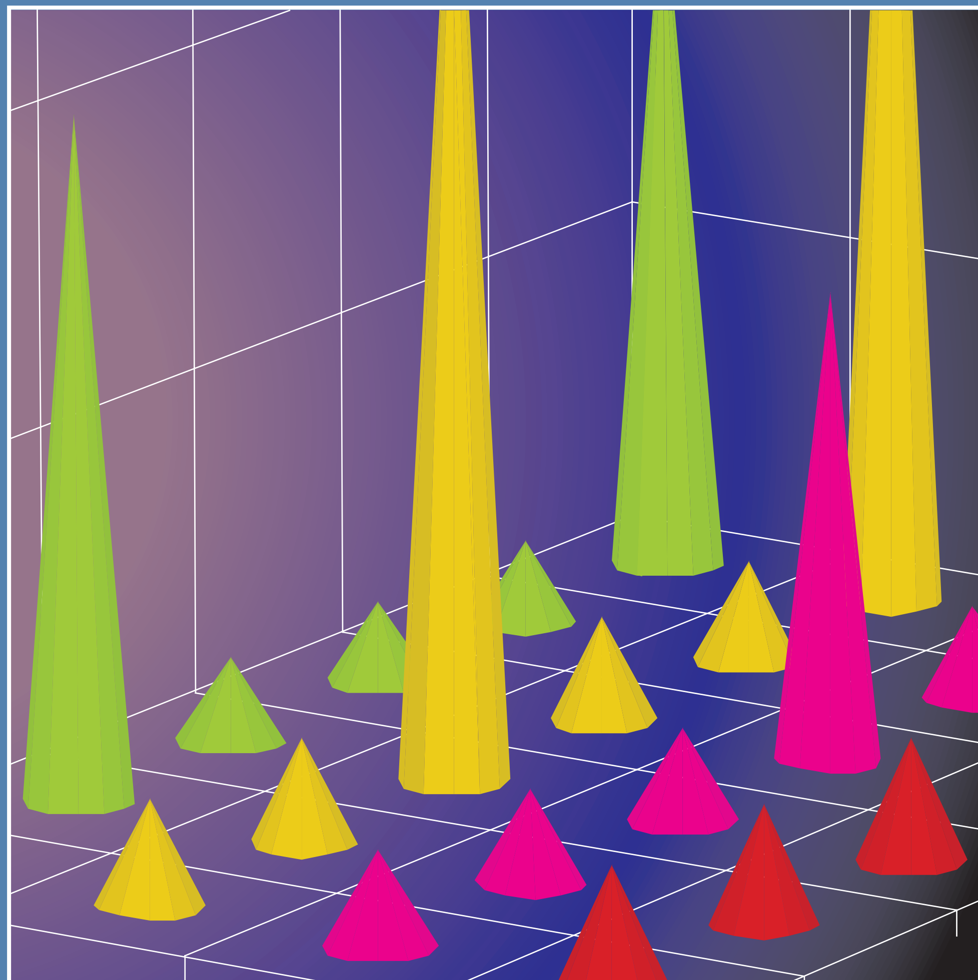

Advanced Sensors and Instrumentation

1

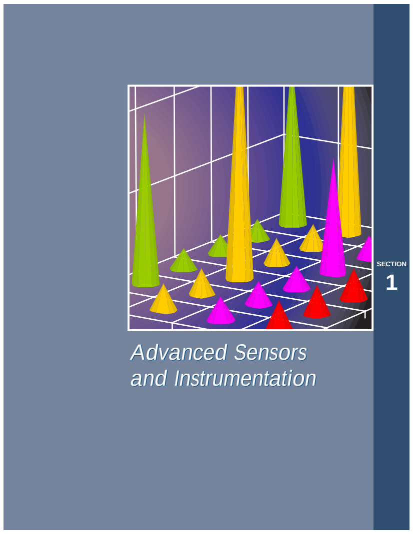

About the preceeding page

Biological Warfare: Detection, Identification, and Tracking Technology. An urgent need exists for the deployment of an effective means for the rapid detection and identification of suspected biological warfare (BW) agents. At LLNL, Fred Milanovich and his team have demonstrated technology that can significantly improve the state-of-the-art for point detection of BW agents by combining two unique inventions, a miniature flow cytometer and a miniature polymerase chain reaction instrument. This technology addresses emerging national priorities in BW counter-proliferation and has extensive applications in the defense, intelligence, and public health communities. This image displays results of experiments using flow cytometry and a multiplex-capable analysis system for identifying BW agents. Read further details about this LDRD project on the facing page.

Biological Warfare: Detection, Identification, and Tracking Technology

F. P. Milanovich, R. P. Mariella, Jr., R. Langlois, M. A. Northrup
96-DI-009

This project was conceived to address a gap in the nation's counterproliferation and counterterrorism preparedness by providing a means to rapidly detect and identify biological warfare (BW) pathogens (bacteria, viruses, and biological toxins). The basis for the work is provided by two unique LLNL technologies: miniaturized polymerase chain reaction (mPCR) and a miniature flow (mFlo) cytometer. The first, mPCR, is a biochemical technique that is very sensitive and eliminates the need for culturing cells or microorganisms. The mFlo cytometer is rugged, easy to align, and precise. Both basic approaches are well established as primary bench-top analytical techniques and already support many facets of the biotech industry. However, their use in point detection of BW pathogens had lagged their laboratory use because of several perceived performance shortfalls, namely, large size, slow response time, and fragility. Our initial goal was to mitigate most if not all of these shortfalls by (1) rapidly developing reliable, fast, and rugged versions of mPCR and mFlo, and (2) field testing them in nationally sanctioned demonstrations. These field tests were all conducted at Dugway Proving Ground in Utah; our mPCR and mFlo both gave outstanding performances. As a consequence, field versions of our mPCR are being built for U.S. Army and Navy medical response teams.

In FY98, we focused on the development of new biodetection concepts: (1) a new broad-spectrum detector suitable for use by nonexpert users (e.g., firemen, police, and medical emergency personnel), and (2) an instrument for detecting multiple BW agents in a single measurement (multiplex flow). For the former, we have designed and build a prototype instrument, and we are now engaged in patenting and technology-transfer activities. For the latter, our progress has been dramatic, and our instrument should overcome the last performance shortfall of the mFlo.

To permit the detection of multiple BW agents, we reduced all flow-cytometer assays to a bead-capture type—where antibodies bound to the bead capture a specific target, which can then be labeled by a second fluorescent antibody for detection by flow cytometry. From a commercial source, we obtained optically encoded beads (with varying ratios of two dyes of different color) with which we can distinguish up to 64 bead types in an arbitrary mixture. By adding the antibody assay (which incorporates a third color dye) to these beads, we established a three-color multiplex system that can theoretically identify up to 64 different BW agents.

The figure shows the results of a series of six experiments run against a four-plex assay system. This combination sample represents the first-ever demonstration of flow cytometry for the multiplex analysis of BW agents.

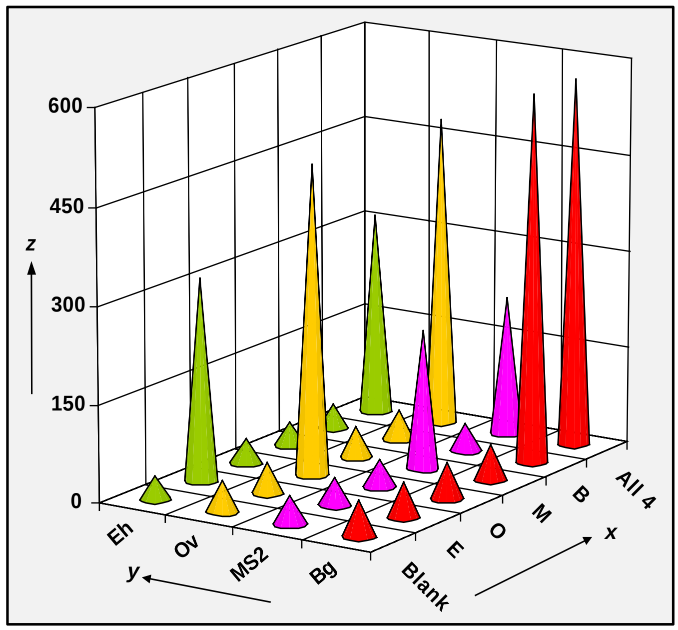

Results of a series of experiments utilizing flow cytometry and a multiplex-capable analysis system for identifying simulants of biological warfare (BW) agents. The *y*-axis displays the assay type, the *x*-axis a series of experiments, and the *z*-axis the concentration of target detected (in units of fluorescence intensity). The samples analyzed were, in order from the origin, first a blank, then a series of samples containing the following surrogates for BW agents: *E. herbicola* (E), *ovalbumin* (O), the virus *MS2* (M), *B. globigii* (B), and lastly, a sample containing all four surrogates.

Development of Chemically Amplified Optical Sensors for Defense and Biomedical Applications

S. M. Lane, T. A. Peyser, C. Darrow, J. Satcher
96-ERD-017

Chemically amplified optical or optochemical sensors represent a new measurement technology in which chemical recognition of target analytes results in a detectable change in some optical property of the sensor. Optochemical sensors may be used to perform local quantification of particular target chemicals in an extraordinary variety of applications, including medicine, biological and chemical research, agriculture, environmental monitoring, industry, transportation, and defense. We are developing sensors for two applications. The first, in concert with the DOE's Enhanced Surveillance Program (ESP), is for *in situ* monitoring of gaseous degradation products in aging nuclear weapons. The second is for use in biomedical applications such as measuring the level of therapeutic agents in the blood or monitoring physiologically interesting quantities in the blood or subcutaneous tissue.

Our research over the past three years was intended to develop a capability at the Laboratory for the efficient design, synthesis, and fabrication of optochemical sensors for a range of applications. In both the defense and biomedical applications, we have developed techniques for separately optimizing the transduction of the target analyte on the one hand and the optical response of the sensor on the other.

During FY98, we tested several new sensors relevant to the ESP application. Tapered optical fibers were chemically coated with sol-gel compounds synthesized at LLNL. These compounds incorporated chemosensitive fluorophores whose fluorescent properties are altered in the presence of the target gaseous species. Their extremely large surface areas allow maximum contact between the gaseous species of interest and the chemosensitive fluorophores.

Two classes of fluorophores were used. For one of the target gases, we employed a fluorescent resonant energy-transfer (FRET) scheme in which sensors utilize the chromophore pairs sulfrhodamine-bromocresol in a sol-gel matrix. In this scheme, two chromophores are used. The first, a fluorophore, is excited by light introduced into the proximal end of the fiber. The observable—the intensity of light emitted by the first fluorophore—depends on the extent to which the second chromophore overlaps spectrally with the first after having undergone an interaction with the analyte. Other sensors were developed using a single fluorescent molecule that directly senses the presence of the analyte. Sensors based on these two schemes were tested in LLNL's hazardous-gas facility. The use of optochemical sensors for the ESP is a subject of discussion and planning at the Laboratory.

Diabetes, a disorder in glucose metabolism, afflicts an estimated 16 million Americans and is a leading cause of death from disease. For the past two decades, numerous research groups in industry and academia have been attempting to develop noninvasive or minimally invasive blood-glucose sensors. During FY98, we developed and tested components for a simple, accurate, minimally invasive system for measuring glucose levels.

Our optochemical glucose sensor consists of two basic components: (1) a small (1-cm-square, ≤1-mm-thick) polymer disk, placed just under the skin for periods of up to a year, which contains fluorescent molecules that convert glucose concentration into an optical signal; and (2) an external instrument containing a light source that excites the fluorescent sensor and a detector that measures the fluorescence. In other words, once the sensor disk is in place, the glucose concentration could be measured by optical means.

First, we synthesized a molecule capable of transducing glucose in solution over the clinical range of interest (40 to 400 mg/dL). Subsequently, we successfully demonstrated that the molecule could be immobilized in a biocompatible polymer while retaining the desired chemical and optical activity. We also (1) explored a number of variations on the original successful recognition molecule in which the excitation and emission wavelength of fluorophore were increased to improve the efficiency of light transmission through tissue, (2) developed and tested a reference compound for calibrating the transduced signal, (3) designed optical-readout instruments to detect the transduced glucose and reference signals, and (4) optimized biocompatible polymers for packaging the implanted sensor.

In October 1998, MiniMed, Inc. and LLNL announced a Cooperative Research and Development Agreement (CRADA) to continue work on optochemical sensors for continuous glucose monitoring. If successfully developed and later commercialized, the new system will permit continuous measurement of glucose levels in the tissue, thereby improving the treatment and management of diabetes as well as reducing the risk of long-term complications of the disease for those afflicted.

Sensitive Detection of Atomic-Scale Defects with Microscopic Spatial Resolution

R. H. Howell, W. Stoeffl, P. Asoka-Kumar, K. Lynn, J. Jean* †
96-ERD-034

There is a national need, identified by DOE programs, the semiconductor and polymer industries, and the materials-science and positron-research communities, to understand the effects of atomic-scale defects resulting from fatigue, processing, irradiation, or other causes. This understanding requires knowing both the defect identity and concentration variations over small distances for many kinds of samples including thin films, small crystals, buried interfaces, and the near-surface regions of many materials. Such knowledge is required for self-irradiation damage in Pu, electromigration in electronic interconnects, polymer properties related to hole volume, and validation of calculations in quantum-mechanical and microscopic materials models. Positron-lifetime spectroscopy is a unique, nondestructive tool for the detection of atomic-scale defects.

We have been investigating the feasibility of extending positron annihilation lifetime spectroscopy to provide three-dimensional (3D) spatial distributions of defects. The positron's lifetime after stopping in a sample is set by the electron density near the positron, and positrons stop preferentially in open-volume or negatively charged defects. This results in distinctive lifetimes that should permit a highly sensitive, defect-specific spectroscopy over a volume that contains positron implants. Our intent was to perform our research at the most intense positron beam in existence—LLNL's 100-MeV linear accelerator (linac)—where we could evaluate the feasibility of producing an intense, variable-energy (1 to 50 keV), pulsed (less than 100 ps), submicrometer-size positron beam that would enable unique experiments not feasible elsewhere. In our research, we planned to obtain high data rates from microscopic implantation volumes while detecting and identifying the depth-dependent concentration of vacancies, voids, gas-filled voids, and other negatively charged defects to a depth of a few micrometers and at depth and lateral resolutions as low as 0.1 µm.

During FY98, we designed and began assembling and testing a prototype charged-particle optics system that integrates proven concepts of pulsing and focusing with new capabilities enabled by the linac's high current. This system—which combines basic pulse-compression techniques with successive stages of positron thermalization and focusing—was designed to develop a high-efficiency, high-brightness, microscopic pulsed beam. We also procured the pulsing and focusing optics required to complete the pulse compression and to focus the beam on a final brightness-enhancement moderator for input to the microprobe's acceleration column.

By the close of FY98, we had (1) converted the wide initial energy spread and short time duration of the primary positron beam to a narrow energy spread and long pulse duration by trapping the positron pulses in a Penning trap and then slowly raising the trap voltage to spill positrons over a fixed voltage barrier; (2) demonstrated a significantly reduced energy distribution at the first pulsing electrodes and used a programmed pulsing shape generated by a fast-waveform generator to obtain high-efficiency, nanosecond pulses in a single stage; and then (3) accelerated and extracted the pulsed beam from the magnetic field of the Penning trap and focused it at the first brightness-enhancement moderator.

Our work demonstrates that solutions to the major problems of producing a highly focused, pulsed positron beam exist, and prototype devices have produced good results. When combined into a fully engineered instrument, varying the energy and position of the positron beam at the focus of the microprobe accelerator column will enable evaluating the application of positron annihilation lifetime spectroscopy to (1) the 3D distribution of spatial defects in near-microscopic features such as grain boundaries, cracks, and precipitates; and (2) buried interfaces in metals and alloys, semiconductor devices, and thin-film and composite polymeric materials.

* Washington State University
† University of Missouri

Solid-State Fireset

G. W. Johnson, T. W. Barbee, Jr., A. V. Wagner
96-ERD-083

Firesets are now based on two major components, an energy-storage capacitor and a vacuum-breakdown switch, which supply energy to explode a detonator. However, firesets fabricated with existing components are too expensive, too heavy, and too bulky, particularly the capacitor and switch structures.

Our objective was to develop a compact, integrated, solid-state slapper fireset system that will significantly advance the design of conventional weapons.

The core technology in our project is nanostructure multilayer synthesis. Multilayer dielectrics and metals offer improved performance and new capabilities when used to fabricate fireset components. First, the synthesis processes applied are generic in that a wide range of materials may be deposited as thin films. Second, these structures are thermally and mechanically robust. Third, there are manufacturing advantages inherent in thin-film processing; that is, multilayer structures can be designed and fabricated to near net form, with resulting low cost and high production rates.

In FY98, we demonstrated two major components in a solid-state fireset system: a solid-state, high-voltage capacitor and a solid-dielectric breakdown switch and trigger circuitry.

For capacitor dielectrics, we use our proprietary reactive sputtering techniques to intermix materials; thereby, we increase the dielectric constant while controlling second-order effects. For example, layering at the nanometer scale reduces leakage current, inhibits interfacial reactions between the metal contacts and the dielectric, and permits some degree of control over crystallographic structure. Our dielectrics are amorphous metal oxides, and their interfaces are atomically smooth.

The process yield in thin dielectrics is determined primarily by the presence of microparticulate contamination, which we control with novel processing techniques. We have demonstrated capacitor yields of 90% at breakdown strengths of 7 MV/cm over 2 cm^2 in alumina. This level of performance means that our capacitors can in fact be manufactured; commercialization efforts are under way.

In addition to energy density, capacitor designs must also address electrical parameters such as effective series resistance (ESR) and inductance (ESL). Pulse-discharge testing on our 2-cm^2, 30-nF capacitors with 2.5-µm alumina/zirconia dielectrics and 4-µm-thick copper-based conductors showed an ESL of 4 nH and an ESR of 120 mΩ. When packaged for testing, our capacitor is 2 cm square and 1.03 mm thick—including the 1-mm substrate.

Switch performance was excellent. The switch, which is based on the same materials as the capacitors, adds a floating trigger electrode embedded in the dielectric. We applied a high-voltage pulse from a transformer to the trigger to quickly distort the electric field, thereby inducing breakdown. Switches operated reliably at applied voltages from 500 V to 2.8 kV, and damped ringdown waveforms were found to meet or exceed those of a commercial vacuum spark gap, as shown in the figure. At 2.8 kV, a peak current of 9.6 kA was achieved with a 168-A/ns rate of rise. These switches show promise for use in miniaturized firesets and other pulsed-power systems where a single-use switch is appropriate. Combining these components into an integrated unit is feasible and offers new options in meeting long-term programmatic goals.

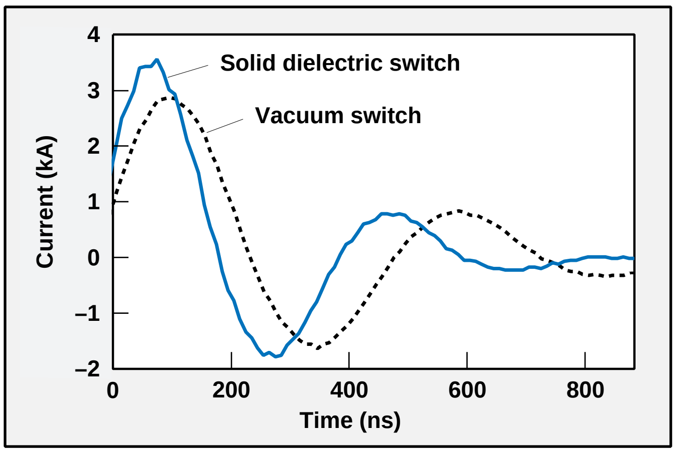

A damped ringdown waveform (transient-current-discharge test) for our solid-dielectric switch is compared with that for a commercial vacuum spark gap. Both were operated at 0.317 µF and 1000 V. Our compact switch works at least as well as the much larger vacuum gap.

Mini-Multichannel, AM/FM, Diode-Laser Absorption Spectrometer

A. J. Ruggiero, M. W. Bowers, R. A. Young
97-ERD-006

We have developed an extremely compact, optical, remote-sensing system for short-range detection of effluents associated with weapons of mass destruction. The sensor system leverages recent advances in photonics and modulation-based detection technologies to make multiple-wavelength, differential-absorption-lidar (DIAL) measurements with low-power diode lasers.

Tunable-diode-laser absorption spectrometers have been used extensively in recent years for monitoring and detecting trace gases. These systems work by changing the frequency or amplitude of the transmitted laser beam in a periodic fashion and then monitoring the changes to this modulation pattern by the target-gas absorption. These changes, which form a chemical's "signature," are impressed on the modulated laser beam and detected at the receiver. Modulation techniques allow high-resolution spectral measurements without requiring a monochrometer or spectral filter. The optical information is down-converted to the radio-frequency (RF) regime, where it can be discriminated from the optical background, detector noise, and system drifts.

Implementing modulation-based detection techniques in DIAL applications requires careful attention to several details. Data at multiple wavelengths—collected within the same atmospheric correlation time—are required to accurately extract most chemical signatures. Broad absorption features at atmospheric pressures also place additional constraints on the modulation frequencies and modulation formats. Last, for systems employing topographical backscatter (laser light scattered from the ground surrounding the target), laser speckle (an interference effect resulting from the coherent nature of the laser light itself) becomes the dominant noise source. Speckle dramatically reduces the signal-to-noise ratio and measurement speed advantages typically obtained with laboratory-based instruments. Extensive signal averaging is then necessary to obtain high-quality data and to overcome carrier losses associated with the geometry of the backscatter.

Our system addresses these issues by exploiting the parallelism made possible by modern diode-laser packaging techniques. The end result is a modulation-based detection system that can support multiple data channels. Simultaneous, multiwavelength, diode-laser modulation spectroscopies offer the sensitivity advantage of a single-channel, tunable laser spectrometer with substantially higher data-acquisition rates and hence more averaging capability. In our system, an independently addressed multiwavelength diode-laser array generates a high-resolution spectroscopic probe field.

By modulating the individual array elements at different RF frequencies, we can configure the system to simultaneously detect multiple absorption lines. We can implement either multichannel versions of a conventional FM spectrometer or a more sensitive, zero-background AM-absorption spectroscopy that we have developed and tailored for this application.

During FY98, we demonstrated the outdoors operation of a prototype, multichannel, AM, DIAL transceiver system (see Fig. 1) using backscatter from building walls at ranges on the order of 100 m. Commercial diode lasers developed for telecommunications were used in the transmitter to acquire near-infrared overtone spectra of both deuterated water and hydrogen iodide vapors. We obtained a quantitative evaluation of the system's performance by first sending the transmitter beam through a calibrated gas cell that contained the effluents at known concentrations and then propagating it to the target. The backscattered returns containing both the impressed absorptions as well as speckle and atmospheric distortions were then collected by the receiver telescope and demodulated to provide the DIAL data. Detection levels approaching 0.4% with signal-to-noise ratios on the order of 4:1 were achieved with only 10 to 20 mW of transmitted optical power and 1-min integration times. We also conducted experiments to characterize the system linearity, averaging capabilities, and range scaling with transmitted power. The results confirmed the performance expectations for our system.

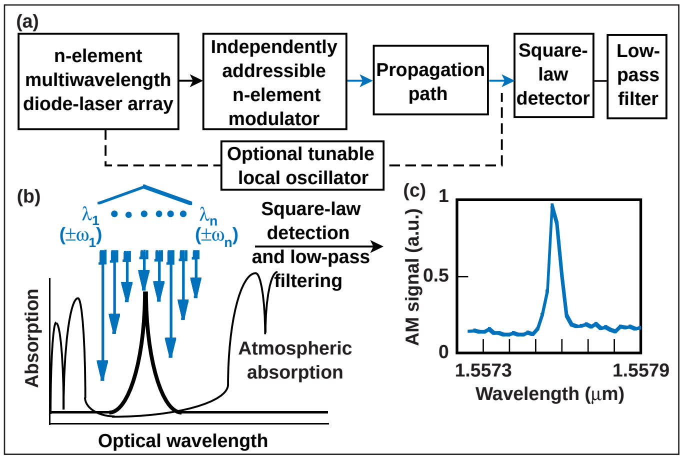

Figure 1. AM differential-absorption-detection (DIAL) experiment: (a) experimental setup, (b) technical approach (using selected DIAL wavelengths from a diode laser array with modulation side-bands), and (c) detached hydrogen iodide overtone spectrum.

Innovative Uses for Conventional Radiation Detectors via Pulse-Shape Analysis

J. Kammeraad, D. Beckedahl, J. Blair, G. Schmid
97-ERD-017

Radiation detectors have many applications in national security programs, including the detection and quantification of nuclear materials of both known and unknown origin. In particular, high-purity germanium (HPGe) detectors have become the international standard for the assay and accountability of nuclear materials. However, prior work in the development of gamma-ray imaging technologies using HPGe has been limited by the very high cost of building large detector arrays or the low detection efficiency associated with smaller, more affordable detector arrays. Our goal in this work is to provide the technical basis for a high-efficiency, low-cost gamma-ray imaging technology with the excellent qualities of HPGe.

Our imaging concept utilizes a HPGe detector with its outer electrode divided into a number (say 36) of electrically isolated segments. When a gamma ray interacts in a segmented HPGe detector, a pulse is generated on each of its segments simultaneously. The pulse shape from each segment depends very precisely in three dimensions (e.g., r, θ, z) upon the location of the interaction relative to the segment. Most gamma rays interact at several locations in the detector, generating a signal on each segment that is the sum of the signals generated for each interaction. A simple example with two interactions is given in the figure. For every interacting gamma ray, all 36 signals are digitally recorded and analyzed by a special algorithm that determines the locations of the gamma-ray interactions very accurately. This information, plus the physics of the Compton interaction, allows us to determine the direction from which the gamma ray most likely came. With just one detected gamma ray, this determination is rather rough. But as the number of detected gamma rays increases, one can obtain a better and better determination of the location of the radioactive source, and in some cases, one can even obtain an image of the source.

We predicted the performance of a segmented HPGe detector as a gamma-ray imager. The performance depends critically upon the accuracy with which one can determine the gamma-ray interaction locations. Using a very realistic pulse-shape model, we determined the location accuracy for 186-keV gamma rays, the most important signature of ^{235}U. For example, if the 186-keV gamma ray interacts twice in the detector, depositing 30 keV at one location and 156 keV at another location 1 cm away, we found that the interactions can be localized to a very small volume of the detector (<0.05 mm^3). This remarkable result implies that this segmented detector concept should have the imaging performance equivalent to a detector array containing more than a million very small, closely packed detectors. In other words, it is indeed possible to build a gamma-ray imager with the excellent energy resolution of germanium and with the high detection efficiency and moderate cost of a large, single detector. A gamma-ray imager based upon this technology holds significant promise for greatly improving the ability to detect weak radioactive sources.

Future research in this project will provide laboratory confirmation of the accuracy with which the interactions can be located in the detector. In addition we are studying the ability of the detector to quickly “localize” a hidden source, rather than obtain a detailed image of it. This usage requires optimum sensitivity to detect a source with confidence in the midst of local backgrounds.

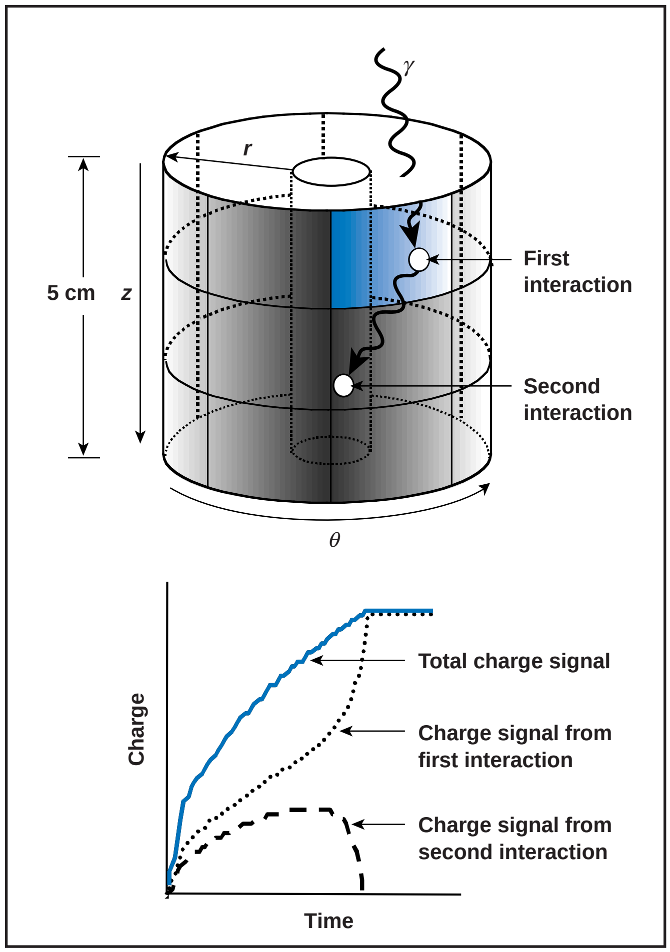

Schematic diagram of a cylindrical segmented HPGe detector. The signal generated in one of its segments is shown for the case where the gamma ray interacts first in the detector volume under the segment, then in the neighboring detector volume.

Eyeglass: A Large-Aperture Space Telescope

R. A. Hyde, S. N. Dixit, I. M. Barton
97-ERD-060

Large-aperture (25-50 m) space telescopes are important both to permit high-resolution Earth viewing from geosynchronous orbit and to extend astronomical observations to greater ranges and of dimmer objects. The Eyeglass is a novel form of large-aperture space telescope, utilizing a diffractive lens as its primary optical element. This diffractive lens, fabricated on a thin membrane, provides a lightweight, easily deployable method of fielding a very large aperture telescope, while virtually eliminating the stringent surface figure requirements faced by reflective telescopes.

Current optical quality Fresnel lenses are centimeters across, not the tens-of-meters sizes needed for Eyeglass. There are two basic reasons for believing that such a huge scale-up is possible. First, on a local scale, creating the necessary diffractive surface profile is quite doable, with size-scales of ~100 µm. Second, the lens does not have to be built as a monolithic unit, but can be seamed together from smaller, more manageable sections.

While last year's LDRD effort concentrated upon the design of Eyeglass telescopes, the primary emphasis this year was upon fabrication. We identified two different fabrication techniques that appear scaleable to the sizes needed for Eyeglass, replication and direct-write. In the replication method, one first creates the diffractive profile on the surface of a "master," then replicates it onto a thin polymer film. In the direct-write approach, one uses a process, such as laser ablation, to directly write the surface profile onto a blank polymer film. During the half-year of this LDRD project, we began to develop both fabrication methods.

Most of our effort was directed towards replication: to build high-precision, 4-in. aperture, *f*/100 Fresnel lenses. This fabrication was carried out in a two-step process, first making chrome masks, then using them with wet-etching to create two-level, phase-plate lenses in fused silica. These lenses have been optically tested, and produce well-focused image spots. We believe that this lithographic procedure, using existing LLNL tooling, can be readily extended to the production of meter-scale fused-silica Fresnel lenses, and we expect to build a 50-cm, multi-level lens in this fashion during FY99.

With the production of meter-scale masters relatively in-hand, we concentrated much of our effort into their replication onto polymer films. Here the challenges are first forming a thin, uniform (but conformal) film, then safely releasing it. Since release is particularly challenging as size is increased, we have concentrated upon an ultraviolet- (UV-) curable process involving photopolymer films. We successfully replicated 4-in. Fresnel lenses from their fused-silica masters onto thin polymer films. These replicated copies accurately match both the surface profile and optical performance of the original masters. The UV-cured process is expected to scale up to the desired meter-sizes, and we will attempt to do so at 50 cm in FY99.

We began direct-write process-development by using an XeCl excimer laser to write a series of parallel grooves on a polyimide film, and we demonstrated that we could form features with the proper size and shape. Scale-up of laser ablation to meter sizes appears feasible, and will involve marriage of diffractive-optics print-heads (capable of writing many grooves simultaneously) with high-quality motion-stages.

In addition to examining fabrication methods, we also investigated a number of material candidates. The prime candidate for unshielded Eyeglass applications remains the low-CTE (coefficient of thermal expansion), "colorless" polyimides. We have made thin films of several polyimides, and have measured their transmissivity from the infrared (IR) down to the UV. We have also characterized polymers (such as parylene), which are both easier to form and optically superior to the polyimides. These are attractive candidates for applications where solar shielding is feasible.

In a second phase of this LDRD project, we have examined large astronomical Eyeglass telescopes. In many ways, this is a less demanding application than Earth observation, requiring less maneuverability and allowing a shielded and higher *f*-number magnifying glass. Optically, however, the typical Eyeglass restriction to isolated spectral windows is not attractive for general-purpose astronomy. We have accordingly designed conceptual prototype Eyeglass telescopes permitting fully continuous diffraction-limited viewing from the mid-IR down to the visible. In the future, we will investigate other laser light applications of Eyeglass technology; these include optical communications, power beaming, and weapons.

A Low-Noise Semiconductor Optical Amplifier

R. P. Ratowsky, S. Dijaili, J. S. Kallman, M. D. Feit, J. Walker
97-LW-014

Optical amplifiers are essential devices for optical networks, optical systems, and computer communications. These amplifiers compensate for the inevitable optical loss in long-distance propagation (>50 km) or splitting (>10×). Fiber amplifiers such as the erbium-doped fiber amplifier have revolutionized the fiber-optics industry and are enjoying widespread use. Semiconductor optical amplifiers (SOAs) are an alternative technology that complements the fiber amplifiers in cost and performance.

One obstacle to the widespread use of SOAs is the severity of the inevitable noise output resulting from amplified spontaneous emission (ASE). Spectral filtering is often used to reduce ASE noise, but this constrains the source spectrally, and improvement is typically limited to about 10 dB. The extra components also add cost and complexity to the final assembly. The goal of this project was to analyze, design, and take significant steps toward the realization of an innovative, low-noise SOA based on the concept of "distributed spatial filtering" (DSF).

In DSF, we alternate active SOA segments with passive free-space diffraction regions. Since spontaneous emission radiates equally in all directions, the free-space region lengthens the amplifier for a given length of gain region, narrowing the solid angle into which the spontaneous emission is amplified. Our innovation is to use spatial filtering in a differential manner across many segments, thereby enhancing the effect when wave-optical effects are included. The structure quickly and effectively strips the ASE into the higher-order modes, quenching the ASE gain relative to the signal.

In FY98, we made further progress on computational modeling, design, and ultimate fabrication of the low-noise SOA. We further enhanced BEEMER, our fast-Fourier-transform, beam-propagation-method code, which includes distributed spontaneous emission and gain saturation. BEEMER calculates ASE power by averaging the output over ensembles of randomly phased sources. The most significant result of our modeling was a definitive calculation that confirmed the fundamental concept for the low-noise SOA: ASE gain is not equal to signal gain. This is illustrated in the figure, where the ASE and signal power are plotted against the number of SOA/free-space stages in a device; the slope of the curves is the gain. The signal power increases exponentially, but the ASE power grows more slowly. Because the multimode nature of the device (essential for DSF) is suppressed, the effect disappears for larger gain. We also obtained an optimized design for a 1-mm DSF SOA device and showed that the signal-to-noise ratio peaks as the duty cycle of the gain region (the ratio of gain region to free-space region) is varied.

In our experiments, we progressed toward the monolithic integration of passive structures that is necessary for fabricating the DSF SOA structure. We found that $SiO_2/Ta_2O/SiO_2$ waveguides fabricated using magnetron sputtering had low propagation loss but high interface loss. We tried using an ion-beam sputtering technique, but then we were unable to achieve low propagation loss.

Because of reduced funding and loss of key personnel, we were unable to experimentally demonstrate the DSF SOA in FY98. However, because the technology has shown sufficient promise, development is continuing in FY99 with outside follow-on funding.

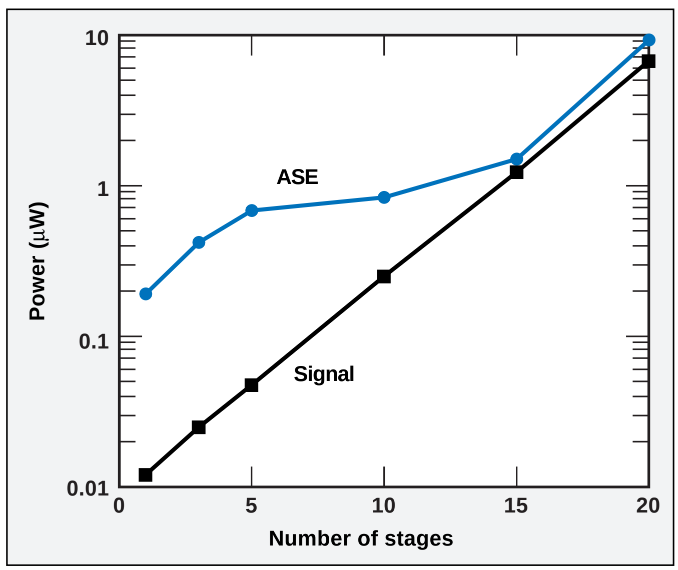

Amplified spontaneous emission (ASE) and signal power vs. number of stages in the distributed spatial filtering semiconductor optical amplifier (DSF SOA). The slope of the ASE curve is smaller in the middle of the plot, showing that ASE gain is smaller than signal gain. This SOA alternates 50-µm gain and free-space segments; the material gain is 100/cm.

LANDMARC: Radar-Based Mine Detection

S. G. Azevedo, J. M. Brase, E. T. Rosenbury, J. E. Mast

97-SI-013

Undetected antipersonnel (AP) land mines from past wars are a serious military and humanitarian problem. However, the removal of these mines is hampered by our inability to detect them rapidly and reliably—better detection strategies are clearly needed.

The micropower impulse radar (MIR) technology developed at LLNL has the most potential for finding the small AP mines that represent the biggest threat to the world's populations. The ultra-wideband nature of the MIR transmission (besides its small size, low cost, and low power) makes it ideal for ground penetration (the low frequencies) and imaging resolution (the high frequencies). Diffraction tomographic imaging from synthetic-aperture or real arrays provides the enhancement needed to reduce clutter in the radar images.

The objectives of our LANDMARC project are to (1) customize LLNL's MIR technology for the land-mine-detection problem, (2) develop models of the radar and clutter signatures, (3) incorporate those models into algorithms for optimal processing, (4) perform experiments to validate the theoretical models, and (5) identify potential collaborators and users of a radar-based mine-detection system. In FY98, we made significant progress towards meeting these goals.

A critical issue is a clear understanding of all signal, noise, and clutter sources in the data. We define noise as any contributor to the radar measurement that degrades our capability to detect the target of interest. During FY98, we modeled the electromagnetic interactions of soil, mine, and environmental factors and used the model to further characterize detection capabilities and to influence radar design. Imaging the subsurface at optimal radar frequencies reduces the effect of clutter because the operator cannot discriminate between a mine and a rock merely on the basis of their shapes.

We found—through tests and simulations—that if the target object (the mine) is smaller than one quarter of the highest wavelength, reconstructive imaging provides little improvement in detection. One of the key results of the modeling effort is that the radar bandwidth necessary for mine detection of near-surface AP mines was found to be 0.5 to 10 GHz; this is higher than that of the current MIR (1 to 4 GHz). Further refinements in the radar antennae and electronics have produced mine-detection capabilities that are beyond the known state of radar technology. Also, refinements to the algorithms—particularly for removal of the first-surface clutter source—have provided step-by-step improvement in the signal-to-clutter ratio. Extending the MIR bandwidth is the subject of on-going effort at LLNL.

During FY98, the prototype system and a Schiebel PSS-12 metal detector (commonly used in most areas of the world) were used in 18 blind, independent tests. The tests employed American-made M14 mines and intentional clutter in three soil types and in generally wet weather. The MIR prototype system demonstrated twice the detection rate (85% vs. 44%) and half the false-alarm rate of the Schiebel PSS-12 metal detector.

Through the scientific methodology thus far followed, we have (1) shown that MIR technology can directly improve the two key performance parameters of AP mine-clearance efforts: reliability and speed of clearance; (2) contributed to the technology of radar-based detection of AP mines; and (3) shown that a first-ever, fully three-dimensional, real-time imaging system is capable of revealing volumes beneath the Earth's surface. Fast algorithms and advances in computer technology will allow the data to be analyzed rapidly enough for humanitarian scenarios. Continued work in this field will likely lead to a fieldable system—see Fig. 1(b)—that can help clear land and save lives.

In the coming year, we plan to continue development in the five areas mentioned above. Extensive systems and field-testing will be required.

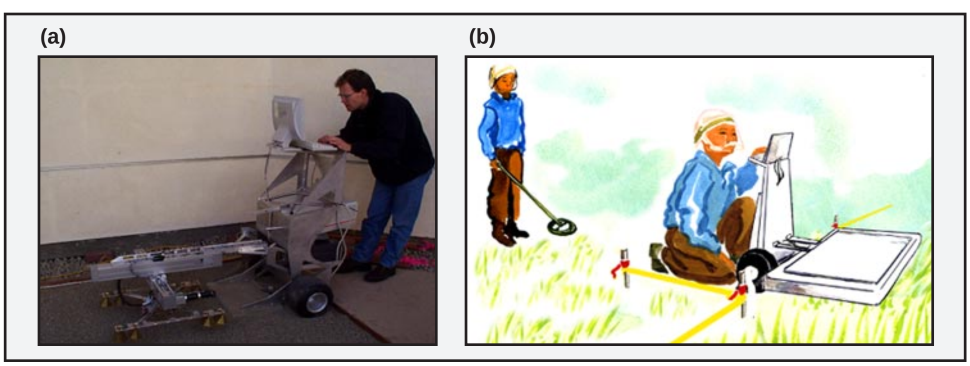

Figure 1. Proposed micropower impulse radar (MIR) mine-detection system: (a) engineering-prototype system for developmental testing, and (b) operational scenario.

Wireless Microsensor Modules for Distributed Network Sensing

A. P. Lee, C. F. McConaghy, J. N. Simon
98-ERD-017

The goal of this work is to develop a prototype sensor for use in low-power wireless sensor networks. The advantages of a network of sensors over a single sensor are improved range, sensitivity, directionality, and data readability. For easy deployment, these sensors and supporting electronics should be small in size and low in power requirements and cost. In addition, these networks must operate with small batteries and operate continuously over long lifetimes. However, because of these constraints, many sensors such as fiber-optic devices that require laser power or sensor technologies that require heaters are precluded from use in these networks.

The focus of our work has been on microelectromechanical systems (MEMS) sensors that use capacitive readout electronics. Capacitive sensing has the advantages of low power, high sensitivity, and wide operational temperature ranges. When a proof mass (the inertial mass that responds to inertial forces such as acceleration) is accelerated, it moves in relation to its surroundings (or package), and the amount of movement is sensed with variable capacitors attached to the proof mass. The effect used to sense acceleration is similar to the crushing feeling felt when one rapidly ascends in an elevator. Because the sensitivity of accelerometers to low accelerations is inversely proportional to the size of the mass, we need a relatively large mass to sense μg accelerations (previous work in the literature used small proof masses fabricated at the surface of the wafer). Our prototype design (see the figure) consists of a thin (2 μm) surface-micromachined polysilicon tether that supports a large proof mass carved out of a bulk silicon wafer by deep reactive-ion etching (RIE). Deep RIE makes these structures possible because it allows for through-wafer etching with aspect ratios greater than 40:1.

As an acceleration is applied, the proof mass tilts around the torsional suspension (the "tether" in the figure), which magnifies the movement of the mass, resulting in changes in the gaps in the sensing capacitor (the space between the fixed and moving electrodes). The basic sensor requires no power; however, low-power electronics are used to measure the variable capacitors and thus convert the acceleration to an electrical signal. Additional electronics are integrated in the same package for signal conditioning, analog-to-digital conversion, and wireless data transmission.

Packaging of MEMS dies requires special considerations because of the small moving parts found on the die, which make traditional packaging and encapsulation technologies unfeasible. To facilitate the integration of the MEMS sensor with other electronics, we developed a flip-chip, multichip-module process for packaging in which the individual chips are flipped over and bonded to a carrier, rather than being interconnected using wire bonds—our process allows for chip-scale packaging of chips from different processes. In addition, MEMS sensors may require contact with a sensing medium, again requiring special packaging considerations.

The entire package for the sensor, wireless electronics, and batteries is designed to fit in a cube 2 in. on a side.

In FY99, we will (1) generate a platform for integrating the multiple chips and wireless components; (2) integrate the micromachined accelerometer with sensing electronics and wireless communication boards; (3) develop multiple and multifunctional sensors on a chip that will cover wide dynamic ranges; and (4) redesign the system to achieve a 1.5-in. by 1.5-in. module.

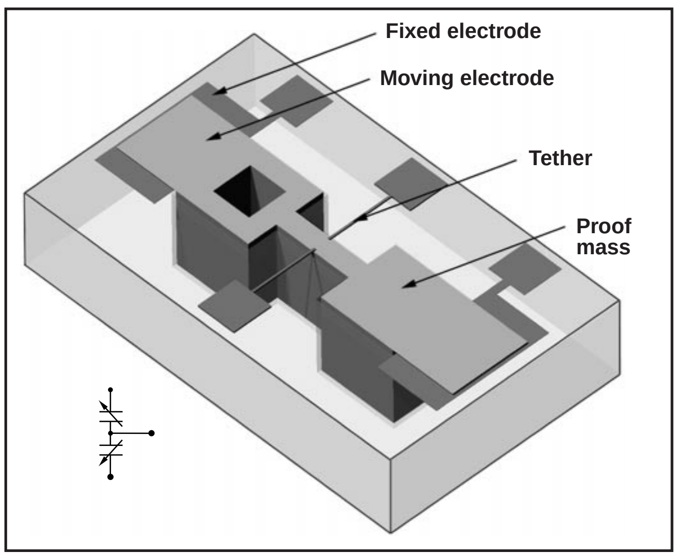

Combined surface- and bulk-micromachined accelerometer with capacitive sensing suitable for use in a distributed network. The combination enables high sensitivity without sacrificing die space. The position sensing is achieved by a differential capacitance scheme that is illustrated in the lower left corner.

FemtoScope: Enabling Femtosecond Diagnostics for Weapons Physics Ignition Experiments

M. E. Lowry, H. W. H. Lee, C. V. Bennett, J. D. Cooke, J. S. Sullivan, B. H. Kolner
98-ERD-027

Many national security missions of interest to LLNL, stockpile stewardship in particular, will require advancement in high-speed signal recording and analysis. For instance, if one performs a simple spatial scaling from the geometries of weapons physics experiments carried out at the Nevada Test Site (NTS) to the geometries of capsules used at the National Ignition Facility (NIF), one could conclude that the latter would require measurement bandwidths in excess of 1 THz. Thus, it is the objective of this work to address this perceived requirement in instrumentation bandwidth scaling by investigating technologies that will lead to a single-transient data recorder—a FemtoScope—with temporal resolutions in the 100-fs to 1-ps range and dynamic ranges greater than 100.

To reduce development risk, we are following two overlapping technology-development tracks. In one approach, we are investigating a novel, all-optical gating technology that will enable the development of high-fidelity, single-transient samplers. Here, all-optical switching gates switch out sequential, short-time slices of the single-transient signal. Multiple low-bandwidth detectors then record the switched time slices in parallel—thereby sampling the optical signal. In the second approach, we are developing a high-performance temporal microscope that expands the time scale of the optical signal beam. This temporal magnification of the signal allows the use of slower samplers. In FY98, we made significant progress in both approaches.

On the optical gating track, we advanced the fullerene waveguide fabrication process significantly, the result being linear losses of about 22 dB/mm at 830 nm. With further improvements in waveguide processing and concomitant loss, we showed that the technology would be suitable for some sampling applications. Second, by successfully demonstrating femtosecond (<60 fs) all-optical switching using cross-phase modulation (XPM) in fullerene thin films and semiconductor quantum dots (QDs), we have shown that optical gating is suitable for 100-fs sampling. Third, the wavelength separation of our XMP experiments—with the signal at 850 nm and the switching beam at 800 nm—is key to a practical sampling device: cross-talk between the signal and switching beams can then be minimized with spectral filtering. Finally, we investigated various gate designs for the optical sampler. One promising design uses nonlinear directional couplers as the gate—this will enable long record lengths and short temporal resolution.

Temporal imaging is based on an analogy that exists between how beams of light spread as they propagate in space because of diffraction and how pulses of light spread as they propagate in a dispersive medium. A “time lens” can be created by any process that imparts either a temporally quadratic phase or (equivalently) a linear frequency chirp to the input waveform. To achieve the required pulse chirp on the signal beam, we have chosen to mix a chirped pump beam with the signal beam using sum-frequency generation in a nonlinear crystal.

In FY98, we developed a successful model of the temporal-imaging system that included various sources of dominant aberration (higher than second-order dispersion). By studying how these aberrations affected the system fidelity (see figure), we were able to identify and classify the sources of the aberrations. We then used this model to design and construct a prototype temporal-imaging system with magnification of +100, a 100-fs resolution, and a 5-ps field of view. Our system uses diffraction-grating dispersive-delay lines for the input and output dispersion as well as to create a chirped pump pulse from the transform-limited output of a Kerr lens mode-locked Ti:Sapphire laser. The chirped pump is imparted to the input signal through noncollinear sum-frequency generation in a 500-mm-thick beta-barium borate (BBO) crystal. Exciting and very promising experimental results are just now emerging.

In FY99, we will (1) demonstrate a time lens with a 100× magnification and measure its aberrations, and (2) model the design of the all-optical sampler and carry out experimental demonstrations of the all-optical gate.

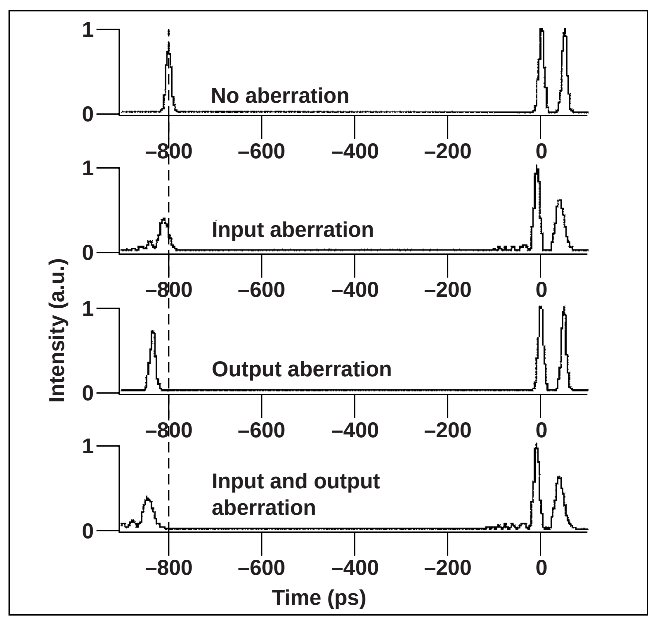

Temporal images with dispersive aberrations calculated with our model. The input waveform is shown at the top, and the temporal images that result from various sources of aberrations are shown below. Aberrations at the input distort the pulse shape; aberrations at the output distort the arrival time. The bottom set of graphs shows the results of various aberrations. By clearly predicting the consequences of these aberrations, we can use this as a design tool to minimize the aberrations.

Qualification of Computer-Based Components for Safety-Critical Applications

J. D. Lawrence, G. L. Johnson, W. L. Persons, G. G. Preckshot
98-ERD-032

The developers of safety-critical instrumentation and control (I&C) systems must qualify the design of the components used in these systems. Examples of safety-critical I&C systems include nuclear power plant protection systems, hazardous area monitoring, and medical devices. For computer-based components, this must include design qualification of the embedded software, which confirms that a component can be trusted to perform its safety functions under the full range of operating conditions. Design qualification is legally required for safety-critical equipment used in many applications.

Design qualification of computer-based systems is currently based upon developing confidence in equipment by gaining confidence in the developer's design, verification, and validation activities. This approach has several undesirable characteristics: (1) it does not directly measure the safety of the product, but draws an inference about safety from observation of the development process; (2) it requires labor intensive inspections of development processes and records; and (3) it often cannot be applied to existing systems because development process records are unavailable.

We are exploring an alternative approach that allows qualification by test for an important subset of I&C components used in safety-critical applications. The goal is to determine if a combination of static analysis and limited testing can be used to qualify this class of computer-based I&C components for safety application. This goal is accomplished by identifying design constraints that enable meaningful analysis and testing. Once such design constraints are identified, digital systems can be designed to allow for testing, or existing systems may be tested for conformance to the design constraints as a first step in a qualification process. This will significantly reduce the cost and monetary risk involved in qualifying commercial components for safety-critical service. The effect will be more rapid introduction of new technology into safety service, thus reducing costs and increasing safety margins.

Mathematical reasoning about computer programs and computer program testing can be done by transforming the program into an abstract structure that preserves aspects essential to the mathematical argument; this procedure eliminates aspects of the program that are irrelevant to the argument. The abstraction used for this project is widely used in computer science—the *flowgraph*.

A flowgraph is a form of directed graph, where the nodes of the graph represent statements in the program and edges in the graph represent possible transfers of control. Paths in the flowgraph can be defined that represent potential paths in the program. Note that there may be an infinite number of such paths if there are loops within the flowgraph. These paths permit the flowgraph to be transformed into a tree structure—the *flowgraph path tree*—with one branch of the tree for every path in the flowgraph. Each path then can be analyzed to give a set of *path conditions* that cause the path to be executed and a *path function* that describes the computation carried out for each path of the tree.

Faults in the program that can affect safety can be classified into at least five types: domain faults, missing path faults, timing faults, computational faults, and input/output faults. It is possible to place limitations on the program structure in such a way that the presence or absence of these types of faults can be detected.

The analysis described above can be carried out if a number of conditions are satisfied. A list of conditions has been found that we believe to be sufficient to carry out the analysis. We do not imply that the list of specific requirements is necessary or that the list is minimal.

Our ultimate goal is to deduce a set of design rules and corresponding validation methods that will enable reusable and qualifiable commercial software to be written for the safety-critical marketplace. We already know that the general problem of qualifying any program is insoluble; we think the problem may be soluble for an important subset.

In FY98, we chose the methods of abstracting and analyzing computer programs and created a list of conditions believed sufficient to enable the analysis to be performed. In FY99, we plan to complete mathematical proofs of the completeness of the methods, study practical examples of applying the methods, and qualify a commercial product.

Doppler Planet Search with a Novel High-Efficiency Spectrometer

D. J. Erskine, J. Ge
98-ERD-054

An important method currently used by astronomers to detect extrasolar planets is to search for a slight Doppler shift in starlight spectra, having a duration of several days to 30 years. The shift is caused by wobble of the star due to the gravitational pull of the planet. Jupiter-sized and Saturn-sized planets at Jupiter-like or Saturn-like orbits create 12 m/s- and 3 m/s-wobbles, respectively, and an Earth-like planet, 0.1 m/s. The 3 m/s best resolution of current grating spectrometers is insufficient to reliably detect sub-Jupiter planets. Their complicated instrument response is susceptible to drifts and is time consuming to calibrate. Their highly individualized character makes consistency over long orbit planet searches problematic. Their low light collection efficiency restricts current observations to bright stars.

The purpose of this project is to evaluate a new kind of spectrometer we have invented, which is superior for the Doppler planet search in particular, and may lead to other useful applications in spectroscopy and metrology in general. This project will enhance LLNL's capabilities in advanced instrumentation and diagnostics (e.g., Doppler-based velocimetry) essential to the Stockpile Stewardship Management Program and the nonproliferation effort. This *crossfringing spectrometer* is a hybrid of an interferometer and a low-resolution spectrometer. The interferometer provides Doppler detection at 1 m/s or better with a dramatically simpler and standardized instrument response. The low-resolution spectrometer increases fringe visibility over interferometers used alone, and improves light collection efficiency over traditional high resolution spectrometers. A larger slit opening can be used, increasing the field of view 200 times over current planet search spectrometers. The increased field of view allows efficient light collection, use of wider optical fibers, tolerance to blurry star images, and multi-object viewing. The instrument can be more compact (the size of a TV set) and can be launched into space.

In FY98, we built a prototype crossfringing spectrometer from off-the-shelf optics and have taken preliminary data on sunlight. Although its eventual use will be at an observatory on starlight, many operational aspects of our instrument can be tested in FY99 on sunlight in our lab at LLNL, seeking evidence of the 12 m/s tugging of the Earth by the moon. Figure 1a shows a small subset of the fringing solar spectrum. Figure 1b explains that overlap of a slanted fringe comb created by the interferometer with the vertical solar absorption lines creates moiré fringes, which shift vertically under Doppler shift. The moiré fringes remain visible even when the spectrometer slits are opened wider than Fig. 1a, to increase light collection. The intensity profile of the fringes is a sinusoidal function, as shown in Fig. 1c, having only 3 degrees of freedom (phase, amplitude, and vertical offset), which simplifies calibration and allows standardization. This is in contrast with current spectrometers with complicated instrument functions having thousands of degrees of freedom, all of which need to be accurately calibrated. Sunlight passing through an iodine vapor cell provides absolute wavelength calibration.

In FY99, algorithms are being created to unwrap the broadband phase shift of the interferogram to a resolution of 1/10000th of a wave, corresponding to Doppler shift of 1 m/s. (This is 20 times the resolution of monochromatic interferometry, and corollary applications to high precision metrology will be investigated.) The optical arrangement will by modified to anticipate use on starlight. Preliminary trials at Lick Observatory are anticipated.

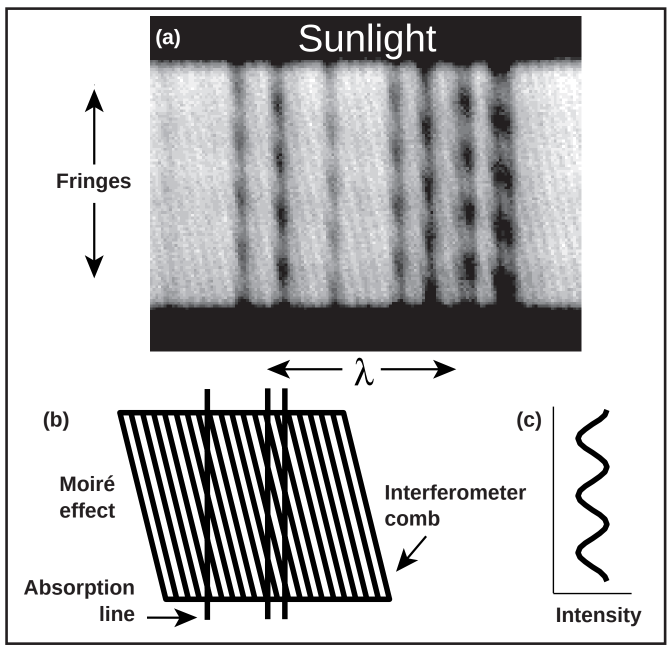

Figure 1a. Solar absorption lines seen through crossfringing instrument. Figure 1b. Overlap of finely spaced interferometer fringe comb with absorption lines creates moiré fringes, which have sinusoidal vertical intensity profile shown in Fig. 1c, where a Doppler shift manifests in vertical translation of moiré pattern.

Photonic Analog-to-Digital Converter Technology

P. D. Sargis, M. E. Lowry, M. W. Bowers, T. M. Tong, R. C. Stafford
98-ERD-092

Many national security missions rely on analog-to-digital converters (ADCs) to digitize a wide information bandwidth (GHz) with high dynamic range and precision. However, the performance of state-of-the-art ADCs has progressed rather slowly. To obtain a leap in performance beyond that of current electronic ADCs, we are developing the enabling technology for a class of photonic ADC architectures, which—along with advanced sensor technology—will allow measurement of many physical phenomena with unmatched speed and accuracy. We are targeting applications that will require sampling rates of 10 Gsamples/s at 12 to 14 bits at one extreme and 100 Gsamples/s at 4 bits at the other extreme. Our approach is to develop a multiwavelength optical-pulse generator that forms the heart of the ADC. To meet our goals for sample rate and dynamic range, this optical source must have a pulse duration of about 1 ps and pulse-jitter specifications of less than 5 fs.

Our basic photonic ADC converter uses a multiwavelength, ultrashort laser-pulse train and a Mach-Zehnder modulator to sample a broadband signal of interest. When pulses of light are present at the optical modulator, they are amplitude modulated in proportion to the input radio-frequency (RF) signal. This effectively samples the RF signal. Our multiwavelength optical-pulse train contains a sequence of optical pulses that progress in wavelength. The time between neighboring pulses is the inverse of the sample rate. This sequence of wavelength-progressing pulses is then repeated at some multiple of the sampling rate. The sampled signal is temporally demultiplexed through a wavelength division multiplexer (basically a spectrometer) to an array of photodetectors; the photodetector outputs can then be digitized by a time-interleaved array of slower-speed, electronic analog-to-digital converters.

Our plans call for a multiwavelength comb with a novel, externally modulated, Fabry-Perot (FP) coupled cavity that will ultimately incorporate optoelectronic feedback. An RF input will drive an intracavity phase modulator that periodically sweeps the optical passband of the FP through the optical source spectrum. A portion of the optical output signal is routed through a fiber delay line back to the phase-modulator input, thus creating a high-Q optical-feedback circuit. This high Q will be essential for low-phase noise and hence for low jitter (recall that our target is <5 fs).

In FY98, we made significant progress on several important elements of our project. We (1) successfully demonstrated the generation of optical pulses from a free-space FP cavity—the FP cavity was driven by a traveling-wave Pockels-cell phase modulator that used 800-nm input from a ring-laser; (2) designed and procured the integrated optical components necessary for the next phase of the source development, which will include the development of a miniature, modulated FP cavity; and (3) built and demonstrated a low-phase-noise (6.3127 GHz) RF source that uses optoelectronic feedback. As shown in Fig. 1(a), a laser operating at 1550 nm is coupled into the optical input of a Mach-Zehnder modulator. The modulator's RF input port is driven by the modulator's optical output through two optical feedback arms. The microwave amplifiers on each arm create enough link gain for the system to break into oscillation. The optical-fiber delay lines provide phase locking at integral multiples of round-trip time and additional frequency narrowing of the allowed oscillation frequency (thus enhancing the Q). The phase noise of the RF output is shown in Fig. 1(b). These results are very encouraging and indicate key progress towards our difficult jitter specification.

Follow-on research will build upon these initial results by further reducing the phase noise, controlling or mitigating the optical pulse amplitude fluctuations, and producing pulses of shorter duration.

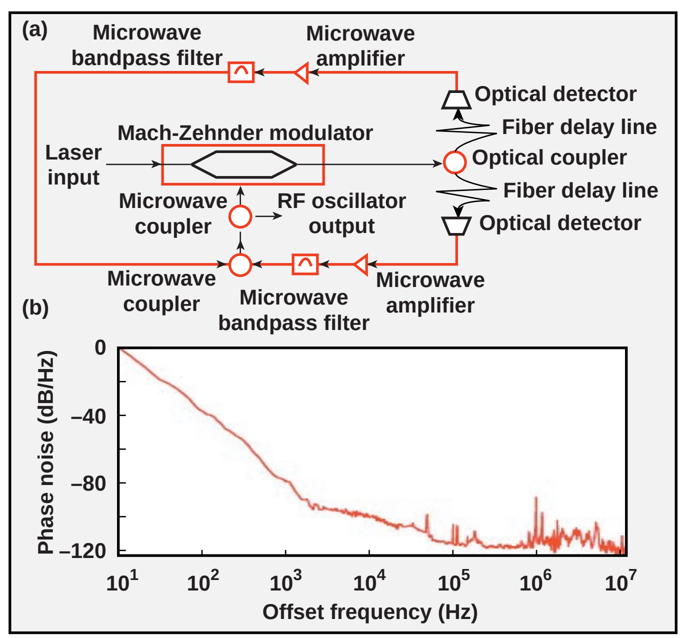

Figure 1. Progress towards a multiwavelength optical-pulse generator, showing (a) our initial low-phase-noise radio-frequency driver, and (b) results of phase-noise measurements.

Miniaturization of Optical Components through Hybrid Integration and Packaging

M. D. Pocha, M. E. Lowry, W. Goward, A. J. Ruggiero
98-ERD-093

Miniaturized optical elements will form the basis of many systems used by the intelligence community. These systems include sensors for the detection of weapons of mass destruction; optical components for communications links (both free-space and fiber-optic networks); and novel, all-optical encryption technology. Miniaturization is crucial in these applications to reduce detectability and also to reduce weight and volume on surveillance platforms.

Quite small individual optical devices can be fabricated using photolithographic processing. This works well for devices that are made from one material (e.g., integrated circuits that are made entirely from silicon). However, for full system functionality it is often necessary to incorporate components from a diverse set of materials. It is generally difficult or impossible to combine these diverse materials on the same substrate—a necessity for truly miniaturized systems.

For example, consider the combination of a semiconductor optical amplifier (SOA) with a laser with selectable output wavelengths. The SOA is an ideal candidate for a miniaturized optical-gain element. SOA development has been focused on III–V materials (semiconducting compounds made up of atoms from columns III and V of the Periodic Table, primarily Ga, As, Al, In, and P). In fact, SOAs made using epitaxial growth and dry-etching technologies are becoming commercially available commodities. A particularly powerful and flexible way of making a laser with selectable output wavelengths is to attach optical fibers with embedded distributed Bragg reflector (DBR) gratings to form an oscillator cavity. Further flexibility and functionality is attained by also attaching fiber-optic phase modulators and mirrors. However, both the fiber-optic DBR and the phase-modulator elements use processing techniques that are totally incompatible with the processing steps for the commercial SOAs.

The goal of this project was to make decisive progress toward integrating optoelectronic devices (such as SOAs or laser diodes) and passive-waveguide elements (such as gratings or modulators) on one substrate. Our approach has been two pronged. First, to provide short-term solutions, we studied our previously developed silicon-microbench technology that allows us to align and attach optical components such as SOAs and optical fiber containing the passive elements to a stable silicon substrate using solder reflowed by on-chip heaters. By the end of the fiscal year, we had further developed our understanding of the thermal behavior of these silicon microbenches by modeling the temperature distribution in and around the SOA on a microbench. This thermal-distribution data will help us to determine the best orientation for mounting the SOA and also will allow us to understand the effects of closely mounted SOA devices in array configurations.

Second, we made significant progress in FY98 on the longer-term monolithic integration of active (SOAs from III–V material) waveguides with passive (glass) waveguides. This level of integration will offer unprecedented miniaturization and functionality, but it will require considerable additional effort.

In a previous project, we had developed a process for fabricating low-loss, tantalum oxide glass, ß passive waveguides on a flat surface. However, to integrate these waveguides with SOAs, we must etch wells down into the active layers that make up the SOAs and deposit the passive layers so that they align with the optical axis, which is normally buried under the gallium arsenide surface. This is not a simple problem because edge effects change the deposition rates and complicate the alignment. In FY98, we simulated the mismatch losses that could be expected, determined the tolerances for the deposition parameters, and then deposited a variety of passive waveguides in passive wells. During this process, we examined the cross sections of the deposited waveguides to optimize deposition and to verify that we could achieve the tolerances needed. We are now ready to try depositing passive waveguides in active wells so that we can (1) experimentally verify the optical coupling we calculated, and (2) demonstrate (for the first time) active and passive waveguides integrated in a single monolithic structure.

RadSensor: An Optical Dielectric Modulation Approach to Prompt Sensing of Ionizing Radiation

M. E. Lowry, H. W. H. Lee, M. C. Larson, G. R. Delgado
98-ERD-095

High-speed detectors of ionizing radiation will have several important applications in weapons physics and inertial confinement fusion (ICF) experiments. For example, diagnostics for fusion burn at the National Ignition Facility (NIF) and gamma detectors for weapons radiography will benefit from advances in high-speed detectors.

Our goal is to develop a novel ionizing-radiation detector that will modulate the intensity of an optical beam in proportion to the intensity of an impinging ionizing-radiation beam. Our approach holds the promise of subpicosecond temporal response and single–x-ray photon sensitivity. With the temporal history of the ionizing radiation beam so encoded in an optical carrier beam, the information can be conveniently transported to a remote location for recording (see the related progress report on the FemtoScope project, 98-ERD-027). We call this new detector concept RadSensor.

Our approach uses x-ray–induced dielectric modulation of a semiconductor or insulator to modulate the phase of the optical beam passing through the material. The effect is analogous to all-optical switching using resonant optical nonlinearities in semiconductors.

As the x-ray photon passes through the material, a large fraction of the deposited energy is stored temporarily as electron-hole (e-h) pair excitations. Rapid relaxation to the band edge alters the absorption spectra of the material by a process known as "band filling." A blue-shift in the absorption edge occurs, effectively modulating the imaginary part of the index of refraction. The Kramers–Kronig sum-rule governs these modulations of the dielectric function, dictating that this absorption change will also modulate the real part of the complex optical index. This modulation of the dielectric function can now be used to modulate an optical carrier beam that is also passing through the material. RadSensor can be configured to operate as either an absorption or phase modulator of this optical carrier beam.

This band-filling effect on the optical index, where one optical beam is used to create a phase change in another beam, has been studied for many materials using optical excitation. The effect is generally called a resonant nonlinear optical phase shift, or cross-phase modulation (XMP).

The e-h pair relaxation processes leading to the band-filling absorption shift are known to be fast (~100 fs) when optical excitation is used. Verifying the rapid rise-time of the shift with x-rays is a key element of this project. However, in a radiation detector that accurately tracks the temporal profile of an x-ray beam, the band-filling process must also rapidly relax to equilibrium after it is formed.

In FY98, we demonstrated that we can epitaxially grow a class of semiconducting materials that have this characteristic, fast relaxation time. We grew low-temperature GaAs (LT–GaAs) test wafers and measured the temporal response of the optically induced index modulation. This measurement was carried out with a femtosecond pump-probe technique, shown in Fig. 1(a), in which an intense femtosecond optical-pump pulse excites carriers in the LT–GaAs. A probe pulse that is time-delayed with respect to this pump pulse then interrogates the carrier population (and hence the index change) by monitoring changes in its reflection off the surface of the LT–GaAs. An example of this measurement is shown in Fig. 1(b), where the intensity of the reflected probe is plotted as a function of the time delay between the pump and probe pulses. As shown, a temporal response of less than 1 ps was observed.

In the coming year, we will fabricate and characterize the response of detectors based on this LT–GaAs material, using both optical and ionizing radiation excitation.

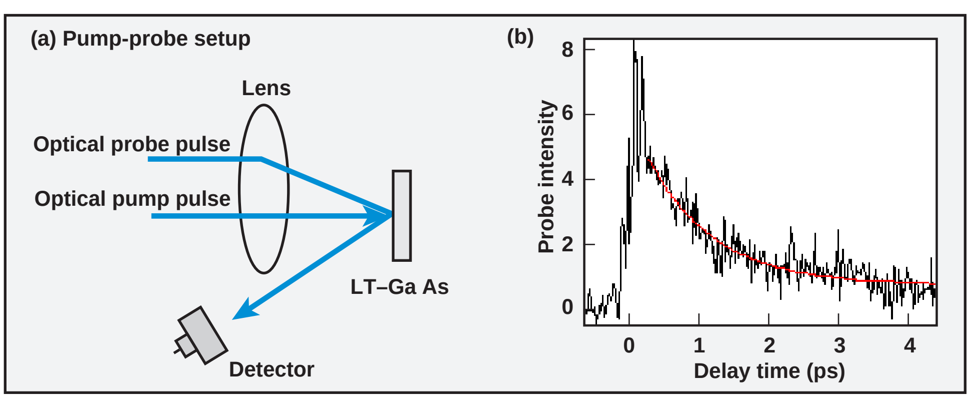

Figure 1. Optically induced temporal response of low-temperature GaAs (LT–GaAs) wafers, showing (a) pump-probe setup, and (b) carrier lifetime of the LT–GaAs. A 813-nm, 100-fs-wide optical pulse was used for the pump probe. The carrier lifetime—at less than 1 ps—verified our ability to grow semiconducting materials with a fast relaxation time.

Real-Time Detection and Identification of Biological Aerosols with Mass Spectroscopy

K. Langry, S. Labov, M. Frank, H. Gregg, J. Horn, F. Magnotta, A. Jordan, F. Milanovich
98-ERD-097

Recent bombings in American cities, the discovery that Iraq had a thriving biological warfare (BW) program, and the release of sarin on a Tokyo subway by the Aum Shinri Kyo terrorist cult have all caused government officials and military planners to re-evaluate the preparedness of the U. S. to defend itself against a catastrophic attack with biological weapons on a major metropolitan area. Experiments with surrogate agents during the late 1960s along with more contemporary atmospheric modeling studies suggest that the U. S. is unprepared for such an event and would sustain massive casualties and deaths if one were to occur in a city like New York. These studies also show that if an attack with BW agents occurs, early detection and agent identification will be paramount in the effort to save lives.

Our research effort is directed at developing the capability for real-time analysis of biological aerosols in urban environments. The goal of our project is to show that biological aerosol particles exhibit a characteristic molecular signature that can be developed using a combination of laser thermolysis and time-of-flight (TOF) mass spectrometry. To achieve our goal, we are exploring laser-based methods for dislodging major identifying proteins from the surfaces of bacterial spores. Proteins liberated with this technique will be analyzed as they are displaced from the spore using a TOF spectrometer equipped with a superconducting tunnel junction (STJ) detector. This combination of laser thermolysis, TOF mass spectrometry, and high molecular mass (>megadaltons) detection with the STJ detector represents a new, sophisticated approach to the real-time analysis of biological aerosols.

With the few months of FY98 funding that was received, we prepared *Bacillus subtilis* spores (see figure) for analysis and have isolated some spore-coat proteins. In collaboration with Henry Benner of LBNL, we obtained preliminary mass spectral data from whole spores and from the isolated coat proteins using the matrix-assisted, laser-desorption-ionization technique on a TOF mass spectrometer equipped with a microchannel plate detector. These data indicate that we must use the STJ detector so that we can evaluate the charge state of the protein signatures as well as their molecular mass.

In addition, we constructed an optical parametric oscillator laser that provides us with a tunable light source ranging from 2 to 4 µm. We will use this pulsed laser to pump thermal energy into the spore to facilitate the release of the coat proteins.

We obtained infrared absorption spectra of cultured *B. subtilis* spores as well as spectra from spores weaponized for use as surrogate biological agents, and we used these data to select other laser-light frequencies that we will exploit to develop protein signatures from spores.

We also made improvements to the LLNL's TOF laser system; in FY99, we will install the antireflection-coated ZnSe windows that we acquired in FY98.

We will perform our first laser-thermolysis experiments in early FY99 with 3-µm light. This spectral region corresponds to the O-H and N-H stretching frequencies in water, alcohols, carboxylic acids, amines, and amides. These functional groups are found in the amino acids that make up proteins, in the peptidoglycans that comprise the spore cortex, and the phospholipids that constitute the principal component of the protoplasmic membrane. Selectively pumping energy into these known resonances will deposit an enormous amount of energy into the spore instantaneously and will result in a ballistic expansion of the spore and dissociation of its structural components into their constituent molecules. Mass spectral detection of these constituent molecules will provide the unique signature necessary to identify different species of bacteria.

We will follow these experiments with laser irradiation at other absorption frequencies, including the 6.3-µm resonance of the C = O bond stretch and a few other modes involving C–H stretching and bending vibrations associated with alkanes and lipids.

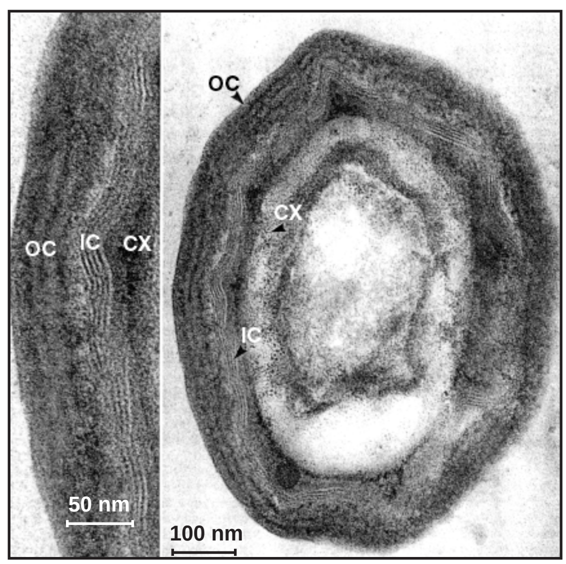

Electron micrograph of a *Bacillus subtilis* spore. The outer core (OC), inner core (IC), and the cortex (CX) are labeled. The protoplasm—the light area surrounded by the IC—is about 50 wt% water. Pulsed irradiation of the spore with a laser will deposit hundreds of microjoules into the cell, causing it to burst. Large, intact proteins will be ejected from the spore coat. Spores, like other cells, possess unique proteins in their outer coat that can be used to identify the species (and even the variant) of the organism; we will detect these ejected proteins by mass spectrometry.

Development of AMS Capability for Plutonium and Other Actinides

J. E. McAninch, T. F. Hamilton
98-ERD-100

Low level actinide measurements have important application throughout the DOE complex, in areas such as monitoring of civilian and worker exposures, following environmental levels and transport, disposing of radioactive waste, and evaluating non-proliferation. Many present day applications require a combination of sensitivity and throughput beyond that of currently available techniques. Development of a robust, high-throughput, and cost-effective analytical tool with the sensitivity to detect these prominent products of the nuclear fuel cycle at environmental levels will have a broad impact in many of these core DOE mission areas.

One analytical tool that has a high potential for meeting these requirements is accelerator mass spectrometry (AMS), a well-established method for the detection of long-lived radionuclides. The Center for Accelerator Mass Spectrometry (CAMS) at LLNL operates the most versatile and most productive AMS instrument in the world. A component of CAMS ongoing development activities is the extension of our AMS capabilities to new isotopes, and the long-lived actinides are an important part of this effort.

The focus of the present project is development of AMS capability and associated sample preparation methods for the detection of the plutonium isotopes ^{239}Pu and ^{240}Pu. One planned use of this tool is in support of the LLNL Marshall Islands Program. Urine bioassays of Marshall Islanders and workers will be performed as part of the ongoing bioassay program associated with island resettlement. This and similar programs involving DOE workers would benefit from an analytical tool sensitive enough to quantify plutonium at the levels found in "unexposed" individuals (i.e., persons exposed only to the environmental levels of plutonium resulting from worldwide fallout). An improved detection sensitivity would lower the threshold for making detect/non-detect evaluations for single individuals and would enhance statistical assessments of the results. Using AMS, we expect to achieve sub-femtogram sensitivity, a capacity for several hundred analyses per year, and a reduced cost per sample.

The AMS capability development will consist of optimizing the operating parameters to maximize the system efficiency, sample throughput, and rejection of interferences. This research effort is taking place in parallel with a series of hardware upgrades to the CAMS spectrometer to improve transport and mass resolution for these high mass ions. The largest component of these upgrades is the installation of a large (4.4-m radius, 45-degree deflection angle) electrostatic analyzer to improve mass separation.

The sample preparation development will be initially based on present LLNL Health and Ecological Assessment (HEA) protocols for alpha spectrometry measurements of actinides. Some simplifications will be allowed by the reduced susceptibility of AMS to interferences; other modifications will be necessary to produce a sample form appropriate for AMS analysis. The major technical challenges are the removal of sample uranium and the attainment of low and reproducible procedural blanks to match the high sensitivity of the AMS measurements. The key element to cost effectively meeting these challenges is an automated, closed-loop fluid management system (FMS), which will minimize contact between the sample and the laboratory environment and will reduce the quantity of reagents required. This is a new application of this system, and the manufacturer is working with HEA to customize the FMS specifically for our requirements.

This research was originally proposed and accepted as a LDRD project beginning in FY99. At the end of FY98, a small amount of funds became available which were allocated for the purchase of the FMS.

In Situ Identification of Anti-Personnel Mines using Acoustic Resonant Spectroscopy

R. S. Roberts, R. L. Perry
98-FS-004

The detection of buried modern anti-personnel (AP) mines is a problem of tremendous importance in many parts of the world. These mines contain very little metal and thus are very hard to locate with conventional metal-detection instruments.

We are investigating a new technique for identifying AP mines. The uniqueness of this approach is that buried objects, detected by other methods, can be quickly identified as AP mines or debris—and removed accordingly. Substantial effort is thus saved because all detected buried objects need not be treated as AP mines.

The technique is based on Acoustic Resonance Spectroscopy. ARS is based on the premise that objects of interest (such as AP mines) have characteristic, nominally reproducible resonant frequencies that we can excite and detect. Since the resonant frequencies of an object are functions of the object's geometry and materials of construction, it follows that objects of a similar nature will have similar patterns of resonant frequencies. Thus, the frequency-response pattern of an object can be used to identify it.

There are several ways to estimate the acoustic resonance spectrum of an object. In the case of an AP mine, the objective is to obtain the spectrum in the most noninvasive manner possible. To begin with, an excitation force spanning the frequency band containing the resonances is applied to (or near to) the object. The magnitude of the excitation force does not need to be large to obtain a useful spectrum. For AP mines, a simple approach is to touch the object with a probe that produces low-amplitude vibrations over the frequency band of interest. Although this requires touching the object, it is perhaps the best way to excite the object's resonant frequencies. Indeed, touching mines with a probe is accepted practice with deminers.

Collecting the frequency response of an object requires a sensor to detect the object's vibrations. In general, radar is well suited for the noninvasive sensing of vibrations. In particular, the micropower impulse radar (MIR) technology invented at LLNL provides a unique means of noncontact, stand-off vibration sensing. Even though the objects of interest are buried, the burial depths are shallow enough that a low-power radar should have little problem sensing the vibrations.

In FY98, we conducted several experiments to assess the feasibility of this identification technique. The experiments consisted of measuring the acoustic resonant spectrum of four objects of similar geometry over a limited frequency range. The objects were secured in a wooden cradle for the experiments; to maximize the signal-to-noise ratio, the objects were not buried while the measurements were being collected. The objects were (1) an M14 mine (inert); (2) a nondescript mine-detection target (MDT); (3) a galvanized nipple covered with duct tape; and (4) a plastic can containing putty. For an excitation signal for the experiments, a signal generator supplied a signal that was amplified and applied to a vibrator. The objects were tested one at a time. A probe about one foot in length was attached to the vibrator and touched to the side of the object; the vibrations of the object were sensed by a low-power MIR. The radar was placed 60 mm from the surface of each object, in an orientation perpendicular to its surface. Spectra from the objects were collected over several frequency ranges. All four objects had distinguishable spectra.

In addition to the experiments described above, several experiments were performed to assess the variability of the spectral measurements. The experiments consisted of multiple measurements of the spectra of the objects over a 200- to 500-Hz band. The multiple measurements were graphed on a raster plot for comparison. The spectra showed some degree of variability, but overall the measurements appeared repeatable. The next step in our development of this technique is to collect spectra from objects buried in soil and submerged in water. The spectra collected from these experiments will be examined for discriminating features and repeatability.

Novel Ultrasound "Scintillator"

J. S. Kallman, A. E. Ashby, D. Ciarlo, G. Thomas
98-LW-035

Ultrasonic imaging is used to inspect parts, monitor processes, and diagnose medical conditions. Soon after x-ray computed tomography (CT) was invented, attempts were made to use ultrasound for tomographic imaging. However, one of the many problems encountered was the difficulty in acquiring the necessary data quickly. The sensor we are developing addresses this problem.

Our sensor is based on frustrated total internal reflection (FTIR), which is a consequence of the wave nature of light. When light moves from a slow medium to a fast one, there is a critical angle beyond which the light is totally reflected. However, an evanescent wave extends a short distance (about one wavelength) into the fast medium; if another piece of slow medium intercepts this evanescent wave, some of the light tunnels across the gap between the slow media. How much light tunnels is a function of the angle of incidence, the indices of the media, and, most importantly from our point of view, the width of the gap.

By separating two media with a pressure-dependent air gap, we can modulate a beam of light to transduce the pressure. A sequence of images, each taken at a different source acoustic phase, enables us to reconstruct the ultrasonic phase and amplitude over an entire two-dimensional (2D) surface. These data can be acquired by a camera and computer.

The inspection technique we are developing is transmission ultrasound. In this modality, an acoustic source sends out pressure waves through a couplant (such as water, oil, or medical ultrasound gel) to the object of interest. The pressure waves are transmitted through the object, along the way being changed in amplitude and phase. The pressure wave emerges from the object of interest and travels, via the couplant, to the acoustic sensor. Our sensor works because the pressure wave causes changes in an air gap, varying it with a phase and amplitude that are a function of that wave.

In FY98, we began our work on this project by modeling as many of the systems and processes as possible. We used LLNL's TSARLITE code to model the optical elements of the sensor, DYNA3D to model the acoustic responses of the air gap, and a modification of the BEEMER code to model the imaging system as a whole. By using TSARLITE, we were able to (1) determine the ranges in which we could expect FTIR to be useful, and (2) bound the permissible width of the air gap. We used DYNA3D to model mechanical designs of our sensor. DYNA3D showed us that our first design had neither the sensitivity nor the frequency response necessary to allow us to acquire the data we needed. Guided by our simulations, we developed a more responsive design. The modified BEEMER program was used to examine the issues that arise when we use the sensor for diffraction tomographic imaging; that is, it was used to model the tomographic data-acquisition processes as well as a variety of reconstruction algorithms.

Simulation eliminated the need to experiment blindly, but we still needed to verify that the simulations were correct and to get proof-of-principle results. For these experiments, we built a test system that consisted of the test sensor, a tank with an acoustic source, and the optics. The test sensor was designed to allow us to examine the responses of a wide range of sensor parameters.

We learned a great deal using the test system, most importantly that (1) we can engineer to the sizes and tolerances necessary to utilize the FTIR physical phenomenon, and (2) we can extract phase and amplitude data at each acoustic pixel from sequences of images.

After performing numerous experimental runs, we were able to arrive at an optimal set of design parameters for the final sensor. By the close of FY98, we had completed the design for the final sensor and had begun fabrication.

In FY99, we will complete the construction of our final sensor, calibrate it, and use it to collect phase and amplitude data from a variety of test subjects. Initially, we will make only 2D transmission ultrasound images; ultimately, we will generate volumetric images of three-dimensional objects using data from this sensor to feed a future diffraction-tomography code.

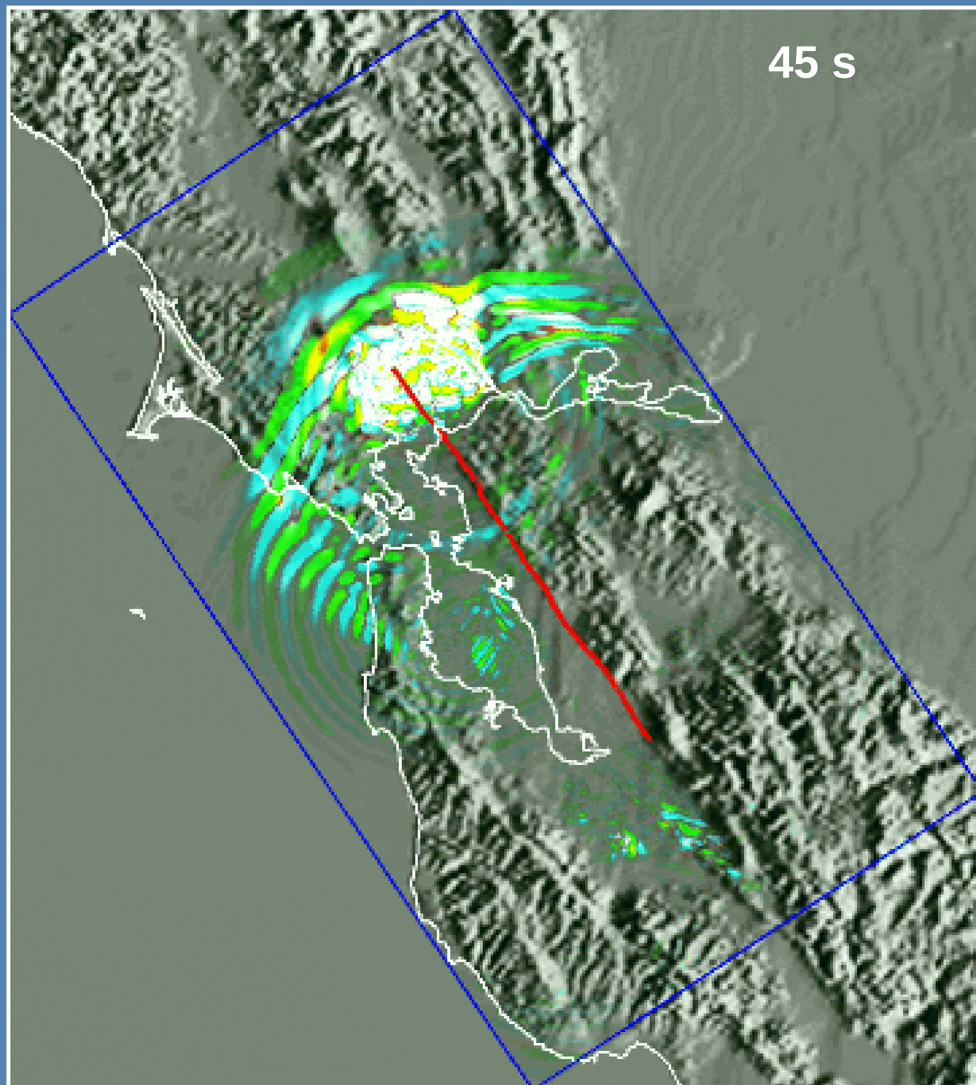

2

Atmospheric and Geosciences

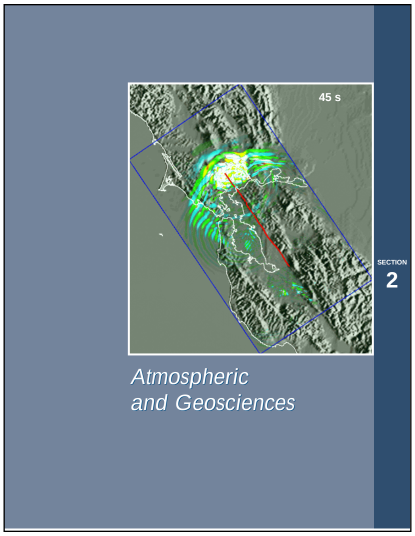

About the preceeding page

Three-Dimensional Simulations of Scenario Earthquakes along the Hayward Fault. The primary objective of this project is to determine the geographical distribution of high-amplitude seismic ground motion computed by 3-D simulations of scenario earthquakes along the Hayward Fault. In addition, Shawn Larsen and his team will integrate the predicted ground motions with structural models of the Bay Bridge. These simulations will be performed with E3D, a sophisticated seismic-wave propagation code developed at LLNL, and a 3-D model of the geologic structure of the Bay Area being developed at the University of California, Berkeley. Shown here is one of the seismic ground-motion intensity maps for a simulated magnitude 7.1 scenario earthquake along the Hayward fault. For details, see page 2-14.

Subduction and Mantle Recycling

H. F. Shaw, K. D. Putirka, F. J. Ryerson
96-ERI-005

Understanding how the Earth has differentiated into chemically distinct reservoirs such as the continental crust, oceanic crust, and mantle is a fundamental goal of geology. In general terms, we know that over time, portions of the mantle have partially melted, forming magmas that rise and form the crust. The flow of material is not unidirectional, however. At the boundaries of convergent tectonic plates, the oceanic crust produced by volcanism at midoceanic ridges is once again returned to the Earth's mantle in subduction zones. Volcanism associated with subduction zones is the principal mechanism for adding new material to the continental crust, and subduction is the principal mechanism of chemical and mass recycling on our planet. To unravel the history of the Earth's differentiation, we must be able to estimate the composition of Earth's mantle and the range of temperatures that exist beneath the oceans' basins. Temperature estimation is particularly crucial because it allows constraints to be placed on the depths of partial melting—the process by which material is added to the crust.

The goal of this project was to apply experimental and computational techniques to elucidate the processes that operate to produce the Earth's crust. In previous years, we studied the partitioning of trace elements between aqueous fluids (as well as silicate melts) and minerals at elevated temperatures and pressures, which allowed us to place limits on the role of aqueous fluids in crustal growth at plate margins. During FY98, we conducted laboratory experiments to calibrate several methods for determining the depths and temperatures for partial melting. These methods involve the clinopyroxene-melt partition coefficient for sodium $K^{Na}_{cpx/melt}$, which is defined as the concentration Na in clinopyroxene (an important Na-containing mantle mineral) divided by the concentration of Na in the coexisting silicate melt. This ratio increases dramatically with increased pressure: the deeper partial melting occurs, the more Na is left behind in the solid residue, and the less Na enters the melt. Measurements of the sodium contents of lavas can thus be used to estimate partial-melting depths. We have also used experimental results from a variety of laboratories, including our own, to examine the quantity of melt produced at a given temperature for a given chemical composition. This quantity, known as "melt productivity," is an important quantity because it relates mantle temperatures to crustal thickness. Finally, we used our experiments to calibrate methods that allow clinopyroxene compositions to be calculated given a magma composition plus either pressure or temperature. These tools help geologists to estimate depths and temperatures of magma crystallization; hence, they can be used to decipher the plumbing system of volcanic centers.

We used the pressure sensitivity of $K^{Na}_{cpx/melt}$ to estimate partial-melting depths for lavas from Hawaii and the East Pacific Rise. To facilitate the comparison, the Na concentrations were normalized to Ti concentrations to correct for the possible effects of crystallization during ascent and eruption. Lavas from Hawaii have much lower Na/Ti ratios than those from the East Pacific Rise, indicating a greater depth of origin for the partial melts that give rise to the Hawaiian lavas. Specifically, our mantle-melting model indicates that at "hot spots" such as Hawaii, melting begins at depths of up to 300 km or more and at temperatures 300˚C above the ambient temperature of the mantle. These findings support the view that islands like Hawaii are produced by the upward movement of hot mantle "plumes," possibly related to the deep melting of subducted, recycled oceanic crust. In contrast, at passive spreading centers such as the East Pacific Rise, partial melting begins at depths of about 100 to 120 km. Such depths are consistent with recent seismic evidence for low seismic velocities in this region, which strongly suggest the presence of partial melt. Finally, others have suggested that if partial melting occurs at depths greater than 80 km at passive spreading centers, then twice the observed thickness of oceanic crust should be produced at such localities. However, our experimental constraints on melt productivity indicate that if melt is removed from the residue as it is produced, then melt productivity could be sufficiently low to allow melting at depths of more than 100 km; yet it would still yield the 8-km-thick oceanic crust that is observed at normal midocean-ridge spreading centers.

This was the final year of this project. In addition to the contributions discussed above, the results of this project have provided explanations for at least three well-known but poorly understood observations. Our work on the partitioning of elements between mantle minerals and aqueous fluids or melts provided an explanation for the anomalously low concentrations of Nb and Ta in subduction-related melts. Those results also explained the systematics of Pb isotopes and Pb concentrations in these melts and the systematic variations of the B/Be ratio as a function of melting depth in subduction zones.

Natural Global Electromagnetic Resonances and Their Security Implications

D. L. Shaeffer, D. R. Rock, J. P. Lewis, S. I. Warshaw
97-ERD-003

Following the end of the Cold War, a Comprehensive Test Ban Treaty (CTBT) was offered to the international community as a partial means of stemming the tide of nuclear proliferation. An international monitoring system (IMS) was proposed as an adjunct to the CTBT to ensure compliance with the CTBT. The IMS—which would also assist in identifying nuclear-test activity of nonsignatory countries—includes four monitoring methods: seismic, hydroacoustic, infrasonic, and atmospheric-radionuclide sampling. However, despite prodigious efforts by a worldwide cadre of scientific experts to design an effective IMS, the task of ensuring the detection of all nuclear-test activity remains daunting.

The objective of this project was to investigate an alternative method of monitoring for the occurrence of explosions (albeit not necessarily nuclear explosions) by demonstrating that explosive events could be detected by monitoring low-frequency (~0.01 to 50 Hz) geomagnetic perturbations induced by acoustic signals emanating from explosions. We postulated that such perturbations might be generated when the upwardly propagating acoustic wave interacts with the ionosphere to generate electron density (and concomitant electrical current) perturbations in the E and/or F regions of the ionosphere. These perturbed regions would correspond to localized peaks in the ionospheric electrical conductivity, and the currents would become sources for the generation of two modes of geomagnetic disturbance. One, called an Alfvén wave (a vibration of a geomagnetic field line analogous to the vibration of a stretched string), propagates along geomagnetic field lines. The other, called a modified Alfvén wave (analogous to a sound wave in air), propagates in a cavity that extends azimuthally around the Earth. We anticipated that this latter wave guide would be leaky because of the imperfectly conducting boundaries of the cavity. Consequently, we expected that—with appropriate instrumentation—we could observe wave-field energy on the ground.

During FY97, we established an experimental program to test our hypothesis by taking advantage of open-pit blasting activity at the Black Thunder Coal Mine (BTCM) near Gillette, Wyoming. Explosions occurring there about every three weeks have yields equivalent to 1 to 3 kT of TNT. We fielded two magnetic observatories 50 km and 64 km geomagnetically north of BTCM. Each observatory consisted of three mutually perpendicular induction magnetometers, a three-component seismometer, a data-acquisition and storage system, Global Positioning System (GPS) timing, and battery power backed up with solar power.

During FY98, our observatories recorded numerous magnetic events, including some caused by mining activities other than at BTCM. Our initial analysis of events corresponding in time to explosions at BTCM tentatively suggested that the observed magnetic signals had arrival times consistent with generation by E- and F-region currents induced by acoustic waves propagating upward from the mining explosions. We observed transient pulses, known as Q-bursts, with spectral energy dominated by the Schumann resonances (~8 Hz). Although normally caused by large lightning strokes, the Q-bursts appeared to be generated by Alfvén solitons (nonlinear waves that travel without change of shape) that were excited by explosion-induced acoustic waves that reached the ionosphere. We also observed late-time (>800 s), ultralow-frequency (ULF) geomagnetic perturbations that appeared to originate in the upper F region (~300 km) and that appeared to be explosion-induced. We suggest that explosion-induced Q-bursts may be discriminated from naturally occurring Q-bursts by association of the former with late-time, explosion-induced ULF perturbations. We observed acoustically induced magnetic signals at both observatories, indicating that magnetometers act as highly sensitive detectors of ground motion. Further work is required to confirm these findings at larger distances (>1000 km) from explosions.

Advances in Atmospheric Chemistry Modeling

D. A. Rotman
97-ERD-051

Changes in the atmospheric distributions of gases and aerosols (either solid or liquid particles) can enhance or mask climate change. Although present in "trace" levels as low as 1 part per trillion (1 pptv), gases and aerosols affect air quality as well as the greenhouse warming of the atmosphere. An important "trace gas" is ozone (O_3), which has radically different purposes and formation routes in the troposphere (the layer closest to the earth, roughly 0–10 km) and the stratosphere (which extends from 10–55 km). Ozone in the stratosphere is beneficial, as it absorbs a significant fraction of the sun's radiation. Destruction of the stratospheric ozone layer (the "ozone hole") may change the chemical and radiative balance of the earth's atmosphere. Ozone in the troposphere, however, is produced differently and considered an atmospheric pollutant that damages crops, vegetation, respiratory systems, and many materials. Aerosols influence climate both directly (by scattering and reflecting radiation) and indirectly, by altering cloud optical properties and lifetimes. Recent results show that atmospheric aerosols may lead to a net cooling effect that partially compensates for the greenhouse warming by gases such as carbon dioxide (CO_2) and water vapor (H_2O).

We have developed a unique model, named IMPACT (Integrated Massively Parallel Atmospheric Chemical Transport model), capable of discerning the global environmental effect of trace gases and aerosols throughout both the troposphere and stratosphere; in particular, we are able to realistically simulate the tropopause (the region separating the troposphere and stratosphere). We are using this tool to analyze the current state and past and future trends of ozone. We will also be able to participate in analysis of data from a variety of campaigns planned for the short and long-term future.

IMPACT uses input meteorological data from the National Aeronautics and Space Administration (NASA) Data Assimilation Office. This high-resolution dataset is a melding of climate model output with observed data to best represent a particular time period. For our studies, we have obtained data representing 1997 to coincide with a major aircraft measurement campaign (named SONEX). We have used these measurements to validate the model. Over the past year, all necessary physics have been added to the model to simulate the combined troposphere and stratosphere. IMPACT is unique in this capability.

Of particular note is our inclusion of wet scavenging. This piece of physics represents the elimination of various chemical species caused by rainfall. The original meteorological data did not provide complete information to model this process. We developed a methodology to *infer* the complete information for this scavenging submodel. We have tested this submodel against observed data for specific chemical species and have found very good agreement. This methodology is now being adopted by various other modeling groups across the United States as well as a major NASA 3D chemistry modeling initiative.

We have applied the IMPACT model to analyze measured data from the NASA SONEX measurement campaign. SONEX was focused on measuring nitrogen species and ozone in the upper troposphere over the North Atlantic aircraft travel route. Measurements showed large variability in ozone. Analysis by the IMPACT model shows this variability to be caused by intrusions of high level stratospheric ozone associated with weather/storm fronts crossing the Atlantic and not associated with in-situ production of ozone. At NASA's urging, this SONEX data analysis may continue and expand to the full range of measured species.

Over the next year, IMPACT will be used to analyze upper troposphere and lower stratosphere distributions of ozone to further our understanding of impacts from energy related activities. In particular, we will investigate tropospheric and stratospheric ozone trends and how biomass and fossil fuel combustion influences these trends.

Measurements of Past ^{14}C Levels and $^{13}C/^{12}C$ Ratios in the Surface Waters of the World's Subpolar Oceans

T. A. Brown
97-ERD-052

In collaboration with the University of Washington, we developed a method to determine past ^{14}C concentrations and $^{13}C/^{12}C$ ratios in the surface waters of the world's subpolar oceans by using archived salmon scales. The overall goal of this research is to develop carbon isotope time-histories for the world's subpolar oceans and to reduce the current uncertainty in the oceanic uptake of anthropogenic carbon dioxide. Since the world's oceans are the most important global sink of fossil-fuel carbon dioxide, our results will lead to improvements in the quantification of the global carbon cycle and elucidation of the fate of anthropogenic CO_2.

During FY98, we measured the ^{14}C contents of salmon scales that had been archived under fisheries research programs in the subpolar North Pacific Ocean. Through the cooperation of Russian scientists, we have been able to make preliminary measurements on scales from Kamchatkan salmon stocks. In combination with archived scales from Alaska and British Columbia, we have now developed time-histories that span the entire subpolar North Pacific and extend back to the mid-1940s. We have also measured the ^{14}C contents of an initial set of scales from North Atlantic salmon caught off the western coast of Greenland in 1988.

The subpolar North Pacific ^{14}C time-series we obtained provide the first determinations of pre-1950s open-ocean ^{14}C concentrations for the subpolar North Pacific surface waters (see figure). These time-series also show the timing and magnitude of the rise in surface water ^{14}C concentrations caused by the influx of ^{14}C produced during atmospheric nuclear weapons tests. The higher "pre-bomb" ^{14}C levels, the very rapid rise in response to increased atmospheric ^{14}C concentrations, and the continuing higher levels shown by the Ocean General Circulation Model (OGCM) results for the central subpolar North Pacific suggest particular deficiencies in the models; they also show the value of our salmon scales-based time-histories in the constraint and validation of computer models of the global ocean. Comparison of our time-series to the few direct measurements of the ^{14}C contents of subpolar North Pacific surface waters (from 1973 and 1991) shows excellent agreement, providing strong evidence that the archived scales are accurate and reliable recorders of the carbon isotope content of the surface waters. Comparison of our North Atlantic salmon ^{14}C data with the single direct measurement available for the western Greenland surface waters shows very good agreement.

Current efforts towards improving our understanding of the impact of anthropogenic fossil CO_2 releases point to the current uncertainty in the oceanic uptake of fossil CO_2 as a significant impediment to improved quantification of the global carbon cycle. OGCMs hold great promise for allowing the accurate quantification of oceanic uptake, and time-histories of the ^{14}C contents of the atmosphere and the oceans provide very strong constraints on the reliability of OGCMs. Initial comparisons of our salmon-scale time-series with OGCM carbon isotope results obtained at LLNL show that the LLNL OGCM results continue to be more consistent with our ^{14}C time-series than previously published model results. However, the OGCM surface water ^{14}C concentrations in the subpolar North Pacific remain somewhat higher than shown by our salmon-scale records, and the nuclear-weapons ^{14}C peak occurs later in our time-series than in the OGCM results. Several improvements to the LLNL OGCM are currently being implemented, which may significantly improve the agreement of model results with our salmon scale ^{14}C time-histories.

Our efforts to expand the research to include $^{13}C/^{12}C$ ratios have been supported by additional funds from the National Science Foundation, and this research is producing additional information on the uptake of fossil CO_2 by the oceans. In FY99, we intend to complete higher time-resolution ^{14}C and $^{13}C/^{12}C$ records for the subpolar North Pacific, to develop initial time-histories for the North Atlantic, and to investigate archived Crabeater Seal teeth as a source of carbon isotope time-histories for the Southern Ocean.

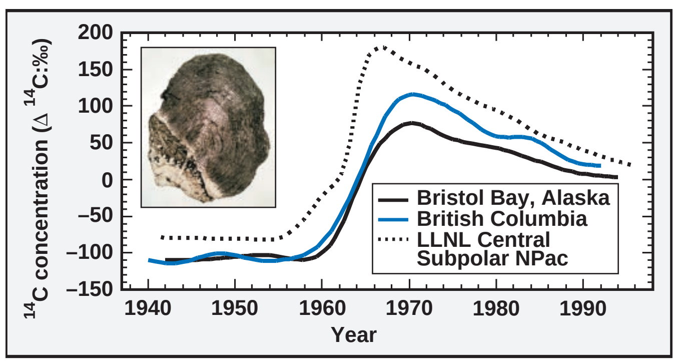

Comparison of radiocarbon time-histories obtained from North Pacific Sockeye Salmon scales to preliminary results obtained from the LLNL OGCM. The scales-based time-histories show the rise of ^{14}C levels, which was caused by the influx of ^{14}C produced in the atmosphere by nuclear weapons testing in the late 1950s and early 1960s. The existence of an east-west ^{14}C gradient in the subpolar North Pacific suggested by OGCM results, with higher ^{14}C levels in the east, is supported by our eastern region (British Columbian) and central region (Bristol Bay, Alaskan) records. The inset shows a scale from a salmon that lived in the open-ocean surface waters of the subpolar North Pacific for just over three years.

Geospeedometry: Application of Cosmic-Ray Surface Exposure Dating to Problems in Active Tectonics

F. J. Ryerson, R. Finkel, M. Caffee

97-ERI-003

The goal of this project is to develop and apply cosmogenic dating methods to constrain rates of tectonic deformation on active faults and folds in the collision zone between India and Asia. Active faulting and seismicity show that deformation in Central Asia is partitioned between thrust faulting in mountain belts and lateral displacement along great strike-slip faults. The extent to which deformation is localized along these faults as opposed to homogeneously distributed throughout Asia is critically dependent upon the rates of slip and bears upon the more general question of how the earth's lithosphere deforms. We, in conjunction with colleagues at UCLA, the Institut de Physique du Globe de Paris, and the Chinese Seismological Bureau, are currently focusing our efforts on sites along Tibet-Tarim Basin boundary, which is defined by the Altyn Tagh Fault System (ATF), as shown in the figure.

The ATF runs along the northern edge of the Tibet-Qinghai highlands for nearly 2000 km, merging with various thrust and other strike-slip systems at its eastern and western termini. Eastward propagation of the ATF may be the primary mechanism by which the northern part of the plateau has grown. In the first two years of this project, mapping and sampling was performed in a number of regions and dated using both ^{10}Be and ^{26}Al to obtain slip rates.

At its eastern termination, slip on the ATF is transferred to other strike-slip fault systems, such as the Haiyuan and Kunlun Faults, and to sub-perpendicular thrust faults such as those in the Tang He Nan Shan. Left-lateral slip along the Kunlun Fault has resulted in several terraced risers offset by various amounts. The cosmic-ray exposure ages of these features yield a slip-rate of 12 ± 2 mm/yr. This is the first quantitative measure of slip-rate on any fault in Asia, and the results from one site were recently published (Van der Woerd et al., 1998). A second paper presenting identical rates over 600 km of the Kunlun Fault is in preparation.

The Tang He Nan Shan is a northwest-southeast trending mountain range roughly perpendicular to the ATF at its eastern terminus. Preliminary data demonstrate that terrace age increases with elevation yielding an uplift rate of 0.5-1.0 mm/yr. Geometric constraints on the thrusts coupled with these uplift rates imply that the central part of the Tang He Nan Shan is being uplifted at a rate of 2.5 mm/yr. This rate predicts initiation of uplift in the Tang He Nan Shan 5 million years ago, an event that would transform the Qaidam Basin into a closed drainage at that time. This prediction is consistent with a dramatic increase in sedimentation rates in the Qaidam Basin at 5 Ma.

Along its western segment the ATF bifurcates with the main branch of the fault turning to the north (the Karakax Valley segment) and smaller branches continuing to the southwest. We obtained an age of ca. 6 Ka for a riser offset by 140 m yielding a slip-rate of ~2 cm/yr for the Karakax Valley segment. Due to the western bifurcation of the ATF, the rate on the Karakax Valley segment sets a minimum rate for the central segment of the fault which, for rigid block kinematics, must accommodate the lateral components on both the Karakax Valley plus the segments to the south.

One of the fundamental results of this ongoing investigation is that the high slip rates we have determined are consistent with kinematic models which assert that a large fraction of Indo-Asian convergence is accommodated by translation and rotation of rigid blocks, rather than by homogeneously distributed diffuse deformation of the Asian lithosphere. Similarly, the high slip-rates we find imply that the ATF is responsible for the eastward extrusion of Tibet, which is in turn accommodated by crustal shortening along its eastern boundary causing pro-

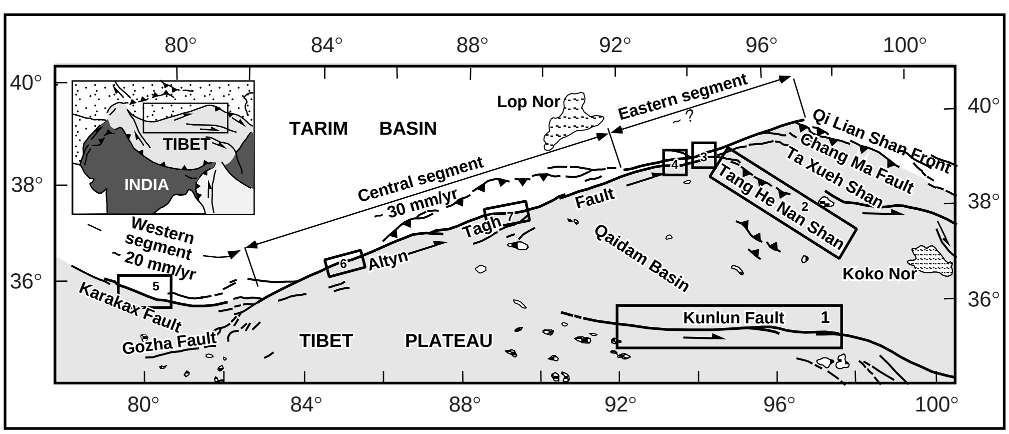

Generalized tectonic map of northern Tibet (area shown in box on inset map of Asia) indicating the areas under investigation in this project. We are attempting to determine rates of strike-slip movement along the Kunlun Fault (1), and the Aksay (3), Subei (4), Karakax Valley (5), Tura (6) and Shur Kholi (7) segments of the Altyn Tagh fault and uplift along the borders of the Tang He Nan Shan (2).

Investigations of Paleoclimate Variations using Accelerator Mass Spectrometry

J. R. Southon, M. Kashgarian, T. A. Brown
97-ERI-009

In this project, we seek to understand mechanisms of climate change on time scales of centuries to millennia, through studies of paleoclimate records in the north Pacific and western North America and through correlations with other records, such as ice cores. We use accelerator mass spectrometry (AMS) ^{14}C measurements to provide chronologies for climate change, and radiocarbon acts as a tracer for the carbon cycle of the past. The ultimate aim is to provide paleoclimate data and overall insights into how climate and the carbon cycle operate, for testing and improving climate models and for enhancing predictive capabilities for climate change.

We have used ^{14}C measurements on marine organisms in annually layered anoxic sediments from the Santa Barbara Basin off Southern California to show that the apparent age of the surface ocean—an index of deep-water upwelling—has decreased over the past 2000 years. The challenge now is to determine if correlated changes appeared elsewhere on the west coast of North America. In FY98, we worked on improving the resolution of the records we are building of ocean-atmosphere radiocarbon differences off British Columbia by dating paired wood and shell from archaeological sites. We also began measurements on a new laminated sediment core taken off Vancouver Island.

We are studying the timing and extent of severe drought events in the Californian Sierra, in the Sand Hills of Nebraska, and in Patagonia, Argentina to investigate possible episodes of widespread dry conditions and to study whether these events are correlated with ocean circulation changes. Through precise dating, we have established the most severe drought in the Californian Sierra in the past 2000 years lasted for at least 170 years and ended in 1240 AD (± 10 years 1σ confidence interval). In FY98, initial dating of materials from the Nebraska Sand Hills suggested that periods of significant dryness in the region were coincident with the drought periods in the Californian Sierra. We obtained first sets of samples from Patagonia under a National Science Foundation grant to a collaborator.

The ^{14}C age differences between surface- and bottom-dwelling marine organisms preserved in ocean sediments provide data on the apparent age of the bottom water relative to the surface ocean. We are measuring these age differences in north Pacific sediments to determine the origin and extent of a well-ventilated water mass ("young" in radiocarbon terms). This water mass existed at 500–1000 m off California during the late glacial period (an abrupt shift to present-day conditions occurred around 10,000 ^{14}C years Before Present). So far, we see no sign of this water mass in cores from the far northwest Pacific, the Bering Sea, the Sea of Okhotsk, or off Vancouver Island. A mid-Pacific source may be most likely.

We will continue to use AMS ^{14}C dates to establish high-resolution chronologies for lake core climate records from the western United States, and for correlation with records in Greenland ice cores and Santa Barbara Basin sediments. Work on Owens Lake, California was completed in FY98. We are currently developing climate records from a more northern site—Pyramid Lake, Nevada—in collaboration with researchers at the United States Geological Survey. In order to refine our AMS chronologies, we are measuring pollen separates in addition to total organic carbon in the sediments.

Since ^{14}C concentrations in the atmosphere have varied over time, a calibration curve is required to convert from radiocarbon to calendar ages (see figure). Such a curve is essential for a detailed picture of the last glacial-to-interglacial climate switch between 14500 and 11500 years ago—a change that is still not well understood. A detailed calibration data set based on ^{14}C dating of wood of known age (determined by tree ring counting) spans the past 11800 years. In FY97, we extended this back another 3000 years at 100-year resolution, by dating carbonate from marine organisms preserved in annually layered ocean sediments, and we related changes in the curve to variations in ocean circulation. In FY98, we began to study fine structure in the record by resampling the sediment cores with 3-fold improved resolution and reduced measurement uncertainties.

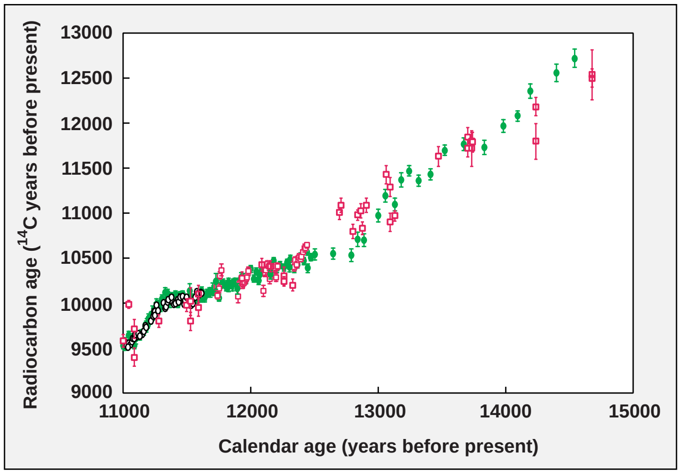

Radiocarbon calibration data (^{14}C dates on known-age materials) for the period of deglaciation. Wiggles in the curve show carbon cycle changes or variations in ^{14}C production due to changes in solar activity. Open circles (black) are tree rings dated by ring counting; open squares (red) are corals dated by U-Th; closed circles (green) are LLNL data: marine carbonate dated by counting annual sediment laminations.

Geologically Precise Hydrogeological Models Enhanced by Monte Carlo Inversion of Geophysical and Hydrological Data

S. F. Carle, A. L. Ramirez, W. D. Daily, R. L. Newmark, A. F. B. Tompson
98-ERD-005

Hydrogeological models inevitably overestimate the performance of groundwater-remediation systems primarily because subsurface permeability (*k*) distributions are more complex than anticipated. The National Ignition Facility (NIF) excavation at LLNL revealed a network of buried, high-*k* stream-channel and stream-flood facies (rock types) embedded in low-*k* flood-plain facies, indicating that an exhaustive characterization of subsurface heterogeneity would require a costly borehole spacing of 3 m or less. Yet, subsurface heterogeneity must be addressed in remediation design at LLNL and at other sites of environmental concern.

In this project, we are integrating three unique LLNL characterization capabilities—geostatistics; electrical resistance tomography (ERT); and the high-performance, finite-difference numerical-flow modeling code, ParFlow, that exploits parallel computing architecture—with the goal of developing more realistic and accurate models of subsurface heterogeneity.

Geostatistics is used to quantify spatial variability of geological facies between boreholes. Multiple, geologically plausible, and equally probable three-dimensional “realizations” are created, rather than one simplistic, manual, geological interpretation. A limitation is that the relative similarity between any single realization and the “truth” is unknown.

The second mode of characterization, ERT, images the subsurface distribution of electrical resistivity (ρ) from voltages induced by currents applied over an array of electrode pairs placed in boreholes. Advantages of using ERT are that ρ exhibits large contrasts that correlate with *k*, and far more points of measurement are obtained than from traditional hydraulic tests. The main limitation of ERT is that accuracy and resolution degrade with distance from the nearest borehole.

In this project, we are simultaneously addressing the limitations of the geostatistical and ERT methods. Figure 1 shows results of our FY98 work. Using 100 realizations of the distribution of *k* and ρ—one is shown in Fig. 1(a)—we generated 100 synthetic hydraulic and ERT data sets. Each set involves 70 ParFlow simulations over a 800,000+ cell finite-difference grid discretized at Δx, Δy, Δz = 0.4 m, 0.4 m, 0.3 m, respectively. The synthetic ERT data sets permitted us to compare inversions—one is shown in Fig. 1(b)—directly to the realizations representing the “truth,” so that we could evaluate ERT in a realistic setting. We assessed the feasibility of a Monte Carlo inversion approach by sequentially designating each realization as the “truth” and comparing the standard deviation (σ) of ERT responses with each of the remaining 99 realizations; this yields 4,950 pairs for comparison. Three realization pairs had $\sigma < 5$ mV; however, typical inversions of good-quality data have $\sigma < 1$ mV.

We concluded that a purely geostatistical Monte Carlo inversion approach is not practical simply because each realization is structurally unique and provides a distinct ERT response. This is good news for ERT—if multiple realizations satisfied the same ERT data, the conclusion could have been made that ERT is insensitive to intra-borehole heterogeneity.

In FY99, we will refine the Monte Carlo inversion technique by using ERT to influence generation of the geostatistical realizations. Then, we will calibrate ρ to geological facies and apply our methods to a remediation site near the NIF excavation. Finally, to speed up the inversion we will integrate calculation of the ERT voltage response by ParFlow into the ERT inversion code.

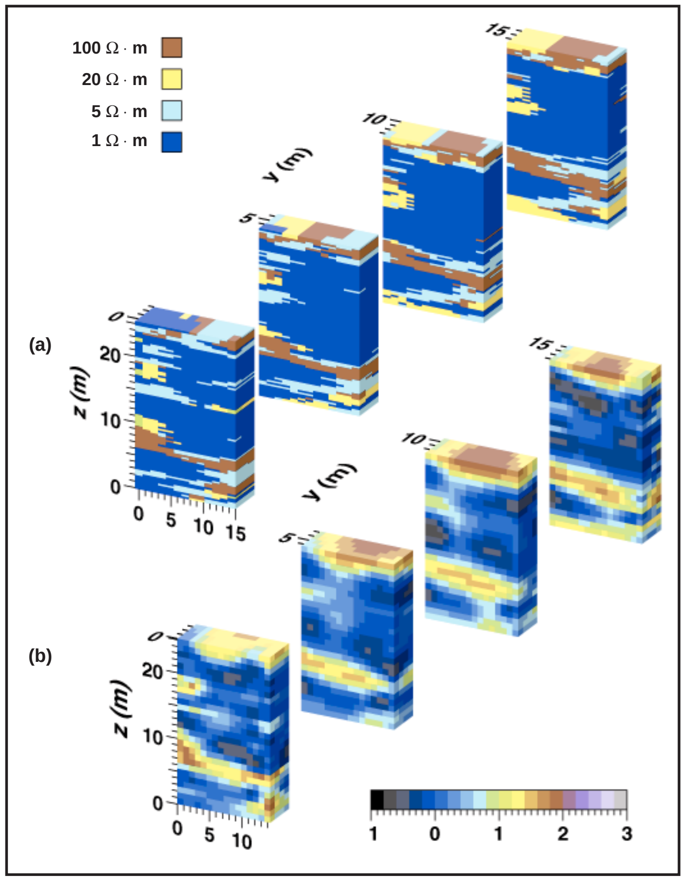

Figure 1. Results indicating that electrical resistance tomography (ERT) can successfully detect subsurface geologic facies architecture: (a) an exploded geostatistical realization of facies architecture beneath LLNL, with representative electrical resistivities assigned to each facies; and (b) an exploded three-dimensional electrical-resistivity tomograph obtained from inversion of synthetic ERT data generated by ParFlow for the realization in (a). The major heterogeneities evident in the realization (a) are detected by the ERT tomograph (b).

Detection of Anthropogenic Climate Change: A Modeling Study

P. B. Duffy
98-ERD-007

This project had two related areas of research: (1) simulating natural climatic variability using a global climatic model, and (2) preparing to use the resources of the Accelerated Strategic Computing Initiative (ASCI) Blue computer for specific problems in atmospheric science and climate.

Understanding natural climatic variability is central to knowing whether or not observed climatic changes result from human activities. Our goals here have been to evaluate (1) whether simulated natural climatic variability is highly sensitive to details of the model used to make the simulation, and (2) whether models can be improved so that the simulated variability agrees with observed variability. In FY98, we successfully parallelized two major components (the atmospheric and sea-ice modules) of the model to be used for this study. The model, developed by Andrew Weaver et al. at the University of Victoria, Canada, consists of (1) a three-dimensional oceanic general circulation model coupled to a dynamic/thermodynamic sea-ice model, and (2) a simplified, vertically integrated model of the atmosphere.

The philosophy behind using a model with a simplified representation of the atmosphere is that in “full” climatic models, the atmosphere takes most of the computer time. At the same time, climatic variability on the time scales we are interested in (decades to centuries) is thought to originate mainly in the ocean and sea ice. Thus, for this problem, a climatic model with a simplified representation of the atmosphere is a sensible choice. In addition, by improving the model’s physics (i.e., the coupling between the oceanic and sea-ice models), we obtained significant improvements in the model’s ability to simulate present-day climate.

Finally, we performed one complete and several partial 1000-year simulations of natural climatic variability using various configurations of the coupled ocean–atmosphere–sea-ice climatic model. Preliminary analysis of the results shows levels of simulated oceanic variability that are comparable to those found in previous model simulations (see figure).

The second area of research was chosen because the community’s ability to simulate climate and other problems in atmospheric science is limited by lack of computer resources. Applying LLNL’s best computational resources to simulations in atmospheric science and climate would give LLNL significant capabilities in these areas. We therefore investigated applying LLNL’s ASCI-related computational resources to a variety of problems in atmospheric and climatic simulation. Specifically, we investigated using LLNL’s ASCI Blue computer for simulating global and regional climate and the transport and fate of hazardous materials in the atmosphere. A major task was to parallelize the U.S. Navy’s Coupled Oceanic-Atmospheric Mesoscale Prediction System (COAMPS), a regional atmospheric model for simulating both regional climate and “transport and fate” of hazardous materials. In FY98, we reached a major milestone in this parallelization project: the successful testing of the model’s dynamics using multiple processors.

Another major task was to port two important global climatic models—the National Center for Atmospheric Research (NCAR) Community Climate Model (CCM3) atmospheric general circulation model and the Parallel Ocean Program (POP) oceanic general circulation model—to the ASCI Blue machine. We have completed this task; however, because of slow interprocessor communication, the parallel efficiency of these models when run with a large number of ASCI Blue processors is relatively poor. A planned system software upgrade should remedy this problem.

Finally, to assess the sensitivity of the results to the meteorological initial conditions used in the simulations, we performed groups of transport and fate simulations. We found that the predicted transport and fate of hazardous materials on the whole are more sensitive to other aspects of the model than to meteorological initial conditions.

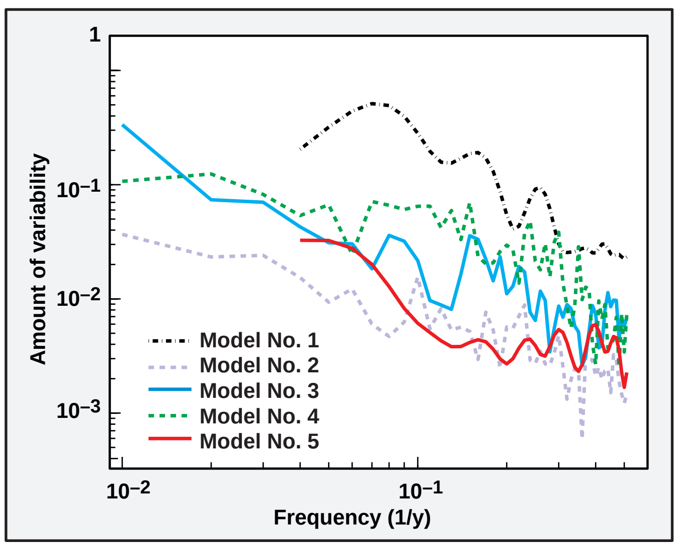

Power spectra of natural climatic variability, as simulated by several climatic models. The quantity being analyzed is global-mean surface air temperature. The results show variability as a function of frequency. Especially at low frequencies, different models predict very different amounts of variability.

A Study of the Basic Properties of Gas Hydrates and Kinetics of their Formation, with an Emphasis on Methane Clathrate

W. B. Durham, W. Zhang, S. H. Kirby, L. A. Stern, S. Circone
98-ERD-008

Gas hydrates (clathrates) are compounds with an ice-like crystalline framework that encages "guest" gas molecules, and methane clathrate is the most commonly occurring gas hydrate in nature. Although it has a number of potentially important applications related to its extraordinary properties and widespread presence in Earth's near-surface environment, methane hydrate has received only occasional and unsystematic laboratory investigation in the several decades since it was discovered. For example, methane hydrate is potentially an abundant source of clean energy, since there is more of it than all the oil, coal, and conventional gas in the world. However, it may be an environmental hazard for the same reason (greenhouse gases that could potentially be released). Also, it is a geological hazard because it can trigger huge undersea landslides and resultant tsunamis. Another clathrate, CO_2 hydrate, may not have direct importance as an energy resource, but it is closely related: it may prove to be a useful carbon-storage medium in the global carbon cycle.

Our work combines recent research breakthroughs with our current expertise and capabilities to advance our general knowledge of the synthesis, basic properties, and behavior of gas hydrates, in particular, of methane clathrate. Our improved understanding of this material will position the Laboratory to play a significant role in serving the nation's future environmental and energy needs.

During FY98, in our laboratory at LLNL and at the laboratory of our coinvestigators at the U.S. Geological Survey in Menlo Park, California, we achieved a number of "firsts."

In many hydrate deposits around the globe—such as in the Gulf of Mexico—the guest molecule is not simply methane, but is a mixture of methane with approximately 5% each of ethane and propane. In FY98, we synthesized pure methane–ethane–propane hydrate in bulk. The availability of this material in the laboratory in pure form complements the availability of pure methane hydrate for properties testing. We have also synthesized CO_2 hydrate, although not without some contamination from free water ice.

We also discovered anomalies in the manner in which methane hydrate breaks down to its components (water and methane gas) when heated. Methane hydrate is stable at elevated pressures and cool temperatures (such as in shallow oceanic sediments). If there is a possibility of exploiting hydrates as an energy resource, we obviously will have to deal with extracting gas molecules. Hydrates are stable at atmospheric pressure only at very cold temperatures, and we see hydrates break down quickly when we exceed about –70˚C at atmospheric pressure. We also see this behavior in the methane-ethane-propane hydrate described above. However, rapid depressurization from high pressure to one atmosphere at warmer temperatures (–40 to –3˚C) does not cause the material to dissociate immediately, even though this places the hydrate well outside its stability region. It can remain for many hours at these extreme metastable conditions, and it will not break down until heated to the ordinary melting point of water ice.

We built a pressure apparatus for measuring sonic-wave velocities in hydrates and successfully measured both shear and compressional wave velocities in the material as a function of porosity. These new experiments have several benefits for hydrates research. For instance, the wave velocities of the fully dense material allow immediate calculation of the elastic constants, which are required in almost any modeling of this material. Also, since velocities change with porosity, they allow us to monitor porosity changes during pressurization, thereby providing an important constraint on material strength.

We measured the ductile flow strength of methane hydrate at warm conditions; this was made possible with our newly developed apparatus. Once again, we see behavior that surprises us: methane hydrate at warm temperatures is much stronger than water ice. We had already found that at low temperatures methane hydrate and water ice have about the same creep strength. However, at temperatures above –30˚C, ice flows hundreds of times faster than hydrate under the same load.

At this point, we have only scratched the surface of research on the basic properties of gas hydrates. To measure—among other things—thermal and optical properties, solid-state diffusion, and the properties of mixtures of hydrates and sediment, we are developing further capabilities and are forming collaborations with other government laboratories and with universities. In FY99, major effort will continue on (1) studying mechanical strength, formation, and dissociation of methane hydrate as well as methane-ethane-propane hydrate and perhaps other hydrates and hydrate–sediment mixtures; and (2) development of hardware and measurement techniques for measuring the other properties mentioned above.

Martian Carbonates: Hot or Cold?

I. D. Hutcheon, A. J. R. Kent, R. J. Ryerson
98-ERD-042

The announcement by a group of NASA scientists in 1996 of fossil evidence of life in a martian meteorite caused a major stir in both scientific and non-scientific circles. Given the obvious scientific and cultural ramifications of such a discovery, scientists around the world have scrambled to test and assess the NASA group's conclusions. To date, numerous techniques have been used to investigate different aspects of the composition and formation of ALH 84001, the meteorite that hosts the putative fossil remnants. In particular, the carbonate minerals which host the microscopic, fossil-like structures have been subject to intense scrutiny. Much of this work has centered on the question of the temperature of formation of the carbonates. As terrestrial life is only viable over a relatively narrow and firmly established temperature range, ~0–150°C, knowledge of the formation temperature and thermal history of the carbonate minerals in ALH 84001 would provide a direct constraint on the possibility this meteorite hosts the fossil remains of ancient, martian biogenic activity.

One particularly elegant method by which the thermal history of these carbonate minerals can be investigated is to use the internal variations in the composition of the minerals themselves. Previous studies have shown that the carbonate minerals in ALH 84001 vary significantly in chemical composition over short distances—changes of up to 10% in the mole fraction of Ca, Fe, and Mg are apparent over distances of only 1–2 microns. Over time, diffusion will act to homogenize such chemical zoning and, since diffusion is a temperature-driven process, we can use diffusion models to constrain the thermal history of the carbonate minerals. The main requirement for this modeling is accurate cation diffusion coefficients in carbonate minerals of the same composition as those found in ALH 84001. Due to low diffusion rates at temperatures below ~500°C, these diffusivities cannot be measured with conventional techniques. This project utilizes LLNL's unique combination of expertise in experimental petrology and secondary ion microscopy (SIMS) to determine diffusivities for Sr, Fe, Ca, and Mg in several carbonate minerals. We use a simple powder-source technique in which carbonate or oxide powders of the appropriate composition are placed next to a cleaved fragment of carbonate mineral in a small platinum capsule. This assembly is then placed in an evacuated silica tube and heated in a furnace for times varying between 12 hours and 120 days. After annealing, the mineral fragment is retrieved and a secondary ion mass spectrometer used to measure the diffusion gradient (change in chemical composition) normal to the mineral surface. Because diffusion at these temperatures is slow, the chemical gradients are only a few tenths of a micrometer long and can only be measured with SIMS depth profiling techniques developed at LLNL.

In FY98, we have measured the diffusion rates of Sr and Mg in calcite for temperatures between 400 – 600°C. In this temperature regime, the diffusivity of Mg in calcite is characterized by an activation energy of 134 kJ/mol and a pre-exponential factor of 1.4×10^{-15} m^2/s. These initial results indicate that at temperatures greater than 300°C, diffusion would homogenize the compositional variations evident in the ALH 84001 carbonates within periods of 100–1000 years. The carbonate minerals in ALH 84001 are thus unlikely to have experienced temperatures above ~300°C for any significant period of time after their formation and, if carbonates formed at high temperatures, they must have cooled very rapidly to low temperature.

Based on work in FY98, our first year of funding, an abstract was submitted to the Fall meeting of the American Geophysical Union. In FY99, we plan to measure the rates of Ca and Fe diffusion in magnesite, another carbonate mineral found in ALH 84001. As magnesite is unstable at relatively low pressures (i.e., 1 atmosphere), this will be done using a piston cylinder apparatus, a method for subjecting samples to high-pressures during heating. By the end of FY99, we will have determined a full suite of cation diffusivities for the major carbonate minerals in ALH 84001 and will have developed the first model-independent constraints on the thermal history of ALH 84001. These data are essential to evaluating the hypothesis that life existed on an ancient, wet Mars and will make a major contribution to the "Life on Mars" story. This work is closely related to on-going, NASA-supported studies of primitive meteorites in the Isotope Sciences Division and has provided the basis for a new proposal to DOE's Office of Basic Energy Sciences to investigate trace element fluid-mineral partitioning and diffusion in terrestrial carbonate minerals.

Diagnostics Systems Approach to Watershed Management

M. L. Davisson, J. E. Moran, C. Koester, G. B. Hudson
98-ERD-046

Due to unregulated land use and development in watersheds, non-point source pollution (NPSP) has become the largest drinking water quality problem in the U.S. today. Agricultural activities, sewage discharge, urban/industrial runoff, and habitat change adversely affect the potability of rivers, streams, and shallow groundwater. For example, total organic carbon (TOC) in raw drinking water, which forms halogenated carcinogens during chlorination, rises with increasing land use. Another example is the recent incorporation of methyl-tert-butyl ether (MTBE) as a gasoline additive, which is slow to degrade and has been shown to accumulate in raw drinking water supplies of California. Currently, drinking water regulations are implemented only on the user end; therefore, water treatment facilities face enormous energy, time, and technological development costs to meet federal regulations. Alternatively, management of the watershed instead is a newly recognized method for regulating water quality at the source end. However, by its very nature, sources of NPSP are difficult to diagnose with traditional water quality investigations, limiting the effectiveness of watershed management strategies.

Isotopic and low-level abundance measurements offer a potentially new tool for delineating sources of NPSP. Natural isotopic abundances of dissolved and suspended constituents in surface and groundwater are intrinsic to their geographic origins and the process of their generation. In addition, accurate measurement of water-quality parameters below drinking water limits provides a basis for discerning contaminant generation and removal.

In utilizing these isotopic and geochemical measurements, the goal of this project is to develop and demonstrate new measurement and investigative approaches in environmental studies of surface water and groundwater. The particular focus is to relate our results to contaminant transport and their applicability to DOE programs and watershed management agencies and consortia.

We have developed measuring techniques and have conducted preliminary investigations of surface water and shallow groundwater environments affected by typical NPSPs. For example, we have developed isotopic measurement techniques for TOC in drinking water. We use ^{13}C and ^{14}C to delineate respectively, the source and mean age of the TOC. Our preliminary results show that isotopic abundances of TOC during spring runoff in the lower Missouri River watershed reflect agricultural sources, while during the winter, the isotopic abundance of the TOC reflects sources from more alpine regions. We have also shown isotopically that dissolved TOC is different from TOC sorbed to suspended sediments in the water column. These results demonstrate that both short and long-range transport of TOC occurs in this large river.

We have also shown in rivers flowing into the southern Sacramento-San Joaquin Delta of California that bromide concentrations reflect sources of salt not related to seawater intrusion, as believed by conventional wisdom. The bromide to chloride ratios indicate an additional salt source with abnormally high bromide levels. Our current investigations are focusing on the agricultural insecticide methyl-bromide as a potential source. Additional evidence for agricultural sources of salts in the Delta is shown by high iodine, uranium, and nitrate concentrations in the same samples.

As another example, a technique was developed using gas chromatography mass spectrometry to detect MTBE down to 15 parts per trillion. MTBE is an additive recently introduced into all gasoline in California. It has been measured as only a point source in several locations in California at a detection limit of 1 part per billion. With our low-level technique, we have observed MTBE from less than 15 to greater than 2000 parts per trillion in over 30 surface water and shallow groundwaters sampled. Its ubiquitous low-level occurrence in drinking water supplies demonstrates MTBE is an NPSP and not related to point sources. We also have shown that it typically occurs at higher levels for surface waters impacted by urban/industrial runoff.

Work for FY99 will focus on mechanisms of NPSP generation. In particular, TOC will be separated in humic and non-humic fractions in order to determine if isotopic variability is also the same in the most refractory parts of the TOC (i.e., humics). There will also be a focus on the source and residence times of salts in watershed soils using a combination of trace metal, anion, ^{36}Cl, and ^{129}I abundances.

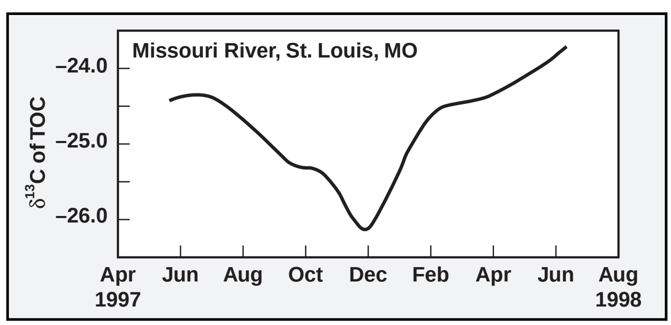

The Missouri River is at high stage in the spring and early summer in St. Louis, and at low stage in late fall and early winter. The $\delta^{13}C$ of TOC correlates with the river height, having low values during low stages and high values at high stages. The change in $\delta^{13}C$ is due to mostly alpine TOC sources (most distal) during low stage, whereas during high stage TOC has more local sources dominated by agricultural areas.

Seasonal-to-Decadal Variability in Pacific Circulation using $\Delta^{14}C$ in Corals

M. Kashgarian, T. P. Guilderson
98-ERI-002

The western tropical Pacific has the highest mean sea-surface temperature; therefore, it plays an important role in the Earth's climatic system. One important feature of Pacific climate is the El Niño–Southern Oscillation (ENSO); these variations in the shallow Pacific circulation and concurrent atmospheric variations are two characteristics of decadal climatic variability in the Northern Hemisphere. Competing explanations are that it is (1) driven by a temperature-anomaly pattern propagated around the subtropical gyre, or (2) initiated by the ventilation of the Pacific thermocline. The latter has been implicated as the moderator of CO_2-induced warming. If changes in oceanic circulation and water-mass distribution are involved in the genesis and evolution of ENSO and decadal climatic variability, we must understand how the circulation varies with other climatological variables—this requires records several decades in length. Such records do not exist—the technologies for continuously monitoring oceanic currents only recently became available. However, geochemical tracers in coral samples taken at small increments parallel to the coral's axis of growth can provide a time series of seawater composition at bimonthly or better resolution. For measuring these tracers in coral samples, we are using LLNL's high-precision accelerator mass spectrometer (AMS). The resultant $\Delta^{14}C$ time series provides information about the shallow circulation of the Pacific that can be used to document circulation, test parameterization of oceanic dynamics in models that contain ^{14}C as a passive advective tracer, and validate the ocean's uptake of fossil-fuel CO_2 in coupled ocean–atmosphere models.

In FY98, we generated $\Delta^{14}C$ records from coral samples recovered from Nauru (166˚E 0.5˚S), Guadalcanal (160˚E, 9˚S), and the Galápagos Archipelago (90˚W, 0˚) [Fig. 1(a)]. We could thus monitor the source regions of upwelling in the eastern Pacific and water transport across the Pacific basin. Our data [Fig. 1(b)] show the long-term increase in $\Delta^{14}C$ (reflecting oceanic uptake of bomb-derived ^{14}C) and the high-amplitude, seasonal-to-interannual variations associated with ENSO. At Nauru and Guadalcanal, these variations reflect the cross-basin advection of surface waters in the tropical Pacific; at the Galápagos, the $\Delta^{14}C$ record reflects variations in upwelling intensity and thermocline dynamics. The interannual redistribution of Pacific surface waters is reflected in the Nauru $\Delta^{14}C$ record because of the large gradient in $\Delta^{14}C$ between subtropical surface waters as documented at French Frigate Shoals and Fiji and by the waters upwelling in the eastern Pacific. A conceptual model of this process can be described as follows: The physical manifestations of ENSO (decreased upwelling—less low-^{14}C water—and weaker easterly trade winds) allow waters of subtropical origin (high-^{14}C water) to directly infiltrate the western Pacific. In non-ENSO years, stronger trade winds cause (1) more upwelling and perhaps water from a deeper level (low-^{14}C water), and (2) rapid transequatorial transport. These results illustrate the dynamic behavior of ^{14}C in the surface ocean and the utility of such time series for studying oceanic circulation over decadal and longer time scales.

In FY99, we will extend these records into the prebomb interval and develop records from new sites in order to (1) further constrain Pacific circulation, and (2) examine the exchange of surface water between the Pacific and Indian Oceans.

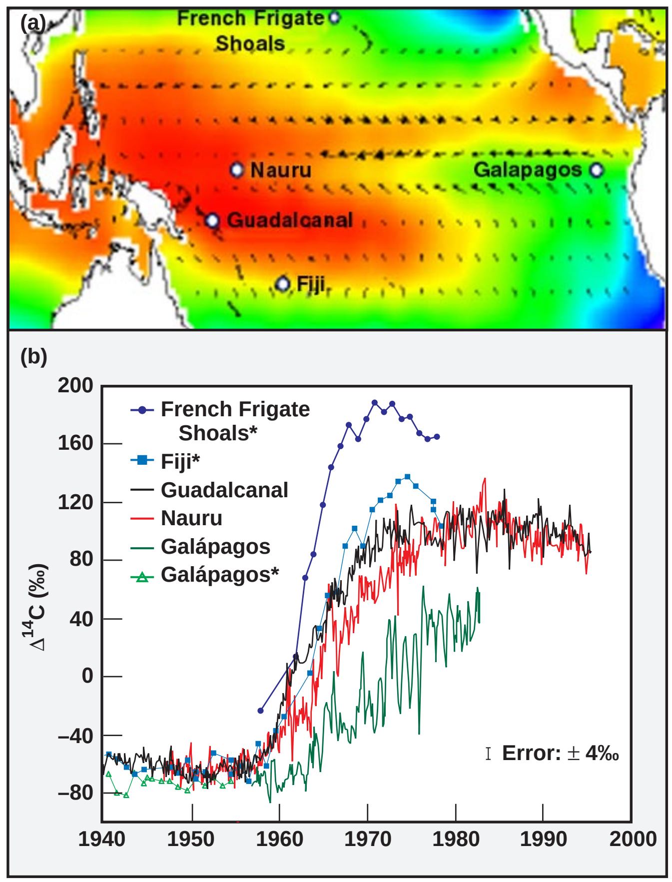

Sources of Pacific corals (a) and results (b) of radiocarbon (^{14}C) time series based on measurements of these corals. Vectors in (a) represent the mean annual surface currents; colors indicate surface temperatures—warmer (red) and cooler (blue). The ^{14}C time series in (b) reflects ocean dynamics (subannual to decadal variability) and the oceanic uptake of bomb radiocarbon (long-term trend). Besides our new, high-resolution records, we include annual and bi-annual data (*) for French Frigate Shoals and the Galápagos (Druffel, 1989), and Fiji (Toggweiler, 1991). The redistribution of surface waters in the western Pacific associated with the El Niño-Southern Oscillation (ENSO) is documented by the large 50 to 80‰ variations in 1965/66 and in 1972/73 in the Nauru record.

Assessing Changes in Solar Activity using Cosmogenic Radionuclides

R. C. Finkel, M. W. Caffee
98-ERI-013

We are engaged in an effort to measure and interpret a high-resolution time series of ^{10}Be and ^{36}Cl in ice cores from Greenland and the Antarctic to test the hypothesis that changes in solar activity influence terrestrial climate. Although it is clear that the sun is the driving force for climate, it is less clear whether changes in solar output play a role in climatic change. Reliable prediction of climatic change requires an assessment of the possible effects of solar luminosity on climate. However, direct measurements of solar output have been made only during the last 20 years. Although numerous publications have shown the plausibility of a connection between solar variability and climatic change, the brevity of direct observations has hindered investigations of the role the sun might play in controlling climate. By developing a time series of solar activity that extends back beyond the era of instrumental measurements, we propose to test this hypothesis in a quantitative way.

To determine solar irradiance before the era of instrumental observations, one must use a proxy for solar luminosity. Our method is as follows: Satellite data show that solar irradiance and the cosmic-ray flux at the Earth are correlated. This is not surprising because changes in solar irradiance and magnetic activity are related to underlying solar-transport properties. The intensity of the solar magnetic field affects the ability of galactic cosmic rays to penetrate the solar system to the orbital distance of the Earth. Concentrations of cosmogenic radionuclides in polar ice cores change with the cosmic-ray flux in the Earth's atmosphere and therefore—through the magnetic-field connection—with solar activity. Nuclide concentrations can thus be used as a proxy to extend the solar-activity record to periods before recorded observations. In fact, earlier measurements from the ice core taken from the GISP2 (Greenland Ice Sheet Project 2) site in central Greenland have shown that during the Maunder Minimum (1645–1715 AD), a period of quiet sun when there were almost no sunspots and of cold climate in Europe and North America, the ^{10}Be concentration was substantially higher than during other periods.

We are using ^{10}Be and ^{36}Cl in polar ice cores as well as published ^{14}C concentrations in tree rings to determine the history of solar irradiance throughout the Holocene, the period since the retreat of the great continental ice sheets. The comparison of ice-core results with those from tree rings will help detect and eliminate perturbing factors other than solar luminosity, such as changes in atmospheric mixing or in oceanic circulation, which might also change concentrations of atmospheric nuclides. Our measurements of the GISP2 ice core during FY98 have shown a good correlation between the main short-term variations of the ^{10}Be and ^{36}Cl record in ice and the ^{14}C record in tree rings between the end of the last glacial period and about 1000 years ago. Part of this record is shown in the figure. These data strongly support the explanation that solar modulation of the galactic cosmic-ray flux is primarily responsible for these fluctuations. During FY99, we will measure a higher-resolution record for the last 1000 years in both Greenland and the Antarctic in order to extend this comparison.

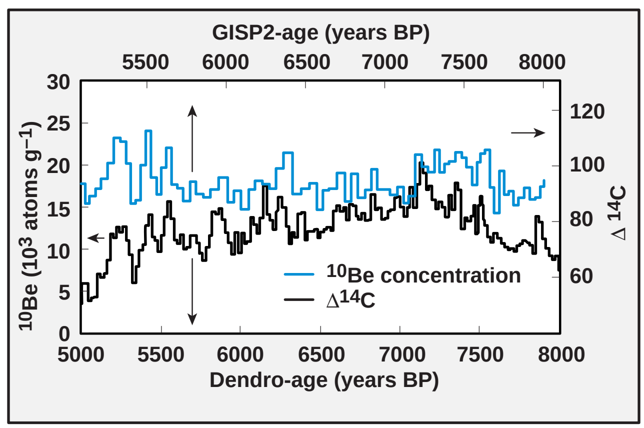

Comparison of ^{10}Be (this work) with bidecadal ^{14}C in tree rings (Stuiver & Braziunas, 1988) demonstrates that solar changes are primarily responsible for fluctuations in nuclide concentrations. Ages are shown in years before the present (BP).

Three-Dimensional Simulations of Scenario Earthquakes along the Hayward Fault

S. C. Larsen, D. Dreger, M. Antolik, C. Stidham
98-LW-028

The Hayward fault runs through some of the most densely populated regions of the San Francisco Bay Area, and is expected to experience a Richter magnitude 6.8 to 7.5 earthquake within the next 30 years. It is estimated that such an earthquake will cause 1,000 to 10,000 fatalities and $50B to $500B in damage. Regions where high-amplitude seismic ground motion is expected must be identified so that appropriate engineering improvements can be made.

The goal of this project is to determine the geographical distribution of high-amplitude seismic ground motion in the Bay Area. To do this, we are combining the seismic ground motions predicted from three-dimensional (3D) simulations of scenario earthquakes along regional faults—with emphasis on the Hayward fault—with a 3D geological model of the Bay Area developed at the University of California, Berkeley. The simulations are computed using E3D, an LLNL-developed, sophisticated, 3D seismic-wave-propagation code that is implemented on high-performance and massively parallel computers.

In FY98, our 3D geological model was updated to include additional sedimentary basins and regions of low seismic velocity. We assessed realistic fault-rupture parameters for the Hayward and other faults and developed algorithms to incorporate complex fault-rupture patterns into the E3D seismic-modeling code. The 3D geological model, fault-rupture parameters, and E3D code were validated by comparing ground motions observed during the 1989 Loma Prieta earthquake with ground motions predicted from 3D simulations of this event. An excellent agreement was obtained. This suggests that 3D seismic modeling is a reliable method for predicting strong ground motion.

We then performed 3D simulations of magnitude 6.9 to 7.3 scenario earthquakes along the Hayward fault. In particular, we simulated south-to-north, north-to-south, and bilaterally propagating ruptures. The figure shows our results for a simulated magnitude 7.1 scenario earthquake. In addition, we completed preliminary simulations of scenario earthquakes along the San Andreas and Rogers Creek faults. These simulations reveal a complex pattern of strong ground motion throughout the Bay Area, with heavy shaking expected in the San Pablo Basin, Santa Clara Valley, and Livermore Valley. In addition, an earthquake along the peninsula segment of the San Andreas fault may be more damaging than expected because the geological structure causes seismic energy to be refocused back into the Bay Area. We also incorporated computed ground motions for two Hayward fault scenario events into a structural model of the San Francisco Bay Bridge. Preliminary analysis indicates that the Bay Bridge may be seriously affected by a large earthquake along the Hayward fault.

The 3D seismic-modeling techniques used in this study are gaining acceptance inside and outside the Laboratory. For example, we are participating in collaborative efforts with outside organizations to investigate seismic hazard in the Santa Clara Valley. The parallel-processing capabilities in E3D and the Laboratory's high-performance computers allow us to perform the largest and most sophisticated simulations in the world.

In FY99, we will (1) simulate a suite of earthquakes for the Hayward and other Bay Area faults, (2) investigate the effect of seismic attenuation on strong ground motions, (3) integrate ground motions with a structural model of the Bay Bridge, and (4) perform a regional hazard analysis of the Bay Area.

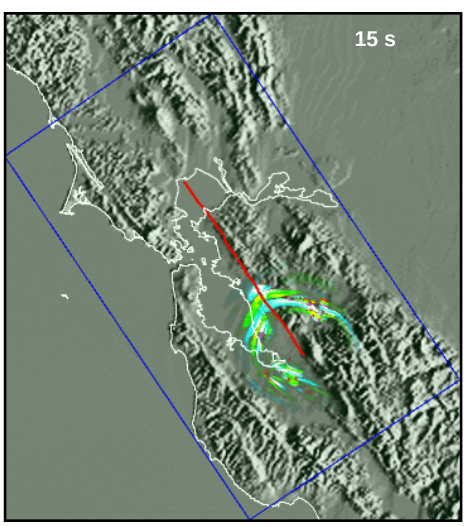

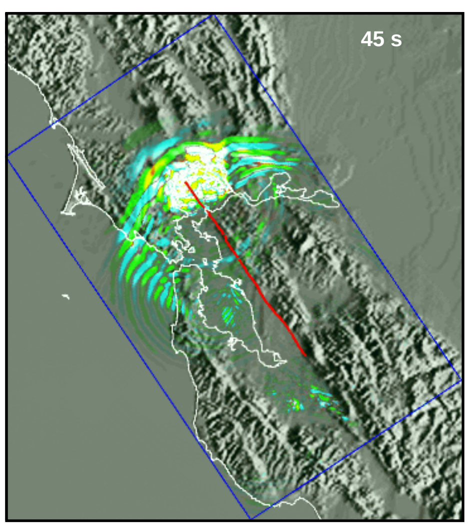

Seismic ground-motion intensity maps for a simulated magnitude 7.1 scenario earthquake along the Hayward fault (in red) at 15 and 45 s after the earthquake initiates. The rupture propagates from the southeast to the northwest. The strongest ground shaking for this scenario earthquake occurs in the San Pablo Basin.

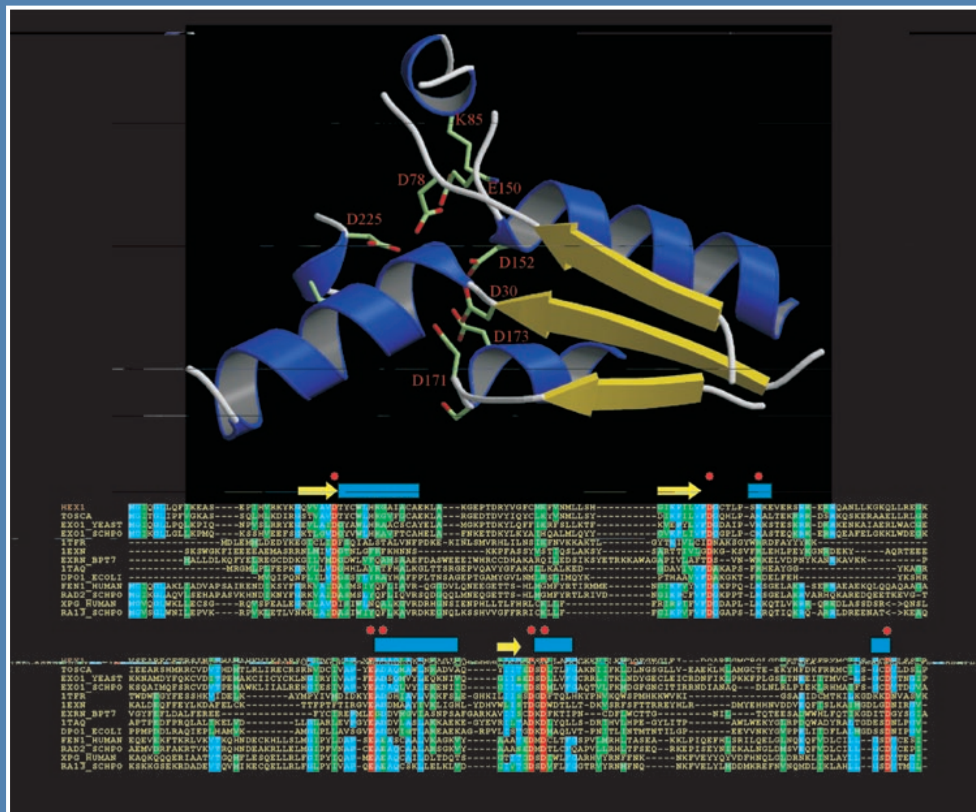

3

Biotechnology and Health Care Technologies

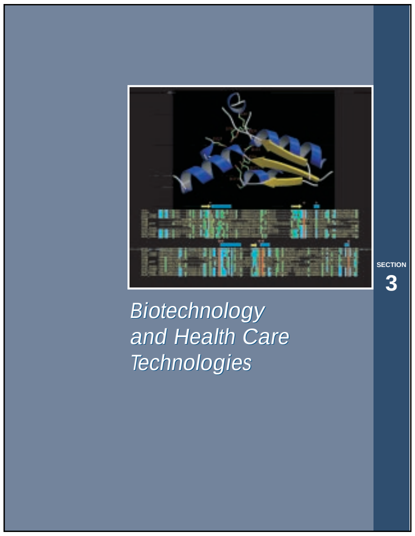

About the preceeding page

Functional Characterization of DNA Repair Proteins. Recently, David M. Wilson III and colleagues reported the identification and initial characterization of a newly identified human exonuclease, *HEX1*. This protein maintains homology to the nuclease elements of the RAD2 family, a group of proteins that includes the structure-specific endonucleases XPG and Fen1. The 5′ to 3′ exonuclease activity of HEX1 reported, in combination with studies performed in yeast and *Drosophila*, suggests that the human protein likely functions in aspects of recombination and/or mismatch repair. Identification of HEX1 denotes an important step towards defining the contribution of mammalian nucleases to such processes and towards determining the relationship of these factors to human disease. This work was reported in *Nucleic Acids Research* (**26**: 3762–3768, 1998) and was featured on the issue’s cover. For additional details, see page 3-5.

PEREGRINE Radiation Therapy Dose Calculations for the 21st Century

C. Hartmann-Siantar, P. Bergstrom, L. Cox, T. Daly, D. Fujino, D. Garrett, B. Guidry, R. House, D. Jong, S. May, E. Moses, R. Patterson, C. Powell, A. Schach von Wittenau, R. Walling
96-DI-006

Radiation therapy is used on more than 700,000 people every year in the U.S. alone. For these patients, survival depends on the physician's ability to target their tumors with a curative dose and to avoid injuring normal tissues. Because the effects of radiation therapy cannot be clinically determined until after the treatment has been delivered, computer-aided treatment planning is a critical part of the treatment process. PEREGRINE enables precision radiation-beam targeting by providing high-accuracy, three-dimensional (3D) Monte Carlo dose calculations. In collaborations with several cancer-treatment centers, we have shown that PEREGRINE dose calculations produce clinically important results for prostate, breast, head and neck, and lung cancer.

The PEREGRINE dose-calculation system is the first tool to provide accurate, 3D Monte Carlo dose calculations that are fast enough and economical enough to use in planning routine treatments for patients requiring radiation therapy. With the patient's computed tomography (CT) scan as input, PEREGRINE simulates, in detail, the important physical processes using a 3D Monte Carlo transport code tailored for radiotherapy applications. Using the atomic and nuclear cross sections from the Laboratory's extensive databases, PEREGRINE calculates the exact distribution of absorbed dose in the patient. Operating on hardware that costs less than $50,000, PEREGRINE can complete a full dose calculation in approximately 15 minutes.

In FY98, we validated PEREGRINE's accuracy by comparing PEREGRINE-calculated dose distributions with more than 1,200 independent dose measurements made by the University of California, San Francisco, and the Medical College of Virginia. In addition, we worked with these institutions to demonstrate the clinical importance of PEREGRINE Monte Carlo dose calculations for lung, head and neck, breast, and prostate cancer. The figure shown below demonstrates how PEREGRINE predicts a significantly different dose distribution than less-accurate conventional methods for a standard prostate cancer treatment configuration.

During FY98, we also demonstrated a manufacturing prototype of the PEREGRINE Dose Calculation Engine by computing over 5 TeraHistories. (A "history" represents a microscopic radiation particle that travels through the patient.) This represents a greater than 10,000 times (speed) improvement over the calculation times required at the beginning of this project.

In addition, we began collaboration with Harvard University and the University of Wisconsin on the use of PEREGRINE for planning proton- and neutron-radiation treatments. In addition, we demonstrated proof-of-principle calculations for Monte Carlo-based planning for automatic treatments that would best meet physicians' goals.

Other activities during the year included filing one patent and two patent disclosures covering software algorithms for Monte Carlo dose calculations, attending several important conferences (including the American Association of Physicists in Medicine and the American Society of Therapeutic Radiation Oncologists), and initiating several papers on transport algorithms, variance reduction methods, validation and verification, clinical treatment strategies, and code/platform design to refereed journals. At both of the mentioned conferences, we had well-attended educational booths and presented multiple papers and poster sessions.

By deploying PEREGRINE, the radiation-oncology community will dramatically improve the accuracy of treatment planning for radiation therapy. Negotiations with commercial vendors are currently under way to facilitate the ubiquitous distribution of PEREGRINE.

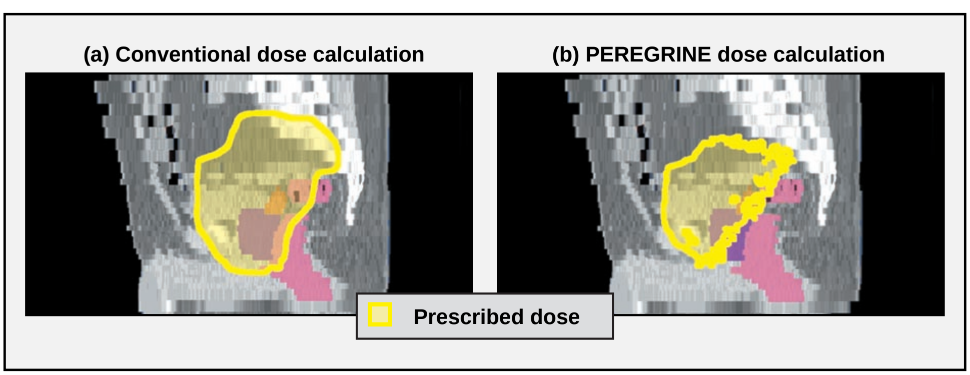

Side views of a prostate cancer patient's pelvis, demonstrating how the more accurate PEREGRINE dose calculations predict a significantly different dose distribution than that predicted by conventional methods. For the conventional calculations, (a), the prostate (purple) and much of the rectum (pink) are shown as targeted with the prescribed radiation dose. In (b), however, PEREGRINE reveals that much of the rectum and posterior prostate were not treated with doses at or above the dose prescription.

High-Resolution Structure Determination and Computational Modeling of Protein and Damaged Nucleic Acids

R. L. Balhorn, J. S. Felton

96-DI-010

A knowledge of the structure of macromolecules, such as proteins and DNA, is critical for a mechanistic understanding of cell function and the molecular defects that lead to cancer and other diseases. The goal of this project is to use structural methods such as x-ray diffraction, nuclear magnetic resonance (NMR) spectroscopy, and computer modeling to determine the structure of macromolecules important to human health and to better understand the interactions that occur between them. Our research focuses on several different problems including (1) identifying how chemical mutagens damage and perturb the structure and function of DNA, (2) characterizing the structure of proteins that synthesize and repair DNA, (3) identifying how genetic changes in DNA coding for proteins involved in lipid metabolism relate to cardiovascular and neurogenerative diseases, (4) determining the structure and mechanism of action of biological toxins related to biological warfare (BW), and (5) predicting protein structure from DNA sequence information. The results provided by these studies will help us identify molecular defects that lead to disease and understand why particular individuals are susceptible to cancer and other diseases. The structural information we obtain about bacterial toxins will play an important role in the development of vaccines, detection systems, and other countermeasures for dealing with exposures to BW agents.

To date, we have over-expressed genes in bacteria (*E. coli*) and insect cells (baculovirus) to provide proteins for structural analysis by x-ray diffraction and NMR spectroscopy. We have examined nine proteins related to DNA repair, including the domain (portion) of the protein XPA that specifically binds DNA. This protein is thought to be responsible for recognizing DNA damage and recruiting the other proteins needed to repair the DNA molecule and to restore it to its original, undamaged state. This work is providing the information we need to understand in a dynamic sense how proteins in the repair complex interact with DNA and function together to excise the damage and repair the gap.

The protein toxin studies have focused on crystallizing the targeting domain of tetanus toxin (the part of the protein that binds to motor neurons) and determining its structure by x-ray diffraction. Using cryo-cooling, the 3D structure of this part of the toxin was determined at high resolution (1.56Å). As shown in the figure, the crystal structure revealed that this domain contains two structural subdomains: one containing the C-terminal part of the protein that binds to and interacts with branched carbohydrates distributed on the surface of the cell (the extracellular portion of gangliosides) and a second domain of unknown function.

Using the atomic coordinates for the protein obtained from the crystal structure, computational methods were also used to model the corresponding domains for six related (botulinum) toxins. While the models have revealed that the basic structure of these domains must be very similar, evidence was also obtained to suggest that each protein might have sufficiently distinct surface structural differences that detection methods could be developed for discriminating among them. Using mass spectrometry, forty percent of the predicted ligands actually bound to the toxin, confirming the utility of this approach to aid the design of new drugs that block or minimize the effects of exposures.

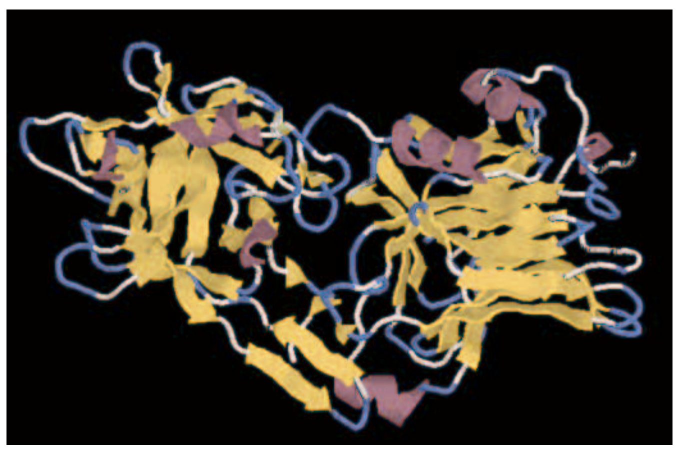

The crystal structure of the targeting domain (C-fragment) of tetanus toxin. This portion of the protein contains two distinct structural domains.

Challenges in Biotechnology at LLNL: From Genes to Proteins

J. S. Albala
96-ERD-076

The focus of this research effort has been to express and purify proteins of interest to the Biology and Biotechnology Research Program for functional studies and structural determination. Genes of high priority were selected at the onset of the effort. Several of the initial DNA repair genes selected for study have been isolated by the DNA Repair group at LLNL, including ERCC4, XRCC2, XRCC3, HEX1, and RAD51B. Additional repair genes selected include ERCC1, APN1, p53, and RAD51C. In FY97, baculoviral expression was optimized for the generation of recombinant viral constructs and subsequent protein expression in insect cells. In FY98, we focused on protein expression and purification of the selected cDNAs using an eukaryotic recombinant expression system. To date, we have obtained soluble protein from all ten recombinant baculoviral constructs expressed. These proteins are in various stages of purification, and much of FY98 focused on tailoring the purification scheme of individual proteins and the generation of larger quantities of these proteins for x-ray crystallography and nuclear magnetic resonance (NMR) analysis.

Unlike cDNAs, proteins are unique in composition and thus more difficult to study. The design of a relevant purification scheme for each individual recombinant protein was the challenge of the past year. Each recombinant protein produced in this expression system contains a six-amino-acid N-terminal histidine tag for purification by metal chelate affinity chromatography. This, however, proved to be only an initial purification step. Subsequent analysis included applying several different experimental conditions to obtain purified protein. The purification scheme for RAD51B has been particularly challenging as metal chelate affinity, ion exchange, and immunoaffinity chromotography have all been applied. The purification scheme for ERCC1 and RAD51B has been successfully completed, and scale-up is under way for structural analysis (see figure). Purification of the additional recombinant proteins will be pursued in collaboration with other members of the DNA repair group at LLNL.

We have continued our efforts to understand the function of the novel DNA repair protein, RAD51B. This work has resulted in two publications to date: Albala et al., “Identification of a novel human RAD51 homolog, RAD51B,” *Genomics*, 1997 and Dosanjh et al., “Isolation and characterization of RAD51C, a new human member of the RAD51 family of related genes, including two-hybrid interactions,” *Nucleic Acids Research*, 1998. A RAD51B-specific polyclonal antibody has been produced that can detect the recombinant protein produced in insect cells. Current efforts are focused on the biochemical characterization of RAD51B with its putative functional partner, RAD51C, by co-immunoprecipitation. Sequence homology suggests that RAD51B has a functional relationship with the RAD51 family of proteins. Recent discoveries define relationships between RAD51 and several tumor suppressor gene products, p53, BRCA1, and BRCA2. Initial studies have shown that RAD51B expression is down-regulated in a malignant breast cancer cell line. Future studies are aimed at the identification of a possible biological role of RAD51B in breast carcinogenesis.

The RAD51B gene has been isolated and initial sequencing has demonstrated that the 3' end of the gene is comprised of three exons including one that is an alternative splice variant. Completion of the RAD51B gene sequence in ongoing. In collaboration with Dr. M. Takata (Kyoto University, Kyoto, Japan), a chicken B lymphocyte DT40 cell line has been generated that is missing the RAD51B gene. This RAD51B-DT40 cell line shows a dose-dependent enhanced sensitivity to gamma radiation. Transfection of the defective cell lines with the human RAD51B cDNA complements this defect. This RAD51B-DT40 cell line also exhibits an enhanced dose-dependent cisplatin sensitivity. These results suggest a role for RAD51B in DNA repair and maintenance of genome stability.

Using the technology of baculovirus expression, another project is currently under way to develop a high-throughput system to express and purify proteins from I. M. A. G. E. (Integrated Molecular Analysis of Genomes and their Expression) cDNAs clones to generate the “human proteome,” the protein complement of the human genome.

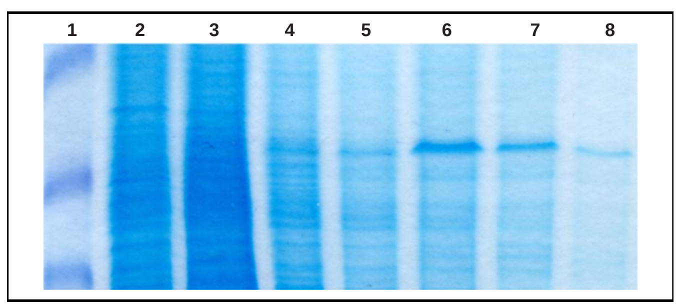

This gel shows the purification of the RAD51B protein from total insect cell lysate by metal chelate chromatography. A single band representing the RAD51B protein becomes apparent at 45 kDa as the protein is eluted from an affinity column. Lane 1: protein standards; Lane 2: total lysate; Lane 3: soluble fraction; Lane 4: fraction after column wash; Lanes 5–8: fractions after elution of the protein from the column.

Manipulation of Individual DNA Molecules Using Optical Traps: Application to Analysis of DNA–Protein Interactions

R. Balhorn, L. Brewer, M. Corzett
96-LW-045

Technical advances involving the use of focused lasers to construct optical traps have made it possible to isolate, manipulate, and perform physical measurements on single biological molecules. By combining optical traps with fluorescence microscopy, we can now design experiments that allow us to visualize and monitor changes in the interactions of proteins with individual DNA molecules. This project addresses several important areas of biological research that will benefit from the development of methods for analyzing individual molecules: DNA-sequence and DNA-damage recognition by proteins, protamine-induced coiling of DNA (torus formation), and studies involving stabilization energies associated with intermolecular interactions. We developed the instrumentation and methodologies required to isolate and manipulate individual DNA molecules on a routine basis. In addition, we demonstrated the utility of this new technology by performing a series of single-molecule experiments that characterize how proteins bind to and alter the structure or conformation of large segments of DNA.

During the first two years of this project, we constructed an infrared optical trap (see figure) and developed more efficient methods for attaching polystyrene spheres to one (monobell) or both ends of DNA molecules. Two different methods (end labeling with terminal transferase and oligonucleotide hybridization) were used to tag the DNA molecules with biotin or digoxygenin and attach them to spheres, and techniques were developed for assessing the efficiency of each step in the process. Using this approach, we determined that DNA molecules in excess of 300 kilobase pairs (~350 Kb was the largest size tested) could be isolated and manipulated without breakage.

To characterize the effects of proteins binding to single DNA molecules, we designed a miniflow cell that permitted the introduction of two sample streams. The DNA molecules are first introduced, then the protein. Binding experiments were initiated by using the optical trap to move a DNA molecule from one side of the cell across the interface into the stream containing protein. To obtain very sensitive measurements of bead displacement and forces exerted, we incorporated a quadrant detector in the imaging system.

In FY98, we used the optical trap and the flow cell to characterize the binding of the protein protamine and related peptides to DNA and monitored in real time their effect on the coiling of DNA into toroidal structures containing as much as 50 Kb of DNA. This process occurs in the testis as developing spermatids mature into sperm and is essential for male fertility; it is being considered for use by biotechnology companies to package DNA for use in gene therapy. We also began experiments to examine the movement of another DNA-binding protein, the helicase RecBCD, as it unwinds long stretches of duplex DNA. This enzyme plays a major role in DNA recombination and the repair of genetic damage.

Our studies provided new information about the kinetics and biophysics of protamine-induced torus formation that could not be obtained from experiments using bulk DNA in solution. Experiments using the peptide arg6 also identified how multiple arg6 DNA binding domains present in protamine molecules increase both the efficiency of torus forma-

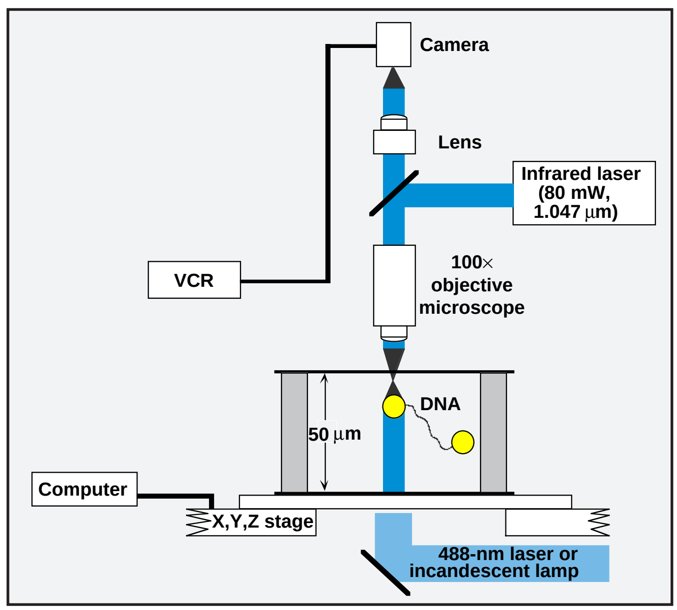

Equipment designed to enable our study of individual DNA molecules, including the infrared optical trap used to manipulate individual DNA molecules. The optical trap pulls the DNA molecule into the protein solution.

Functional Characterization of DNA Repair Proteins

D. M. Wilson III

97-ERD-002

Genetic material (DNA) is susceptible to spontaneous decay or to attack by environmental or food mutagens, or by reactive chemicals produced naturally in cells. DNA modifications can lead to permanent genetic changes that in turn can lead to human disease (e.g., cancer) or aging. To combat the deleterious effects of DNA damage, organisms are equipped with multiple DNA repair systems. The focus of our investigations has been to elucidate the molecular details of two critical DNA repair processes, namely Base Excision Repair (BER) and Recombinational Repair (RR). Our efforts involve a collection of molecular biology, biochemical, and structural biology approaches to determine the precise mechanism of damage recognition and to understand the repair process as a whole. These studies provide important insights into the relationship of DNA repair to human disease and may help develop more effective cancer treatment schemes.

Sites of base loss (or AP sites) in DNA are frequently formed mutagenic lesions that are corrected by a multistep pathway initiated by an AP endonuclease. In mammals, the predominant AP endonuclease is Ape1. Although many of the general properties of Ape1 have been elucidated, how this protein specifically targets abasic sites in DNA is not understood. In the past year, we have tested several models for site-specific recognition by Ape1 and recently presented a new recognition model for this enzyme based on our findings. We are now combining standard biochemical assays with x-ray crystallography, nuclear magnetic resonance (NMR), fluorescence spectroscopy, circular dichroism, and computational methods to better define those elements that influence recognition and catalysis and to characterize the molecular nature of the Ape1-DNA complex.

The most commonly employed repair process is likely BER, a pathway that corrects modifications that form either spontaneously or from attack of DNA by naturally produced reactive chemicals. BER involves the sequential activity of several repair proteins, which act in concert to remove and replace specific forms of DNA damage. To better understand this repair process and delineate the biological contributions of the various BER components, we have overexpressed and purified three central BER proteins—Ape1, Polβ, and Fen1—and have begun to reconstitute the repair pathway in collaboration with colleagues at LLNL and other institutions.

Free radicals, which are generated during normal oxygen metabolism or from exposure to agents such as ionizing radiation, attack chromosomal DNA to form oxidative DNA damages, most notably strand breaks harboring 3'-oxidative termini (3'-phosphate or 3'-phosphoglycolate). The repair of these 3'-damages, which pose both a cytotoxic and mutagenic threat, is not well understood. We are currently designing assays to identify repair factors that are involved in removing these obstructive 3'-ends and restoring DNA to its original state.

Genomic integrity is maintained by several DNA repair systems that often involve exo- or endonucleases for processing of chromosomal damage. We have identified a human gene, named HEX1 (for human exonuclease 1), that is homologous to *Saccharomyces cerevisiae* EXO1 (see figure). Based on its homology to this and other DNA repair proteins of the RAD2 family (a family of DNA nucleases), HEX1 likely functions as a nuclease in mismatch repair or recombination. We are presently working to define the biological role of HEX1 in mammals. Identification of this gene was recently reported by us and was featured on the cover of *Nucleic Acids Research*.

Finally, in collaboration with others at LLNL, we are screening for genetic variation in the human population in genes of BER and RR that leads to a reduced repair capacity and predisposes one to cancer development. Understanding the basic molecular and biochemical details and complex relationships within DNA repair in conjunction with gaining more information on the impact of genetic variation in the human population will be critical for addressing questions relating to human health and environmental exposures. Our efforts to unravel the molecular and biochemical details of damage recognition and processing and to understand the protective machinery of the cell will continue in FY99.

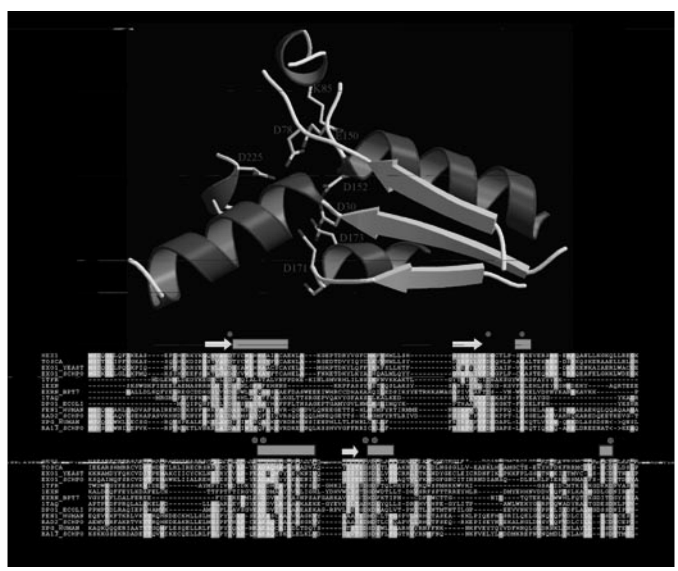

Identification and initial characterization of a new member of the RAD2 nuclease family, HEX1, was featured on the cover of *Nucleic Acids Research*. (See the Biotechnology and Health Care Technologies section page for additional information.)

Chemiluminescent Assay for Detecting Biological Warfare Agents

K. Langry, J. Horn, A. Jordan
97-ERD-008

The end of the Cold War ushered in a new threat to the U.S.—attack by terrorists or rogue nations with biological warfare (BW) agents. This threat was confirmed by Iraq's thriving biological weapons program. The World Trade Center bombing and the deliberate bacterial contamination of food in Oregon have shown that the U. S. is vulnerable to terrorism.

To counter these threats and mitigate the effects of an attack, new sensitive methods and instruments are required to detect BW agents in military and urban settings. We have developed a uniquely sensitive chemiluminescent assay for detecting biological agents. We use immunoanalytical techniques like those in biomedical research and home pregnancy testing; however, our assay uses two antibodies, each one specific to a different binding site on the surface of the agent. Each of the two groups of antibodies is labeled with one enzyme of a proximal enzyme pair such that when the two enzymes are in very close proximity, the product of one enzyme is used by the second enzyme to produce a signal indicating the presence of the agent. Only when both enzyme-linked antibodies are attached to the agent will there exist a local concentration of substrate high enough for the second enzyme to generate the transduction signal. This two-antibody system makes the assay highly specific, minimizes the occurrence of false-positive results, and—because it is homogeneous—does not require the separation of antibody-bound antigen. We enhance the sensitivity by using a chemilumophore that, when oxidized by the product of the second enzyme reaction, produces light. Consequently, this chemiluminescent proximal-pair assay is highly specific and extremely sensitive.

Figure 1(a) shows results from a 2-s exposure of a CCD detector to an assay. Bacteria-size antigen-labeled beads are in a solution containing the enzyme-linked antibodies along with chemilumophore and first-enzyme substrate. The beads glow with light generated by antibody-linked enzymes attached to antigens on the bead's surface. No reaction occurs in the bulk solution because the concentration of substrate produced by the first enzyme of the pair is too low to effectively activate the second enzyme.

This assay has great potential for detecting BW agents and antigens of medical and industrial significance. We envision the assay as part of camera-size, hand-held monitor used to detect aerosol and water-borne agents [Fig. 1(b,c)]. Antibodies can be raised to recognize specific polysaccharide or protein molecules on the surface of a cell or spore, a protein dissolved in water, or even small molecules such as those in drugs; thus, antibody-based assays are used to detect bacteria, viruses, proteins, and small molecules such as toxins. This versatility suggests the assay/personal detector could be used for monitoring air and water for BW agents, for testing for airborne pathogens in hospitals or pathogens on hotel-room surfaces, or as an assay system in a doctor's office. Commercialization would target assay portfolios for specific applications (medical, veterinary, military), and each film would test for 10 or 20 antigens on each assay frame [Fig. 1(b)]. There would be many exposure frames on each assay film, and frames either would be exposed directly with a drop of liquid through a special inlet, or a fan would draw air to test for airborne antigens.

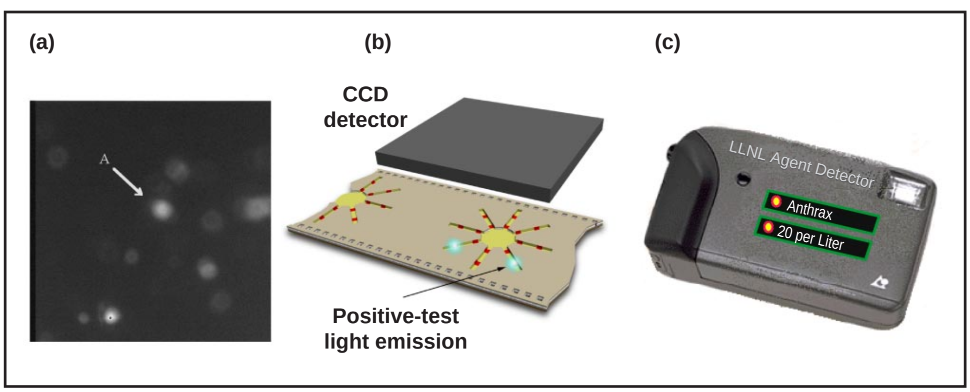

Figure 1. Chemiluminescent detection of biological warfare agents: (a) a digitized, charge-coupled device (CCD) image from a 2-s exposure of antigen-labeled beads treated with enzyme-linked, proximal-pair antibodies (arrow points to a luminescing bacteria-size bead), (b) conceptual image of assay film showing a multi-analyte with two positive spatially resolved antigen tests detected by a CCD detector, and (c) a camera-size prototype multi-analyte detector.

Incorporating Biomechanical and Clinical Data into Design of an Ergonomic Computer Pointing Device

P. Tittiranonda, S. R. Burastero
97-ERD-031

The incidence of musculoskeletal disorders (MSDs) continues to rise steadily and now accounts for 62% of occupational illness. The total economic impact of MSDs was over $50 billion in 1995. Computer-related MSDs have been reported to increase ten-fold within the past five years, with notable increase among mouse users. MSD risk factors such as repetition, force, contact stresses, and awkward postures have been linked to intensive use of pointing devices. Repetition and high finger force are apparent during "button down and dragging." Extreme postures such as pinch grip, wrist deviation, forearm and shoulder abduction can occur when the pointing device is held with fingers in a pinch grip and when there is excessive reach due to inadequate workspace. The goal of this project is to integrate LLNL's expertise in ergonomics, occupational biomechanics, and computational modeling to evaluate and design a "biomechanically rational" computer pointing device prototype.

During FY98, we used stereolithography to produce a prototype from several design concepts generated in FY97 and based on field, laboratory, and modeling data. To further evaluate the effect of a typical pointing device configuration on upper extremity joint postures, we used our existing 3D motion analysis system to measure joint postures of the fingers that are commonly used to operate the mouse buttons. Our findings will be used to optimize the mouse button location on our second-generation prototype in FY99.

In FY97, our analysis of heavy computer users showed that non-neutral, upper extremity posture can be caused by poor product design and individual work style. In FY98, we extended our studies to develop a taxonomy of pathmechanical "mousing" and "gripping" styles based on workplace video postural analyses of a subset of heavy users. Our taxonomy enabled us to further identify and select muscle groups that correspond to harmful work styles. Activity in these extrinsic forearm muscles will be compared when subjects use the prototype and the conventional pointing device.

The challenge in measuring muscle activity during pointing device work using surface electromyography has been the ability to isolate the relevant upper limb muscle groups with minimal interference from the adjacent muscles. In collaboration with the University of Michigan during FY98, we also developed an improved technique to accurately and repeatedly measure electromyographic (muscle) activity of the extrinsic forearm muscles on the skin surface during pointing device tasks. In addition to improving the surface electromyography technique, we also made significant progress towards improving our proprietary biomechanical measurement systems, which we will continue to use to test our working prototype against the conventional products in FY99.

Recently, our biomechanical measurement tools have generated interest from clinicians applying them to new rehabilitation and training techniques for injured computer users. Many of the tools that we used in the project have found practical applications in back injury prevention, clinical rehabilitation, and product design.

In FY99, we plan to (1) create a working prototype, (2) compare muscle activity patterns of the extrinsic muscles and upper limb postures on the prototype vs. conventional pointing device, (3) conduct field trials of the working prototype in heavy computer users as resources permit, and (4) patent intellectual property. We will apply our new ergonomic measurement techniques in clinical rehabilitation settings and explore applications in workplace training and job analysis.

Tracer-Isotope Development in Environmental and Biological Sciences

J. S. Vogel, M. A. Davis, A. Marchetti, M. W. Caffee
97-ERI-007

Proteins, as hormonal, enzymic, or structural entities, form key components of physiological cycles and act at concentrations that challenge even the most sensitive techniques. Proteins and their pathways have long been studied by labeling them with iodine isotopes, specifically with ^{125}I ($t_{1/2}$ = 60 days). However, ^{129}I ($t_{1/2}$ = 16 My) is an attractive alternative to ^{125}I as a radiotracer in biomedical tracing because it eliminates the hazards associated with highly radioactive materials. However, the more significant value of ^{129}I is the increased sensitivity in protein detection when it is quantified with accelerator mass spectrometry (AMS). Using ^{129}I, labeled proteins could be administered to human subjects for in vivo studies of enzyme and hormone effects using the low activity and high sensitivity of AMS tracing. Even in animal studies, obtaining sufficient radioiodine for decay detection in a tissue of interest may require a physiologically unrealistic protein dose. Further, the long-term behavior of a labeled protein in an animal is not quantifiable with short-lived isotopes, because sensitivity is lost with time as the protein undergoes biological elimination and the isotopic label is itself decaying.

In this project, we demonstrated the sensitivity and usefulness of ^{129}I as a new isotopic label for protein tracing in animals with expected extension to humans. We first developed an iodine-separation process that was robust, efficient, and simple for extracting ^{129}I quantitatively from biological materials. By using an alkali-fusion process, large numbers of biological samples can be simultaneously oxidized in separate crucibles within a single furnace. The solubilized iodine is taken up in an acid solution and precipitated to silver iodide for AMS measurement. Our FY98 goal was the completion of the demonstration that proteins could be labeled at very low levels of ^{129}I without damaging their biological activity.

We labeled purified acetylcholinesterase (AChE)—an enzyme involved in the neurotransmission and metabolism of toxic esters such as nerve agents—with ^{129}I. We purified the labeled proteins with size-exclusion chromatography (SEC) to measure the specific labeling activity through the quantitation of the protein concentration and the measurement of the protein-bound iodine. Finally, to determine any denaturation we assayed the protein's enzymatic activity both before and after the addition of the isotopic label. This process of labeling, purification, label quantification, and activity assay demonstrates the essential steps of protein tracing using ^{129}I.

We originally planned to develop our chemical methods using ^{125}I detection through decay counting; however, the health hazards prompted us to use gas chromatography to quantify the iodination of proteins with stable isotopes. By careful control of background iodine in containers and solvents, we reached a sensitivity of 10 pmol of iodine, enough to determine the level of initial protein labeling without the use of radioisotopes. AMS detection of ^{129}I is 10,000 times more sensitive, with detection available to 1 fmol and lower. We were able to label AChE proteins at low-enough levels (one iodine atom per 2.7 ± 0.4 proteins) that the active site of the enzyme was unlikely to be perturbed. This binding represents 42 fCi of ^{129}I per µg of protein. A similar labeling with ^{125}I would yield a specific activity of 4 µCi/µg, constituting a serious radiation hazard for experimenters and subjects. Iodine binds to one of the 12 tyrosines in AChE, and one of the tyrosines is in the protein's active site. Measurements of enzymatic activity showed that the proteins were 20% more efficient at cleaving target chemicals after they had been labeled with iodine. The enhanced activity may indicate that the iodine preferentially binds in the active site but does not hamper esterase cleavage. The level of isotope label on the AChE is sufficient to detect a dose of labeled proteins as low as 10 fmol (10^{-15} mol) administered to a 250-g rat, or a 1.2-µg dose of AChE to a 100-kg human.

Human growth, development, actions, and even thoughts are mediated by low levels of proteins and their interaction with cellular receptors. AMS tracing of ^{129}I-labeled hormones and signal proteins will enable the study of elusive processes directly in humans without disturbing natural protein levels and without any danger from isotope radiation.

The Biomechanics of Osteoporosis

J. Kinney, A. Ladd
97-LW-016

Osteoporosis is a significant public health problem. It is known that fracture risk is strongly correlated with the loss of bone mass, but the majority of patients with low bone mass do not suffer from osteoporotic fractures. This has led us to search for factors other than bone mass, such as changes in geometric structure, and differences in tissue properties, to help explain the occurrence of fracture in some osteoporotics and not in others. Much of our research has focused on trabecular bone.

Connectivity, the number of closed loops in the trabecular bone network, is a topological measure that attempts to relate biomechanical behavior to architecture. Because of the difficulty in measuring connectivity, the relationship between connectivity and mechanical strength has never been established. The objective of our present research is to determine whether there is a functional relationship between connectivity and strength in trabecular bone. This research is of great importance, since we have now established that none of the approved or pending treatments for osteoporosis can restore trabecular connectivity.

We have used unique LLNL resources in three-dimensional imaging, materials modeling, and nanoprobe technology to investigate the relationships between trabecular bone structure and strength. The three-dimensional images provided us with a quantitative measure of trabecular connectivity and became the template for finite element modeling of the strength. Nanoprobe methods (atomic force microscope indentation) were used to independently measure the mechanical properties of the trabecular bone tissue. With this information, we were able to directly study the role of connectivity on bone strength. The results of our study demonstrated that recovery of mechanical function depends on preserving or restoring trabecular connectivity. However, in early stages of osteoporosis we have also found that strength can be recovered without restoring connectivity. We have therefore focused our remaining efforts into resolving this paradox.

Understanding why, at least in early stage osteoporosis, it is possible to recover strength without restoring connectivity has required us to develop new methods of characterizing trabecular microarchitecture. One avenue that is proving particularly fruitful is a technique of cellular disassembly, where the three-dimensional architecture is deconstructed into a Euclidean graph. We have used this method to find a linkage between connectivity and thickness. Indeed, there appears to be a universal relationship between the number of trabeculae and their thickness that provides a resolution to our paradox; namely, trabecular strength can be recovered without restoring connectivity only by thickening the remaining trabeculae significantly beyond baseline values. These results have significant implications for treating severe osteoporosis.

High-Precision Short-Pulse Laser Ablation System for Medical Applications

M. D. Feit, A. M. Rubenchik, B.-M. Kim
97-LW-074

Ultrashort laser pulses (i.e., pulses of duration shorter than a few picoseconds) can deposit laser energy at high density into a thin layer of material. Because of the short time and high energy density, the affected material can be ablated away before appreciable heat conduction or energetic shock-wave generation takes place. Previous LDRD-sponsored research has shown the advantages of this regime for processing metals and dielectrics such as high explosives. In this project, we are developing the science and associated technology needed to apply ultrashort laser pulses to the surgical ablation of soft and hard tissues. This involves scientific understanding of the laser–material interaction (energy absorption, heating, shock waves, ablation) along with exploration of the necessary technology for application (feedback-control system, delivery system). Our project combines sophisticated computational simulations with experiments to provide the necessary scientific and technical knowledge.

Since each laser pulse removes only about one micrometer of material, it is necessary, for most applications, to run the laser at a high repetition rate to achieve adequate removal rates. In a typical system, a 1-kHz pulse-repetition rate results in material removal rate of about 1 mm/s. At such high rates, issues of safety and the effects of high average power must be addressed. To combine a high rate of material removal with high precision and safety, it is necessary to monitor the cutting and to employ a feedback system to shut off the system when appropriate.

We previously reported the development of a luminescence-based feedback system that allows distinguishing between soft and hard (bony) tissue for neurological procedures. This system allows the laser to be automatically shut off when the tissue type being ablated changes. Actual shut-off occurs fast enough so that not more than about 1-μm thickness is removed from the tissue not to be ablated.

Thermal effects deep in the tissue resulting from high repetition rates have been modeled and measured. During FY98, we measured the changes in the effective ablation threshold in dental tissue (enamel and dentin) caused by both high repetition rates and beam size. The determining physical parameter is the thermal-diffusion length during one cycle compared to the beam size. At smaller beam sizes, residual deposited energy is more easily transported away by heat conduction. At high repetition rates, residual heat cannot be transported away from the ablation area before the next pulse arrives. Another multiple-pulse effect involves "incubation," that is, the accumulation of invisible absorbing defects (e.g., color centers upon repeated irradiation). We measured the effective ablation threshold in dentin and found that it decreased with the number of pulses used. This decrease is only in part a matter of detection sensitivity; the remainder is attributed to incubation.

Figure 1 shows results from our study of the effect of pulse length upon ablation. Very short pulses minimize collateral damage, but lasers producing the shortest pulses are more expensive than those producing longer pulses. Optimal pulselength can be determined by studies, such as illustrated in the figure, in which tubular structures in dentin are undisturbed after ablation by 130-fs pulses, while evidence of melting appears for pulses longer than a few picoseconds.

During FY98, we began making fundamental measurements of the temperature and pressure effects in material near the ablation site. This is necessary to assess the biological significance to tissue adjacent to the cut of the residual thermal and mechanical stresses.

In FY99, we will continue the pressure and temperature measurements to develop a more complete picture of the collateral effects of laser ablation. Time- and space-resolved measurements away from the ablation site of the ablation-induced shockwave will be determined and compared to our detailed theoretical modeling to validate the theoretical models used to understand the ablation process.

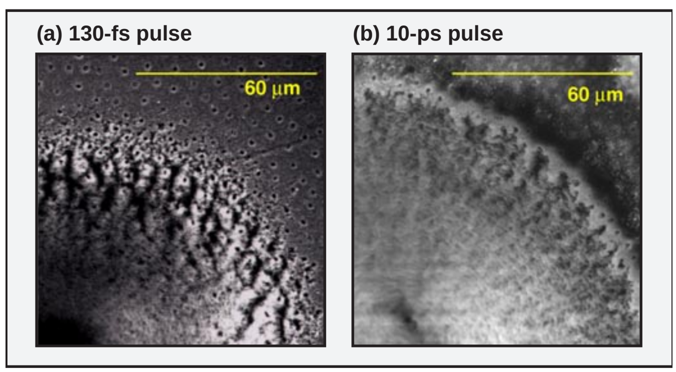

Figure 1. Comparison of the morphologies of holes ablated in dentin by ultrashort laser pulses at two pulse durations: (a) a 130-fs laser pulse removes material without modifying the tubular structure of dentin; and (b) at the longer pulse length, some melting and modification occur.

Dielectrophoretic and Electrophoretic Focusing of DNA for Improved Capillary Electrophoresis Injection

R. R. Miles, A. W. Wang, K. A. Bettencourt, J. Hamilton
98-ERD-082

The Laboratory is part of a larger cooperative effort between various institutions to sequence the entire 3 billion base pairs of the human genome. Our research involves manipulating biological particles independently of the suspending media by using electric fields so that we can better integrate sample handling with improved biological assays. In particular, we seek to move and concentrate DNA at the input to electrophoresis channels to improve the repeatability and resolution of DNA sequencing assays.

The primary method for sequencing or decoding DNA is gel electrophoresis. Electrophoresis involves subjecting molecules, such as proteins, carbohydrates, nucleotides and others, suspended in a medium, such as paper, gel, or aqueous solution, to a high voltage. The ionic particles are attracted to the electrodes of opposite polarity, and the particles separate consistent with their mobility through the media. Since DNA molecules exhibit an inherent negative charge, they are attracted to a positively charged electrode. However, since DNA strands all have the same charge-to-mass ratio, polyacrylamide gel is used to impede the progress of longer chains of DNA. Electro-osmotic flow is suppressed, resulting in a device that can measure lengths of DNA strands to within 1 base pair such that the DNA sequence can be discerned.

In the late 1980s, gel-filled micromachined channels began to appear for performing DNA sequencing. The channels are etched in glass plates using the same photolithographic techniques as are commonly used to make electronic semiconductor devices. Use of channels decreases analysis time from 12 hours per run to 1 hour per run over commonly used slab-gel techniques.

The primary drawback of the use of channels is the inability to introduce the analytes at the beginning of electrophoresis channel prior to testing. The degree of concentration of the sample directly relates to the signal-to-noise at the detection end of the channel. While others use cross-channel techniques to inject a reasonably concentrated sample, we decided to introduce the analytes at the input region using electrical means. We placed thin film electrodes into the input region of etched channels, as shown in the figure below. Each electrode could be activated independently.

Several techniques were tested and one has been selected for further studies. The selected technique seems to concentrate the DNA, and it proved successful for sequencing. However, we have not yet established if that is an improvement over competing methods. We will continue this effort in FY99.

Also in FY99, we plan to develop a system for electrical manipulation of both cellular material and DNA, which is capable of preparing a sample for a DNA amplification polymerase chain reaction (PCR) assay. These assays are used extensively in DNA sequencing, forensic analyses, and pathogen detection systems.

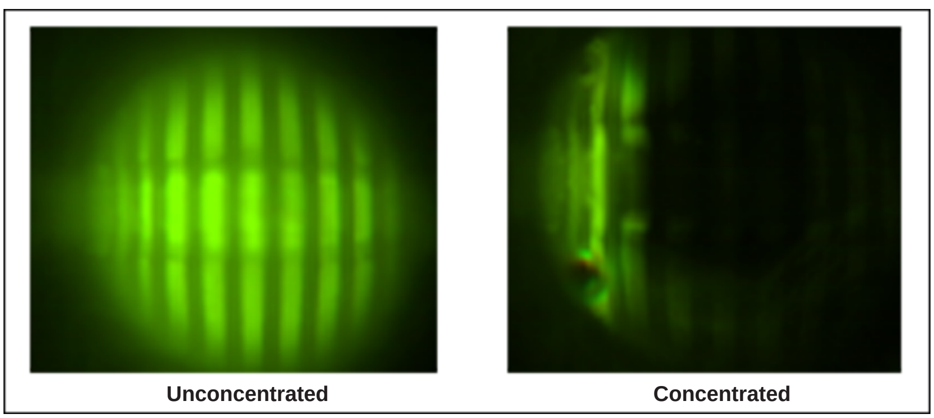

Fluorescently labeled DNA is smeared throughout the injection end of an electrophoresis capillary in the unconcentrated form. By properly applying voltage, the DNA is concentrated, which leads to improved DNA sequencing information.

Novel Microfluidics: A Magnetohydrodynamic Micropump

A. P. Lee, A. V. Lemoff
98-ERD-089

Microfluidics is the field of manipulating fluids in micromachined channels. Microfluidic systems would find immediate application in biowarfare detection, for detecting and cleaning up hazardous materials, and in bioinstrumentation (e.g., in support of the Human Genome Project and for drug delivery). Most micropumps developed thus far have been complicated, both in fabrication and design, and often are difficult to reduce in size—negating the possibility of many integrated fluidics applications. In a majority of these pumps, the fluid is indirectly pumped by a moving component; the result is a pulsatile flow instead of a continuous flow. With moving parts involved, dead volume is often a serious problem, causing cross-contamination in sensitive biological processes.

Our ultimate goal is to integrate pumping, valving, mixing, reaction, and detection on a single chip. The micromachined pump would propel fluids using magnetohydrodynamic (MHD) force. In FY98, our immediate goal was to study the scalability of MHD to microsystems and to design, fabricate, and evaluate a prototype MHD micropump.

In FY98, we successfully designed, constructed, and tested a prototype MHD micropump and developed a microfabrication process for integrating the microchannels with thin-film metallic electrodes. The microchannels of our MHD micropump are fabricated in silicon by first patterning the channels photolithographichally and then by using potassium hydroxide (KOH) wet etching to define them. In this bulk-micromachining process, KOH etches different crystallographic planes in silicon at different rates, resulting in the silicon v-grooves shown in Fig. 1(a). Once the microchannels have been defined, a thin oxide is deposited onto the substrate to provide electrical isolation, followed by evaporation of titanium and platinum for electrodes. The electrode patterns are then defined by a shadow mask. The silicon microchannel is bonded between two plates of glass using an anodic bonding process. The top glass plate has holes for electrical contact to the platinum electrodes and for fluidic loading into the microchannel. An electromagnet provides a uniform magnetic field. Our MHD packaging and test setup are shown in Fig. 1(b).

During tests, an alternating current was generated between opposing electrodes in the microchannel to avoid electrolytic bubbles that can impede flow. We chose an NaCl solution for the conducting liquid because it is used for biological applications. The frequency and phase of the current across the microchannel were matched to the frequency and phase of the electromagnet so as to produce a force in the same direction. We determined the optimum frequency for driving the most electrical current through the solution without generating bubbles in the microchannel and also for producing a high magnetic field in the electromagnet. We found that a frequency of 1 kHz allows a current of about 90 mA through 1*M* of NaCl solution in the microchannel without bubble generation. At this frequency, the maximum magnetic field that can be generated is 240 G. The average force produced can generate flow rates up to 1 μL/min.

Further experimentation showed that the flow rates could be increased if we used an electromagnet with a ferrite core. At the end of the fiscal year, we were able to pump the liquid via AC MHD force. By placing polystyrene beads in the solution (5 μm diam) and tracking their motions, we observed a bead velocity of 1.06 mm/s with an electrode current of 75 mA and electromagnet current of 375 mA, corresponding to a magnetic field of 251 G at the surface of the magnet (quite a bit lower in the channel). If we assume this to be the average flow velocity, the volumetric flow rate is then calculated to be 13 μL/min. This is the first ever demonstration of such a micropump; it could enable integrated fluid systems for applications in genetic analysis and combinatorial chemistry.

In FY99, we plan to test different conducting solutions used in biological applications and other microchannel configurations. We will also test the MHD effect in other microfluidic devices such as a microflowmeter, micromixer, and microviscosity meter.

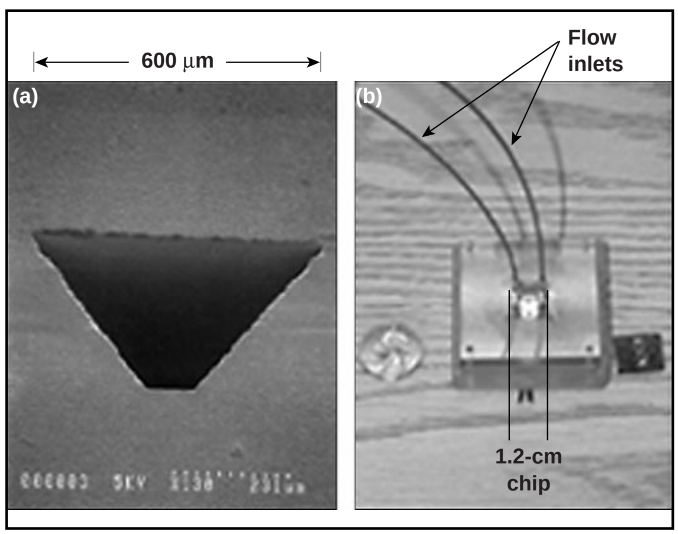

Figure 1. A magnetohydrodynamic (MHD) micropump: (a) scanning electron microscope picture of a microchannel's cross section, and (b) packaging and test setup of the micropump.

Base-Calling for Microchannel DNA Sequencers

L. M. Kegelmeyer, J. P. Fitch
98-ERD-098

To determine all 3 billion bases of the human DNA sequence by 2003, the international Human Genome Project has a critical need for high-quality, high-throughput sequencing instruments. LLNL has applied unique capabilities in microfabrication to design and prototype a high-throughput microchannel electrophoresis DNA sequencer. As with the best current sequencing systems, the output of the microchannel sequencer is a four-color (one for each base) electropherogram. The best available software to process electropherograms, from the University of Washington, is called *plan* and *phred*; it was optimized for conventional sequencers by "training" on extensive amounts of data from commercial slab-gel instruments. Unfortunately, the microchannel sequencer utilizes a different gel and a different geometry for sequencing. Consequently, electropherograms of the same DNA with comparable resolution (the ratio of peak spacing to full-width-half-maximum) when run through *plan* and *phred* produce better base call scores for the slab-gel than for the microchannel electrophoresis data. Here, we report models of the microchannel data acquisition system that accounts for scan speed, channel spacing, and signal-to-noise ratios (SNR) of the instrument. We also demonstrate the systematic incompatibility of microchannel data with the standard software suite and show LLNL software modifications that significantly improve the sequence accuracy of microchannel data.

The modeling effort began with simple techniques for synthesizing electrophoresis data from a list of bases. In this small project, we implemented and analyzed models that simulate arbitrary length strands of DNA with both nonlinear time scale distortions and color cross-talk (the spectral overlap of different dyes that tag the four bases as well as overlap in the optical detection bandwidths). The ability to synthesize data allows both the testing of *plan* and *phred* and the evaluation of parameter estimation codes that are essential for utilizing any base-calling software. We plan on applying this simple model to evaluating SNR and non-uniform sampling in the near future.

Software modifications focused on the fundamental differences between conventional instruments and the microchannel instrument. By replacing the baseline correction algorithms with a more adaptable and robust morphology-based algorithm, the noisy microchannel peaks retained their resolution, while losing most of the overlying high frequency noise. The morphological approach is nonlinear and allows dynamic shape-based computations throughout the data trace.

We have developed tools to generate dye-molecule mobility correction to account for the unique media/dye combination and channels of different length. We are now able to generate customized compensation tables for various types of lanes and obtain improved performance. These tools were applied separately to long and short lanes, with performance results shown in the figure below. Because the microchannel plate has lanes that vary in length, the electric field and thus velocity of the specimen vary as a function of position along each channel. As a result, the single look-up-table in *plan/phred* that corrects for non-uniform signal spacing along the length of a lane were not flexible enough to accommodate the range of lane lengths in the microchannel data, and we implemented a dynamic spacing correction for microchannel lanes.

Lastly, we found that the *plan/phred* software does not trim the beginning of the signal adequately for microchannel data, as evidenced by the "original *plan/phred*" performance curves; therefore, we trimmed the beginning of the sequences by 100 bases before analysis. The improvement realized by these software changes is illustrated in the performance chart, which shows promising advancement towards a practical sequencing goal of 95 to 98% maintained performance accuracy.

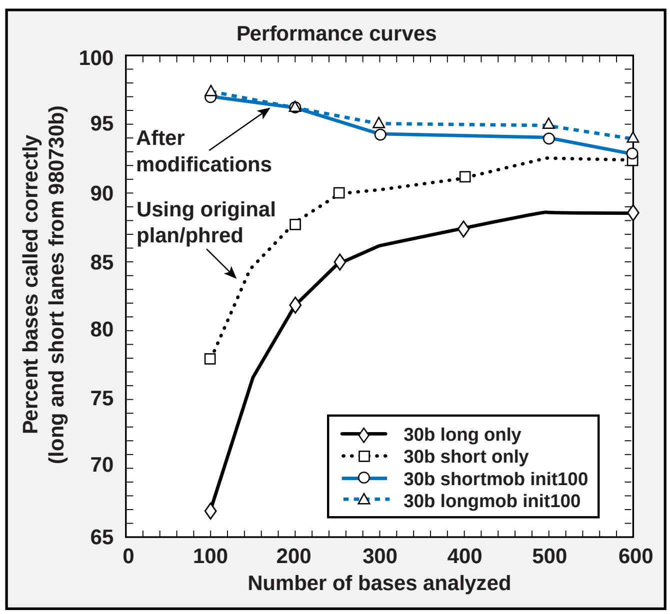

Performance improvement by modifying plan/phred software measured as an increase in the percent of correctly called bases from running known DNA samples in the microchannel sequencer. The two lower curves represent results from the original plan/phred software; the improved performance shown by the two upper curves is the result of applying all software modifications described in the report.

Identification of Population with Lifetime ^{41}Ca-Labeled Skeletons

S. P. H. T. Freeman
98-ERI-003

Osteoporosis is a major public health problem. In the United States alone, there are over a million osteoporotic fractures a year; these have an attendant annual financial cost of more than $10 billion. Consequently, there are considerable efforts to develop therapies and a great need for better diagnostic tools.

Osteoporosis is a disease characterized by reduced bone-mineral density (BMD). Skeletal calcium deposition and resorption are usually closely coupled, but prolonged slight net imbalances ultimately deplete the skeleton. Many current therapies are directed at redressing this imbalance by partially blocking bone resorption. The evaluation of these, and of other therapies more generally, requires good measurements of skeletal calcium loss. However, current x-ray techniques are insensitive to changes, and the preferred alternative techniques of using urine/serum proxy biomarkers only poorly predict an individual's BMD. The goal of this project was to establish a potentially more powerful method for monitoring bone degradation: the direct measurement of resorbed and excreted skeletal calcium. This promises better, faster, and less-expensive development of therapies.

Recent work has demonstrated the necessary labeling of the human skeleton with an isotope novel to calcium kinetics research—(^{41}Ca), coupled with ultrasensitive accelerator mass spectrometry (AMS) detection of the minute amounts of the tracer resorbed and excreted in any day. Although a single tracer administration can usefully label the skeleton for life, a significant outstanding issue was that it might take years of normal skeletal remodeling before the ^{41}Ca signal of resorption would usefully reflect skeletal resorption. Then, in 1997, we realized that historical experimental subjects had received previously unrecognized ^{41}Ca tracer as an impurity in other radiotracers in unrelated experiments performed by other researchers even many years in advance. Thus, it transpires that there exist thousands of one-time experimental subjects who, by virtue of having been accidentally labeled sufficiently long ago, now have skeletons with thoroughly equilibrated tracer. If even a small fraction of this unique population were available for enrollment into contemporary protocols, then these subjects might prove the ideal population for evaluating osteoporosis therapies.

Our goals were to (1) confirm the magnitude and extent of historical ^{41}Ca dosing, (2) characterize the long-term ^{41}Ca signal by comparing it with conventional measurements of skeletal health, and (3) demonstrate the utility of the historically labeled population in evaluating an actual potential therapy for osteoporosis. However, rather than investigate historical records to learn the identity of those inadvertently dosed, find them, and if possible enroll them into a new protocol, this project was to be particularly efficient through using a multiyear archive of samples from original, inadvertent ^{41}Ca-dosing experiments at Creighton University in Omaha, Nebraska. Because the subjects had been dosed in conventional studies of calcium kinetics, much important correlating historical data would also be available for comparison. Measurements of contemporary urine samples specifically provided for this project by selected identified subjects would follow.

To confirm widespread ^{41}Ca dosing among the subjects of the Creighton University studies, during FY98 we investigated the neutron-irradiation genesis of the ^{41}Ca impurity in the original radiotracers by analyzing historical radiotracer dosing solutions. This involved reconstructing the historical experiments from Creighton records. We concluded that the 10,000 or so subjects were dosed with variable but typically large-enough amounts of ^{41}Ca that should result in a measurable signal today. The likelihood is that none of the historical subjects have been adversely affected by their inadvertent radiological exposure. We ultimately obtained permission to analyze archived actual human samples, but measurement of these samples was delayed by lengthy deliberations on the ethical and legal implications. However, we did discover a second archive at the University of Texas Southwestern Medical Center. This is potentially a better source of material because the samples were generated in numerous historical evaluations of actual osteoporosis therapies in which ^{41}Ca-impure radiotracers were used. The therapies might now be retrospectively evaluated, both to contribute powerfully to our understanding of the therapies and to highlight the potential use of the ^{41}Ca tracer and LLNL's measurements.

Our results during FY98 were presented at the Second Joint Meeting of the American Society for Bone and Mineral Research and the International Bone and Mineral Society.

Low Charge-State AMS for Biological Research

I. D. Proctor, J. S. Vogel, M. L. Roberts, J. P. Knezovich, K. W. Turteltaub*
98-ERI-012

The first application of radiocarbon accelerator mass spectrometry (AMS) to biomedical research was reported nine years ago by LLNL scientists. By providing a tenfold greater sensitivity than stable-isotope labeling and decay-counting techniques, this technology allows the study of molecular interactions and permits a direct assessment of the relationships among genetic damage, DNA, and protein adducts and metabolism at low levels of exposure to natural or anthropogenic chemical compounds. LLNL is now recognized as the world leader in a technology that not only can address fundamental issues of environmental and biomedical science but also can change research and clinical practices. We will couple the LLNL expertise in biochemical AMS with research opportunities in University collaborations using a new, low-voltage spectrometer now under construction and fabricate the major components of this spectrometer.

Existing AMS instrumentation is large because it is designed primarily for geochronology analyses that require very high precision and high sensitivity plus the ability to detect a range of isotopes. The biomedical spectrometer that we are assembling is relatively small (i.e., 1 MV, 400 ft^2); ultimately, it will be an integrated analytical system that will provide both biomolecular speciation and isotope-ratio determinations. It will provide ready student access to an easily operated AMS. This new spectrometer will offer a number of advantages. For example, it will permit research projects that require an order of magnitude more sample measurements than are used in current projects.

During FY98, we worked closely with a vendor of AMS components to specify a spectrometer system that is optimized for particular application to biochemical analysis. We (1) performed detailed calculations of ion trajectories through the spectrometer to maximize the design of the 1-MV electrostatic accelerator, the mass-analysis magnets, the location of lenses, and other active components of the system; and (2) modeled the very high output of LLNL's ion source to ensure complete transmission of the ion beams with our expected ion currents (100 to 250 mA $^{12}C^{-}$)—almost an order of magnitude higher that those produced by commercial ion sources. We also explored energy-loss and ion-identification schemes for the low-charge-state ions. The results of our studies particularly affected the choice of the first mass-analysis magnet and the positioning of lenses near the ion-source. In FY99, the components of this system will be delivered, assembled, and tested.

Beginning in FY99, university students and faculty will use the spectrometer for projects that include (as examples) the calibration of clinical bioassays (University of California, San Diego—UCSD); kinetics of vitaminic fractions through *ex vivo* (external) labeling (University of California, Davis—UCD); and the identification of protein targets of drugs and toxins (University of California, San Francisco).

Disease states, diagnostics of the cause of disease, and the value of therapies against a disease are often quantified clinically using assays of biomarkers to the disease. Assays, however, often offer poor quantification of protein biomarkers because of the difficulty in calibrating low levels of protein solutes. In the UCSD collaboration, assays will be absolutely calibrated against isotope-labeled targets whose fluid concentrations can be accurately quantified with AMS. The sensitivity, selectivity, and rapid response of traditional bioassays will thus be linked to accurate quantification.

Many small molecules are distributed throughout the body by carrier proteins such as albumin. Nutritionists at UCD propose to bind isotope-labeled forms of the compound (parent or metabolite) to the human subject's carrier proteins *ex vivo*. Kinetics of the chosen protein-bound component can then be easily determined through quantification of the isotope label present in the excreta. Multisubject studies of kinetic parameters of nutrient compounds in a wide human population are required to understand the relation between disease and diet. This is a task that requires fast and accessible AMS measurements.

By modifying DNA or important protein functions, chemical binding can lead to cellular mutation or cancer. In collaboration with UCSF, we are developing techniques to identify the damaged proteins by combining two-dimensional gel electrophoresis with AMS detection of the labeled compound bound to the isolated protein. There are hundreds of protein spots visible on such a gel separation, and these can all be excised for AMS detection of bound components. However, there could be thousands of samples per gel that need AMS quantification to find the modified proteins that do not show up with staining.

* Deceased

Opto-Acoustic Enhanced Drug Delivery

S. R. Visuri, H. L. Campbell, L. B. Da Silva
98-LW-030

There have been few evolutions in the administration of therapeutic drugs since the syringe was invented; medicines are most always either taken orally or injected. Therefore, the entire body generally receives some dose of the drug, even when it is desired to target a single site. Significant benefits can be realized by locally delivering and enhancing the uptake of drugs across cell barriers. There are many applications: delivery of thrombolytics to dissolve blood clots, delivery of drugs to prevent artery restenosis, localized delivery of chemotherapeutics for cancer therapy, and delivery of gene vectors for gene therapies.

We are developing an opto-acoustic technique that could greatly improve the efficacy of local drug delivery; it has the potential to decrease dosages and side effects and to enable revolutionary therapies (we have filed Records of Invention). The concept is similar to transdermal ultrasound, which can increase drug transfer across the skin by up to 5000 times. However, transdermal ultrasound is impractical for targeting internal tissues. Figure 1(a,b) shows how ultrasound produced via our opto-acoustic technique is postulated to transiently disorder the cell membrane, creating channels through which compounds can enter the cell. This temporary disruption of a cell's barrier can increase intracellular concentrations of compounds that normally either cannot penetrate the cell's membranes or have low diffusion rates.

Initial research in FY98 established thresholds for cell damage caused by stress waves. Cells can withstand pressures greater than 200 bar for short durations of less than 100 ns. We intend to operate at pressures less than 20 bar, which should prove harmless to cultured cells. We have optically generated ultrasound that has parameters similar to those used in transdermal drug delivery (e.g., 1 bar at 20 kHz). Using these values as a starting point, we applied a nonpenetrating dye and optical ultrasound to cultured cells. Results have demonstrated the successful delivery of flourescein dye into cells.

In FY98, we tested two methods of quantifying the improvement of dye/drug concentration in cells. One method, spectrofluorometry, relies on the inherent fluorescence of a drug of interest, for example, the chemotherapy drug doxorubicin. When doxorubicin enters a cell, its fluorescence is quenched. Quantification of intracellular drug concentration involves measuring fluorescence of the cell media, pre- and post-treatment. This method can be used with a variety of cell types. The second quantification technique involves performing fluorescent intensity scans on cultured cells. Following application of a fluorescent dye and subsequent ultrasound treatment, the cells may be viewed under fluorescence microscopy and the image digitally captured for analysis. To quantify the dye uptake, the fluorescence activity of treated cells can be compared to controls and standard concentrations. Multiple dyes of varying size or polarity with distinct emission spectra can be simultaneously investigated.

Our goals for FY99 are to define the boundaries of our technology and to concentrate on specific clinical applications and feasibility. That is, we will (1) explore parameters of frequency, intensity, and duration of treatment; (2) monitor cell function via vital-dye staining and clonogenic assays; (3) explore mechanisms of action; (4) design clinically practical transducers; and (5) study clinical applications of cancer, restenosis, and gene therapy by using appropriate cell lines and drugs. The information derived from our work will provide the base for developing a clinically viable drug-delivery device.

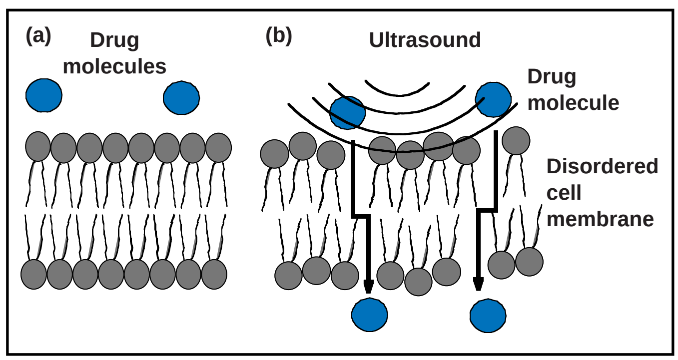

Figure 1. Drug transfer across a cell barrier (a) without and (b) after application of ultrasound. Ultrasound disorders the cell membrane, allowing molecules to diffuse through the membrane that otherwise would not. In (a), the drug remains in the extracellular fluid; in (b), the drug penetrates to the cytoplasm.

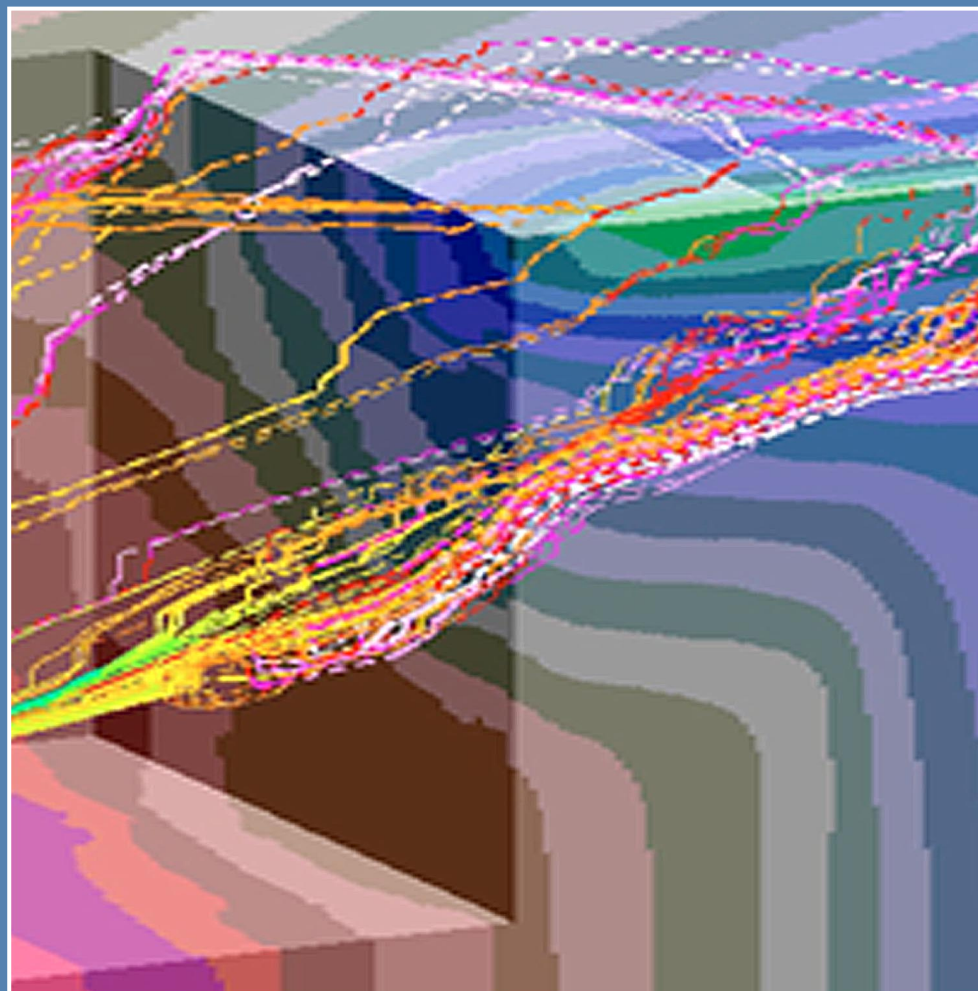

4

Computing / Modeling / Simulation

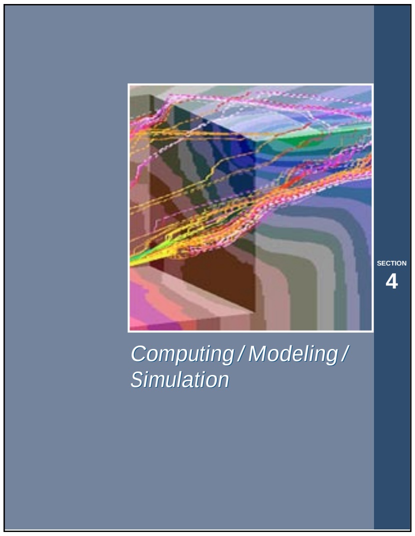

About the preceeding page

Enabling Computational Technologies for Subsurface Simulations. Rob Falgout and colleagues are collaborating with LLNL's Environmental Programs Directorate to develop and apply advanced computational methodologies for simulating multiphase flow through heterogeneous porous media. They have applied their computational technologies in the simulation code ParFlow to study water resource management issues for the Orange County Water District. For additional information, see page 4-5.

Surface Morphology Evolution in Silicon during Ion-Beam Processing

T. Diaz de la Rubia, P. Bedrossian
96-ERD-009

To cut development time and costs, the semiconductor industry makes extensive use of simple models of dopant implantation and of phenomenological models of defect annealing and diffusion. However, the production of a single device often requires more than 200 processing steps, and the cumulative effects of the various steps are far too complex to be treated with these models. New atomic-level models are required to describe the point-defect distributions produced by the implantation process and the defect and dopant diffusion resulting from rapid thermal annealing steps.

The goal of this project has been to develop predictive tools that would simulate the process of manufacturing integrated semiconductor circuits. During the first two years of this project, we dedicated our efforts to coupling experiments and simulations aimed at obtaining the properties of point defects and defect clusters in silicon. We validated the point- and cluster-defect properties with specific experiments at LLNL and obtained secondary ion mass spectroscopy results from Intel Corporation for 40-keV boron implants in silicon that had been annealed at several different temperatures and for several different times.

In FY98, we used the results of our earlier investigations to model actual front-end-of-line manufacturing of silicon devices. Our simulations involved the use of the previously obtained data for interstitial and vacancy diffusivities and cluster binding energies in our own kinetic Monte Carlo code. As a global validation of the results and of the approach, we modeled the same conditions of ion implant energy, dose, and annealing temperatures and times as in the Intel experiments. The results of our simulation agree very well with Intel's experimental results. (It is worthwhile to note that our simulations cover over 14 orders of magnitude in time scale, during which the kinetics of many types of defects and defect complexes were modeled.)

Because our simulations had been validated experimentally, we were able to use them in FY98 to explain the transient-enhanced diffusion (TED) of boron during implantation and annealing. Our results show that boron diffusion is a consequence of the early disappearance of vacancy complexes and the remaining subsequent migration of silicon self-interstitials coupled to boron atoms. These results also corroborated the early disappearance of vacancy complexes after implantation and annealing that had been postulated and experimentally proven in the first year of this project.

Our results also predict the fraction of electrically active substitutional boron in the silicon lattice during annealing; that is, they predict that there exists a time window—between 0.01 s and 10 s for 800˚C annealing of 40-keV boron implanted in silicon—during which 98% of the implanted boron is electrically active. This is in contrast to only 25% being active at the beginning of the anneal, immediately after implantation, or to 75% being active at the end of the anneal (which occurs at about 1000 s). Our results may provide guidance for the exploration of new time–temperature processing windows where residual damage is minimized and the fraction of electrically active dopant is maximized. Our work on this project has resulted in several refereed publications.

As a result of the success of this LDRD project, a funds-in cooperative research and development agreement (CRADA) with Intel Corporation and Applied Materials corporation has been signed. The CRADA is in place for one year. The ultimate goal is to accelerate and optimize development and insertion of new technology for ultra-shallow junction manufacturing, as required by the National Roadmap for Semiconductors in the year 2003.

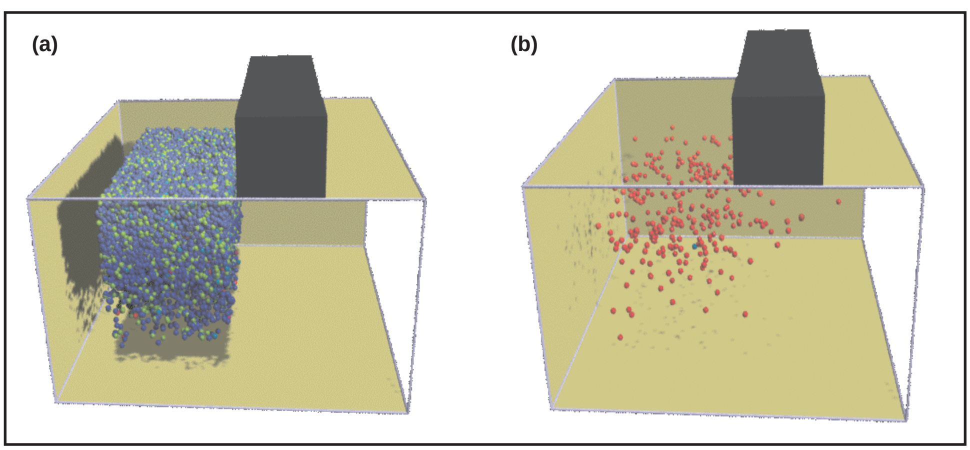

Figure 1. Computer models of a 40-keV boron implant in silicon showing (a) the three-dimensional distribution of implant damage, and (b) how the boron has undergone transient-enhanced diffusion and how all damage disappears after the sample has been annealed at 800˚C.

A New Approach to Orthopaedic Implant Design

K. Hollerbach, S. Perfect, E. Ashby, H. Martz
96-ERI-003

Total joint replacement has become a major industry and will expand dramatically as our population ages and our life expectancy increases. However, the present joint replacement market is served by an inadequate product. As a group, US implant recipients can anticipate anywhere from 1 to 6 revision surgeries by age 75. Today's implants typically fail in one or more of three modes: failure to reproduce normal joint kinematics, material failure at the articular interface, and bone-implant interface failure. The failure of most implants to reproduce normal joint kinematics results from a lack of understanding of specific joint kinematics and a lack of means to quantitatively assess the effects of implant geometry modification on the kinematics of the implanted joint. Material failure is common at the articular surfaces. Bone-implant interface failure can lead to bone fracture and implant loosening. There is a clear need for an improved approach to implant design. Any new approach should provide a way to shorten the time to market for improved designs. Finite element modeling of joints with implants offers an opportunity to evaluate designs before they are manufactured or surgically implanted. This is an attractive alternative to current methods that use only expensive, time-consuming experimental testing for design evaluation, where retrieved implants serve as a post-failure demonstration of poor design strategies.

We used the on-site facilities and expertise of LLNL's Non-Destructive Evaluation Division to obtain computed tomography (CT) data to determine bone and, to some degree, tendon geometry. To extract three-dimensional surfaces from the CT volume images, segmentation and surface reconstruction tools were developed, implemented, and applied to the data. The tools have been integrated into an interactive software environment to facilitate use by others at the Laboratory. Finite element analysis was performed by staff and students in the Laboratory's Institute for Scientific Computing Research, using the LLNL's NIKE3D code.

In FY98, implant models, chosen to represent current market products, were further developed and tested. The designs were evaluated by examining the interface contact stresses and material deformation, following loading representing *in vivo* conditions. The designs modeled include two knee joints (ExacTech, Inc. and the Biomedical Research Foundation), a thumb carpo-metacarpal joint (Avanta Orthopaedics, Inc.), and a generic ball and socket design that has been used for the thumb carpo-metacarpal joint replacement in the past and is currently being used extensively in the hip joint. The prosthetic and human joint models developed within the context of the LLNL project have led to contracts with outside industry.

Material properties for the ultra high molecular weight polyethylene (UHMWPE— one of the materials commonly used in prosthetic joint implants) were taken from the literature and incorporated into a NIKE3D material model. Boundary conditions were taken from the literature and from experimental results provided by outside collaborators.

To ensure that the implant models can be used as clinically predictive tools, the finite element simulations have been compared to failed implant surgeries in the thumb carpo-metacarpal joint. Model validation has included comparisons with experimentally measured contact stresses, contact areas, and joint kinematics.

The work performed in this project has resulted in an extension of LLNL core competencies in non-destructive evaluation techniques, in finite element modeling techniques (using the NIKE3D code), and in computational model development techniques; furthermore, it has directly resulted in separately funded (by DOE and others) spin-off projects in the orthopedic industry and in other industries. Future goals include continued validation of the human joint models, improvement of data processing algorithms, and development of a combined implant-human model, and continued refinement of the models and modeling techniques.

3D Massively Parallel CEM Technologies for Design of Advanced Accelerator Components

D. J. Steich, J. S. Kallman, D. A. White, G. J. Burke, S. T. Brugger

97-ERD-009

Many of today's design projects at LLNL require increasingly complex modeling capabilities. For example, the Advanced Hydrotest Facility (AHF) requires accelerator components never before designed. To aid in their design and to ensure the high beam-performance characteristics essential for the success of AHF, certain vital components require fields to be simulated by advanced computational electromagnetic (CEM) modeling. In this project, we are addressing this need by investigating flexible abstractions for numerical algorithms on massively parallel processor (MPP) platforms using object-oriented methods. These algorithms are being integrated into a time-domain-generalized excitation and response (TIGER) platform that will allow plug-and-play capabilities for newly introduced physics packages. Our plan is to demonstrate TIGER's capabilities by modeling various accelerator components vital to AHF.

In FY97, we built a prototype version of TIGER that achieved a 100-fold reduction in the number of cells required to simulate wakefields (integration Lorentz forces experienced by a test particle) produced by a simplified accelerator-kicker component. Run times were reduced from weeks of central processing unit (CPU) time to hours by simultaneously using (1) better boundary conditions—to truncate the problem space much closer to the kicker; (2) conforming nonorthogonal grids—to avoid stair-stepped approximation errors; (3) extensive, complex source modeling—to increase accuracy; and 4) improved wakefield physics—to reduce run time and required data storage.

In FY98, we (1) extended the TIGER code to include higher-order wakefield physics; (2) made substantial capability, efficiency, and flexibility improvements to our core framework; (3) made huge progress in the parallelization of TIGER; (4) explored abstractions for the hybridization of meshing (structured/unstructured, orthogonal/nonorthogonal, and homogeneous/mixed elements) and numerics (finite difference, finite volume, and discrete surface integrations); and (5) performed extensive research into interface-boundary conditions to improve accuracy by correcting both magnitude and phase of reflection and transmission through interfaces.

In FY98, we successfully modeled a full, three-dimensional kicker structure that was built as a prototype design for AHF; we obtained wakefield results for modes $m = 0$ to $m = 4$. The TIGER calculations for the kicker showed significant high-order wakefields. Our calculations agreed with preliminary experiments on the actual kicker structure, which showed a triangular-shaped image of the beam hitting a foil for a large-radius input beam and suggested a strong sextupole ($m = 3$) wakefield. Previous modeling had been limited to $m = 0$ to $m = 1$ for a simplified geometry. Understanding these high-mode wakefield impedances is critical to the success of LLNL's AHF.

Also in FY98, we focused on the next major parallel version of TIGER. This new version is much more capable, efficient, and flexible. The figure depicts speedup factor vs. the number of processors for TIGER's preprocessor on the Accelerated Strategic Computing Initiative (ASCI) Blue machine. The mesh is a 234,000 tetrahedral cell mesh of a kicker structure that is domain decomposed into various numbers of processors. Note the excellent speedup of roughly 30 while using 32 processors. We also performed extensive testing and validation of the physics, which led to the results described in the paragraph above.

Our FY99 goals are to complete parallelization of the TIGER solvers and focus on the efficient simultaneous implementations of hybridized meshing and numerics abstractions. These object-oriented abstractions will allow us to implement various algorithms using a collection of operators, fields, sources, and materials that are almost entirely independent of issues such as mesh type, parallel communication, and input/output methods.

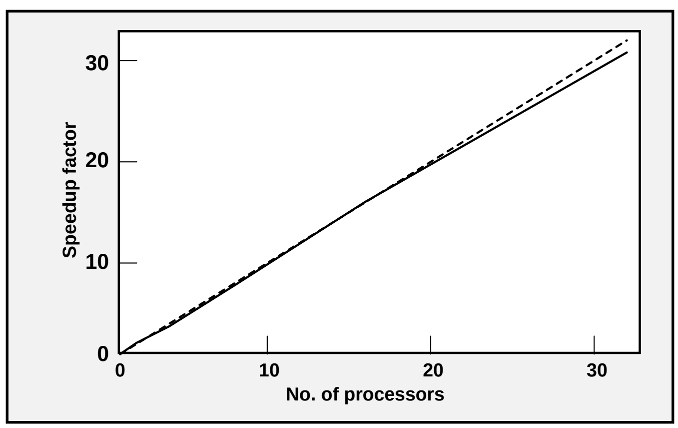

Reduced run times required for the modeling of an accelerator-kicker component for LLNL's Advanced Hydrotest Facility with increasing number of processors for TIGER's preprocessor on the Accelerated Strategic Computing Initiative (ASCI) Blue machine. We used a 234,000 tetrahedral-cell mesh. The dashed line represents the maximum possible speedup.

DataFoundry: Data Warehousing and Integration for Scientific Data Management

C. R. Musick, Jr.
97-ERD-033

As scientific enterprises evolve, the integration of and access to large, complex, and heterogeneous data collections stored throughout scientific communities has become a key challenge that will either enable rapid scientific progress, or restrict it. For data to be valuable, scientists must be able to access and manipulate it as structured, coherent, integrated information. Specifically, a consistent interface with the community's data resources—one that supports *ad hoc* queries, data mining, and domain-analysis tools—would be a major contribution in many areas. Data warehousing addresses this requirement for a consistent interface; it is a set of techniques for gathering data from external sources into one location and one format for storage and analysis. Unfortunately, the content, representation, and interfaces typical of scientific data sources are highly dynamic, and standard warehousing approaches fail in dynamic environments.

The DataFoundry project is a computer-science research effort focused on extending our ability to integrate and provide online, functional access to data from external, autonomous sources. Our primary goals for FY98 were to (1) implement a prototype useful to the genomics researchers with whom we have been working, (2) integrate several data sources into the warehouse, and (3) demonstrate progress in automating warehouse construction and maintenance tasks. We achieved these goals.

During FY98, we began using highly structured metadata (or, "ontology") to capture domain-specific knowledge and represent it in an organized, declarative form such that a computer program can make use of it. We have developed a metadata infrastructure that makes use of this information to automatically generate code needed in the data-integration process. To date, we have shown a reduction of about 50% of the effort required to incorporate a new source into the warehouse. We then developed a prototype warehouse in the human-genome domain (a scientific community with over 200 databases using different formats, models, and interfaces). This prototype provides multiple ways to access integrated data from several external sources. Along the way, we published our research progress in the proceedings of several technical conferences.

The prototype warehouse uses a specific architecture in which the integration of data takes place in a series of modular steps according to a unified model of the data. The bulk of the resulting integrated data is stored locally (for performance). The prototype includes fully integrated data from several biological databases: PDB (protein structure), SWISSPROT (protein sequence), and SCoP (structural taxonomy). In total, it contains information on more than 60,000 proteins, 90,000 contributing authors, and 33,000,000 atoms. These data are kept up to date with a data-ingest process that runs nightly. There are multiple interfaces with the data, including (1) forms-based interfaces designed by domain scientists, (2) a graphical query interface for more flexible access, (3) a pure standard query language (SQL) interface, and (4) a mechanism for directly accessing the data from C or C++. The interfaces include ways for the scientist to extend the warehouse data with results from individual analyses. Finally, we developed a data-mining interface that allows the user to automatically select or construct the input features in real time from warehouse data, run clustering and classification algorithms on those features, and manage the results. Our prototype is already supporting the core structural-biology research being done at LLNL.

During FY98, we also made significant progress towards automating data-management tasks. We have determined the type and level of detail of metadata needed to support code generation in the data-integration process. This highly structured metadata has been incorporated for the protein structure, sequence, and taxonomy data. We built an engine that uses the metadata to automatically generate C++ code for the applications programming interface (API) and for the mediator (the API and the mediator are the core elements needed to integrate and load data). We used this engine when we incorporated the structural taxonomy data—from start to finish, the new process took less than half the time it would have taken without the ontology engine. Finally, we made progress on a novel approach based on "genetic algorithms" (a machine-learning approach based on the natural-selection process) for managing sources that frequently change their data representations and interfaces.

Our primary goals for FY99 are to (1) add data and interfaces that further support functional genomics, (2) extend the ontology engine to further automate the data-integration process, and (3) implement new architecture and integration plans to improve the system's scalability.

Enabling Computational Technologies for Subsurface Simulations

R. D. Falgout, C. Baldwin, W. Bosl, S. Smith, C. Woodward, A. F. B. Tompson
97-ERD-035

We are collaborating with LLNL's Earth and Environmental Sciences Directorate to develop and apply advanced computational methodologies for simulating multiphase flow through heterogeneous porous media. The goal is to enable detailed simulations currently not tractable with conventional approaches, allowing applications scientists to both pose and answer new research questions. Our work has primarily been focused on the (1) scalable and efficient solution of the nonlinear Richards' equation used to model two-phase (variably saturated) flow, and (2) large-scale simulation of subsurface fluid flow and chemical transport in the context of water resource management applications. The simulation code ParFlow is being developed in support of this work.

In FY98, we completed the implementation of a variably saturated flow capability based on the Richards' equation model and investigated the scalability of a new multigrid, preconditioned Newton–Krylov method to solve the nonlinear systems of equations that arise at each timestep. This method uses a globalized, inexact Newton method for linearization, a Krylov iterative method as the linear Jacobian system solver, and the symmetric part of the Jacobian with a multigrid solver as a preconditioner. By using this combination of solvers, we can take advantage of the fast convergence properties of Newton's method, the robustness of a Krylov algorithm, and the parallel scalability of a multigrid preconditioner.

To implement the Newton–Krylov method, we used KINSOL, a package from the parallel variable ordinary differential equation (PVODE) code being developed at LLNL. As a preconditioner for the generalized minimum residual (GMRES) Krylov algorithm, we used the semi-coarsening multigrid method in ParFlow, applied to the symmetric part of the Jacobian. Numerical studies were done to demonstrate the scalability of the method, and we showed scaled speedups in overall solution time of more than 70%, scaling up to 7 million spatial zones on 128 processors of the IBM SP-2 initial delivery system at LLNL.

We have also applied our computational technologies in ParFlow to support investigations of aquifer recharge in a groundwater resource management application in Orange County, California. Here, management is interested in water-quality issues such as those related to the reuse of recycled water (e.g., treated wastewater). Results suggest that subsurface heterogeneities can have a dramatic effect on the distribution of wastewater age at extraction wells (see figure), thereby demonstrating the importance of the affect of geologic heterogeneity on flow paths, mixing, and residence times in the vicinity of recharge basins and wells.

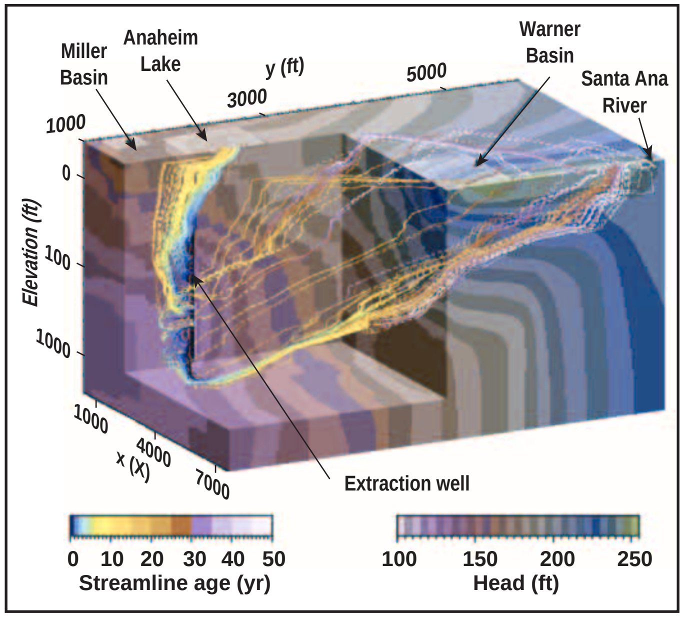

Streamlines representing backward travel pathways of water from an extraction well to their surface recharge points. Streamlines are shaded to indicate backward time-of-flight between the well and the surface. The hydraulic head is superimposed on the background domain block. These results demonstrate how the age of groundwater entering a production well can be highly distributed because of subsurface heterogeneity. This simulation used about 18 million spatial zones.

Portable Implementation of Implicit Methods on Parallel Computers—Maintaining the Leading Role of UEDGE in Magnetic Fusion Energy

T. D. Rognlien, X. Xu
97-ERD-045

Research for developing magnetic fusion energy (MFE) devices for power production is increasingly utilizing sophisticated computer codes to provide new physical insights and minimize cost. In assessing the viability of MFE devices, it is now recognized that the edge region where the confined fusing plasma contacts the "outside" world of the vacuum vessel plays a very major role for three reasons. First, the plasma that leaks to the walls of the confining vessel does so in a narrow strip that can produce large local heat loads on material walls, thereby causing high erosion. Second, helium ions (ash) produced by the fusion reactor must be pumped at the plasma edge to prevent dilution of the deuterium/tritium fuel. And third, the energy confinement of the core plasma is known to depend sensitively on the edge plasma conditions.

This project is a continuation of the work begun last year to capitalize on the large increase in computational power available from parallel (multiprocessor) computers for comprehensive simulations of the edge regions in MFE devices. Such a computational tool allows us to more realistically assess various MFE configurations for energy production and thus help decide which warrant the expense of constructing an experimental device. In addition, these simulation models are being used extensively to interpret experimental behavior and suggest new ways to operate the devices to optimize performance.

The two major components of our simulation model of the edge-plasma region are a two-dimensional fluid transport code UEDGE and a three-dimensional turbulence code BOUT (for BOUndary Turbulence). UEDGE evolves the plasma and neutral gas profiles in the edge region on long time and space scales to obtain equilibrium profiles; it was parallelized as part of this project last year. A crucial component of UEDGE is the model for leakage of particles and energy across magnetic fields lines owing to plasma turbulence. This model is provided by BOUT, which simulates the turbulence level and resulting transport driven by plasma instabilities with short wavelengths and fast timescales, whose existence is confirmed by diagnostic measurements.

This year, we made important advances to the BOUT computational model in three areas. First, we developed a parallel version of the BOUT code, which utilizes the implicit solver routine PVODE (a suite of parallel solving systems for ordinary differential equations), also used by UEDGE. The use of this implicit solver has resulted in an order of magnitude speedup in the computation time. In the parallel version, the problem is divided into several subdomains (domain decomposition) that are worked on separately by the different processors of the computer; we have been able to utilize 32 processors with further enhancement anticipated.

The second advance to BOUT is the improved coupling with the UEDGE transport code. We have now coupled the realistic magnetic field and plasma profile data from UEDGE to the BOUT code, making it the most realistic and complete simulation model of the edge-plasma turbulence available. This has allowed us to perform detailed simulations of the edge turbulence in the DIII-D tokamak at General Atomics and to obtain good quantitative comparisons with experimental measurements of the electrostatic turbulence frequency spectrum and the resulting fluxes of particles and energy across the magnetic field lines.

Finally, we have assessed how best to couple the BOUT information concerning the effective turbulent diffusion coefficients back to the UEDGE code. Because the direct coupling of the two codes is costly, we are developing a reduced model, with researchers from Lodestar Corporation, based on a linear stability. We are also finding that the parameter dependence of the diffusion coefficients can sometimes be expressed in terms of dimensionless combination of plasma variables for a type of similarity scaling. These improvements to the BOUT code have greatly enhanced our ability to understand and predict the important role of boundary turbulence in MFE devices.

Lung-Cancer Risk from Low-Level Exposures to Alpha Emitters: Critical Reappraisal and Experiments Based on a New Cytodynamic Model

K. T. Bogen
97-ERD-050

A cytodynamic two-stage (CD2) cancer model was proposed to explain how a negative ecologic association between residential radon exposure and age-adjusted 1980s lung-cancer mortality (LCM) in white males in U.S. counties might be consistent with a positive association between cumulative occupational radon exposure and LCM estimates for underground miners. The primary goal of this project was to refit the CD2 model for radon to sets of epidemiological data different than those used initially by the author—data that better address the estimation of radon concentrations in U.S. homes, as well as potentially confounding effects of smoking on the interpretation of radon–LCM associations. For this purpose, new data were obtained on age-specific LCM and estimated corresponding residential radon concentrations in white females of age 40+ y (about 11% of whom ever smoked) in 2,821 U.S. counties during 1950–54, and on LCM in five groups of underground miners (a total of 2,488 miners worldwide) who never smoked. The county-level LCM data (previously unavailable in any form) were generated from raw U.S. mortality data, and new estimates of county-specific mean residential radon levels for all U.S. counties were recently generated by Lawrence Berkeley National Laboratory (LBNL). Corresponding county-level census, climatological, and geophysical data were also assembled at LLNL. Person–year data summarizing individual-level exposure and LCM information on nonsmoking miners were obtained through the National Cancer Institute.

During FY98 (the final project year), we first analyzed these improved epidemiological data and found that radon levels were significantly negatively associated with corresponding county-level LCM rates in U.S. women who died in 1950–54 at age 40+ or 60+ years, after adjustment for age and many other factors considered. The similarity in results obtained for 40+ and 60+ year-olds indicates that intercounty differences in smoking are unlikely to explain the observed negative associations. Additionally, it was found that a single fit of the CD2 model was able to predict both the improved residential and the improved occupational data, as summarized in Fig. 1(a,b). (The actual fit involved more than 50 data points relating exposure to age-specific LCM.) The CD2 fit obtained happens also to predict the "inverse dose-rate" demonstrated (for the first time) to occur in nonsmoking miners—that is, the CD2 fit predicts entirely independent data to which the CD2 model was not fit.

Additional related epidemiological studies were also conducted, as well as experimental work at LLNL in collaboration with investigators at the University of California, Davis, School of Veterinary Medicine.

In conclusion, modeling results from this LDRD study support the biological plausibility of the hypothesis that LCM is not increased by exposure to radon at residential levels. They are consistent with a mechanistically based U-shaped (or "hormesis") dose-response pattern for radon's effect on lung-cancer risk, but by no means prove that this pattern either is the case or is as large as suggested by the U.S. ecologic data considered. The U-shaped CD2 fit obtained in this study predicts LCM risks far less than do linear-no-threshold models currently used for radon risk extrapolation[Fig. 1(a,b)]. This study thus indicates that formal uncertainty analysis ought to be emphasized in risk management for residential radon. The results also pose testable mechanistic hypotheses concerning the effect of subchronic or chronic exposure to relatively cytotoxic genotoxins, such as alpha radiation, on growth kinetics of premalignant foci. One such test, mentioned above, is being completed as part of this study.

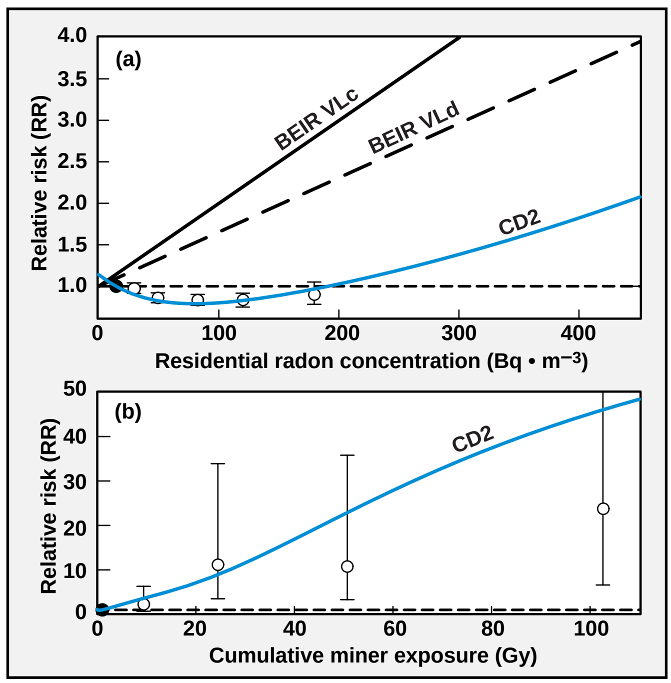

Figure 1. Results of fitting LLNL's cytodynamic two-stage (CD2) model (in blue) with epidemiological data (data points and error bars) relating exposure to radon gas to relative risk (RR) of lung cancer mortality in: (a) U.S. white females during 1950–54 (among whom very few ever smoked), and (b) 2,488 nonsmoking miners (adjusted for age, cohort, and previous work exposures). Dashed lines represent an RR value of 1.0. Solid and dashed curves in (a) show the two linear risk-extrapolation models (labeled VIc, IVd) for radon now recommended by the "BEIR VI" committee of the National Research Council. The linear models predict a substantially greater lifetime risk of lung cancer at residential exposure levels ≤ 4 pCi/L than does the CD2 model.

LATIS3D: The Gold Standard for Modeling Laser–Tissue Interactions

R. A. London, B-M. Kim, A. J. Makarewicz
97-ERD-056

LATIS3D is a computer program that models the essential physical processes of laser–tissue interactions; it is designed for use in research about and the practice of laser medicine. The overall goals of our project are to (1) enhance the capabilities of LATIS3D so that it becomes the world's leading program in laser medicine, and (2) apply LATIS3D to several important problems, particularly to the study of laser-light distribution and dose as applied to photodynamic therapy for arthritis and cancer. This project will lead to fundamental advances in the design of several laser medical therapies and to the establishment of LLNL as the top location for the application of computer modeling to laser medicine. This project is also enhancing LLNL's competency in radiation-hydrodynamics by pushing simulation codes into new parameter regimes and by attracting external expertise. The project will advance our capabilities in radiation-transport modeling in several ways. We are adding new features to the codes, such as refraction and polarization. We are also addressing complicated, three-dimensional (3D) geometries, and developing methods of generating 3D meshes from medical images. By applying our codes to current experiments, we will contribute to their verification and validation. We will also attract external expertise to help develop and apply our codes. This effort will also lead to the recruitment and training of young scientists in the field of radiation transport.

The essential physical processes being modeled by LATIS3D are laser transport, thermal-heat transport, material and chemical properties, and hydrodynamics. Laser-light transport is treated via the Monte Carlo method; heat transport via the "bioheat" equation (a heat-transport equation that includes laser heating, heat conduction, and cooling by the flow of blood through the tissue). Local processes include the equation-of-state (EOS), which describes the dependence of the pressure and internal energy of a material on its density and temperature; protein chemistry; and material failure. The hydrodynamics model in LATIS3D includes compressible flow and material strength and failure effects. Our development effort is highly leveraged by the continuing development of KULL, an Accelerated Strategic Computing Initiative (ASCI) code.

Our work is focusing on (1) programming special physics models, such as opacity, angular scattering functions, and tissue chemistry; (2) adding specific input parameters for the laser–tissue interaction modeling into developing packages (e.g., boundary conditions and sources); (3) developing packages in other codes such as the two-dimensional (2D) LATIS program that will be ported to LATIS3D, and (4) developing a customized user interface. In addition to code development, we are continuing to explore applications for LATIS3D, particularly with researchers from the world's premier laser-medicine research groups.

Our accomplishments in FY98 included the following. In the area of ultra-short-pulse, hard-tissue ablation for ultra-high-precision surgery, we enhanced a wave-equation package to calculate the propagation and absorption in hard tissues. We performed a set of coupled laser-propagation–hydrodynamic simulations in which we explored three ablation mechanisms: vaporization, melting, and spallation. By comparing numerical simulations to experiments, we determined that melting and spallation are important effects in determining the ablation.

On the application of development of focusing opto-acoustic transducers for lithotripsy (breaking up kidney stones), we developed and incorporated an analytical EOS for use in the acoustic regime and performed simulations that will be used for designing experiments.

In the area of laser transport, we incorporated (1) a polarization-dependent tracking and scattering capability into LATIS, and (2) anisotropic scattering, boundary conditions, and surface sources into the KULL Monte Carlo package (and validated the results against a public-domain 2D Monte Carlo code). We also developed and tested a code that translates meshes from the format generated by medical images to the format required for KULL.

Our goal for FY99 is to develop and provide LATIS3D with a complete capability to predict laser-light doses for photodynamic therapy. To achieve this goal, we will develop accurate, three-dimensional (3D) numerical models of the anatomy targeted for arthritis therapy (e.g., the knee joint). These models will be based on medical images obtained from magnetic resonance imaging (MRI) and computerized axial tomography (CAT). Achieving our goal also requires completion of the 3D laser-transport package. We will use the models to design optimal delivery systems (e.g., diffusing optical fibers) and delivery protocols (e.g., fiber placement and irradiation times).

The Information Operations, Warfare, and Assurance (IOWA) Initiative

J. A. Smart
97-ERD-070

With the rapid growth of global computing and communications, information security is a critical issue in all discussions about protecting national infrastructures. The purpose of this Information Operations, Warfare, and Assurance (IOWA) initiative is to advance the enabling core technologies of this field. Special emphasis is placed on computer networks and telecommunication systems. Our effort requires (1) techniques for identifying the topology of large, complex computer networks; (2) data representation models for these systems; (3) high-performance methods for visualizing the resulting complex models; (4) automated analysis methods for processing large network representations; (5) specialized search techniques for isolating vulnerabilities; (6) a foundation for simulating network operation; and (7) an assessment methodology for determining the consequences of system component failure or disruption. The figure illustrates the multidimensional aspects of the problem.

To automate information system protection, we must first identify the visible components that an intruder might attempt to access and determine the specific information that might be inferred about each component. We began by developing a set of software modules for analyzing Internet-related protocols. This software examines the information that flows across a computer network and extracts network topology and details about each component's configuration. At present, the tool suite processes over 20 popular Internet protocols and retrieves over 50 system operating parameters.

Since modem computer networks have grown considerably in size (i.e., to >25,000 nodes), we developed a specially designed model to capture the enormous amount of information that the tools process. Our resulting model uses a unique blend of relational database technology integrated into a graphical, theoretical framework that provides rapid information retrieval in an environment conducive to mapping and analyzing large networks. We demonstrated a platform-independent viewer for browsing the graphical model that has integrated access to the relational database. To better manage the complexity of large networks, we incorporated several powerful dependency constructs, graphical operations, and reduction functions into the model. We also developed and demonstrated a diverse suite of generic graphical, fault-tree, and Internet-specific processing algorithms.

To better understand the nature of computer and network vulnerabilities, we developed a taxonomy of known vulnerabilities. This taxonomy formed the basis of a new vulnerability database that was populated with vulnerability facts from industrial and private sources. The end result is a tool that can now be used to automate the search for weaknesses in our computer systems.

While developing the modeling tools, we constructed an environment in which to perform high-fidelity simulations of computer networks. The resulting tools can be used to simulate computer networks captured in the IOWA model. To test and calibrate the network-mapping tools, arbitrary computer networks can also be constructed in the simulation environment and used to generate network traffic. While limited consequence modeling was performed in FY98, the application of our new modeling tools and simulation environment on actual systems will provide a strong foundation for future consequence assessment work.

In FY99, we will demonstrate IOWA's core technologies by constructing a comprehensive IOWA model of the Laboratory's entire unclassified computer network, applying IOWA's analysis and vulnerability tools, and precisely identifying exploitable weaknesses in these systems. The completion of this work will enable validation of IOWA's

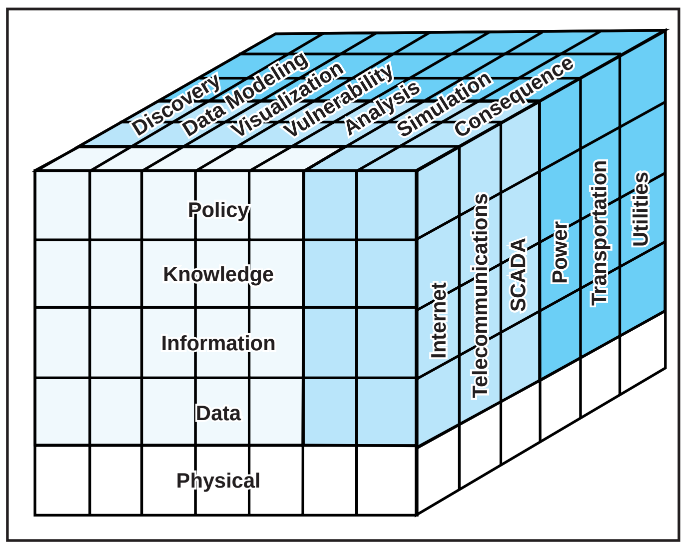

Critical infrastructure protection is a multidimensional issue. The labels on the front of this cube indicate the various levels of abstraction represented in the models we are developing, the labels on top identify the methodologies used to analyze the infrastructure, and the side labels show the vulnerable infrastructure components modeled (SCADA stands for supervisory control and data acquisition).

Unified-Element Technology for Explicit/Implicit Structural Mechanics

P. Raboin, J. I. Lin
97-ERD-072

For years, the finite-element (FE), structural/continuum mechanics codes DYNA3D and NIKE3D have been the workhorse computational tools at the Laboratory. Both codes are designed to solve problems with specific regimes of loading, deformation, or frequency characteristics. DYNA3D uses an "explicit" time-integration approach, which requires small integration-time increments but avoids solving large systems of simultaneous equations. NIKE3D employs an "implicit" integration scheme, which affords a large time increment but requires solving simultaneous equations in each increment. Because of these different philosophies, DYNA3D is particularly effective in simulating transient events of impulsive loading, high nonlinearities, and complicated contact conditions; NIKE3D is more suited for long-duration, quasi-static problems.

The continuous advancement of computer technologies and computational methods in the past decade has drastically expanded the application scope of these codes. Simulations involving multiple phases of distinctive characteristics have become commonplace—problems associated with initial stress (e.g., failure analysis of fan blades in aircraft engines), residual stress (e.g., sheet metal forming with spring-back), or the behaviors of visco-elastic/plastic materials are obvious examples. The explicit DYNA3D would have difficulty either attaining an equilibrium state for the rotation-induced initial stresses in the fan blades or sustaining a long-duration simulation of the spring-back phenomenon. Although the implicit NIKE3D is perfectly suited for these purposes, the fast-changing contact conditions and highly nonlinear deformations exhibited in the transient phase of these problems usually render NIKE3D ineffective and necessitate the use of DYNA3D. The goal of this project has thus been to link DYNA3D and NIKE3D in a serial arrangement so the advantages of both codes can be fully utilized for multiphased problems.

Because of their explicit/implicit nature, the codes favor different element formulations. In general, explicit FE codes prefer "under-integrated" elements, which use fewer spatial integration points than mathematically required because the stress evaluation at these points consumes the majority of the computation resource. Implicit codes usually prefer elements with more accurate spatial-integration methods because solving simultaneous equations replaces stress evaluation as the main computational burden. To have a seamless linkage between these codes, the necessary element information (e.g., stresses and strains) must be properly passed between them by either (1) stress interpolation/extrapolation, or (2) element formulation unification.

The first approach lets each code use its preferred elements to analyze a model and to generate necessary data through either interpolation or extrapolation procedures, as required by the other code. For example, DYNA3D, which contains fewer spatial sampling points, must extrapolate the stresses at these points to the NIKE3D sampling points before it can pass the data to NIKE3D. Conversely, NIKE3D must condense its sampling-point information to DYNA3D's sampling points through interpolation. The second approach adds each code's element technologies to the other. However, because of the high cost associated with using fully integrated elements in DYNA3D, it is more efficient to combine these two approaches. Then, a user could deploy the more expensive elements only where high-fidelity data transfer is required and utilize the interpolation/extrapolation scheme on the rest of the model. This aspect of our work was completed in FY97. In FY98, we concentrated on and completed the element technologies unification phase and implemented the new elements in both codes.

A shortcoming associated with under-integrated elements is the existence of spurious zero-energy modes, so-called "hourglass" modes, that exhibit deformation but yield no strain energy. Without numerical procedures to control them, hourglass modes often cause spatial instability and render the simulation results useless. The hourglass-control algorithms in DYNA3D and NIKE3D rely on a user-defined numerical parameter to determine the magnitude of the anti-hourglass forces. Only experience gained through past analyses can help in choosing the value of the parameter. In FY98, we developed new and improved physical hourglass-control methods and implemented them into DYNA3D and NIKE3D. This work involved research related to new projected strain fields and generated one journal publication.

Another important issue that we resolved in FY98 was to have comparable multibody contact features in both codes. Although popular contact algorithms are available in both codes, NIKE3D did not have the convenient and flexible automatic contact feature. This useful option, which relieves the user from the burden of defining detailed contact components, was added to NIKE3D in FY98.

The completion of this project brings forth a flexible and powerful numerical simulation tool for Laboratory analysts. Via a series of DYNA3D and NIKE3D runs, an analyst can take full advantage of the codes' characteristics in solving multiphased problems.

Enabling Computational Technologies for Terascale Scientific Simulations

S. F. Ashby
97-ERD-114

We are developing scalable algorithms and object-oriented code frameworks for terascale scientific simulations on massively parallel processors (MPPs). Our research in multigrid-based linear solvers and adaptive mesh refinement enables Laboratory programs to use MPPs to explore important physical phenomena. For example, our research aids stockpile stewardship by making practical detailed 3D simulations of radiation transport.

The need to solve large linear systems arises in many applications, including radiation transport, structural dynamics, combustion, and flow in porous media. These systems result from discretizations of partial differential equations on computational meshes. Our first research objective is to develop multigrid preconditioned iterative methods for such problems and to demonstrate their scalability on MPPs.

Scalability describes how total computational work grows with problem size; it measures how effectively additional resources can help solve increasingly larger problems. Many factors contribute to scalability: computer architecture, parallel implementation, and choice of algorithm. Scalable algorithms have been shown to decrease simulation times by several orders of magnitude.

Multigrid is an example of a scalable linear solver. It uses a relaxation method such as Gauss-Seidel to damp high-frequency error, leaving only low-frequency (smooth) error—which can be efficiently solved for on a coarser (smaller) grid. Recursively applying this to each subsequent coarse-grid system creates a multigrid V-cycle, so named because one first descends a hierarchy of successively coarser grids, solves a small problem, then ascends the hierarchy of grids. Interpolation and prolongation are used to traverse the hierarchy. If these operations are defined properly, the algorithm's computational costs grow linearly with problem size.

We research geometric and algebraic multigrid techniques. Geometric multigrid is typically used in problems on structured meshes. Such an algorithm, based on Shaffer's semi-coarsening method, sped up the linear algebra in an Accelerated Strategic Computing Initiative (ASCI) code by a factor of 27, reducing overall simulation time 10-fold for a 2D test problem (128,000 unknowns). Algorithmic scalability was shown in 3D test problems on the ASCI Blue Pacific and Red MPPs. In particular, using Red we solved a problem with 134 million unknowns in 24 seconds on 2048 processors. We investigate algebraic multigrid methods for problems defined on unstructured meshes. We have parallelized Ruge and Stuben's algebraic multigrid method and will run scalability experiments in FY99.

Our second research objective is to develop an object-oriented code framework for structured adaptive mesh refinement (AMR) applications, as shown in the figure. AMR allows efficient use of computing resources (CPU time and memory) by focusing numerical effort locally within the computational domain with varying degrees of spatial and temporal resolution. This makes practical simulations—especially those involving complex physics and large spatial domains—that would be too expensive on a uniform mesh. Our framework, a structured adaptive mesh refinement application (SAMRAI), provides extensible software support for rapid development of parallel AMR applications.

We completed the basic framework in FY98, including grid hierarchy management, adaptivity control, and visualization support. This parallel 3D framework is being used to develop several simulation codes, most notably one for studying laser-plasma interactions. SAMRAI is also used by the Utah ASCI Alliance Center of Excellence for its fire safety simulation code. In FY99, we will implement numerical methods and will work with application teams to run large-scale simulations on ASCI platforms.

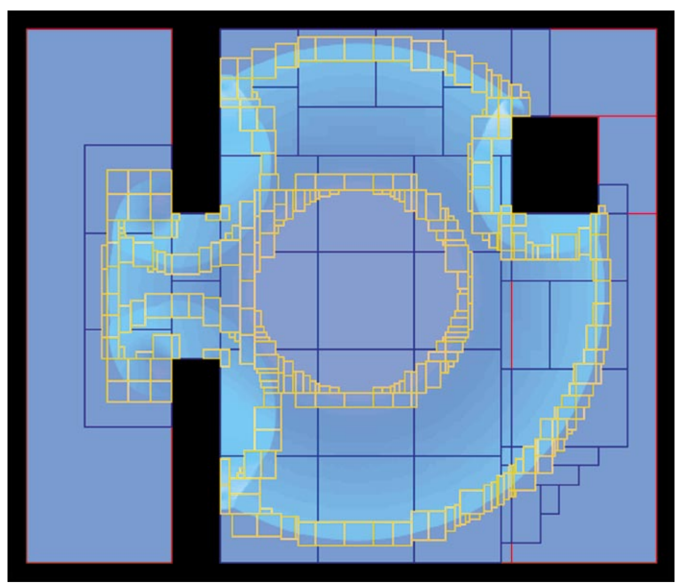

Adaptive mesh refinement dynamically focuses computational effort in the areas of interest, such as near the shock fronts in this hydrodynamics simulation.

Experimental Validation for Atomistic Simulations of the Deformation of Tantalum

G. H. Campbell, J. F. Belak, J. A. Moriarty
97-ERD-117

Atomistic simulations are an increasingly popular means of modeling materials. With this technique, an assembly of thousands, or even millions, of atoms are defined in a computer and allowed to interact according to certain rules. The boundary conditions include temperature and states of stress, allowing the calculation of such properties as the equation of state or ideal shear strength. The rules of interaction are very simple in order to speed computation. This simplification requires approximations to the physics of the interacting atoms. Hence, in the development of models of interatomic interactions, an evaluation is necessary to determine if the essential physics have been successfully incorporated.

The models are tested by comparing their predictions with experimental observations. The models are developed by deriving a form of the interaction from physical considerations containing some number of adjustable parameters. These parameters are fit to experimentally observed quantities or to quantities calculated for more detailed ab-initio methods. These quantities are usually equilibrium quantities; thus a good test of the model is how well it predicts properties away from equilibrium. The atoms residing in the core of a crystal defect experience an environment that is different in terms of neighboring atom distances and angles from those in an equilibrium-perfect lattice site. A convenient crystal defect to study is a grain boundary.

Recently developed models of interatomic interactions incorporate angularly dependent contributions to model materials with directional bonding, such as the body-centered-cubic (bcc) transition metals in which the d–bands participate in bonding. The strength of the directional component of the bonding has a major influence on the structure of grain boundaries. A model of interatomic interactions with angular dependence called the Model Generalized Pseudopotential Theory (MGPT) has been applied to modeling grain boundaries in tantalum (Ta) and molybdenum (Mo). One model for Mo is shown in Fig. 1(a) and (b). This boundary is a symmetric tilt grain boundary with the [001] crystal direction as the axis of tilt. It is seen in the view of the atomic model perpendicular to the tilt axis that the crystal planes are not perfectly aligned; rather there is a shift of one crystal with respect to the other. This shift depends critically on the strength of the angularly dependent terms in the model; without directional bonding, no shift is predicted.

In order to experimentally investigate the structure of the grain boundary shown in Fig. 1, we fabricated it by diffusion-bonding precisely oriented single crystals of high purity Mo. The atomic structure of the boundary was then investigated by high-resolution-transmission electron microscopy. The images acquired are shown in Figs. 1(c) and 1(d) and are projections of the structure in the two directions shown in the model in Figs. 1(a) and 1(b). The top image is a view of the boundary along the tilt axis. The bottom image is acquired in the direction perpendicular to the tilt axis. Viewed in this direction, only one set of atomic planes can be resolved in the microscope; thus only a single set of fringes is visible in the image. If this image is viewed at a glancing angle, to sight down the fringes as the fringes cross the position of the grain boundary, a shift is seen. The fringes in the top half of the image do not align with the fringes on the bottom half of the image. Thus the shift between the crystals predicted by the MGPT is confirmed by this experiment.

This observation is the first of its kind. Although symmetric tilt grain boundaries in the bcc metals have been studied by atomistic simulations for many years and this shift has been predicted, its existence has only now been confirmed. These results are a strong validation that the angularly dependent interatomic interactions incorporated in models such as the MGPT are a necessary component for the accurate atomistic modeling of the bcc metals. A grain boundary with the identical $\Sigma 5$ (310)/[001] geometry has been prepared in Ta as well as the closely related $\Sigma 5$ (210)/[001] boundary. Plans for FY99 include high resolution electron microscopy analysis of those boundaries and comparison with theoretical predictions.

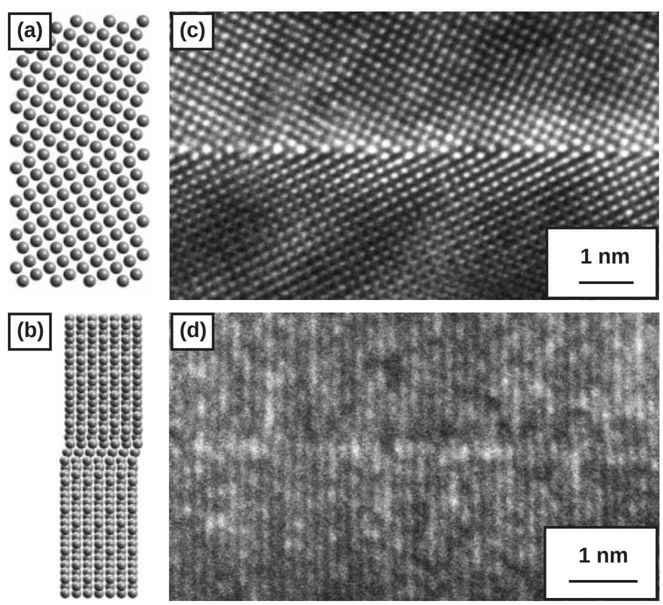

Figure 1. (a) Predicted atomic structure of the (310) symmetric tilt grain boundary in Mo, viewed parallel to the tilt axis and (b) perpendicular to the tilt axis. (c) High resolution electron micrograph of the boundary in the same orientation as (a) and (d) in the same orientation as (b).

New Conflict-Simulation Capability for Assessing Military and Civilian Health Effects from Exposures to Chemical or Biological Warfare Agents

J. I. Daniels, F. J. Gouveia, M. J. Uzelac, F. Y. Shimamoto, T. M. Kelleher, H. R. Brand, T. J. McGrann
98-ERD-006

Many potential aggressor nations, as well as some well financed extremist groups, have recently demonstrated covert capabilities for manufacturing, transporting, and offensively using chemical and biological warfare agents. Although incidents involving the use of these substances are of low probability, they potentially are of high consequence. Therefore, national and international attention is now focusing on procedures for preparing for and responding to military or terrorist acts involving the threat or actual use of chemical or biological weapons. Unfortunately, scheduling and conducting field exercises routinely to train for such incidents is often expensive, time consuming, logistically demanding, and not always productive. Accordingly, both military and civilian responder communities desire a more robust and cost-effective operational training tool that can be used frequently.

To meet this very important need, we have been exploring ways of enhancing the Joint Conflict and Tactical Simulation (JCATS) system so that it could be used for developing both military and civilian preparedness and responses to chemical or biological incidents. The LLNL-designed JCATS system is ideally suited for this purpose because it is an advanced, interactive computer-software model that simulates the performance of individually controlled opposing military personnel, noncombatants, and equipment under differing conventional battlefield scenarios. System output is a real-time visualization on a geographical landscape of evolving impacts on personnel and tactics. Furthermore, the JCATS system accommodates multiple operators and different terrain features and can be distributed for use at many locations.

During FY98, we focused on proving that the JCATS system could be enhanced to reliably and effectively assess the spectrum of consequences for military personnel of a scenario involving the release into air of an organophosphorus nerve agent. This required coupling a suitable atmospheric-dispersion model (for location and type of release and specific exposure concentrations) and dose-response algorithm (for exposure and toxic effects) to the JCATS system. We selected and employed a Gaussian puff-tracking model developed by the U.S. Naval Surface Warfare Center; this model contains reasonably well described release mechanisms for chemical agents and allows incorporation of time-variable meteorological data. For the dose-response algorithm, we adopted models that were physiologically based and that accounted for the inhibition of acetylcholinesterase by organophosphorus nerve agents. (Acetylcholinesterase is the enzyme responsible for hydrolyzing acetylcholine and preventing its accumulation—accumulated organophosphorus nerve agents produce continuing excitation of cholinergic-nerve fibers and disrupt nerve and organ function.)

The figure shows a snapshot of the JCATS visualization of impacts on performance of individual military personnel exposed to the plume created by an atmospheric release of an organophosphorus nerve agent adjacent to a collection of buildings. Our calculations demonstrated the feasibility of enhancing the JCATS model so that it can track a toxic substance released into the atmosphere and identify the spectrum of doses and corresponding effects on different individuals as a function of their behavior, location, and exposure time.

In FY99, we are favorably positioned to further improve the system scientifically and to customize it for potential military and civilian applications. Our objective is to further enhance the JCATS system so it can dynamically and systematically educate individuals on how best to address the impacts of adverse health effects from exposures to a wide variety of chemical and biological warfare agents—as well as other substances that might be employed as opportunity poisons—during acts of terrorism or warfare.

Joint Conflict and Tactical Simulation (JCATS) system visualization of performance and mission impacts resulting from exposures to a toxic plume created by the atmospheric release of an organophosphorus nerve agent adjacent to permanent buildings (numbers 200 and 211 identify specific personnel; "K" means killed).

Hybrid Ray and Wave Optics for Laser–Target Interaction

R. P. Ratowsky, J. S. Kallman, B. B. Afeyan, M. D. Feit
98-ERD-019

The goal of our project was to create a computational tool that would move easily between ray and wave optical regimes. This is an important capability in areas such as laser propagation in plasma and multimode photonics, where systems can be optically large, but where we require calculating diffraction and interference effects. Our approach was to use phase-space methods, where a set of rays distributed in a particular way in position and angle retain many essential features of wave propagation. By launching the right set of rays, diffraction and interference can be calculated directly from the ray distribution without explicitly solving a wave equation. In this way, a problem domain can easily use both ray and wave optics in the regions where the descriptions are most appropriate. To characterize and enhance our understanding of the method, we developed a tool based on a graphical user interface (GUI); this tool can analyze light propagation in systems with a variety of axial and transverse refractive-index profiles.

We conceived a wave-propagation algorithm as follows. From an initial complex electric-field distribution, we calculate a ray distribution function in position and angle known as the Wigner transform. By integrating the Wigner distribution over angle or position, we obtain what are called the nearfield or farfield, respectively. Since in wave optics the nearfield and farfield amplitudes are related by Fourier transform, the complex electric field can be reconstructed (up to a constant phase factor) from the ray intensity distributions in position and angle.

The code developed for this project, which we call Phase Space Techniques for Electromagnetics Research (PHASTER), allows us to set up an arbitrary initial beam consisting of a sum of Gaussians with selected widths and amplitudes. After computing and displaying the Wigner distribution for the beam, PHASTER will solve the ray equations for a set of points in the ray phase-space that samples the distribution in a prescribed manner. The rays are traced through a variety of refractive-index profiles having both transverse and axial variation. After propagating the prescribed set of rays to the exit plane, the code displays the phase-space distribution at the exit plane, as well as the x-space and angle-space intensities. PHASTER gives useful insight into the dynamics of the rays in phase space and their effect on the wave optical distribution. It also allows us to study systematically the important issue of sampling. Sampling is critical: if we do not sample wisely, we suffer in computational efficiency for a given accuracy.

We used PHASTER to study a number of practical problems. For example, we calculated that the evolution of a beam is incident at an oblique angle on a linear index gradient—a model for a laser propagating in a plasma. A subset of the rays is reflected by the plasma index gradient, while the rays getting through form a distorted distribution on the high-density side. This example is of particular interest because the problem admits an exact solution in terms of Airy functions, thus allowing direct evaluation of accuracy. We also (1) added high-frequency speckle to the beam, an important feature of laser propagation in plasma and in multimode optical fibers; and (2) calculated propagation in waveguiding structures, important for plasma propagation and multimode photonics applications. The evolution of speckle in multimode fiber allowed us to calculate modal noise, which is the random variation in power that often occurs in multimode optical systems.

Our FY98 project has resulted in a new propagation capability that is now being applied to LLNL's photonics needs. The project was successful in implementing a phase-space propagation technique in a practical tool, elucidating the advantages and limitations of the method, and pointing the way for further development.

Modeling of Anisotropic Inelastic Behavior

D. J. Nikkel, A. A. Brown, J. Casey
98-ERD-020

We are working to develop better physical models of the behavior of metals subjected to large inelastic deformations, models that accurately reflect the anisotropic behavior of these materials. To this end, we are using an experimental capability that we developed at LLNL to study the yield behavior of elastic–plastic materials under multiaxial, nonproportional, large-deformation conditions. Our experimental results show that actual material responses can differ significantly from those predicted by the simple, idealized models commonly used in numerical-simulation codes.

Polycrystalline metals subjected to loads or deformations initially behave elastically. However, if the deformations or loads become large enough, the material begins to exhibit plastic behavior. That is, there is no longer a one-to-one correspondence between stress and strain, the response is dependent on the loading path taken to reach a given state of deformation, and residual (plastic) deformations remain after the external loads have been removed. This gives rise to the theoretical idealization of an elastic–plastic material and, in particular, to the notion of a yield criterion that describes the boundary between loads (or deformations) that result in only elastic behavior and those loads that result in inelastic deformation. The analytical description of this criterion, the yield function, is a central feature of the constitutive theory of elastic–plastic materials. Viewed geometrically in stress (or strain) space, this criterion represents a surface bounding the region where only elastic behavior occurs. We are experimentally measuring representative points on the multiaxial yield surface at a given elastic–plastic state. After additional inelastic deformation, the surface is again measured and its evolution can then be observed. In the figure, each closed curve represents the measured stress-space yield surface at a particular inelastic state. Yield surfaces at several states for three sets of experiments are shown: tensile loading followed by shearing (O–A_1–A_2); a pure shearing path (O–B_2), and axial compression followed by shearing (O–C_1–C_2).

In FY98, we made significant progress in refining experimental procedures to reduce errors in the measurements and to ensure repeatability. We have measured yield surfaces along paths of varying conditions of tension, compression, and torsion. As seen in the figure, with sufficient deformation the yield surface no longer contains the origin in stress space. A high level of accuracy is required for the two kinds of experiments we are performing: (1) the measurement of yield surface evolution to guide model development as discussed above; and (2) critical experiments to resolve a basic scientific question regarding the appropriate way to identify the plastic strain tensor under general nonlinear deformations.

In addition to the experimental effort, we have begun to examine numerical issues related to implementation of anisotropic plasticity models into LLNL's codes. To evaluate methodologies for integrating the evolution equations, we have implemented a general quadratic yield function model into the parallel version of the ALE3D code (Alec). ALE3D is a multiphysics code used to predict the thermomechanical response of structures under high-loading-rate, large-deformation conditions. More general models, which better represent the data being generated, will be numerically implemented in FY99. A model of crystal plasticity has also been implemented into NIKE3D, LLNL's nonlinear, implicit, solid-mechanics code. This allows for the explicit modeling of microstructural details in order to be able to predict what the effective macroscopic yield surface should be for known microstructures. This capability will be exploited in the coming year.

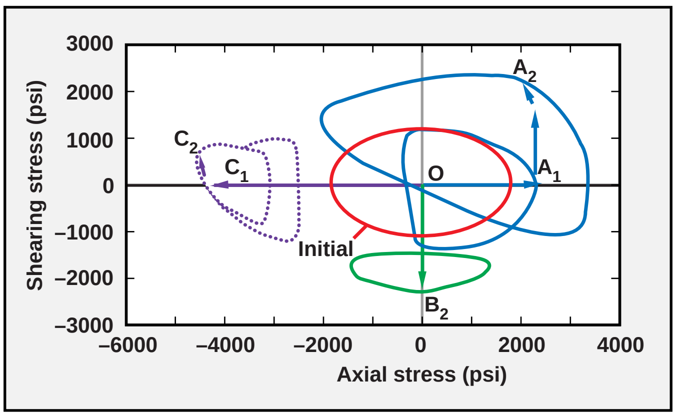

Experimentally measured stress-space yield surfaces from three sets of experiments (differentiated by color) on 1100 Al. Initial yield is well represented by the elliptical Mises-yield surface; however, subsequent yield surfaces, for all loading paths, exhibit hardening that is clearly anisotropic.

Novel Parallel Numerical Methods for Radiation and Neutron Transport

P. N. Brown, B. Chang, U. Hanebutte, F. Graziani, C. S. Woodward
98-ERD-022

In this project, we are developing scalable solution methods for the equations that model the transport of photons and neutrons through materials. In many of the multi-physics codes at the Laboratory, transport generally comprises anywhere from 30–50% of the time for a simulation. When using Monte Carlo methods, the percentage can be as high as 80%. Our goal is to reduce the transport solve time in these simulations via more advanced numerical methods along with their parallel implementations. In particular, scalable methods are a necessity. By *scalability,* we generally mean that the time to solution remains constant as the problem size grows and additional computer resources are used. For iterative methods, scalability requires that the number of iterations to reach convergence is independent of, and the computational cost grows linearly with, problem size.

We are focusing on deterministic approaches to transport, building on our earlier work in which we performed a new detailed analysis of some existing methods for transport and developed some new approaches. The underlying equation to be solved is the Boltzmann equation, and various solution methods have been developed over a long period of time. Many production codes are based on these methods, which are in some cases decades old. For the transport of x-rays through partially ionized plasmas in local thermodynamic equilibrium, the transport equation is coupled to nonlinear diffusion equations for the electron and ion temperatures via the highly nonlinear Planck function. We are investigating the suitability of traditional solution approaches to transport on terascale architectures as well as designing new scalable algorithms, and in some cases hybrid approaches combining both.

Our other research areas include structured adaptive mesh refinement (SAMR) techniques and first-order-system least squares (FOSLS) methods. We began working on the design of a SAMR neutron transport code during FY98. The FOSLS technology is by design a scalable multilevel approach. We made significant progress on a FOSLS code during FY98, and anticipate having a parallel FOSLS code by the end of FY99. We also are investigating the use of multilevel techniques in traditional methods. In FY98, we developed a parallel-diffusion-based preconditioned iterative scheme for our existing neutron transport solver, and have shown it to be algorithmically scalable.

Since the radiation transport equations are nonlinear, the time integration methods in many codes are based on operator splitting, which effectively time-lag the nonlinear terms in order to avoid solving nonlinear systems. During FY98, we developed a fully coupled nonlinear solver for radiation transport. Recent advances in solver technology now allows consideration of the fully coupled approach, and has suggested that fully coupled methods offer the same (or increased) accuracy for comparable computational cost. The fully coupled approach must solve linear and nonlinear systems on each time integration step. We use a Newton-Krylov nonlinear iteration, where the linear Krylov method is the generalized minimal residual (GMRES) method. Preconditioning is essential to accelerating the convergence of the iterative Krylov methods. Our preconditioner uses a parallel semicoarsening multigrid method (SMG) developed at LLNL to invert the main diagonal blocks of the linear system matrix.

We have verified the accuracy of our solver using test problems having analytic solutions. Specifically, a two temperature Marshak wave problem developed by Olson and Su at LANL was used in this comparison. We also have begun investigating the parallel scalability of our approach on a 3D version of this problem. The figure shows the scaled efficiency of the total runtime (blue line) and the scaled efficiency of the solve part of the parallel SMG preconditioner for a typical linear solve (black line).

Our plans for FY99 include putting our fully coupled nonlinear solution method into the ASCI code ARES to perform the radiation transport. As ARES includes realistic physics and sophisticated spatial discretizations, this will be a good test of our solution approach. We also will pursue additional preconditioning approaches for problems that involve significant particle scattering, and will continue developing solvers based on SAMR and FOSLS.

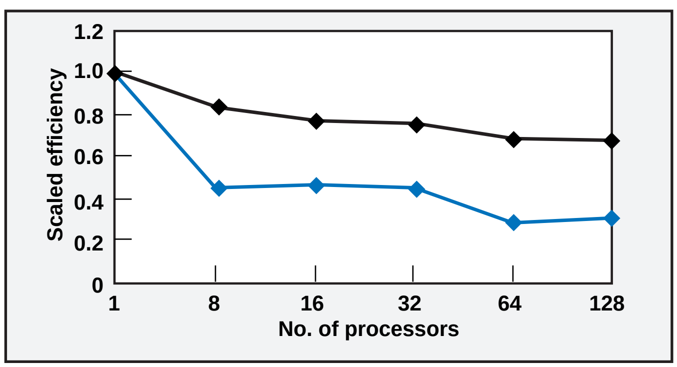

The blue line shows a plot of scaled efficiency for the entire runtime of our solver (100 time steps) on a 3D version of the Olson-Su test problem. There were $N = 40^3$ spatial mesh points per processor. The black line shows a plot of scaled efficiency for a typical solve using the SMG preconditioner.

An Object-Oriented Framework for Magnetic-Fusion Modeling and Analysis Codes

R. Cohen, T.-Y. Brian Yang
98-ERD-033

The magnetic-fusion energy (MFE) program, like many other scientific and engineering activities, has a need to efficiently develop (1) complex modeling codes that combine detailed models of components to make an integrated model of a device, as well as (2) a rich supply of legacy code that could provide the component models. There is also growing recognition in many technical fields of the desirability of steerable software: computer programs whose functionality can be changed by the user as it is run. This project had as its goal the design and development of two key pieces of infrastructure that are needed to combine existing code modules written mainly in FORTRAN into flexible, steerable, object-oriented, integrated modeling codes for MFE. These two pieces are (1) a set of tools to facilitate the interfacing of FORTRAN code with a steerable, object-oriented framework (which we have chosen to be based on the Python interpreted language), and (2) a skeleton for an integrated modeling code that defines the relationships between the modules. The first of these activities has immediate applicability to a spectrum of projects; the second is more focused on the MFE application, but may be of value as an example for other applications.

During FY98, we developed tools to automate the Python–FORTRAN interface. The tools consist of two sets of Python codes: (PYCOMMON), which makes FORTRAN common blocks (groups of globally defined variables) accessible to the Python interpreter; and (PYCFORTRAN), which enables the Python interpreter to invoke FORTRAN functions and subroutines.

The input to PYCOMMON consists of files containing standard FORTRAN-77 common-block and variable-type declarations. The output consists of files containing wrapper functions written in C. These output files can then be compiled and linked with the FORTRAN-77 code to form dynamically loadable Python modules. When imported by Python, these modules contain Python objects with attributes corresponding to the items in the FORTRAN common blocks. The values of these attributes correspond exactly to those of the FORTRAN common-block variables. Furthermore, the values of the FORTRAN common-block variables can be altered by changing the corresponding attributes from the Python interpreter. Such capability, usually referred to as "steerability," gives users flexibility both during code development and while running production simulations.

The input to PYCFORTRAN consists of files containing standard declarations of FORTRAN-77 subroutines, functions, and variable type, with an extension to specify arguments as input or output variables. The output of PYCFORTRAN consists of files containing wrapper functions written in C. In the input file for PYCFORTRAN, users can also specify which input files to PYCOMMON should be included as parts of the Python module, so that the wrapper functions for the corresponding common blocks are included in the output of PYCFORTRAN. This way, the resulting Python module contains Python objects for FORTRAN common blocks as well as functions that invoke FORTRAN functions with proper argument-type checking and array-bound checking. We also performed successful but limited testing of the tool with FORTRAN-90 modules. (FORTRAN-90 is a relatively recent extension of FORTRAN that is becoming somewhat popular for scientific computing.)

The second key piece of infrastructure is a skeleton for an object-oriented transport code—the basic prototype for the desired code. A key element of such a code is the development of a class hierarchy—a definition of logical components, or objects, of a code, based on structure and function and grouping similar objects as specific instances of more general "classes" (which can themselves be descendants of still more general classes). Such a design, properly executed, facilitates code maintenance and enhancement by localizing specific functionality that is likely to change to small, isolated parts of the code.

Over the course of the year, we developed a class hierarchy for a prototype Python transport code, as well as (and in fact via experience with) an operational code. We started with the transport models, and over the course of the year extended (and revised) the class structure to include all aspects of a functioning transport code. This activity has facilitated our entrance into, and our influence on, the National Transport Code Collaboration (NTTC), an initiative launched by the national Magnetic Fusion Energy Program in May 1998. In late FY98, our Python prototype was adapted as the basis for development of the initial physics core for the NTTC demonstration code, an activity that is now ongoing.

Computational Theory of Warm Condensed Matter

T. W. Barbee III, M. P. Surh
98-ERD-052

Laboratory missions such as science-based stockpile stewardship (SBSS) demand accurate materials-modeling capabilities. Among these, calculations of the equation of state (EOS) and opacity play important roles. SBSS programs require knowledge of these properties over an extreme range of densities and temperatures. In the low-density/high-temperature limit, models based on plasma physics are very accurate, whereas models based on condensed-matter physics perform best in the high-density/low-temperature regime. In this project, we are focusing on "warm" condensed matter, i.e., on the region of intermediate temperature and density where the high-temperature or low-temperature approximations may no longer be valid.

Current models for the EOS of warm dense matter are primarily based on theoretical models that are most accurate in the low-temperature limit and that treat the effect of finite temperature as a perturbation of the zero-temperature solution. These models are largely untested above the melting point—especially approaching the Fermi temperature (the characteristic energy scale for the interacting electrons in a material). Thus, the goal of the current project is to develop rigorous extensions of existing state-of-the-art condensed-matter techniques that are valid in this intermediate-temperature regime.

Our approach focuses on three areas: improving theoretical treatments of the thermal contributions to the EOS; calculating optical properties (e.g., opacity) at finite temperature; and developing a new theoretical formalism that can be used to solve the quantum-mechanical, many-electron problem at finite temperature.

During FY98, we concentrated on the first and third of these three areas. We took existing band structure and total-energy computer codes for condensed matter at zero temperature and added the capability to calculate thermal contributions to the EOS. These contributions arise from two sources: (1) the thermal excitation of electrons into higher-energy states, and (2) the thermally induced motion of the ions. These improvements allowed us to model experiments in which a semiconductor crystal heated by a femtosecond-pulse laser was found to thermally induce structural instabilities within a few picoseconds (10^{-12} s) of heating. On this short a time scale, the electrons remain hot while the ions are relatively cold; therefore, melting of the crystal cannot explain the experimental results. Several groups have proposed that heating the electrons into excited states alters the forces that act on the nuclei, resulting in the observed lattice instability. To simulate the experimental conditions, we used the codes we developed to calculate the vibrational properties of a silicon crystal with cold (stationary) ions and hot electrons. The figure shows that at a sufficiently high electron temperature (a few eV), the crystal lattice becomes unstable—as reflected by a negative force constant. This calculated result agrees with what was seen in the experiment.

We have also implemented a simple model for the interacting electron gas at finite temperature and have begun testing how this more accurate description of the electrons in warm condensed matter affects observable properties such as the EOS.

During FY99, we plan to study the effects of ion motion and disorder on the EOS of warm condensed matter and to begin calculating the optical properties of simple metals, such as Be and Al, at temperatures near and above their melting points.

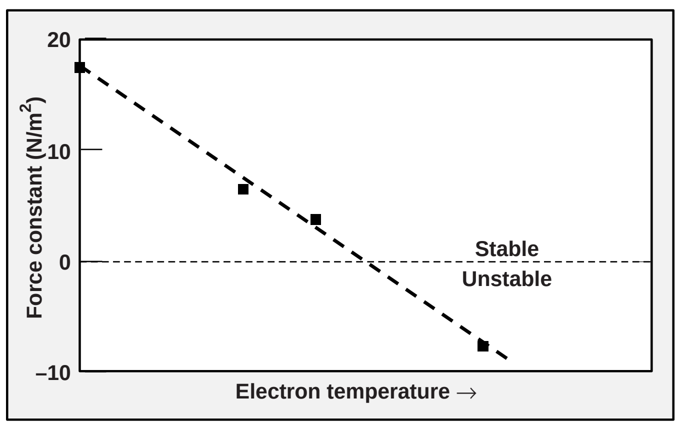

Calculated force constants in silicon as a function of electron temperature. With increasing electron temperature, the force constant becomes negative, indicating a lattice instability, as seen in ultrashort-pulse laser experiments. The squares are calculated values, and the dashed line is a guide to the eye.

LambdaConnect: Multiwavelength Technologies for Ultrascale Computing

R. J. Deri, M. E. Lowry, M. C. Larson, M. D. Pocha, H. E. Garrett, H. E. Petersen, R. R. Patel, W. Goward, M. A. Emanuel

98-ERD-057

Ultrascale computing—the integration of large numbers of processors into a single, highly capable multiprocessor system—is of great interest for several national security missions. These systems contain hundreds to upwards of 1000 central processing units (CPUs) to attain computing capabilities from 100 Gflops (floating-point operations per second) to 100 Tflops and beyond. The provision of fast data communications within such systems poses a significant challenge. The communications bottleneck among these processors can substantially degrade computational performance, significantly complicate programmability, and cause inefficient use of costly memory resources. This work, which we call LambdaConnect, addresses technology to solve this bottleneck.

The recent emergence of byte-wide optical interconnects, which use linear arrays of multimode optical fibers in a ribbon-cable assembly, has substantially improved the cost and performance of Gbyte/s point-to-point communications. To fully leverage this technology, however, the latency and congestion issues with distributed electronic switching must be overcome.

Earlier, we had proposed source-routed switching in the optical domain using a wavelength-switching mechanism to address these issues, and we had demonstrated the advantages through simulation. Now, in this LambdaConnect project we are focusing on developing prototypes of required components to enable byte-wide, multiwavelength optical interconnects for ultrascale computers. These components—optical transmitters capable of fast wavelength tuning and fixed optical filters—differ substantially from existing telecommunications fiber optics. All components must be compatible with existing multimode fiber-ribbon cables, and they must provide compact form factors suitable for populating electronics boards.

In FY98, we achieved remarkable progress in both the wavelength-selectable transmitter and the fixed-wavelength filters. We developed optical-filter modules based on the packaging of thin-film interference filters within a housing comprising ribbon-cable connector ferrules. The advantages of this approach are that the module is assembled primarily by passive alignment using interlocking guide pins, and it automatically mates to ribbon-cable connectors.

Our initial filter designs were single-cavity Fabry-Perot filters that achieved acceptable insertion loss and filter bandwidths as small as 4 nm. Modules with the broader (14 nm) passband have been cascaded in series to improve cross talk suppression and to achieve somewhat narrower passbands. However, filter modules with a flatter top and sharper skirts than obtainable from the Lorentzian lineshape associated with single-cavity designs are valuable because they (1) improve system tolerances to variations and drifts in the wavelengths of individual transmitter and filter modules, and (2) enable tighter spacing of wavelength channels.

We have demonstrated such a filter module, which is based on a multicavity interference-filter design. Its response (see figure) shows a flatter top and substantially sharper filter skirts than achievable with single-cavity devices, and it exhibits cross talk suppression better than 30 dB. This device is suitable for channels spaced 8 to 10 nm apart, and provides a 5-nm tolerance window for variations in component wavelength (at 1-dB excess loss).

These filter achievements and our demonstration in FY98 of 2- and 4-wavelength, vertical-cavity, surface-emitting, laser-based transmitter technologies position us for our FY99 goal of an 8- to 32-wavelength link prototype. We have also solved some significant mechanical/optical packaging difficulties and demonstrated both a 2- and 4-wavelength, vertical-cavity, surface-emitting, laser-based transmitter technology. Thus, we are well positioned to achieve our FY99 goal of an 8- to 32-wavelength link prototype.

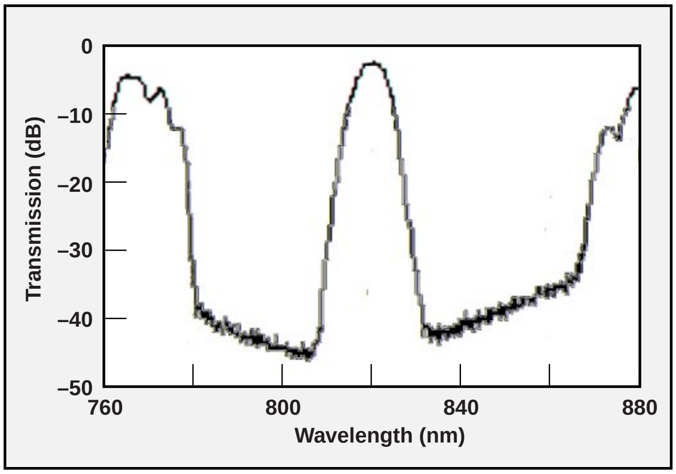

Transmission response of our newly developed multicavity filter module. The high shoulders and low skirts of this response function will greatly reduce wavelength cross talk from that of earlier designs.

Simulator for an Integrated Computer Control System Based on a Common-Object Request-Brokering Architecture

P. J. Van Arsdall, R. M. Bryant, F. W. Holloway
98-ERD-065

Risks associated with distributed control systems can be great for complex, mission-critical scientific facilities. That is, problems with the control-system architecture can hinder construction or limit scientific utility of the facility later during operations. LLNL is developing an abstract software framework, the Integrated Computer Control System (ICCS), for building event-driven control systems for current and future facilities. ICCS integrates data acquisition and control hardware with a supervisory system and reduces the amount of coding necessary by providing prebuilt components that are reused and extended to meet additional requirements. It is interoperable among computers of different kinds and provides plug-in software connections by leveraging a common-object request-brokering architecture (CORBA) to transparently distribute software objects across the computer network. However, because object-brokered distribution applied to control systems is relatively new, and its inherent performance is roughly one-third that of traditional point-to-point interprocess communications, CORBA presented a performance risk to designers.

In this project, we evaluated CORBA and the underlying network and software architecture against high-stress-control scenarios to determine distribution performance and scaling properties. Results were used to optimize the ICCS architecture. We studied both UNIX and real-time operating systems with tools we developed in the object-oriented Ada95 language. By measuring software prototypes on a computer test bed, we estimated the performance of potential deployment schemes; we used discrete-event simulation techniques to scale prototype data to the desired operating regime. To demonstrate their utility in a demanding real-world application, the tools developed for this project were applied to predict the performance of the ICCS architecture under deployment scenarios relevant to the design of the National Ignition Facility (NIF).

Most control-system messages average 100 bytes of data. In this operating regime, CORBA transacts over 2,800 messages/s, while using up to 80% of a powerful processor. For small messages the processor is the limiting resource, because network bandwidth is not heavily used. As messages become larger (e.g., spatial sensor data), the network eventually becomes the limiting factor. These factors led designers to partition facility computers into smaller, isolated network segments so that the communications design point for any one segment would average about 500 control transactions/s or less. This approach reserves network capacity for traffic peaks as well as processing capacity for other computational tasks.

The local area network, which delivers timely and reliable communication between control applications, is another critical resource that impacts CORBA performance. We selected a network modeling tool (Mil3 Opnet Modeler) and developed simulations of a hybrid network that uses both Ethernet 10- and 100-Mbit/s and asynchronous transfer mode 155-Mbit/s technologies to interconnect computers. By simulating operation under worst-case conditions, we derived performance estimates of key control-system tasks. Actual performance data collected from the test bed verified our simulation parameters. In an example scenario taken from NIF's alignment system, the expected traffic will be the simultaneous transfer of control messages along with high-bandwidth digital video. Our analysis of simulation results indicates that a properly partitioned network will meet NIF's throughput and latency requirements. Additional simulation results also showed that some trigger signals as fast as 1 ms could be reliably broadcast over the network, obviating the need for separate trigger-distribution hardware. Analysis of NIF's network showed that this technique could save approximately $250K over conventional methods.

To complement our CORBA measurements and network simulations, we used another general-purpose simulation tool (CACI Simprocess) to model the performance of CORBA-distributed objects. The scenarios modeled placed heavy demands on system infrastructure and included computer-system restart, subscription-based equipment status monitoring, and control-loop interactions between supervisory workstations and front-end processors. The topology studied included image processors, supervisory workstations, video digitizers, and motion-control systems. Our simulation results led to changes in the design (e.g., change-threshold status filtering) and hardware fixes (e.g., improving manipulator reaction time) that would lead to acceptable system performance.

From the outset, the ICCS was designed so that it could be reused on future projects at LLNL and elsewhere. This project developed simulation tools that successfully guided the integration of CORBA as the key enabling technology in the architecture.

A General Method for Coupling Atomistic to Continuum Mechanics Simulations with Application to Stress-Corrosion Cracking

A. A. Quong, W. G. Wolfer
98-ERD-087

Stress-corrosion cracking (SCC) is the most common mode of failure for a wide range of materials and is responsible for the failure of bridges, fiber-optic cables, nuclear-waste containers, and reactor pressure vessels; it costs the public and industry billions of dollars every year. In typical failures, the growth rates of the cracks are very slow, and it is very hard to predict when a device will fail. Environmental effects, macroscopic stress fields, and thermally induced materials changes are just a few of the many effects that must be included in the analysis when we try to understand SCC. Because many of these effects are macroscopic, it is very difficult to understand how they will affect the breaking of single atomic bonds at the tip of the crack.

In the traditional way to deal with SCC, the environmental aspects are accounted for in an empirical fashion. There is no mechanistic coupling of chemistry at the crack tip with fracture mechanics at the macroscale. Our method will enable us to make this connection for the first time in a rigorous and general manner.

In the present project, we are developing a new computational approach that will enable us to treat the crack tip on an atomistic level and also incorporate macroscopic fields. Stanford University will provide experimental data to apply and test our method. We achieve this by embedding an atomistic region in an elastic medium. The atomistic region contains the crack—this allows us to treat the chemistry at the tip properly. The macroscopic region is modeled as an elastic medium, and the boundary conditions are applied to this region. The difficulty is in coupling the two regions to each other. The virtual atoms will ensure that the real atoms in the atomistic region see the correct environment even when they are adjacent or near the continuum/atomistic interface. In the figure, we illustrate a model of the system. Included in the atomistic region are two orientations of a bulk material with a crack at the interface. There are also impurities and vacancies. The elastic continuum is modeled using linear elasticity theory—the corresponding equations are solved using the boundary-element method (BEM). The atoms in the continuum are virtual or quasi-atoms, which perform two roles: (1) they provide the correct environment for the atoms near the continuum–atomistic interface, and (2) they provide the interaction between the two regions.

In implementing the BEM for two-dimensional isotropic elastic media and the atomistic codes, we have treated the atomic interactions as pair potentials. At the close of FY98, we were testing the algorithm used to generate the boundary conditions at the interface between the continuum region and the atomistic region for accuracy and efficiency, and we were beginning to extend the BEM to anisotropic elasticity. In FY99, we will first study defects in alpha-alumina by examining, in vacuum, the effect of relationships between crack orientation and applied stress on the strength of atomic bonds at the crack tip. The next step in the development of the method will be to include a quantum-mechanical description of the interatomic forces. This will allow us to study how the addition of corrosive molecular species at the crack tip will change the strength of the atomic bonds at the crack tip.

The development of this computational tool will provide a framework for a comprehensive study of SCC. Understanding SCC is important to a wide range of LLNL's missions, including nuclear-materials stewardship, stockpile stewardship, and programs such as Yucca Mountain. Furthermore, this tool is not restricted to studying SCC, but can be used for a wide range of problems in materials science (e.g., noninteracting defects such as point defects or dislocation-core structures). This tool will provide us with a way to study materials problems on the mesoscale.

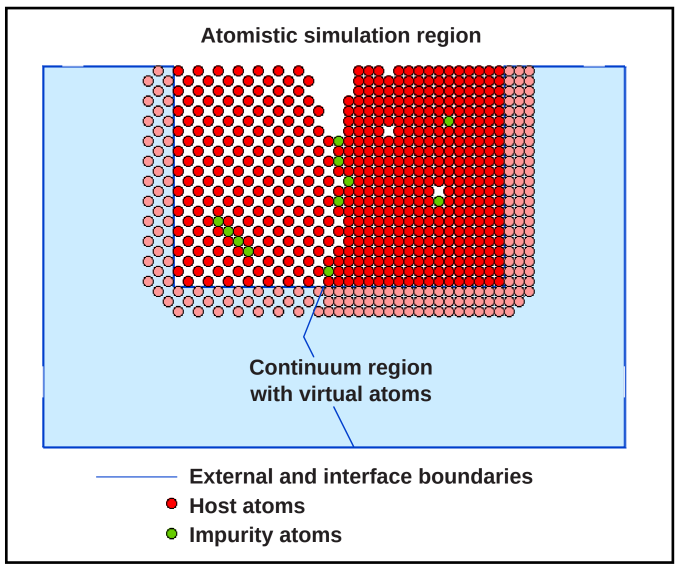

Example of simulation cell containing an atomistic region embedded in a continuum region. The virtual atoms aid in coupling the two regions.

Effects of Radiation on the Mechanical Properties and Structural Integrity of Nuclear Materials

T. Diaz de la Rubia
98-ERD-090

The lifetime of structural materials in nuclear power systems is often limited by their interaction with environmental variables such as radiation damage, temperature, stress, and the chemical environment. As nuclear reactors around the world are aging, the ability to predict accurately the status of various nuclear components is becoming critical from the point of view of nuclear safety and the extension of reactor operating life.

To meet the need to develop a multiscale model of mechanical property changes in metals exposed to high radiation environments in nuclear power plants, we began, in mid-FY98, a project to develop and apply tools for simulating atomistic and dislocation dynamics. These are tools that will enable us to describe microstructure evolution in irradiated materials over 14 orders of magnitude in time scale (from picoseconds to seconds) and 4 to 6 orders of magnitude in length scale (from nanometers to tens of micrometers). As a result, we will be able to describe within a multilength and time-scale simulation the nonequilibrium response of the material to an irradiation field as well as the changes in mechanical properties that ensue.

In the first half year of this study, we focused on developing a flexible boundary-condition methodology for calculating by molecular-statics methods the interactions among point defects, defect clusters, and dislocations. The method is based on the use of anisotropic elasticity and Greens functions to couple an atomistic region to an elastic continuum. We have implemented this technique into our molecular dynamics and statics simulation code MDCASK and have begun to use it to model point-defect and cluster interaction with dislocations in body-centered cubic (bcc) iron and vanadium.

In addition, we have carried out extensive molecular-dynamics simulations of high-energy (up to 20 keV) displacement cascades in copper, vanadium, and iron. The results obtained in these simulations clearly show the drastic difference in the primary damage state between face-centered cubic (fcc) and bcc metals. Our results predict that in fcc metals the displacement cascade results in large vacancy clusters surrounded by self-interstitial clusters. In bcc metals on the other hand, the simulations show that—although interstitial clusters form in the periphery of the cascade—vacancy clusters do not form in the center. We believe that these results provide insight into the drastically different damage-accumulation behavior observed between bcc and fcc metals.

To validate this claim, and to further understand these differences, the primary damage state obtained from our molecular dynamics simulations has been coupled with our kinetic Monte Carlo code BIGMAC in order to predict the rate of damage accumulation in iron, vanadium, and copper as a function of irradiation dose. Results have been obtained to date for irradiation doses up to 0.005 displacements per atom (dpa), and the results agree very well with the experimental database. The results predict that—although in copper the density of visible defect clusters in the transmission electron microscope should be of the order of $10^{17}/cm^3$—in iron, no visible clusters should appear at this dose. This simulation result is in excellent agreement with the experimental database.

In addition to the atomistic calculations, we have initiated a systematic dislocation-dynamics study of the effect of irradiation-induced decoration of dislocations in bcc iron. The preliminary results already show an increase in yield stress with irradiation dose, in good agreement with experiments. Further work aimed at elucidating the phenomenon of flow localization and plastic instability in irradiated metals is under way.

In FY99, we will (1) focus attention on calculating defect and precipitate interaction energetics with dislocations in bcc metals; (2) continue to carry out our molecular dynamics/kinetic Monte Carlo studies of damage microstruture evolution over macroscopic time scales; and (3) use the outcome of these simulations to predict—using the dislocation-dynamics tool—the evolution of the mechanical properties of irradiated bcc metals with age. In particular, we will develop an understanding based on these calculations of the increase in yield stress with irradiation dose in bcc metals—with the ultimate goal in FY00 of understanding the ductile-to-brittle fracture transition in these systems.

Algorithm for Wave–Particle Resonances in Fluid Codes

N. Mattor

98-ERD-099

This project (which was begun late in FY98), aims to develop a simpler way to view one state of matter: the collisionless fluid (e.g., hot plasmas or self-gravitating astrophysical gases). If it is successful, the dimensionality of such systems will be reduced by a factor of two—by eliminating the need to resolve particle velocity—and physicists can greatly increase the accuracy of present-day models.

In the general sense, a “fluid” is a collection of many similar particles, each of which moves freely; examples are air, water, the sun, stellar nebulae, fusion plasmas, and exploding hydrogen bombs. In physics, we want to predict the behavior of these things. However, tracking the motion of each individual particle is simply impossible; it requires too much information for even the most advanced computers imaginable. Fortunately, it was shown by physicists such as Boltzmann, Chapman, and Enskog that many such fluids can be greatly simplified. Specifically, if particles collide with each other frequently enough, the fluid takes on a simple collective behavior, and it is possible to describe all the particles in terms of three quantities: density, velocity, and temperature. Such a highly collisional system is a “fluid” in the restricted sense and is described by “fluid equations,” an accurate but vast simplification of the full dynamics.

Air molecules around us collide about every 0.06 µm (the smallest bacteria are about 1 µm), and so the fluid description generally works well here. However, there are many systems that are not so collisional. At 160 km above sea level, air molecules travel about 50 m between collisions; in the solar corona, hydrogen ions travel about 100 km. Phenomena on shorter scales than these are generally thought not to be fluid. Still, such systems are commonly studied with fluid equations; although these miss a number of known phenomena (e.g., resonances between waves and particles), they are used anyway because they are solvable.

Extending the simple fluid description to collisionless systems has long been thought impossible by most physicists, but recent breakthroughs have shown the feasibility of this extension. Specifically, a new mathematical technique known as the “phase velocity transform,” was developed making it possible to eliminate particle velocities from the kinetic equation. A surprising finding of this study is that all the necessary information seems to be contained in the phase velocities of the fluid averages (density, fluid velocity, and temperature); individual particle velocities are not needed, as formerly thought. The practical result of this work is a term in the fluid equations in the collisionless limit, roughly analogous to the viscosity that comes in a collisional fluid. This term contains (in principle) numerous effects that were previously thought impossible to include in fluid equations, such as linear and nonlinear wave–particle resonances, nonlocal transport, flux limits, and others. Such effects are often neglected in present-day models, thereby reducing their accuracy.

The FY98–99 work in this project has two parts. The first involves finding a practical method to calculate the collisionless closure term. Eulerian and Lagrangian methods were devised that are accurate but somewhat time consuming and a local approximation that sacrifices some of the accuracy but has a large payoff in simplicity. Future studies will determine what level of accuracy is necessary. The second part involves extending the collisionless closure term to a very general class of collisionless fluids (Hamiltonian systems). Once this generalization has been completed, the fluid equations can be applied to nearly any collisionless fluid considered in physics.

Feasibility Study for Analyzing Plasma–Aerodynamic Effects

J. W. Sherohman, B. M. Penetrante
98-FS-002

Experimental work conducted by the United States Air Force Research Laboratory (AFRL) at Wright-Patterson Air Force Base has verified Russian claims that, for an object moving at supersonic/hypersonic speed in endoatmospheric flight, plasma–aerodynamic effects can cause "anomalous relaxation" of the bow shock wave and result in a major reduction in drag. The purpose of this feasibility study is to examine the facilities and modeling capabilities that LLNL could provide in support of AFRL's plasma–aerodynamic research program for supersonic/hypersonic flight.

The phenomenon of anomalous relaxation, although verified experimentally, is not yet understood. For a number of years, Russia has conducted a research and development effort aimed at utilizing unconventional hypersonic technologies to achieve a significant breakthrough in hypersonic flight. The Russian program, known as Ajax, has the goal of building a Mach 12 or greater aircraft based on the integration of three novel subsystem technologies: plasma–aerodynamic shock-wave modification, endothermic fuel conversion, and magnetohydrodynamic (MHD) power generation. In particular, plasma–aerodynamic experiments to modify shock-wave behavior have generated much interest in the United States aerodynamic community as well as internationally. This interest has been stimulated in large part by the experimental work conducted by AFRL.

The scope of our study is two fold: (1) determine what facilities, capabilities, and technical expertise within LLNL could be applied to conduct research on shock-wave–plasma interactions at high-Mach numbers, and (2) conduct preliminary modeling calculations to simulate AFRL's experimental results on shock-wave propagation in a weakly ionized plasma.

In FY98, we completed both an evaluation of the expertise and capabilities at LLNL that could be applied to plasma-aerodynamic research of interest to the USAF and a preliminary investigation, via one-dimensional (1D) modeling studies, of the shock-wave "relaxation" caused by a weakly ionized plasma. Our study of LLNL's capabilities relevant to plasma–aerodynamic research indicated that there are several important areas to which the Laboratory could contribute: (1) high-Mach projectile acceleration, specifically, through the use of the Super High-Altitude Research Program (SHARP) facility; (2) techniques for shock-wave generation; (3) advanced plasma diagnostics; (4) advanced concepts for the development of a high-Mach-number wind tunnel (e.g., LLNL is part of a team effort sponsored by the USAF to examine advanced technologies for the development of a new, national, hypersonic wind-tunnel facility); and (5) three-dimensional (3D) modeling/simulations.

Our 1D calculations in FY98 demonstrated several of the shock-wave characteristics observed experimentally when the shock waves are propagating through a weakly ionized plasma. Although to some extent the results could be explained by thermal gradients, 1D calculations cannot explain the extreme damping of the shock wave in the presence of the plasma.

In FY99, we will conduct 3D calculations in order to understand and interpret the experimental effects associated with the shock-wave–plasma interaction. Such calculations will be necessary to examine how radial perturbations (i.e., radial thermal gradients and shock-front irregularities) may influence shock-wave damping. These calculations will support our understanding of the plasma–aerodynamic effects and provide insight as to how the Laboratory might contribute to this area of research.

Strategic Initiative in Computational Biology

M. E. Colvin, F. Gygi, G. A. Galli, K. A. Fidelis, D. Barsky, F. C. Lightstone, T. A. Kuczmarski, M. Cosman

98-SI-008

The emerging understanding of biology in terms of its underlying chemical processes is one of the great triumphs of science; it means that a growing fraction of biology can be simulated by computer modeling. We are bringing together LLNL's capabilities in parallel computing, computational chemistry, and structural biology to establish a new state of the art in biological simulation. This project involves both developing new modeling methods and applying them to problems in biology.

Our primary developmental goal is to create methods for simulating biochemical processes using an accurate quantum mechanical description of the molecular interactions. This method, called first-principles molecular dynamics (FPMD), is much more realistic and accurate than the ball-and-spring atomic models used in conventional molecular dynamics. FPMD will allow nearly exact simulations of the time evolution of chemical systems, simulations that will require the capabilities of LLNL's fastest computers. Another goal is the development of a homology-based algorithm for predicting the folding of proteins that is based on the analysis of all known protein structures. Other goals include implementing parallel versions of software for analyzing gene sequences and, in collaboration with Sandia National Laboratories, developing methods for high-accuracy quantum chemical predictions of static chemical properties.

During FY98, we made good progress in both the methods development and the biological applications. Our FPMD software was efficiently implemented on the Accelerated Strategic Computing Initiative (ASCI) parallel computer. For the protein-structure prediction, we completed the amino-acid-based structure descriptors that classify protein structures at an unprecedented level of detail. Finally, both the gene-sequence analysis software and quantum chemistry software were successfully ported to the ASCI computer. We applied these methods to several problems, including comprehensive studies of the weak hydrogen bonds that underlie most biochemical processes, including DNA replication. These simulations involved some of the largest FPMD, quantum chemical, and gene-comparison calculations ever performed.

We also made significant progress on a number of biological applications. For example, we used protein homology modeling methods to predict the structure of DNA-repair protein REC1. We also modeled the initial DNA binding reaction of a class of cancer-causing chemicals found in cooked foods and worked on several other collaborative projects, including studies of anticancer drugs that chemically bind to DNA. Finally, in support of the computational simulations, we made progress on experimental nuclear magnetic resonance (NMR) studies to determine the structure and flexibility of damaged DNA helices and of a unique, parallel-stranded DNA structure.

We collaborated with LLNL's molecular biologists on a multilevel study of the mechanism of human apurinic/apyrimidinic endonuclease, the enzyme that repairs the most common form of natural DNA damage. This research includes molecular-dynamics simulations of the damaged DNA helix (see figure) as well as accurate quantum chemical simulations of the damage site and of the mechanism by which the enzyme cuts the damaged DNA strand. We also used protein homology methods to create a model of the DNA-enzyme complex. The emerging conclusion from this project is that this enzyme detects the DNA damage because of its increased flexibility, rather than by recognizing the specific shape of the damaged region.

In FY99, our focus will be on continued development to the FPMD method, including algorithmic improvements that will allow much larger biochemical systems to be simulated. In collaboration with university researchers, we will perform detailed comparisons between the FPMD and traditional MD simulations on the chemical building blocks of DNA. We also plan to begin work on several new biochemical applications, including simulations of the initial metabolic step in the activation of food mutagens.

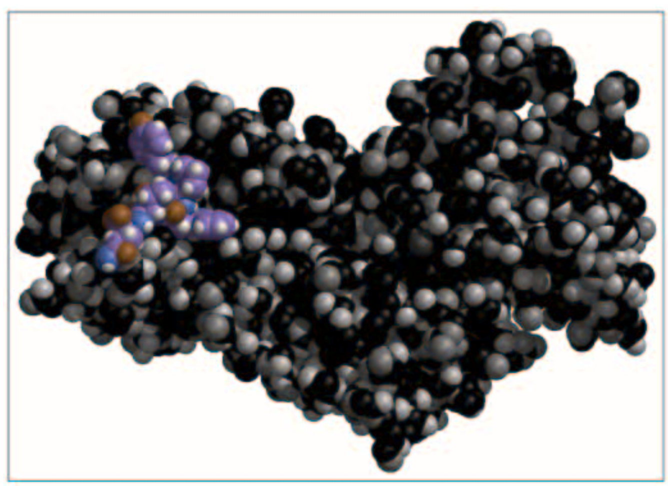

Results of a simulation of a DNA double helix that has undergone spontaneous loss of a single base (center right). Atoms are colored by their relative motion during a molecular-dynamics simulation (red moves least; blue moves most). It can be seen that the damage increases the DNA flexibility, which is hypothesized to be how the DNA-repair enzymes recognize this damage.

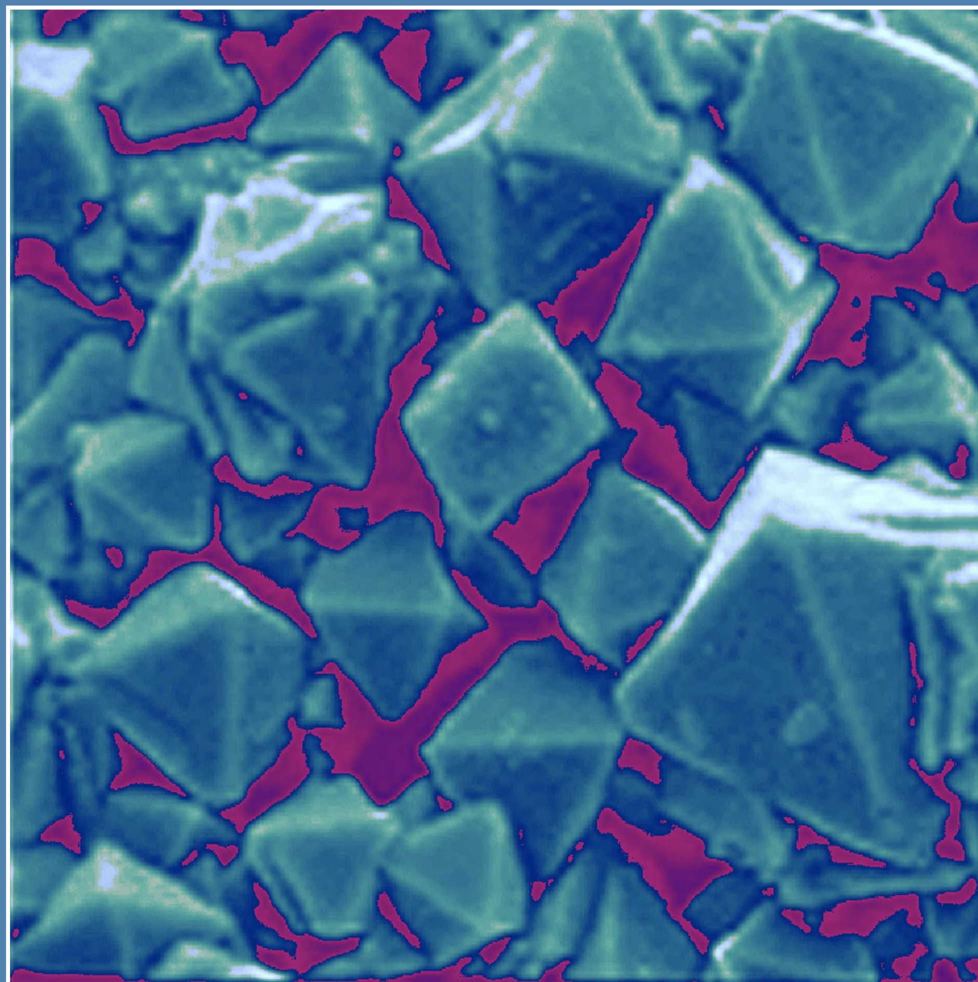

5

Energy and Environmental Technologies

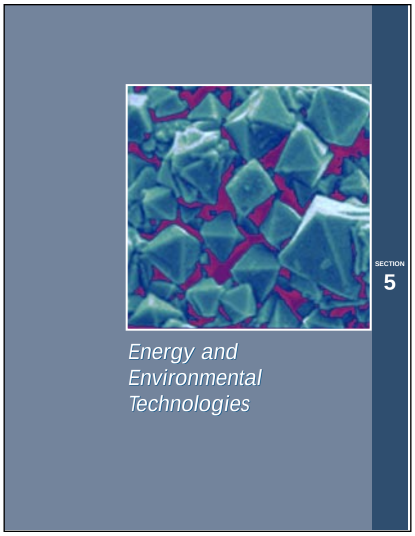

About the preceeding page

Neptunium Solubility: Kinetic or Thermodynamic Control. The DOE is pursuing the establishment of a permanent, geological disposal site for high-level nuclear waste at Yucca Mountain, NV. Cindy Palmer's team is investigating an apparent discrepancy in terms of thermodynamic and kinetic control by conducting laboratory experiments specifically designed to determine the rate of precipitation NpO_2, as a function of pertinent variables (e.g., pH, time, and ionic strength). Shown is a colorized SEM micrograph of the NpO_2 solid obtained in a 102-day 200°C solubility experiment. See page 5-4 for more information.

Remediation of Chlorinated Hydrocarbons and Metals in Groundwater using Zero-Valent Reducing Agents and Electrolytic Processes

W. W. Mcnab, Jr., D. J. Bishop, S. A. Martins, R. Ruiz
96-ERD-059

Contamination of groundwater resources by halogenated solvents and metals poses a significant environmental problem at DOE, DoD, and private commercial facilities. Existing cleanup technologies for remediating groundwater suffer from several disadvantages, including the need to construct surface facilities and pipelines and the need to employ different technologies to treat different contaminants. Another problem of particular concern is that many conventional treatment technologies merely transfer the contaminant from one medium (water) to another (e.g., activated carbon).

In response to these problems, we have investigated the application of zero-valent reducing agents to destroy dissolved halogenated solvents through dehalogenation reactions and to chemically reduce dissolved metals to immobile forms. This approach offers the advantage of a potentially compact and versatile groundwater remediation technology. Our previous experiments had shown that chlorinated solvents found in LLNL groundwater (perchloroethylene, trichloroethylene, dichloroethylene, carbon tetrachloride), could be rapidly dechlorinated using electrolytically generated hydrogen as a reducing agent in the presence of a palladium catalyst in a flow-through reactor design (catalytic reductive dehalogenation, or CRD). As shown in the figure, the principal end product of the reductive dehalogenation reactions is ethane, which is environmentally benign. Rapid reduction of hexavalent chromium, a common groundwater contaminant, was also achieved using electrolytically generated hydrogen as well as with an alternate design utilizing metallic iron as the reducing agent. In FY98, experiments conducted with the bench-top CRD unit indicated that a variety of additional halogenated compounds were also subject to rapid reduction (e.g., reaction half-lives of less than 30 seconds). These include ethylene dibromide, trichloroethane, bromoform, pentachlorophenol, and various chlorobenzene isomers. These results suggest the CRD technology may be broadly applicable to a wide range of common halogenated contaminants. Also, CRD exhibited the capacity to reduce nitrobenzene to benzene, suggesting this technology may be useful for remediating groundwater contaminated by nitroaromatic compounds associated with high explosives.

A pilot CRD unit, based on a flow-through reactive well design, was previously installed at LLNL to remediate groundwater in situ that is contaminated with both chlorinated solvents and tritium. The strategy behind the CRD deployment is to treat the dissolved chlorinated hydrocarbons in the well bore without having to bring tritiated groundwater to the surface environment. Tritium remains in the subsurface to self-remediate via radioactive decay. Much progress was achieved in FY98 in optimizing the performance of the pilot CRD system. Employing both electrolytically generated hydrogen and methods of direct hydrogen injection and dissolution, destruction efficiencies greater than 98% for total chlorinated hydrocarbons (primarily tetrachloroethylene and trichloroethylene) were obtained using flow-through rates of 4 liters/min, corresponding to a contaminant mass destruction rate of approximately 1 g/h of operation. Earlier problems involving deactivation of the catalyst material appear to be related to microbiological activity within the CRD unit. This may occur as a result of biofilm formation associated with the presence of hydrogen, sulfate, and ethane in the flow-through treatment stream as it passes over the catalyst bed. We have found that periodically draining the column and exposing it to atmospheric oxygen alleviates this difficulty.

Based on the results of this study, the CRD pilot test unit has won acceptance as the groundwater treatment method of choice from the regulatory agencies involved in the groundwater restoration effort at LLNL. Scientists and engineers participating in groundwater cleanup at other DOE facilities are also expressing interest in this technology.

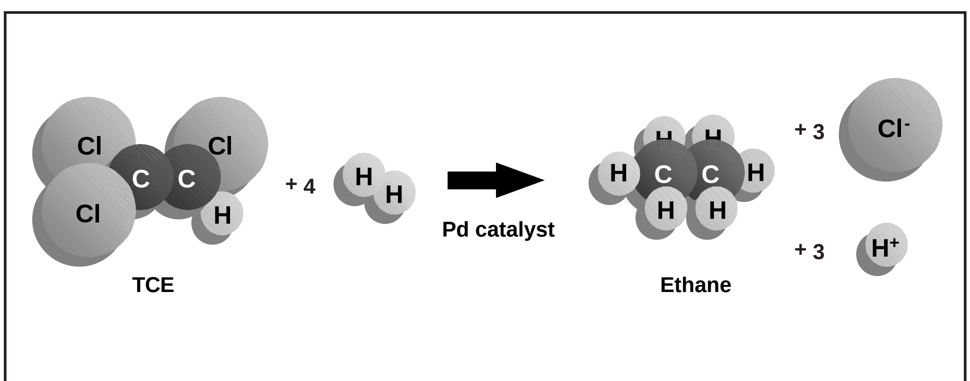

Abiotic reductive dehalogenation of trichloroethylene (TCE) by aqueous hydrogen to form ethane and hydrochloric acid. Reaction proceeds rapidly in the presence of a palladium catalyst.

Removal of Mercury from Waste Streams

T. F. Baumann, J. G. Reynolds, G. A. Fox
97-ERD-015

As a result of increasing environmental concerns about waste water remediation, major efforts are under way to design new materials that can effectively remove and recover toxic metal ions from aqueous solutions. One approach to this problem has been to utilize organic ligands anchored to solid supports. Specific binding properties of the ligands can be exploited to selectively remove a desired metal ion from a complex solution of cations. The utility of polymer pendant ligands for the extraction of a variety of metal ions from aqueous media has been previously demonstrated in the literature (see Publications).

The chemistry described here is designed to remove and separate low level concentrations of mercury (Hg) found in aqueous waste streams using polymer pendant ligands. Removal, immobilization, and characterization of Hg in waste streams are major target topics for DOE's Offices of Energy Research and Environmental Management and specific DOE contractor sites. Many waste streams generated by DOE-sponsored activities contain high levels of Hg, such as the 2 million gallons of acidic radioactive waste at Idaho National Engineering and Environmental Laboratory. These streams require removal of Hg, then immobilization to effectively meet environmental criteria for disposal.

Our initial effort was development of the synthesis of thiacrown polymer. We have been exploring the use of thiacrowns, sulfur-containing macrocycles that are cyclic carbon systems with multiple sulfur binding sites, to specifically bind Hg. The new crown thioether, 2-hydroxymethyl-1, 4,8,11,14-pentathiacycloheptadecane ([17]aneS_5-OH), **1**, was synthesized in a 25% yield through reaction of 2,3-dimercapto-1-propanol with 4,7,10-trithiatridecane-1,13-di-p-toluene- sulfonate (see the figure showing Scheme 1), using the cesium-carbonate-mediated cyclization. Advantages of this technique are twofold: first, it is general for synthesizing sulfur crown of various sizes; and second, the hydroxymethyl moiety does not need to be protected prior to the condensation reaction.

Next, [17]aneS_5-OH was treated with thionyl chloride to form 2-chloromethyl-1,4,8,11,14-pentathiacycloheptadecane ([17]aneS_5-Cl), **2** (89%), followed by conversion to 2-(N-methyl) aminomethyl-1,4,8,11,14-pentathiacycloheptadecane ([17]aneS_5-NHMe), **3** (65%), through reaction with methylamine. The synthesis of the 4-vinylbenzyl-substituted thiacrown, **4** (60%), was readily accomplished by treating **3** with 4-vinylbenzyl chloride. Copolymerization of the 4-vinylbenzyl-substituted thiacrown **4** with DVB (80% divinyl benzene). Using AIBN as the radical initiator generated the highly cross-linked crown thioether polymer 5. Elemental analysis of the resulting polymeric material showed that each gram of the polymer contained 1.53 mmol of [17]aneS_5 crown (based on wt% of S).

In our Hg uptake studies, solid-liquid extraction capabilities of the polymer-supported thiacrown ether were tested in aqueous solutions. Here, 20-mg samples of the polymer were tested at various Hg concentrations, pH values, and reaction times. Amounts of Hg in the sample were measured directly on the reaction solutions before the reaction with the polymer and are not calculated from dilution factors on stock solutions. The approximate concentration of Hg in the solution being extracted (20, 200, and 2000 ppm working Hg solutions were used) is calculated from dilution. As a reference point, 200 mg of polystyrene-co-divinylbenzene, without thiacrown ligand, was reacted with an aqueous solution at pH 1.46 containing 1.54×10^{-4} g Hg (~40 ppm) for 30 min. After filtration, the product solution contained 1.27×10^{-4} g Hg. This translates to a 2% removal for a 20-mg sample.

These tests show that the polymer bound [17]aneS_5 thiacrown is very effective for chelating Hg. At mixing-separation times as short as 30 min., 97+% removal was afforded at 4 and 40 ppm at pH values 1.5 to 6.5. In the presence of excess metal ions, Pb, Cd, Al, and Fe, the thiacrown still removed 97+% of the Hg at pH 1.6. The thiacrown polymer was also tested for potential reuse. A 20-mg sample was used to treat a 40-ppm Hg solution. The polymer was isolated and the Hg removed. The regenerated thiacrown polymer was used to treat another 40-ppm solution of Hg. Again 97+% removal was found. In addition to the [17]aneS_5 thiacrown, a [14]aneS_4 thiacrown was also synthesized by the method shown in the figure. Although not tested as extensively as the [17]aneS_5 thiacrown polymer, the S_4 material exhibited identical extraction capabilities: 97+% extraction at pH 1.5 and 30 min. reaction-separation time.

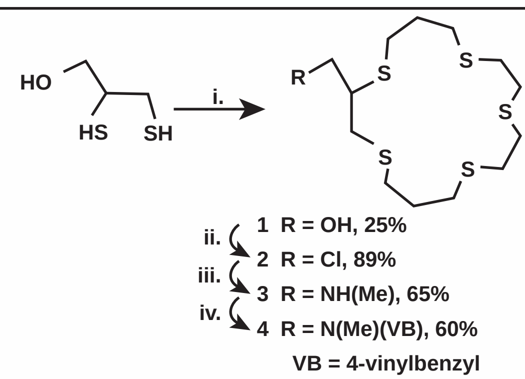

The synthesis of thiacrown polymer, used for removing Hg from aqueous, acidic waste streams. Scheme 1 (reagents and conditions): i. $S(CH_2CH_2SCH_2CH_2CH_2OTs)2$, Cs_2CO_3, DMF, 90°C; ii. $SOCl_2$, CH_2Cl_2, RT; iii. $MeNH_2$, Na_2CO_3, MeCN, 0°C; iv. 4-vinylbenzyl chloride, Na_2CO_3, MeCN, 81°C.

Optimization and Monitoring of an In Situ Biodegradative Process

A. M. Happel, J. M. Horn, S. R. Kane

97-ERD-030

Because of its widespread use as an industrial solvent, trichloroethylene (TCE), a suspected carcinogen, is a common groundwater pollutant. Several DOE sites (including LLNL) have been contaminated with TCE. We are investigating the use of methanotrophs (bacteria that use methane for carbon and energy) for in situ biodegradation of this contaminant and also of alkyl ethers. Biological treatment of contaminants such as TCE is often more cost effective than chemical or physical methods and results in the complete breakdown of TCE to carbon dioxide.

Methanotrophs produce an enzyme, soluble methane monooxygenase (sMMO), that oxidizes both methane and TCE. The methanotrophic bacteria, including *Methylosinus trichosporium* OB3b and *M. sporium*, have been shown to have the greatest rates of TCE degradation relative to bacteria with other TCE-degradative enzyme systems. Therefore, these organisms are being used by our group to study the control of sMMO synthesis, with the aim of optimizing sMMO production and, thus, effecting efficient TCE degradation.

Currently, the literature records that at least two factors limit the utility of methanotrophs for TCE remediation in situ. First, the gene encoding sMMO is not expressed (translated into an enzyme) in the presence of low levels of copper. Second, the enzyme is produced only in the presence of methane; however, if methane is present, then sMMO preferentially degrades methane over TCE. To overcome these obstacles and increase the utility of these organisms, copper-resistant mutants have been produced by others and by our group by using classical chemical mutagenesis. Using this approach, mutants have been obtained of OB3b that express sMMO regardless of environmental conditions; that is, these strains produce sMMO in the absence of methane or other substrates of the enzyme, and even in the presence of copper. However, because these mutants are somewhat slow-growing relative to the original strain, we are continuing mutagenesis efforts to obtain improved strains for remedial use. In addition, we have applied the same approaches to obtain mutants of *M. sporium*.

Our initial studies were directed at comparing growth rates and TCE degradation rates for the two methanotrophic strains. TCE-degradation studies have shown that older cultures of *M. trichosporium* OB3b have higher degradation rates (and thus higher sMMO activities) than actively growing, low-cell-density cultures. However, we find that growth stage does not appear to influence TCE degradation rates to this extent in *M. sporium*. In FY98, we began evaluating the regulation of sMMO production by analyzing the amount of sMMO messenger RNA produced in cultures of both strains at different stages of growth. In addition, we are using TCE-degradation assays to determine whether sMMO expression is a function of the physiological age of cells (known to trigger the expression of a whole suite of genes) or whether sMMO expression is governed by when the culture attains a critical cell density. We found that *M. sporium* grew better in low methanol concentrations (0.001%); there was no apparent sMMO inhibition. Feeding deregulated mutant strains of *M. sporium* on methanol in the subsurface, while still producing sMMO and degrading TCE, would thus be feasible.

In recent years, alkyl ethers such as methyl tertbutyl ether (MTBE) have been added as octane enhancers to unleaded gasoline. Although fuel hydrocarbons from leaking underground fuel-storage tanks are often degraded naturally in the environment, MTBE is not. Since there was evidence that sMMO might be capable of degrading alkyl ethers, in FY98 we tested the ability of methanotrophs to degrade four EPA-approved fuel additives (MTBE, ethyl tertbutyl ether, diisopropyl ether, and tertiary amyl methyl ether). Unfortunately, we detected no degradation of any of the fuel additives that were tested.

In FY98, we also began developing monitoring techniques with which we could directly measure biodegradative enzymatic activities. A "reporter gene," whose product is easily measured, will be used to assess expression of sMMO (which is more difficult to assay). The green fluorescent protein (GFP) is being fused with the regulatory region of the sMMO gene cluster such that the reporter gene is under the same genetic control as sMMO is normally. Thus, under conditions where sMMO is expressed, the reporter-gene product, GFP, is produced. GFP can be directly measured online, nondestructively, and in real time. Replacement of the sMMO gene with GFP will enable (1) studies involving the regulation of sMMO production, and (2) monitoring and quantification of TCE degradation in field applications. For example, by using whole methanotroph cells containing the GFP reporter fusion, we will be able to easily discern environmental conditions favorable for sMMO production—and thus TCE degradation. This work will continue through FY99.

Neptunium Solubility: Kinetic or Thermodynamic Control

C. E. A. Palmer, T. J. Wolery, K. E. Roberts
97-ERD-047

The nation is faced with the serious issue of disposing of high-level nuclear waste. Currently, the U.S. is using a conservative approach when conducting potential radiation dose and repository performance calculations. Incorporation of published neptunium (Np) concentrations observed in short-term experiments has yielded calculated doses in excess of proposed long-term dose-based regulatory limits. These results may grossly exaggerate the long-term reality in an actual repository, such as Yucca Mountain, by ignoring the role of certain insoluble Np solids that may form only at very slow rates.

Existing thermodynamic data at 25˚C show that experimentally observed, approximately ~10^{-3} M Np concentrations at pH 6 are supersaturated with respect to Np(IV) oxide, NpO_2. However, the observed solid phases were Np(V) solids, both $NaNpO_2CO_3$ and Np_2O_5. Thermodynamic calculations made using the computer code EQ3/6 confirm equilibrium with these phases but cannot show why NpO_2 was not obtained instead.

Our hypothesis is that NpO_2 is slow to form on the time scale of the earlier laboratory experiments. Accordingly, we are studying the precipitation kinetics of NpO_2 at higher temperatures. Under these conditions, the formation of this phase should occur faster if our hypothesis is correct. Our goal is to better understand the ambient-temperature equilibrium distribution of the Np(IV) and Np(V) solution and solid species by using high temperature to accelerate any slow reaction kinetics. The precipitation of a crystalline NpO_2 solid phase would go hand in hand with *significantly* lower aqueous Np concentrations. Such concentrations, if observed, would support calculated doses far below proposed long-term dose-based regulatory limits.

During FY97, we prepared our equipment and materials, and we conducted our first elevated temperature solubility experiment. After two weeks of reaction time, the 200˚C experiment showed a significant decrease in the aqueous Np(V) concentration. A small amount of precipitate was collected from the elevated temperature experiment. During FY98, we analyzed the solid obtained in the 200°C solubility experiment by x-ray powder diffraction (XRD), x-ray absorption spectroscopy (XAS), and scanning electron microscopy (SEM). Based on the results from all three analyses, we concluded that the reduction in the aqueous Np concentration was accompanied by the precipitation of crystalline NpO_2. This is the first time that crystalline NpO_2 has been observed to precipitate from an aqueous solution of initially Np(V). It appears that thermodynamic calculations made using EQ3/6 were correct: that NpO_2 is the solubility controlling solid phase under near-neutral aqueous solution conditions, and that slow kinetics has prevented the experimental observation of this precipitation reaction until now. To confirm this result, a second experiment was conducted. All conditions were identical to the first experiment other than a five-fold increase in the solution volume and switching from a teflon-lined, stainless steel reaction vessel to a titanium metal reaction vessel. This was done so that periodic measurement of the aqueous Np concentrations could be made.

Figure 1(a) shows the measured aqueous Np concentrations as a function of time for the second 200°C solubility experiment. After 102 days of reaction time, steady state had been reached, so that the experiment was terminated. The solids were collected and analyzed by XRD, XAS, and SEM. The resulting data confirmed the first experiment's result in that crystalline NpO_2 precipitated from a near-neutral solution of initially Np(V). Figure 1(b) shows a SEM micrograph of the solid obtained from the second experiment. The octahedra ranged in size from a few tens of microns to nearly 100 microns, and indicate the formation of high-purity NpO_2 crystals.

Additional experiments have been started to investigate the pH dependence on this precipitation reaction and will be accompanied by work at other temperatures to determine the activation energy associated with the formation of NpO_2 in aqueous solution. Following the closed-vessel precipitation experiments, additional work will be performed using the "stirred-flow" apparatus acquired in FY98 to measure dissolution rates of crystalline Np(IV) oxide as a function of solution composition while the reaction vessel is at elevated temperature. The final goal of FY99 will be to model both the dissolution and precipitation kinetics of Np(IV) oxide.

(a)

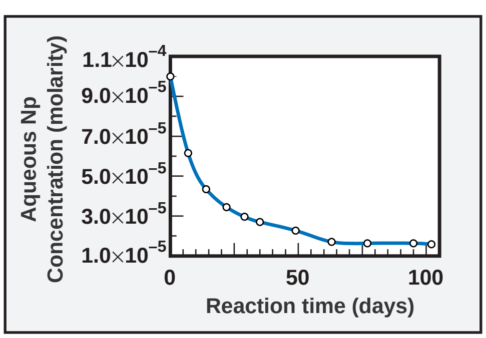

(b)

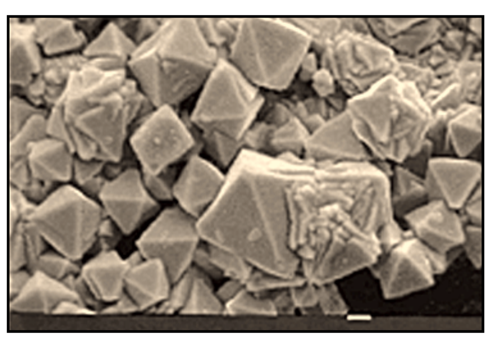

Figure 1. (a) Aqueous neptunium concentration as a function of time. (b) SEM micrograph of the NpO_2 solid obtained in the 102-day 200°C solubility experiment.

Global Sustainability and Strategic Modeling

A. Lamont
97-ERD-048

The sustainability of our modern way of life is a major concern of both our domestic and international policy. Energy is a key component in global sustainability since obtaining and using it have major environmental effects. If our energy systems are to be sustainable for the long run, they must have a minimal impact on our environment and be reasonably economical. Because economic considerations and government policies determine the development of the energy system, economic and systems modeling can help us understand ways that new technologies and policies can be used to obtain a more sustainable system. Through the Global Sustainability and Strategic Modeling Project, we developed economic modeling tools and models to help us better understand these issues and applied them to the analysis of energy and environmental problems in China.

Tool development this year focused on the META•Net economic modeling system. META•Net is a system for building models of economic systems and solving them for a price-quantity equilibrium over time. Last year, the project worked with both the META•Net modeling system and SuperCode, a constrained optimization system designed to work with other models. We plan to connect the two systems to take advantage of the more efficient solvers in SuperCode. This year, we took the initial step to combining the systems by restructuring the META•Net solution algorithm so that it can be controlled by an external solver. Several other small improvements have been made in META•Net, which speed convergence and allow it to more accurately meet constraints.

During the past two years, we developed a long-term model of the Chinese energy system. This year we used the model for several analyses. The first application examined the impact of improved industrial technologies on sulfur emissions in China. Improvements in industrial efficiency can reduce emissions since Chinese industries use from two to five times the energy per unit output, compared to US or European industries. Working with LLNL's Environmental Protection Department, we explored the magnitude of emissions reductions that could result from using modern industrial practices. We found that modern industrial technologies can moderate the growth of sulfur emissions for about 25 years. This indicates that one of the most effective emissions control policies will be the financing and development of modern industrial facilities.

In conjunction with the DOE Office of Fossil Energy, a second analysis focused on controlling emissions in the Chongqin region of China. A modified version of the China model was developed to illustrate the effects of policies to control sulfur emissions. The model indicates a mix of measures that can economically be used to meet environmental goals. These include turning to natural gas, using coal gasification technologies, and shifting to cleaner coal technologies in the electric sector.

During the past year, Professor Toshihiko Nakata of Tohoku University in Japan was visiting LLNL on a Fulbright Grant to study modeling of energy systems. The project assisted him in modeling the Japanese energy system using META•Net. He compared Btu taxes and carbon taxes as strategies for reducing carbon emissions in Japan, in accordance with the Kyoto Protocol. He found that although the carbon tax is somewhat more efficient in reducing carbon emissions, the Btu tax tends to produce a broader mix of fuels, which is important for Japanese energy security.

Through the Global Sustainability and Strategic Modeling Project, we have developed both data and software for understanding the impacts of new technologies and energy policies. We expect that the capabilities we have developed will provide a basis for future work. The China model in particular has been the basis of two proposals submitted in conjunction with the Office of Fossil Energy for further analysis of the Chinese energy system and the role that new coal technologies can play in China's future development.

Proliferation-Resistant Fuel Cycles

N. W. Brown, J. A. Hassberger, E. Greenspan
97-ERD-068

During the next century, the worldwide demand—especially by developing countries—for clean electrical energy will continue to extend the use of light-water reactors (LWRs) and the development of sodium-cooled fast reactors. The resultant large inventories of recycled plutonium will demand inspection and accountability requirements that are not easily achieved.

In response to this situation, we embarked on a study with the goal of establishing (1) requirements for improving the proliferation resistance of fission-energy systems, and (2) conceptual designs for fission-energy systems with improved (relative to the large-LWR, once-through fuel cycle) proliferation resistance that would have application in developing countries.

During the first year of this project, we found that one of the most important approaches to proliferation resistance appeared to be the elimination of on-site refueling through the use of very long-lived cores. We identified four nuclear-fission systems that appear capable of meeting such an objective: light-water, liquid-metal, gas, and molten-salt systems. In FY98, we continued the development and evaluation of these systems and began developing a decision-analysis tool for selecting the preferred system.

During FY98, we expanded our interactions with outside organizations that have experience in fission-energy technology and in determining the potential for its use in developing countries. These organizations included the International Atomic Energy Agency (IAEA), Los Alamos National Laboratory, Argonne National Laboratory, and the Westinghouse Technology Center. Our interactions allowed us to expand and refine the requirements and design concepts identified in FY97. For example, we learned that additional variations in the lead-bismuth-cooled reactor-core design indicate a potential for core-neutronic lifetimes approaching 30 years—fuel and structural-material factors that limit the life of this system remain to be investigated. We also confirmed through these external interactions that the four fission-energy systems that we identified in FY97 remain viable candidates for development into more detailed designs.

We expect that, with the support of the organizations identified above, these systems will be developed further under a program being proposed to the DOE's FY99 Nuclear Energy Research Initiative (NERI). An IAEA advisory group is also now recommending further study of these proliferation-resistant fission-energy systems.

We completed—to the point of testing with trial parameters—development on the multi-attribute decision model for evaluating the value of the four systems listed above. The principal attributes of this model are cost, environmental safety and health, institutional goals, and proliferation resistance. Proliferation resistance has been further separated into proliferation resistance during the periods of manufacturing and installation, transportation, operation, and waste and recycling. We demonstrated that the commercially available Logical Decisions computer code is capable of processing the large tree structure necessary to cover the scope of attributes used in the multi-attribute decision model. We expect that this work also will be completed under a program being proposed to NERI.

Multilayer Catalytic Membranes for Selective Oxidations of Hydrocarbons

A. Q. Pham
97-LW-009

We have been developing a new energy-efficient technology for the exploitation of natural gas as an alternative feedstock. Currently, the process for upgrading natural gas consists of a steam-reforming or partial-oxidation step for the preparation of syn-gas (a mixture of CO and H_2) followed by the synthesis of chemicals such as methanol, ammonia, and liquid fuels. The steam-reforming process is highly capital- and energy-intensive and has thus limited the widespread upgrading of natural gas.

Our approach to replacing the expensive steam-reforming or partial-oxidation process is to utilize ceramic electrochemical membranes that simultaneously perform oxygen-gas separation and catalytic partial oxidation of hydrocarbons. An additional oxygen-separation unit is thus not required. Existing electrochemical membranes for oxygen separation are mainly a single-layer, mixed ionic–electronic conductor. This implies that a single material must perform as a (1) catalyst for oxygen reduction, (2) diffusion medium for oxygen and electron transports, and (3) catalyst for the partial oxidation of hydrocarbons. Limited performance and materials-stability problems have been observed. Our approach is to separate entirely these functions by the use of multilayer membranes; each layer is selected and tailored to optimize one of the above tasks. Although the main purpose of the current project is to upgrade natural gas to syn-gas, our concept of multilayer membranes, which has the advantage of large materials selection, can be developed for other partial-oxidation processes at temperatures lower than 700˚C, such as the oxidation of propylene to propylene oxide.

In FY97, we developed the basic science of the oxygen-permeation process and used thick membranes to demonstrate the feasibility of the multilayer-membrane approach. Our theoretical work suggested that for thick membranes, the membrane resistance to the diffusion of oxygen ions can contribute up to 30% of the total energy loss of the process, the remaining being attributed to the loss due to the slow surface exchange of chemicals at the electrodes. Thus, we decided to use thin-film membranes to reduce the diffusion resistance. In a joint effort with another project (LDRD 98-ERD-031), we successfully developed a novel thin-film deposition technique based on colloidal deposition. The new technique is simple, low cost, and highly versatile. A patent application has been filed.

In FY98, we concentrated our effort on the application of our multilayer membrane to the generation of syn-gas. For this purpose, we processed a trilayer membrane. Using fixed-bed reactor experiments, we identified nickel as the most active nonprecious-metal catalyst for the partial oxidation of methane. To avoid the sintering of Ni resulting from high-temperature operation, Ni was dispersed in a matrix of doped ceria, in a similar way to that done for solid-oxide fuel cells. Then, using the new thin-film deposition technique, we deposited a thin (5-µm-thick) layer of doped ceria on the Ni/ceria cermet. As a catalyst for the oxygen reduction, we screen-printed a layer of mixed iron and cobalt oxide on the ceria membrane.

Tests showed that the oxygen flux through the multilayer membrane using 5% methane in nitrogen was as high as 3 mL • min^{-1} • cm^{-2} at 900˚C. In pure methane, the flux increased to 12 mL • min^{-1} • cm^{-2}, which is about 50% higher than published data for single-layer ceramic membranes. We believe, on the basis of our theoretical work, that higher oxygen fluxes can be achieved if the electrode surface area is optimized. The selectivity to CO formation was excellent, exceeding 95% in all cases and confirming that Ni/doped-ceria cermet is an excellent partial-oxidation catalyst. The conversion efficiency was more than 80%, which is a significant improvement from the preliminary result of 45% obtained in FY97.

This project demonstrated for the first time the possibility of combining gas-permeable membranes with catalytic reactions in a single device. This approach is very general and can be applied to other gases such as hydrogen. A spin-off project has been generated from this research (“Natural-Gas-Assisted Steam Electrolyzer,” funded by the DOE Hydrogen Program).

Sustained Spheromak Physics Project

E. B. Hooper, D. N. Hill, R. D. Wood, Jr.
97-SI-009

Construction of the Sustained Spheromak Physics Experiment (SSPX) is nearing completion, and experiments begin soon. The experiment is designed to study energy confinement and other physics in a toroidal magnetic field configuration, which is generated primarily by currents flowing in the plasma. The resulting device is simpler and more compact than most other magnetic fusion geometries, and thus offers significant reactor opportunities if the plasma can be made hot enough and its energy confined long enough to generate net power.

A magnetic field is generated in the spheromak by a magnetic dynamo, similar to those which generate the magnetic fields of the earth and sun, although in a very different regime. Although simple in concept, the dynamo involves fluctuations in the magnetic field that can cause energy to leak out of the basic toroidal configuration. Detailed study of the physics is thus needed to determine how to optimize the energy confinement of the high temperature plasma.

Figure 1 shows two major components of the experimental facility. In preparation for mounting the spheromak hardware, the vacuum vessel is baked to minimize gas evolution. Power systems providing 2 MJ of electrical energy stored in capacitor banks are shown during testing.

State-of-the-art diagnostics are essential to measure the properties of the plasma. One of these, the reflectometer, is being constructed in collaboration with the Applied Science Department at U. C. Davis. It is essentially a radar in which microwaves are reflected from various locations in the plasma. The round-trip time is determined by the density and magnetic fields, providing a measurement of their values. The reflectometer will also provide data about magnetic turbulence in the plasma. This turbulence, part of the dynamo current drive mechanism, is poorly understood. Thus, our measurements, made for the first time in the core of a hot, low collisionality plasma, will provide new information on processes critical to our device and elsewhere. In preparation for interpreting the data, we have applied a model of the reflectometer to plasma profiles generated by the CORSICA code, a comprehensive computer model developed under previous LDRD funding.

We are also developing descriptions of spheromak physics to better understand and extrapolate results. Previous models of the coupled spheromak and exterior current, which drives the dynamo, focused on the processes by which the magnetic geometry is formed. However, these include a strong acceleration of plasma from the exterior discharge region into the volume where the final plasma resides. This is much like the acceleration of gas in a supersonic nozzle. Once this acceleration phase is over, the plasma will form a steady state in which there is little plasma mass flow from the discharge. In this state, the current-carrying plasma is better described by a force-free model of the current and magnetic field in which the discharge acts like a subsonic nozzle. We have used this model to predict the behavior of the steady-state plasma. The calculations show many features of previous experiments, including a strong bending of the magnetic field lines where they enter the spheromak volume and a short-circuiting of the discharge if the current is too low.

In FY99, we plan to bring SSPX into operation and to begin the experimental studies. The combination of experiments and theoretical modeling will generate the data and understanding needed to evaluate the potential of the spheromak configuration. If positive, we anticipate moving to larger experimental devices, potentially leading to a fusion power reactor.

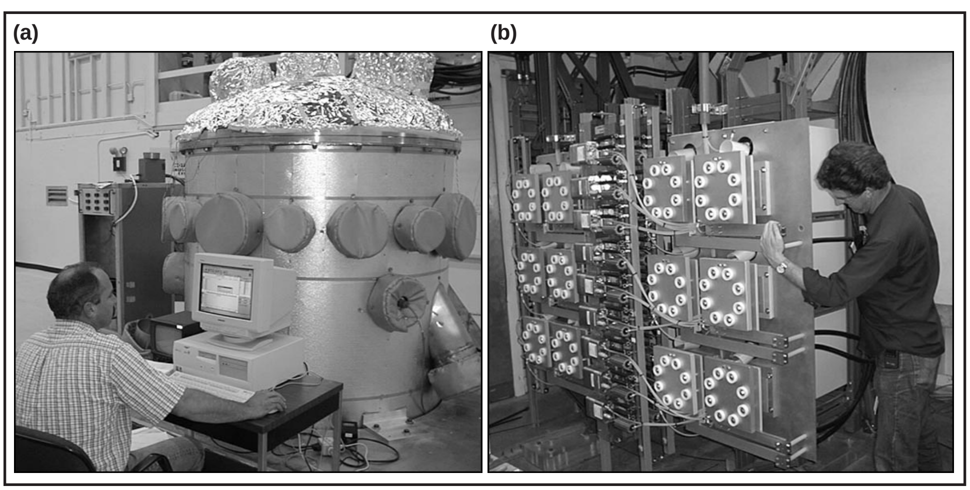

Figure 1. The two major components of the experimental facility: (a) The Sustained Spheromak Physics Experiment (SSPX) vacuum vessel during initial bakeout; and (b) The formation capacitor bank for SSPX.

Performance Prediction for Large-Scale Nuclear Waste Repositories

W. E. Glassley, J. J. Nitao, T. Bulous, M. Gokoffsky, C. W. Grant, J. W. Johnson, J. Kercher, J. A., Levatin
97-SI-017

The success of many major DOE and US nuclear programs ultimately depends on the ability to safely and securely dispose of high level nuclear waste. Yucca Mountain, Nevada is seen as a potentially suitable repository site because of its arid climate and remote location. Although the present day characteristics of Yucca Mountain are important, it is essential to have the ability to simulate how the potential repository will evolve over its 10,000-year lifetime. The purpose of our work is to use the massively parallel computational hardware being acquired by LLNL to increase the reliability and accuracy of simulations that will model how such a nuclear waste repository may evolve.

Rock at Yucca Mountain contains a small volume of water in its microscopic pores. Heat from radioactive decay will boil water in the near vicinity of the waste. The water vapor will migrate away, condense, and accumulate in cooler areas. The condensed water will slowly dissolve small quantities of the minerals composing the rock, and it may precipitate other minerals. The structure of pores and fractures will be modified by this process, as well as by mechanical effects as the rock expands and contracts during the heating cycle. These processes affect the movement of water, since they modify the spaces through which the water must migrate. Realistic simulation of a repository requires the ability to calculate how these various feedback loops interact with each other over thousands of years at high spatial resolution. This becomes of great importance since these interactions determine where, when, and how much water may reach waste containers. A single simulation to model these coupled processes would require many years to complete on standard work stations. Many such simulations must be done to evaluate various "what if" scenarios for repository behavior.

Recent acquisition by LLNL of computers that utilize massively parallel processor (MPP) architecture have made it possible to greatly reduce the simulation time. The MPP capabilities being acquired by LLNL are part of the Accelerated Strategic Computing Initiative (ASCI). We are constructing a new software package that exploits these capabilities, and we are using this new tool to develop detailed models of how Yucca Mountain may evolve.

The first step in developing this tool required our solving important conceptual problems about how to mathematically couple the thermal (T), hydrological (H), and chemical (C) processes. After solving this problem and conducting comparisons with experiments and observations to demonstrate validity of the calculations, we applied this technique to models of the potential repository. The figure shows that coupled THC effects lead to significant, irreversible changes to the rock around the waste tunnels. However, in simulations that compare different strategies for emplacing the waste, these effects are seen to be sensitive to the heat output of each waste package. Through more detailed studies, it will be possible to determine the optimum waste emplacement program. We have shown that these effects are predictable and potentially controllable by careful engineering. In addition, this simulation capability provides a tool with which to monitor performance of the repository. By simulating repository evolution during the first few decades of operation, we can predict where specific changes may occur, and thus guide a monitoring program designed to establish at an early time whether the repository evolves as it is predicted to evolve. This can provide an additional means for safeguarding the integrity of the waste containers.

Our future work will focus on expanding the chemical complexity represented, developing efficient solvers, and acquiring high resolution visualization capabilities, in order to make intelligible the large data sets output from these simulations. We will also focus on methods for demonstrating that the results produced by the model are physically and geologically reasonable.

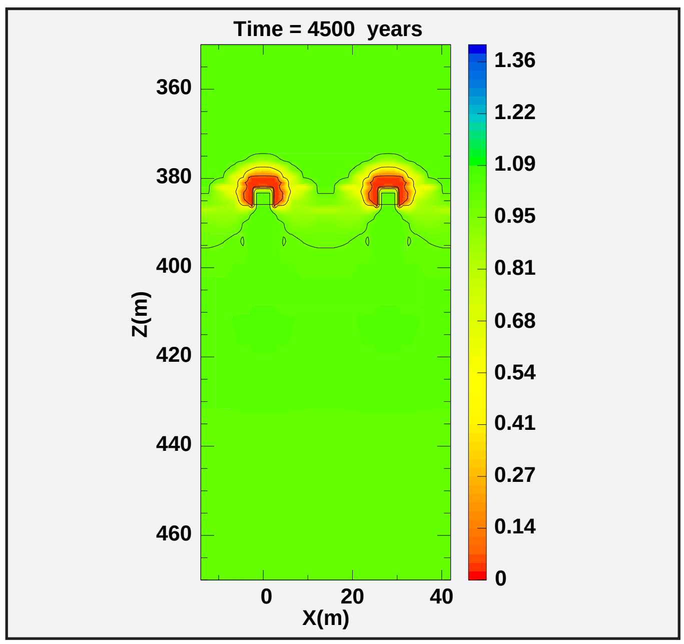

Extent of fracture sealing around waste emplacement tunnels, modeled using our new simulation capability. The simulation used the initial conditions expected for the potential Yucca Mountain repository. The color scale indicates the fraction of the fracture porosity remaining 4,500 years after waste emplacement.

High-Power-Density Solid-Oxide Fuel Cells

A. Q. Pham
98-ERD-031

A solid-oxide fuel cell (SOFC) is a solid-state electrochemical device that converts the chemical energy in fuels directly into electricity. Because SOFCs are highly efficient and have very low emissions, they are an attractive option for clean power generation. However, despite many successful demonstrations by Siemens–Westinghouse, actual commercialization of the SOFC is still not envisioned for the near future because of its excessively high fabrication cost. In this project, our goal is the development of low-cost SOFCs. Our strategy is based on (1) developing low-cost thin-film processing techniques, and (2) optimizing the materials design in order to increase the power density of the fuel cell.

The presence of a thin-film electrolyte is known to be the key factor in reducing the resistance of the fuel cell. In FY98, we successfully developed a novel, low-cost thin-film deposition technique that is an improved version of the well known colloidal deposition technique. Conventional colloidal deposition consists of dipping the substrate in a colloidal solution and then drying and sintering at high temperatures. This technique is limited to very thin films (only a few micrometers thick) and is very sensitive to the surface defects that are not unusual for SOFC ceramic materials. Our new approach overcomes all the above problems. Very high-quality thin films of yttria-stabilized-zirconia (YSZ) of thickness ranging from a few to 100 µm have been successfully deposited on porous Ni/YSZ cermet substrate (the cermet also serves as the anode of the fuel cell). We have also been able to deposit a wide variety of oxide thin films, including ceria, alumina, and iron oxide. We are applying for a patent on this process.

When thin-film electrolytes are used, the electrodes become the predominant source of the electrical loss in a fuel cell. Reducing the electrode thickness does not reduce the electrical loss because the electrochemical reactions occurring at the electrodes are non-ohmic but catalytic in nature. To improve the electrode performance, it is necessary to improve the catalytic oxygen exchange reaction at the electrolyte/electrode interfaces. Doped ceria is known for this catalytic effect. Multilayer thin-film electrolytes made of YSZ and doped ceria have thus been proposed to enhance the electrode performance. However, because of the thermal expansion mismatch between the two layers, cracking and/or delamination have been observed [see Fig. 1(a)].

To relax the stress at the interface, in FY98 we designed a graded thin-film structure in which the composition of the film changes progressively from pure YSZ to pure doped ceria. Using our novel thin-film deposition technique, we successfully prepared such a graded film. As seen in Fig. 1(b), this graded film is highly homogeneous and shows no cracking; the interface between the YSZ and doped-ceria layers has completely disappeared. Electron microprobe analysis confirmed the graded composition. This graded film is unique among ceramic materials; it has allowed us to reduce the electrode polarization loss by almost one order of magnitude.

In FY99, we will optimize the electrode materials and build and test a complete prototype fuel cell.

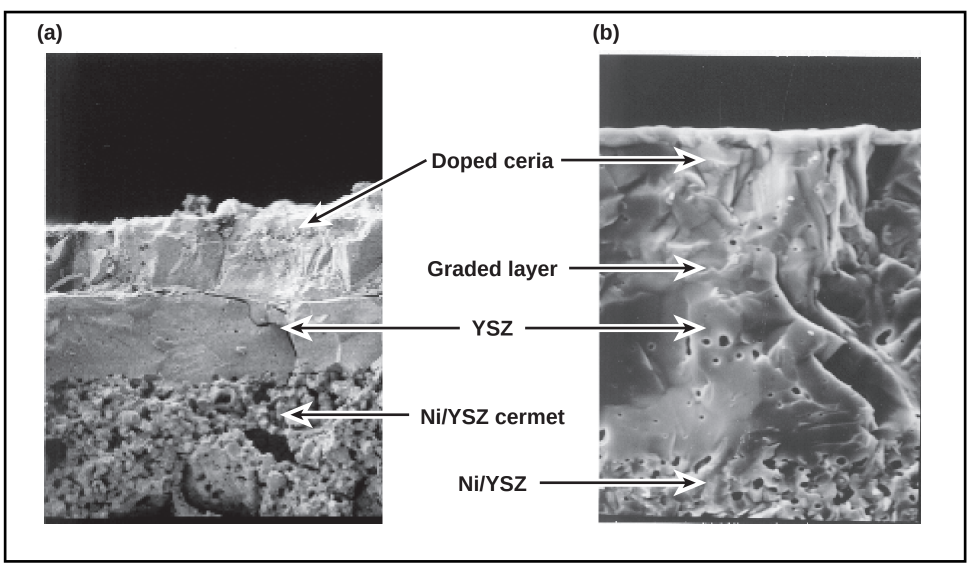

Figure 1. Scanning electron micrographs of the fracture surfaces of: (a) a bilayer composed of thin-film yttria-stabilized-zirconia (YSZ) and doped ceria on a porous Ni/YSZ cermet substrate, and (b) a multilayer thin film with continuously graded composition, prepared using our new technique. Note that the ceria film delaminates in (a) because of the thermal expansion mismatch whereas the interface between the YSZ and doped-ceria layers in (b) has been suppressed.

Stability Issues in Passive Magnetic Bearings

R. F. Post
98-ERD-035

The Laboratory has pioneered the development of a new breed of magnetic bearings for a variety of possible future applications such as flywheel-energy storage or high-speed rotating machinery. A patent containing broad claims has been issued, and others are pending. The concepts involve the use of axially symmetric permanent-magnet elements to provide levitation, coupled with special “stabilizer” elements that employ periodic Halbach arrays of permanent magnets. These arrays interact dynamically with inductively loaded circuits to provide stabilizing forces. Although this combination of elements overcomes the limitations of Earnshaw’s theorem (i.e., the absence of a stable static equilibrium for magnetically levitated systems composed only of permanent-magnet elements), there remains the ubiquitous issue of rotor–dynamic instabilities. Rotor–dynamic instabilities can arise in rotating systems when there exist displacement-dependent torques from whatever source. In mechanical systems, such instabilities are stabilized in a variety of ways, usually either involving dampers utilizing viscous forces in liquids or dissipation in bearing mounts. In all such mechanical damping elements, inertial effects are present that introduce frequency dependence. That is, mechanical dampers that may function well at low speeds may become ineffective at higher speeds, so that the system becomes “whirl” unstable above a critical speed.

Magnetically levitated systems must face the same kinds of rotor–dynamic instability problems as those encountered in the use of mechanical bearings, but these problems can be attacked by new means. For example, in so-called “active” magnetic bearing systems, the approach has been to use sensors and electronic feedback circuits to sense and control rotor–dynamic instability, but with the down side of added complexity and cost. In our passive magnetic bearing systems however, there are other options, ones involving electrodynamic damping effects. One major advantage of electrodynamic damping means over mechanical dampers is that they are “inertialess.” That is, the damping forces, since they are electrodynamic in origin, can be arranged to be as effective (or even more effective) at high speeds as they are at low speeds— something generally not possible (for the reasons cited) with mechanical dampers.

The investigations performed during FY98 included theoretical analyses, experimental studies, and the design and construction of a special test rig for bearing elements. The analytical studies included derivations of (1) stability criteria, (2) the damping coefficient of eddy-current dampers suitable for use with our passive bearing systems, and (with certain approximations) (3) the destabilizing coefficient (displacement-dependent drag coefficient) of two permanent-magnet discs in attraction. Elements similar to these latter are employed in our passive-bearing system designs. It was evident from the magnitude of the predicted destabilizing coefficients that, in the process of designing passive bearing systems that are to be both Earnshaw-stable and free from rotor–dynamic instabilities, it will be important to measure both these coefficients and those of the stabilizing dampers. To this end, we designed and constructed a test rig that will permit such measurements.

During the year, we tested a previously constructed rotating-model system that incorporated passive magnetic suspension (but no eddy-current dampers) by attempting to spin it up to design speed. However, before this speed was reached, rotor–dynamic vibrations were excited that prevented the model from reaching higher speeds. These tests emphasized the importance of carrying out the measurements of critical coefficients that were described in the preceding paragraph.

In FY99, we plan to focus on developing an experimental database on both dampers and destabilizing coefficients. From this focus could come the information and understanding necessary to design complete bearing systems that should—according to the theory—be both Earnshaw-stable and stable against whirl-type rotor–dynamic instabilities.

Evaluation of Electro-Osmotic-Aided Remediation of Dense, Non-Aqueous Phase Liquid Contaminated Aquitards

T. M. Pico, D. G. Hill, S. Pamukcu

98-ERD-038

Groundwater contamination by chlorinated solvents is a major environmental problem at DOE sites, Department of Defense facilities, and industrial sites across the United States and around the world. Cleanup of aqueous-phase contaminant plumes in ground-water is limited by our inability to remediate fine-grained soils in the contaminant source areas. These contaminated fine-grained soils become secondary sources of contamination, slowly diffusing dissolved contaminants into adjacent high-permeability zones. This diffusion from the low-permeability zones into high-permeability zones extends the time to reach cleanup standards that will prevent site closure.

There is no proven technology for removing dense non-aqueous phase liquid (DNAPL) and the resulting aqueous-phase contaminants from aquitards, a layer of fine-grained sediments in an aquifer system that is much less permeable than the aquifers themselves. We urgently need a technology to remediate fine-grained soils in source areas to reduce the cleanup mortgage at LLNL and similar sites around the world.

Electro-osmotic-aided remediation may prove to be a cost-effective and efficient technology for remediation of DNAPL contamination in fine-grained soils. When an electrical potential is applied across a saturated soil mass, cations are attracted to the cathode (negative electrode) and anions are attracted to the anode (positive electrode). As the ions migrate, they carry their water of hydration and drag the water around them. Since there are more cations than anions in a soil containing negatively charged clay particles, there is a net water flow toward the cathode. The bulk movement of a liquid phase through a stationary solid phase in the presence of an electric field is called electro-osmosis.

Our project focuses on organic contamination in fine-grained soils at a depth of 100 feet. We propose to combine electro-osmosis technology with the existing pump-and-treat remediation systems to remove DNAPL and the resulting aqueous-phase contamination from fine-grained soils. Electro-osmosis transports contaminated water from the fine-grained soils to the combined cathode/extraction well, where it is pumped to the surface, treated, and discharged and/or reinjected.

Since initial funding was received in late March FY98, qualitative experiments were designed by LLNL and conducted at Lehigh University using LLNL sediment and groundwater samples. The purpose of these tests were (1) to estimate the increase in water flow due to electro-osmosis, (2) to determine if mass flux from the fine-grained materials can be reduced to a level where groundwater in the adjacent coarse-grained materials would meet cleanup standards, and (3) to evaluate Lehigh's experimental setup and use the lessons learned to design the next generation test apparatus. In addition, the effectiveness of electro-osmosis was simulated using a two-dimensional, steady-state flow, transient transport, finite element simulator. The effects of electro-osmosis were emulated by increasing hydraulic conductivity in the zone to be impacted by electro-osmosis.

We concluded the following: (1) approximately two-orders-of-magnitude increase in aqueous flow can be achieved under electric potential gradient, as compared to hydraulic gradient; (2) aqueous-phase trichloroethylene is transported by electro-osmosis; and (3) electro-osmosis continues to show promise for significant enhancement to contaminant removal and should be studied further.

During FY99, we plan to design and construct a new test cell for qualitative and quantitative electrical and fluid flow measurements. The primary objective of bench-scale experimentation is to demonstrate that electro-osmotic-aided remediation can successfully reduce chlorinated solvent contamination in LLNL fine-grained sediment samples to achieve cleanup standards. If successful, we will continue with parameter optimization to support a field-scale demonstration, including electrode spacing, electrode material, applied voltage gradient, power requirements, treatment needs, length of treatment time, and changes in process performance over time.

MEMS-Based Fuel Cell for Micropower Conversion

J. D. Morse, A. F. Jankowski
98-ERD-091

We are developing a novel approach to the manufacture and assembly of fuel-cell stacks by combining expertise with thin-film materials with microfabrication and microelectromechanical systems (MEMS) techniques. This MEMS-based fuel cell offers a highly compact power source with high specific energy compared to existing battery techniques, is scalable over a broad range of portable power applications, is easily recharged, and complies with all environmental and safety requirements.

During the past year, we demonstrated the use of silicon micromachining techniques to form a free-standing, solid-oxide, electrode-electrolyte stack on a silicon substrate and assessed other systems based on electrolytic materials such as polymer-based electrolytes. By incorporating manifold structures within the host substrate through micromachining techniques, we have realized a complete fuel-cell device that can be readily attached to fuel and oxidant sources. In this approach, we form efficient, monolithic, solid-oxide fuel-cell (SOFC) stacks and electrode structures and allow for distributing fuel to the entire stack without the need for bulky, complex manifolding. Furthermore, since the stack is now only a small percentage of the mass of the entire structure, appropriate thermal design of the fuel-cell device, package, and resistive heating elements will allow efficient, low-power heating of the stack.

The SOFC stack is formed of a layered combination of a Ni–yttria-stabilized zirconia (YSZ) anode, a YSZ electrolyte, and a Ag-YSZ cathode. This arrangement allows for the transport of oxygen ions through the electrolyte via a diffusion-moderated process. We use integrated-circuit microfabrication processes (the silicon substrate is selectively etched with potassium hydroxide with patterned silicon nitride being used as the mask) to pattern electrode contacts and to form a resistive heater element within the stack structure, and selective etching of the substrate to form the stack into a free-standing membrane. Manifold channels are micromachined in another silicon substrate, which is subsequently bonded to the fuel-cell substrate. When bonded together, these components form a fuel-cell module having inlet and outlet channels with approximately 50-µm by 200-µm openings for fuel delivery.

The thin-film SOFC sits atop a windowed Si wafer that is bonded on the anode side to a quartz tube with a ceramic epoxy. The anode and cathode tabs on the Si wafer are bonded with Ag epoxy to Ag wires. The wires are connected to a semiconductor parameter analyzer that controls the applied cell potential. The Si wafer-mounted tube is O-ring sealed within a larger-diameter quartz tube that is placed within a conventional (Lindbergh) clam-shell furnace. Feedthroughs at either end of the assembly, on both the anode and cathode sides, allow for passage of the oxidant (air) and fuel (hydrogen) as gases.

To test our MEMS-based, thin-film fuel cells, we sent a fuel mixture of 3% hydrogen (in helium) through the anode tube at a rate of 1 to 3 standard cm^3/s. Air was sent to the cathode surface at the same rate. We measured the current output of the SOFC as a function of temperature to 600°C, as the voltage was increased from nil through and above the open-circuit voltage (OCV). The resistivity of the electrolyte was measured to typically exceed 1 MΩ·cm. We found that a maximum OCV of about 1.1 V existed for the combination of oxygen and hydrogen using this SOFC structure.

Our test results exhibited the expected overpotential for this electrolyte materials system with no output current, along with increasing current output as the temperature increased. Although the output current densities were low, inherent limitations were present in the performance of the fuel cell because of the high density of the nickel cathode layer. Thus, whereas fuel can readily diffuse through the nickel film to the electrolyte interface, the by-product of the electrochemical reaction (water) is unable to diffuse away from the interface. Therefore, the reaction ions were quenched, and the result was limited efficiency of the fuel-cell stack.

In FY99, we will (1) continue the development of a MEMS-based fuel cell with a YSZ-based solid-oxide electrolyte, and also (2) fabricate fuel-cell modules having proton-exchange membrane (PEM) electrolyte stacks. The main focus will be on the formation and integration of porous electrodes, flow-field host structures, and membrane electrode assemblies with MEMS-based manifold systems. This work will result in a standalone fuel-cell module component.

Chemical Aspects of Actinides in the Geosphere: Towards a Rational Nuclear Materials Management

P. G. Allen, K. R. Roberts
98-ERD-094

A complete understanding of actinide interactions in the geosphere is paramount for developing a rational Nuclear and Environmental Materials Management Policy. One of the key challenges towards understanding the fate and transport of actinides is determining their speciation (i.e., oxidation state and structure). Since an element's speciation directly dictates physical properties such as toxicity and solubility, this information is critical for evaluating and controlling the evolution of an actinide through the environment. Specific areas within nuclear and environmental management programs where speciation is important are in waste processing and separations, wasteform materials for long-term disposition, and aqueous geochemistry.

The goal of this project is to develop actinide X-ray Absorption Spectroscopy (XAS) as a core capability at LLNL and integrate it with existing facilities, providing a multi-technique approach to actinide speciation. XAS is an element-specific structural probe that determines the oxidation state and structure for most atoms. XAS can be more incisive than other spectroscopies because it originates from an atomic process and the information is always attainable, regardless of an element's speciation. Despite the utility, XAS is relatively complex due to the need for synchrotron radiation and significant expertise with data acquisition and analysis. The coupling of these technical hurdles with the safe handling of actinides at a general user synchrotron facility makes such experiments even more difficult. As a result, XAS has been underutilized by programs that could benefit from its application.

From the initial point of funding (midyear FY98), we began developing various key components for actinide XAS experiments. We also coordinated the preparation of environmental samples with existing LLNL programs to conduct the first series of actinide XAS experiments at the Stanford Synchrotron Radiation Laboratory.

Of the constituents present in spent nuclear fuel, ^{237}Np is of particular concern because it is the primary source of radiological hazard to the biosphere for waste storage times in excess of 10,000 years. Compounding the long half-life of this isotope is neptunium's preference to present itself in the Np(V) oxidation state under oxidizing environmental conditions. This oxidation state tends to be more soluble than Np(IV) in aqueous solutions and less strongly sorbed by geologic material surrounding a nuclear waste repository (e.g., Yucca Mountain).

In our first XAS measurements, we studied a series of Np solid precipitates. These compounds were prepared in related experiments conducted to study the solubility and thermodynamic stability of Np at Yucca Mountain. The figure shows Np L_{III}-edge XAS Fourier Transforms (FTs) for the Np(V) species NpO_2^+, the Np(IV) solid compound NpO_2, and one of the solid Np precipitates. The FTs represent pseudo-radial distribution functions of the structure surrounding the Np atoms in these samples. The FT peaks correspond to nearest-neighbor atoms (O and Np) at discrete distances from a central Np atom (e.g., Np-O or Np-Np bonding). The results of this study demonstrate that the Np precipitate has a local structure similar to that of the known tetravalent Np compound NpO_2. The figure shows that the starting material for the solubility experiment was composed of a pentavalent Np species possessing a dramatically different bonding pattern. The detection of Np(V)—>Np(IV) transformation may prove to be important for understanding the fate of Np at Yucca Mountain.

In FY99, we plan to continue developing the actinide XAS capability using new custom-designed x-ray detectors and sample positioning devices. The systems we plan to investigate include (1) plutonium sorbed onto colloidal silicate minerals representative of systems found in the vicinity of the Nevada Test Site; (2) uranium and neptunium absorbed and reacted with cementitious materials intended for use in repository construction at Yucca Mountain; and (3) a continuation of the studies on neptunium precipitates derived from solubility experiments discussed above. Determining the oxidation state and structure of the actinide elements in these laboratory-based systems is crucial for understanding their fate and transport in the environment.

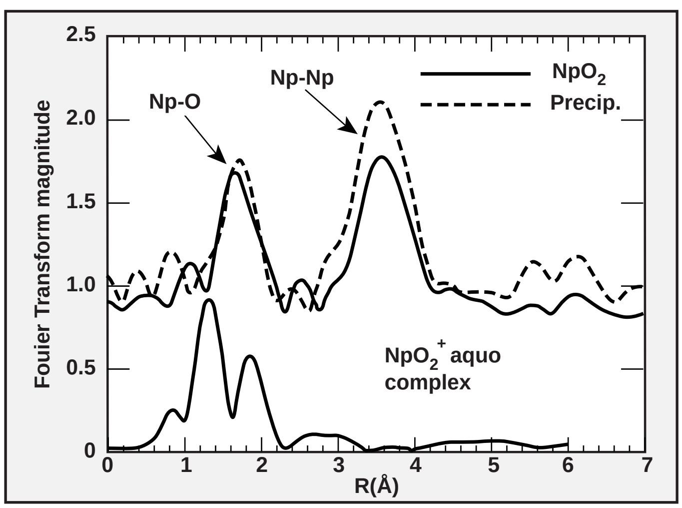

Neptunium L_{III}-edge XAS Fourier Transforms (FTs) for the Np(V) species NpO_2^+, the Np(IV) solid compound NpO_2, and a solid Np precipitate. The FTs show peaks that correspond to near-neighbors at discrete distances from a central Np atom (e.g., Np-O or Np-Np bonding).

Mechanisms of Entry for Inhaled Metals into the Central Nervous System

G. Bench, P. Grant, J. Lewis, K. Divine, T. Carlsen, J. Woollet
98-ERI-004

The DOE sites requiring environmental restoration are characterized by various mixtures of inorganic and radionuclide constituents. Levels of some of the constituents are sufficient to present human health risks. However, human exposure risk evaluation is hindered to the extent that environmental exposure conditions deviate from controlled laboratory studies. Laboratory studies are often not validated through analysis of tissues from subjects environmentally exposed to these contaminants. To improve risk evaluation, a method that can perform rapid, quantitative, multi-element analyses of biological matrices to expedite analysis of field samples is desirable. Field verification using such methods should allow better extrapolation of laboratory data and better prediction of ecological and human health impacts in situations where contaminant exposures occur.

We are assessing the capability of microbeam Proton Induced X-ray Emission (μPIXE) to provide such analyses by investigating, as a demonstration project, factors controlling the central nervous system (CNS) transport and toxicity of inhaled inorganics in rodents. Metals and specifically their entrance into the CNS via the olfactory pathway are of great interest since it has been hypothesized that chronic exposure to environmental or workplace metals are possible causes of neurodegenerative diseases. By extrapolating the animal model data to humans, data obtained from the proposed work can be incorporated into risk assessment processes, which can enable risk analysts to more effectively prioritize the risks that levels of toxicants at DOE facilities pose to human health.

Successful demonstration of the utility of the μPIXE method for environmental analyses has the potential to lead to further investigations at DOE sites. We envisage examining legacy contamination at DOE sites that are intersected by a variety of ecological areas encompassing recreation and some potential residential use. The proposed research on the olfactory epithelium as a portal of entry for inhaled toxicants to the central nervous system will also address issues that are of interest to the National Institute of Environmental Health Sciences, Environmental Protection Agency, and the Health Effects Institute. In the future, we intend to examine mechanisms underlying inhaled metal uptake into the CNS and determine factors that result in increased olfactory epithelial permeability, increased uptake of inhaled inorganics, and subsequent deposition in the olfactory bulbs; we expect to use this technique to follow the onset of neurodegenerative diseases.

In FY98, we demonstrated that μPIXE is a useful, rapid technique for examining inorganic metal uptake and distribution in the olfactory and brain tissues of mammalian species. Specifically, the sensitivity of the method and the quantitation and spatial localization capabilities allow better detection of metals not uniformly distributed throughout samples. We have also completed construction of a new microprobe system that can collect data at rates up to a factor of 6 faster than our previous system. We have investigated methods to rapidly locate metal-containing regions on the specimen, using large-current, coarse spatial resolution beams to further speed up analysis times. The results of this work are currently being incorporated into a paper for submission to a peer-reviewed scientific journal.

We are examining mechanisms underlying inhaled metal uptake into the CNS by exposing rats to inhalation of metal-containing compounds. We are testing the hypothesis that factors that increase olfactory epithelial permeability will result in increased uptake of inhaled inorganics. We have shown that both soluble aluminum chlorhydrate and (surprisingly) insoluble aluminosilicates entered the CNS of ~25% of animals via deposition in the olfactory bulbs, while control animals showed no evidence of aluminum. Animal exposures to the other metals are currently in progress.

In FY99, we will start to assess whether the uptake and distribution of inhaled inorganics in field animals can be predicted from information on the exposure medium and the laboratory data on biological uptake, distribution, and clearance. The field work will be performed on ground squirrels trapped at Site 300. Because many areas at Site 300 have been well characterized, they will suffice to test the validity of our laboratory data on CNS accumulation of inorganic toxicants. The studies will focus on ground squirrels because this species is abundant, and is known to have a narrow range that can be confined to a single exposure area. In addition, ground squirrels burrow and, by virtue of this activity, are exposed to inhalation of contaminants in soils.

We realize the difficulties in interpretation of data from multiple exposure (inhalation, ingestion, and dermal contact) pathways in our field studies. However, the fact that we can characterize differences in our field sites and potentially utilize that information to help interpret any differences in results both between sites and between field and laboratory data should provide us with valuable tools to define future research. At the very least, a refinement of some of the uncertainties related to these exposures should be possible.

A New Magnetic-Fusion System: The "Kinetic Tandem"

R. F. Post, J. A. Byers, T. D. Rognlien
98-FS-001

In the now nearly 50 years that fusion research has been under way, major progress has been made in the magnetic confinement of plasmas. In earlier days, the research spanned a variety of "closed" and "open" field configurations. Closed systems have the topology of a doughnut, while open ones have the topology of a tube open at both ends. Both types have their advantages and disadvantages. However, in the 1980s, with declining fusion budgets, it was decided in the U.S. that only closed systems, in particular the tokamak, would be pursued. That approach had made the most progress in attaining long-time plasma confinement, achieved mainly through scaling up the size of the apparatus. Recently, however, it has become apparent that technical problems (e.g., the required large size) associated with the tokamak raise questions about its economic viability.

This situation prompted us to re-examine open systems. The criterion: any system considered should place minimal demands on plasma confinement and minimize the probability of encountering plasma turbulence. The simplest magnetic-field topology satisfying both these requirements is a long solenoidal field, the intensity of which is maximum at the midpoint and tapers off toward each end. This configuration should be stable against flute-type magnetohydrodynamic (MHD) modes and, being axially symmetric, is free from the transverse particle drifts that can occur in nonaxially symmetric open systems.

Though free from MHD modes and particle drifts, the long solenoid has a major deficiency: Nothing prevents plasma from streaming out the ends. The "kinetic tandem" idea addresses this problem as follows: In the tandem mirror concept of Dimov and of Fowler and Logan, end plugging requires short mirror cells at each end. These end cells contain plasmas at higher densities than that of the plasma in the central cell. In mirror-confined plasmas, a positive potential, higher at higher plasma density, automatically builds up to hold back the electrons so that their outward flow rate matches that of the slower-moving ions. Thus, the potential in the end cells, higher than that in the central region, "plugs" the ends against ion losses. However, complex, non-axially symmetric fields are required to avoid MHD modes, and this introduces particle-drift problems.

In the kinetic tandem, the ion-density peaks needed to produce the plugging potentials are generated by shooting ion beams in from each end of the solenoid. The injected ions, aimed at small angles to the field lines, pile up and are reflected partway up the magnetic gradient, forming density peaks. Following their reflection, those ions are caught in "direct converters" to reduce the power required to maintain the plugs.

During FY98, we performed both analytical and computational studies of the buildup of the ion-density peaks in the kinetic tandem. Our analyses employed realistic ion-source angular distributions and magnetic-field intensities and took into account the limits imposed by the "firehose" and the "mirror" MHD instability modes. We found large ion-density compressions, of order 5000:1, which yielded ion densities of practical interest. Also, we obtained preliminary results about the effect of the potentials on the motions of the ions themselves.

The analytical approach was checked and extended using LLNL's Inertial Confinement Experiments Particle-in-Cell (ICEPIC) computer code. ICEPIC follows the guiding centers of ions moving in the presence of a magnetic field and the ambipolar field of electrons of a given kinetic temperature. The code results confirmed and extended those obtained analytically. When run with the same initial conditions as those assumed in the analysis, the code closely reproduced the analytical results. As the electron temperature was increased, the results showed clearly the effects of the ambipolar potential, which moved the peak back to a location with lower magnetic-field values. Turning up the ion energy then restored the peak to its previous position. No instability of the ion streams was seen. We conclude that the kinetic tandem idea has passed its first hurdle.

Interaction of a Magnetized Plasma with Structured Surfaces—From Fusion Devices to Spacecraft

D. D. Ryutov, R. H. Cohen, G. D. Porter

98-LW-023

Our research is directed towards developing a basic understanding of a new class of phenomena: the effects of surface structure on the processes in a magnetized plasma near surfaces and at some distances from them. The surface structures can be of various kinds, including topographic features ranging from smooth "waviness" to a coarse "roughness," non-uniformities of the secondary emission coefficient, and dielectric impregnations into conducting surface. The expected effects are strongest when the magnetic field forms a shallow angle with the surface. Applications of this new branch of plasma physics include fusion devices, gas-discharge and plasma processing devices, large spacecraft, and physical phenomena in the vicinity of celestial bodies without atmospheres (e.g., the Moon).

In the theoretical part of our project, we developed a methodology that allows one to study, in a unified way, effects of rough surfaces with arbitrary scales of topographic features in the most interesting case of a grazing magnetic field: from sizes much below the electron gyroradius to sizes approaching the ion gyroradius. The results can be presented in a dimensionless form so that they would be equally applicable to the micrometer-scale roughness of the fusion devices divertor plates, and to 10-km-scale structures of a Lunar surface. We have identified the following key effects: (1) the plasma is absorbed by only a small fraction of the total surface, near the "mountain tops" of the bumps; (2) regions inaccessible for one or both plasma species (known as "shadows") are formed behind the bumps; generally speaking, the size of these inaccessible domains is different for the electrons and the ions; and (3) this latter fact leads to formation of fine potential structure both near the surface and in the bulk plasma, bringing about enhanced plasma transport.

The aforementioned shadowing effect turned out to be particularly important in the distribution of the potential around satellites in the geomagnetic environment. Development of large electric potentials over the surface of spacecraft may cause arcing and lead to failure of the spacecraft equipment. Fluxes of fast suprathermal electrons that are usually the primary cause of the charging have to be neutralized by adjustment of the current delivered to the surface by the ambient plasma. However, as the plasma electrons are strongly tied to the magnetic field lines, the zones "shaded" from plasma electrons (and by virtue of quasi-neutrality, from plasma ions) are formed at some orientations of the spacecraft. The charge neutralization of fast electrons gets strongly inhibited in these zones, and large potentials develop. The other type of shadowing occurs if the velocity of the spacecraft is much higher than the ion thermal velocity. In this case, the density of the neutralizing plasma is small outside the zones determined by the Mach angle. We have developed a "three-vector model" that allows one to describe these phenomena in a unified way.

A key issue with regard to the shadowing effect (in all the aforementioned applications, from fusion devices to spacecraft) is whether the plasma can fill shadows smaller than the ion gyroradius by some fast "anomalous" processes associated with plasma microturbulence. Theoretical predictions in this regard are still not very reliable, and we have studied this problem experimentally at a small-scale experimental device called *Bluebell* (we modified for our purposes the previously existing device, called *Helicon Plasma Source*). The shadowing effect was studied by introducing a collimating mask that allowed us to produce plasma streams with radii smaller than the ion gyroradius. It turned out that these jets persist at distances considerably greater than the initial diameter of the jet. In other words, the anomalous broadening of the jets, if at all present, is a slow process, and the aforementioned concept of "shadowing" works in its direct form. The results obtained in the course of this work will have an impact on an understanding and improvement of performance of a broad range of laboratory devices and spacecraft.

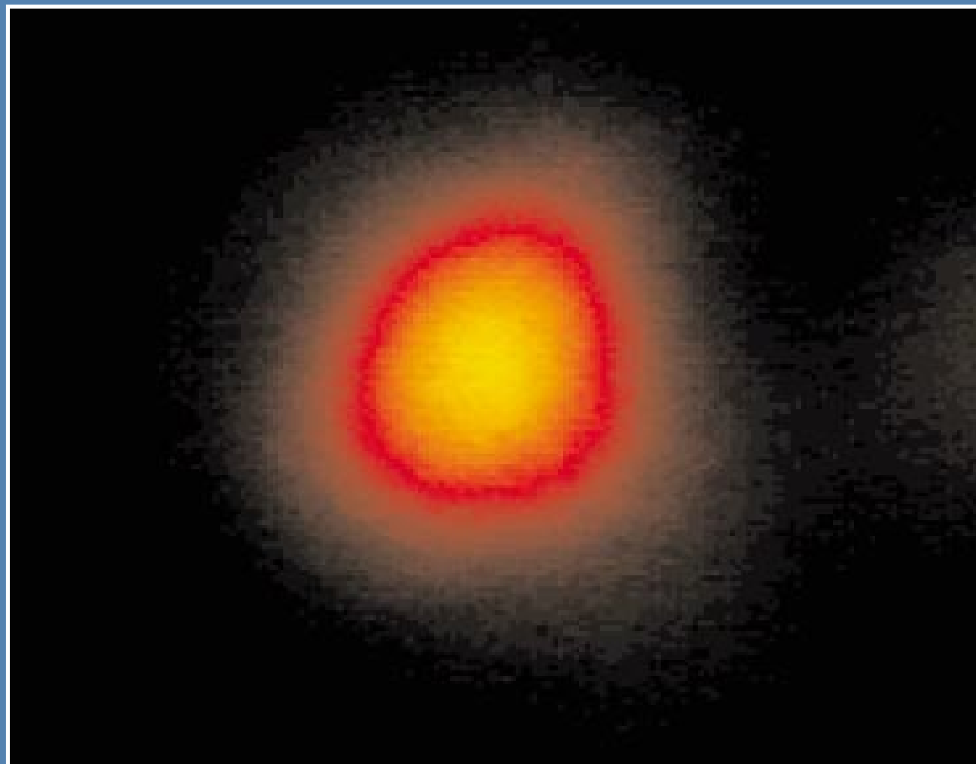

6

Lasers / Electro-optics / Beams

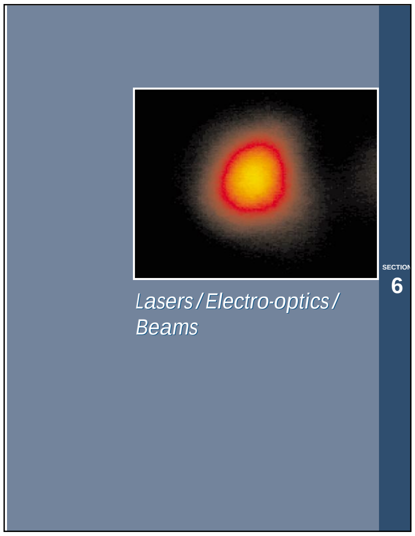

About the preceeding page

Pulsed Ti:Sapphire Laser Power Amplifier. Numerous Laboratory applications require pulsed lasers operating at 10 kHz or higher with high beam quality and electrical-to-optical efficiency. The unique thermal properties of titanium-doped sapphire (Ti:Sapphire) at low temperatures allow scaling this laser material to high powers while maintaining excellent beam quality. Earl Ault's team intends to demonstrate an all-solid-state, high-power Ti:Sapphire laser system that satisfies requirements for beam quality and electrical-to-optical efficiency at high average powers. The figure shows the spatial profile of the Ti:Sapphire laser with an output power of 23 W. The symmetric and uniform structure of the output beam indicates the excellent beam quality of the Ti:Sapphire laser. See page 6-17 for more information.

Beam Control for Ion-Induction Accelerators

T. C. Sangster, L. A. Ahle
96-ERD-048

LLNL is developing new, precision techniques for the control of space-charge-dominated (SCD) ion beams. Such beams are a key element of the heavy-ion fusion approach to a post-National Ignition Facility inertial fusion driver for electric power production. The development platform for this project is the Small Recirculator, a circular, SCD ion induction accelerator. Our goals for FY98 included beam characterization around a 90-degree bend, longitudinal and transverse control demonstration, steering algorithm optimization, beam propagation through an insertion/extraction module, and detailed data comparisons with WARP3D (a three-dimensional particle-in-cell beam simulation tool for accelerator design).

The transverse control of the Recirculator beam is accomplished by coordinating a voltage ramp on the electrostatic bending dipoles with the acceleration schedule. During FY98, we implemented a new dipole pulser capable of producing an arbitrary voltage ramp at the dipoles based on a computer-generated digital waveform. Acceleration and longitudinal control are achieved by providing precise current pulses to the induction cores. Unfortunately, a feedback circuit in the first production modulators, which provide this current pulse, was too unstable to reliably drive the induction cores. Therefore, we were unable to perform longitudinal control experiments or demonstrate acceleration using the existing five induction cores. Although the design of the insertion/extraction module was completed in FY98 through to the final drawing package, funding was not adequate to fabricate the module for testing with the beam.

The first drifting beam transport to 90 degrees was accomplished in early FY98. Well over 99% of the beam current was measured in a Faraday cup at 90 degrees. In- and out-of-bend plane emittance measurements were made with both parallel slit scanning devices and the LLNL Gated Beam Imager (GBI). Innovative GBI algorithm improvements rectified initial discrepancies with the standard slit measurements. Indeed, a new vacuum-compatible, insertable GBI has been fabricated to provide complete beam phase space information at every half-lattice period around the ring (this cannot be done with slit devices). A custom data acquisition and control system was also implemented during FY98 along with a complete set of capacitive probes to monitor the position of the beam. The figure shows an example of c-probe(capacitive beam position monitor) data as a function of bend angle through 90 degrees; the betatron oscillation of the beam is apparent.

Integrated WARP3D simulations from the source injector through the 90-degree transport lattice originally did not agree with the emittance measurements. The discrepancy was traced back to emittance oscillations that begin in the matching section, where the injected beam is matched to the bend lattice. Subsequent improvements to the beam matching, the metrics used to determine a good tune, and the input beam source distribution in WARP3D brought the predicted emittances into relative agreement with the measured values along the full length of the Recirculator.

Finally, two general strategies for controlling the transverse position of the beam in the Recirculator were developed and tested numerically. Although the strategies differ only in the frequency and magnitude of the steering impulses, there are significant differences in the physical implementation. Both approaches appear to work well in simulations, and the final selection will depend on detailed emittance growth calculations using WARP3D.

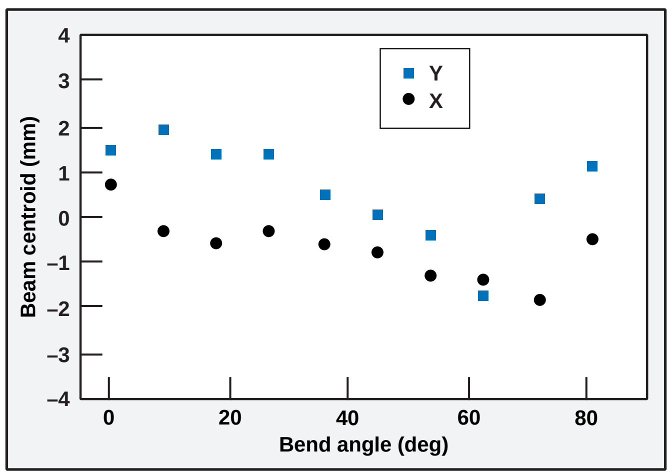

Beam position vs. beam angle. The in- (X) and out-of-bend plane (Y) beam position, in millimeters, measured using the capacitive probes is plotted as a function of bend angle. The absolute position accuracy is approximately 0.1–0.2 mm and is dominated by alignment tolerances rather than the basic measurement uncertainty (<0.1 mm).

Parametric Instabilities in Laser/Matter Interaction: From Noise Levels to Relativistic Regimes

H. A. Baldis, C. Labaune, W. L. Kruer
96-ERI-011

One of the most complex processes in laser–plasma interaction physics is the growth and saturation of parametric instabilities occurring in the interaction of a high-power laser beam and a plasma. This is of particular importance to inertial confinement fusion (ICF). Many aspects of the interaction remain unexplained, even after many years of intensive experimental and theoretical efforts. The primary instabilities of interest are stimulated Brillouin scattering (SBS), which consists of the decay of the incident electromagnetic wave (EM) into a scattered EM wave and an ion-acoustic wave (IAW), and stimulated Raman scattering (SRS), which consists of the decay of the incident EM wave into a scattered EM wave and an electron-plasma wave (EPW). The study of these instabilities is further complicated by the competition and interplay between them and, in the case of ICF, by the presence of multiple, overlapping interaction beams.

Our research during FY98 concentrated on the modification of the instabilities in the presence of multiple interaction beams. Enhanced forward-SBS has been theoretically predicted both for crossing beams with different frequencies in homogeneous plasmas and for beams with the same frequency in the presence of plasma flow. This enhanced forward-SBS can produce either energy transfer from one beam to the other or a redistribution of the laser energy in the forward direction.

During FY98, we reported the first observation and spectral analysis of enhanced, forward-scattered light of a laser beam in the presence of a second, identical, laser beam that is crossing the first one at 22.5˚. Results obtained with parallel and crossed polarization for the two beams demonstrate that the coupling between the beams must happen through the ion-acoustic waves. Enhanced forward scattering is likely caused by enhanced forward-SBS through some type of resonant process, similar to what has been predicted theoretically for symmetric modes or observed experimentally for waves propagating along the bisector of two beams. Linear theory predicts no growth when the two laser beams have the same frequency; however, because of the small angle between the two beams (22.5˚), the frequency of ion-acoustic waves involved in this process is very small compared to the laser frequency. The resonance conditions should be easily satisfied if one includes all possible modifications of laser frequencies through hydrodynamic effects, density evolution, local heating, or modifications of ion-acoustic frequency through a Doppler effect in the flowing plasma. The large width of the red-shifted component also indicates that a broad spectrum of ion-acoustic waves can contribute to the coupling. If SBS is in the strongly coupled regime, nonresonant ion modes could be driven by the laser beam, with the frequency of these modes depending on the laser intensity.

Another aspect of our study and analysis of parametric instabilities during FY98 was the localization of SBS in a plasma irradiated using random phase plates (RPPs) to produce a statistically predictable intensity distribution in the focal spot. RPPs are used to spatially smooth the laser-intensity distribution in the focal region. We presented the first experimental evidence of the localization of SBS emission in a plane perpendicular to the axis of the laser beam—thereby demonstrating that only a few small interaction regions contribute to the total SBS emission. When we evaluated SBS emission from these small speckles, we found that the local reflectivity was much higher than the average SBS reflectivity, by a factor of about 100. These observations are consistent with our recent theory that the RPP produces a convective amplification of SBS in randomly distributed speckles. This new approach is important because it can explain (1) the moderate, observed average SBS reflectivity (because of the limited number of SBS-active speckles), and (2) pump depletion within these speckles. It also demonstrates the importance of the microscopic description of SBS.

The project has achieved its goals by providing a detailed characterization of the behavior of parametric instabilities in the presence of overlapping laser beams. The study of forward-SBS has unique results that will help the interpretation of the interactions among the different parametric instabilities.

Supernovae to Supersolids: Science for the National Ignition Facility

B. A. Remington
97-ERD-022

Intense lasers offer heretofore unavailable opportunities for conducting astrophysics-relevant basic research on compressible radiative hydrodynamics. We are focusing on two fundamental, important problems in astrophysics: (1) the differences between two-dimensional (2D) and three-dimensional (3D) evolution of nonlinear hydrodynamic instabilities relevant to the evolution of core-collapse supernovae (SN), and (2) the differences between radiative and nonradiative hydrodynamics as relevant to the formation of SN remnants (SNRs) and astrophysical jets. In collaboration with several universities and laboratories, we are developing experiments on intense lasers such as Nova, Petawatt, and Falcon (LLNL); Omega (University of Rochester); Trident (Los Alamos National Laboratory); and Gekko (Osaka University, Japan). Experiments being planned for the National Ignition Facility (NIF) will span from SN hydrodynamics to the dynamics of supersolids (solids at extreme pressure and compression).

In collaboration with the University of Arizona and CEA-Saclay, we continue to develop experiments using Nova to answer specific questions about hydrodynamic instabilities relevant to the evolution of core-collapse SNs. In particular, the high velocities of the core elements Ni, Co, and Fe in SN1987A are still unexplained (3000 km/s observed vs. predictions of about half that). We are also testing the hydrodynamics of the SN code PROMETHEUS. Experiments in 2D were successfully completed during FY98. We also developed scaling criteria that address the validity and limitations of laser-based laboratory experiments for SN research. In FY99, we will study how the instability evolution in 3D differs from that predicted in 2D, an issue that may help explain several remaining questions surrounding SN1987A (e.g., high peak core velocities and early observation of gamma rays from ^{56}Ni and ^{56}Co).

In collaboration with the Universities of Colorado and Michigan, we are conducting experiments on Nova to benchmark the astrophysical codes used to model the hydrodynamics of SNR evolution, particularly the SNR now developing around SN1987A. The ejecta from this SNR are on a collision course with its circumstellar ring nebula, with impact imminent. The expected Rayleigh–Taylor instability could induce clumping and change the nature of the much-awaited collision from a smooth, one-dimensional (1D) sweeping up of the ring to something like "hydrodynamic bullets" that impact the ring in radiative bursts ("sparkles"). In FY98, we began 1D experiments to observe ejecta plasma flowing into a low-density ambient plasma; the result was a classic forward shock-reverse shock system, much like in the astrophysical SNR. We also developed scaling that addresses the validity and limitations of laser-based laboratory experiments and examined shock-induced 2D effects.

In collaboration with Rice and Osaka Universities, during FY98 we began using Falcon in an experimental study of blast-wave propagation in a gas-cluster target. Our goal is to examine the properties of radiative blast waves that are relevant to SNR formation and evolution. In our experiments, gas-jet targets of N_2, Ar, and Xe are irradiated by a 30-fs, 15-mJ Ti:Sapphire laser pulse. The gas jet forms clusters of molecules when injected into the target chamber, which is at vacuum. The laser absorption of the gas clusters is very efficient; a high-initial-temperature, low-density plasma is generated. Initial results indicate that for high-Z gas, radiative preheat causes the generation of an ionization precursor ahead of the shock wave. The precursor is not evident for low-Z gas. In FY99, these experiments will be done at higher laser power, hence at higher initial plasma temperatures. This should strengthen the radiative effects in the blast wave.

Astrophysical jets (e.g., the well-known Herbig-Haro jet HH47) have emerged as galactic laboratories for the study of radiative hydrodynamics. If we can produce similar radiative jets in the laboratory, the underlying physics can be investigated in more detail. In collaboration with the University of Maryland and Osaka University, we are developing experiments on the Nova and Gekko lasers. In FY98, we used five Nova beams to drive the interior of a gold cone, which coalesced to form a hot, radiative, high-velocity (~700 km/s) jet. The initial high temperature (~1 keV) triggered strong cooling by radiative losses—the result was a radiative collapse of the jet on-axis. Without radiative cooling, the jet would remain much hotter, "puffing up" to achieve pressure equilibrium, rather than collapsing. These experiments will continue in FY99 on Gekko.

Blue Laser Diode Process Development

G. A. Meyer, G. A. Cooper, S. L. Lehew, T. Sigmon, D. Toet, S. DenBaars
97-ERD-082

Gallium nitride (GaN) is a unique wide-band gap (~3.4 eV) semiconductor material that enables the fabrication of semiconductor lasers capable of spanning the entire visible spectrum, from blue to red. GaN materials technology will enable the development of 490-nm laser diodes for use in compact, light-weight, portable bio-detection instrumentation for national security and other applications. Our objective was to develop process and device technologies that directly advance the state-of-the-art performance of blue laser diodes fabricated in GaN. One of the main obstacles to the full realization of the potential of GaN as a material for optoelectronic devices is the difficulty in reaching high doping levels in this material.

Ion implantation may offer a practical solution to the problems associated with achieving high doping levels in GaN. This technique is widely used in semiconductor device fabrication technology. Several researchers have investigated this technique for GaN but have encountered problems that do not appear for silicon or GaAs. One of these problems is that annealing temperatures in excess of 1200°C are required to incorporate the implanted dopant atoms into the crystal lattice correctly. Since heterojunctions and quantum wells are particularly sensitive to annealing temperatures in excess of 900°C, an activation process that selectively heats the doped layer is preferred.

In FY98, we focused on developing a pulsed laser processing method for improving the activation process for ion implanted dopants in GaN. A pulsed excimer laser can deposit large amounts of energy into a thin layer at the GaN surface in a very short time. Deeper layers, containing the sensitive quantum structures, do not experience the high temperatures. The laser annealing actually melts the implanted layer. During the recrystallization of the molten layer, the dopant atoms assume the appropriate lattice positions, allowing realization of the desired low sheet-resistance contact layer.

The GaN films used in our experiments were 2 µm thick, grown in a modified two-flow horizontal reactor on c-plane sapphire, using low pressure metalorganic chemical vapor deposition (MOCVD). The samples were then ion implanted with either silicon (Si) or magnesium (Mg) to doses of 8×10^{16} cm^{-2} at 150 keV (Si) or 5×10^{14} cm^{-2} at 220 keV (Mg). Laser processing of GaN films was performed using a XeCl excimer laser with a 35-ns pulse length at a wavelength of 308 nm. The transformation induced in the GaN by this pulse was monitored in-situ and in real time by measuring the time-resolved transmission (TRT) of an IR laser beam passing through the center of the spot irradiated by the XeCl laser.

From the TRT data, we determined that we successfully melted and recrystallized the implant layer in less than 120 ns. Secondary ion mass spectroscopy (SIMS) was used to measure the silicon profiles of the samples before and after laser processing. The SIMS data is used to determine the laser fluence at which silicon redistribution occurs. As shown in the figure, the silicon surface concentration increases with corresponding increased laser fluence. This indicates that laser processing enables the implanted atoms to mobilize during the short melt duration. Attempts to measure carrier type and concentration yielded inconsistent results. We feel that lower dose implants should resolve this problem.

We have demonstrated that pulsed laser processing for the activation of dopants in GaN shows compelling promise. However, additional process development is required before this technology can be applied to actual devices.

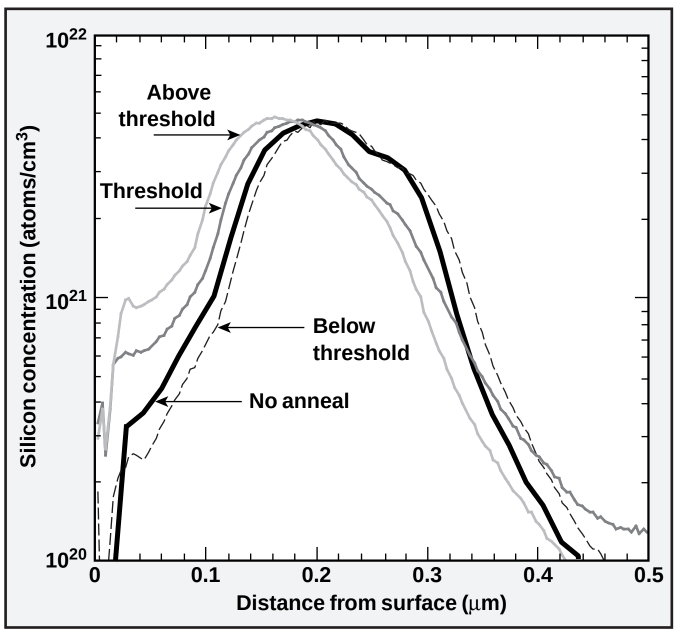

Secondary ion mass spectroscopy (SIMS) profile of ion implanted silicon in GaN (dose of 8×10^{16} cm^{-2} at 150 keV) laser processed at laser fluences above, at and below threshold. Silicon redistribution is evident at threshold laser fluence.

Technologies for Advanced Induction Accelerators

M. A. Hernandez, D. A. Autrey, R. L. Hanks, W. M. Sharp
97-ERD-086

This project, aimed at developing the technologies necessary for a fusion energy source, has focused on the concept of indirect drive targets using a heavy ion accelerator. A 1991 study showed that a recirculating accelerator (or recirculator) is a promising candidate for a cost-effective inertial fusion energy (IFE) driver. A recirculator is exactly what its name implies: an accelerator in which the beam travels around a ring-shaped configuration, repeatedly passing through each accelerating element.

We have utilized the heavy-ion fusion (HIF) Small Recirculator as a test bed. Our work in FY98 concentrated on developing the components necessary for tailored beam acceleration and bending, continuing modeling efforts aimed at constructing efficient beam steering correction algorithms, and conducting beam dynamics experiments to further our understanding of the beam control parameters.

Acceleration of the recirculating beam requires high efficiency induction core materials driven by high-rep-rate, programmable pulse waveforms. As the beam is accelerated, it gains both kinetic and electrical energy. In addition, our acceleration scheme calls for compressing the beam to help reduce emittance effects. The induction core modulators must thus be able to produce precise, fast rise-time waveforms with varying shapes, amplitudes, and widths. During FY98, we designed and built two prototype versions of the required modulator. One version is based on four parallel metal oxide semiconductor field-effect transistors (MOSFETs) and associated drivers configured as switching circuits; the other version employs the MOSFETs as linear control elements, complete with feedback and proportional drive circuitry. The linear version has demonstrated acceptable voltage regulation at average currents in excess of 200 A, and peak currents in excess of 800 A. This performance level is consistent with that required for the recirculator. We expect to build and install prototype modulator boards (based on the linear prototype) to drive the induction cells on the existing 90˚ recirculator early in FY99.

The dynamic beam parameters also require that we drive the beam bending dipoles with varying voltage levels. As the beam becomes more energetic, the dipole voltage necessary to provide the proper bending increases. During FY98, we installed and tested a prototype bending dipole pulser on the Small Recirculator. Pulser performance was mixed. Its power stages performed as expected, but we experienced unexplained failures in some of the output transformers. In addition, we worked to modify the pulser's waveform generation and control feedback elements, in order to integrate the pulser into the existing recirculator timing, control, and diagnostics sub-systems and to compensate for the effects of output loading and filtering. We conducted beam dynamics experiments using the modified pulser, which determined the relative effects of timing, voltage level, and output ripple on beam bending. We will conduct further bending experiments once the induction core modulators have been brought online.

We have used beam modeling throughout this project to develop steering control algorithms and to identify critical beam control issues. During FY98, we studied the relative merits of two fundamental steering methods, which will help determine the best configuration for steering modules on the Small Recirculator. The first method applies steering corrections based on measured values of beam position, velocity, and momentum. This method tends to impart larger "kicks" to the beam using relatively fewer steering modules. The second method is based on solving simultaneous equations designed to minimize functions based on measured beam displacements and steering module voltages. This method tends to apply smaller "kicks" using steering modules in more locations. We will carry out experiments in this area during FY99.

Equation-of-State Experiment with the Ultrashort-Pulse Laser

G. Guethlein, K. Widmann, P. Springer, M. Foord
97-ERD-107

The ultra-short pulse (USP) laser facility allows us to access the regime of strongly coupled plasmas near solid density and temperatures of several tens to hundreds of eV. This plasma regime is present in inertial confinement fusion (ICF) plasmas and stellar interiors and is also of great interest to the Stockpile Stewardship Program. Theoretical predictions of the atomic state of such plasmas are highly challenging. Thus, simulations of the surface expansion of these hot expanding states strongly depend on the equation-of-state (EOS) tables used for the calculation, which can differ by a factor of two or more.

In FY97, we developed and implemented Fourier domain interferometry (FDI) to measure the surface expansion. We demonstrated that this technique is capable of detecting changes in the optical path of the probe pulses of less than 1/1000 of the wavelength, i.e., an equivalent displacement of 6 Å for our measurements.

A significant factor in the accuracy of our surface expansion experiment is the certainty of the initial energy density from which the expansion begins. Thus, one experimental effort during FY98 focused on the precise measurement of the pump-laser intensity at the location of the target. Although we now routinely measure the absorbed laser intensity with less than 5% uncertainty, the energy density that is deposited in the target is known only within 10% accuracy. This is due to the conduction losses within the target; therefore, the goal is the implementation of thin free-standing foils. In FY98, we successfully produced free-standing aluminum foil targets of 100 Å thickness; we plan to acquire expansion data from such targets by the end of FY99. Another experimental effort during FY98 was devoted to the studies of the impact of the target surface to the measured expansion. Measurements using aluminum targets with surfaces of 20 Å and 150 Å roughness, respectively, did not show any dependence upon surface roughness of the target. This owes to the transverse averaging of the probe imaging system.

However, simulations have shown that the P-polarized probe pulse interacts with a very localized part of the plasma, namely, the critical surface. As such, the P-probe has sensitivity to extremely thin layers of the initial surface. In particular, the figure shows the difference between two LASNEX (a radiative hydrodynamics code) calculations assuming a pure aluminum target (solid line) and an aluminum target that is coated with a 2-Å-thick CH_2 layer. Comparison with the measured phase shift and reflectivity data (symbols in the figure) suggest that the target might have a non-aluminum top layer. The result of an independent target assay, indeed, confirms the existence of such a layer. Additional experimental confirmation of this extraordinary sensitivity of the P probe will take place during FY99. The current status of the experimentally achieved precision and reproducibility of the measured phase shift and reflectivity data, shown in the figure, allowed us to benchmark the technique by studying the expansion of aluminum.

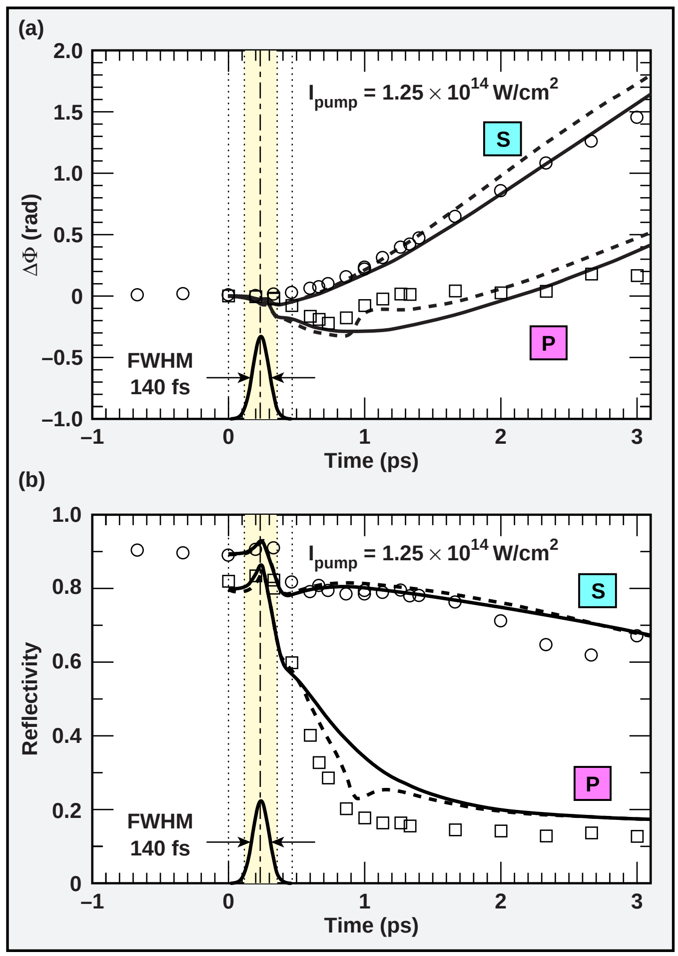

Temporally resolved phase shift (a) and reflectivity (b) measurements (symbols) of the S- and P-polarized probe pulse using a pump-pulse intensity of 1.25×10^{14} W/cm^2. The curves are LASNEX calculations using ACTEX EOS tables for a pure aluminum target (solid line) and an aluminum target coated with 2 Å of CH_2 (dashed line).

Aluminum-Free Semiconductors and Packaging

M. A. Emanuel
97-ERD-111

The goal of this project is to develop and investigate high-power laser diodes for pumping solid state lasers, such as neodymium-doped yttrium aluminum garnet (Nd:YAG). The laser diodes investigated are of a relatively new type, which contain no aluminum in or around the region in the device where the light is generated. Some early evidence indicates that such aluminum-free active region (Al-free) devices based on the InGaAsP/GaAs material system may offer performance and reliability advantages over devices based on the commonly used AlGaAs/GaAs material system for the 800-to 1000-nm range. This difference has been attributed to the apparent negative effect that aluminum has on various aspects of semiconductor crystal quality. However, the evidence presently available thus far is not sufficiently compelling to declare Al-free to be superior, especially in light of the fact that these structures tend to be more difficult to grow and have greater temperature sensitivity than their AlGaAs counterparts. The thrust of our FY98 work has been to develop wafer growth processes and device structures to investigate Al-free laser diodes and compare these results to our long-term experience with AlGaAs-based structures. In addition, we initiated a collaboration with two laser diode manufacturers in which they perform detailed evaluation of LLNL-grown Al-free laser diode wafers and share the resulting data with us. This is beneficial to all involved in that it helps the diode manufacturers evaluate Al-free structures and gives us access to "industrial strength" device testing and statistics capabilities.

The Al-free structure that we have concentrated on for FY98 consists of a thin (<20 nm) InGaAsP active region (where the light is generated) surrounded by InGaP waveguide layers. Beyond the waveguide layers are thick (~1 µm) AlGaAs layers. Even though there is aluminum present in the structure, it is away from the active region, so it is not expected to have a negative impact on the device performance. The first few months of FY98 were devoted to developing the wafer growth process using our metalorganic chemical vapor deposition (MOCVD) crystal growth reactor. After identifying and solving some unexpected growth problems concerning intermixing of materials at AlGaAs/InGaP interfaces, work was begun to investigate the performance of devices having different types of active (light generating) regions.

Three different active regions were investigated: (1) compressive strained, in which the natural lattice constant of the active region is larger than that of the GaAs substrate; (2) tensile-strained, in which the natural lattice constant of the active region is smaller than that of the GaAs substrate; and (3) strain compensated, in which a compressive strained active region is surrounded by tensile strained layers to give a net strain of zero. The compressive and tensile strained structures exhibited similar performance characteristics, while the strain compensated structures exhibited slightly poorer characteristics, perhaps because of the added complexity of their growth. However, reliability testing of the strained compensated devices yielded impressive results. Pulsed testing of such bars showed useful lifetimes of greater than 2×10^8 shots for 750-µs pulse widths. This is to be compared to lifetimes of less than 5×10^7 shots under similar conditions for AlGaAs-based devices. Under continuous-wave testing, projected lifetimes of several thousand hours at 40-W optical output were observed with the Al-free structures, compared to approximately one thousand hours for AlGaAs-based bars. Even with our very limited test data, it appears that Al-free structures in fact offer some advantages over AlGaAs-based counterparts. Preliminary testing of our wafers by an industrial partner has also shown good reliability, and this partner has expressed strong interest in continuing this interaction.

For our work in FY99, we will continue our collaboration with our industrial partners. We will also investigate variations on the structures studied in FY98 in order to optimize performance and ease of device fabrication.

Accelerated Thermal Recovery for Flashlamp-Pumped Laser Amplifiers

A. Erlandson, J. Beullier, R. London, C. Marshall, S. Payne, C. Petty, L. Smith, S. Sutton, L. Zapata
97-ERD-133

Flashlamp-pumped neodymium glass lasers used for inertial confinement fusion (ICF) experiments must produce high-quality laser beams to heat targets to high temperatures and densities. To be productive and cost effective, they must also maintain high repetition rates. These two requirements are often difficult to meet simultaneously, however, because of waste heat deposited in the amplifying neodymium-doped laser slabs by flashlamp-pumping processes. The resulting thermal gradients, which occur not only in the laser slabs but also in the gas that is convectively heated by the slabs, cause refractive-index variations and beam-wavefront distortion that can persist for many hours after each shot. In modern ICF laser systems, in which the beam is passed through the amplifiers several times for efficient usage of hardware, temperature variations as small as 0.1˚C in the laser slabs can produce several waves of beam distortion. Thus, management of thermal distortion will be a critical factor in determining, for example, the performance and scientific productivity of the National Ignition Facility (NIF), a $1.2B, 192-beam, 1.8-MJ laser now being built at LLNL for ICF experiments. While the NIF laser is expected to produce high beam quality while maintaining a repetition rate of at least three shots per day, a higher rate would increase the scientific productivity of this important national facility. We have therefore undertaken this work to study thermally induced wavefront distortions in flashlamp-pumped neodymium-glass amplifiers and to develop methods for accelerating the thermal recovery of the amplifiers.

During the past year, we performed both experiments and modeling to characterize the recovery of thermal wavefronts. Our experiments included a successful demonstration of a full-scale prototype amplifier in which thermal recovery was accelerated by flowing turbulent air over the flashlamps. Temperatures of selected slabs, blast shields, flashlamps, and reflectors were measured with thermocouples, and wavefront distortions were measured with a Twyman–Green interferometer. The amplifier was tested in two- and three-slab-long configurations. Measurements were compared with predictions made with a three-dimensional (3D), finite-element thermal model that simulated thermal radiation and conduction processes and forced-air cooling.

Our analysis—see Fig, 1(a)—shows that the prototype amplifiers should meet their thermal-recovery criteria within 3 to 5 h after each shot, provided the flashlamps are aggressively cooled with slightly chilled, turbulent gas. Flashlamp cooling is effective because most of the waste pump heat in the amplifier remains in the flashlamps immediately after a shot. Average slab temperatures measured after flashlamp shots were in close agreement with predictions made with the 3D model. Measured gas distortions varied nearly linearly with the difference between the average slab temperature and the ambient temperature, as shown in Fig. 1(b).

To estimate the effect of the gas distortions on the NIF laser beams, we scaled the measured gas distortions to account for the greater path length through the NIF amplifiers and used a beam-propagation code to calculate the beams' focal spot. Our estimate shows that the gas distortions will meet the NIF requirement (less than 5 µrad added beam divergence) within 2 to 3 h after the shot, provided the temperature of the flashlamp-cooling gas is about 1˚C below the ambient temperature. Further, the measured distortions of the slabs were of sufficiently low order and magnitude to be correctable—within 3 to 4 h after each shot—by the deformable-mirror system now anticipated for the NIF.

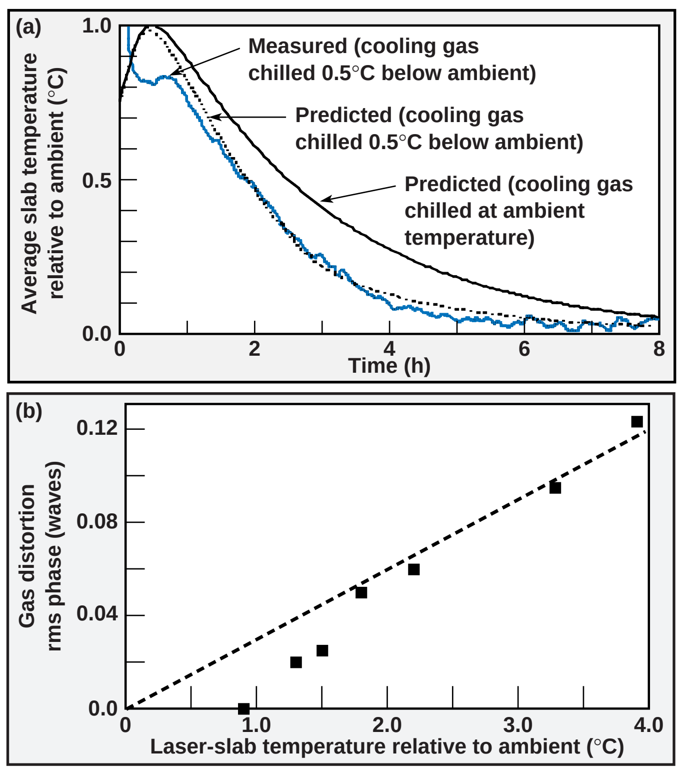

Figure 1. Results obtained from tests of prototype amplifier: (a) average laser-slab temperatures measured after flashlamps were fired, compared with those predicted by a three-dimensional, finite-element thermal model (note close agreement between the measured and predicted temperatures when thermal recovery was accelerated by slightly chilling the gas used to cool the flashlamps); and (b) how temperature gradients within the gas inside the prototype amplifier produced wavefront distortion with root-mean-square (rms) amplitude that varied nearly linearly with the temperature difference between the laser slabs and the top and bottom reflectors.

Theoretical Modeling of Fast Ignition

M. H. Key, S. P. Hatchett
97-ERD-127

Fast ignition continues to be an attractive advanced concept for obtaining higher gain in inertially confined fusion and to offer a possible route to inertial fusion energy with laser drivers of limited efficiency. This LDRD project is the theoretical component of an experimental and theoretical effort directed towards evaluating fast ignition. Estimates of the gain in a hypothetical adaptation of the National Ignition Facility (NIF) laser for fast ignition suggest that 300 × gain could be possible. The high gain relative to the 15-fold gain expected for NIF's main goal of ignition by indirect drive clearly illustrates the significant potential of fast ignition.

Monte-Carlo modeling of electron transport with a code named ITS was used to interpret experiments that measured the yield of a Kα fluor layer in a solid target irradiated at fast ignitor-relevant intensity. An important result was a demonstration that more than 28% of the laser energy was converted to electrons of mean energy close to 700 keV.

Numerical modeling with a hydrodynamic code LASNEX was used to interpret experiments in which the thermal x-ray spectrum from a layer of Al in CH targets was used to determine the heating by electrons. The LASNEX modeling was linked to measurements of pre-cursor irradiation of the target, which caused significant ablative modification—in particular, changes to the initial density of the Al layer before the arrival of the main heating pulse. Similar modeling for thin foil targets aided the interpretation of experimental studies of the process of plasma hole boring. The modeling showed the limiting level of precursor radiation that would make thin foil targets underdense and transmit prior to any hole boring. LASNEX modeling was used to simulate interferometric measurements of the preformed plasma where good consistency with the experiments was obtained. The effects of electrostatic potential in the Kα electron transport study were simulated with LASNEX. A spherical approximation was used and sensitivity to different conductivity models was assessed. Experimental study of thermonuclear reactions in CD2 targets using a large aperture neutron scintillator array (LANSA) was initiated, based on LASNEX modeling of the heating associated with hot electrons in solid targets. Data interpretation was aided with a statistical model of the neutron detector results, which gave a convincing proof of a thermal peak in the neutron energy spectrum. Another Monte-Carlo code (TART) was used to describe the neutron transport to the neutron detector.

Particle-in-cell (PIC) modeling with a 2.5 dimensional code Zohar produced important insight into the relativistic laser target interaction. Effects studied include self-focussing, hole-boring, hosing instability, hot electron generation and transport, including angular patterns, magnetic fields due to hot electron currents and cold return current, and Weibel-like instability of the hot electron flow. A powerful new technique of tracking "characteristic" electrons to illustrate the physics was developed. Other PIC modeling with 2D Zohar concentrated on the subcritical plasma contribution to the energy spectrum of the hot electron source. The modeling was specific to preformed plasma profiles deduced from LASNEX simulations. Adaptation of a diffraction/propagation code F3D enabled treatment of relativistic self-focussing; development also of a massively parallel algorithm produced detailed modeling of intense beam propagation at subcritical densities for realistic imperfect focal spot characteristics.

The net effect of all this theoretical work was to guide the experiments and to extend and develop basic understanding of the new relativistic laser plasma interaction physics at the core of the fast ignitor concept.

Time-Resolved Raman and Photothermal Deflection Studies of Laser-Induced Heating and Damage in NIF-Related Optical Materials

H. B. Radousky, S. G. Demos, M. Yan, M. Staggs, J. J. De Yoreo

97-ERI-006

It is currently believed that laser-induced damage in National Ignition Facility (NIF) optics is initiated by light absorbing "particles," whose size might be of the order of 10 nm. Our research effort to understand the photophysics associated with intrinsic properties and laser-induced damage in potassium-dihydrogen phosphate (KH_2PO_4, also known as KDP) was designed to find these particles by looking for emission sites in this material using microscopic fluorescence imaging.

The experimental set up consists of a Q-switched neodymium-doped yttrium-aluminum-garnet (Nd:YAG) laser, a continuous-wave (CW) argon laser, a microscopic optical imaging system, and a charge-coupled device detector. The 514-nm CW output of the argon laser is overlapped with the 3-ns, 355-nm third harmonic of the Nd:YAG laser and focused into the sample using a 7.5-cm focal length cylindrical lens. The imaging plane of a microscopic system is matched with the focal plane of the illumination slit beam. A 700-nm-long pass filter is incorporated into the imaging system so that the image is formed by near infrared photons emitted following absorption of the 514-nm laser light. The samples used were fast grown and conventionally grown KDP crystals.

Figure 1(a) shows an image of a 70-×70-×25-μm^3 section of a fast grown KDP crystal, denoting the presence of light-emitting clusters inside the bulk. The size of the observed emission clusters is nearly 1 μm, indicating that this is not due to their actual size but to the resolution limit of the imaging system. The overall measured emission cluster concentration is 10^4–10^6 per mm^3, depending on the crystal growth method and crystal sector. Conventionally grown crystals typically have much smaller concentrations than fast grown crystals. Furthermore, the prismatic sector in fast grown crystals contains a much smaller emission cluster concentration than the pyramidal sector. This effect is best depicted in Fig. 1(b) where the microscopic fluorescence image of a 1500-×1500-×25-μm^3 section of a fast grown KDP crystal across the sector boundary is shown. The difference in the emission intensity arising from the defect clusters in the two crystal sectors allows for the extrapolation of their spectral characteristics. The spectral profiles were measured in both crystal sectors. The difference spectrum allowed for the removal of the Raman scattering component and enhancement of the visibility of the emission due to the defects and impurities that are mostly concentrated in the prismatic sector. The experimental results show an emission band in the 550–800-nm spectral region with peak value at ≈610 nm.

The effect that the 355-nm, 3-ns high-power laser irradiation has on these optically active defect clusters is shown in Fig. 1(c). The crystal was illuminated with average power of ≈5 J/cm^2, approximately half of the damage threshold of this crystal. Figure 1(c) shows that the number of emission clusters decreases, exhibiting a laser "conditioning" result. In addition, the image intensity of the uniform background decreases, indicating the presence of "unclustered" defect centers in the material. The intensity of the individual centers also decreases under exposure to the 355-nm pulsed irradiation

It is known that 355-nm pulsed laser illumination of KDP crystals at sub-damage laser threshold intensities leads to increased laser damage threshold (laser conditioning). Figure 1(c) shows a dramatic change in the cluster concentration, which could be described as laser conditioning. These optically active clusters may contribute to laser-induced heating, enhancement of absorption, and lowering of nonlinear optical performance. The role of the observed emitting "particles" in laser-induced damage and the origin of these particles will be the focus of our future experimental effort.

Our work is in collaboration with Professor Harry Tom and student Jason McNary at the University of California, Riverside.

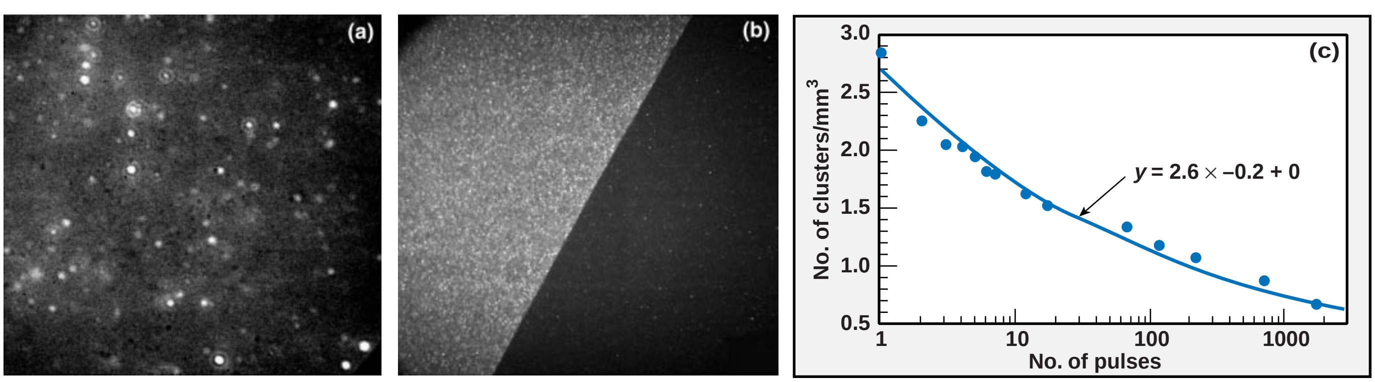

Figure 1(a) shows microscopic fluorescence images of a 70-×70-×25 μm^3 section of a fast grown KDP crystal; (b) the image of a 1500-×1500-×25-μm^3 section of a fast grown KDP crystal at the boundary between prismatic (upper left) and pyramidal (lower right) sectors; (c) the emission cluster concentration as a function of irradiation to sub-damage threshold 5 J/cm^2, 355-nm, 3-ns pulses.

Mercury: Next Generation Laser for High Energy Density Physics

C. Bibeau, R. Beach, C. Ebbers, M. Emanuel, S. Fulkerson C. Orth, S. Payne, K. Schaffers, J. Skidmore, S. Sutton, S. Telford, L. Zapata

97-SI-014

We have made significant progress in developing and building the “Mercury” prototype laser system as the first in a series of a new generation of rep-rated diode-pumped solid-state inertial confinement fusion (ICF) lasers. Primary performance goals include 10% efficiencies at 10 Hz and a 1- to 10-ns pulse with 1ω energies of 100 J and with $2\omega/3\omega$ frequency conversion. Achieving high-energy, good beam quality while operating at average power level within a 10% efficiency envelope and incorporating an architecture that allows scaling to megajoule-class systems makes Mercury a technically challenging project.

Over the past 25 years, LLNL has established itself as the world leader in the development and application of high-energy lasers. Thirty years of flashlamp-pumped Nd:glass lasers will soon culminate with the construction of the National Ignition Facility (NIF) at LLNL. The slow shot rate of once every few hours, however, limits the number of experiments. If successful, this LDRD research effort will enable a new class of high repetition-rate fusion lasers and will produce the first rep-rated solid-state fusion laser facility.

We have assembled a design for the prototype laser system shown in the figure below. The laser design uses a Yb-doped crystalline gain media (Yb:S-FAP), which offers better storage lifetime. The final amplification stages are accomplished through four passes of the beam through two gas-cooled amplifier head assemblies.

We completed a one-dimensional propagation code, which includes the impact on beam quality of (1) optical aberrations for Yb:S-FAP slabs determined from as-grown crystals, and (2) aberrations for other optics based on an appropriate 7-cm sized optics for Mercury. From code calculations, we find that a deformable mirror will remove the nine waves of thermal distortion accumulated in four passes; we verified that the laser could deliver its goal of 100 J. We have begun more detailed two-dimensional calculations.

The first production laser diode array tiles were fabricated this year. Each array consists of forty 900-nm laser bars, procured from an outside vendor, that are packaged internally on precision-sawed BeO heatsinks. These laser bars were designed for the aggressive operating conditions of Mercury, with strict attention paid to control of wavelength uniformity over large batches of bars. All Mercury diode specifications were demonstrated. Preliminary lifetests demonstrated successful operations for 10^8 shots in excess of 100 W/bar. In addition, two key improvements: higher slope efficiency and lower packaging resistance enabled us to demonstrate 45% wall plug efficiency at the design point (4 kW). Radiance conditioning of the output facets is accomplished by fabricating precision lens frames formed from lithographically etched Si wafers. The angular divergence in the collimated direction was measured to be within 30+10 mrad with 85% collection of the output energy. Low angular divergence was accomplished by maintaining strict alignment/location tolerances. Our modeling indicates that the collective tolerances in the vertical and horizontal directions are +10 mm and +5 mm, respectively.

The goals of the crystal growth efforts for the Mercury project are to assess the growth potential of Yb:S-FAP [Yb^{3+}:$Sr_5(PO_4)_3F$] crystals and to investigate the capability and integrity of the fusion bonding process in the event that full size crystals are more difficult to grow. We have identified four possible defect structures in Yb:S-FAP: cloudiness, bubble core defects, cracking, and grain boundaries. Each of the defects has been clearly identified and current growth techniques have produced 4-cm-diam, crack-free crystals with limited defects. We plan to grow 4.5-cm-diam crystals and cut two half slabs, which will be fusion-bonded together while studying the growth potential for larger diameters. Fusion bonding has been proven acceptable for meeting the Mercury specifications.

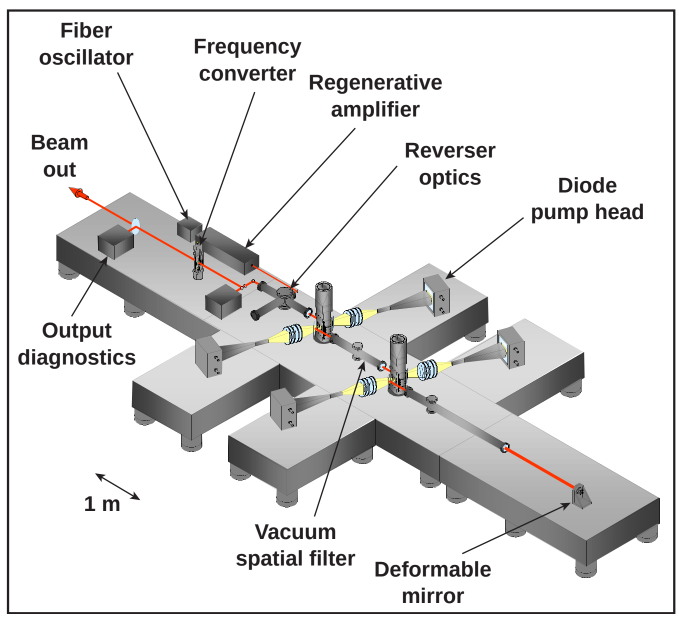

Mercury is the first prototype of a new generation of rep-rated ICF lasers. The layout of Mercury prototype laser system shows four diode arrays, two gas-cooled laser heads, and four-pass extraction geometry.

Photonic Doppler Velocimetry

P. D. Sargis, M. E. Lowry, N. E. Molau, O. T. Strand, D. E. Sweider
98-ERD-016

We are developing a novel fiber-optic implementation of laser Doppler velocimetry as a diagnostic for characterizing the performance of high-explosives tests. Other researchers have demonstrated laser Doppler velocimetry using single-mode fiber optics; our system is unique in that it uses multimode fiber optics. If successful, this technique will enable the fielding of significantly more data channels than is possible using current methods. In the past year, our purpose has been to demonstrate the feasibility of this diagnostic through laboratory experiments and field trials.

Currently, LLNL physicists measure surface velocities using a technique called Fabry-Perot velocimetry. This system employs free-space Fabry-Perot interferometers and streak cameras for each data channel. Although the Fabry-Perot velocimeter yields excellent data, overall channel count will always remain low because of its size, cost, and complexity.

Our technique uses multimode fiber optics, an optical detector, radio-frequency electronics, and moderate-sample-rate, analog-to-digital converter technology. All the components fit into a small chassis. The advantage of using multimode fiber optics is the significant increase in optical light collection from the target compared to that from single-mode fiber optics.

The target for our first refereed test was a shock-driven copper foil, with the Fabry-Perot velocimeter acting as the referee. The copper foil was in close proximity to a bridgewire, which was driven by a capacitive discharge unit (CDU). Green (532 nm) light from a frequency-doubled $Y_3A_5O_{12}$ (YAG) laser was focused onto the copper target through a probe lens. The Doppler-shifted light was reflected back through the probe lens and was simultaneously processed by both the Fabry-Perot velocimeter and the photonic Doppler velocimeter. The Doppler beat frequency signal, plotted in Fig. 1(a), was converted first into frequency vs. time and then into velocity vs. time, as shown in Fig. 1(b). Velocity values were hand-digitized from the Fabry-Perot data and then plotted on the same graph in Fig. 1(b). The negative velocity at the end of the data record is consistent with the rebounding of the copper foil after the shock event.

In a later experiment conducted at Livermore's Site 300, the Fabry-Perot velocimeter and the photonic Doppler velocimeter were again operated side by side. This time, the target was an aluminum plate that was driven by high explosives. Because the Doppler beat frequency was expected to be too high to be recorded directly on a transient digitizer, we used a microwave phase discriminator to measure the frequency-dependent phase shift of the incoming signal. Despite some system noise, the results compared favorably.

In the coming year, we plan to conduct further research into system stability and reliability issues. Our work will include making detailed measurements of the changes induced in the optical polarization state, the mode populations, and their relative phases by the moving surface and the optical elements in the system. Once we have gained a better understanding of these issues, we will design and build an optimized system. Finally, we will demonstrate the optimized system on an experiment in which a foil target is driven by high explosives.

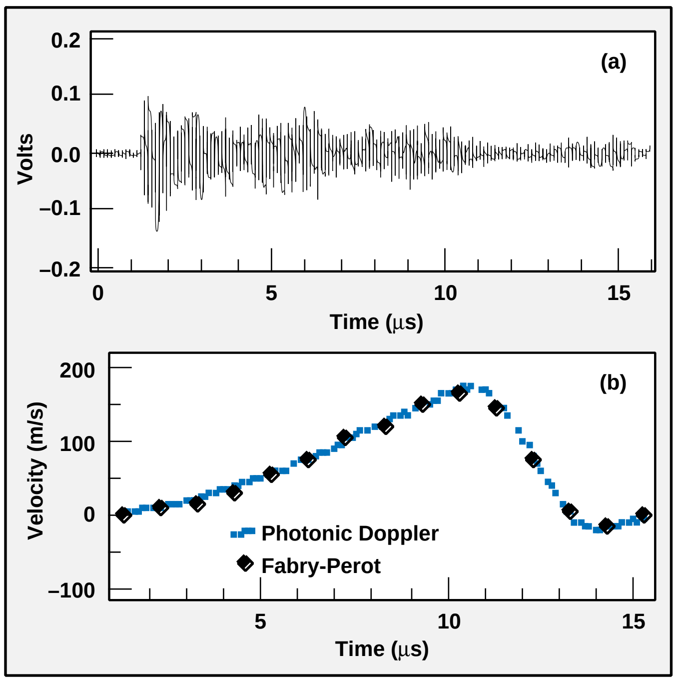

Figure 1. Results of a test of our photonic Doppler velocimeter using shock-driven copper foil: (a) raw data from the photonic Doppler velocimeter are a digitized record of the Doppler beat frequency, and (b) processed data from the Photonic Doppler velocimeter compare favorably with results using the Fabry-Perot velocimeter.

Wavefront Control with Adaptive Optics Technology

K. Avicola, J. M. Brase, M. Johnson, S. S. Olivier, T. Salmon, S. Winters
98-ERD-061

Nearly every new large-scale laser system application at LLNL has requirements for beam control that exceed the current level of available technology. For applications such as the National Ignition Facility and Atomic Vapor Laser Isotope Separation (AVLIS) or for new concepts in tactical laser weapons, the ability to transport significant power to a target and put the power where it is needed is critical. This ability requires precise control of the laser wavefront. The objective of this research is to demonstrate a new level of high-resolution wavefront control technology to address current and future needs.

Laser wavefront quality can be degraded by many effects including heating of the laser medium (e.g., Nd:glass disks), motion of heated gases in amplifiers, errors in optics manufacturing, and propagation through the atmosphere. All these effects degrade our capability to control the intensity distribution of light at the target. In our current approach to wavefront control, we use deformable mirrors to correct the disturbances to the beam. These mirrors have reflective glass faceplates, which can be deformed by piezoelectric or electrostrictive actuators, typically separated by about 1 cm. The cost of scaling these mirrors is approximately $1K per actuator, which makes them prohibitively expensive for many applications that require more than a few tens of actuators. Many current and emerging laser applications fall into this high-resolution category—edge curl on the AVLIS beam, correction of high spatial frequency aberration in the Petawatt laser, and atmospheric correction of the lasers are examples.

Two new wavefront control technologies are emerging which can address the need for affordable high-resolution wavefront control: (1) liquid crystals and (2) an approach using micro-deformable mirrors built from silicon lithography. Liquid-crystal (LC) technology can be used to control the phase of linearly polarized light. This technology is being driven by the image display industry and offers the potential for controlling phase at millions of points on a small device. Our main activity in FY98 has been to investigate these devices for laser beam control applications. One of the principal technical issues is the damage threshold of liquid crystal devices. Because they are transmissive by nature, some light will be absorbed in the device. At high powers this absorbed energy can cause damage, particularly in the transparent electrode structures necessary for controlling the device. Very little is known about the power levels that can be used with this technology; one of our initial FY99 tasks will be to quantify the permitted power levels for operating LC phase modulators. We have worked with two manufacturers (Hamamatsu and JenOptik) to develop prototype devices. Both can control the phase of up to approximately 10^6 points on the device. The phase to be applied to the beam is written to the LC device by illuminating it with an image—this avoids the pixelization and dead space problems of electrical addressing. Our principal objective for FY99 will be to demonstrate high-resolution wavefront control of an AVLIS-type beam using these devices.

The second emerging approach for high-resolution wavefront control used micro-deformable mirrors, which are built using silicon lithography—the same technology, used to make integrated circuits. We are working with several groups (particularly the Air Force Research Laboratory at Wright-Patterson Air Force Base and an engineering group at LLNL) to develop these prototype devices. These are essentially identical to the traditional macroscopic deformable mirrors discussed above, but with actuator separations of less than 200 µm rather than 1 cm. These mirrors have advantages over LC devices—they are not sensitive to polarization and, in principle, can have higher damage thresholds. The first prototypes are just emerging from the device research groups mentioned above. Our objective in FY99 is to demonstrate phase correction in a laboratory setup using a micro-deformable mirror. Demonstration in a laser application will follow in FY00.

Advanced Imaging Catheter

L. B. Da Silva, M. J. Everett, B. W. Colston, Jr.
98-ERD-062

Catheter-based, minimally invasive surgery is one of the fastest growing sectors of all surgical procedures. These medical procedures are performed by making a small incision into a main artery (e.g., the femoral artery in the thigh) and then inserting a long, thin, hollow tube and navigating it through the artery to the treatment area. The important advantages of this technique are reduced patient trauma and fast recovery. In the United States, over 700,000 catheter procedures are performed annually, and this number will increase significantly with improvements in catheter technology.

Currently, catheter procedures rely on radiography and manual manipulation for navigating and positioning the device. The difficulty can be appreciated when you consider that catheters can be as long as 2 m and that they taper down to outside diameters of 800 µm and working channel diameters of 500 µm. In addition, to reduce the possibilities of perforating arteries or damaging the arterial wall, the catheters are made of soft and pliable polymers. This makes the control problem similar to pushing on a string.

Over the past year, we have applied LLNL expertise in optical imaging, microfabrication, and modeling to begin the development of the next-generation catheter. Ultimately, this catheter will offer surgeons imaging and active control capabilities that can be used to accurately guide and position the medical device.

Our advanced catheter project involves incorporating optical fibers into the polymer wall; these fibers, when combined with a novel imaging technique, can be used to image the vicinity of the tip. In FY98, we demonstrated that optical coherence tomography (OCT), a noninvasive, noncontact optical technique, can image through highly scattering blood and detect artery walls. Although analogous to ultrasound imaging in many ways, OCT offers superior depth (<10 µm) and lateral (<10 µm) spatial resolutions. We constructed a single-fiber device with an outside diameter of 250 µm that incorporated a compact grin lens and corner cube at the distal end to focus and direct the optical beam.

To evaluate the imaging capabilities of OCT in blood-filled arteries, we used the device in *in vitro* experiments. In Fig. 1(a), we show an OCT image of a porcine artery with a metallic stent and flowing saline solution. The metallic struts of the stent are clearly visible as casting a shadow through the image, which was obtained by rotating the fiber device through a complete revolution. In Fig. 1(b), we show an OCT image of an artery with flowing blood. The results clearly indicated that OCT can image through approximately 1.5 mm of blood with high spatial resolution (~15 µm). These images will allow surgeons to confirm stent placement during balloon angioplasty and to quantify the condition of the artery.

Significant progress was made in FY98 towards developing the next-generation catheter. In FY99, we will extend this work and tackle three key areas in the development of the advanced imaging catheter. Our tasks will be to (1) miniaturize and multiplex multifiber OCT imaging technology to allow video-rate imaging, (2) develop fabrication technology to economically embed (or extrude) optical fibers within the thin polymer wall of a catheter, and (3) develop materials and techniques for incorporating active control into the distal end of the catheter. Aside from the catheter applications of OCT, we will also investigate its potential uses for imaging high explosives and fiberglass composites. In addition, we will model photon transport in highly scattering media—this will ultimately assist the surgeon in interpreting OCT images.

The image data collected in this project will be a critical test of our radiation-transport models, which play an important role in the inertial confinement fusion (ICF) and weapons programs.

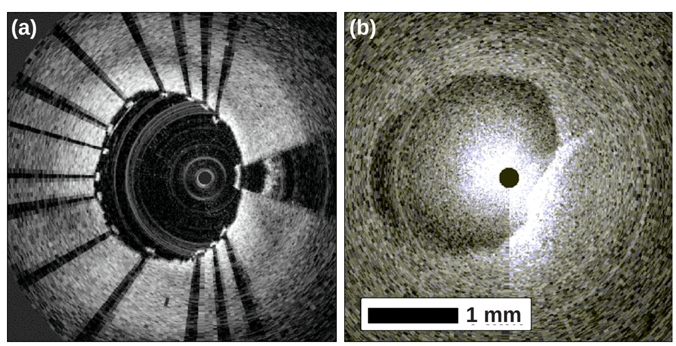

Figure 1. Optical coherence tomography (OCT) images of porcine arteries with (a) a metallic stent and flowing saline solution, and (b) flowing blood.

3ωLaser Damage II

M. R. Kozlowski, M. D. Feit, F. Y. Genin, L. M. Sheehan, Z. Wu
98-ERD-063

Laser-induced damage to optical materials for high power lasers, such as the National Ignition Facility (NIF), is largely initiated by surface or bulk defects. As the quality of optics increases, the size and density of defects leading to laser-induced damage continue to decrease, making their detection and identification more difficult. This project represents a combined modeling and experimental effortsfocused on understanding the initiation and growth of laser damage to optical materials under irradiation with high fluence ultraviolet (UV) laser light (355 nm). Our modeling efforts identified several potential mechanisms for laser damage in the optics. These mechanisms included absorption at nm-scale particles and enhanced E-fields at near-surface cracks. In order to differentiate among possible mechanisms, our experimental plan consists of two efforts. In the first effort, we are developing diagnostic tools that will allow us to locate and identify defect sites which are precursors to damage. In the second, we are identifying the optic and laser parameters that control continued growth of damage sites upon further illumination. The results are then integrated into modeling efforts to understand both damage mechanism and optic functional lifetimes.

During the past year several techniques were developed and applied, alone and in combination with each other, to locate and characterize defect sites in as-manufactured optics. Total Internal Reflection Microscopy (TIRM) studies of scatter sites provided insight into the effects of polishing parameters on the optical surface quality. By comparing our pre- and post-damage data, we were able to identify a sub-set of defects that ultimately lead to damage. Photothermal Deflection Microscopy (PDM), a technique that specifically detects defects that are heated by laser illumination, also showed promise. We found, however, that by combining the advantages of TIRM and PDM, we obtained a hybrid technique called Laser Modulated Scatter (LMS), which is simpler and more sensitive than PDM while still selectively detecting defects heated by laser illumination. A patent application has been filed for the LMS technique. In another example of combined techniques, Near-field Scanning Optical Microscopy (NSOM) used in a TIRM mode (in collaboration with another LDRD effort—97-ERD-013) has located features below the optic surface that indicate the direction of damage crack growth upon subsequent illumination pulses, thus providing insight into the damage growth process.

The second part of the effort employed experimental and theoretical techniques to determine the influence of various illumination and sample parameters on damage density and growth rate for multi-pulse illumination of fused silica. The radial growth-rate of damage sites increased linearly with laser fluence but decreased with laser wavelength. The laser damage growth rate did not vary with laser pulselength. In contrast, the fluence threshold for initiation of damage scales with the square-root of the pulselength. Extreme statistics theory was used to address the issue of dependence of damage site density on diameter of the test beam. A procedure was developed to allow comparison of data obtained with millimeter-scale test beams with data obtained at NIF-like m^2-size apertures. This improved understanding of the statistical nature of damage has resulted in a move away from the “damage threshold” specification for laser damage, which dominated the laser damage field for the last three decades.

FY99 activities will focus on refinement of our precursor detection tools with a shift towards an emphasis on precursor identification. This effort will rely on the addition of spectroscopic capabilities to the detection techniques developed in FY98. Damage growth experiments will examine issues of coated optics, vacuum environments, and macroscopic (>1 mm) damage sites. Through the study of both damage precursors and damage growth, we will continue to develop a mechanistic model for laser-induced damage while improving our predictive capabilities for optic lifetimes.

Measuring Parameters of Large-Aperture Crystals used for Generating Optical Harmonics

R. E. English, Jr., R. L. Hibbard, R. B. Michie, P. J. Wegner, J. M. Auerbach, M. A. Norton, M. D. Summers, S. A. Perfect
98-ERD-066

Optical harmonic generation has long been known as a very effective means for extending the operating wavelength range of high-peak-power lasers. Generating optical harmonics in laser systems such as the National Ignition Facility (NIF), Inertial Fusion Energy (IFE) lasers such as Mercury, or lasers for isotope separation requires careful control of several parameters. Efficient transfer of power from the input beam to the harmonic beam requires the input and output waves to be phase-matched; this is most often done by using the birefringence of a nonlinear optical crystal to cancel the effects of dispersion.

The purpose of this project was to develop tools for understanding the influence of crystal quality and crystal mounting on harmonic-generation efficiency at high irradiance. Measuring the homogeneity of crystals interferometrically, making detailed physics calculations of conversion efficiency, performing finite-element modeling of mounted crystals, and designing a new optical metrology tool were key elements in obtaining that understanding.

For this work, we used the following frequency-tripling scheme: type I second-harmonic generation followed by type II sum-frequency mixing of the residual fundamental and the second harmonic light. The doubler was potassium dihydrogen phosphate (KDP), and the tripler was deuterated KDP (KD*P). With this scheme, near-infrared light (1053 nm) can be frequency tripled (to 351 nm) at high efficiency (theoretically >90%) for high irradiance (>3 GW/cm^2).

Spatial variations in the birefringence of the large crystals studied here (37 to 41 cm square by about 1 cm thick) imply that the ideal phase-matching orientation of the crystal with respect to the incident laser beam varies across the crystal. We have shown that phase-measuring interferometry can be used to measure these spatial variations. We observed transmitted wavefront differences between orthogonally polarized interferograms of $\lambda/50$ to $\lambda/100$, which correspond to index variations of order 10^{-6}. On one plate that we measured, the standard deviation of angular errors was 22.3 µrad; this corresponds to a 1% reduction in efficiency.

Because these conversion crystals are relatively thin, their surfaces are not flat (they deviate ±2.5 µm from flat). A crystal is mounted against a precision-machined surface that supports the crystal on four edges. This mounting surface is not flat either (it deviates ±2.5 µm from flat). A retaining flange presses a compliant element. The load thus applied near the edges of the crystal surface holds it in place. We performed detailed finite-element modeling to predict the resulting shape of the mounted crystal. The prediction agreed with measurements of mounted crystals.

We computed the physics of the frequency-conversion process to better quantify the effects on efficiency of variation in the crystal's axis, changes in the shape of the crystal, and mounting-induced stress. We were able to accurately predict the frequency-conversion performance of 37-cm-square crystals on Beamlet, a one-beam scientific prototype of the NIF laser architecture, using interferometric measurements of the mounted crystals and the model. In a 2ω measurement campaign, the model predicted 64.9% conversion efficiency; 64.1% was observed. When detuned by 640 µrad, the model and measurement values (both 10.4%) also agree.

Finally, we completed the design and initial testing of a new optical metrology tool to measure the spatial variation of frequency conversion. This system employs a high-power subaperture beam from a commercial laser oscillator and rod amplifier. The beam interrogates the crystal's aperture by moving the crystal horizontally on a translation stage and translating the laser beam vertically on an optical periscope. Precision alignment is maintained by means of a full-aperture reference mirror, a precision-machined surface on the crystal mount, and autocollimators (the goal for angular errors is 10 µrad). The autocollimators track the mounting angle of the crystal and the direction of the laser beam with respect to the reference mirror. The conversion efficiency can be directly measured by recording 1ω, 2ω, 3ω energy levels during the scan and by rocking (i.e., tilting) the crystal mount over an angular range.

During this project, we developed frequency-conversion modeling knowledge, refined optical-interferometry techniques, and demonstrated new metrology-tool capabilities. These are being used in the design of crystal-fabrication and assembly-verification equipment for NIF.

Pulsed Ti:Sapphire Laser Power Amplifier

E. R. Ault, G. V. Erbert
98-ERD-069

Numerous isotope-separation applications based on frequency-doubled, tunable near-infrared light require lasers with power levels and beam quality that have heretofore been unavailable. These applications require pulsed lasers operating at 10 kHz or higher with high beam quality and electrical-to-optical efficiency.

The unique thermal properties of titanium-doped sapphire (Ti:Sapphire) at low temperatures allow scaling this laser material to high powers while maintaining excellent beam quality—this has been demonstrated with an argon-ion pumped, continuous-wave Ti:Sapphire laser presently used as a source of process light in the uranium atomic vapor laser isotope separation (AVLIS) project. However, the output power and efficiency of the Ti:Sapphire laser is limited by the argon-ion pump lasers.

The recent development of solid-state, high-average-power, frequency-doubled neodymium-doped $Y_3A_{l5}O_{12}$ (Nd:YAG) lasers in the AVLIS program suggests that Ti:Sapphire can indeed be efficiently pumped with the second harmonic of these lasers. The goal of our project has been to demonstrate an all-solid-state, high-power Ti:Sapphire laser system that satisfies requirements for beam quality and electrical-to-optical efficiency at high average powers.

For a pump laser, we used a solid-state, diode-pumped, frequency-doubled Nd:YAG laser that had been designed and assembled at LLNL. This laser is acousto-optically Q-switched, and the second harmonic is generated with a 5-×5-×18-mm lithium triborate (LBO) crystal. Output powers up to 140 W at 532 nm can be achieved; output-beam quality was measured to be 30 times diffraction limited.

For the Ti: Sapphire laser that we designed and constructed for this project, we concentrated on two important features: control of thermal gradients in the rod and conversion of a multimode pump beam into anear-diffraction-limited output beam.

The output power of Ti:Sapphire lasers with stable, high-quality beams is limited by thermal gradients generated in the rod. Beam distortions induced by these gradients can be reduced significantly by cooling the rod to liquid-nitrogen (LN_2) temperature. Therefore, the rods in our Ti:Sapphire laser are mounted to a copper block that is cooled with flowing LN_2; the laser is enclosed in a vacuum vessel to prevent condensation on the rod surfaces when they are cooled to low temperatures. An optical breadboard inside the vacuum chamber allows the laser to be easily configured to various resonator designs.

An important feature of our laser design is its ability to convert a multimode pump beam into a near-diffraction-limited output beam. The spatial overlap of the pump and resonator beams within the rod is a critical design consideration. To optimize the optical design of both the delivery optics of the Nd:YAG pump laser and the resonator of the Ti:Sapphire laser, we performed extensive modeling using a Gaussian beam-propagation code coupled to a Frantz Nodvik pulsed-amplifier model.

With the laser configured as a single-rod oscillator, the output power of the Ti:Sapphire laser was 23 W when pumped with 100 W from a single-pump Nd:YAG laser. The laser was operated in a broadband mode centered at 870 nm. The optical-to-optical efficiency was 23%; the electrical-to-optical efficiency was 1.25%. For comparison, the argon-ion-pumped Ti:Sapphire laser currently used in the AVLIS project has an electrical-to-optical efficiency of 0.02%. The excellent beam quality of the Ti: Sapphire laser is illustrated in the figure.

We achieved our goals in FY98 and demonstrated the feasibility of a Nd:YAG-pumped Ti:Sapphire laser for the desired applications. With the use of this system, savings of millions of dollars in capital and significant savings in operating cost are possible. In FY99, we plan to scale the output power of the Ti:Sapphire laser to the 100-W level by adding additional Nd:YAG pump lasers and a second rod configured as a power amplifier. We will also make detailed measurements of beam quality.

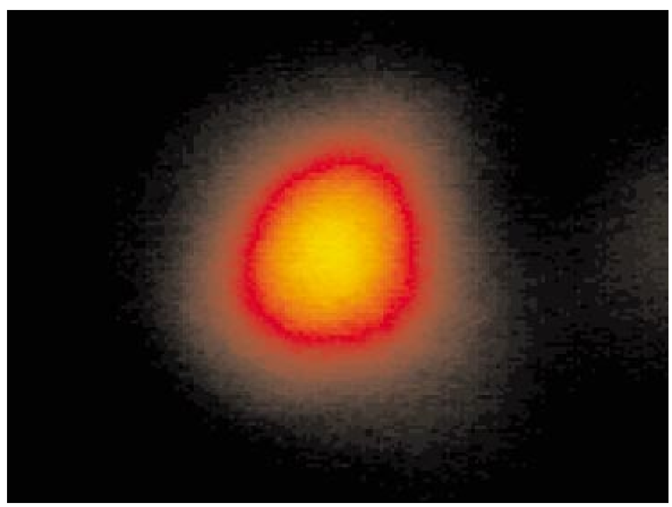

Spatial profile of the Ti:Sapphire laser with an output power of 23 W. The excellent beam quality of the Ti:Sapphire laser is indicated by the symmetric and uniform structure of the output beam shown here.

Advanced Wavefront-Control Techniques

K. Avicola, S. E. Winters, C. A. Thompson, M. A. Johnson, J. T. Salmon
98-ERD-071

Adaptive-optics (AO) systems are finding increased application in energy research programs such as the National Ignition Facility (NIF) and Advanced Vapor Laser Isotope Separation (AVLIS), in laser defense applications, and in astronomy. Especially in the energy research programs, large numbers of these systems are being planned (order of 200 for NIF and AVLIS), and high-performance, lower-cost systems are desired. This project is aimed at these goals and has three areas of concentration: modeling and analyzing deformable mirrors; designing, constructing, and testing low-order wavefront correctors; and designing heterodyne wavefront sensor systems. This AO technology is a vital part of LLNL's Laser Program, and advancing this technology is expected to be important to future programs.

Our work on deformable mirrors includes developing improved modeling tools, improving fabrication techniques for deformable mirrors, and linking the mirror models to beam-propagation codes. Our improved model utilizes the finite-element method to predict the response of the mirror surface from input forces or displacements on the back of the mirror. The output of the model is the axial displacement of the surface at regularly spaced points on the mirror's surface. These points uniquely determine the response of the mirror surface for the displacement of each actuator and serve as input to a model of the AO system. Previous models use a set of Gaussian approximations of the surface response for the displacement of each actuator. Our new method provides a significant improvement in predicting residual errors and was tested on NIF and AVLIS applications in FY98. In FY99, we will develop and apply an integrated AO modeling tool.

Traditionally, deformable mirrors have been used to correct wavefront aberrations. Unfortunately, when the aberrations are primarily of low order, deformable mirrors add unneeded complexity to the system. In FY98, we investigated the Alvarez lens—which is based on an idea proposed by Luis Alvarez in the 1970s—as a simpler means of correcting low-order aberrations. We designed a set of lenses that, when translated orthogonally to the optical axis, introduce a variable amount of astigmatism to the incoming wavefront. Figure 1 shows a pair of Alvarez lenses and illustrates how they are operated. As the lenses are translated in equal and opposite directions—see Figs. 1(a) and (b)—an increasing amount of astigmatism is introduced along that axis. This allows for control of astigmatism in two axes and for power (when the *x*-axis shift is equal to the *y*-axis shift). In FY98, we designed and toleranced a lens pair and began assembling mounting and translating hardware. A set of lenses is being fabricated by a commercial source using a small-tool polishing technique; another set is being fabricated at LLNL using a lithography technique. In FY99, we will test the lenses and explore reflective designs.

Most AO systems to date have used Hartmann sensors to detect the wavefront errors needing correction. Rather than measuring phase directly, these sensors measure the local wavefront slopes. A Hartmann sensor uses an array of lenslets in front of a charge-coupled-device (CCD) camera; each lenslet produces a spot on the CCD. The centroid position of these spots is a measure of the local wavefront slope. To apply correction signals to a wavefront corrector, the wavefront must be reconstructed from this centroid information. These processing steps are very computer intensive, and the computer hardware and software costs usually make up a major part of the total system cost. We are investigating the heterodyne sensing approach in which known flat reference beams, frequency shifted by a fixed amount from the beam to be corrected, are combined and mixed on an array of lenslets and photodiodes. As in the Hartmann sensor, the beam is spatially sampled by the array; however, in our heterodyne sensing approach the relative phase information is directly available at the output of the photodiodes.

In FY98, we set up a two-beam experiment with a deformable mirror, acousto-optic frequency shifter, and heterodyne detectors. We have successfully locked the phase of the two air paths together with a simple analog control loop; the residual error is less than 0.08 wave peak-to-peak. In FY99, we will extend our work to a full-beam experiment, which is more representative of what is needed in typical system applications.

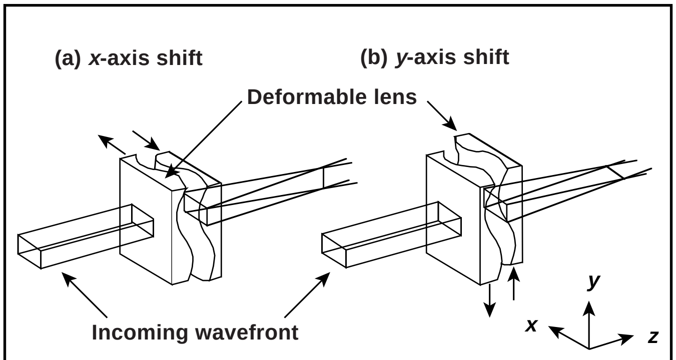

Figure 1. Alvarez lens pair (with surfaces greatly exaggerated). These lenses provide independent control of (a) *x*-axis astigmatism, and (b) *y*-axis astigmatism.

Visible Solid-State Laser for Isotope Separation and Advanced Manufacturing

J. J. Chang, I. L. Bass, E. P. Dragon
98-ERD-073

This project focused on the development and demonstration of 200-W-class green solid-state lasers pumped by laser diodes. High-power generation of a pulsed green laser is important for applications such as material processing, pumping Ti-sapphire and dye lasers, and the laser guided star. Efficient green generation is also a critical step to achieve high-power UV output for excimer laser replacement. In FY98, we demonstrated greater than 300 W of pulsed green output from a diode-pumped Nd:YAG laser. This side-pumped laser uses compound parabolic concentrators for efficient coupling of continuous-wave (CW) diode radiation into a closely coupled laser pump chamber. With a 6-mm, Nd-doped YAG rod and a flat-flat short resonator, we obtained a CW infrared (IR) output of greater than 500 W with an optical-to-optical efficiency of 40% and an electrical-to-optical efficiency of 15%.

We have improved the laser resonator design in FY98 for intra-cavity frequency doubling. The use of an advanced four-mirror Z-resonator enabled us to adjust the laser spot size in the doubling crystal for optimum second-harmonic generation. This resonator also compensated the large thermal lensing introduced by the KTP doubling crystal. As a result, we have achieved a frequency-conversion efficiency (i.e., from IR to green) of as high as 82%. In FY98, we have also enhanced pulsed laser operation through better designs of the laser rod and the acousto-optic Q-switches used in the system. These improvements enabled us to generate a world record 315 W of pulsed green output with a 5-mm long KTP crystal. This power level exceeded the previous record by greater than 150 W. This performance represented an optical-to-green (O-to-G), efficiency ratio of green power to diode power) of 24% and an electrical-to-green (E-to-G) efficiency of 8.2%. These numbers were significantly better than the 17% O-to-G and 5.5% E-to-G efficiencies achieved previously. With an 18-mm-long lithium triborate (LBO) doubling crystal, we have also obtained 304 W of green output with pulse duration of 75 ns at 17 kHz. The output was 272 W at 13 kHz.

To evaluate the long-term performance of the diode-pumped green lasers, we built four rack-mountable laser packages for around-the-clock operation in the Solid-State Laser Test Facility (SSLTF). They were 140-W class lasers based on current design. By the end of FY98, we accumulated >25,000 device hours of operation with an average on-time output of 143 W per device. To our knowledge, this is the world's first demonstration of continuous operation of high-power, diode-pumped solid state lasers in an industrial type environment.

We have improved the laser design and system reliability based on what we learned during the long-term laser operation. As a result, a laser degradation rate as low as ~0.003% per hour has been demonstrated. The figure shows a 400-hour run of one of the engineering laser using an LBO crystal. The stability of the laser performance is clearly demonstrated. During the later part of FY98, we built an advanced 200-W class laser package for around-the-clock operation. This higher power unit passed the initial 100-hour life test with an average power of 221 W of green output. We will continue the operation of the advanced laser at the SSLTF.

In conclusion, we have achieved all the project goals in FY98. We developed diode-pumped Nd:YAG lasers with record levels of green output and system efficiency. These lasers have passed the reliability test in a hands-off around-the-clock operation facility. The robust performance of the key laser components (i.e., doubling crystals, laser diodes, Q-switches, and optics, etc.) demonstrates the economical viability of high-power, diode-pumped solid-state lasers for industrial applications.

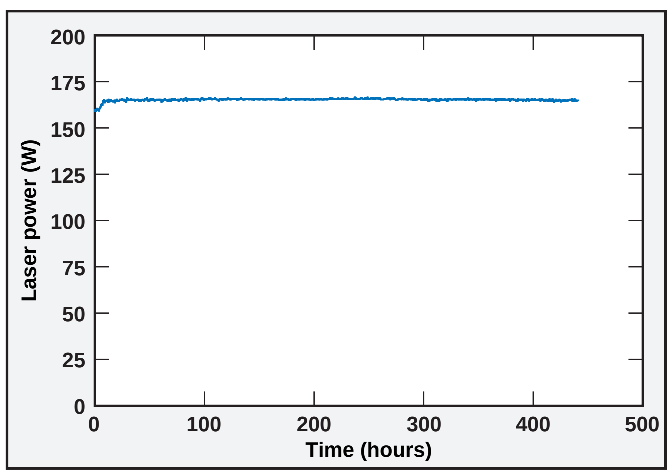

The continuous operation of a diode-pumped Nd:YAG laser with pulsed green output using an intracavity LBO doubling crystal.

Second Harmonic Generating Material Development for High Average Power Visible Solid-State Lasers

C. A Ebbers, K. I. Schaffers
98-ERD-074

A solid state, high-average-power, long-lifetime, visible laser is a useful source for many applications, such as pump sources for other lasers (i.e., Ti:Sapphire). The critical element with the highest risk of failure within the solid state laser is the intracavity frequency doubling crystal. In addition, intracavity frequency conversion intimately links the performance of the laser with the performance of the frequency conversion crystal. Utilizing both $KTiOPO_4$ (KTP) and LiB_3O_5 (LBO) for the frequency doubling element, we have achieved an unprecedented average output power and power conversion efficiency: greater than 300 W of 532-nm light with an intracavity power conversion efficiency approaching 70%. However, there exists variability in the lifetime of these lasers that is dependent upon the nonlinear optical crystal. We are evaluating commercially obtained KTP and LBO crystals grown by different vendors and/or differing growth methods to evaluate the lifetime and average power capability of each crystal source. We are also examining issues such as nonlinear absorption, angular acceptance, thermal acceptance of the frequency conversion crystals, and the effect of these parameters on the laser performance.

Degradation of the KTP due to “graytracks” is directly correlated to performance degradation of the laser. In addition, we find that due to nonlinear optical absorption, the effective thermal lens developed in KTP can be as short as 10 cm. In an optical cavity that is unstable to the induced lens, this nonlinear-absorption-induced-lens can cause the beam size at the crystal to decrease, causing an even greater increase in the thermally induced lensing in the crystal. This runaway situation causes a collapse in the spot size at the crystal, dramatically reducing the available power. By accounting for this effect in the optical cavity design, this runaway, nonlinear-absorption-induced thermal lens can be circumvented.

Different issues surround the use of LBO as the intracavity doubling crystal. In contrast to KTP, under the same average power loading the LBO crystal will act as a negative lens, eliminating the runaway thermal lensing issue discussed above. In addition, the absorption in LBO tends to be lower than that of KTP, and the LBO crystal thus has a minimal effect on the optical cavity design. However, the nonlinear coefficient of LBO is 1/4 that of KTP, requiring the use of much longer crystals to achieve the equivalent performance. Due to the longer length and higher optical scattering present in the LBO, the maximum second harmonic power extracted is nearly always ~10% lower than in the equivalent laser utilizing KTP. Finally, the thermal acceptance of LBO is much smaller than that of KTP, requiring more stringent control on the crystal cooling water to maintain peak conversion efficiency.

The ideal nonlinear optical material would combine characteristics of both KTP (fast growth, low thermal sensitivity) and LBO (high transparency, photochemically stable). We are examining the properties of a new class of nonlinear crystals with the potential to replace both KTP or LBO for intracavity frequency conversion. These new crystals will have properties similar to LBO assuring that optical absorption and graytrack effects will be minimized. In addition, we expect that the thermal acceptance and growth rate of these new crystals will improve upon the existing properties of LBO. We have made significant progress towards these goals and are in process of scaling the new crystals to apertures suitable for complete characterization.

We are also examining the potential of another new material, periodically poled lithium niobate (PPLN), for use in intracavity doubled lasers. The large nonlinearity (5 times larger than that of KTP) makes PPLN appear attractive for harmonic generation of these high-average-power lasers. However, PPLN currently suffers from photorefraction and nonlinear absorption. We are attempting to improve PPLN by reducing the defects in the lithium niobate substrates. In FY99, we will continue to improve the bulk material and coatings of existing nonlinear optical crystals as well as characterize and test new materials as they are developed, enabling greater reliability of the intracavity doubled laser.

All-Solid-State Tunable Laser Source Using Sum-Frequency Mixing

R. H. Page, R. J. Beach, C. A. Ebbers
98-ERD-078

Tunable, narrow-band visible laser light finds many applications in spectroscopy, sensitive detection of atoms, and other fields. Traditionally, dye lasers have been used to generate tunable visible light; a notable example of an engineered dye laser system at LLNL is the atomic vapor laser isotope separation (AVLIS) Laser Demonstration Facility. It is inherently difficult to design, operate, and maintain a dye-based front end (master oscillator) of such a system because of stringent requirements on line width, pulse-repetition frequency, wavelength stability, and reliability. Our primary goal is to create a solid-state laser prototype system that produces continuous-wave, tunable, visible light, with a clear pathway to deployment as an improved alternative to a pulsed dye-laser master oscillator.

Various solid-state laser systems can be enhanced with nonlinear-optical components (e.g., frequency doublers) to produce visible light, but the scheme we have selected leverages recent developments in the fiber-optics, nonlinear-optics, and telecommunications industries. The wavelength region of interest can be reached by producing the "sum frequency" of two long-wavelength infrared light beams at ~1000 nm and ~1300 nm.

The prototype system we are developing has four major components: (1) a high-resolution, oscillator for the 1000-nm range; (2) an amplifier to boost the oscillator output to the few-watt level; (3) Nd:YAG laser; and (4) a crystal for performing sum-frequency generation with the infrared beams. The fiber oscillator and amplifier both employ doped silica-based glass as gain media and are very similar to the 1550-nm components based on Er-doped glass that are used in telecommunications. We are acquiring custom-made fiber oscillators, which are capable of controlling the wavelength. For the amplifier, we used a "cladding-pumped" fiber that boosted the 10-mW oscillator output to over 2 W, while preserving the single-spatial-mode quality of the injected signal. The Nd:YAG laser is commercially available and has excellent beam quality and ultranarrow line width. For sum-frequency generation, we used a 50-mm periodically poled lithium niobate crystal, valued for its high conversion efficiency (of infrared to visible light). The figure shows the crystal in its holder, with a visible light beam being produced.

Experiments were conducted to characterize each of the components and examine performance of the integrated system. Two separate oscillator vendors learned how to make spectrally pure lasers tuned close to a target wavelength (1064 nm in our case, to facilitate system testing with a Nd:YAG laser at the same wavelength). We procured a stand-alone amplifier unit (not yet tested) of 3-W nominal output power, and have also demonstrated 2-W output with our home-built system. Our integrated breadboard system has generated over 55 mW of orange light. Scaling to over 100 mW of output looks feasible, and the line width is below 50 MHz.

In FY99, we will be enhancing the utility of the visible light source by controlling its spectral format. We will also be working on tuning and stabilizing the output wavelength.

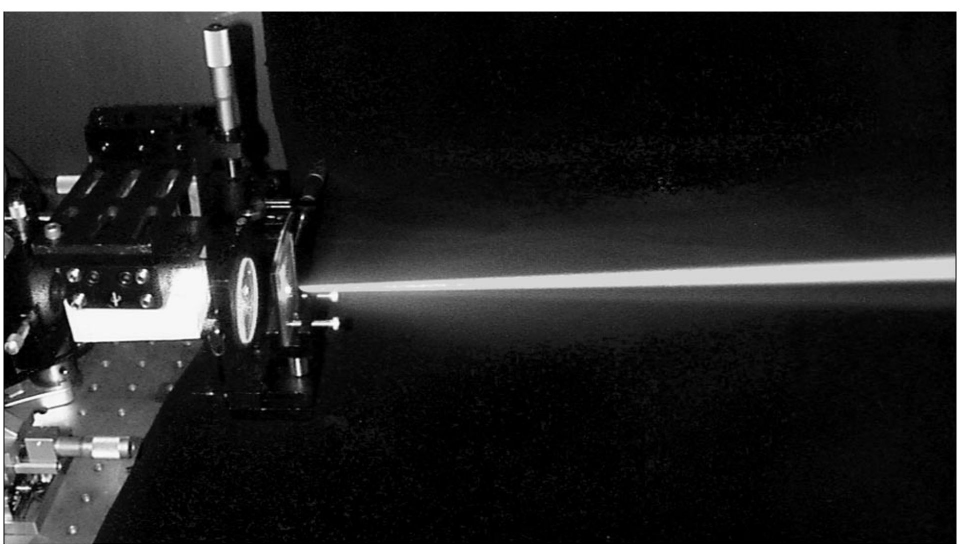

Orange light beam emerging from a crystal of periodically poled lithium niobate used for sum-frequency mixing of solid-state laser beams at 1.0- and 1.3-μm wavelengths.

Laser-Driven Radiography

M. D. Perry, M. H. Key, J. A. Sefcik, T. E. Cowan, C. Sangster, M. Singh, R. Snavely, M. Stoyer, E. Henry, T. Phillips

98-ERD-079

Emission of MeV x rays is efficiently produced by bremsstrahlung of relativistic electrons in high-*Z* targets. X-rays of photon energy from 2 to 6 MeV are required for dynamic radiography of dense objects in the Stockpile Stewardship Program. Pulsed relativistic electron beam machines generating multi-kilojoule pulses of electrons of about 15 MeV are presently used for this purpose. Improved systems are in the planning stage.

When an intense laser pulse strikes a dense plasma target, it is efficiently absorbed and its power is transferred to forward-directed relativistic electrons. Although the details of this interaction are quite complex, theoretical modeling suggests that multi-petawatt (PW) lasers generating multi-kilojoule pulses focused to 10^{21} W/cm^{-2} could produce a quasi-Maxwellian electron source of 10-MeV mean energy. This offers an advanced conceptual alternative for dynamic radiography with many potential advantages. The key question is whether sufficient x-ray brightness can be achieved. Investigation of the viability of this application was the purpose of this project.

Experimental effort was concentrated on quantitative characterization of the laser-produced electron and x-ray sources. Control of the PW laser wavefront using adaptive optics was implemented in FY98 and gave peak intensity in vacuum up to 3×10^{20} W/cm^{-2} for 1-PW power in 0.5-ps pulses.

Electron energies up to 100 MeV were observed by magnetic electron spectrometers, and the angular pattern was forward peaked. Positrons from pair production from bremsstrahlung in 1-mm-thick Au targets were also seen at the theoretically predicted flux level relative to the electrons. The quasi-Maxwellian slope temperature of the electrons for energies >10-MeV energy was in the range of 5 to 10 MeV. The spectrum, angular pattern and absolute intensity of x rays were determined for irradiation of 1-mm-thick solid Au-targets, which modeling showed were close to optimized converters. The spectrum from 0.2 to 10 MeV was obtained from thermoluminescent dosimeters (TLDs). Between 10 to 50 MeV, it was deduced from multiple orders of (γ xn) photonuclear processes which caused measurable nuclear activation of Au disks placed close to the target. The results showed a strongly nonthermal x-ray spectrum with a slope temperature of about 1.5 MeV at 2 MeV energy, rising steadily to more than 5 MeV at 20 MeV energy. The angular pattern of >1-MeV x-ray emission was recorded with an array of 96 TLDs. The emission pattern was in a ±60˚ cone with ±10˚ peaks, the latter not reproducible in direction. The maximum intensity of the source measured in this way reached a value of 2 rads at a distance of 1 m, in peaks of the angular pattern. Measurements of nuclear activation with an array of up to 20 Au disks showed, with less resolution, the angular pattern of the photons of about 15-MeV energy. This was broadly similar to the TLD patterns. High-quality radiographs were obtained through 170 g/cm^2 of Pb, as shown in the figure. Given further development to improve the collimation of the x-rays, combined with fast detectors that can utilize the rapid dose to improve the image contrast by gating out the scattered background radiation, this source potentially offers a new approach to time-resolved radiography.

An important issue in the research is the angular pattern of the electron source; work elsewhere suggests that better collimated electrons may be obtained with no preformed plasma. A limited data set will be obtained under these conditions to complement the PW data. Interpretation of the data will be assisted by collaboration with theorists at LLNL and others who will model the experiments using a variety of computational techniques.

Essential for the development of laser radiography and other applications of PW lasers, notably fast ignition, is development of diffraction-grating laser pulse compressors capable of multi-kilojoule energy. A 60-cm grating will be fabricated to give an energy-handling capability estimated at 4 kJ. This estimate will be validated by damage testing on smaller gratings. An engineering study will address the gravity induced deformation and consequent minimum thickness of gratings at this aperture and determine the related minimum pulse duration at full power.

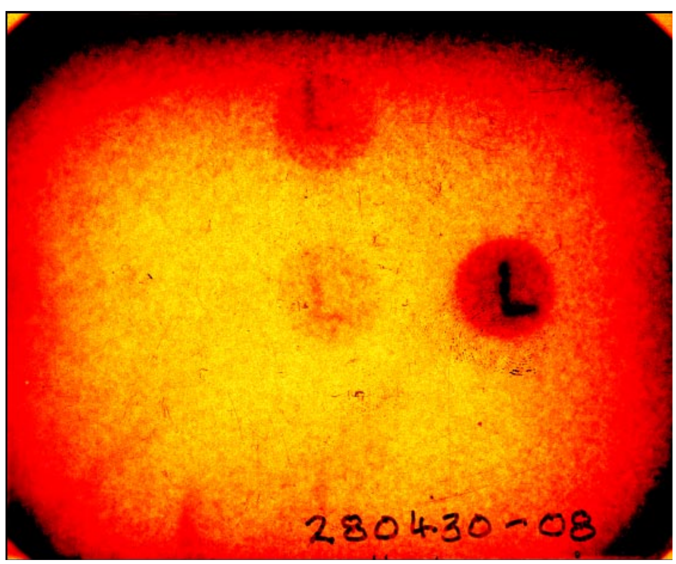

Radiograph of object through 150 mm (center), 120 mm (right) of Pb. The "L" feature is 1.2 mm in line width.

High Intensity Physics with a Table-Top 200-TW Laser System

T. Ditmire
98-ERD-084

Recent experiments at LLNL as well as at a number of facilities and universities around the world have demonstrated the utility of short pulse (<100 fs), very high peak power (>10^{12} W) lasers based on chirped pulse amplification (CPA) in several interesting applications. The development of CPA roughly 13 years ago has fueled a rapid increase in the focused laser light intensity that is accessible. This development has culminated in the Petawatt laser currently in operation at LLNL. The most important uses of these lasers have only recently come to light, however, and include such applications as the production of very-high-temperature, high density plasmas and the production of pulsed x-rays with pulse width below 1 ps. For example, ultra-high intensities focused on solid targets can produce MeV energy x-rays in sufficient quantities to potentially permit time-resolved radiography of hydrodynamic tests. Another application includes the creation of plasmas whose conditions are relevant to astrophysical studies.

The purpose of this project was to develop a high-peak-power laser system (100 TW) and begin initial high intensity experiments that exploit its short pulse width (30 fs) and high repetition rate (1–10 Hz). Such a laser system presents unique capabilities, such as permitting ultrafast time-resolved plasma physics experiments by probing the plasma with the 30-fs laser pulse. The high repetition rate also allows detailed, systematic studies of phenomena, not possible with large, single shot laser systems.

In FY98, we made good progress on the development of the laser. We have demonstrated the production of pulses up to 5 TW at 10 Hz and have installed an additional amplifier to take the system to 20 TW. We have pulse compressed the pulses to 30 fs and have developed several diagnostics to characterize the laser prepulse. During this year, we also activated a target chamber to begin plasma physics experiments in gas jet targets.

One of the first set of experiments we performed involved the study of radiative blast waves in a low density gas. Understanding such radiative blast waves is crucial to understanding the structure of the interstellar medium. To create a radiative blast wave we focused the 1-TW laser pulse into a clustering gas (such as argon or xenon) and created a high temperature plasma filament. Because of the low density of the gas and high temperature of the plasma created by the 30-fs laser, radiation transport is sufficiently strong to ionize the gas ahead of the shock and to affect the shock propagation. To probe this phenomenon, we conducted interferometry with a second 30-fs laser pulse, split from the main laser. Data from this experiment is shown in the figure. The ionization ahead of the sharp shock front is clearly visible in the xenon case. This represents the first radiative hydrodynamics experiment conducted with a table-top laser.

In FY99, we intend to further pursue these hydrodynamics experiments, including an examination of the effects of an external magnetic field to yield information on radiative magneto-hydrodynamics. The possibility of conducting fusion experiments with exploding deuterium clusters will be explored as well. We will also study a host of other high-intensity experiments, such as MeV photon production from laser accelerated electrons in solid target interactions, picosecond x-ray production via K-alpha generation in solid targets, and high-order harmonic generation in gas jets. Such experiments will hopefully lead the way toward the application of laser-plasma interactions to the development of a laser-based, next-generation light source.

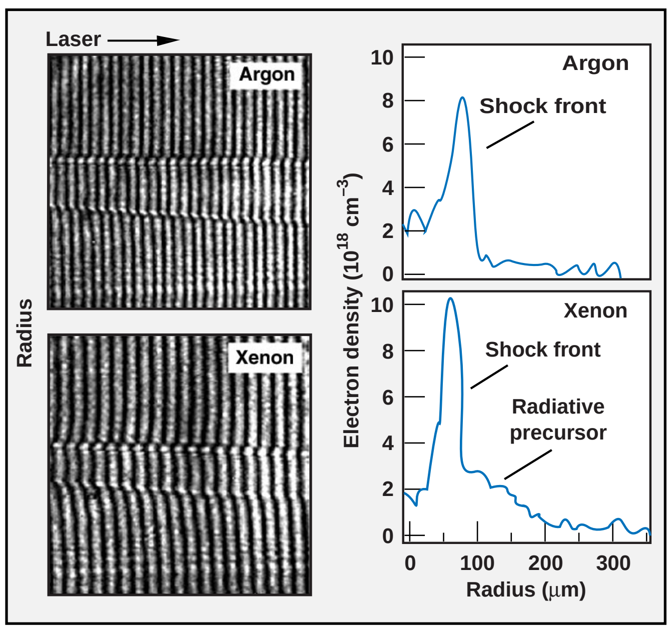

Interferograms (and deconvolution of electron density) of shock waves generated by a 1-TW pulse in argon and xenon gases. The high laser energy absorption by clusters in these gases forms a high temperature plasma and leads to the formation of a radiative precursor ahead of the main shock front.

Extreme States of Matter on Nova

B. A. Remington
98-ERI-009

Understanding the processes behind the propagation of strong shocks in solids under extreme compression is important to LLNL's stockpile stewardship program, the National Ignition Facility (NIF), and astrophysics. In this project, we have—in collaboration with the University of Oxford, the University of California, San Diego, and Los Alamos National Laboratory—developed experiments on the Nova laser at LLNL and the Trident laser at Los Alamos to investigate the dynamic response of solids to strong shocks.

The response of a solid-state material to shock loading is typically described by a constitutive model such as the Steinberg–Guinan model. This is a semi-empirical model that describes the material response using parameters that have been normalized against shock-wave measurements of the shear stress and yield stress. This model is an elastic–perfectly plastic model; that is, when a stress is applied to a sample, it responds elastically up to the point where the stress exceeds the yield stress. At that point, the sample yields to plastic flow.

However, the application of a semi-empirical constitutive model is speculative at the high strain rates that may be achieved with a laser-driven shock experiment. In reality, the material has a microscopic lattice structure that is not accounted for in such an empirical description. When the solid undergoes deformation at high pressure, stresses that occur at a lattice level result in the generation and subsequent propagation of mobile lattice dislocations. It is the rearrangement of the lattice structure by transport of these mobile dislocations that is the microscopic mechanism behind solid-state plastic flow. As a result, it is important to characterize the shock response of materials at high strain rates with a technique that probes the lattice structure itself.

To probe the lattice structure, in FY98 we developed a technique in which time-resolved x-ray Bragg diffraction was used to record the response of crystal lattices to the shock compression of solids. We applied this technique to shock experiments on Nova using a hohlraum x-ray drive and to experiments on Trident using direct laser illumination. We constructed experiments on the Nova laser in which single-crystal Si samples were shock-compressed using a hohlraum x-ray drive at pressures of 100 to 500 kbar. A cylindrical, gold hohlraum target was used to generate a Planckian soft–x-ray drive. The crystal sample was mounted over a hole in the side of the hohlraum at the midplane. The x rays in this cavity ablatively drove a shock into the crystal, which we diagnosed using time-resolved x-ray diffraction. The backlighter foil created x rays that were diffracted from the crystal and recorded with an x-ray streak camera.

We recorded an x-ray diffraction signal before and during the shock breakout at the back (free) surface of a Si crystal for (111) and (400) orientations for "low" (160 kbar) and "high" (500 kbar) shock strengths. The shocked (400) Si showed a double Bragg signal from the compressed lattice, suggesting that the crystal had potentially undergone a phase transition, that is, the transition from uniaxial (one dimensional) to hydrostatic (three dimensional) compression. We observed shifts in the diffraction peak that indicated a reduction in the lattice spacing of about 5 to 10% relative to the initial (111) Si lattice spacing. We also measured a streaked transmission-diffraction (Laue) signal off planes perpendicular to the Bragg planes.

By the end of FY98, we had begun comparing the time-resolved diffraction structure with post-processed simulations. Our model combines numerical simulations of the hydrodynamics with lattice-diffraction theory to predict the diffraction features observed in the experiment and also incorporates the strained-crystal rocking curves and Bragg diffraction efficiencies.

A Source for Quantum Control: Generation and Measurement of Attosecond Ultraviolet Light Pulses

K. C. Kulander
98-LW-013

This project has pursued the possibility of producing ultra-short pulses of coherent light using harmonic conversion of a mid-infrared (IR) light source, focused into an atomic gas medium. High-order harmonic generation (HHG) in noble gas media using short-pulse visible and near IR lasers has become an established method for producing coherent, short-pulse radiation at wavelengths from the ultraviolet to soft x-rays. We recently proposed that this approach could lead to extremely short pulses, potentially less than one fs, provided the unavoidable frequency chirp of the highest harmonics, could be removed by compressing the pulses with a grating pair. Sources of sub-fs pulses would provide unique opportunities to study dynamical processes on time scales short compared to those associated with nuclear motion; for example, truly stroboscopic pictures of chemical reaction dynamics would be possible. In this research project we have chosen much smaller driving frequencies than used previously in HHG studies (by a factor of 3 to 4) for two reasons. First, this will allow us to measure the pulse lengths of the compressed harmonics because they will be in the vacuum ultraviolet where coincidence measurements are possible. Second, the wavelengths of these harmonics will be ideal for pump-probe experiments of quantum dynamical control studies.

Our theoretical effort was concentrated in two areas. We used our time-dependent quantum numerical codes to evaluate the harmonic response of alkali atoms to the mid-IR laser excitation. Results were obtained for potassium, the initial species to be used in the experiments, then sodium and rubidium to investigate the possibility of higher conversion efficiencies. In fact, rubidium was found to be significantly better than potassium, both because it provided a stronger harmonic response and because the target gas could be maintained at about an order of magnitude higher pressure than with potassium. The second theoretical focus was the development of an adiabatic approximation for solving the equations governing the propagation of the generated harmonic fields through the laser-excited medium. A code was constructed using this approximation and the first phase matching calculations in this ultra-short pulse regime were carried out. Two papers have been written about this work, one published and a second soon to appear, both in *Physical Review A.*

Although the experimental effort was slowed by difficulties with the potassium source (which were solved), photoelectron and harmonic spectra were obtained, the first ever at these wavelengths. These preliminary experiments were carried out using a picosecond laser source and an estimate of the bandwidth of the harmonics was obtained. The spectral width indicated that our prediction that the harmonic pulse lengths can be two orders of magnitude shorter than the driving field appears probable. Soon the experiments will switch to a 100-fs driver, and the attempt to reach the sub-fs regime will then be possible. We found that potassium, the target in the initial studies, had a lower than expected conversion efficiency so that experiments were initiated using rubidium. This has proved to be better by more than three orders of magnitude. A large fraction of this improvement was due to the metal source running at a much higher pressure. A further increase will be obtained when the shorter pulse driver is installed. An additional paper on these preliminary results is now being prepared.

Although successful, the project is a bit behind schedule because of experimental problems. The theoretical predictions seem to have been corroborated by the measurements thus far. We also found some unexpected differences in the behavior of the different alkali atoms to mulitphoton excitation and ionization at these wavelengths.

This project was a joint effort with Louis DiMauro’s experimental group at Brookhaven National Laboratory and in collaboration with Ken Schafer from Louisiana State University and Mette Gaarde from Lund University on the theoretical aspects.

7

Manufacturing Processes and Technologies

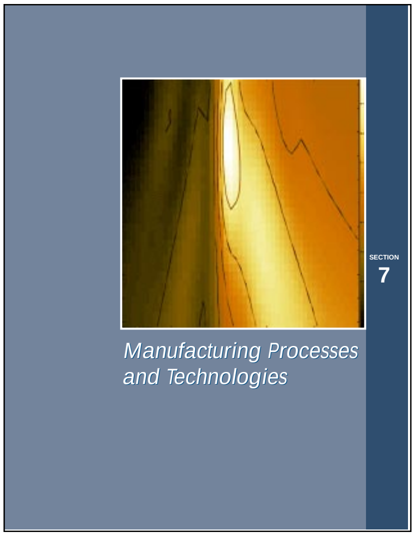

About the preceeding page

Techniques for Enhancing Application of Laser-Based Ultrasound to Nondestructive Testing. Graham Thomas and his team are investigating ways to increase the sensitivity of laser-based ultrasound, which offers many advantages over traditional piezoelectric-based ultrasound for the noncontact, nondestructive testing and characterization of materials and structures and for process control. The figure shows a colorized version of an enhanced, laser-based ultrasonic image of a flaw (a drilled hole) in an aluminum block. The experimentally obtained data were processed using matched-field processing. See page 7-5 for details.

Thin-Film Transistor Printing

D. Toet, T. W. Sigmon, M. O. Thompson, P. M. Smith
96-ERD-053

The fabrication of microelectronic devices by laser-induced material transfer is expected to have a fundamental impact on the field of semiconductor processing, because this procedure does not involve photolithography. Instead, the structures making up a device are directly "printed" onto the desired substrate with a high spatial selectivity, using pulsed laser irradiation of a target. Therefore, materials are deposited only on locations where they are actually needed, and the processing steps used in conventional manufacturing can be bypassed. This leads to significant reductions in the fabrication throughput, in materials waste, and in the use of hazardous materials. Moreover, the printing procedure is compatible with inexpensive, low-temperature substrates (glass, polymers) because its thermal budget is minimal.

During the first two years of this project, we developed a printing technique for silicon. This procedure, illustrated in Fig. 1(a), consists of irradiating the backside of a hydrogenated amorphous silicon (a-Si:H) film with an excimer laser. The ensuing transfer results from the explosive effusion of hydrogen as the a-Si:H film is melted. The transfer process is monitored in real time by transient optical measurements. Analysis of these experiments allowed us to develop a consistent model for the transfer mechanism.

In FY98, we took three decisive steps towards the realization of a fully printed device. The first step consisted of optimizing the quality of the transferred Si. The main challenges overcome here concerned the adherence, uniformity, and roughness of the transferred films. Our transfer process now enables us to consistently obtain well-adhering, uniform, polycrystalline Si films. Using atomic-force microscopy (AFM), we found that the initial roughness of the printed material can be drastically reduced by exposing it to a high-fluence excimer pulse. A 900-mJ/cm^2 pulse, for instance, resulted in a reduction of the mean roughness of a printed Si film from 570Å to 75Å. The second step consisted in fabricating thin-film transistors (TFTs) in the printed-and-smoothed material (using conventional lithography). The resulting devices show consistent switching behavior, with reasonable performance characteristics, ON/OFF ratios of 10^5, OFF-currents on the order of 1 pA, and mobilities of 0.1 cm^2/V • s. The successful fabrication of electronic devices demonstrates that our printed Si is now compatible with conventional semiconductor processing. Finally, we demonstrated the printing of Si and Al lines with widths of 5 to 15 mm—we used a reflective grating mask defined on the target substrate by photolithography prior to the a-Si:H deposition. The metal features were printed by depositing Al on the top of the a-Si:H reflective-mask stack. Upon laser exposure, the hydrogen pressure in the a-Si:H film resulted in the ejection of both the Si and the overlying Al. As shown in Fig. 1(b), the lines printed with this method are straight, show few discontinuities, and have sharply defined edges. The main challenge here was to keep the transferred material from spreading beyond the intended areas, which occurs if the separation between target and receptor and/or the transfer fluence is not carefully chosen. Systematic investigation of the dependence of the structure of the printed feature on the target/receptor separation and the transfer fluence allowed us to identify the optimal transfer regime.

We feel that we have made significant advances in our endeavor to fabricate electronic devices using the laser-induced transfer technique. Although we need to overcome several hurdles (e.g., optimization of the structure of the printed material), the feasibility of this objective now appears very realistic. We are presently planning further experiments aimed at improving our procedure; we are also investigating alternative methods, such as the transfer of entire structures.

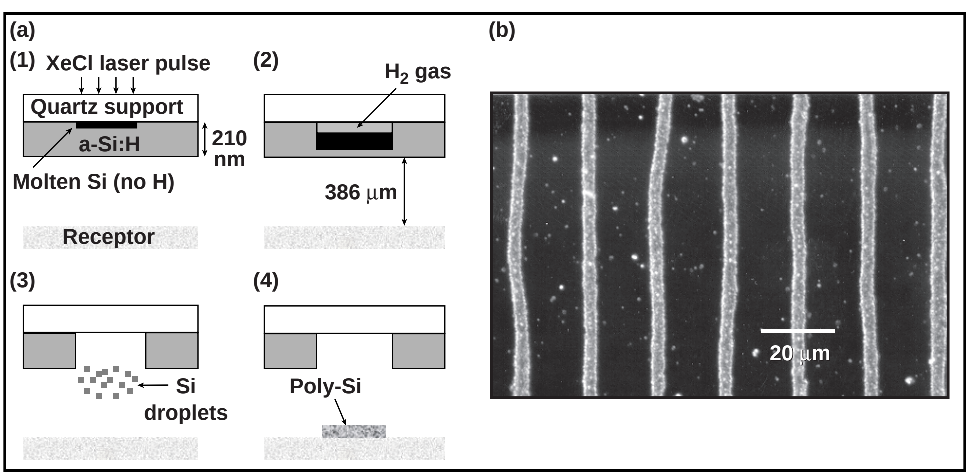

Figure 1. Progress in thin-film transistor printing. In (a), we show the H-assisted printing technique: (1) the exposure of an a-Si:H film through the quartz support leads to melting in the film; (2) hydrogen diffuses out of the molten Si to the film/support interface; (3) the pressure exerted by the accumulated H_2 induces the ejection of the film; and (4) the ejected droplets coalesce on the host substrate, resulting in a polycrystalline Si film. In (b), we show an example of laser transfer of patterned polycrystalline silicon lines (the line width is about 5 μm).

Improved Printed Circuit Board Fabrication through Etch Rate Control

M. P. Meltzer, J. F. Cooper
97-ERD-032

The goal of this LDRD project is to develop alternative approaches to the manufacture of printed circuit (PC) boards that offer significant environmental and cost advantages over present methods. In these approaches, we identify and control the factors that drive etch rates so that we can selectively etch certain parts of a PC board at reduced rates. This selective etching eliminates the need for lead-bearing etch-resist application, which is a typical operation in PC board fabrication. By eliminating these lead-bearing etch resist applications, we reduce the generation of lead waste and eliminate time-consuming and expensive manufacturing steps.

The focus of our FY98 work was to identify and exploit the parameters that most strongly govern copper etch rates. Toward this end, we fabricated a variety of electrodeposition cells that permitted rapid variation in copper plating parameters believed to affect the etch rate. These parameters included composition and temperature of the electroplating bath as well as electrical potential across the layer being deposited. This setup allows us to monitor the complex impedance of the copper electrode, which may be important for etching selectivity. Control of surface characteristics appears to have been neglected in prior attempts to increase etching selectivity. Such surface characteristics include (1) interfacial films, (2) anodic oxide barrier layers, and (3) viscous layers of hydrated oxides and concentrated salts. These films or surface conditions form during etching dissolution.

Another approach we are exploring is to co-deposit, with the copper, other metals that show enhanced resistance to etching. We are also designing bimetal deposition systems that allow either of two metals to be selectively deposited out of the same bath through varying reduction potentials. This may be done by pulse deposition techniques that alter the potential of the deposition process by greatly changing the current density. We have verified that an extremely thin layer of a second metal on top of a copper deposit will reduce etch rates by at least an order of magnitude. This result is environmentally beneficial, because of the other metal's low toxicity relative to lead. The successful implementation of a bimetal, selective deposition bath will also have significant advantages by eliminating the need for separate etch resist deposition and stripping operations and by allowing more PC board production per unit of time.

Finally, we have examined the effect of surface morphology on copper etch rates. Roughened surfaces present more surface area to the etchant and have been demonstrated much faster.

A recently finished and related project with the Environmental Sciences and Engineering Department of the University of California, Los Angeles, examined the cost and pollution prevention benefits resulting from implementation of the differential etch process on industry production lines. The study indicated that the differential etch approach can reduce wastes as well as be profitable. Though some savings would be realized from reduced waste management costs, the greatest financial gains would typically come from the added daily production resulting from a shorter, more efficient manufacturing process.

Our main focus for FY99 will be to develop the differential etch process as fully as possible and to implement it in LLNL's printed wiring board line. Particular attention will be given to development of bimetal baths that allow selective deposition of either metal.

Radiation Hardening of CMOS Microelectronics

T. W. Sigmon, A. M. McCarthy

97-ERD-066

The goal of this project is to demonstrate a technology that permits the use of state-of-the-art silicon electronics in weapon systems subject to radiation-intense environments. Heretofore, there have been no reasonable schemes—methods that have not required costly process or redesigning—for hardening commercial, state-of-the-art, digital microelectronics to meet this requirement for weapon surety. Using a novel methodology developed at LLNL—silicon transfer to arbitrary substrate (START)—we are developing a process for manufacturing radiation-hardened, complementary metal-oxide semiconductors (CMOSs); test structures; and simple circuits.

In FY98, we made significant progress toward implementing novel uses of integrated circuit (IC) technologies for weapon surety. To demonstrate the decreased radiation sensitivity of CMOS technology, we fabricated circuits and devices and, using the START methodology, transferred them to glass substrates. Our improvements to this transfer technology have resulted in the development of processes amenable to manufacturing.

LLNL's silicon-transfer technology forms thin-film silicon microelectronics on almost any material—metal, glass, plastic, etc. The transfer is achieved by bonding a fully fabricated silicon wafer of microelectronics, circuit-side down, on a holding substrate and removing most of the wafer—silicon is left only in the transistor-device areas. In FY98, by improving the transfer methodology and through collaborations with SEZ America Inc., Sandia National Laboratories (SNL), and the University of California, Berkeley, on experiments to perform radiation tests on transferred circuits, we continued to extend the technology to render standard circuits insensitive to radiation.

We have addressed issues relating to manufacturing thin-film silicon microelectronics by adopting a new approach to silicon bonding and thinning. To ensure optimum silicon removal (to within 5 μm of the device surface), we have emphasized treating the back side of the silicon wafer with chemicals prior to etching—this smoothes the surface in preparation for an extended etch. An example of a bonded and thinned silicon wafer containing circuits and devices is shown in the figure. At the top of the photograph is a view through a glass substrate to which a silicon wafer is bonded. The aluminum-metal interconnections of the circuits and devices are plainly visible. The reverse view below shows the same metal interconnections visible through the remaining 3.5 μm of silicon.

In FY99, SNL will provide LLNL with circuits and devices fabricated on their 6-in., radiation-hard, CMOS, silicon integrated-circuit fabrication line. LLNL will, using the START methodology, transfer these samples; SNL will then perform radiation testing to study the impact of the LLNL transfer technology on improving the radiation insensitivity of these circuits.

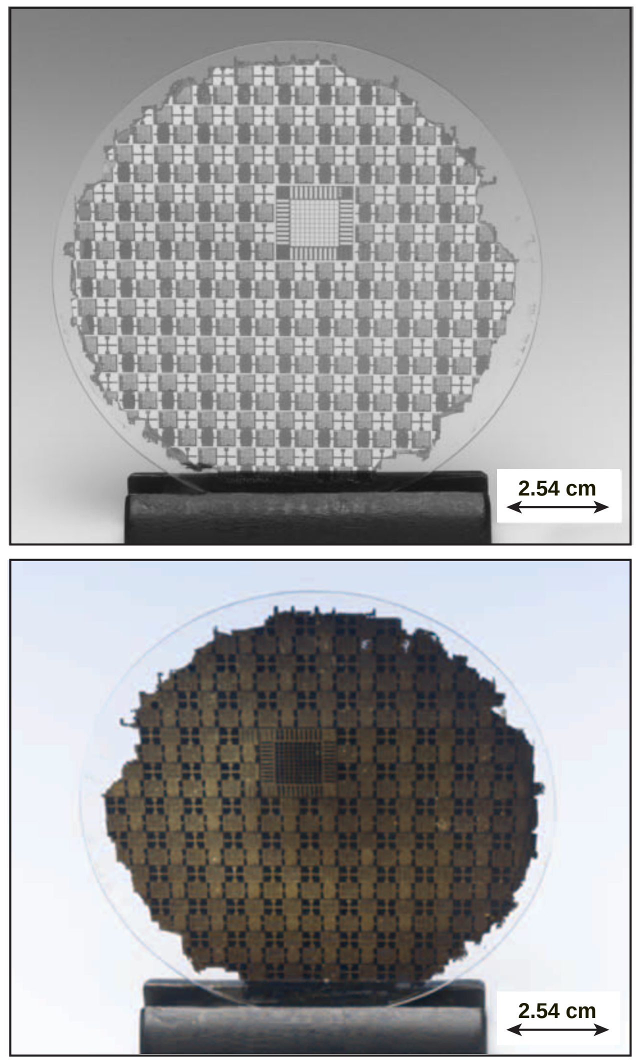

Views of a silicon wafer bonded to a glass substrate using LLNL's silicon-transfer technology and then thinned: (top) view through the glass substrate—the interconnections of the circuits and devices are plainly visible; and (bottom) a reverse view—the interconnections are visible through the remaining 3.5 μm of silicon. The process achieves silicon microelectronics that are less sensitive to radiation.

High-Density Arrays of Micromirrors

J. A. Folta, J. Y. Decker, J. Kolman, C. Lee, J. M. Brase
97-ERD-078

We have been exploring designs for high-spatial-density micromirror arrays (MMAs) for use in maskless lithography, pattern generation of photolithographic masks, and adaptive optics (AO) for imaging and laser-beam control. In particular, MMAs offer a potentially high-payoff application to maskless lithography, which would require MMAs with tiny pixels capable of precise and small displacements (~90 nm).

In FY97, we selected a scalable MMA design that called for a highly compressible material sandwiched between two electrodes. Aerogels, which potentially satisfy the modulus requirement (on the order of a few hundredths of MPa), cannot be successfully and economically processed into the required thin films. Therefore, we investigated commercial elastomers as the compressible material for our device. However, at issue was whether elastomer films can be processed into uniform, thin films. Commercial elastomers are typically formulated for use as bulk samples or thick films (>70 µm thick).

In FY98, we established and achieved our goal to (1) fabricate and evaluate test structures based on the FY97 optimized micromirror design, (2) perform system analysis and code development for our MMA concept, and (3) identify specifications for MMAs for LLNL's AO applications and conceptualize new devices.

We successfully developed the fabrication process for producing thin, uniform elastomer films with commercial elastomers. We also developed a process for coating the elastomer films with other thin films as the top electrode. For both the bare and coated films, we achieved surface roughness of less than 10-nm root mean square (rms).

The second issue in using elastomers for MMAs was reduction of the elastomer bulk modulus. We identified a highly elastic material with a nearly negligible amount of hysteresis and a measured bulk modulus of 0.5 MPa. Although extremely low for elastomers, the modulus is still an order of magnitude higher than desired. Prototype devices made with this elastomer produced lower displacements than required even for a 100-V applied voltage. We carried out an experiment for evaluating and reducing the bulk modulus of patterned elastomer films. We also developed a process for patterning the elastomer films. At year end, we were evaluating the bulk moduli of these patterned films.

During FY98, we developed an algorithm for designing input signals for a lithography system. The input signal can represent various types of static masks or spatial light modulators (i.e., our MMAs). The forward model (propagating light from the mask to the wafer) employed by the algorithm describes the full optical system: source condenser, mask or MMA, projection optics, and photoresist. Our algorithm also works in the reverse direction (i.e., it constructs an input signal that yields the desired printed pattern) by evaluating the quality of the pattern and iteratively adjusting the input. Our techniques for speeding up the calculations and extending the model allow practical-sized problems to be solved with no reduction in quality. Extensions to the model consider arbitrary complex objects and constraints that allow portions of the input signal to be fixed. The constraints may be useful for modeling defects in multilayer masks.

For wavefront control, advanced AO systems require a deformable mirror with extended high spatial and temporal bandwidths and low cost. No commercially available deformable mirrors meet LLNL's requirements. In FY98, we investigated three new MMA designs that could be used as deformable mirrors for AO applications. Unlike maskless lithography, where we require MMAs with small pixels and small displacements, deformable mirrors for AO require MMAs with large pixels (~100 µm) and larger (up to 10 µm) displacement. The new designs were chosen for their potential to provide 10-µm displacement over large arrays. All designs (1) offer operation at high spatial and temporal frequencies—proper design and coating of the micromirror surfaces would extend operation to high-intensity illumination; (2) are based on electrostatic, magnetic, and piezoelectric actuation; and (3) leverage LLNL's extensive capabilities in microfabrication and microelectromechanical (MEM) devices. Our preliminary finite-element analysis of the actuation forces required for correcting a typical wavefront with high-spatial-frequency aberrations indicated that reasonable forces (tens of µN) are required for actuating the individual mirror pixels. We are analyzing the feasibility of these new designs for AO applications in FY99.

Techniques for Enhancing Application of Laser-Based Ultrasound to Nondestructive Testing

G. H. Thomas, R. D. Huber, J. V. Candy, D. J. Chinn, J. B. Spicer
97-ERD-083

Laser-based ultrasound offers many advantages over traditional piezoelectric-based ultrasound for noncontact, nondestructive testing, characterization of materials and structures, and process control. For example, whereas piezoelectric transducers require couplants between the transducers and the object (e.g., the object must be placed in a tank of water), laser-based ultrasound does not require a coupling medium to get the acoustic energy to and from the test object. Thus, because it is undesirable to use couplants on many objects (or to place the objects in a tank filled with water), laser-based ultrasound may be a viable alternative for many applications. For example, its noncontact and remote-sensing capabilities make laser-based ultrasound of interest during work with hazardous materials (e.g., radioactive materials or objects at elevated temperatures) or in hostile environments. In addition, because only laser beams touch the object being investigated (there is no mechanical loading of the object), the ultrasonic equipment does not affect the ultrasound propagating through the part. However, despite the tremendous advantages of laser-based ultrasound over more traditional piezoelectric-based ultrasound, the overall lower sensitivity of laser-based ultrasound greatly limits its use.

We are studying ways to increase the sensitivity of laser-based ultrasound. Last year, we applied various signal-processing techniques that improved the signal-to-noise ratios of the experimentally obtained, laser-based ultrasonic data. Further processing of these data to form images has allowed us to develop techniques to locate flaws from laser-based ultrasonic data.

In FY98, we improved sensitivity and defect detection through matched-field imaging of the laser-based ultrasonic signals. Matched-field imaging is a signal-processing technique that uses a novel correlation-canceling approach to locate flaws in parts. It works by comparing laser-based ultrasonic data obtained from a real part to data obtained from a flawless reference. The choice of an appropriate reference part is extremely important. Through this processing, information that is the same in the two sets of data is eliminated. What is left represents any flaws that are present.

Simulations obtained with a theoretical model of an aluminum block with a hole in it showed the feasibility of this method and guided the experimental demonstration. Our experimental method involves generating ultrasound in one location with a pulsed laser, and then using a simulated array of interferometers to detect the ultrasound at numerous detection sites. The source location is then moved, and the ultrasound is again detected by the simulated array of detectors. By gathering information from numerous locations, we increase the effective detection ability of laser ultrasonics.

Initial results using this technique—obtained on a part with a single flaw—are promising; we plan further studies using parts containing several flaws. An image of a flaw as produced by matched-field imaging is shown in the figure. First, reference data were obtained on an aluminum block; then, a flaw (a drilled hole) was introduced into the same part. The figure that is derived from an array technique displays the hole, whereas traditional single-point generation and detection of the ultrasonic energy does not sense the hole.

This technique could also be used to monitor degradation of parts by comparing initial data obtained from a part to subsequently obtained data.

The signal and image processing techniques developed for this project, coupled with the equipment now available in the laser ultrasonic laboratory at LLNL, are helping to make laser-based ultrasound a more widely applied technique.

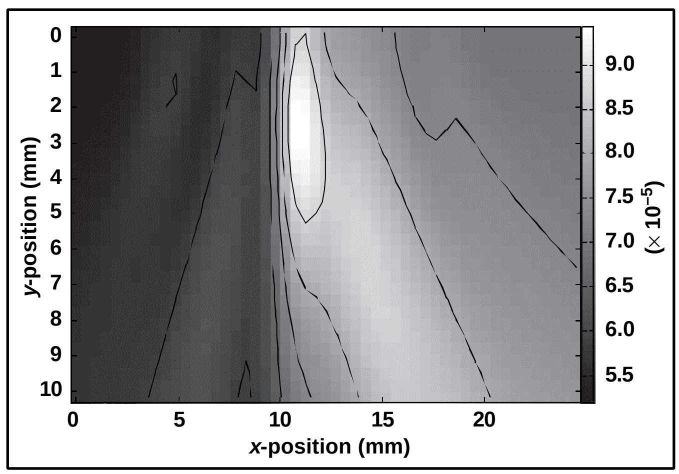

Enhanced, laser-based ultrasonic image of a drill hole in an aluminum block. The experimentally obtained data were processed using matched-field imaging. The hole is clearly displayed near the top of the image.

A Spatial-Frequency-Domain Approach to Designing Precision Machine Tools

D. A. Krulewich
97-ERD-084

The aim of this project is to develop an error budgeting methodology for designing machines used to manufacture parts with spatial-frequency-based specifications, thus reducing risk while maintaining accuracy. Increased precision in manufacturing is demanded by LLNL programs in areas ranging from National Ignition Facility (NIF) optics manufacturing and inertial confinement fusion (ICF) target positioning to the production and alignment of optics for extreme ultraviolet (EUV) lithography.

Recently, many of the component tolerances have been specified in terms of the spatial frequency content of residual errors on the surface. During the design of a new machine tool, we use an error budget as a sensitivity analysis tool to ensure that the parts manufactured by this machine will meet the specified component tolerances. Error budgets provide the formalism whereby we account for all sources of uncertainty in a process; we sum the uncertainties to arrive at a net prediction of how "precisely" a manufactured component can meet a target specification. Using the error budget, we are able to minimize risk during the design stage by ensuring that the machine will produce components that meet specifications before the machine is actually built. Minimizing the risk while maintaining accuracy is a key manufacturing goal for programs that cannot tolerate yield factors less than 100%, such as in fabricating components for the nuclear weapons program.

However, the current error budgeting procedure provides no formal mechanism for designing machines to produce parts with spatial-frequency-based specifications. Current efforts to embrace the frequency aspects of error budgeting typically divide the frequency spectrum into a small number of bins (e.g., figure, ripple, and finish), and then perform an error budget summation within each of those bins. This may be acceptable when the manufacturing specifications can be simplified into two or three frequency bins. However, recent specifications are being posed in terms of the continuous spatial frequency spectrum of the surface errors on the machined part. Based on these requirements, it is no longer acceptable to specify tolerances in terms of a single number that spans all temporal and spatial frequencies.

The error budgeting procedure consists of six steps: (1) identify the physical error sources, (2) determine how the errors couple to the machine, (3) transform the errors into the frequency domain, (4) combine the errors in the frequency domain, (5) consider the material removal transfer function, and (6) map the errors to the part coordinate system. During FY97 and FY98, we identified the physical error sources and determined the coupling mechanism for a diamond turning operation. We transformed these errors into the spatial frequency domain by acquiring the error measurements with appropriate sampling rates and anti-aliasing filters, then performing a Fast Fourier Transform to the data. The Fast Fourier Transform is a rapid algorithm that transforms time domain signals into the frequency domain. We developed a generalized combinatorial algorithm to sum errors in the frequency domain with its foundations in the statistical nature of the process. With this combinatorial algorithm, we have the ability to place confidence intervals about the error budget prediction.

We determined a simplified relationship for the material removal transfer function. The material removal transfer function predicts the frequency content of the forces induced by the material removal process given the frequency content of the instantaneous depth of cut, feed rate, and other cutting parameters. The structure then responds to these forces with cutting-induced errors. Finally, we determined a procedure to map the errors into the part coordinate system through a sample and filter routine. Given the frequency content of the error motion of the tool during cutting, we must take into consideration the path of the tool and the tool geometry to determine the frequency content of the residual surface errors on the workpiece. This sample and convolution procedure maps the errors into the part coordinate system. We have put this entire procedure together to predict the spatial-frequency content of errors along a radial trace of the machined part and verified this procedure through software simulation.

We are performing experimentation and validation of each step in the error budgeting procedure on a T-based lathe. We will compare the error budget prediction of the spatial-frequency content of errors along a radial trace to measurements of the actual machined part. During experimentation and validation, we have been able to measure the contributing errors. However, during the design process, we will not have this luxury. Therefore, we must relate the physical properties of the machine to the general types of errors that are created.

During FY99 we will relate the physical properties of general machine components to the frequency content of errors that are associated with these types of systems. We will also study the non-linear behavior and higher order terms of the material removal transfer function.

Materials Processing using Short-Pulse Lasers

B. C. Stuart, P. S. Banks, M. D. Feit, A. M. Rubenchik, M. Shirk, A. Komashko, M. D. Perry
98-ERD-068

The use of femtosecond-pulse lasers allows materials processing with extremely high precision and minimal collateral damage. Advantages over conventional laser machining (using pulses longer than a few picoseconds) are realized by depositing the laser energy into the electrons of the material on a time scale that is short compared to the transfer time of this energy to the bulk of the material. This results in increased ablation efficiency and negligible shock or thermal stress. Numerous applications, ranging from industrial processes to Stockpile Stewardship issues, can be achieved with this new machining technology.

Our goal in this project was to develop a better understanding, via experiments and computations, of using short-pulse lasers for the ablation and machining of materials.

During FY98, we improved our computational model of the interaction between intense laser pulses and metals by including electromagnetic-wave propagation within the radiation hydrodynamic code Hyades. This addition allows a self-consistent description of laser absorption in the expanding plasma that is independent of arbitrary assumptions regarding the plasma distribution where the laser energy is absorbed. In particular, plasma resonance absorption is automatically included along with inverse-Bremstrahlung absorption.

Because material removal by a femtosecond-pulse laser occurs on time scales very long compared to typical ultra-short-pulse lengths of 1 ps or less, an estimate of the ultimate amount of material removed must be based on numerical simulations over much shorter times. We studied two measures: (1) the time-integrated mass flux through a plane just outside the initial surface, and (2) the zero-mass velocity point inside the initial surface at “long” times. The zero-mass velocity point appears to be a better measure, at least for metals where long-time evaporation is less significant than in the case of insulators.

We carried out numerical estimates of energy-absorption and material-removal efficiencies as functions of laser polarization, fluence, and pulse duration. These theoretical studies predicted that an optimally timed prepulse (5 to 10 ps before the main pulse) would enhance laser-energy coupling to the material because it would create a plasma with a scale length that promoted resonance absorption of the main pulse.

We then experimentally measured the effect of a prepulse on machining rate and quality. High-average-power laser systems that are used in short-pulse materials processing typically include a regenerative amplifier, which can produce prepulses both from leakage at each round trip and from spectral modulation. Depending on the mechanism, the separation between the prepulse and the main pulse can range from less than 1 ps to more than 10 ns. With sufficient intensity, the prepulse forms a plasma before the arrival of the main pulse. In contrast to our calculations, our experiments showed that the presence of a prepulse was always detrimental to the machining process. Both holes and lines were machined using linear and circular polarization. The peak of the effect occurred when the prepulse arrived 0.5 to 1 ns before the main pulse; then, drilling times increased by over a factor of ten (depending on fluence and depth), and the hole’s morphology was random and indicative of melting. Knowledge of these effects will be invaluable in designing new short-pulse-laser machining systems.

We investigated numerous methods for drilling round and shaped holes in metals with steeper side walls, namely, phase plates, amplitude imaging, rotating wedge, rotating linear polarization, and variations in laser fluence and pulse duration. We achieved substantial improvement in hole quality and also found a way to reduce damage to a second substrate (behind the laser-drilled hole).

To measure the expansion of the plasma away from the sample surface, we activated two new plasma diagnostics. An interferometer on a variable time-delayed line (up to 10 ns) was set up to probe the expansion over short time scales. We also used a gated imager (2-ns gate) to watch the plasma expansion over longer times.

These diagnostics can be used to correlate the plasma velocity (temperature) and spatial distribution of the plasma expansion with the laser-processing parameters (intensity, fluence, cut-depth and shape, etc.). If spectral dispersion is added, the atomic and ionic species present in the plasma can be investigated.

High-Precision, Droplet-Based Net-Form Manufacturing of Advanced Materials

A.B. Shapiro
98-ERD-085

In collaboration with the University of California, Irvine (UCI), we are working on a new technology that relies on the precise deposition of nanoliter molten-metal droplets that are targeted onto a substrate by electrostatic charging and deflection. This way, three-dimensional (3D) structural materials can be manufactured microlayer by microlayer. UCI is responsible for an experimental investigation of the manufacturing feasibility of this process. LLNL has unique expertise in the computational modeling of 3D heat transfer and solid mechanics and has the large-scale computer resources necessary to model this large system. Applications at LLNL include rapid prototyping of metal parts and manufacturing new alloys by co-jetting different metals. In addition, success would mean that we could manufacture hybrid microelectromechanical systems (MEMS) by fabricating 3D structures on etched substrates.

Parts manufactured at UCI from 190-µm-diam solder droplets are shown in the figure. Because the droplets have small volumes, they rapidly solidify on impact, bringing forth a material component with the fine grain structures that lead to enhanced material strength. Rapid solidification also leads to high geometric fidelity because there is no macroscopic fluid flow of the deposited droplets.

To successfully apply our research to a technology suitable for industrial use, it is critical to understand the droplet-to-droplet and droplet-to-substrate mechanical and thermal interactions. That is, we must understand the transient thermal behavior of a droplet during time of flight, the mechanical deformation and solidification of a droplet on impact with a substrate, the deformation and thermal interaction of an incoming partially liquid droplet with the previously deposited and solidified material, and how the microstructure is formed.

Our collaborative approach is both experimental and numerical: we are using the modeling effort at LLNL to guide the experiments at UCI, and experimental studies at UCI are being used to corroborate the predictions of our numerical models. In FY98, we modeled the liquid-metal splatting on a substrate with DYNA3D, a Langrangian solid-mechanics finite-element code, and ALE3D, an arbitrary Langrangian-Eulerian code. The Eulerian part of ALE3D was better able to model the very large deformation and flow of the liquid metal on impact with the substrate. However, neither code successfully matched data in the literature. In FY99, we will investigate the problem area, namely, the requirement for a constitutive model that can better represent the reduced strength at high temperature of the just-solidified metal.

During FY98, UCI began moving the technology forward from using solder droplets to more interesting materials with higher melting points. A new facility came online in August 1998. By the end of the year, metallurgical investigations of a variety of metals will be completed. Early tensile tests were promising: with measured yield stresses greater than both the yield stress for the starting metal ingot and published handbook values

In FY99, UCI will reduce the oxides and porosity by fabricating the parts in a vacuum or inert-gas environment, while we continue to improve our modeling capability to help define the process parameters for manufacturing a quality part.

Examples of successful net-form manufacturing using 200-mm solder droplets. These axisymmetrical parts were fabricated in a prototype facility at the University of California, Irvine.

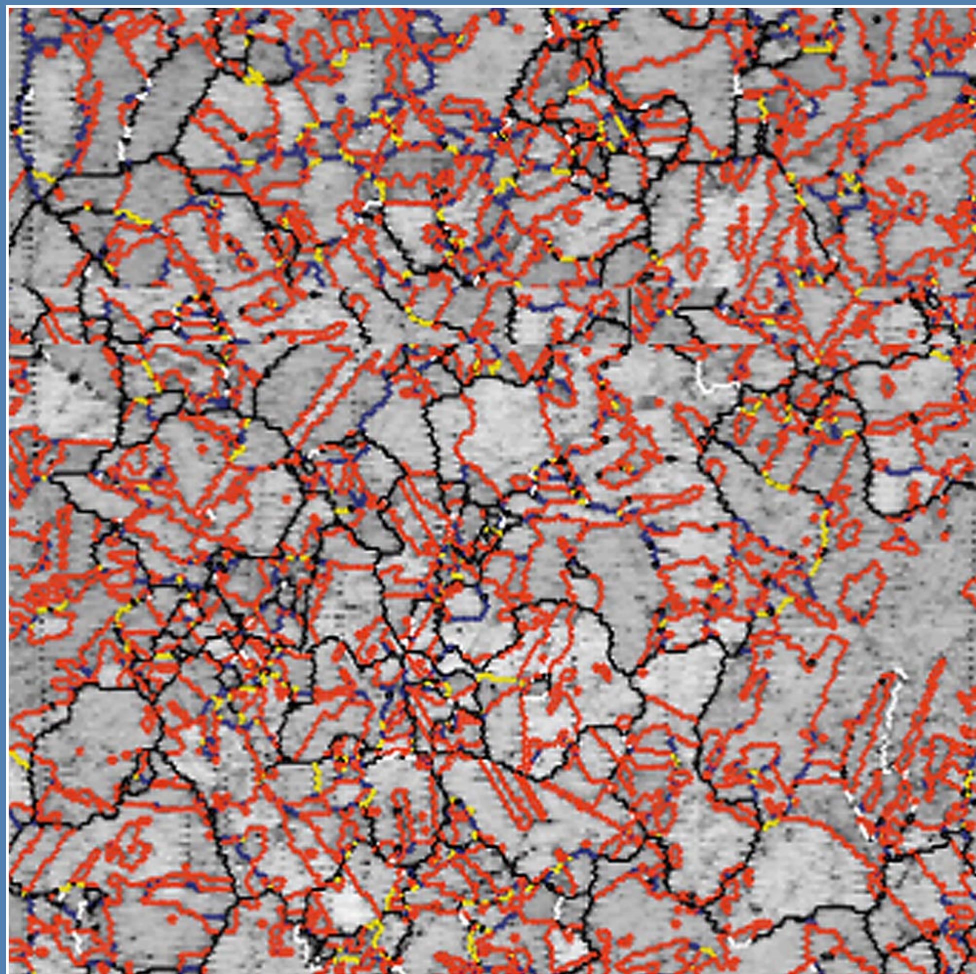

Materials Synthesis and Characterization

8

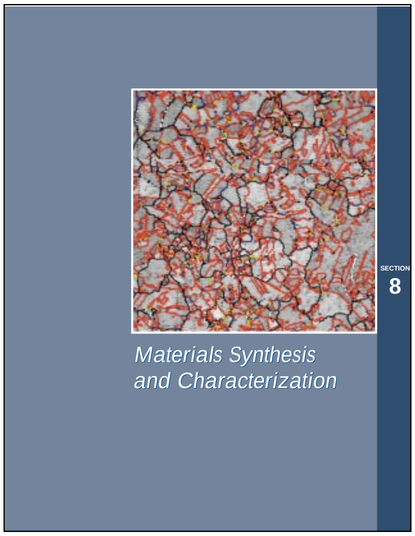

About the preceeding page

Research on the Potential to Engineer Grain Boundaries through Thermomechanical Processing. The principal technical challenge for Adam Schwartz and his team is to develop methods to systematically alter the grain boundaries in a polycrystalline material to produce a range of test microstructures. They are probing the role that intercrystalline defects, grain boundaries, have in the high-rate deformation and failure of polycrystalline metals. The image shows orientation imaging microscopy maps of strain-recrystallized oxygen-free electronic-Cu. For details, see page 8-19.

Exploration of Unconventional Properties of Ceramic Shaped-Charge Jets

D. Baum, J. B. Chase
97-ERD-005

A shaped-charge jet is produced when a piece of solid high explosive (HE) with a hollow formed in one side is detonated opposite the hollow. A jet useful for penetrating armor can be made by lining this hollow with metal. After detonation, the metal forms a long, solid rod moving with great speed. For our project, the lining of the conical cavity in the HE is a hollow cone of aluminum oxide instead of metal. This lining forms a coherent jet of very fine, rapidly moving ceramic particles that result in unusual target-penetration properties.

The original objectives of this project were to characterize this jet and predict its interaction with target materials. We planned to (1) use standard diagnostics to optically and radiographically “look” at the jet formation and compare the formation with computer models, (2) collect the jet particles and compare those to the ceramic liner’s microscopic structure, and (3) examine the jet’s penetration into a variety of targets. However, we found that most of the “standard” diagnostics (such as high-energy radiography and electrical shorting switches) did not provide useful data for these unusual jets. Therefore, we changed the objectives of this project so that in FY98 we would focus more on the means of gathering relevant data rather than on the data itself. We achieved some major successes.

Using an image-converter camera, we obtained stereo-pair images that showed that these powdered jets maintained a very high degree of coherence. Color framing cameras succeeded in following the jet through most of the formation period; computer models of the jet formation are remarkably similar to the framing-camera pictures. However, it is the flash–x-ray images that have been the most astounding. As reported last year, we had made several attempts to x ray these low-density jets. This process culminated in FY98 with very low x-ray–energy images that showed good contrast over the density range of the jet. This year, we analyzed these x-ray images to extract the spatial profile of the jet density. Figure 1(a) shows the x-ray film exposure; Fig. 1(b) shows the tomographically extracted alumina density. The most striking feature in Fig. 1(b) is the uniformity of the density across the diameter of the jet. More analysis is required to remove the apparent drop in density near the jet tail, which results from bad calibration of the film exposure density range.

Our principal discovery on this project was that the depths of penetration of the powdered jets did not scale as Bernoulli theory suggests (a principle adhered to by all-metal jets). The standard way of studying target penetration is with shorting switches placed at intervals in depth through the target material. We found that nonconductive jets do not close shorting switches; therefore, we obtained our data by measuring the hole depth after the shot. Not having the rate of penetration drastically reduces the information available. However, preliminary scaling for these powdered jets suggests that when the strength of the target material is less than the average impact pressure of the jet, Bernoulli scaling works. When the impact pressure is less than the strength of the target material, the penetration is greater than Bernoulli theory would suggest.

This research is just beginning—there is much yet to understand. However, very important strides have been made; that is, we (1) analyzed a first useful x-ray, (2) discovered some mysteries of target penetration, and (3) identified new diagnostic-technique shortcomings.

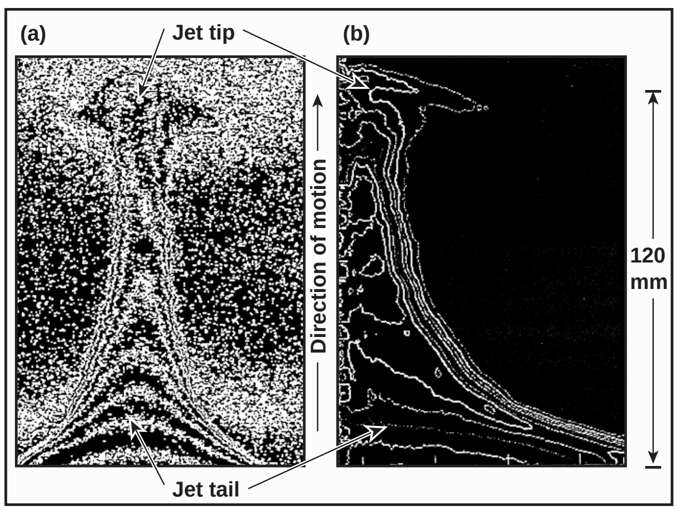

Figure 1. Studies of the density range of a penetrating, ceramic shaped-charge jet: (a) a contour plot of the x-ray film exposure density of the x-ray image of the jet, and (b) a contour plot of the alumina density extracted by tomographical analysis. In (b), only half the assumed axisymmetric jet is shown.

Defect Studies of Optical Materials using Near-Field Scanning Optical Microscopy and Spectroscopy

M. Yan, J. McWhirter, S. Oberheiman, T. Huser, W. Siekhaus, M. Kozlowski, J. De Yoreo
97-ERD-013

Defects and impurities are generally the key material properties governing the quality and lifetime of optical components. Progress in materials synthesis has advanced so that today, for high-power laser applications such as the National Ignition Facility (NIF), laser-induced damage is typically initiated at the site of submicrometer defects. Thus, developing tools for optical characterization at the submicrometer scale, such as near-field scanning optical microscopy (NSOM), is essential for investigating such defects and their correlation with laser damage.

We are using NSOM to detect the electric-field enhancement at small cracks and pits in the surface of fused silica and to demonstrate that electric-field enhancement is strongly correlated with damage initiation and growth.

During FY98, we used a fiber probe to detect the near-field evanescent wave produced by a laser beam that was totally internally reflected at the surface of the sample. By controlling the height of the probe relative to the surface of the sample, we found that the decay length of the evanescent wave was about 100 nm; this agrees with the calculations for our incident-beam geometry. The calculations also show that the intensity of the evanescent wave at a flat surface is four times the intensity of the incident light. Thus, because other processes (such as scattering and stray light) have cross sections less than unity, the evanescent wave is the dominant signal in our NSOM measurements. Therefore, NSOM's fiber tip directly probes the evanescent wave that is proportional to the intensity of the electric field at the surface of the sample.

Using this near-field evanescent wave, we found that (1) the electric field is enhanced near pits in the fused silica surface, and that it varies with the defect size and the polarization of the incident laser; (2) the local laser intensity at defect sites is enhanced by as much as a factor of three relative to sites where there is no defect; and (3) such field enhancement is not limited to surface defects, but is also produced by subsurface defects such as nodular defects in optical coatings and subsurface defects in fused silica.

Our measurement is the first direct experimental observation of electric-field enhancement near defects. This technique provides a nondestructive optical method to probe field enhancement at surface and subsurface defects in optical materials.

During FY98, we also correlated the electric-field enhancement with local laser damage. In Fig. 1, we show three pairs of topographic (a) and near-field evanescent-wave (b) images of a fused silica surface. The topography is obtained concomitantly with the NSOM image, using the atomic-force microscopy (AFM) signal of the fiber probe. The left-hand image pair shows regions of enhanced evanescent waves, which are correlated with the surface pits identified in the topographic image. In the middle pair of images, we show the result of a factor of 10 local intensity enhancement: laser-induced damage occurs at the location of high evanescent-wave intensity and also generates surface cracks. We continued to irradiate the same site with an additional laser pulse with sub-threshold fluence, and the right-hand image pair shows increased damage at the cracks generated by the previous laser irradiation. Note by comparing the right and middle image pairs that of the two image types (evanescent-wave vs. topographic), the evanescent-wave image is the better predictor of subsequent damage morphology.

In FY99, we will continue our investigation of defects on a submicrometer scale and correlate such defects with in situ laser damage. We will focus on (1) establishing the correlation between optical defects as observed by NSOM and laser damage, and (2) using the fluorescence capability of NSOM to investigate the local variation of impurities and contamination in potassium dihydrogen phosphate (KDP) crystals and fused silica.

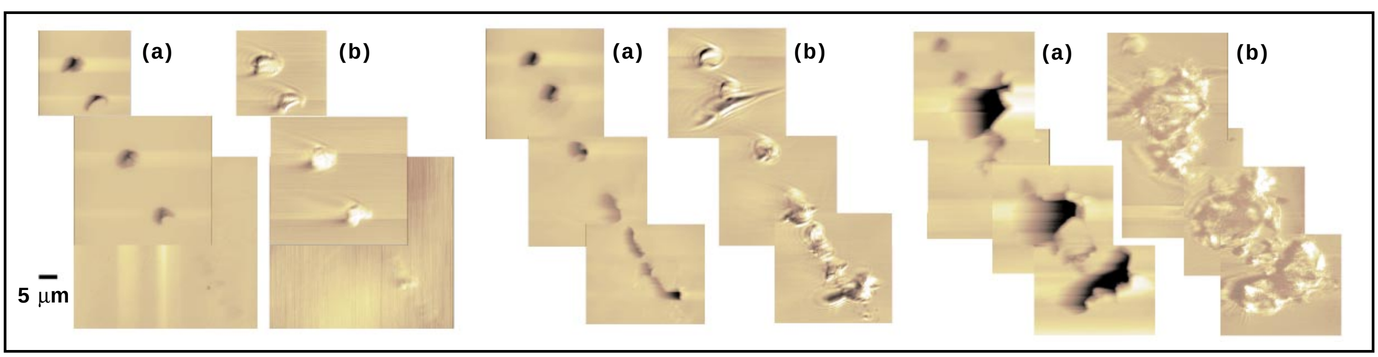

Figure 1. Atomic-force microscopy (AFM) topographic (a) and evanescent-wave (b) images of a fused-silica surface. The images are, left to right: prior to laser damage; after irradiation with a 355-nm, 7-ns laser pulse at a fluence near the damage threshold; and after an additional sub-threshold pulse.

High Performance Polyimide Coating Technology

S. A. Letts, C. C. Roberts, R. C. Cook
97-ERD-016

Polyimides form one of the few classes of plastics that have excellent thermoxidative stability, high mechanical strength, and superior resistance to chemicals. Process difficulties have limited the uses of these materials, although one relatively new polymer-fabrication technique—vapor deposition (VD)—has shown obvious potential for the microelectronics industry. Polyimides are traditionally synthesized from dianhydride and diamine monomers in a solvent. For example, Kapton results from the solution polymerization and thermal curing of pyromellitic dianhydride (PMDA) and 4,4'-oxydianiline (ODA). The stoichiometry of monomers determines the molecular weight of the resulting polymer, which inherently determines the tensile strength. Under optimum conditions, VD can be used to form conformal, solvent-free polymer coatings of controlled thickness.

One National Ignition Facility (NIF) target design calls for a 2-mm-diam capsule with an ablator that is about 160 µm thick. These capsules will be fielded at cryogenic temperatures with an 80-µm deuterium-tritium (DT) layer. At room temperature, the DT would produce a pressure of 360 atm, which corresponds to an internal tensile stress of 120 MPa. The current ablator materials do not have enough strength to hold this fill, and these capsules must always be handled at cryogenic temperatures. This process is both extremely expensive and limiting with respect to fielding options. Commercial polyimide films, such as Kapton and Upilex, have reported tensile strengths in the range of 230 to 420 MPa. Thus, this project was initiated to research high-strength capsule-fabrication techniques by (1) developing polyimide VD techniques and expertise, (2) demonstrating flat polyimide films with adequate properties for the National Ignition Facility (NIF), and (3) applying these techniques to shell-coating technology.

In our VD experiments, PMDA and ODA were codeposited by heating them in separate evaporators and directing the vapor fluxes down to a flat substrate or bounce pan. We calibrated the VD process by characterizing the evaporation and deposition rate of PMDA and ODA as a function of temperature. The evaporators were weighed before and after heating at a given temperature. From this data, we determined the molar-mass-loss rate for each monomer as a function of the reciprocal of temperature for PMDA and ODA. A quartz-crystal deposition-rate monitor determined the deposition rate as a function of evaporator temperature for each monomer, independently. Hence, we determined the stoichiometry as a function of monomer evaporator temperatures; using the molar-mass-loss ratio, one may infer a stoichiometry for a given VD experiment.

To optimize the strength of cured polyimide films, we deposited a number of coatings at various monomer molar-mass-loss ratios onto KBr-precoated glass substrates. Typical cured-polyimide films were 9- to 10-µm thick. We used infrared spectroscopy to confirm the chemical structure of the films.

In the figure, we compare the tensile strengths and the stoichiometry for a selection of VD polyimide films as calculated from the observed molar-mass loss of each monomer. The biaxial tensile strength of the films was measured using a film-burst apparatus; the tensile stress at burst was calculated using the measured differential pressure and the radial strain. For example, the strongest film was pressurized to 365 KPa and rose 0.89 mm from the initial horizontal position just before bursting. This film was 9.0 µm thick, and the calculated radius of curvature was 4.65 mm. Thus, the stress at burst for the strongest film was 94 MPa. Tensile stress at burst for our sample films varied from about 5 to 94 MPa. As expected, the strength of the films varied, in a qualitative sense, with the flux ratio of the monomers. The strongest films, which were vapor deposited closest to an equal molar ratio of PMDA and ODA, are close to the minimum strength specification for an NIF-quality capsule.

During FY98, we also successfully vapor-deposited films up to 80-mm-thick and recently began coating shells instead of flat substrates. In FY99, we plan to switch to another polyimide formulation, Upilex, that has a reported tensile strength of 400 MPa. Therefore, if by using our VD process we obtain a conservative 40% of the reported strength value, we will have a reasonable safety margin for a NIF target. In addition, future efforts will be focused on the deposition of thick films (50 to 200 µm) and coatings on spheres.

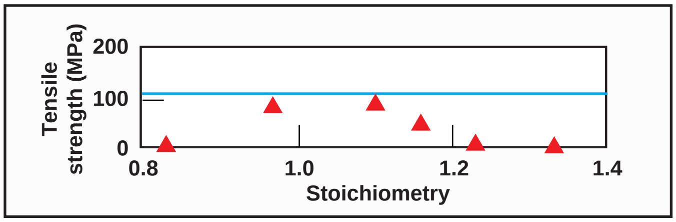

Tensile strengths vs. stoichiometry for vapor-deposited polyimide films containing various monomer ratios tested in this study. The tensile strengths of two of the films are close to the minimum strength (blue line) that is required by NIF targets. Note that (1) a correlation between stoichiometry and strength is observed, and (2) the films with stoichiometry of about 1.1 gave the best data.

Hydrogen at High Pressures and Temperatures

W. J. Nellis
97-ERD-055

Achieving a metallic state of hydrogen has been a major goal in condensed-matter physics ever since hydrogen was first solidified in 1899 and found to be an insulator at 1 atm rather than an alkali metal as expected. In 1935, Eugene Wigner predicted that solid hydrogen would become metallic at some sufficiently high but unknown pressure. Today, the metallic state of solid hydrogen has not yet been observed at pressures up to 3.4 million atm (3.4 Mbar) at room temperature.

It is important to reach the metallic state because hydrogen is the first element ($Z = 1$) in the Periodic Table of the Elements; thus, it is expected to be the simplest element to understand. However, because of its quantum-mechanical nature and the extreme difficulty in achieving a prediction made several decades ago, the exact opposite is true. A fundamental understanding of this supposedly simple material is not in hand, which raises the possibility that new phenomena might be found. Also, it is important to understand hydrogen because it is 90% of all atoms. For example, Jupiter and Saturn are mostly hydrogen. Therefore, to understand how and where the magnetic fields of these planets are generated, we must determine the electrical conductivity of hydrogen at high pressures and temperatures.

Possible scientific and technological uses of metastable solid metallic hydrogen—if the metallic state could be retained at ambient pressures and temperatures—include a dense fuel for higher-energy yields in inertial confinement fusion; a diatomic quantum metallic solid with novel physical properties, including room-temperature super-conductivity; a very lightweight structural material; a fuel, propellant, or explosive, depending on the rate of release of stored energy; and an aid in the synthesis of novel, hard materials.

The purpose of this project was to measure the electrical conductivity and equation of state of dense hydrogen at pressures of 0.5 to 3 Mbar and temperatures in the range of 1000 to 10,000 K. Of specific importance are the dependencies on pressure of the temperatures of metallization, melting, and the formation of the simple two-component plasma of protons and electrons. Determination of these phase lines would greatly advance the theory of dense hydrogen.

In FY96, we made the first observation of a metallic state of hydrogen, at 1.4 Mbar and 3000 K in the fluid state. Our laboratory is the only one in the world today that can perform these hydrogen experiments. We achieved these pressures and temperatures with a reverberating shock wave that was generated by impacting a projectile at velocities up to 7 km/s onto a cryogenic-sample holder containing liquid hydrogen at 20 K. The highest temperature achieved in hydrogen statically is only 500 K at 0.2 Mbar.

Because we were measuring electrical conductivities of hydrogen in a regime in which experiments had never before been performed, it is essential to measure conductivities of other materials to verify that different materials give different results. For this reason, in FY98 we measured electrical conductivities of water at pressures in the range 0.7 to 1.8 Mbar. Water was chosen because it is hydrogen-rich, and the electrical-charge carrier is the proton—which has a lower conductivity than the electron charge carriers in hydrogen. The experimental results (see figure) were as predicted: the measured conductivities for water have lower values and a different pressure dependence than those for hydrogen. These results with water show that our results with hydrogen results are, indeed, representative of hydrogen, and not of some other aspect of the experiment. During FY98, we also (1) refurbished and successfully tested our existing liquid-H_2 coolant system, which had become inoperable after 20 years of use—this refurbishment enables us to do hydrogen experiments starting from liquid density at 1 bar, as before; and (2) built a new cryogenic cooling system that uses the flow of cold helium gas to cool the sample holder and make a liquid-H_2 sample.

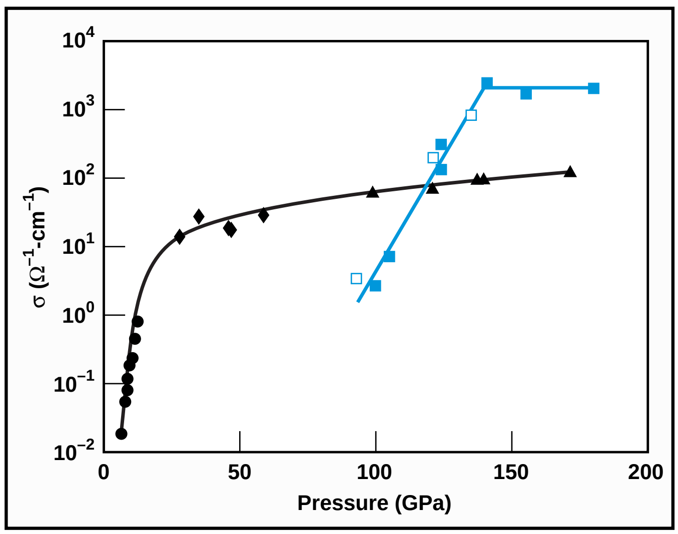

Electrical conductivities of hydrogen (D_2, open squares; H_2, solid squares) and water (blue triangles, this work; solid diamonds, Mitchell and Nellis, 1982; solid circles, David and Hamann, 1960).

Origins of Laser Damage in Crystals of KDP

J. J. De Yoreo, M. Yan, M. Staggs
97-ERD-098

The ability of optical materials to withstand high power ultraviolet (UV) laser irradiation without sustaining irrevocable damage is critically important in two areas central to LLNL: laser fusion and UV lithography. In particular, the output fluence of the National Ignition Facility (NIF) is limited by the laser damage thresholds at 351 nm of the potassium dideuterium phosphate or KH_2PO_4 (KDP) frequency conversion crystals. The ability to increase the laser output would increase the odds for successful achievement of ignition, allow target physicists to assess target performance at higher drives, and provide higher temperature-density conditions for studies of the physics of stellar interiors. Moreover, in order to meet the current design criteria for advanced fusion laser systems like NIF, crystals of KDP must be conditioned by illumination with low fluence laser irradiation, which increases the damage threshold by about a factor of two. Although existing studies indicate that damage is caused by extrinsic defects, little of the basic science needed to understand the process of damage or conditioning of KDP or the defects responsible for damage has been performed.

Our work to date has shown that there is no direct correlation between micron-size inclusions and laser-induced damage. In fact, damage almost always occurs in locations that contain no visible inclusions! In addition, we have shown that there is no direct correlation between the damage threshold and either overall high but homogeneous impurity levels or dislocations in the crystals. However, we find that damage is always accompanied by emission of visible radiation during and subsequent to the laser pulse. This emission decays with a time constant characteristic of electronic trapping states (~20 µs), and has a broad spectrum consistent with black body radiation from a hot electron plasma with a temperature of 10^3–10^4 K. Both Raman spectroscopy and photothermal deflection spectroscopy have demonstrated that these high temperatures are restricted to regions with diameters less than 100 nm. More careful analysis of the emission spectra reveals significant structure in the infrared, which is strongly sample dependent. This shows that much of the emission is fluorescence from defect states following the intense emission from the initial "damage fireball." Consequently, the observed spectra are unlikely to represent the temperature of the lattice; rather it is probably a mixture of gray-body radiation from a hot electron plasma and fluorescence from crystal defects. These results allow for only two potential sources of damage: (1) sub-micron, highly-absorbing inclusions, which are too small to be visible with conventional scatterometry; and (2) optically active electronic defect clusters, which essentially amount to diffuse sub-micron inclusions.

In both cases, we hypothesize that, during laser irradiation, localized heating due to absorption by the inclusions results in vaporization of the inclusion, followed by damage through local melting and through fracture due to thermal stress. Low fluence laser conditioning reduces the probability of damage by heating the inclusions to temperatures below the vaporization point. This increases their solubility and diffusivity so that they become more dispersed and less absorbing.

We are now engaged in an effort to identify the composition of these inclusions. Transition metal phosphates are particularly suspect because they are highly insoluble, should be present in the starting materials, and have high absorption coefficients in the UV. For example, measurements on iron phosphate ($FePO_3$) show that its absorption coefficient at 35 nm is of order 10^4 cm^{-1}, which is large enough to generate temperatures in excess 103 K at typical damaging fluences. Through careful chemical etching and ion beam milling, we have exposed sites of laser damage at the surface for secondary ion mass spectrometric analysis. Our initial measurements have identified sub-micron regions that are rich in Ca, Fe, Cr, and Cu. During FY99 we expect that the completion of this analysis combined with time-resolved spectroscopy on the initial emission "fireball" will lead to positive identification of these damage precursors.

High Performance Explosive Molecules

L. E. Fried, C. J. Wu, P. F. Pagoria, T. F. Baumann, G. Fox
97-ERD-101

In this project, we are seeking to substantially accelerate the development of new high-performance or enhanced-safety explosive molecules. By combining state-of-the-art quantum chemistry calculations with the aggressive synthetic pursuit of promising candidate molecules, we hope to significantly advance the state-of-the-art in this field.

Our approach is based on the tight linkage of theory with chemical synthesis. By linking the thermochemical code CHEETAH with the *ab initio* electronic-structure code GAUSSIAN and the molecular-packing code MOLPAK, we have established a high-explosive performance-prediction code. Stability is predicted on the basis of calculations of first-principles electronic structure.

In FY98, we synthesized the target molecules DNBP. We are also a single step away from synthesizing TNBP which has record-breaking predicted performance.

DNBP has predicted performance nearly equal to that of HMX, but has much better thermal and impact stability. We believe that it may find future application in the DOE as a material with a superior combination of safety and performance. Given the importance of stability to the usefulness of an energetic material, much effort has been put into stability calculations. We have established that modern, gradient-corrected density functional methods can reliably calculate bond-breaking energies in energetic materials.

We have applied these methods to determine the energy required to break the weakest chemical bond in the target systems. In TNBP, the N–NO_2 bond was found to be the weakest; in DNBP, the C–NO_2 bond was the weakest. We find that our target molecules are stable, with relatively large dissociation barriers. TNBP has bond-breaking energies near that of RDX; DNBP was found to have a bond-breaking energy near that of TATB. We predict that the target molecules are all sufficiently stable to be synthesized and isolated, and that the stability of DNBP should be outstanding.

The latter prediction was confirmed experimentally by the successful, initial synthesis of 35 mg of DNBP, which decomposes in the differential scanning calorimetry apparatus at a temperature of 330˚C. Therefore, its thermal stability is significantly better than that of HMX, whereas its predicted performance is the same. No current material combines DNBP's predicted performance with its measured thermal stability.

During FY98, we scaled up our initial 35-mg synthesis of DNBP to produce 3 g of material. The material was then subjected to impact safety testing. We found that the DNBP material explodes when struck by a weight falling from a height of 69 cm. This compares well with the impact sensitivity of HMX, which is 33 cm.

In FY99, we are planning—in coordination with the DoD—another scale-up of the synthesis to produce enough material to measure its detonation performance. We will also pursue the synthesis of TNBP and MNTO, the two target materials that we have not yet synthesized. DNBP and DABP will be fully characterized with regard to safety, performance, density, and heat of formation.

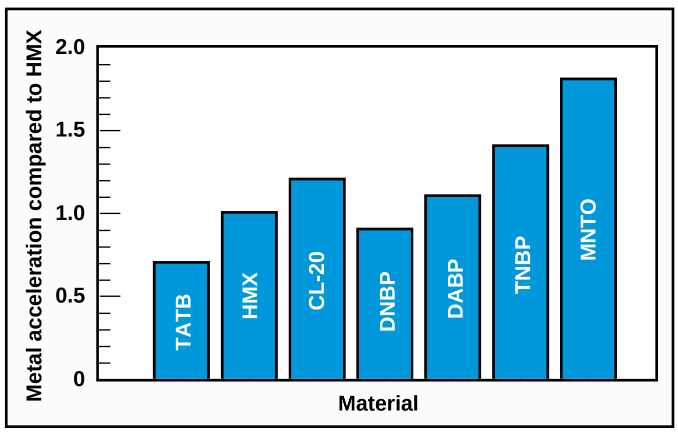

Explosive molecules, showing predicted metal-acceleration performance of the target materials DNBP, DABP, TNBP, and MNTO compared to the known materials TATB, HMX, and CL-20.

Novel Approaches to Surface Analysis and Materials Engineering using Highly Charged Ions

A. V. Hamza, T. Schenkel, A. V. Barnes, D. H. Schneider

97-ERD-102

Complex problems in materials science require very sensitive, high-spatial-resolution (<50 nm) determination of chemical (molecular) structures in near-surface volumes. Highly charged ions (HCIs) provide a new, unique tool for probing chemical structure on a nanometer scale.

We are exploring the potential of this new technique in studies of materials with programmatic significance such as hydrogen-getter technology and high-explosive mixtures. Specifically, we are (1) developing the use of slow HCIs from LLNL's electron-beam ion trap (EBIT) for this regime, and (2) studying HCI-based surface-analysis techniques (such as secondary-ion mass spectroscopy, SIMS) that are capable of boosting sensitivity limits to more than 10^9 atoms/cm^2. This surface sensitivity and quantification can be applied to Laboratory missions in enhanced surveillance and nonproliferation.

The unique competitive advantage of HCIs over conventional, singly charged ions is the extreme, high energy density that is deposited into a nanometer-sized near-surface volume at the impact of a single HCI. For example, a Au^{69+} ion deposits about 0.5 MJ/cm^3. This high energy density causes the emission of large numbers of secondary particles (electrons, ions, neutral atoms, and clusters) from the surface. The emitted particles act as probes of the energy-dissipation mechanism, and their yields are of technological significance.

Our initial study of HCI-impact electron-emission measurements led in FY98 to the design and construction of a low-magnification, proof-of-principle, HCI-based SIMS microscope. By accumulating time-of-flight cycles in SIMS event by event, we can differentiate among impact events that require the presence of characteristic "fingerprint" ions. By building spectra with characteristic requirements, we can see correlations among the secondary ions that were emitted following the impact of a single primary ion. We estimate the emission area of secondary ions to be only about 10×10 nm. The uniquely high secondary-ion yields enable the use of an HCI–SIMS microscope to probe the chemical structure and homogeneity of complex target surfaces on a nanometer scale.

During FY98, we used our HCI–SIMS technique to collect images of test wafers in several runs at the EBIT facility. Contrast provided by the number of emitted electrons, secondary-ion time-of-flight, and total emitted intensity was demonstrated at a micrometer scale. The figure shows the results for a run using a W/SiO_2 test wafer that was impacted with Th^{75+}. In constructing the wafer, the tungsten was deposited by reduction of WF_6 in disilane (Si_2H_6). Silicon fluoride compounds, most of which are volatile (e.g., SiF_4), are byproducts of this process. The full spectrum shows signatures of tungsten oxide and silicon dioxide from a W/SiO_2 test wafer. If we require the presence of tungsten features, we find a very strong correlation with Si_xF ions—this indicates the presence of silicon fluoride on the tungsten areas. If we require the presence of an SiO_2 feature, results reveal that no silicon fluoride is present on the SiO_2 areas of the test structure. Information gained from this coincidence-counting HCI–SIMS analysis can be used to optimize process parameters.

Sputter yields are fundamental characteristics of the interaction of HCIs with surfaces. In FY98, we measured the sputter yields of uranium oxide and GaAs when they interacted with HCIs and found that up to 70 U atoms and 1400 Ga and As atoms were removed by Th^{70+} ions. The low ionization probability for the GaAs surface was unexpected and contrary to the atomic mechanisms in HCI-surface interactions as predicted by existing models. We adapted a laser–surface interaction model from Stampfli to describe these results.

The data from the test microscope are guiding our decisions for the final design, which will be constructed in FY99. Removal of 1400 atoms per incident highly charged ion begs investigations of the possible surface modification that highly charged ions can achieve. We will investigate the nanoscale modification of silicon surfaces by highly charged ions with atomic force microscopy (AMF) and photoluminesence.

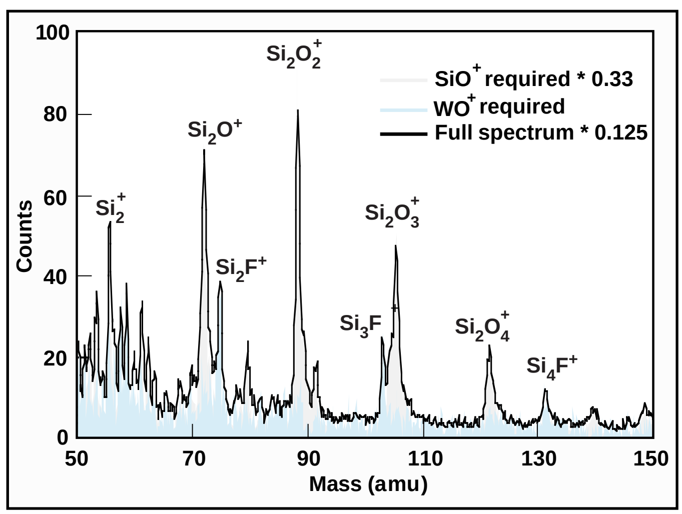

Coincidence-counting, time-of-flight, positive secondary-ion mass spectra from a W/SiO_2/Si test wafer impacted with a Th^{75+} primary beam. The black line is the full spectrum. The SiO^+ coincidence spectrum is shown in gray; the WO^+ coincidence spectrum is shown in blue. The spectra are scaled by the number of events in each spectrum.

Tailoring Material Properties of Sputtered Beryllium

R. L. McEachern
97-ERD-129

Doped beryllium is a material of considerable interest both to the inertial confinement fusion and the weapons communities. It could also find applications in specialized industrial settings (e.g., x-ray windows and mirrors). Some of these uses require conformal coating of thin films on (possibly) irregularly shaped surfaces. Physical vapor deposition is often used to accomplish this, and sputtering is often the technique of choice. Among the advantages of sputtering is that the depositing atoms are relatively energetic, leading to more compact films even at low substrate temperatures. Moreover, if we apply a voltage bias to the substrate, ambient noble-gas ions will bombard the growing film—causing further densification and other modifications to the microstructure. Sputtering is also well suited to the introduction of dopants, even those that are insoluble.

Most applications of these novel doped Be materials will require fundamental knowledge of their properties. However, because so many can be devised, such information is generally unavailable. The objective of our effort is to systematically study the properties of films produced under different conditions, with an emphasis on their surface finish, hydrogen permeability, and strength.

In FY98, we focused on two areas: (1) the addition of boron to improve the surface finish and bulk morphology of deposited Be films, and (2) measurements of their permeability at relatively low temperatures. The doping experiments were performed both on flat substrates and on plastic spheres, with boron concentrations ranging from 3 to 35 at.%. Permeation experiments were performed by placing capsules with Be coatings in a heated vessel pressurized with deuterium gas.

The inclusion of boron had a pronounced effect on the Be films. The most striking result from the experiments on flat substrates was the observation of an abrupt transition in the film morphology at approximately 11 at.%B. Below this level, the films were similar to one another, each with a root-mean-square (rms) roughness of about 20 nm—as measured using atomic force microscopy—and grain sizes of about 200 nm. At 13 at.%B and above, the films were an order of magnitude smoother, with subnanometer finishes measured at 18 at.%B and above. The grain size dropped to less than 50 nm. Deposition on plastic capsules yielded notably different results. At 10 at.%B, the coatings were similar to those on flat substrates, although about 50% rougher. At 15 at.%B, however, rather than a smooth coating the capsules had a nodular surface with an rms roughness of over 50 nm. The grain size was similar to that on the flat substrates; in both cases, scanning electron microscope images of film cross sections revealed a homogeneous bulk structure. We are still researching the cause of this discrepancy.

In a recent series of experiments, we compared BeB films deposited on flat silicon substrates, as in the initial studies, with ones deposited on plastic-coated flat substrates at various temperatures. Our results showed that boron-doped films adhere poorly to plastic, and that the high intrinsic compressive stress in the films causes delamination at substrate temperatures as low as 150˚C. We attempted to deposit lower-stress BeB films on capsules by increasing the pressure of the argon sputter gas, but the results were similar to previous experiments. Since we could not increase the pressure enough to eliminate the stress, it is still possible that this factor contributes to the unusual morphology observed on capsules.

Most of our permeability experiments have been performed at a temperature of about 200˚C. This choice was based on results from Los Alamos National Laboratory in which thin palladium coatings on both sides of a Be foil were found to significantly increase its permeability to hydrogen at that temperature. The Pd layers protect the Be from oxidizing and may hasten the uptake of hydrogen by the Be by providing a catalytic surface at which the hydrogen molecules can readily dissociate. Although literature values for Be permeability are not generally consistent with these results, we have attempted to duplicate them by depositing thin (~100 nm) layers of Pd on plastic capsules, overcoating them with Be, and then finishing with another thin layer of Pd. These capsules were kept in a 200˚C chamber under 10 atm deuterium for several days, then crushed inside a calibrated volume to measure the gas fill. None of the capsules showed significant fill, suggesting that this approach is probably not feasible for coatings on capsules.

Microfabrication and Characterization of High-Density Ferromagnetic Arrays

C. Cerjan, A. Fernandez
97-LW-037

The dramatic increase in magnetic disk storage capacity has been driven by scale reduction of the bit arrays and improved component engineering. In the conventional bit storage scheme, high-density arrays of magnetic stripes are written onto a spinning disk. These are typically much longer in their radial extent than in the spacing between the stripes. Thus the information is arranged in concentric rings of magnetic tracks much like radially distributed, closely spaced stripes. The distance between any two of these stripes (bit distance) and the number of tracks (track density) determines the areal storage density of the magnetic disk. Improvements in the material properties of the media and the reduction in size of the magnetic sensor head required to read the bits are essentially responsible for the remarkable increase in storage density over the past decade.

As the bit distance per track continues to decrease, fundamental limitations on the magnetic response of the individual bits arise. These limitations are caused by the microcrystalline nature of the thin film media—the deposition process used to form the magnetic films produces large statistical variations in the grain size and orientation of the film. As the bit dimensions shrink, the intrinsic noise associated with the reading head overwhelms the desired signal from any one bit. In essence, the reading head can no longer distinguish when it has successfully read one bit of information from the noise of the background, inter-bit media. This source of noise is termed transition noise and is predicted to dominate the read signal when the areal density is greater than 10 Gb/in^2. The primary object of the present project is to circumvent this limitation by developing a transition noise-free media.

One promising technique to overcome the signal-to-noise problem in magnetic storage is the use of patterned arrays. In this method, the conventional thin film media is replaced by patterned media using interference lithography that creates arrays of submicron sized magnetic dots. Thus the role of the magnetic stripes is now taken by individual dots of magnetic material. There is no transition noise associated with this scheme since there is no magnetic material between the bits (dots). The interference lithography process is rapid since large arrays may be prepared with one exposure, in contrast to the previously used electron beam patterning promoted by other research groups. Electron beam exposure is limited to serial, one-dot-at-a-time, production whereas interference lithography is parallel.

It was demonstrated in FY97 that such a technique could successfully be used to produce uniformly magnetized arrays. This step was critical since other groups had observed very non-uniform magnetic response from electron beam generated arrays. In contrast, the interference lithographic technique applied to substrates coated by thermal evaporation produced small dots that had very simple magnetic field response. Additionally, the magnetic field response of these elliptical cylindrical dots was numerically simulated using the so-called micromagnetic simulation technique. The resulting magnetic force microscopy (MFM) images and the hysteresis loops derived from vibrating sample magnetometry (VSM) matched the simulations quite well, thus confirming the observation of uniform magnetic response.

In order to make this process attractive, very high areal densities must be demonstrated. The primary goal of the FY98 project was to extend the interference lithographic approach to very high densities, exceeding the 10 Gb/in^2 range, which is a five-fold increase over the highest density currently manufactured. This objective was not completely realized since arrays of 7 Gb/in^2 were successfully prepared. On the other hand, a clear pathway to extending this work was realized by the end of FY98. Specifically, the scaling of the achievable density is quadratically dependent upon the laser wavelength. Thus changing the laser system to 193-nm illumination using the developed process will effect at least a four-fold increase in density. Since this extension required the acquisition of a shorter wavelength laser system, the intended higher density regime could not be accessed. It is believed that this straightforward extension will produce uniform arrays with densities exceeding 40 Gb/in^2.

Physical Basis for Materials Synthesis using Biomineralization

J. J. De Yoreo, C. A. Orme
97-LW-069

Crystals found in biology often display a complex organization that is difficult to reproduce in the laboratory. Although it is thought that the interplay between organic and inorganic materials conspires to control both the phase and facets expressed, the processes are poorly understood. We are measuring fundamental material parameters of the biologically relevant crystals calcium carbonate (calcite), calcium phosphate (brushite), and ice both in pure systems (to provide a baseline for subsequent work) and in solutions with organic additives. Our goal is to work towards an understanding of the processes that control crystallization in biological systems.

We are using atomic force microscopy (AFM) to image calcite and brushite growing from solution (see figure). Because AFM has atomic resolution in the *z*-dimension and molecular resolution laterally, the motion of atomic steps is easily seen. Images obtained while a temperature-controlled solution flows over the sample show topographic information. The morphology reveals both the mode of growth and the facet directions for step motion. A sequence of images reveals the velocity of the steps as well as the critical length needed for the step motion. Because the solutions can be changed while the surface is being imaged, it is possible to observe the effects of solution variations on microfaceted structure and surface dynamics.

For calcite, we measure the step velocities in the different crystallographic directions as a function of the supersaturation of the solution. We then extract the kinetic coefficient—a measure of the barriers involved in moving atoms from the solution into the solid form. We also measure the critical length needed for step motion as a function of supersaturation and obtain the step-edge free energy. Gibbs and Thompson (early 1900s) derived the scaling of critical length with supersaturation from simple thermodynamic arguments; although historically important, this law had not been experimentally verified. We have obtained the first direct measurements.

To understand the effect of organic element on crystal dissolution, during FY98 we added amino acids to the solution of calcite. We chose glycine and aspartic acid because they are commonly found in the proteins associated with biogenesis. We found that the amino acids alter the pit structure from the rhombohedral symmetry found in natural calcite, but they express different microfacets. For example, aspartic acid creates trapezoidal pits with none of the four steps expressed coincident with the original rhombohedral step directions. Calcite has rows of calcium along the diagonals of the rhombohedron, but the two perpendicular directions have different calcium–calcium spacing. One of the steps stabilized by aspartic acid is along these rows of calcium; however, only one calcium row direction is stabilized—indicating that the spacing of calcium atoms is important for the binding to take place.

In FY99, we will supplement this study by looking at the systematic effect of aspartic acid on crystal growth of calcite and at the effect of a well-characterized peptide designed specifically to interact with calcite. These peptides, which are modeled after those found in fish to inhibit ice nucleation, have been shown to alter the macroscopic crystal shape. We hope to connect the morphological changes to microscopic step motion.

During FY98, we began examining the brushite system because of its relevance as a structural material in mammals. Brushite exhibits a large anisotropy in the step velocities, with the slowest step being approximately 10 times slower than the fastest. We began analyzing the step velocities and critical lengths of brushite as a function of supersaturation.

We also (1) completed an environmental chamber and temperature-control system that allow imaging down to –20˚C (vs. the 20 to 50˚C allowed by our previous setup), (2) imaged evolving ice surfaces, and (3) began working to control the nucleation of specific facets for more quantitative studies.

This work is being done in collaboration with the Georgia Institute of Technology (calcite), the State University of New York, Buffalo (brushite), the University of California (ice), and Boston University (peptides).

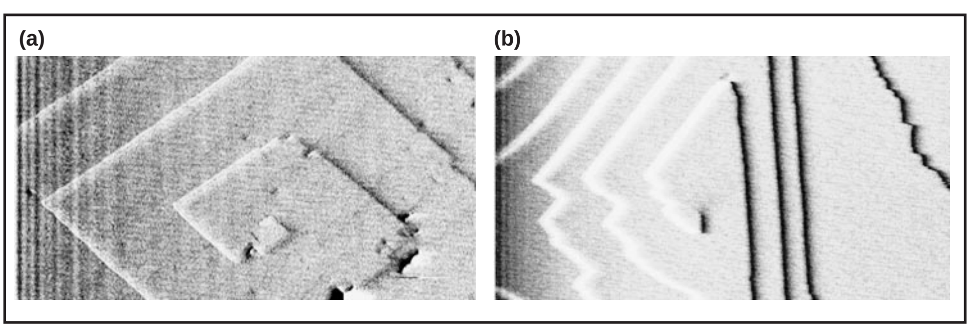

Figure 1. Atomic force microscopy images of calcite and brushite surfaces while they are growing in solution: (a) calcite, 4×2 μm, T = 25˚C; and (b) brushite, 4×2 μm, T = 37˚C. The lines represent atomic steps. Over all supersaturations examined, both calcite and brushite grow from polygonalized spiral defects. The clarity of the atomic steps makes possible quantitative measurements of their motion.

Dislocation Dynamics at the Microscale: Experiment and Simulations

D. H. Lassila, W. E. King, T. Diaz De La Rubia, D. J. Nikkel, J. Moriarty, N. Holmes
97-SI-010

Since the development of quantum mechanics, great strides have been made in understanding materials phenomena based on "first principles" associated with atomic structure (e.g., in the fields of microelectronics and nuclear energy). However, when we consider the mechanical behavior of metals, the connections between the fundamental nature of atomic structure and important properties are problematic because—in addition to atomic structure—other structural aspects of the material at longer length scales are important. Although general relationships between the composition of metals and their mechanical properties have been established, we lack a detailed understanding of the effects of the composition and microstructure based on first principles.

Multiscale modeling approaches can be employed to rigorously "link" information from atomistic simulations to models that are used in continuum computer-code simulations. The methodology employed at LLNL for studying the mechanical behavior of body-centered cubic (bcc) metals is based on information that passes between simulations at three different length scales: atomistic, microscale, and mesoscopic/continuum. In this project, we are developing experimentally validated microscale simulations for predicting strength properties.

The microscale simulation, referred to as "dislocation dynamics," is the principal deliverable of this project. Dislocations, which are the fundamental crystalline features associated with the strength properties of metals, have been modeled at the atomistic-length scale for over 30 years. The movement and interactions of large numbers of dislocations caused by an applied load give rise to plastic deformation. Dislocation-dynamics simulations can be used to study the forces required for these movements and interactions—in essence, the fundamental strength properties.

Our technical plan involves three closely coupled work areas: (1) simulation development, (2) single-crystal deformation experiments, and (3) characterizations of deformed crystals. Our FY98 progress in each area is described below:

Simulations: We are predicting stress-strain response and the corresponding dislocation structures of single crystals of tantalum; our predictions are in good agreement with experiments. The physics associated with dislocation motion and interaction that has been incorporated into simulations has improved dramatically; for example, we can now predict temperature dependence on flow stress. Also, we have begun to implement parallel versions of the simulation codes, and large problems have been run on the Accelerated Strategic Computing Initiative (ASCI) computers.

Deformation experiments: These center on the preparation, deformation, and subsequent characterization of single crystals of Ta and Mo. Single crystals with low defect and dislocation densities are being produced using a float-zone refinement technique and purified at high temperature in an ultrahigh vacuum designed to reduce the interstitial impurities (e.g., carbon, oxygen, etc.) that can have substantial effects on dislocation motion. We made considerable progress in designing and fabricating the test fixtures required for compression tests that will be performed over a wide range of test temperatures (4 to 600 K) and strain rates (10^{-5} to 10^{3} s^{-1}). We met most experimental milestones, including conducting several preliminary tests on single-crystal compression samples.

Characterizations: We characterized deformed single crystals of Ta and Mo using transmission electron microscopy (TEM) and orientation imaging microscopy (OIM) to determine dislocation structures and microtexture, respectively. We also (1) completed detailed characterization of dislocation structures in well-annealed materials—this information is being used to establish initial conditions for the dislocation dynamics simulations, and (2) investigated changes in dislocation density and character related to the strength properties of single crystals.

In June 1998, we hosted an international meeting and workshop titled "Dislocations in Materials." We are collaborating with six universities and one commercial company and maintaining a website (www.multiscale.llnl.gov).

Our plans for FY99 center on detailed and extensive comparisons between experimental data and results of simulations. The strength properties and associated dislocation structures that evolve when Mo and Ta are deformed at low vs. high temperatures are dramatically different. Consequently, our comparisons will first focus on these extreme-deformation conditions.

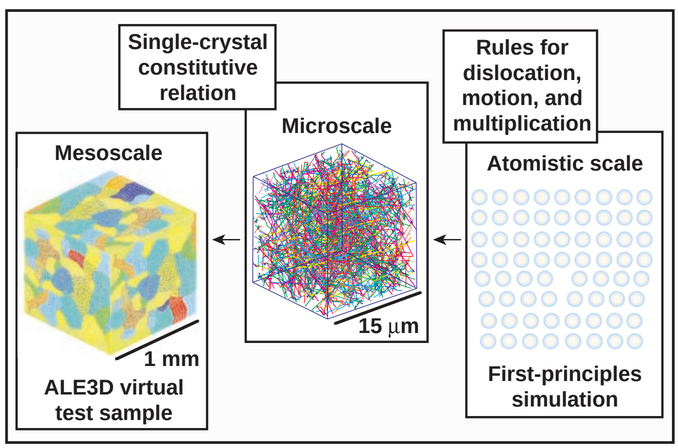

LLNL's multiscale modeling approach involves simulations at three length scales, where carefully defined "information passing" from the shorter- to longer-length scales enables "bridging of the length scales." Of the three simulations, the microscale ("dislocation dynamics") simulation is the least developed and is the critical link between the atomistic and mesoscopic (continuum) length scales.

Micromechanics of Highly Filled Polymers

S. W. Groves, S. J. DeTeresa, B. J. Cunningham
98-ERD-015

Highly filled polymers (HFP) are used throughout the Laboratory, in applications that include plastic-bonded explosives, propellants, a variety of specialized, highly filled rubber systems for stockpile explosives and highly filled epoxy dielectric materials for the National Ignition Facility (NIF). Our objective is to develop a suite of tools and models for predicting the long-term mechanical response of HFPs. One of the critical components to lifetime analysis of plastic-bonded explosive (PBX) and other HFPs used at the Laboratory is to understand the contribution of the individual components to the mechanical response. Our efforts have focused on determining the contribution of the plastic binder. Since the binder is still a continuous phase, it dominates the mechanical response, even at low concentrations for PBX.

Long-term modeling requires accurate thermo-visco-elastic models with the ability to capture microstructural/in situ properties of the constituents. Developing material models that can relate constituent properties to macroscopic composite properties will provide significant benefits, especially in the case of energetic materials. These tools would also facilitate incorporation of any identifiable chemical or physical aging mechanism, as well as the effects of microstructural damage. In FY98, our efforts included macroscopic (bulk) characterization of the binders used in PBXs, limitation and eventual curtailment of efforts to measure thermal-visco-elastic properties of PBX, an evaluation of techniques to characterize the local microstructure and in situ properties, and micromechanical modeling. None of these proved to be simple tasks.

In our efforts to characterize the local microstructure of PBX, we investigated the use of atomic force microscopy, microcomputed tomography (small beam x-ray), optical microscopy, and scanning electron microscopy. Through application of these analytical techniques, we hope to determine the distribution and in-situ properties of the binder. To date, the best images of PBX microstructure were obtained at LANL using polarized light microscopy (thru-transmission) of very thin wafers [see Fig. 1(a)]. We have explored a relatively new technique called *atomic-force microscopy with nano-indentation* to investigate the in-situ mechanical response of binder in mock high explosive (HE). In our investigation, it became quickly apparent that current probe designs are inadequate to determine the required in-situ properties. For our purpose, we must develop a high aspect ratio probe with a diameter less than 0.1 micron and with the ability to measure and impart nano-newton forces and nanometer displacements [see Fig. 1(b)]. We are working with the microtechnology center to fabricate these new tips. Our goal is to measure the visco-elastic properties of the binder material within the PBX matrix. Overall, we believe this is a promising method for mapping the microstructure of PBX because of the large differences in mechanical properties between the binder and relatively hard HE crystal. Also, we hope to explore extensively the use of a new type of scanning electron microscope with organic materials; our approach would eliminate the need to apply a conductive coating, such as gold, which is known to mask some details.

In our micromechanical modeling effort, we are assessing the merits of two different approaches: a generalized self-consistent scheme and a finite element analysis. The former is both analytic and quite simple to construct, but does not accurately account for the geometry of the particles in that it assumes that the particles are spheres of constant radius. The finite element method has the capability of accounting for these geometric difficulties, but it suffers from the fact that it is more cumbersome due to the numerical nature of the approach [see Fig. 1(c)]. In FY99, we will focus on studying the micromechanics of HFPs.

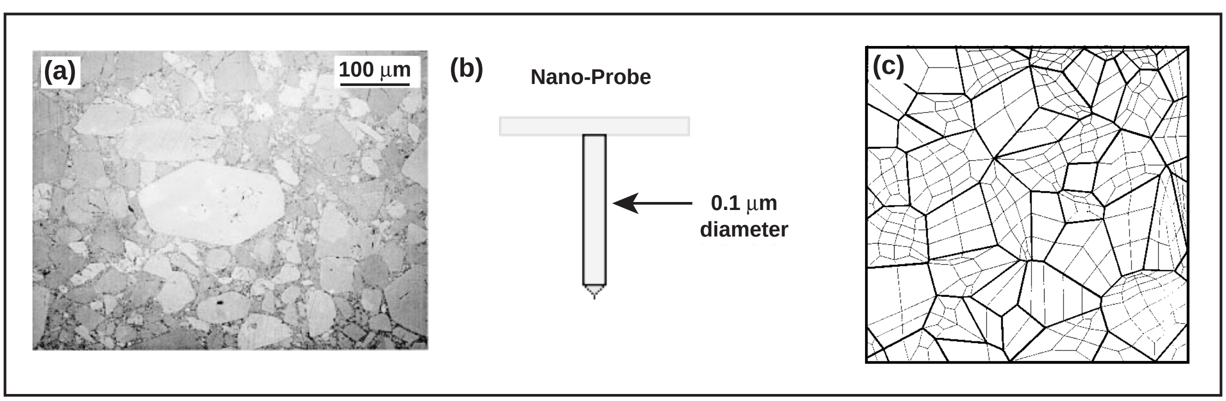

Figure 1. (a) PBX microstructure (courtesy LANL); (b) new nano-probe design that will be used to measure binder properties around HE crystals; (c) a possible finite element mesh for the microstructure shown in (a).

Fundamental Aspects of Radiation-Induced Microstructural Evolution in Plutonium–Galium Alloys

M. J. Fluss, T. Diaz de la Rubia, M. Caturla, M. Wall, T. Felter.
98-ERD-028

The prediction of microstructural evolution as a result of the approximately 5-MeV alpha-particle decay of Pu in its alloys is a scientific and technological challenge to today's stockpile stewardship program. Radiation-damage accumulation can lead to microstructural evolution on a scale that might affect a weapon's performance. Using materials models to predict these microstructural changes poses both technical and scientific challenges. Experimental data on materials can help to provide better problem definition, model component validation, and critical physical parameters needed as input to the materials models. Our experimental investigations focus on the underlying science; hence, they are an important component in the development of predictive molecular-dynamics (MD) modeling of radiation-induced microstructural changes. Our experiments thus have two related goals: (1) model validation, and (2) determination of the critical parameters of mass-transport kinetics.

In FY98, with experiments that combined heavy-ion irradiation and transmission electron microscopy (TEM) of Pb specimens, we validated the MD numerical models that describe the radiation-damage cascade of heavy ions in high-*Z*, low-melting-temperature materials. We also designed, built, implemented, and qualified new experimental facilities for low-temperature radiation damage. We used proton- or alpha-particle irradiation followed by four-point precision resistometry during a program of thermal annealing at successively higher temperatures. This apparatus will be used to obtain key kinetic parameters relevant to the microstructural evolution in Pu alloys that is driven by radiation-damage accumulation, time, and temperature.

To confirm that the irradiation-annealing apparatus has the requisite sensitivity and accuracy, we performed experiments on thin (10 µm thick) Pb specimens. We used heavy-ion irradiation of these specimens by 180-keV Er ions to simulate that part of the cascade model that follows the recoiling 80-keV U ion produced when Pu decays via a 5-MeV alpha particle. These Er–Pb irradiations were performed at near-liquid-nitrogen temperatures (–182˚C) on Pb specimens of 99.999% purity. The MD modeling predicts the number and type of radiation-damage sites that would be produced and also predicts the growth and dissolution of defect clusters (collapsed interstitial and vacancy loops) with increasing temperature. All relevant predicted features were observed by TEM, and the model-predicted annealing characteristics were confirmed. Such experiments on a high-*Z*, low-melting-temperature metal such as face-centered-cubic (fcc) Pb give us great confidence that we will be able to characterize the similar behavior in Pu–Ga delta-stabilized fcc alloys.

In the past, Pb has been well studied by electron irradiation at liquid-He temperatures, followed by isochronal annealing and resistometry. The annealing stages of the accumulated damage are used to deduce the key kinetic parameters. There are five major annealing stages, each with well-defined temperature boundaries. We had to ask, "Would irradiation with alphas and/or protons reveal the same stages?" In FY98, we completed our first irradiation with alpha particles at 10 K (above the superconducting transition of Pb); exactly the same stages two through five were revealed as we had seen with electron irradiations. An important side benefit was that stage five annealing—which accounts for excess, freely migrating vacancies that might lead to void nucleation and swelling—was thermally coincident with dissolving of collapsed loops, a thermally activated process that is a key to modeling subsequent radiation effects.

In FY99, we plan to obtain similar data for Pu–Ga. We will then be able to make accurate predictions about the critical temperature range in which void growth might be extant. In addition, through experiments we will deduce key parameters required by the kinetic Monte Carlo models that are used to follow the long-term evolving microstructure. The experimental data will (1) be used in materials-modeling codes to predict those microstructural changes that might be important to the reliability of nuclear weapons, and (2) provide a basis for interpreting engineering experiments related to the surveillance of the stockpile.

Solid-State Physics of Transuranics

L. J. Terminello
98-ERD-040

With the demise of nuclear weapons testing, the focus of the Laboratory has turned towards a science-based stockpile stewardship (SBSS) approach to evaluating and predicting the life span and long-term safety of our nuclear stockpile. A great many modeling and measuring efforts are underway to address these concerns.

We are addressing a fundamental component of this SBSS endeavor: the experimental validation of first-principles calculations of U, Pu, and their alloys—calculations that are the basis of many weapons-system models. We have two primary goals. One is to validate our first-principles calculations by measuring the electronic structure (density of states, or DOS) of the material using valence-band photoemission spectroscopy (VBPES), soft–x-ray fluorescence (SXF), and x-ray absorption spectroscopy (XAS). These are complementary techniques that allow us to probe the bulk occupied (VBPES and SXF) and unoccupied (XAS) electronic states of a material. These measurements will allow a direct comparison between the calculated and measured densities of electronic states, thereby identifying the degree of f-electron localization in the alloys and permitting selection of the best modeling code for determining additional material properties.

A second goal is to develop the stringent materials-handling procedures for the synchrotron-radiation techniques at the core of the project—procedures that will be valuable to broader stockpile-related missions. Many of the safety issues that surround the safe handling of actinides at a user facility like a synchrotron ring cannot be underestimated or overlooked.

During FY98, we began the synchrotron-radiation SXF and XAS experiments and made significant progress in developing the radioactive-materials preparation, handling, and analysis procedures needed for the success of this project. We measured the SXF of U, UO_2, and UO_3 samples at LBNL's Advanced Light Source (ALS) and the XAS of U and U–Nb alloys at the Stanford Synchrotron Radiation Laboratory (SSRL). We measured the uranium oxide series to evaluate our sample integrity as well as to identify the DOS features that we expect to see shifting in our uranium-metal/niobium-alloy samples. Our initial interpretation of these results (see figure) indicates that our sample-preparation methods are producing unreacted surfaces that remain pristine throughout the experiments. Our results also indicate evidence for charge transfer from Nb to U in the U–Nb alloy from our observation of the relative increase in the unoccupied niobium DOS when compared to the pure metal. The greater than 1000-Å penetration depth of the photon-based fluorescence and absorption measurements ensures that we are sampling primarily bulk electronic features. No other techniques can assess this phenomenon, which has a direct bearing on the materials properties of the alloy.

Our goal for FY99 is to measure the electronic structure of U, Pu, and their alloys to compare to current state-of-the-art calculations, with pending calculations on uranium alloys by others at LLNL. One interesting phenomenon that we will be looking for is the localization of the 5f electrons in the alloys of Pu that result from alloying the metal. These electrons should have properties that are intermediate between itinerant (delocalized) 5f electrons in Pu and lower actinides and localized 5f (Kondo effect) electrons in americium. This effect is important for understanding the complex and novel properties of the actinides that are associated with their 5f electronic structure. With the localization/delocalization of the 5f electrons is an accompanying structure/property change of the material that has critical importance for the actinides. The degree of localization for the 5f electrons in Pu alloys has direct bearing on the macroscopic properties of these materials (such as heat capacity) and thus underlies the importance of this project to measuring the electronic structure of these actinides as a means of model validation for SBSS.

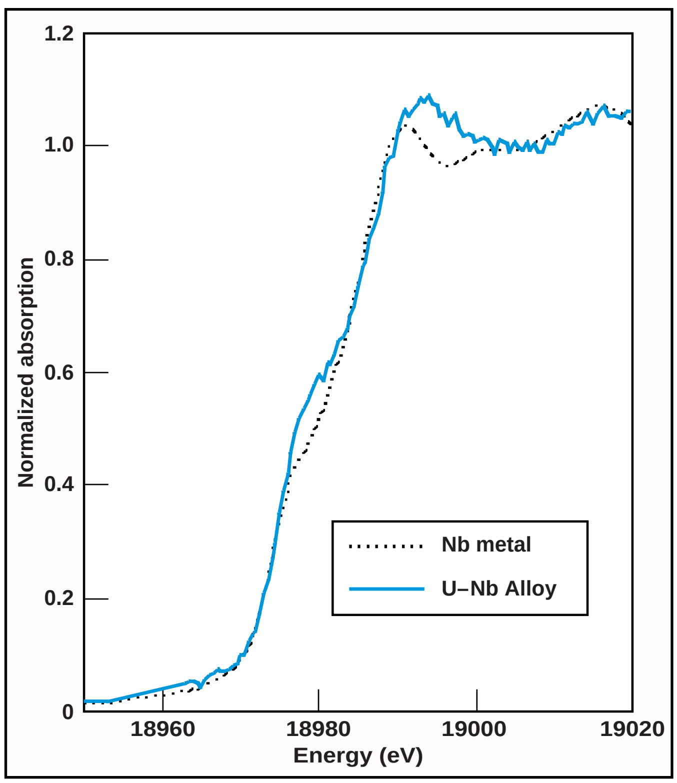

The Nb K-edge x-ray absorption near-edge structure (XANES) of Nb metal and U–Nb alloy, indicating charge transfer from Nb to U in the alloy.

Multilayer X-Ray Waveguides for X-Ray Analysis Instrumentation with Ultra-High Spatial Resolution

T. W. Barbee, Jr.
98-ERD-044

The ability to characterize crystallographic and compositional distributions in macroscopic material samples significant to DOE-relevant materials as well as a more general class of technologically important materials at sub-100-nm resolution levels is not possible with traditional x-ray technologies. This ability would offer the materials community new understanding of relationships among synthesis, structure, and property and would enable materials engineering at the mesoscopic-to-microscopic scales.

Our project goals were to model, synthesize, and characterize thin-film, x-ray waveguide structures to determine whether such nanostructures can be fabricated with the precision required for true waveguide operation at x-ray energies. In FY98, we designed, fabricated, and characterized (at the Stanford Synchrotron Radiation Laboratory) optimized, thin-film, x-ray waveguide structures (XWGs) as resonant concentrators of x rays that may be applied as diffraction-limited, linear x-ray sources. We fabricated nine waveguide structures that were optimized to operate in the cavity modes m = 1,2,3 and tested them at x-ray energies of 6 to 10 keV. The observed performances were compared to the calculations based on the design structures; excellent agreement was demonstrated.

Our critical experiment involved an XWG with a 0.4-nm-thick layer of a fluorescent material, Ta, deposited in the center of its cavity. The angular-dependence Ta L_α fluorescent intensity from this marker layer excited by incident 10-keV x rays allowed us to determine of the guided x-ray intensity in the cavity for comparison with model calculations. When a waveguide is operated atm = 1,3,5..., the maxima of the guided x-ray wave intensities in the cavity are at its center. For even cavity modes m = 2,4,6…, minima in the guided x-ray wave intensities lie at the cavity's center. The experimentally observed angular dependence of the Ta L_α fluorescent intensity presented in the figure—maximum for the odd cavity modes (m = 1,3,5...) and minimum for the even cavity modes (m = 2,4,6...)—is definitive proof of x-ray waveguide performance**.** The figure also shows that the intensity of the Ta L_α fluorescent at m = 1 is greater than 40 times that expected at angles of incidence near 1000 mdeg, where no waveguide performance is expected. This waveguide-action-enhanced intensity in this cavity is therefore at least 40 times the incident intensity, in agreement with the calculations from our model. We obtained similar results from tests of other XWGs that were fabricated and studied in this project.

Our work has shown that XWGs, when developed, can provide an intense, diffraction-limited, point source of x rays that will enable projection x-ray microscopy at the sub-100-nm level. The scientific and programmatic importance of these XWGs and the instrumentation based on these devices is multifaceted. This point source can be re-imaged and applied to high-resolution composition analysis as well as to microdiffraction studies of fine-grain-size materials with resolutions exceeding 100 nm. Direct evaluation of strain distributions at similar resolution levels will also be possible. This linear 20- to 100-nm source will also make very high-resolution x-ray tomography possible. Although this technique will not reach the atomic scale, it will provide a tool for studying materials in a quantitative manner at that intermediate level between microscopic and macroscopic.

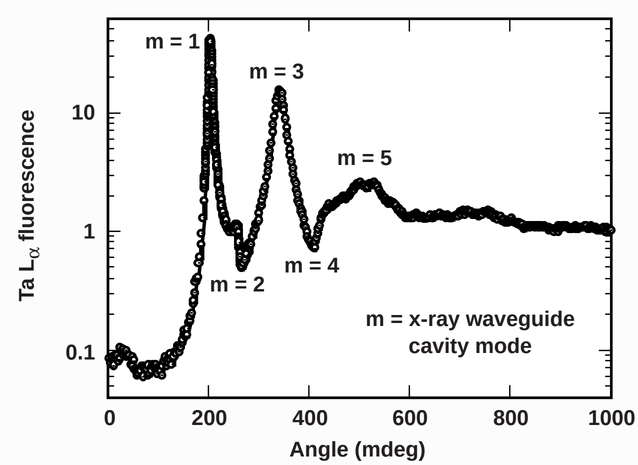

Experimentally observed Ta L_α fluorescent intensity from a 0.44-nm-thick Ta layer at the center of the waveguide cavity excited by 10-keV x rays injected into the cavity, shown as a function of the angle of incidence of the 10-keV x rays. The intensity is seen to be near zero for the even cavity modes m = 2,4,6... and maximum for the odd cavity modes m = 1,3,5.… Our calculations showed that x-ray waveguiding would be confirmed if the intensity of the Ta marker-layer L_α fluorescence approached zero for the even cavity modes and was maximum for the odd cavity modes; this was experimentally demonstrated.

Nano-Structure High Explosives using Sol-gel Chemistry

T. M. Tillotson, R. L. Simpson, L. W. Hrubesh, R. S. Lee, R. W. Swansiger
98-ERD-048

This project represents the first scientific inquiry using sol-gel chemistry in explosive synthesis. The use of sol-gel methodology offers the exciting possibility to control the microstructure of energetic materials on the nanometer scale, resulting in new or improved properties. The new micro- and meso-porous materials will also enable understanding initiation and detonation mechanisms, mass transport, and intramolecular reaction kinetics in the nanometer range.

Sol-gel chemistry produces high surface area, porous solids, which may be cast to near-net shape. The microstructure, comprised of nanometer-sized pores and linked primary particles, as well as the elemental composition, can be controlled by solution chemistry. In the general sol-gel process, monomers are reacted in a solution to produce 2–20 nanometer diameter primary particles, called “sols,” which can be linked to form a solid network surrounded by a liquid, called a “gel.” Controlled evaporation of the liquid phase results in a dense, porous solid, or “xerogel.” Highly porous, lightweight solids, “aerogels,” are produced by removing the liquid by supercritical extraction without collapsing the structure.

Several problems in energetic materials may be addressed by this methodology. One example is the fabrication of detonator materials where low manufacturing rates, difficulty in handling fine powders, and the inability to produce geometric shapes are current limitations. Using sol-gel chemistry, the intimacy of mixing can be controlled and dramatically improved over the state-of-the-art mixing of granular solids while providing a method for easily casting complex geometric shapes. Increased dimensional control will also enable high quality experiments to be run where chemical and mass transport limited kinetics may be determined more accurately than by conventional approaches. The next generation detonation models will focus on chemical kinetics and species equilibrium that rely on these data.

Numerous synthetic routes are possible utilizing this method in processing energetic materials. We have focused this work on four approaches: solution crystallization, powder addition, nano-composites, and functionalized/explosive solid networks. In FY98, we produced nano-structured high explosives by the first three approaches. Differential scanning calorimetry (DSC) confirmed the presence of the energetic materials in the final dried products. Monolithic aerogels were prepared by the solution crystallization of hexahydro-1,3,5-triazine (RDX). Monolithicity was maintained up to 45 wt% RDX in a 55% SiO_2 matrix. In the lowest composition, 17 wt% RDX, the crystals are not visible to the naked eye, while increasing compositions result in micron-sized orthorhombic crystals. Using the powder addition approach, high solids loading was accomplished and reported for the first time by a gel-mending method. The impact sensitivity of an energetic material to unintended initiation is an important safety factor in its use. Counter to expectations, drop hammer sensitivity tests showed that the presence of the gel structure decreased the impact sensitivity of an explosive. De-sensitized materials are only an improvement in technology if they can still be initiated with reasonable power outputs. A flyer-plate experiment demonstrated that possibility when an 80% RDX xerogel moulding powder pressed into a detonator pellet could be initiated. Remarkably, we found that RDX in silica-based xerogels failed to initiate when shocked at pressures adequate to initiate TATB.

A prototype nano-composite (see figure) was made by crystallizing ammonium perchlorate (AP) within the pores of an organic gel. In this composite, the solid hydrocarbon skeleton comprises the fuel with the AP acting as the oxidizer. Compositions with the energy density of HMX have been made. Transmission electron microscopy (TEM) indicated no crystallites greater than 20 nm. Near-edge soft X-ray spectroscopy performed at LBNL’s Center for Microscopy showed that nitrogen was uniformly distributed to the resolution limit of 80 nm. With this technology readily scaleable to large quantities, a material goal—that has eluded conventional technology—to create a material that has the energy of strategic rocket propellant with the power of an ideal explosive may be possible.

In FY98, collaboration with the Navy resulted in nano-composites where aluminum, a fuel, was crystallized within skeletal structures using in-situ chemical processes. Other accomplishments include synthesizing aerogel gas generators by polymerizing 1,3 diaminobenzene, and developing a non-aqueous based organic aerogel route, which significantly reduces processing time. In FY99, we will continue to develop new sol-gel synthetic routes, emphasizing characterization of the new energetic materials.

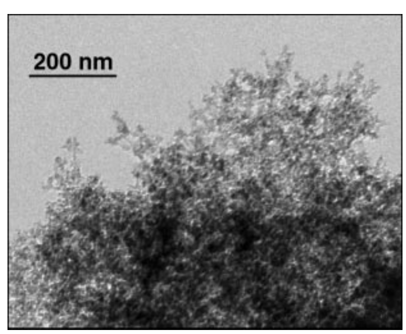

Ammonium perchlorate/ resorcinol-formaldehyde (AP-RF) nano-composite made by crystalling ammonium perchlorate within the pores of an organic gel. Resorcinol-formaldehyde is the classic polycondensation reaction for making organic nano-structures.

Production of High-Value Isotopically Separated Materials

K. F. Scheibner, B. Comaskey, M. J. Shaw, J. G. Wilder
98-ERD-072

The purpose of this project was to complete the development of the laser systems and separator systems needed to investigate the potential for the economical separation of high-value isotopes used in medical and industrial applications, then demonstrate this separation capability. The project was to focus on the isotopic purification of lead for use as solder in high-end electronics, and on the isotopic enrichment of thallium for medical applications. Ultimately the goal is to demonstrate the economical and technical viability of the technology for lead and thallium and to develop a more general capability for other possible isotope separation missions. Both lead and thallium are useful applications in this context because they require dye lasers, solid-state lasers, and a frequency doubling capability of some of the lasers. This later capability allows access to the wavelength range 250 to 450 nm, with tunable, high-power and high repetition frequency lasers. Until recently, these wavelengths have been largely inaccessible in combination with these other laser characteristics. In addition, up to two new potential laser-isotope separation applications would be conceptually developed through a process of needs analysis and technical feasibility studies.

Because of an unanticipated reduction in funding, the project had only enough funds to allow an orderly closeout of the research activities. Two key technical steps in the laser development were accomplished during the closeout phase, both of which are required for lead and thallium isotope separation. The first accomplishment successfully demonstrated the power scalability of a master-oscillator, power amplifier (MOPA) approach to a high-power Ti-sapphire laser host material. The net result output power produced, after a series of amplification stages, was around 50 W of tunable (red) laser light. In addition, the output power showed no signs of power saturation as the input power was varied. The demonstration verified the design intent of the amplifiers as well as that of the host material. This result is suggestive that greater than 100 W should easily be achievable from this laser architecture. Such powers are likely required for many applications such as efficient frequency doubling of red radiation to obtain blue, or near UV radiation, and for medium to large scale isotope separation.

The second accomplishment was the successful demonstration of a dye master oscillator that pulse-amplified, at pulse repetition frequencies greater than 10,000 pulses per second, an injected continuous-wave input signal with low-signal gains greater than 500. This is important to potential isotope separation missions (and other applications) that require narrowly tuned, high pulse repetition frequency dye laser light and would normally be the first step in a dye MOPA chain to achieve the required high average power. As part of this demonstration the low signal gain was measured as a function of pump pulse power and injected signal strength. Both measurements are required in order to specify the requirements for an eventual system that uses such a master oscillator.

Elastic Constants of Metals at High Pressures and Temperatures

C. S. Yoo, H. Cynn

98-ERD-059

The elastic properties of solids under high pressure are fundamental to our understanding of intermolecular potential, equations-of-state (EOS), melting, anharmonicity, and phase transition in condensed matter. Simple combinations of elastic constants, on the other hand, yield a wide variety of mechanical properties such as Young's moduli, shear moduli, bulk moduli, Poisson's ratio, etc. Therefore, elastic constants provide a way of correlating an atomistic theory to a macroscopic material model; this has long been a challenging problem in the physics of condensed matter. The elastic EOS data for metals at high pressures and temperatures are also of importance to DOE defense programs, where they are required for hydrodynamic simulations of the performance of conventional and nuclear weapons.

The conventional experimental methods for determining elastic constants use acoustic scattering of light or ultrasonic wave and are typically limited to transparent, single crystals at relatively low pressures below 10 Gpa (1040 atm); they are not applicable to either opaque metals or polycrystalline aggregates. Furthermore, these methods often require very specific orientations of single crystals in order to determine individual elastic constants.

Therefore, the purpose of this project is to develop a new experimental technique—stress- and angle-resolved synchrotron x-ray diffraction (SAX)—that can accurately determine single-crystal elastic constants from opaque and polycrystalline metals at high pressures and temperatures. We are emphasizing the study of transition metals, including iron and tantalum. Because the Earth's core is largely made of iron, the elastic properties of iron are fundamental to our understanding the internal structure and dynamics of the Earth's core. For example, the elastic constants and crystal anisotropy of iron at the temperature and pressure of the Earth's core are needed for quantitative interpretation of the observed seismic anisotropy, whereas the mechanical strength of iron at those conditions is fundamental to modeling geodynamics such as convection in the outer core and the rotation of the inner core. Tantalum, on the other hand, is a simple body-centered cubic (bcc) metal without any known phase change to 1000 Gpa. For tantalum, system theory can calculate the elastic constant reasonably well, and a new experimental technique can be developed. It is also a critical programmatic material whose elastic properties are needed to verify models used in current weapons' design codes such as Steinberg–Guinan's strength model.

In FY98, we made substantial progress in this project: (1) We developed the SAX, which is capable of determining elastic constants above 100 GPa and a few 1000 K from non-transparent polycrystalline samples such as tantalum. Our experimental concept for the SAX is shown in the figure. (2) We determined the bulk modulus of tantalum up to 200 GPa, which is the first angle-resolved measurement above 100 GPa. The angle-resolved x-ray data provide a more highly accurate relation of elastic constants than the conventional energy-dispersive x-ray diffraction. (3) We investigated the elastic constants and shear moduli of tantalum up to 60 GPa, thereby providing the first elastic data for tantalum above 10 GPa. These data are being used to understand the intermolecular potential for tantalum and to develop materials-strength models for various Laboratory programs.

Our elastic data may, however, contain a relatively large experimental uncertainty that is associated with the less well characterized stress of the sample in a diamond-anvil cell. To address this issue, we are developing an internal stress gauge.

In FY99, we will concentrate on determining the elastic constant of iron at Earth-core conditions (120 to 360 GPa and 2000 to 7000 K). The elastic properties of iron will provide constraints for quantitatively modeling the seismic anisotropy observed in the Earth's core and Earth's dynamo actions—such as the convection motion of the liquid outer core and the recently discovered rotation of Earth's solid inner core.

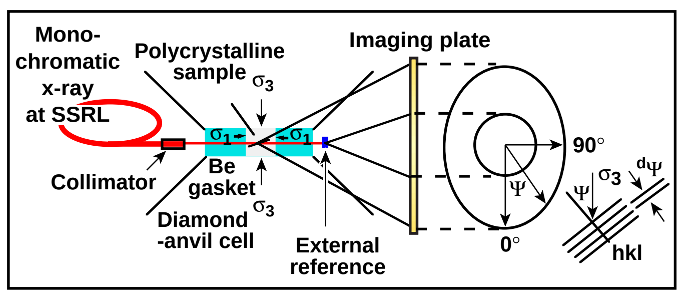

An experimental concept for stress- and angle-resolved synchrotron x-ray diffraction, using an x-ray source at the Stanford Synchrotron Radiation Laboratory (SSRL). The polycrystalline sample is contained in a very small hole (less than 20-μm diam) in a Be gasket without any pressure medium and is uniaxially compressed between two diamond anvils. The stress condition of the sample is then biaxial: the major stress (σ_3) along the axial compression direction and the minor stress (σ_1) along the radial direction of the gasket. In this case, the stress conditions of the sample will vary depending on their orientation and can be resolved as a function of angle (Ψ) between the σ_3 and the hkl-lattice normal. The elastic constants of the sample are then determined from the elliptically distorted strain (d_Ψ) and the stress condition (σ_3- σ_1) using angle-resolved synchrotron x-ray diffraction (SAX).

Research on the Potential to Engineer Grain Boundaries through Thermomechanical Processing

A. J. Schwartz, W. E. King, M. Kumar
98-ERD-080

Many important physical and mechanical properties of materials are known to be intimately dependent on microstructural features such as chemistry, grain size and shape, texture, and the presence of secondary phases and precipitates. Intercrystalline defects, such as grain boundaries and triple lines or junctions, have been observed to exert a significant influence on corrosion resistance, stress-corrosion cracking, creep, total elongation to failure, fracture, and the morphology and type of grain-boundary precipitates. Numerous reports in the literature have demonstrated that it is possible to exert control over the types of grain boundaries in the microstructure of different materials. Thus, in principle, these physical and mechanical properties could be tailored for specific applications in a manner similar to that used to modify microstructure through solid-state phase transformations.

The grain-boundary character distribution (GBCD) as measured by orientation imaging microscopy (OIM) is a microstructural feature that describes the proportions of "random" and "special" grain boundaries as defined by the coincident site lattice (CSL) model. Grain-boundary engineering involves thermomechanical processing, that is, deformation and annealing. During the annealing step, the intent is for special boundaries to replace random boundaries in the boundary network.

As part of this research, we investigated two fundamentally different approaches to the optimization of the GBCD. The strain-annealing treatment—which (because of low deformation strain) does not induce full recrystallization—has been shown to increase the special fraction and to reduce the average deviation from the exact "special" boundary misorientation. However, the strain-recrystallization sequences appear to be more effective in increasing the special fraction while reducing the grain size and the level of preferred orientation (texture). The GBCD of the as-received and strain-recrystallized copper are revealed in the OIM images of Fig. 1. The fraction of special boundaries, shown in color, is observed to dramatically increase during the sequential thermomechanical processing that constitutes the strain-recrystallization treatment.

We have demonstrated that the fraction of special boundaries in Cu can be increased through thermomechanical processing. Using commercially practical processing methods, we have shown that the special fraction increases from starting values of about 0.15 to over 0.70, while at the same time the grain size decreases and develops no significant texture. The new microstructure is composed of a network of random boundaries interrupted by special boundaries.

To further evaluate and understand the influence of processing on the GBCD of materials, we are investigating the widely used commercial alloy Inconel 600. In FY99, we will employ microstructural characterization with OIM as well as transmission electron microscopy (TEM) in order to understand the critical stages in the optimization process. Our early efforts will focus on the deformed state and the spatial distribution of the stored energy in the cold-worked material. We also plan to develop quantitative methods for describing the spatial distribution of triple junctions though their characterization and categorization.

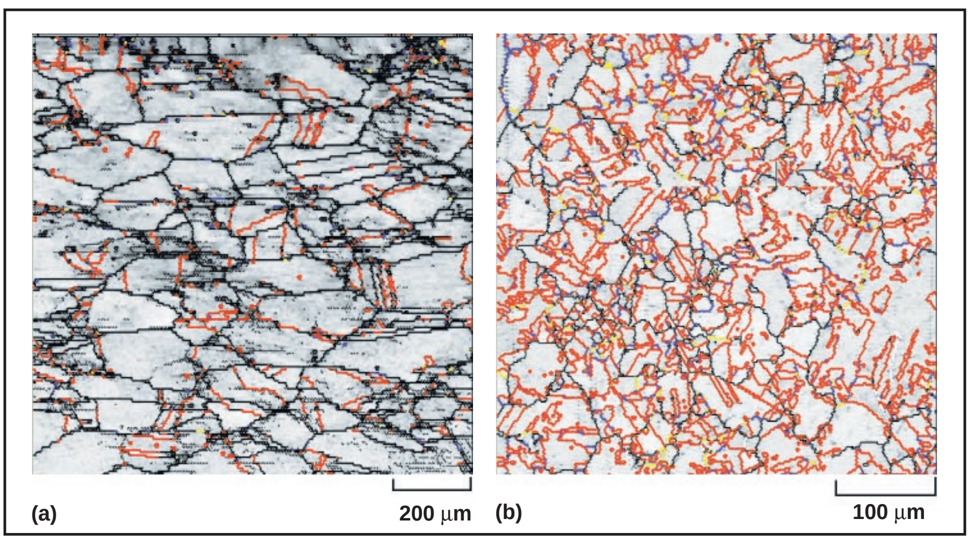

Figure 1. Orientation imaging microscopy maps of (a) as-received oxygen-free electronic (ofe)-Cu with a special fraction of about 0.15, (b) strain-recrystallized ofe-Cu with a special fraction in excess of 0.70. The fractions of special boundaries are shown in red; random boundaries are drawn in black.

New Si-Based Compound Clusters and Their Application in Field Emission Devices

M. Balooch, L. N. Dinh, W. McLean, II
98-LW-006

The work function of materials, defined as the minimum energy required to remove an electron from the material into the vacuum, plays a major role in the efficiency, durability, and economic viability of field emission devices. Field emission is defined as the emission of electrons from the surface of a condensed phase into a vacuum under high electrostatic fields. The emission current is exponentially dependent on the work function of the surface as well as on the applied field; the field strength can be enhanced by reducing the radius of curvature of the electron emitting surface (typically a "tip" with radius of curvature ~10 nm). Field emitting devices, will become very attractive economically and technologically for flat-panel displays if materials with stable and low work functions are used to realize extraction voltages of <15 V in a gated structure. This is especially true if one wishes to fabricate low cost planar emitters. Presently, extraction voltages up to 100 V are being used in gated (triode) devices and 300 V in ungated (diode) structures.

The purpose of this research is to produce and investigate the properties of the silicon/alkali metal/oxygen compounds films, consisting of small clusters with low work function (down to 1.2 eV). The small radii of curvature inherent to these clusters provides an easy path for emission of electrons in an electrostatic field. This, in turn, means that the conventional gated field emission structures could be drastically simplified, and the required sharp tips, which are extremely difficult to make, could either be relaxed or eliminated.

In FY98, we employed a physical thermal vaporization technique to produce films with nano- to micrometer-scale constituent clusters. Experimentally, a Cs dispenser is directed at a resistively heated Si vapor source which, in turn, is directed towards a substrate. A Cs/Si/O compound is formed by gas-gas collisions of the Cs/Si vapor with oxygen deliberately leaked into the synthesis vessel. The average size and composition of the clusters synthesized by this technique could be varied by controlling the Si source temperature, the oxygen buffer gas pressure, the source to substrate distance, or a combination of all of these parameters. The resulting films have the current-voltage characteristics needed for good cold cathode emitters.

The structure and size distribution of the clusters has been obtained by scanning probe microscopy (SPM). The complex indices of refraction and band gaps of the clusters have been derived from spectroscopic ellipsometry. The elemental and chemical composition of the clusters were monitored with Auger electron spectroscopy (AES) and x-ray photoelectron spectroscopy (XPS). Finally, the electronic density of states near the Fermi level, the absolute and temporal-spatial work function study of the clusters and their derivative films were examined by ultraviolet photoelectron spectroscopy (UPS) and photoelectron emission microscopy (PEEM).

In FY99, we will produce the compound clusters by pulsed laser deposition (PLD) technique that offers the possibility of providing smaller clusters. We will also continue the basic studies of the clusters to understand their chemical structure and electronic properties by using solid state nuclear magnetic resonance (NMR) spectroscopy, transmission electron microscopy (TEM), and synchrotron radiation. In addition, we will build a variety of field emission structures capable of low turn-on voltage to assist in the reduction of energy consumption in field emission devices and apply the technique to produce sensitive and stable x-ray detectors.

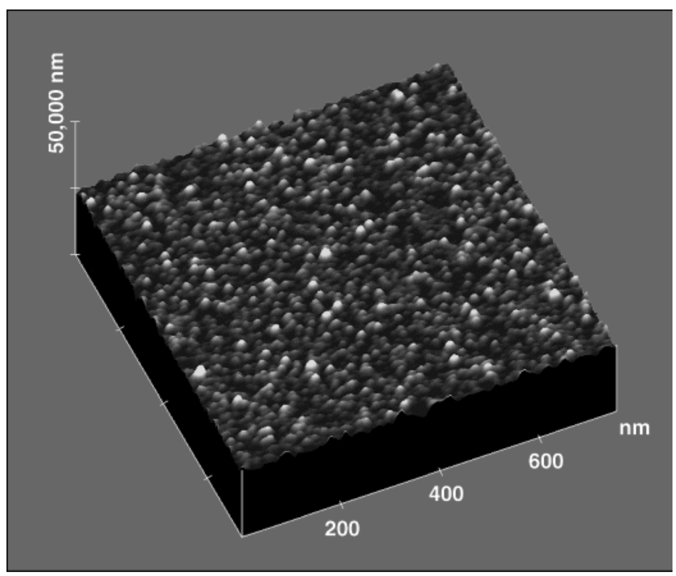

An atomic-force microscope image of low work function Si/Cs/O nanoclusters with average size of 5 ± 2 nm.

Semiconductor Quantum Dots for Advanced Blue Light-Emitting Devices and Laser Diodes

H. W. H. Lee

98-LW-058

Intense worldwide research and development underscore the importance of blue light-emitting devices (LEDs), which are critical to the development of advanced photonic devices such as full-color, flat-panel displays; optical memories; and ultrahigh-density, optical data-storage systems. Currently, the ZnSe and GaN material systems dominate the field. However, crucial obstacles remain for these materials. For example, growth-related defects—which arise from lattice-matching problems—degrade the devices, limit operational lifetimes, and increase costs.

Semiconductor quantum dots (QDs), which are nanometer-size crystals of semiconductors, represent a new material form. They present an innovative and potentially superior alternative to bulk material systems. The properties of QDs are highly dependent on their size because of quantum confinement, e.g., the color of light emission from QDs changes dramatically as their size changes. This allows simple control over the output color with a single material and enables higher performance than bulk materials. Advantages include higher emission efficiency, broader tunability of the output color, longer lifetime, simplicity of processing, miniaturization, and lower cost. Our goal is to understand the fundamental properties of QDs and to apply this knowledge to the development of advanced blue LEDs and laser diodes that exploit the unique optical and electronic properties of semiconductor QDs.

During FY98, we developed in-depth understanding of the fundamental properties of Si, Ge, ZnSe, and GaN QDs. An important aspect of QD physics concerns the dependence of the QD energy gap (which relates to the color of light emission) with QD size. This is particularly relevant to the design of QD light-emitting diodes (QD–LEDs) and lasers because it specifies the QD size needed for a specific light emission or lasing color. We found that for these QDs, the energy gap is poorly described by simple effective-mass theories, which have been commonly used. Instead, our results corroborate more recent pseudopotential calculations.

We also performed power-dependent and femtosecond spectroscopy on Si and Ge QDs; our results directly affect our design of QD–LEDs and lasers. Power-dependent spectroscopy shows that photoluminescence (PL) below the energy gap saturates at high excitation powers, whereas band-edge PL does not. This suggests that the saturated peaks arise from traps, in turn implying that high optical power densities saturate traps and favor band-edge emission. Our femtosecond spectroscopy results corroborate these findings. At high excitation powers, a fast initial decay dominates—this fast decay results from the relaxation of multiple excitations near the QD band edge and confirms that high optical power densities saturate traps and favor band-edge emission.

Our results profoundly affect the fundamental understanding and design of LEDs and lasers based on QDs. The spectral output of these LEDs can be tuned by quantum confinement and traps. Since band-edge emission dominates at high power densities, QD lasers will preferentially emit near the band edge regardless of the traps present. LEDs, which operate with lower optical power densities, can emit either near the band-edge or from traps.

Finally, based on the new QD physics we advanced, we successfully fabricated and demonstrated the operation of the world's first and only blue QD–LEDs. The active layer of a multilayer device was comprised of Si or Ge QDs dispersed in a polymer matrix. Indium tin oxide and aluminum served as the anode and cathode, respectively. The turn-on voltage was as low as 2 to 6 V— the lowest turn-on voltage for blue LEDs of this kind (suggesting the first real possibility for battery operation of these blue emitters). A blue QD–LED that we fabricated with Si QDs is shown in the figure.

In FY99, we will (1) expand our understanding of the physics of semiconductor QDs, focusing on their light-emitting properties (particularly in the blue); and (2) develop designs for and demonstrate milestones leading up to the proof-of-existence of a blue QD laser. A blue QD laser will enable many future photonics technologies; its realization is critical and has yet to be demonstrated.

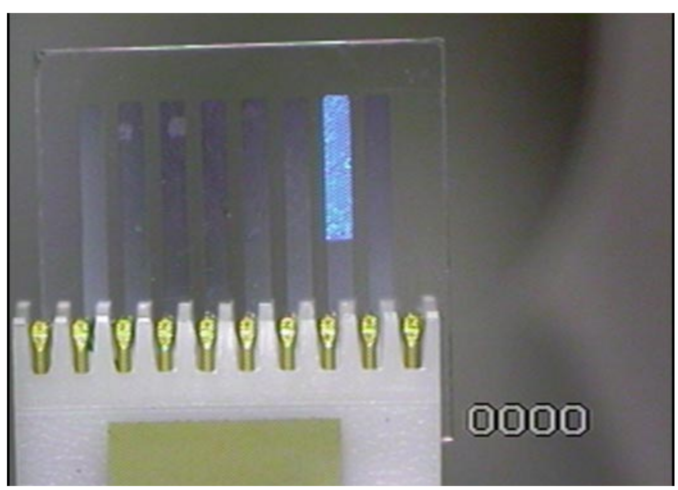

Blue light-emitting diode fabricated with Si quantum dots.

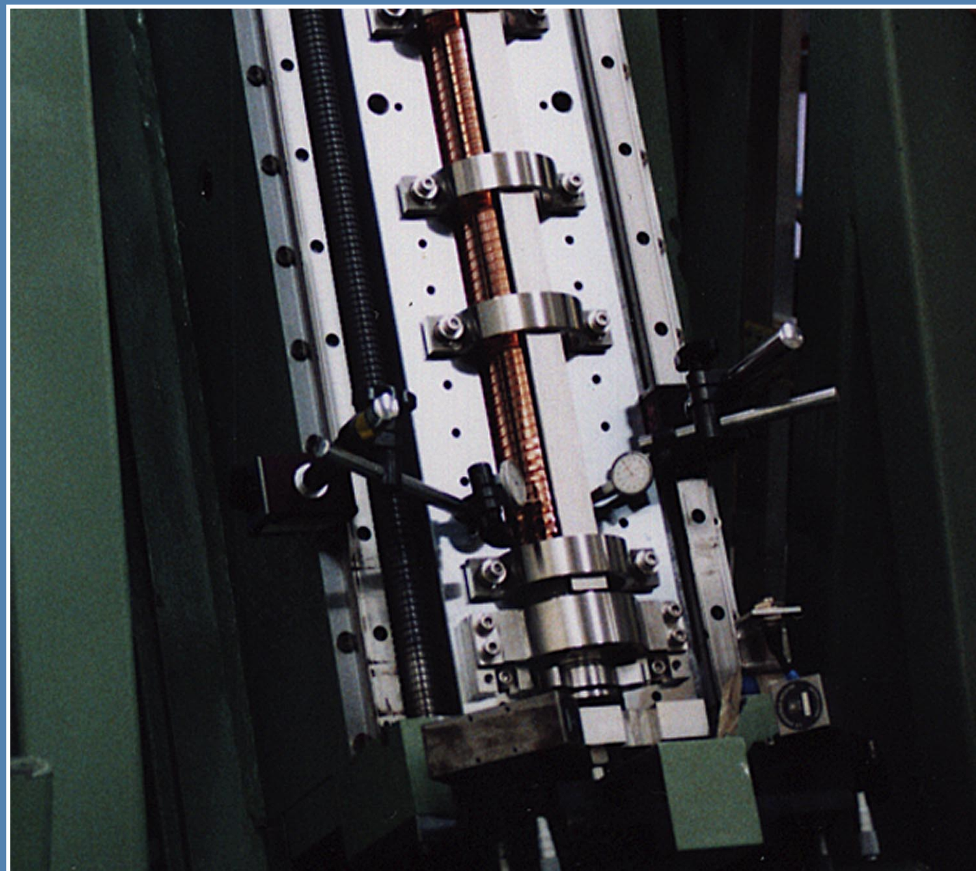

9

Nuclear / Atomic Science and Technology

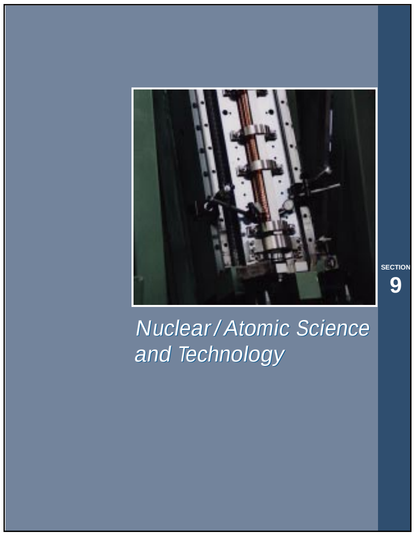

About the preceeding page

Intense Laser-Electron Beam Interactions. Karl van Bibber and his team are developing a world-leading program on intense laser-electron beam interactions, focussed toward next generation light source and advanced accelerator research, which involves multiple LLNL directorates and university collaborations. The figure shows a prototype 1.8-m X-band (11.4 GHz) accelerator structure. The more than 200 cells, fabricated at LLNL with different critical internal dimensions, are stacked with micron-level alignment tolerances. Vacuum-diffusion bonding near 1000˚C will produce a monolithic precision structure. See page 9-6 for further information.

Studies with Highly Charged, Ultracold Ions: Binary Mixtures

L. Gruber, J. Steiger, B. R. Beck, D. Schneider, J. P. Holder, D. A. Church
96-ERD-052

The electron-beam ion trap–cryogenic Penning trap (EBIT–RETRAP) facility at LLNL offers a unique opportunity for investigating highly charged ions and one- and multicomponent plasmas at very low temperatures (<10 K) and in a quiescent environment. EBIT is an unique ion source that allows us to produce high-charge-state ions, up to U^{90+}. The development of efficient cooling schemes for ions confined in storage rings and ion traps has enabled precision measurements that have greatly improved our understanding of basic atomic physics, collisions, and charge-exchange processes, as well as of the behavior of strongly coupled, one-component plasmas. The concept of extracting from EBIT and trapping highly charged ions in a Penning trap is new, and cooling of ions at rest allows spectroscopy in a new regime of precision. Multicomponent, strongly coupled plasmas—which are of considerable interest in an astrophysical context—have not been studied experimentally at all because of experimental and technical difficulties. For example, to create a low-temperature binary ionic mixture in a Penning trap, the mass-to-charge ratios of the ion species must match; otherwise, a centrifugal separation of the plasma will take place before the plasma becomes strongly coupled. This difficulty can be avoided by using highly charged ions. Unfortunately, the most effective cooling technique, laser cooling, cannot be applied to high-charge-state ions because of a lack of suitable transitions accessible with lasers.

The initial phase of the experiment was concerned with optimization and improvement of the ion confinement. This has been accomplished, and up to 1000 highly charged ions can be confined for longer than 1000 s. We implemented a sympathetic cooling scheme at RETRAP. In brief: First, Be^+ is caught and confined in the trap. Then, the ions are cooled electronically with a tuned circuit and optically by a laser. Highly charged ions are merged into the cold Be plasma, and energy is exchanged by collisions—thereby reducing the kinetic energy of the highly charged ions to the temperature of the Be plasma.

In FY98, we successfully applied this cooling scheme for highly charged ions to Xe^{44+} ions. A charge-coupled device (CCD) camera, placed in the radial plane of the trap, was used to image the plasma—which consisted of Be^+ and Xe^{44+}—by measuring the scattered photons from the Be. The figure shows a typical image. These data, in combination with plasma-composition measurements obtained with a tuned circuit detector, revealed the number of ions (10^5 Be^+ ions, 400 Xe^{44+} ions) as well as the Be^+ density. By measuring the Doppler-broadened line width of the cooling transition and observing a centrifugal separation, we could establish an upper temperature limit of 1.7 K. By applying a fluid model for the plasma, we estimated the density of the highly charged ions (Xe^{44+}) to be greater than 3×10^7 cm^{-3}. These parameters indicate the formation of a strongly coupled, highly charged ion plasma. The Coulomb coupling parameter (the ratio of kinetic to potential energy) is greater than 1000 under these conditions, possibly enough to force the ions into an ordered structure.

This work accomplished the first experimental demonstration of the formation of a mixed, strongly coupled ion plasma using a sophisticated, sympathetic cooling scheme and state-of-the-art trapping techniques. It opens up new research possibilities—experimental verification of binary ionic mixtures can serve to benchmark astrophysical plasma modeling, and cooling of highly charged ions allows unprecedented precision in laser spectroscopy and may be useful for coherent quantum control experiments.

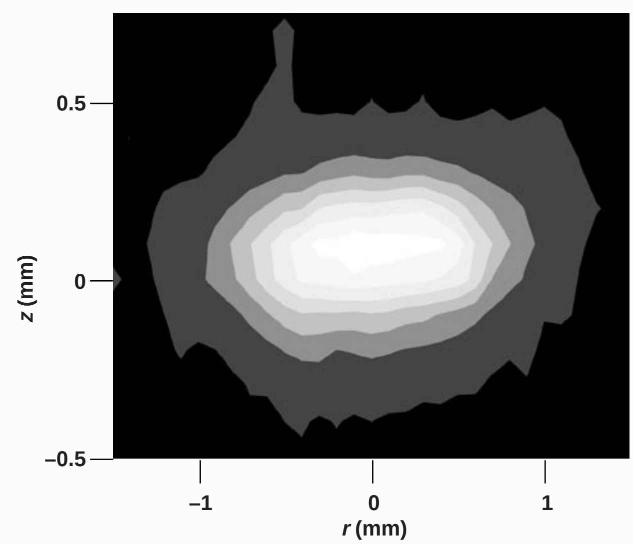

A cryogenic charge-coupled device (CCD) camera is used to gain information about the spatial distribution of trapped Be^+ ions. The image shown here is a side view of the plasma cloud. The elliptical shape can be used to determine the Be^+ density, which is constant over the full extent of the cloud. The total number of ions in the cloud can then be determined by measuring its size.

Proton Radiography for the Advanced Hydrotest Facility

E. P. Hartouni, M. Aufderheide, P. D. Barnes, Jr., R. Bionta, P. H. Park, R. Porata, D. Wright
97-ERD-058

Proton radiography is a technique for studying the dynamics of imploding systems. High-energy protons (>1 GeV) illuminate the object, are absorbed and scattered by it, are brought to a focused image by a magnetic lens systems, and then are detected by a set of integrating, imaging detectors. Proton radiography offers mature source technology, long interaction lengths, high detection efficiency, and multiple types of radiographic information. Therefore, LLNL has been actively exploring the fundamentals of proton radiography in order to develop applications for the Advanced Hydrotest Facility (AHF), which will be designed—as part of LLNL's Stockpile Stewardship Program (SSP)—to determine primary yield, study weapons safety, and provide data on various related physics questions.

Our purpose is to assess the science of proton radiography as a tool for doing experiments involving time- dependent hydrodynamics of imploding systems. Our experimental program is directed at producing data and technology relevant to hydrotests. At Brookhaven National Laboratory (BNL), we are trying to understand the limits, if any, to high-precision, quantitative radiography. These experiments utilize *static* objects chosen to provide data on radiographically derived measurements of density and material composition. At the Los Alamos National Laboratory's Los Alamos Neutron Science Center (LANL/LANSCE), we are conducting experiments with *dynamic* systems aimed at developing framing-camera systems and providing information regarding the hydrodynamics of shocked metal–gas interfaces.

In FY98, we focused on analyzing data we gathered as part of the BNL experiment E910 collaboration. The goal of experiment E910 was to investigate the production of strange particles in the interactions of protons with nuclei. We have concentrated on the general features of these interactions because of their relevance to proton radiography, which can then be applied to proton radiography. These data (1) have indicated that secondary-particle production from the inelastic interaction of the protons with the object will result in less than 1% image backgrounds—negligible at angles comparable to multiple-beamline facilities, and (2) are an important benchmark for computer codes (being developed at LLNL as part of this project) to simulate the production of secondary particles. These codes, which will be completed in FY99, provide a computational tool for studying detailed radiography setups and understanding our various experiments.

Another basic science experiment is being performed by our group at BNL—experiment E943. The central goal of this experiment is to determine the absorption cross sections of proton–nucleus interactions to less than 3% for a number of materials spanning the periodic table and for energies from 1 to 10 GeV. These cross sections are important for making accurate estimates of the performance of proton radiography and for planning experiments.

In another set of experiments being performed in collaboration with scientists at Los Alamos, we are using the multiple-time-frame capability of the Line-C proton radiography facility (see figure) to study the dynamics of high-explosive-shocked metals. The goals are to measure density evolution, surface definition and velocity, and composition of the metallic surface. These experiments were designed and built during FY98 and will run through FY99.

We are also developing instrumentation and detectors that are crucial to the use of proton radiography. Our detectors, which are being used in the LANSCE experiments, include (1) static charged-coupled device (CCD) camera systems to obtain single, high-resolution images; and (2) a "line out" streak camera to measure proton intensity along a line for a maximum of 256 time frames with 150-ns spacing. These camera systems are designed to image either a plastic scintillator fiber bundle (to measure proton intensity) or a Xerogel Cerenkov radiator (to measure proton energy loss through the object). The Xerogel was developed at LLNL specifically for this experiment. Further detector development through FY99 includes a prototype of a two-dimensional streaking camera as well as variants on the Cerenkov-imaging camera systems.

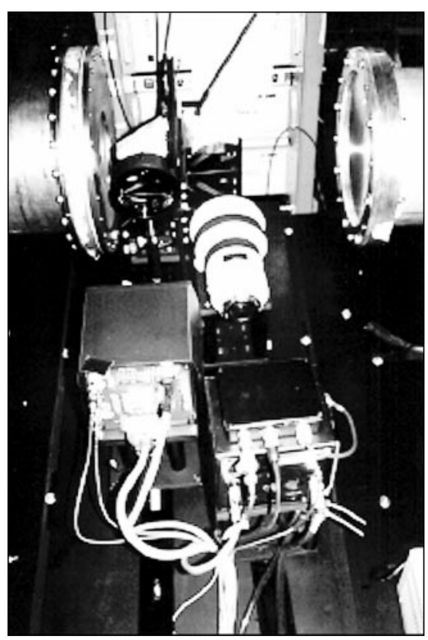

Our charge-coupled-device (CCD) and one-dimensional streak cameras in the Los Alamos Neutron Science Center C-line proton radiography facility. The proton beam enters from the left, traversing a plastic scintillator-fiber bundle. The streak camera on the left side records the motion along a vertical line. The CCD camera on the right records a single, high-resolution image.

Imaging Techniques for X-Ray Computed Tomography in Limited Data Environments

D. M. Goodman, J. A. Jackson, M. B. Aufderheide, E. M. Johansson
97-ERD-085

There is an increasing requirement throughout LLNL for nondestructive evaluation using x-ray computed tomography (CT); efforts include DOE's Enhanced Surveillance Program (ESP), the Advanced Hydrotest Facility (AHF), scanning waste drums, and photothermal radiometry. Conventional CT methods are non-iterative algorithms that require low computational effort, but are not sufficiently adaptable to incorporate prior information or non-Gaussian statistics. Frequently, restrictions on acquisition time, geometry, and budgets prevent acquiring projection data over enough views to achieve desired resolution. Conversely, most iterative algorithms use methods that converge very slowly, if at all. Our goal was to develop limited-data CT reconstruction tools and demonstrate their usefulness on a variety of LLNL problems.

This year, we continued developing reconstruction tools and demonstrated their effectiveness on several important problems. Our ability to solve difficult tomography problems is the result of two specialized optimization algorithms that we have developed. The first is an extension of the conjugate gradient algorithm that incorporates bound constraints on the variables. This constrained conjugate gradient (CCG) algorithm is unique in that it incorporates a bending linesearch, which permits multiple bounds to be attained during a single iteration. The second algorithm is a limited-memory quasi-Newton (QN) algorithm that also permits bounds on the variables. This year, we completed implementing the QN algorithm.

We also completed work on and demonstrated the usefulness of robust tomography. In a simulated example involving outliers, our robust technique reduced root-mean-square error between reconstruction and true object by a factor of two. Although robust statistical methods have been applied to a variety of problems, to our knowledge, this is the first application to tomography. Several tomography problems are plagued by outliers: our methods show promise for solving many real problems.

The application of emission tomography to characterize mixed waste drums has been studied at LLNL for several years. Our active and passive computed tomography (A&PCT) technique first uses active tomography to map the attenuation within a waste barrel. This attenuation map defines the matrix for the passive or emission tomography problem. Our new techniques gave us the flexibility to implement the correct likelihood function, thereby greatly reducing bias in the waste assay. This also gave us the opportunity to demonstrate the effectiveness of our techniques for general emission tomography problems.

LLNL is developing a high-energy (10-to 15-MeV) neutron imaging system for use in support of the ESP. This approach is a powerful technique for probing dense objects that may be opaque to x rays and lower energy neutrons. Imaging experiments using neutron radiography were conducted in FY98 at the Ohio University Accelerator Laboratory; our techniques gave significantly better reconstructions than conventional filtered back projection.

Last year, we adapted our CCG algorithm to cone beam tomography problems. This year, we used the resulting algorithm, CCG-Cone, for extensive studies of limited-view reconstruction for the AHF. The CCG-Cone has been indispensible in these studies, which have allowed the AHF design group to make recommendations on the number of views needed and their placement. In addition, CCG-Cone has been used to study the effect of constraints on reconstruction quality. A judicious use of constraints will help the AHF to achieve its objectives. More programmatic work will continue in this area.

In collaboration with other institutions, including the University of California, Irvine Medical School, and the University of Texas at Austin, we continued to apply our optimization-based methods to pulsed photothermal radiometry. This tomographic method inverts data from the time evolution of the heat equation to see inside an opaque object. This year we obtained the first high-quality 3-D images of port-wine-stain blood vessels.

We will continue refining our algorithms and applying them to practical problems. Immediate plans include parallelizing the algorithms, refining forward models, and including a point-spread function for the AHF problem.

Uncharted Frontiers in the Spectroscopy of Highly Charged Ions

P. Beiersdorfer
97-ERD-103

The Laboratory is at the forefront of producing and trapping ions of any element and charge state, which in principle can be used for previously impossible experiments. New capabilities would enable definitive tests of fundamental theories, including quantum electrodynamics and nuclear structure theory, and provide the basis for developing new diagnostic techniques of high-temperature plasmas such as those generated with the National Ignition Facility (see figure). To exploit this unique availability of trapped ions and this potential for basic and applied research, we need innovative and sophisticated spectral diagnostics that are tailored to the source. Many areas of atomic physics that have been opened up by Livermore's ion production facilities have not yet been accessible to scientific scrutiny. For example, we can produce copious amounts of hard x-rays from the K-shell emission of heavy ions stripped to one or two electrons, but the spectrometers to measure such radiation and resolve individual transitions do not exist. Similarly, knowledge of the natural line shape of x-ray transitions used as diagnostics on the Nova laser are crucial for accurate determinations of the density and temperature; however, no measurement of the natural line shape under controlled laboratory conditions exists. Spectral line emission in the extreme ultraviolet represents a prime source of information about astrophysical plasmas surrounding cataclysmic variables and the interstellar medium; again, no controlled laboratory measurement capabilities exist for the required densities and charge states.

We are systematically creating new research tools tailored to Livermore's novel ion source that enable entirely new classes of measurements. We constructed the first high-resolution hard x-ray spectrometer to measure individual lines from highly charged heavy ions, improving the resolving power with which such lines can be measured by more than an order of magnitude. In FY98, we used this unique instrument to determine the electron-impact excitation cross sections of the K-shell lines from one-electron Xe^{53+} and two-electron Xe^{52+}. Such measurements were previously possible only for elements with half the atomic number. We found that the cross sections are strongly influenced by the magnetic interaction between the bound and free electron. The interaction is much stronger than was predicted by Livermore calculations, thus stimulating the development of improved atomic physics computer codes. Efforts are now under way to determine the effects of the magnetic interaction on dielectronic recombination in such high-energy systems.

We constructed very high-resolution spectrometers to measure the line shape of the lines used as spectral diagnostics in laser fusion. The technique was demonstrated on the most prominent L-shell x-ray transition in neonlike cesium. In FY99, we will apply this technique to neonlike xenon and heliumlike argon, the two gases most often used as line shape diagnostics in laser fusion. These new instruments have also yielded the world's best determination of energy shifts due to quantum electrodynamics in heavy nuclei.

In FY98, we constructed the first spectrometer to investigate transitions from iron, tungsten, and uranium in the extreme ultraviolet under controlled laboratory conditions from low-density plasmas. The measured line intensities are in some cases dramatically different from those calculated in standard spectral models. This will undoubtedly result in a revision of these models.

The capabilities created under this LDRD project have dramatically strengthened the experimental core competencies in basic atomic physics and our readiness for evolving programmatic needs. They have been the basis for nearly a dozen scientific publications, including one Ph.D. thesis, and have served to train several graduate students and post docs. Our research is providing new spectral diagnostics for NIF, unsurpassed benchmarks for basic atomic and nuclear physics, and the database for the analysis of astrophysical x-ray spectra.

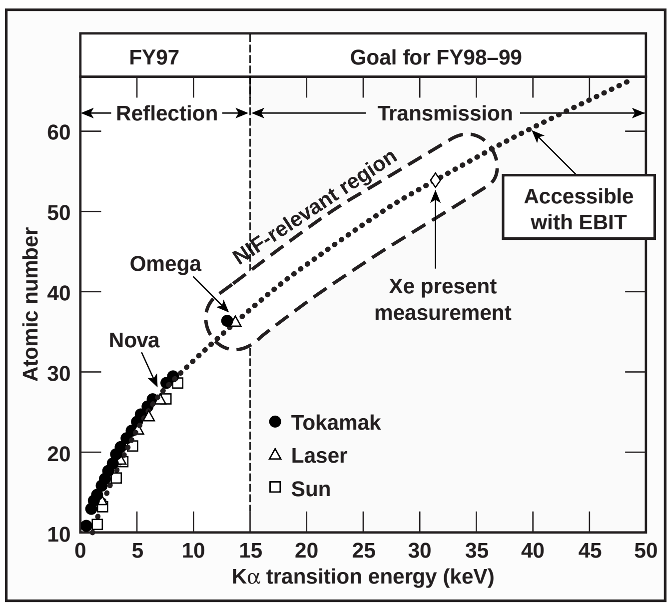

Energy of the K-shell emission lines for different elements. Present-day plasma sources, such as tokamaks, the Nova and Omega lasers, and our Sun, have produced x-ray energies up to 15 keV from elements with atomic number as high as krypton ($Z = 36$). This is a first-ever measurement for xenon at an x-ray energy of 31 keV, paving the way for similar measurements on NIF.

Development of Short-Pulse, Laser-Pumped X-Ray Lasers

A. L. Osterheld, J. Dunn
97-ERD-105

We are developing transient collisional excitation (TCE) x-ray lasers excited by picosecond optical lasers. These TCE lasers can be pumped at high repetition rate with tabletop laser systems; they have applications in imaging and diagnostics of high-density plasmas, in chemistry and material science, and in x-ray lithography. During the second year of our project, we improved the COMET laser facility (a compact multipulse terawatt laser system) and developed a series of efficient x-ray lasers that are well matched to multilayer x-ray optics. In addition, we reduced the energy required to produce these lasers, and experimentally and theoretically characterized their behavior. In the third year of the project, we will increase the energy output of the x-ray lasers and use them for plasma imaging experiments to systematically test predictions from hydrodynamics codes. These experiments will validate the codes used to design and analyze laboratory experiments in the Stockpile Stewardship program.

The TCE scheme is highly efficient because it separates the formation of the plasma amplifier from the production of high gains, and allows these processes to be optimized separately. Our implementation of the TCE scheme uses a low intensity, long pulse laser to produce the plasma amplifier, and a high intensity, picosecond laser to rapidly heat the plasma and pump the lasing transition. The plasma is formed by heating a material to a modest temperature and waiting approximately a nanosecond for the plasma to expand to the appropriate density (about 100–1000 times less dense than a solid). A lot of energy is saved by not heating the plasma to high temperatures during the expansion phase. Because the excitation pulse heats the plasma on a time scale shorter than the relaxation times of the plasma, very large transient gains can be produced. These gains are about 10–100 times larger than the quasi-steady state gains produced when the plasma is heated slowly.

Our experiments are conducted on the COMET laser facility. This laser has two arms driven by a common oscillator. These arms can deliver 7.5 J in 0.5–3 ps, and 15 J in 500–800 ps. The long pulse arm was added during this year. Previously, low energy pulses of the nearby Janus laser were used for the plasma-forming beam. Combining the two arms into a single laser system eliminates problems with fluctuations in the timing of the two laser pulses, enables the x-ray laser work to progress year round, and allows the Janus laser to be used to create a separate plasma for some of the plasma probing experiments.

During the past year, we have developed a series of TCE lasers using low-*Z* nickel-like ions (elements ionized until they have 28 electrons remaining). These lasers have wavelengths between 100–200 Å; a band well matched to current high quality multilayer optics. These lasers can be created with as little as a joule of energy, and are the brightest lasers in this band that have been produced with tabletop pump lasers.

We have characterized the output of these TCE lasers as a function of the energies in the plasma formation and excitation laser pulses, as well as the temporal separation of the two beams. The output of the x-ray laser depends critically on these parameters, and the details depend on the element that comprises the x-ray laser. We have modeled these results with a one-dimensional hydrodynamics and atomic kinetics code coupled to a transient ray tracing post-processor. The careful experimental characterization and theoretical analysis has allowed us to increase the efficiency of these lasers.

The emphasis in the third year of the project will be to apply the TCE lasers to plasma imaging. Because the brightness of these lasers is critical to many applications, we will also continue to improve the performance by the use of structured targets and a travelling wave line focus. Initially, we will use the x-ray laser in combination with multilayer mirrors to probe the x-ray laser plasma itself. In later experiments, we will use the x-ray laser to probe a separate plasma. These experiments will be used to test predictions from hydrodynamics codes. In these experiments, the short pulse of the x-ray laser is important, as it allows the dense, rapidly moving part of the plasma to be probed.

Intense Laser-Electron Beam Interactions

K. A. van Bibber, J. L. Klingmann, T. E. Cowan, T. R. Ditmire, G. P. Le Sage
97-SI-001

The next decade promises to usher in what will be one of the most exciting chapters in the history of science. The Standard Model of particle physics, which describes the fundamental constituents and forces of the Universe, has been found to be in perfect agreement with all experimental data for the last quarter century. Despite its uncanny success, however, it is known that the Standard Model is incomplete and new physics will very likely be discovered in the energy range between a hundred billion and a trillion electron volts (TeV). Proton colliders, such as the Fermilab Tevatron that discovered the top quark, or the Large Hadron Collider under construction at the European High Energy Physics Laboratory (CERN), will likely see the first evidence of this new physics, but a high-luminosity TeV-scale electron-positron linear collider will be required for detailed high-precision studies. Such a linear collider would be the most technologically challenging accelerator ever built, requiring bunches of electrons and positrons to be accelerated down opposing 15-km long linacs, squeezed down to 5 nm, and brought into collision. In order to be able to accelerate the electrons and positrons without emittance growth, the technical specifications for the linac structures are very demanding and require precision manufacture. However, advanced manufacturing development will also be required if the 20 km of structures are to be affordable.

Towards this end, we have partnered with the Stanford Linear Accelerator Center (SLAC) and the Japanese High Energy Accelerator Research Organization (KEK) to carry out R&D on X-band (11.4 GHz) accelerator structures, both to test the performance of new electromagnetic designs and to develop innovative manufacturing strategies for them. Our principal milestone in FY98 was a joint-venture prototype 1.8-m structure. LLNL developed the procedure and carried out the diamond-point machining of more than 200 copper cells, each slightly different in critical dimensions, with micron-level tolerances. KEK developed the procedure and carried out the vacuum diffusion bonding of the cells into a monolithic structure, to achieve alignment tolerances also at the micrometer level (see figure). SLAC completed the structure and will be the site for all microwave and beam-based performance studies.

Additionally, we have conceived of an entirely new mechanical design for the structure that could dramatically reduce the amount of precision machining required. In FY99, we will make several sub-structure prototypes to test this concept.

We have also investigated acceleration schemes based on lasers rather than conventional microwave power sources. In FY98, as part of experiments where the PetaWatt laser was focused onto solid targets to observe high energy electrons, we discovered the phenomenon of laser transmutation. In this process, bremsstrahlung from high energy electrons induces photoneutron and photofission processes within the target itself, which were detected by off-line gamma spectroscopy. Significant progress was also made to begin systematic studies in laser acceleration.

In FY99, we will focus on the upgrading of the 100-MeV linac with a low-emittance electron source, and the completion of the Falcon ultra-short pulse laser. The marriage of these two provides the tool for systematic studies in the interaction of intense laser and electron beams. These include both experiments in ultra-high gradient acceleration, as well as production of sub-picosecond hard x-rays for basic materials science and programmatic applications.

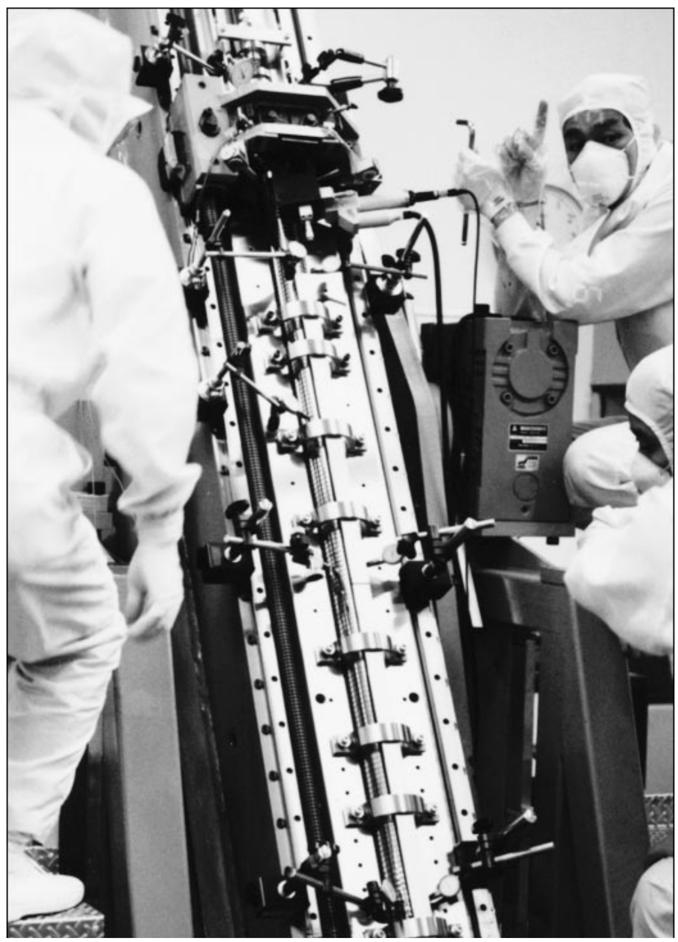

A prototype 1.8-m X-band accelerator structure being prepared for bonding. The more than 200 cells, fabricated at LLNL with different critical internal dimensions, are stacked with micron-level alignment tolerances. Vacuum-diffusion bonding near 1000˚C will produce a monolithic precision structure.

Full-Volume-Imaging Gamma-Ray Detectors for Enhanced Sensitivity

K. P. Ziock, D. Archer, A. Dougan, J. Luke, L. Nakae
98-ERD-025

Smuggling of special nuclear materials (SNM) is of overwhelming concern since the cost of successful delivery of even one nuclear device is staggering. Although SNM can be located by detecting the penetrating gamma radiation that it emits, this signal may be shielded so that it is weaker than the natural radiation background. To improve the sensitivity of gamma-ray detectors, we are developing a prototype full-volume gamma-ray imager. If successful, this detector will significantly enhance the sensitivity of gamma-ray detection equipment by obtaining information on the direction of arrival of each gamma-ray photon. We can then distinguish the background radiation, which will be distributed over all space, from the smuggled materials, which will appear as a localized "hot-spot."

To achieve real images at the gamma-ray energies of interest (~0.2 MeV to 2.0 MeV), we take advantage of the fact these photons can "bounce off" electrons (i.e., Compton scatter). By measuring the energy of the recoiling electron and the energy and direction of travel of the recoiling gamma ray, we can reduce the incident direction of the initial gamma ray to a narrow ring that is typically less than a percent of the area of all possible incident directions. To take full advantage of Compton scattering requires a detector that is sensitive throughout its volume to the energy deposited by both the recoiling electron and gamma ray and that provides the location and energy of each interaction site. We will achieve this through the use of a noble gas-time-projection chamber.

We began with a design study of the detector; our goal was to develop an experimental test bed the following year. Several research issues have been investigated. Of particular concern to such a device is understanding the signature of the recoiling electron as it traverses the gas. Ideally, if we can detect the track it leaves behind, then we can further reduce the possible incident directions of the initial gamma ray from a ring to an arc, further improving sensitivity. The electron's range will be an inverse function of gas pressure, decreasing as the gas pressure is increased. However, the likelihood that a gamma ray will interact in the detector and be measured is an increasing function of the gas pressure. We must balance the ability to localize the incident gamma ray against the possibility of not detecting it at all. The first result obtained from the simulations is that the traditional modeling codes derived from high energy physics—GEANT (a detector description simulation tool) and EGS (electron gamma shower)—are not well benchmarked to experimental data at the lower electron energies of our interest (~100 keV) and disagree at the 25% level. However, the results are sufficient to show that a position resolution of order 300 µm (our target resolution) will allow us to restrict the incident direction of many of the incident photons to less than a full ring.

To fully understand the sensitivity trade-off, we must understand the background signature. Our modeling effort includes a study of how to best find a point source in a diffuse background, given the ring-like signature of the individual photons. An example of that work is shown in the figure below, where just 25 source photons are overwhelmingly visible in a diffuse background of 300 photons.

In FY99, we will extend our work to the laboratory, where we are developing a prototype detector to verify the simulations. We will focus on understanding the physics requirements that drive the design criteria (gamma-ray stopping power vs position resolution). This work will involve both additional simulations and laboratory experimentation.

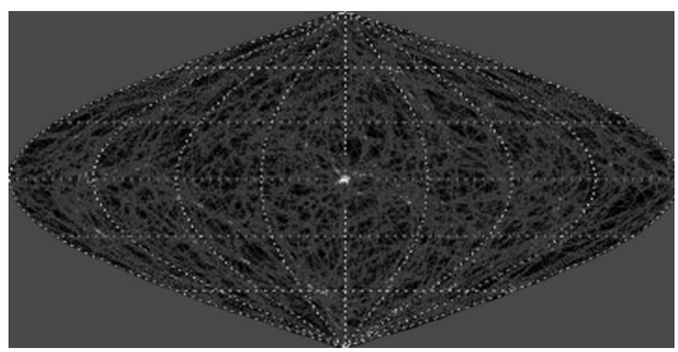

Grayscale image of a point source of radiation (25 photons) in a distributed sea of 300 photons. The source is seen as the white spot in the center. All possible directions are shown in the plot, which is a theta, sin theta representation of the entire "sky."

Mapping of Enhanced Nuclear Stability in the Heaviest Elements: Identification of Element 114

K. J. Moody, R. W. Lougheed, J. F. Wild, N. J. Stoyer, M. A. Stoyer
98-ERD-050

In 1989 and prior to this LDRD project, we began a collaboration with scientists at the Joint Institute for Nuclear Research (JINR), Dubna, Russia, to search for and map out a region of enhanced nuclear stability against spontaneous fission, predicted to fall around the nucleon numbers $Z = 108$ and $N = 162$. In the succeeding years, we were successful in discovering isotopes of elements 106, 108, and 110 with lifetimes of up to five orders of magnitude greater than they would have had if there were no enhanced stability. Furthermore, our work established that the center of the region of enhanced stability matched the modern predictions. Our discovery of the mass-273 element 110 isotope may have earned LLNL a share of the credit for discovery of the element.

We are continuing our collaboration with the Russian scientists at JINR. We are performing experiments to discover and characterize very heavy isotopes around the magic nucleon numbers $Z = 114$ and $N = 178$ to 184. In contrast to the deformed $N = 162$ nuclides, these nuclides are representative of the next higher spherical doubly closed shell nucleus, the higher homolog of ^{208}Pb. Measurements of the nuclear decay energies and lifetimes in this region will be of substantial value in characterizing the behavior of very heavy nuclei; this region has been investigated for many years using only theoretical methods. In common with previous experiments in this collaboration, this is a high-risk experiment, which aims for a major scientific discovery.

In the principal experiment, we will bombard a target of ^{244}Pu with ions of the rare isotope ^{48}Ca to produce the compound nucleus [114]-292, which comes as close to landing directly at the center of the "Island of Stability" as can be done with today's technology. Due to the unusual stability of the ^{48}Ca projectile, we can form a compound nucleus with considerably less excitation energy than the other reactions we have used, which increases its chances for survival greatly as it de-excites. We expect that between two and five neutrons will evaporate from the compound nucleus to leave the residual nuclei that we intend to observe. These product species will recoil from the target into the Dubna gas-filled separator, which kinematically isolates the compound-nucleus residues from other reaction products and the unreacted beam particles and directs them into a detector array. The time- and position-correlations of the implanted residues and their subsequent decays, combined with the suppression of background events due to the action of the separator, allow us to unambiguously identify products introduced into the detector array at a rate of less than one atom per month.

In FY98, in preparation for the main experiment, we bombarded targets of ^{232}Th and ^{238}U with ^{48}Ca ions. The purpose of these experiments is two-fold: to study the performance of the separator with reacting systems kinematically similar to that of the main experiment, and to try to measure the cross sections of reactions of ^{48}Ca ions with actinide targets, which are currently unknown. The evaporation products arising in these experiments are also previously unknown nuclides, and their detection and characterization would provide additional information on the structure of the lower edge of the new region of spherical nuclei; analysis of these data is in progress. We are responsible for supplying the exotic isotope ^{244}Pu for the targets; the material has been purified, packaged and sent to Dubna, where it is being fabricated into targets. We are also responsible for a data-acquisition computer system, which we set up, tested, and shipped to Dubna; it is currently functional, and we are able to extract data from it over the Internet.

We are scheduled to start the principal experiment to search for element 114 in November 1998, and expect it to run until March 1999. Livermore experimenters will be in Dubna in November and December of 1998. The remainder of the fiscal year will be taken up with data reduction and interpretation and documentation of our results.

Development of High Velocity Launcher Technology

R. G. Finucane, T. W. Alger, A. J. Higgins
98-ERD-055

The objective of the High Velocity Launcher project is to carry out analysis, design, construction, and test of a new class of gas dynamic launchers with the capability to conduct high velocity impact equation-of-state (EOS) measurements in a laboratory setting up to 2-TPa (20 Mbar) pressure levels in high-*Z* materials. The motivation for the project is to expand the pressure range of the conventional two-stage light gas launcher to overlap and validate the regimes previously attainable only with shock waves generated by nuclear explosions, lasers, or multistage conventional explosions.

Our High Velocity Launcher design is a new concept in the ancient art of ballistics. The fact that conventional or two-stage light gas launchers do not efficiently apply their high breech pressures to the projectile has led to the idea of distributing the propellant over the launch tube; this concept has been tried a number of times since the late nineteenth century. Our design, developed in collaboration with researchers from John's Hopkins Applied Physics Laboratory, McGill University, and elsewhere, is to inject the propellant onto the base of a tapered boattail projectile as it passes a series of reservoirs distributed along an extended launch tube. Theoretical arguments indicate that this approach can increase the maximum projectile velocity by a factor of two or more with the same gas reservoir conditions.

In the first year, we focussed on demonstrating some of the crucial technical issues required to make our new concept work in practice. To accelerate a projectile already travelling at 8 km/s, or 8 mm/μs, one has to release a high-pressure gas reservoir in a few hundred ns with a total jitter of a few tens of ns. Once the valve or diaphragm is opened, the design requires that the gas pressure contained in the reservoir be applied to the rear surface of the projectile at the right moment in its flight path. To fulfill these requirements, we designed and tested two different fast diaphragm-opening techniques, one using a small explosive charge and the other an exploding bridge wire (EBW) driven by a high voltage capacitor discharge. Both of these techniques met the timing requirements, but we settled on the EBW technique for further development because it is faster, has less jitter, and avoids explosive safety handling issues.

We designed and built a gas release test fixture to study the rate of rise of pressure at a fixed distance from the bursting diaphragm. Theoretical approximations to this flow phenomenon suggest that, in a typical configuration, the pressure will be effectively applied to the projectile in a time short in comparison to the few μs traverse time, and our experimental program supported these estimates. The final phase of these trials will involve doing the two measurements simultaneously in the same fixture: pressurizing the reservoir, breaking the diaphragm with the exploding bridge wire, and measuring the resultant pressure rise. With this test completed, we will have successfully demonstrated the essential technical issue associated with our distributed injection approach.

In parallel with these analyses, designs, and tests, we have initiated design and fabrication of the prototype distributed injection launcher itself. The basic design consists of a helium prelauncher, designed to accelerate the boattail projectile to an initial velocity of 1.5 km/s, a distributed injection acceleration section, and a target chamber. The helium prelauncher consists of a commercial pressure intensifier used to boost the helium bottle pressure from 10 MPa to 100 MPa, a 100-MPa gas breech, and a new 5-m-long, 20-mm-dia barrel. All these components have been designed and are in fabrication. As a result of a previous collaboration with Professor Andrew Ng of the University of British Columbia in Vancouver, we have obtained a complete operational two-stage light gas launcher, which we disassembled, loaded aboard a moving van, and shipped to LLNL. We are in the process of reassembling this system into our launcher laboratory, where we will convert it to the distributed injection configuration for our proof of concept tests.

In FY99, we plan to demonstrate the fundamental feasibility of our distributed injection approach, using the equipment described in the previous paragraph. We plan to launch the projectile with the gas breech to a velocity around 2 km/s into our distributed injection equipment, then inject cold argon as the acceleration medium. By measuring the velocity and accelerations of the projectile as it travels down the barrel, we will be able to confirm our analytical and numerical predictions and to extrapolate the performance to lighter gases (hydrogen).

New Physics at the B Factory: Search for CP Violation

D. M. Wright
98-ERD-058

The existence of CP (charge-parity operator) violation, a fundamental process that favors particles over antiparticles, remains a crucial problem for both particle physics and cosmology. CP violation is a necessary ingredient in cosmological models that result in a universe dominated by matter over antimatter, such as the universe in which we live. Only one CP violating process has ever been discovered, but the observed effect, within the context of current particle theory, is too small to provide the mechanism required by cosmology. Either the current theory is incomplete, or the CP violation required by cosmology has remained undetected. Unraveling this mystery is of paramount importance to particle physics, and LLNL plays an important role in a new experiment that is dedicated to resolving this problem.

The current theory, the Standard Model of particle physics, has been extremely successful at explaining data from particle physics experiments over the past 50 years. CP violation arises as a natural consequence from the part of the theory associated with radioactive decay. While the theory is consistent with all current data, the model for CP violation has never been stringently tested. In the late 1980s, it was realized that by studying the decay of B mesons (a heavy form of matter produced in accelerators) a definitive set of experiments could be conducted to test the model. Every major accelerator laboratory in the world now has a high-priority experimental program to search for CP violation in B mesons.

LLNL is part of an international collaboration of particle physicists that is assembling at the Stanford Linear Accelerator Center a detector called BaBar, which could be the first experiment to come on-line to address the mystery of CP violation. For a particular class of B meson decays, the Standard Model predicts a large asymmetry in the time evolution in the decay of B mesons and anti-B mesons. By studying these special decays, BaBar can determine whether CP violation exists for B mesons and whether it is consistent with the predictions of the Standard Model. This could lead to the first observation of physics beyond the Standard Model.

The most sensitive test of CP violation at BaBar can be made from the K^0_S decay channel of the neutral B meson. This mode is relatively easy to reconstruct. Equally sensitive, but more challenging to detect, is the K^0_L have the exact opposite asymmetry as that of the K^0_S channel. In order to make a convincing discovery the experiment should see a signal in both channels. LLNL has been involved in the design and construction of the system that detects K^0_L particles in BaBar; therefore, we have focused our physics efforts on the important K^0_L decay channel. Leveraging our hardware and software responsibilities, we have developed expertise in K^0_L reconstruction. Using simulations, we have conducted a preliminary analysis that demonstrates the feasibility of the K^0_L measurement.

Based on our detector optimization work, we proposed to enhance the K^0_L detector system in BaBar with a cylindrical layer of resistive plate chambers (RPCs) between the magnet coil and calorimeter. The design was based on LLNL technology developed for an experiment at the Supercollider. With support from BaBar to construct the full 32-detector system, in less than seven months, we designed the final detector system, set up a production facility and constructed the entire detector and support system at LLNL. We delivered and installed the detector on schedule in August 1998. We also created the software that processes the data from the cylindrical RPC in the BaBar off-line reconstruction program. The software fully integrates the complex geometry of the cylindrical RPC with the reconstruction algorithms for the planar portion of the K^0_L detection system.

BaBar will begin to collect data in 1999, and statistically significant results will be possible by the year 2000. In this next phase of the project, LLNL will operate and calibrate the cylindrical RPC system, build a physics analysis to reconstruct the K^0_L decay channel and extract the CP violation signal. The BaBar collaboration expects to discover or rule-out CP violation in B meson decay and LLNL is well positioned to play a crucial role in producing evidence for a convincing discovery.

Exploratory Research for a Proton Radiography Demonstration Experiment

E. P. Hartouni, O. Alford, P. D. Barnes, Jr., A. Chargin, J. Hockman
98-ERD-088

In this era of the Comprehensive Test Ban Treaty (CTBT), no nuclear weapons tests are allowed. Therefore, to continue certifying the safety and reliability of the U.S. nuclear weapons stockpile, the weapons complex will require a major new radiographic facility—the Advanced Hydrotest Facility (AHF). This facility will provide multiple radiographic pulses on multiple axes. The high-energy proton beam is one of the radiographic probes being considered.

Since we have almost no experience with proton radiography, a series of experiments should be performed to develop the tools and techniques needed to provide the data required to design a proton AHF. These experiments should use appropriate objects and materials and should include high-explosive-driven dynamic systems. We would be able to extrapolate the radiographic requirements for proton accelerators from these preliminary experiments. However, there are no suitable facilities in the U.S. in which to perform these demonstrations, either because of classification, the specific nature of the experiments, material, or other issues.

The purpose of this project was to determine whether it is possible to build a 20-GeV proton synchrotron suitable for the experimental program. Specifically, this synchrotrom must be built (1) as quickly as possible, that is in two or, at most, three years; and (2) as economically as possible, that is, for a price in the \$50M to \$100M range.

An accelerator design consisting of 80 B1 dipoles and roughly 100 Q4 quadrupoles from the Fermilab Main Ring and other associated hardware can be configured to accelerate a 300-MeV beam of protons from a linear accelerator (linac) injector to 20 GeV. The major difficulty in this design was to determine the effect of the large sagitta of the beam trajectory through the magnets. The solution to this problem required a detailed study of the magnetic-field properties of the dipole magnets, which was used in a comprehensive simulation of the proton-beam dynamics.

Our synchrotron would provide a 20-GeV beam of ten bunches (or frames), 10^{11} protons each and of 20-ns duration, spaced 250 ns apart. This beam would be delivered once every 1 to 5 min to a single-axis radiographic station centered at the Big Explosives Experimental Facility (BEEF) facility at the Nevada Test Site (NTS). These parameters are sufficient to demonstrate the potential capabilities of a proton-based AHF, as well as to return valuable information to the stockpile program that cannot be obtained in any other way.

If protons prove to be a suitable radiographic probe, there is a natural upgrade path from our synchrotron to the full AHF, thereby allowing a staged approach to the final facility. It is possible to accelerate and extract the proton beam at 40 and (maybe) even at 50 GeV. With a more advanced kicker magnet, it will also be possible to extract one proton bunch at a time and achieve an arbitrary frame spacing over a long time interval. The addition of a small, rapid-cycling booster will increase the proton-beam intensity by an order of magnitude. A large external collector ring adds the capability to simultaneously extract several beam bunches along multiple axes.

This approach to building an experimental synchrotron for proton radiography has been central to defining a practical strategy for realizing the AHF. Work on these plans is proceeding with support from the weapons program.

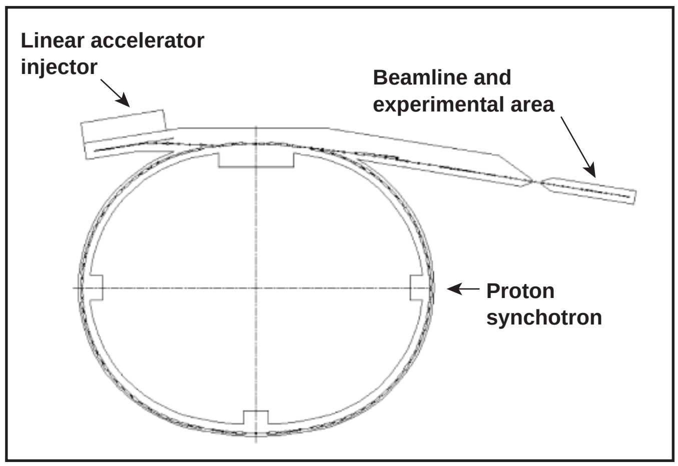

Plan view of a possible accelerator facility to be located at the Nevada Test Site (NTS). The proton synchrotron measures 318 m by 294 m.

The Fundamental Nucleon-Nucleon Interaction: Probing Exotic Nuclear Structure using GEANIE at LANSCE/WNR

L. A. Bernstein

98-LW-051

The goal of this project is to study the in-medium nucleon–nucleon interaction by testing the fundamental theory of nuclear structure, the shell model, for nuclei between ^{80}Zr and ^{100}Sn. The shell model predicts that nuclei with "magic" (2, 8, 20, 28, 40, 50, and 82) numbers of protons or neutrons form closed shells in the same fashion as noble gas atoms. A "doubly magic" nucleus with a closed shell of both protons and neutrons has an extremely simple structure and is therefore ideal for studying the nucleon–nucleon interaction. The shell model predicts that doubly magic nuclei will be spherical and that they will have large first-excited-state energies (~1 to 3 MeV). Although the first four doubly magic nuclei exhibit this behavior, the $N = Z = 40$ nucleus, ^{80}Zr, has a very low first-excited-state energy (290 keV) and appears to be highly deformed. This breakdown is attributed to the small size of the shell gap a $N = Z = 40$. If this description is accurate, then the $N = Z = 50$ doubly magic nucleus, ^{100}Sn, will exhibit "normal" closed-shell behavior. However, measurements of the structure of $N = Z$ nuclei with $A > 60$ are very rare because of the Coulomb repulsion between protons that favors nuclei with $N > Z$. The last spectroscopic information about a $N = Z = 40$ magic nucleus, ^{80}Zr, was obtained more than a decade ago.

We have pioneered a unique approach to the problems of studying highly neutron-deficient nuclei between ^{80}Zr and ^{100}Sn by using high-energy ($E > 100$ MeV) beams of neutrons to induce (n,xn) reactions with $x \geq 13$. We are using the Germanium Array for Neutron Induced Excitations (GEANIE) spectrometer at the Los Alamos Neutron Science Center/Weapon Neutron Research (LANSCE/WNR) neutron source to study the structure of these neutron-deficient nuclei.

Our accomplishments during the first year of this project include (1) completing and reporting a preliminary analysis of a late-FY97 test run at GEANIE using a ^{112}Sn target, and (2) making major improvements to GEANIE's electronics. The improvements we have made to GEANIE this year include (1) increasing the detector throughput by a factor of 2, (2) adding 6 more detectors (bringing our total to 26), (3) increasing the neutron time and energy resolution by a factor of 3, and (4) adding a 100-ms-range clock that allows us to use gamma rays observed during beam-off intervals to measure reaction yield and isomeric-state decay.

We also studied nuclei near ^{80}Zr, using GEANIE to study neutron-induced reactions on a recently acquired ^{92}Mo target, and we discovered new isomeric states in this data set. A spectrum showing the new isomeric transitions is shown in the figure.

Finally, we proposed and had accepted an experiment to study new high-spin states in ^{80}Zr using GAMMASPHERE—the premier international gamma-ray spectrometer—at Argonne National Laboratory. This experiment complements the GEANIE data, which are restricted to studies of low-spin states. This experiment was run at the close of the fiscal year.

Our goals for FY99 include completing our study of the ^{112}Sn data set—this will include (1) analysis of the prompt and delayed spectra for neutron-deficient nuclei and reaction product yields, (2) comparison with LLNL's reaction-model codes (HMS-ALICE, CASCADE etc.), and lifetime measurements of isomeric states for use in codes that model shells. During FY99, we will begin and complete a similar analysis of the ^{80}Zr run at GEANIE and also analyze the ^{80}Zr run at GAMMASPHERE.

We also plan to publish our results from both the GEANIE and the GAMMASPHERE experiments. By adding a large-volume detector to the GEANIE array, we plan to increase the array's efficiency for detecting high-energy gamma-rays by an order of magnitude.

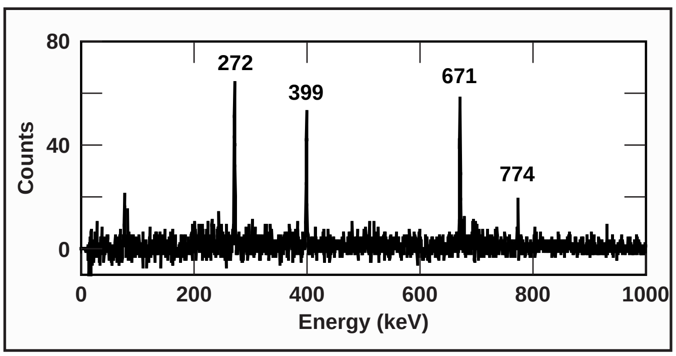

Isomeric gamma-ray transitions from the ^{92}Mo experiment using the Germanium Array for Neutron Induced Excitations (GEANIE) at Los Alamos. These gamma-ray transitions connect the isomeric to the low-lying 4^+ and 5^- states.

Experimental Test of Nuclear Magnetization Distribution and Nuclear Structure Models

P. Beiersdorfer
98-LW-057

A correct description of the internal composition of an atomic nucleus is fundamental to our understanding of the building blocks that make up our universe. While we know such basic characteristics as the number of protons and neutrons in the nucleus of each element and isotope, we have a more limited understanding of the actual arrangement of these particles and their interaction. Much of our understanding of nuclear structure has come from scattering experiments. For example, bombarding a nucleus with electrons and counting the number of electrons deflected by varying degrees gives detailed information on the arrangement of protons and the associated distribution of electric charge in the nucleus. Similarly, bombarding the nucleus with magnetic monopoles and measuring the amount of scatter would give us information on the distribution of currents and magnetic fields in the nucleus. The problem, however, is that no magnetic monopoles are available to carry out such experiments. In fact, it is not clear that they even exist. As a result, our understanding of collective effects in the nucleus, such as nuclear currents and the distribution of magnetic fields within the nucleus, is very limited.

Models exist that ascribe the nuclear magnetic fields to the presence of a single nucleon whose spin is not neutralized by pairing it up with that of another nucleon; other models assume that the generation of the magnetic field is shared among some or all nucleons throughout the nucleus. All models predict the same magnetic field external to the nucleus since this is an anchor provided by experiments. The models differ, however, in their predictions of the magnetic field arrangement within the nucleus for which no data exist. The only way to distinguish which model gives the correct description of the nucleus would be to use a probe inserted into the nucleus. The goal of this research is to develop exactly such a probe and to use it to measure fundamental nuclear quantities that have eluded experimental scrutiny. The need for accurately knowing such quantities extends far beyond nuclear physics and has ramifications in parity violation experiments on atomic traps and the testing of the standard model in elementary particle physics.

Unlike scattering experiments that employ streams of free particles, our technique to probe the internal magnetic field distribution of the nucleus rests on using a single bound electron. Quantum mechanics shows that an electron in the innermost orbital surrounding the nucleus constantly dives into the nucleus and thus samples the fields that exist inside. This sampling of the nucleus usually results in only minute shifts in the electron's average orbital, which would be difficult to detect. By studying two particular energy states of the electron, we can, however, dramatically enhance the effects of the distribution of the magnetic fields in the nucleus. In fact about 2% of the energy difference between the two states, dubbed the hyperfine splitting, is determined by the effects related to the distribution of magnetic fields in the nucleus. A precise measurement of this energy difference (better than 0.01%) would then allow us to place stringent bounds on the models predicting currents and magnetic fields in the nucleus.

We have implemented our method by constructing a very high-resolution spectrometer sensitive to light near 3800 Å, which is the wavelength of light corresponding to the hyperfine splitting of the orbital of a single electron bound to a thallium nucleus, Tl^{80+}. The spectrometer is unique in its design and consists of two independent arms, each with an ultra sensitive CCD camera, a large-diameter transmission grating, and various focusing elements. The gratings were manufactured using Laboratory facilities and leveraging unique Livermore expertise in manufacturing of high-throughput optics. The spectrometer was successfully tested at the Livermore SuperEBIT (electron beam ion trap) facility and found to enable measurements with an accuracy of about 1 part in 100,000, exceeding the design requirements.

The SuperEBIT facility is the only device capable of producing Tl^{80+} ions in sufficient quantities to carry out the planned measurements. However, unrelated to our project, the machine was completely incapacitated in May 1998 by a failure of the vacuum and cooling systems. The expected date of the resumption of operation has progressively shifted into the future and is now slated for February 1999. Although our LDRD project was only funded in FY98, we still hope to come to a successful completion of our measurements provided we obtain about one month of runtime on SuperEBIT in FY99.

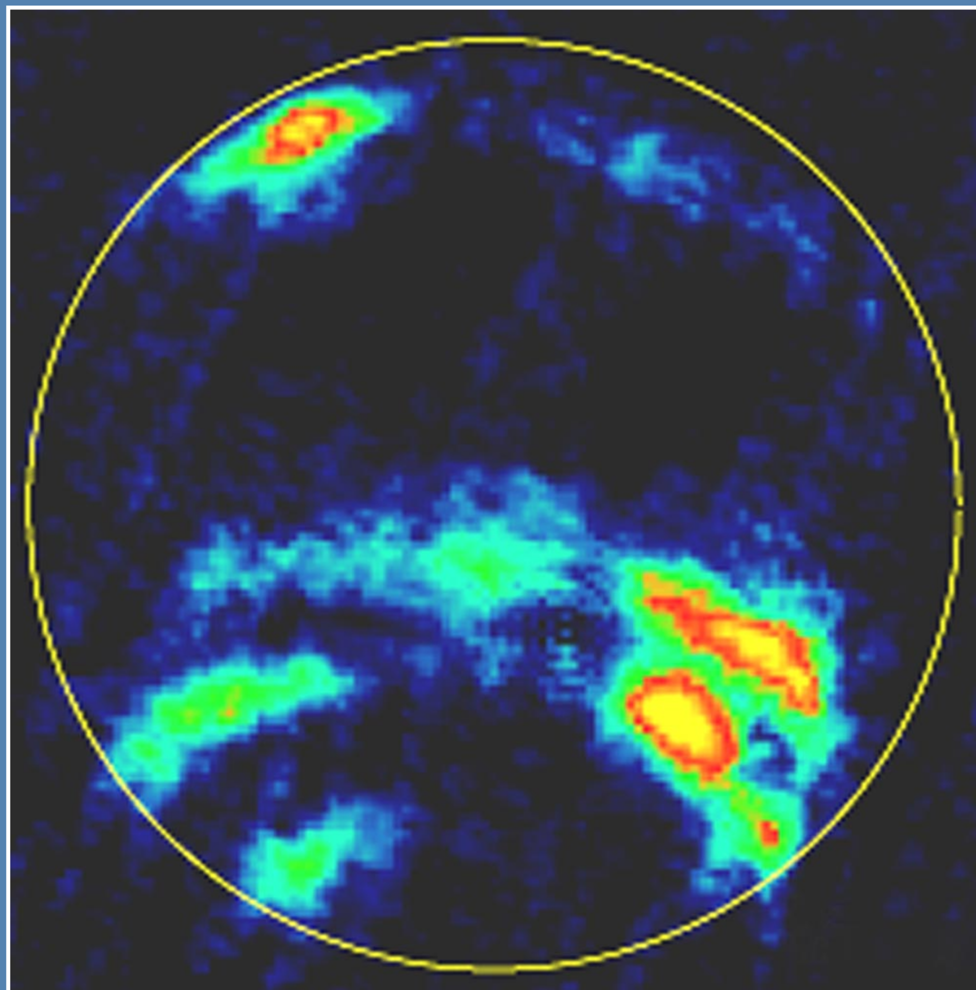

10

Space Science and Technology

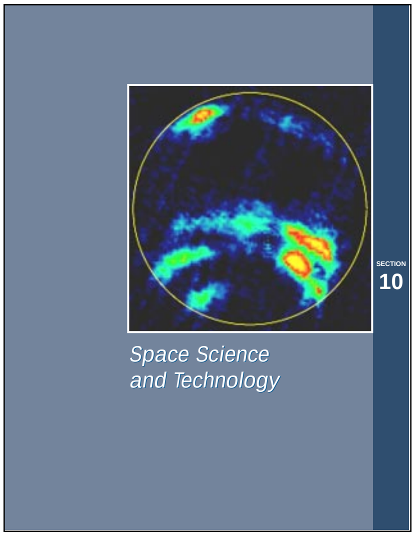

About the preceeding page

Observation of Solar System Events at High Spatial Resolution. Don Gavel and his colleagues are applying LLNL-developed speckle imaging techniques to make high-spatial-resolution observations of planets, moons, and other objects in our Solar System using ground-based telescopes. Whereas space-based observations are only snapshots in time, speckle imaging in the infrared (IR) allows observations over a long period of time. This figure shows a 1.65-µm near-IR image of Neptune from the 10-m W. M. Keck Telescope, the world's largest. Page 10-2 shows three such images, produced using high-resolution image processing speckel interferometry and with a resolution of 0.04 arcsec, better than the Hubble Space Telescope.

Very Fast Control and Response for Astronomy

C. R. Alcock, T. Axelrod, K. H. Cook, S. Marshall, D. Minniti
96-ERD-044

Modern astrophysics is confronting a revolution brought about by the advent of modern, digital imaging sensors. These sensors have allowed astronomers to collect well-calibrated data at unprecedented rates and have allowed the search for important but extremely rare events. The most prominent example of this work is the Macho Project, which has successfully detected extremely rare gravitational microlensing events (this was accomplished in another LDRD project: 93-ERD-032).

This deluge of data is both a blessing and a curse. The blessing is obvious: astronomers can now look for phenomena that were beyond their dreams only a few years ago. The curse is very serious: analyzing massive datasets is a daunting challenge; analyzing in a timely manner so that real-time decisions can be made is much more so. It was the goal of this LDRD project to develop the software and protocols to analyze a massive dataset as it was collected, to search for evidence of rare transient phenomena, and to provide reliable alert information to the international astronomical community so that time-critical follow-up observations could be made.

Our specific goal was to develop these software tools and apply them to the data stream from the Macho Telescope System and to alert the astronomical community to rare events as soon as they were detected. This system is used to search for distant stars that are magnified by the gravitational microlens effect. It has proved stunningly successful in detecting these extremely rare events. Over 300 microlensing events have been recorded since 1993, more than seven times the total reported by all other groups in the world. In one night, the Macho Telescope System takes more than 5 Gbytes of data, and it can record the brightnesses of over 40 million stars. The system has produced the world's premiere data set for studying variations in astronomical objects.

We developed the initial version of the software for this "alert system" during FY96 and implemented it during FY97. The early implementations allowed significant progress to be made on the analysis path and on the software. In addition, our early alerts to the community proved reliable, and we were able to establish trust in our system. The improved, current version of the alert system was implemented in FY98 and has been an outstanding success.

Our most spectacular success came with the detailed observations of a very special gravitational microlens event. Some gravitational microlenses are unusual in that they consist of two masses instead of one. The resulting magnification pattern is radically different from that due to a single lens. During FY98, we detected—with the Macho Telescope System—a spectacular example of this phenomenon, and our response system worked extremely well. Four other international groups of astronomers joined with us to complete the recording of this event, which was the best-sampled event of its kind in history. The data for this event are shown in Fig. 1.

In another FY98 accomplishment, we were awarded time with the Keck telescope in Hawaii to obtain spectra of stars normally too faint to observe. We successfully argued that we could observe such stars that were sufficiently magnified by microlensing. During the observation period in August 1997, the combined power of the telescope and gravitational microlens effectively made the 10-m Keck a 15-m telescope. From the resulting spectra, we also detected, for the first time, lithium in a star near the center of the Milky Way.

Two lasting consequences of this project add to the particular scientific results published in the refereed literature. First, we have demonstrated that a highly automated data-gathering and analysis system can be relied upon to find rare, time-critical events as they occur. Second, we have shown how to exploit fully the modern digital sensors that are now available to science. The legacy of this work will be the enabling of ever more ambitious surveys of the universe.

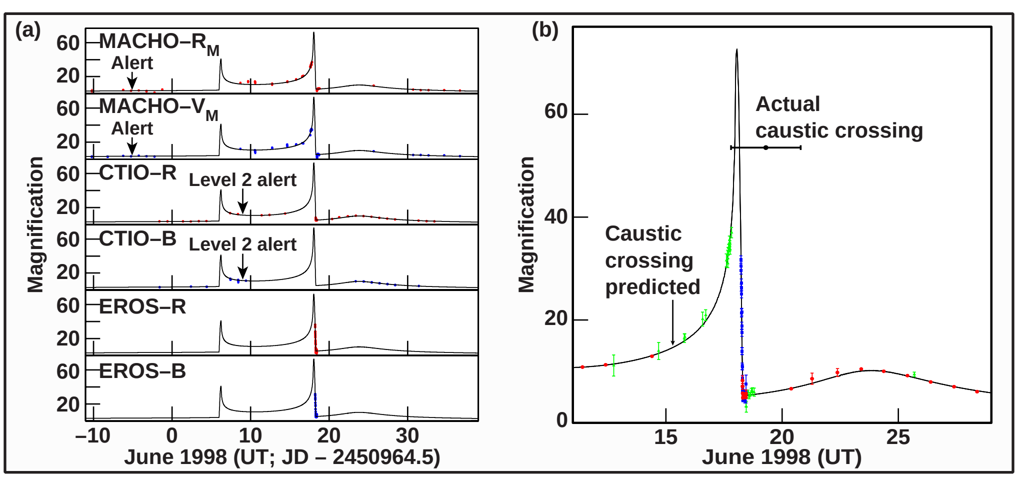

Figure 1. Forty days of observations of MACHO-98-SMC-2. Part (a) shows the Macho alert date and the "level 2 alert" when we realized this event was unusual. Data sources for the panels are (top two) Macho Telescope System, (middle two) Cerro Tololo, Chile; and (bottom two) La Silla, Chile. Part (b) is a blowup of the detail revealed during the late stages of this event. Data from three telescopes are shown.

Observation of Solar System Events at High Spatial Resolution

D. T. Gavel
96-ERI-002

Until recently, astronomical observations from the ground were limited by the blurring effects of earth's atmosphere to a resolution of 0.5 arcsec or worse. This precluded ground-based observations of details of the solar system's moons, asteroids, and outermost planets. With the maturing of high-resolution image processing techniques, such as speckle interferometry, and of adaptive optics systems, this limitation can now be overcome. The fundamental diffraction limit of resolution is a function only of the diameter of the telescope (larger being better) and of wavelength, and it can be ten times sharper than the atmospheric blur. Over the past three years, we have applied the technique of speckle imaging at the 10-m W. M. Keck telescope in Hawaii to observe (1) Titan, the largest moon of Saturn and the only moon with an atmosphere; (2) Io, the innermost moon of Jupiter and the most volcanically active body in the solar system; and (3) Neptune, which has continually changing planet-encircling storms. In addition, we have used the Lick Observatory 3-m telescope to observe these objects using an LLNL-developed adaptive optics system.

Titan has an atmosphere which, like Earth, is composed of 80% nitrogen, but is saturated with hydrocarbon aerosols (methane, ethane, and other molecules) that completely obscure the moon's surface at visible wavelengths; the Voyager spacecraft missions saw Titan only as a hazy orange ball. At certain infrared (IR) wavelengths, however, Titan's atmosphere is relatively transparent.

Titan, when viewed from Earth, subtends an angle less than one arcsecond, so conventional IR imaging shows no details. Our Keck speckle imaging observations show Titan's surface at a resolution of 0.02 arcsec per pixel (160 km/pixel) with 50 pixels across the moon. We see continent-sized bright regions, perhaps highlands of rock and ice, and very black areas, which may be pools of liquid hydrocarbons—the only liquid seas in the solar system other than on the Earth.

Applying a radiative transfer model to our observations we can recover both Titan's surface reflectivity and properties of the atmospheric hydrocarbon haze. Because Titan's atmosphere resembles that of Earth before the formation of life with no oxygen but complex organic chemistry, there is considerable interest in this moon as an example of Earth's prebiotic conditions.

The same technique was used to observe the IR light emitted by volcanoes on Io, the innermost moon of Jupiter. Io is subject to intense tidal stresses that cause frequent volcanic activity. We observed new, bright transient outbursts and variations in the energy of known volcanoes. The high spatial resolution allows us to pinpoint the location of the volcanoes and place limits on their size. Observations at different wavelengths allow us to characterize the temperature of the hot spots, which gives clues to the composition of the lava flows.

Neptune is so distant from the sun that its active weather (first observed by the Voyager spacecraft) comes as a surprise. The enormous energy in these storms is not derived from the sun's incident radiation but from the planet's internal heat. In a program of observations at Keck, we have observed storm sizes, locations, and velocities. The figure shows Neptune's storm systems at three different epochs, as seen from the Keck Telescope. Adaptive Optics observations, funded under the LDRD project entitled "Laser Guide Star Based Astrophysics at Lick Observatory," 97-ERD-037, are being combined with our narrow-band observations made at Keck to measure the altitude of these cloud features.

In addition to our publications listed at the end of this annual report, we have plans for more. We will write a follow-up paper on Titan, which incorporates our latest observations, and a paper on Neptune observations, in collaboration with Imke de Pater and her student Henry Roe at U.C. Berkeley, which combines data from our high-resolution speckle images with their low-resolution, narrow-band images.

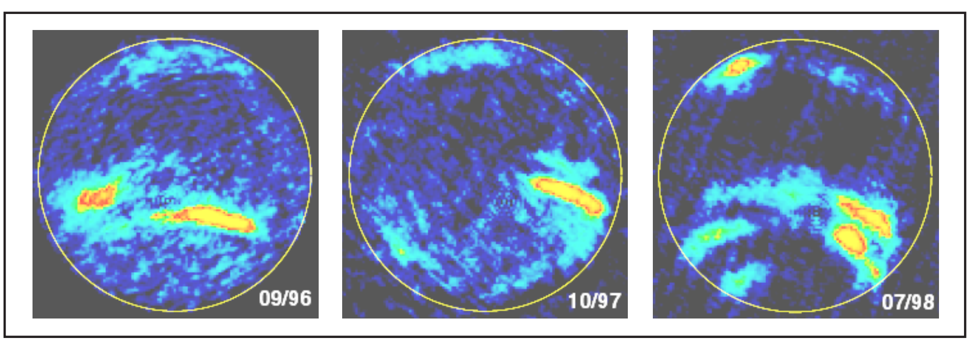

The figure shows 1.65-μm near-IR images of Neptune from the 10-m W. M. Keck telescope, the world's largest. The images were produced using high-resolution image processing called speckle interferometry and have a resolution of 0.04 arcsec, better even than the Hubble Space Telescope. The three images show evolution of storm features from September 1996 to July 1998.

Implementation of a Large-Scale, Dark-Matter Galactic Axion Experiment

C. Hagmann, D. Kinion, W. Stoeffl, K. van Bibber
96-LW-061

There are strong reasons for believing that most of the matter in our universe is in the form of exotic particles left over from the Big Bang. These relic particles interact extremely weakly with ordinary matter or light and make up most of the dark matter in the universe. A likely candidate for this dark matter is the hypothetical axion, a very light, neutral, and penetrating elementary particle. If axions exist, they would be very abundant in the dark halo of our galaxy, with a local number density of order ten trillion per cubic centimeter.

Our experiment attempts to detect halo axions by their stimulated decay into microwave photons in a strong magnetic field.

Our detector began taking data in early 1996 and has been online since then except for only minor interruptions. The magnet, which is a superconducting solenoid with a length of 1 m and a clear bore of 50 cm, produces a central field of 8 T. Housed within the bore is a tunable, low-temperature microwave cavity to trap the signal photons. A very low-noise microwave receiver amplifies the power for further processing by the room-temperature electronics.

The search for halo axions is difficult because the axion's mass and its corresponding microwave frequency are only poorly known. We scan in frequency by stepping the cavity frequency with tuning rods. For each setting, the cavity signal is averaged for about 30 min to increase the signal-to-noise ratio.

In early FY98, we completed a scan of our first frequency range (700 to 800 MHz) without finding an axion signal and published our null result. Since then, we have more than doubled the frequency coverage; at present, the excluded range is roughly 550 to 810 MHz (axion mass of 2.28 to 3.35 µeV).

The detector is expected to run for at least one more year, and we plan a scan in the 1.5-GHz region using a pack of four smaller cavities. In preparation, we developed and tested piezoelectric stepping motors for tuning the new cavity array. The piezo-driven motors are very compact and work at cryogenic temperatures and in high magnetic fields. The tuning precision must be high, since the four cavities must be kept in tune at all times. In our tests, we achieved a tuning resolution of about 500 Hz, adequate for our purpose.

In FY98, our collaboration achieved an important milestone in our program to develop sensitive, superconducting quantum interference device (SQUID) microwave amplifiers for the axion search. For the first time, SQUIDs were demonstrated to be useful microwave amplifiers above 100 MHz. Several units were built and tested at the University of California, Berkeley. They proved to have good power gain (about 20 dB), reasonable bandwidth (about 10%), and a noise temperature near 0.5 K at a physical temperature of 1.8 K.

At the close of the year, we were expecting to improve the noise performance by another factor of 5 by cooling the devices to 0.3 K, and we had begun tests employing a ^{3}He-based cooler.

Laser Guide-Star-Based Astrophysics at Lick Observatory

C. Max, K. Avicola, J. Brase, H. Friedman, D. Gavel, S. Olivier, B. Macintosh
97-ERD-037

Because of the blurring effects of atmospheric turbulence, the resolution of ground-based telescopes is typically limited to about 1 arcsec. Adaptive-optics (AO) technology senses and corrects for the optical distortions due to turbulence hundreds of times per second using high-speed sensors, computers, and a deformable mirror technology similar to that developed for the atomic vapor laser isotope separation (AVLIS) program.

The goal of this project is to make sodium-laser guide-star AO systems into widely useful astronomical instruments. Alone, AO provides up to a factor of 10 improvement in the spatial resolution of astronomical images, but requires a bright nearby reference star. The sodium-laser guide star provides a reference beacon that allows AO correction on dim science targets virtually anywhere in the sky.

With AO correction, for the past two years we have been able to achieve the diffraction limit of the Shane 3-m telescope at Lick Observatory at near-infrared wavelengths (0.15 arcsec), which is slightly better than the Hubble Space Telescope at these wavelengths. During FY98, we improved the capability and efficiency of the AO system enough so that making AO astronomical observations using natural-starlight beacons became routine. The AO system was used in a natural guide-star mode in dedicated science-observation runs in which several University of California faculty and graduate students participated. Astronomy projects included imaging of newly formed stars, a search for giant planet companions to nearby stars, and studies of weather systems on the giant planet Neptune (see figure). The AO system performed extremely well, operating with faint (down to magnitude 12) natural guide stars—in the case of Neptune, the guide-star beacon was Neptune itself, at magnitude about 8—and achieving diffraction-limited resolution and high-contrast images.

We had previously designed, built, and tested the laser guide star on the Shane telescope. The laser is a 20-W, tunable, dye, master-oscillator/power-amplifier design. It is tuned to resonate with a layer of sodium atoms, residue from meteorite ablation, that is located 100 km above the Earth's surface. The resonant backscatter from the sodium layer provides an artificial guide star sufficiently bright for the AO system. Without the laser, the AO system must use a bright, natural guide star (12th magnitude or brighter) as a beacon for the atmospheric correction, limiting its operation to only a small fraction of the sky. With the laser, the system is limited only by the need for a faint star (15th to 16th magnitude) to use as an overall tip/tilt reference; most of the sky is thus opened to AO observation.

During FY98, we improved our techniques for using the laser guide-star/AO system. Alignment and calibration procedures now provide the AO system with stable, predictable performance. Changing the laser amplifier to a bounce-beam configuration resulted in a better-quality laser wavefront and a smaller guide-star spot in the sky—thereby improving the measurement sensitivity of the AO system. Improvements to the tip/tilt sensor and its control system decreased the requirements on the tip/tilt star brightness to near the theoretical limit—thereby allowing practical laser guide-star operation over most of the sky and providing astronomers with the ability to observe faint galaxies and other objects that are not near bright reference stars. The net result was that the laser guide-star AO system could now achieve a Strehl ratio of about 35%. (The Strehl ratio is a performance measure for AO systems; it represents the ratio of the actual peak intensity to that of a theoretically perfect telescope with no turbulence.)

As a return benefit to LLNL, AO technology has become a routine component within other LLNL program applications, including beam correction for lasers in the National Ignition Facility (NIF).

In FY99, we plan to continue our program of natural guide-star AO astronomical observations with University of California faculty and students and to expand it to include objects such as faint galaxies that are accessible only by using the laser guide star.

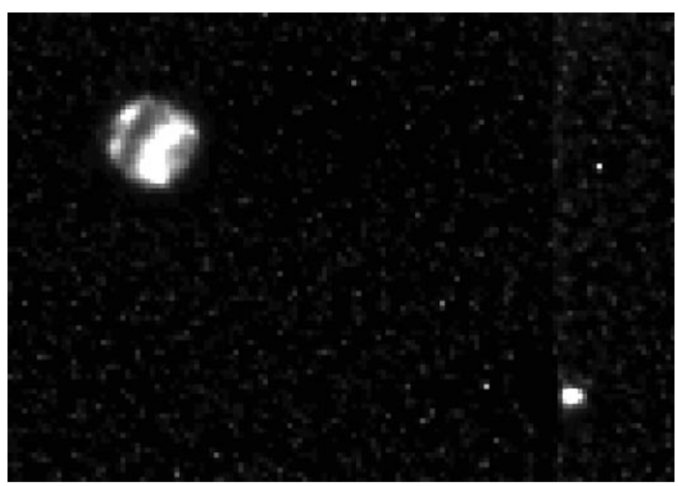

Adaptive optics image of Neptune and its moon Triton at a 1.6-μm wavelength, showing longitudinally extended storm systems in the southern hemisphere of Neptune. North is to the upper left.

A Comprehensive X-Ray Spectral Code for High-Energy Astrophysics

D. A. Liedahl, C. W. Mauche, K. B. Fournier
97-ERD-057

Hot cosmic plasmas such as are found in stellar coronae, supernova remnants, and clusters of galaxies cool by emitting x rays. When plasma temperatures exceed about one million Kelvin, highly ionized species of several elements radiate in a set of discrete spectral lines over the 1- to 200-Å range. The wavelength distribution of this radiation can be used to infer temperatures, densities, velocities, and chemical compositions of the emitting plasmas—information that can then be used to constrain models of the structure of the sources being studied.

Cooler, less-ionized plasmas can also emit x-ray lines. This occurs when matter is irradiated by high-energy continuum radiation, such as that produced near black holes and neutron stars. A high-energy photon is absorbed by a near-neutral ion, resulting in the ejection of an electron from the innermost atomic shell. The radiative decay of this excited state produces an x ray with a wavelength that is characteristic of the ion. Finally, the absorption of x rays by material that is "backlit" by a source of continuum x rays can imprint features on the spectrum. For example, these features allow one to measure properties of cold interstellar matter in the Milky Way Galaxy that intercepts radiation from distant quasars as it propagates towards Earth.

The application of x-ray spectroscopy to cosmic phenomena is about to become a major focus of astrophysical research. By 2000, the launches of three major "facility-class" observatories are scheduled: National Aeronautics and Space Administration's (NASA's) Advanced X-Ray Astrophysical Facility (AXAF), European Space Agency's (ESA's) X-Ray Multi-Mirror Mission (XMM), and Astro-E, a joint Japan/U.S. project. Instruments aboard these spacecraft will achieve order-of-magnitude improvements in spectral resolving power. With projected lifetimes of up to 10 years, these missions are expected to return data of very high quality from hundreds of celestial targets.

The aim of our project is to develop a spectral-analysis tool with a level of quality commensurate to that expected in the data. This is challenging. An x-ray spectrum from a celestial x-ray source may consist of tens of thousands of lines, a fraction of which (a few hundred, say) will be individually resolved; the rest form line complexes—blends of hundreds, or even thousands, of weaker lines that cannot be individually resolved and identified. Our project can be broken down into three primary tasks: (1) generation of the bulk of the atomic database using LLNL's computer codes; (2) compilation, critical assessment, and incorporation of atomic data that cannot be generated at LLNL in a timely manner; and (3) design of a user interface that will allow rapid access to and manipulation of the database. The overall package is called the Livermore X-Ray Spectral Synthesizer (LXSS).

During FY98, we used the Hebrew University–Lawrence Livermore Atomic Code (HULLAC) suite to generate approximately three-fourths of the database. For easy interface with fitting packages provided by NASA centers, we are storing atomic data in flexible image-transport system (FITS) format. We have written several "pipeline processing" codes in Interactive Data Language (IDL) to facilitate uniform data conversion and storage. We are also constructing (1) an extensive IDL graphical user interface that will allow access to a number of simulation and display functions, and (2) a database-query function.

The issue of benchmarking is being addressed through close collaboration with LLNL's electron beam ion trap (EBIT) team and with various tokamak groups in the U.S. and Italy. On the astrophysical front, we are participating in the analyses of spectroscopic data from the Advanced Satellite for Cosmology and Astrophysics (ASCA), using models that constitute the raw ingredients of LXSS. Members of our team are also active in the field of x-ray astronomy. For example, we have been awarded AXAF Guest Observerships, and are participants in the XMM Guaranteed Time program. Thus we foresee—in the near future—many excellent opportunities for exercising the full capability of LXSS.

In FY99, we will focus on refining the LXSS graphical user interface and on implementing an array of auxiliary functions. For example, LXSS will allow the calculation of radiative cooling curves or the calculation of non-local-thermal-equilibrium opacity in the x-ray range. We plan to release a beta version of the code near the end of FY99.

Astrophysical Opacity Experiments: Radiative Transfer in Relativistic Media

P. T. Springer, R. G. Eastman, P. A. Pinto
97-ERD-108

Laboratory experiments relevant to astrophysics are used to benchmark the opacity and the radiative transfer models for Cepheid Variable pulsation and type Ia supernova luminosity—the cosmological standard candles. Classical Cepheids serve as an extra-galactic distance indicator to 60 million light years. Type Ia supernovae—the best tool for understanding the age and curvature of the Universe—can serve as a cosmological distance indicator to 6 billion light years. A detailed understanding of these standard candles is essential in astronomy. The experimental techniques and spectroscopic diagnostics developed in this project are also important for the Stockpile Stewardship Program (SSP). They enable the capability for precision opacity experiments of interest to SSP on multimegajoule DOE plasma generation facilities and for prototype diagnostics and techniques important for such experiments on the National Ignition Facility. Cepheid Variables are pulsating stars whose luminosity is correlated with the pulsation frequency. Astronomical observations of double-mode Cepheid Variables indicated a lack of understanding of these stars resulting in poor agreement between the stellar pulsation and evolution predictions. An improved understanding of the opacity of M shell $\Delta n = 0$ transitions in iron and direct experimental confirmation have resolved these long-standing differences. Using the 500-kJ Saturn facility at Sandia National Laboratory, we created and measured the opacity of iron and nickel plasmas at stellar envelope conditions, validating and improving the accuracy of the OPAL opacity code for these systems. New methods were developed to obtain local thermodynamic equilibrium (LTE) opacity data for plasma density 100 times lower than previous measurements. Experimental requirements include high spectral resolution, large homogenous plasma sources, and Planckian radiation fields lasting tens of nanoseconds. Experiments showed that detailed line-by-line treatments in OPAL were accurate for these systems, providing that a complete atomic data set comprising 25 million transitions was employed.

These experiments were modified and conducted in order to test and refine supernova radiative transfer models and to address systematics in the supernovae derived cosmological distance scales. This requires accurate and complete atomic models and also accurate models for radiative transport in the presence of large velocity gradients. In FY98, we conducted experiments to address the physics of radiative transfer in a scaled analog of the supernovae plasma, using low-density, expanding plasmas created in the pulsed power experiments. In these experiments, plasmas were created with high velocity gradients, in excess of 200 km/s. As in the supernovae, these plasma are in the Sobolev regime, in which the Doppler shifts in radiation crossing the plasma exceed the intrinsic atomic line widths and the typical interline spacing. The absorption in the expanding plasma is increased as a result of the expansion, and it is measured in the Saturn experiment

The experimental setup is shown in Figure 1(a). A high-resolution spectrometer records the plasma absorption in two samples at the same time, both parallel and transverse to the plasma expansion. The plasma is characterized using spectroscopic tracers for temperature and the spatial profile to derive the density and velocity field. The increased attenuation due to the plasma expansion is measured and modeled. Approximations for the atomic physics used in the OPAL opacity code are being applied with various approximations for the radiative transport, then compared with the experimental absorption. These techniques are also applied to code that models supernovae light curves. The use of OPAL line lists results in higher opacity for supernova plasma as compared with standard models using the Kurucz line lists shown in Figure 1(b). The importance of these differences to the cosmological distance scale is being explored.

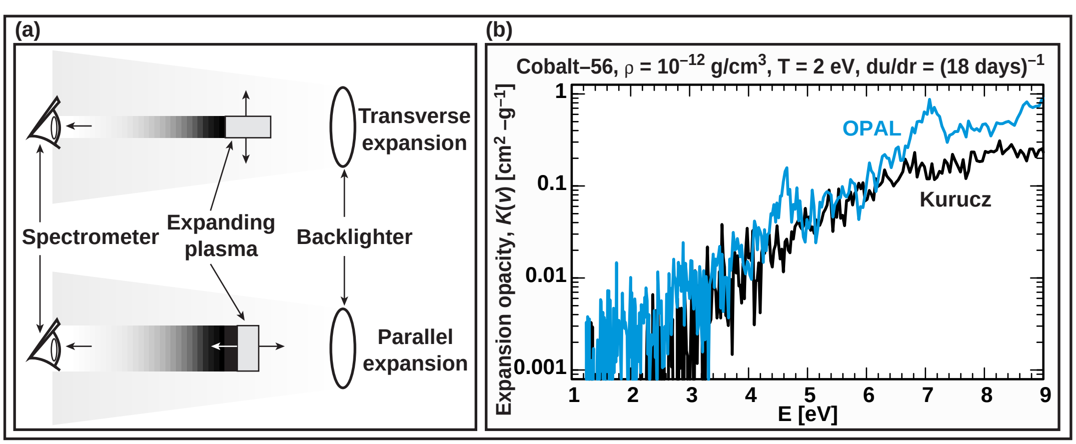

Figure 1. (a) Experimental setup allows absorption measurements parallel and transverse to expansion. (b) OPAL opacity models verified in the experiment differ significantly from standard supernova opacity models, using the Kurucz line list.

Asteroids and Comets: Completing the Inventory of the Solar System

C. R. Alcock, K. H. Cook, S. Marshall
97-ERI-004

Following the detection of solid objects in the trans-Neptunian region, the observed frontier of the solar system progressed from about 10 AU in the early 1600s—when Kepler deduced his "laws" of planetary motion, only six planets were known to orbit the Sun—to about 50 AU today. During these four centuries, three planets, hundreds of comets, and thousands of asteroids have been detected in orbit about the Sun, and dozens of moons as well as four ring systems have been observed to orbit planets. Progress is very slow beyond Neptune because the objects are mostly small, solid bodies, and the brightness in reflected sunlight declines as the inverse fourth power of distance.

Although no objects have been observed beyond 50 AU, a rich population of comets has been inferred. This population acts as a reservoir from which new comets can enter the inner solar system, become active, and be discovered as their brightnesses increase by many orders of magnitude.

The populations and distributions of these objects are not known; in the case of the comets, the uncertainties span orders of magnitudes. Scientifically, these objects serve as probes of the primordial solar system because they preserve a record (in ice) of the conditions at that epoch. Programmatically, interest is growing regarding ways to mitigate the hazards of asteroid or comet collisions with Earth. The region of interest for us is the Kuiper Belt, which lies just beyond the observed frontier of the solar system. It is believed that there are between a billion and a hundred billion comets in the Kuiper Belt, in orbits with semimajor axes between 50 and 200 AU.

During FY97, we designed a novel survey for taking an inventory of the comets in the Kuiper Belt—we would use the occultation of nearby stars by the comets to estimate the total population of small (~2 km) objects. Our system consists of an array of telescopes at a dark site; each telescope has a wide-field-of-view, charge-coupled-device (CCD) camera system pointed at the same region of the sky. Our design study determined the architecture and parameters of the system, that is, the number of telescope elements, the size of the telescopes, the kind of cameras, etc.

Three is the minimum number of telescopes for systematic control and measurement of the false-positive rate; we adopted this minimum to minimize the overall cost of the array. With three telescopes—and the design goal of a false-alarm probability per measurement of about 10^{-12}—the false-alarm probability per measurement at one telescope should be no poorer than about 10^{-4}. This sets the signal-to-noise requirement for each telescope in the system. The optimum telescope for this design has an aperture of 50 cm and a focal length of approximately 95 cm. This couples well to a moderate-cost, commercially produced CCD camera.

During FY98, we completed the design for the three-telescope array. This included design of the optical corrector cell for the telescope system, which ensures that most of the flux from a star will be collected into one camera pixel over the entire three-square-degree field of view. We also (1) identified a small telescope manufacturer who can fabricate the needed telescopes at moderate cost, (2) selected the digital camera for the project, and (3) invented a novel photometry scheme that allows us to perform photometry on several thousand stars five times per second (much faster than allowed by conventional astronomical photometry schemes).

Also during FY98, we employed an analog system at Los Alamos National Laboratory to acquire test data for the simulations used in the ongoing design of the analysis path for the full, three-telescope system. The analog system is also used to test the robotic-control software that we are writing.

In FY99, we will (1) assemble and test a complete three-telescope system—this includes procuring the telescopes and cameras and integrating the telescope control and camera operations into one software environment; and (2) complete the software needed to acquire the data, process it to photometry, and archive the results. Our goal is to have most of the system shipped to Taiwan for preliminary testing in the field before the end of FY99.

A Search for Simultaneous Optical Counterparts of Gamma-Ray Bursts

H-S. Park, R. A. Porrata, R. M. Bionta, G. G. Williams
97-LW-019

Once a day orbiting satellites detect brief flashes of gamma rays from random points in the sky. Despite 25 years of effort, these gamma-ray bursts (GRBs) remain poorly understood and are difficult to study due to their short lifetimes and the poor angular resolution of the gamma-ray detectors. Recently, an Italian–Dutch satellite provided accurate locations for fading x-ray emission that accompanied some GRBs. Later, large telescopes observed fading optical afterglows in some of these locations. They measured redshifts of >0.835 establishing that GRBs are at cosmological distances and are therefore the most energetic and relativistic events since the *Big Bang*. The fading afterglows observed for hours to days later do not originate in the GRB but are understood to be the consequence of the release of large amounts of energy into the surrounding medium. The goal of this research is to measure prompt optical emissions from GRBs while they are still emitting gamma rays, thereby providing clues to the underlying GRB physics.

To achieve this goal, we constructed an innovative automatic telescope that images a 17.6- × 17.6-deg field of view and responds to GRB triggers within 10 seconds. The experiment, LOTIS (for Livermore Optical Transient Imaging System), is located at LLNL's Site 300 and began routine observation in October 1996.

During two years of operation, LOTIS has recorded images of over 40 GRB locations taken 6 to 15 seconds after the start of the bursts. Careful study of these images, published in *Astrophysical Journal Letters*, has established that prompt optical activity associated with GRBs must be dimmer than m_V~12. Our limits constrain theoretical GRB models that predict some visible light emission early in the burst. During FY98, we upgraded our cameras, increasing the sensitivity to m_V~15. The upgraded system is running continuously and is always ready to respond to GRB triggers from NASA's GRB coordinate distribution network.

Of particular interest was GRB971227, which occurred December 27, 1997, because it was detected by three satellites and its location scrutinized by telescopes from all over the world. LOTIS had the earliest images—taken 10 seconds after the start of the burst—whereas images from the other telescopes were taken at least 10 hours later. The figure shows LOTIS' detection of GRB971227. For this event, the gamma-ray flux was low, and no convincing afterglow was observed. This deepens the mystery of the GRB production mechanism since only about half the interesting events have afterglows. Nothing is known about early time optical activity. Some theories predict that the brighter GRBs will produce visible light signals at early times that are detectable by the upgraded LOTIS. While waiting for GRB triggers, LOTIS surveys the sky continuously. These data can be used for studying other optical transient phenomena such as variable stars, near-Earth objects, or supernovae. In FY98, we began constructing robust photometry algorithms to process large quantities of data on the Livermore Computing Facility. This work is still in progress.

In response to new NASA and European GRB satellite missions (HETE2, INTEGRAL, IPN, RXTE, and MIDEX), we are installing a 0.6-m telescope, sensitive to m_V~19, at the Kitt Peak National Observatory in spring, 1999. This telescope can respond to satellite GRB coordinate alert triggers within 30 seconds at m_V~19 sensitivity level. By acquiring image data this early, we can learn about the GRB production mechanism. No other telescopes can respond this rapidly. The early observation of optical activity will produce important measurements to understand GRBs.

In FY99, we are planning one team meeting following the construction of the 0.6-m telescope, publications related to the topics of real-time optical flux limits to the GRBs and optical transient searches, and an expansion of our work toward all-sky-survey database production.

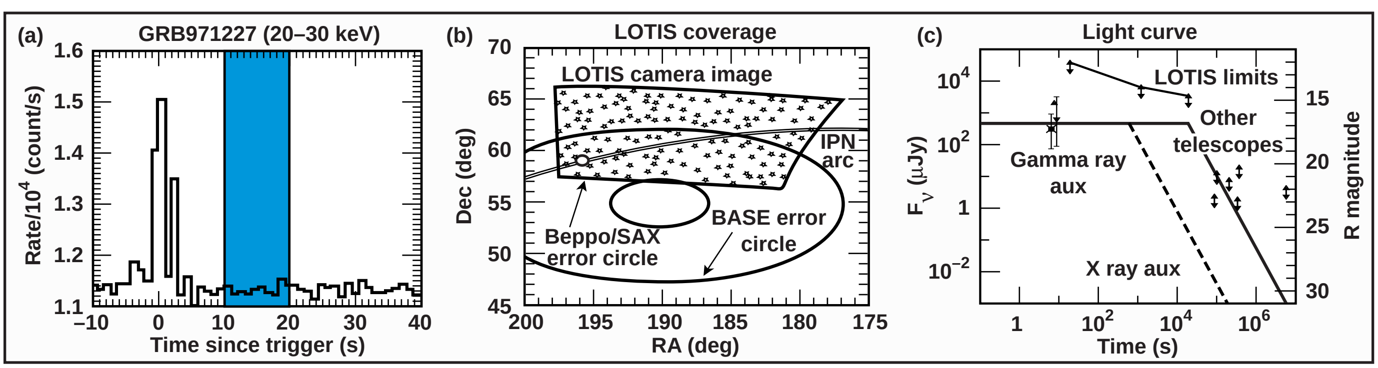

LOTIS detection of GRB971227. The first panel (a) shows the gamma-ray light curve of this event, and the shaded area indicates the time when LOTIS started imaging. The second panel (b) shows the LOTIS coverage of the GRB error circles constrained by three satellites. The third panel (c) shows optical flux limits from LOTIS and other telescopes for this event.

Ultrahigh-Contrast Imaging

C. Max, C. Olivier, B. Macintosh, C. Carrano, D. Gavel, J. Brase
98-ERD-036

The recent indirect detection of planets around more than 10 nearby stars has stimulated the popular imagination and galvanized the scientific community. We now have an unprecedented opportunity to characterize these new extra-solar-system planets from the ground through the development of new techniques for ultrahigh-contrast imaging. Only by direct detection can we separate the light from a planet from that of its parent star; only then can we measure the planet's color, broad-band spectrum, and orbital elements.

In this project, we are exploring ultrahigh-contrast imaging techniques in which we use adaptive optics (AO) to detect very faint objects close to very bright ones. In particular, the goal of this project is to use the Keck Observatory telescopes in conjunction with AO to focus on the direct detection of planets around nearby stars. We are investigating two approaches: (1) the use of a single Keck telescope with AO and a coronagraph, and (2) synthetic aperture-imaging methods using the two Keck telescopes and four smaller outrigger telescopes in interferometry mode. This project is the outgrowth of an LDRD feasibility study that was funded in FY97.

We made significant progress during FY98. In accordance with our research plan, our major emphasis was on the internal calibration of AO systems—minimizing internal aberrations is a crucial enabling condition for the execution of our technical strategy. Two techniques were investigated for this purpose: (1) phase retrieval, and (2) phase-shifting diffraction interferometry.

Phase-retrieval techniques have been used for a number of years to characterize aberrations in optical systems. For instance, phase-retrieval techniques were used to diagnose the pre-repair-mission aberrations of the Hubble Space Telescope. As a precursor to their future use at Keck, we applied phase-retrieval techniques to evaluate the internal aberrations in our AO system at Lick Observatory. Then, to optimize the image quality, we used this information to adjust the calibration of the AO control system. With this procedure, we corrected the internal aberrations to the 50-nm root-mean-square (rms) level.

Phase-shifting diffraction interferometry was developed in LLNL's Advanced Microtechnology Program for use in the Extreme Ultra-Violet Lithography Project. This patented, award-winning method holds the record—at less than 1-nm rms—for absolute phase-measurement accuracy. We adapted the phase-shifting diffraction interferometer for use on the Lick AO system, as a prototype for future use at Keck. This technology allows characterization of the aberrations of an AO system to extremely high accuracy. The interferometer was installed in the Lick AO system and used to measure the aberrations at the 10-nm rms level.

In addition to the work on AO calibration, in FY98 we carried out a series of high-contrast AO observations at the Lick Observatory in which we searched for structure around selected, bright young stars. These observations resulted in the discovery of a previously unknown stellar companion to one of the program stars, and set strong upper limits to the size of potential stellar and substellar companions to most of the other program stars.

During FY98, we also continued to assess the characteristics of the scattered light from the primary mirror of the Keck telescope. These observations prepared us for the high-contrast imaging observations planned for FY99, following commissioning of the Keck AO system. During FY99, we plan to (1) perform our first high-contrast-imaging observations on the newly commissioned Keck AO system, (2) implement phase-retrieval techniques at Keck, and (3) complete an initial search for stellar and substellar companions to nearby stars using the Lick Observatory's AO system.

On the basis of innovations resulting from this research, the National Aeronautics and Space Administration (NASA) Origins of Solar Systems Program has selected a complementary proposal for seed funding.

The Study of the Hydrodynamics of Single-Bubble Sonoluminescence

P. E. Young, R. W. Lee, W. Moss
98-ERD-081

Sonoluminescence (SL) is a mysterious phenomenon in which sound waves aimed at a container of fluid nucleate, grow, enlarge, and then collapse many gas-filled bubbles to create ultrashort light flashes representing a trillion-fold focusing of the initial sound energy. Although discovered in 1933, the phenomenon could not be studied in detail until 1990, when SL was successfully obtained from a single air bubble. Thus, SL is the production of visible light by a gas bubble that is suspended in a fluid (normally water) by an acoustic standing-wave field. Present understanding of the phenomenon suggests that sonoluminescence may result in temperatures of over 10^5 K (which approaches the temperature found in the solar corona), pressures of over 10^7 bar (close to the pressure at the center of the planet Jupiter), light emission of less than 10^{-9} s duration, and concentration of mechanical energy of up to 10^{12}. In sonoluminescence, a small (10-µm-diam, or about 1/10 the width of a human hair) bubble oscillating in an audio-frequency (25 kHz) ultrasonic field synchronously emits on the order of a million photons in a short pulse each acoustic period (the time from one compression part of the cycle to the next). The process by which the acoustic energy is converted into electromagnetic energy is not well understood; it is being investigated by numerous research groups around the world.

The purpose of this project is to address several topics of importance to understanding SL, including hydrodynamics, the properties of matter at extreme conditions, and the source of the light flash. Our experiments will look at the hydrodynamic collapse of a bubble—the spherical nature of the collapse and the details of the simulations that need to be exercised can provide rigorous tests of the hydrodynamic codes (e.g., codes for inertial fusion, plasma diagnostic source development, or astrophysical modeling. The fact that there is still no reasonable solution regarding the source of the emissivity from the bubble has led to studies that have impact on the equation of state of the gases in the bubble as well as that of the water at extreme conditions. We are able to bring unique techniques to bear on this problem—such as ultrafast laser probing of the collapsed bubble—that will provide basic information on the ability of codes to map out the implosion phase correctly. Finally, understanding the light emission may provide a path for the use of this rather interesting phenomenon.

Since beginning this project at the start of FY98, we have set up and quantified a stable SL cell and have also set up diagnostics to monitor the temperature, gas concentration, and driving pressure in the cell. A laser-probing system is obtaining images of the bubble with 10-ns time resolution; this system is being used to measure the maximum and ambient bubble radii during the acoustic period. We have also set up a thermoelectric system to allow control of the water temperature (which is critical to the amount of light emission from the bubble) and an optical streak camera to measure the duration and time shape of the light emission from the bubble. Furthermore, we have been able to investigate the duration of the light emission as a function of water temperature, driving pressure, and gas concentration; we are observing pulse durations of 50 to 300 ps. These measurements will provide data that rigorously test the hydrodynamic models.

Our project has successfully engaged high-quality students, young, bright individuals who are being attracted to the Laboratory to participate in research in which they become fully involved: during FY98 the project supported several undergraduate students and Summer Research Institute students. One of the students represented the Laboratory at two national undergraduate research conferences and was one of four students nationally to be selected to appear before the Secretary of Energy's Advisory Board on Undergraduate Research. The student participation has proved to be an exceedingly effective method for introducing researchers to LLNL and for gaining public awareness.

In future work, we will use ultrashort-pulse lasers to diagnose the conditions of the bubble near its collapsed phase by imaging the bubble and fluorescing trace materials seeded into the bubble.

Primordial Quasars and Protogalaxies

W. van Breugel
98-ERI-005

The goal of this LDRD project is to use radio surveys to search for massive protogalaxies, primordial quasars, and ultra-luminous infrared (IR) galaxies. Using space- and large ground-based observatories, we will then investigate the relationships between galaxy formation, quasar activity, starbursts, and galaxy merging.

The existence of galaxies and the expansion of the universe have been known for over 70 years. Ever since Edwin Hubble made these first discoveries, one of the main questions in astronomy has been how galaxies form and, indeed, how the universe formed. Nearly 35 years ago, this mystery was deepened by the discovery of quasars, point-like objects that are the most luminous in the universe.

Standard models of galaxy formation assume that it is a hierarchical process in which smaller mass objects collapse first into stars and star-forming regions, then into galaxies and large clusters of galaxies. Quasars, located at the centers of galaxies, are thought to be active black holes, emitting more than a million solar masses within a region of space only a few light years in diameter. Some models suggest that black holes may grow together with their host galaxies through the capture of gas, stars, or the end products of rapid stellar evolution in the galaxy centers. Other models suggest that conditions in the very early universe may be such that massive black holes form already, well before the main body of their host galaxies develop. These "primordial" black holes, or quasars when they are active, may then be the cores of future massive galaxies. Regardless of the details of these theories, it appears very likely that the formation of massive black holes and of massive galaxies may be closely related.

From previous work at the Institute of Geophysics and Planetary Physics (IGPP), we found that powerful radio sources are amazingly good beacons for locating massive forming galaxies in the early universe. In FY98, we combined two methods to build a very efficient sample for finding such radio sources. These methods employ two properties of powerful radio sources and their host galaxies: the steepening of their radio emissivity with frequency, and an inverse relationship between near-IR galaxy brightness and distance. The former will allow us to select promising candidates from existing large radio surveys; the latter will allow us to further improve on this by using near-IR identifications. The two most important surveys we used are the FIRST survey (Faint Images of the Radio Sky at Twenty Centimeters), which is being conducted at the LLNL IGPP, and the WENSS survey (Westerbork Northern Sky Survey) at Leiden Observatory, The Netherlands.

Using these surveys, we have completed our selection of a sample of "Ultra-Steep Spectrum" (USS) sources. Our final sample covers both the northern and southern hemispheres, consists of approximately 700 objects, and reaches 10–100 times lower flux density limits than previous samples. It has the promise of probing much larger redshifts than has been previously possible. Using this sample, we have subsequently begun a vigorous program to obtain near-IR identifications of these sources. The faintest USS radio sources, which on average are also the most distant, are being observed with the Keck 10-m telescopes; the brighter sources are observed at Lick Observatory and Cerro Tololo Interamerican Observatory (Chile). As expected, we have discovered many extremely faint near-IR objects, which, on the basis of the near-IR/redshift relationship, are expected to be at very high redshifts.

We have also used the FIRST radio survey to search for extremely high redshift quasars, using multi-color digitized optical plates from the Palomar Optical Sky Survey. We observed 22 point-like objects with red colors at the Lick and Palomar observatories. These initial observations have been plagued by poor weather. Nevertheless, we have now uncovered the two most distant quasars selected from the FIRST survey to date, FIRST 1410+3409 (z = 4.36) and FIRST 0100-0128 (z = 3.85), proving that the method works in principle.

In FY99, we will continue our near-IR identification program, and will obtain optical spectra to search for the highest redshift galaxies and quasars. We will begin a statistical analysis of the radio and IR properties of the samples as a function of cosmological parameters and evolution. This research is in collaboration with faculty members and graduate students at the University of California at Berkeley, University of California at Davis, California Institute of Technology, and Leiden University (The Netherlands).

Appendix

Publications
Principal Investigators Index
Tracking Code Index

Publications

These documents were published under the auspices of the Department of Energy and denote DOE publication numbers in compliance with contract W-7405-Eng-48.

Abare, A. C., et al., *Measurement of Gain Current Relations for InGaN Multiple Quantum Wells*, UCRL-JC-130773. 97-ERD-082.

Adam, N., R. Musick, T. Slezak, "Digital Libraries and Bioinformatics," submitted to *IEEE Transactions on Information Technology in Biomedicine*, UCRL-JC-131329. 97-ERD-033.

Ahle, L. A., and H. S. Hopkins, "Gated Beam Imager for Heavy Ion Beams, Beam Instrumentation Workshop," Palo Alto, CA, May 1998, to be published in *NIM*, UCRL-JC-130010. 96-ERD-048.

Ahle, L. A., et al., "Recent Progress in the Development of a Circular Ion Induction Accelerator for Space Charge Dominated Beams at LLNL," *LINAC98*, Chicago, IL, August 1998, to be published in *NIM*, UCRL-JC-130606. 96-ERD-048.

Albala, J. S., C. Prange, W. Fan, M. Thelen, G. G. Lennon, "Isolation of a novel member of the RAD51/RECA family of DNA repair proteins," *American Society for Cell Biology*, San Francisco, CA, December 1996, UCRL-JC-126574Abs. 96-ERD-076.

Albala, J. S., et al, "Identification of a novel human RAD51 homolog, RAD51B," *Genomics* **46**, 476–479, UCRL-JC-127970. 96-ERD-076.

Albala, J. S., I. R. McConnell, F. Farrahi, J. E. Lamerdin, "Characterization of RAD51B and its role in genomic stability and DNA repair," *Keystone Meeting on Molecular Mechanisms of DNA Replication and Recombination—Keystone Symposia, Molecular Mechanisms in DNA Replication and Recombination*, Taos, New Mexico, February 1999, UCRL-JC-132399Abs. 96-ERD-076.

Alcock, C., et al., "EROS and MACHO Combined Limits on Planetary Mass Dark Matter in the Galactic Halo," *Astrophys. J*. **499**, L9, UCRL-JC-130244. 96-ERD-044.

Alcock, C., et al., "First detection of a gravitational microlensing candidate towards the Small Magellanic Cloud," *Astrophys. J. Lett*. **491**, L11, UCRL-JC-129380.

Alcock, C., et al., "MACHO Alert 95-30: First Real-Time Observation of Extended Source Effects in Gravitational Microlensing," *Astrophys. J*. **491**, 436, UCRL-JC-127208. 96-ERD-044.

Alcock, C., et al., "Optical identification of the LMC supersoft source RX J0527.8-6954 from MACHO Project photometry," *Monthly Notices of the Royal Astronomical Society* **291**, L13, UCRL-JC-129384. 96-ERD-044.

Alcock, C., et al., "Optical photometry of the eclipsing Large Magellanic Cloud supersoft source CAL 87," *Monthly Notices of the Royal Astronomical Society* **287**, 699, UCRL-JC-129383. 96-ERD-044.

Alcock, C., et al., "The Macho Project Large Magellanic Cloud Variable Star Inventory. III. Multimode RR Lyrae Stars, Distance to the Large Magellanic Cloud, and Age of the Oldest Stars," *Astrophys. J*. **482**, 89, UCRL-JC-129360. 96-ERD-044.

Alcock, C., et al., "The MACHO Project LMC Variable Star Inventory. VII: The Discovery of RV Tauri Stars and New Type II Cepheids in the LMC," *Astronom. J*. **115**, 1921, UCRL-JC-129361. 96-ERD-044.

Alcock, C., et al., "The MACHO Project LMC Variable Star Inventory: VII. The Discovery of RV Tauri Stars and New Type II Cepheids in the Large Magellanic Cloud," *Monthly Notices of the Royal Astronomical Society* **115**, 1921, UCRL-JC-127090. 96-ERD-044.

Alcock, C., et al., "The RR Lyrae Population of the Galactic Bulge from the MACHO Database: Mean Colors and Magnitudes," *Astrophys. J*. **482**, 189, UCRL-JC-128779. 96-ERD-044.

Alcock, C., et al., "The Zero Point of Extinction Toward Baade's Window From RR Lyrae Stars," *Astrophys. J*. **494**, 396, UCRL-JC-128951. 96-ERD-044.

Altschuler, E. L., N. V. Hud, J. A. Mazrimas, B. Rupp, "Random Coil Conformation for Extended Polyglutamine Stretches in Aqueous Soluble Peptides," *J Peptide Res.*, in press. UCRL-JC-122953. 96-DI-010.

Altschuler, E. L., N. V. Hud, J. A. Mazrimas, B. Rupp, "Random Coil Conformation for Extended Polyglutamine Stretches in Aqueous Soluble Peptides," *J. Peptide Res.* **50**, 73. UCRL-JC-122953. 96-DI-010.

Amann, J. F., et al., "High-Energy Test of Proton Radiography Concepts," *11th Biennial Nuclear Explosives Design Physics Conference (NEDPC'97),* Livermore, California, October 20–24, 1997, LA-UR-97-4721. 97-ERD-058.

Anderson, D., et al., “A general multi-link kinematic representation for human limbs,” *16th Congress of the International Society of Biomechanics*, UCRL-JC-127344Abs. 96-ERI-003.

Annese, C. E., and M. G. Miller, *Simulation of Beamline Alignment*, **1**, 1, NIF-15961. 98-ERD-065.

Annese, C. E., *NIF Countdown Messages Simulation*, **1**, 1, NIF-15962. 98-ERD-065.

Armstrong, G. H., *T-1 Ethernet Network Trigger Simulation*, **1**, 1, NIF-4127. 98-ERD-065.

Armstrong, G. H., *Video Capture Trigger Simulation*, **1**, 1, NIF-4128. 98-ERD-065.

Ashby, S. F., W. J. Bosl, R. D. Falgout, S. G. Smith, A. F. B. Tompson, T. J. Williams, “A Numerical Simulation of Groundwater Flow and Contaminant Transport on the Cray T3D and C90 Supercomputers,” *Intern. J. High Perform. Comp. Appl.* **13**(1), pp. 80–93 (1999). UCRL-JC-118635 Rev. 1. 97-ERD-035.

Ashby, S.F., et al., “A Numerical Simulation of Groundwater Flow and Contaminant Transport on the Cray T3D and C90 Supercomputers,” *Int’l J. Supercomp. Apps. and H-P Comp*., February 1999, in press, UCRL-JC-118635. 97-ERD-114.

Asoka-Kumar, P., R. Howell, W. Stoeffl, D. Carte, “High Intensity Positron Program at LLNL,” ed. J. Duggan, *Applications of Accelerators in Research and Industry ’98*, North Holland, Amsterdam, UCRL-JC-132024. 96-ERD-034.

Atherton, C. S., *Biogenic and Biomass Burning Sources of Acetone to the Troposphere*, UCRL-ID-127304. 97-ERD-051.

Athreya, R. M., V. K. Kapahi, P. J. McCarthy, W. van Breugel, “Large Rotation Measures in Radio Galaxies at $Z > 2$,” *Astronomy and Astrophysics* **329**, 809, UCRL-JC-129387. 98-ERI-005.

Averback, R.S., and T. Diaz de la Rubia, “Damage production in metals and semiconductors,” *Solid State Physics* **51**, 281, UCRL-JC-128998. 96-ERD-009.

Bailey, D. S., R. A. London, W. E. Alley, “Hard-tissue ablation simulations using the LATIS computer code,” *Laser-Tissue Interaction IX*, Ed. S. L. Jacques, *SPIE* **3154**, 232, UCRL- JC-130048. 97-ERD-056.

Baldis, H. A., and C. Labaune, “Interplay between parametric instabilities in the context of inertial confinement fusion,” *Plasma Physics and Controlled Fusion* **39**, A51, UCRL-UR-121871. 96-ERI-011.

Baldis, H. A., C. Labaune, J. D. Moody, T. Talinaud, V. T. Tikhonchuk, “Localization of stimulated Brillouin scattering in random phase plate speckles,” *Phys. Rev. Lett.* **80**, 1900-1903, UCRL-JC-128618. 96-ERI-011.

Barbee, T., D. Young, F. Rogers, “Equation of State of Warm Condensed Matter,” *Proc. Mat. Res. Soc*. **499**, 105, UCRL-JC-130201. 98-ERD-052.

Barnard, J. J., et al., “Emittance Growth from Bend-Straight Transitions for Beam Approaching Thermal Equilibrium,” *LINCA98*, Chicago, IL, August 1998, to be published in NIM, UCRL- JC-130607. 96-ERD-048.

Barnard, J. J., et al., “Emittance Growth in Heavy Ion Rings due to Space Charge and Dispersion,” *Workshop on Space Charge Effects in Hadron Rings*, Shelter Island, NY, May 1998, UCRL-JC-130694. 96-ERD-048.

Barnard, J. J., et al., “Heavy Ion Fusion Experiments at LLNL,” *ICFA Advanced Beam Dynamics Workshop*, Bloomington, IN, October 1995, UCRL- JC-122314. 96-ERD-048.

Battersby, C. L., L. M. Sheehan, M. R. Kozlowski, “Effects of wet etch processing on laser-induced damage of fused silica surfaces,” *Laser-Induced Damage in Optical Materials: 1998*, UCRL-ID-131224. 98-ERD-063.

Baumann, T. F., J. G. Reynolds, G. F. Fox, “Synthesis of Novel Pendant Arm Crown Thioethers for Mercury Removal from Acidic Aqueous Solutions,” *ACS Division of Environmental Chemistry*, UCRL-JC-127988Abs. 97-ERD-015.

Baumann, T. F., J. G. Reynolds, G. F. Fox, “Polymer pendant crown thioethers: synthesis and Hg(II) extraction studies of a novel thiacrown polymer,” *Chem. Comm.*, 1637 (1998), UCRL-JC-130647. 97-ERD-015.

Baumann, T. F., J. G. Reynolds, G. F. Fox, “Polymer Pendant Crown Thioethers: Synthesis, Characterization, and Hg^{2+} Extraction Studies of a [17]ane-S_5 Thiacrown Polymer,“ submitted to *Green Chemistry* (1999), UCRL-JC-133064. 97-ERD-015.

Baumann, T. F., J. G. Reynolds, G. F. Fox, “Polymer Pendant Crown Thioethers for Removal of Mercury from Acidic Wastes,” *Proc. 1999 Waste Management Conference*, Tucson, AZ, UCRL-JC-132856. 97-ERD-015.

Baumgartner, T. R., and J. R. Southon, “A 1500 year radiocarbon record of near-surface ocean reservoir ages obtained from the sediments of the Santa Barbara Basin,” *EOS* **77**, 299, UCRL-JC-133208. 97-ERI-009.

Bedrossian, P. J., “Vortex Symmetry and Domain Stability in Micron- and Sub-Micron Scale, Patterned Co Films,” *MRS Spring 1997 Meeting*, March 4, 1997, San Francisco, CA, UCRL-JC-125748. 97-LW-037.

Bedrossian, P. J., and S. P. Vernon, “Binding of Confined Vortex-Pairs in Micron-Scale, Patterned Co Films,” *MRS Fall 1996 Meeting*, December 2–6, 1996, Boston, MA, UCRL-JC-124501. 97-LW-037.

Bedrossian, P. J., M. J. Catrula, T. Diaz de la Rubia, “Damage Evolution and Surface Defect Segregation in Low-Energy Ion-Implanted Silicon,” *Appl. Phys. Lett.* **70**, 176–178, UCRL-JC-125294. 96-ERD-009.

Bedrossian, P. J., M. J. Caturla, T. Diaz de la Rubia, “Defect Diffusion During Annealing of Low-Energy Ion-Implanted Silicon,” *Proc. Materials Research Society Symposium* **439**, 53–58, UCRL-JC-125294. 96-ERD-009.

Bedrossian, P., M. Caturla, T. Diaz de la Rubia, “Damage Evolution and Defect Segregation in Low Energy Ion Implanted Silicon,” accepted by *Appl. Phys. Lett.*, UCRL-JC-125294. 96-ERD-009.

Beiersdorfer, P. “High-Resolution X-Ray Spectra from Low-Temperature, Highly Charged Ions,” *AIP Conference Proc. No. 389*, **121**, UCRL-JC-125360. 97-ERD-103.

Beiersdorfer, P., “Linear X-ray Line Polarization Effects on Spectral Measurements using an Electron Beam Ion Trap,” *NIF Publication Series* **37**, 67, UCRL-JC-130147. 97-ERD-103.

Beiersdorfer, P., A. Osterheld, J. Scofield, J. López-Urrutia, K. Widmann, “Measurement of QED and Hyperfine Splitting in the $2s_{1/2}$-$2p_{3/2}$ X-ray Transition in $^{209}Bi^{80+}$,” *Phys. Rev. Lett.* **80**, 3022, UCRL-JC-127437. 97-ERD-103.

Beiersdorfer, P., et al., “Spectral Catalogue of the Intermediate Ionization States of Iron in the Extreme Ultraviolet,” *Proc. NASA Workshop on Laboratory Space Science*, UCRL-JC-130832. 97-ERD-057.

Beiersdorfer, P., J. R. Crespo López-Urrutia, P. Springer, S. B. Utter, K. L. Wong, “Spectroscopy in the Extreme Ultraviolet on an Electron Beam Ion Trap,” *Rev. of Sci. Instr.*, in press, UCRL-JC-131082. 97-ERD-103.

Beiersdorfer, P., K. Widmann, J. R. Crespo López-Urrutia, “QED and Hyperfine Splitting in the $2s_{1/2}$-2p X-ray Transition in Lithiumlike Bi^{80+},” *Hyperfine Interaction*, in press, UCRL-JC-128718. 97-ERD-103.

Benson L. V., J. W. Burdett, M. Kashgarian, S. P. Lund, F. M. Phillips, R. O. Rye, “Climatic and hydrologic oscillations in the Owens Lake Basin and the adjacent Sierra Nevada, California,” *Science* **274**, 746, UCRL-JC-125154. 97-ERI-009.

Bergstrom, P., et al., “Monte Carlo Transport Physics Algorithms and Variance Reduction Methods in PEREGRINE,” *Med. Phys*. **25**, A186, UCRL-MI-131471. 96-DI-006.

Bergstrom, P., L. Cox, R. Mohan, “Monte Carlo Transport of Photons and Electrons Through Beam Modifiers in the PEREGRINE Dose Calculation System,” *Med. Phys.* **25**, A186, UCRL-MI-131468. 96-DI-006.

Bernstein, L. A., et al., “Probing Reaction Dynamics with the 196Pt(n,xng) Reactions for x≤15,” *Physics Review C - Rapid Communications* **57**, R2799, UCRL-ID-130176. 98-LW-051

Blair, J., D. Beckedahl, J. Kammeraad, G. Schmid, “Spatial Resolution Attainable in Germanium Detectors by Pulse Shape Analysis,” accepted by *Nucl. Instr. and Meth. in Phys. Res.*, UCRL-JC-129137. 97-ERD-017.

Bogen, K. T., “Do U.S. County Data Disprove Linear No-Threshold Predictions of Lung Cancer Risk for Residential Radon? A preliminary assessment of biological plausibility,” *Human Ecol. Risk Assessment* **3**, 157–186, UCRL-JC-125331. 97-ERD-050.

Bogen, K. T., “Mechanistic model predicts a U-shaped relation of radon exposure to lung cancer risk reflected in combined occupational and U.S. residential data,” *BELLE Newsletter* **7**, 9–14, UCRL-JC-130731. 97-ERD-050.

Bogen, K. T., *Biologically based prediction of empirical nonlinearity in lung cancer risk vs. residential/occupational radon exposure*, UCRL-JC-132063. 97-ERD-050.

Bogen, K. T., D. W. Layton, “Risk management for plausibly hormetic environmental carcinogens: the case of radon,” *Human Exper. Toxicol*. **17**, 463–467, UCRL-JC-129909. 97-ERD-050.

Brenan, J. H. Shaw, F. Ryerson, “Experimental constraints on the origin of B/Be variations of arc magams: the role of aqueous fluids,” *7th Annual V.M. Goldschmidt Conference*, Tucson, AZ, June 2-6, 1997, UCRL-JC-126285. 96-ERI-005.

Brenan, J. M., H. F. Shaw, F. J. Ryerson, “Experimental evidence for the origin of lead enrichment in convergent margin magmas,” *Nature* **378**, 54, UCRL-JC-125596. 96-ERI-005.

Brenan, J. M., H. F. Shaw, F. J. Ryerson, “Trace element partitioning between pargasite and melt: development of a predictive model using elastic strain theory,” *Geol. Soc. Amer. Annual Mtg. Abstracts with Programs* **A430**, UCRL-JC-125593. 96-ERI-005.

Brenan, J., E. Neroda, C. C. Lundstrom, H. Shaw, F. J. Ryerson, D. L. Phinney, “Behavior of B, Be, and Li during melting and crystallization: constraints from mineral-melt partitioning experiments,” *Geochemica Cosmochemica Acta* **62**, 2129, UCRL-JC-129052. 96-ERI-005.

Brenan, J., F. Ryerson, H. Shaw, “Li/V as an indicator of the redox state of MORB sources,” (Abstracts) *GAC/MAC Conference*, May 19–21, 1997, Toronto, Canada, UCRL-JC-126373. 96-ERI-005.

Brenan, J., H. Shaw, F. J. Ryerson, “Experimental Evidence for the Role of Aqueous Fluids in the Slab-to-Mantle Transfer of Boron During Subduction,” *Geochemica Cosmochemica Acta*, in press, UCRL-JC-129053. 96-ERI-005.

Brookman, K. W., J. E. Lamberdin, J. S. Albala, R. S. Tebbs, W. Fan, L. H. Thompson, “Candidate recombinational repair genes XRCC3 and hh5RAD51 are yeast RAD51 homologs” *Gordon Conference on Mammalian DNA Repair*, Ventura, CA, February 1997. UCRL-JC-126210Abs. 96-ERD-076.

Brooks, E., and K. A. Warren, “A Study of Performance on SMP and Distributed Memory Architectures Using a Shared Memory Programming Model,” *Supercomputing 97*, UCRL-JC-127449. 97-ERD-114.

Brotherton, M. S., B. J. Wills, A. Dey, W. van Breugel, R. Antonucci, “Spectropolarimetry of 3CR 68.1: A Highly Inclined Quasar,” *Astrophys. J*. **501**, 110, UCRL-JC-129159. 98-ERI-005.

Brown, G., P. Beiersdorfer, D. Liedahl, S. Kahn, K. Widmann, “Laboratory Measurements and Modeling of the Fe XVII X-Ray Spectrum,” *Astrophys. J*. **502**, 1015, UCRL-JC-128877. 97-ERD-057.

Brown, N. W., J. A. Hassberger, “New Concepts for Small Power Reactors Without on-site Refueling for Non-Proliferation,” IAEA-AG-1021, IWGFR/97, July 98, UCRL-JC-131317. 97-ERD-068.

Brown, N. W., J. A. Hassberger, E. Greenspan, E. Elias, “Proliferation Resistant Fission Energy Systems,” *International Conference on Future Energy Systems, Global 97*, UCRL-JC-127959, 97-ERD-068.

Brown, T. A., P. D. Quay, R. C. Francis, D. Holmgren, “Radiocarbon time-histories for subpolar North Pacific surface waters spanning the last 50 years,” *EOS, Transactions of the AGU* **79**(17), 167, UCRL-JC-130385Abs. 97-ERD-052.

Bryant, R. M., *ICCS Network Simulation LDRD Final Report Summary*, **1**, 1, UCRL-ID-133085. 98-ERD-065.

Bryant, R. M., *NIF ICCS Network Simulation Final Report*, **1**, 1, NIF-15957. 98-ERD-065.

Caleria, K., G. Rau, P. Duffy, “Predicted oceanic degassing of radiocarbon and increase in atmospheric radiocarbon content,” *Geophys. Res. Lett.*, in press, UCRL-JC-127868. 98-ERD-007.

Campbell H. L., S. R. Visuri, L. B. Da Silva, “Effects of Stress Waves on Cells,” *SPIE* **3254**, 92–96, UCRL-JC-130131. 98-LW-030.

Campbell, G., et al., “Multi–Scale Modeling of Polycrystal Plasticity: A Workshop Report,” *Mat. Sci. and Eng. A* **1**, 251, UCRL-JC-129124. 97-ERD-117.

Campbell, G., W. King, D. Cohen, “Data Preparation for Quantitative High Resolution Electron Microscopy,” *Microscopy and Microanalysis* **3**, 299, UCRL-JC-124741. 97-ERD-117.

Candy, J. V., G. H. Thomas, D. J. Chinn, J. B. Spicer, “Laser Ultrasonic Signal Processing: A Model-Reference Approach,” *J. Acoustical Soc. Am*. **1**(1), 278–284, UCRL-JC-122414. 97-ERD-083.

Caturla, M. J., and T. Diaz de la Rubia, “Dose Rate Effects During Damage Accumulation in Silicon,” *Proc. Materials Research Society Symposium* **439**, 125–129, UCRL-JC-126223. 96-ERD-009.

Caturla, M. J., M. D. Johnson, T. Diaz de la Rubia, “The Fraction of substitutional Boron in Ion implanted silicon, *Appl. Phys. Lett*. **72**, 2736, UCRL-JC-129148. 96-ERD-009.

Caturla, M. J., T. Diaz de la Rubia, P. B. Bedrosian, “Modeling Ion Implantation and Diffusion in Silicon,” *Materials Science Forum*, 248–249, UCRL-JC-125676. 96-ERD-009.

Caturla, M., and T. Diaz de la Rubia, “Modeling Ion Implantation and Defect Diffusion in Si,” *Nuc. Instru. and Meth. B.*, UCRL-JC-230994. 96-ERD-009.

Caturla, M., T. Daiz de la Rubia, L. Marques, G. H. Gilmer, “Ion Beam Processing of Silicon at keV Energies: A Molecular Dynamics Study,” *Phys. Rev. B* **54**, 16683, UCRL-JC-122487. 96-ERD-009.

Chang, J., E. Dragon, C. Ebbers, I. Bass, C. Cochran, “An efficient diode-pumped Nd:YAG laser with 451 W of CW IR and 182 W of pulsed green output,” *Trends in Optics and Photonics* **19**, 300, 1998, UCRL-JC-129704. 98-ERD-073.

Claybourn, R. V., *Video Capture Timing Trigger Analysis*, **1**, 1, NIF-4130. 98-ERD-065.

Cleary, A. J., R. D. Falgout, V. E. Henson, J. E. Jones, “Coarse-Grid Selection for Parallel Algebraic Multigrid,” *SIAM Workshop*, UCRL-JC-130893. 97-ERD-114.

Cohen, B. I., B. F. Lasinski, A. B. Langdon, E. A. Williams, H. A. Baldis, C. Labaune, “Suppression of stimulated Brillouin scattering by seeded ion wave mode coupling,” *Phys. Plasmas* **5**, 3402–3407, UCRL-JC-129490. 96-ERI-011.

Cohen, B. I., E. B. Hooper, M. C. Spang, C. W. Domier, "Theoretical Aspects of the Use of Pulsed Reflectrometry in a Spheromak Plasma," accepted by *Rev. of Sci. Instr*., UCRL-JC-129499. 97-SI-009.

Cohen, B. I., L. L. LoDestro, E. Hooper, C. Bickford; A. Thomas, "Simulations of Ultra-Short-Pulse Reflectrometry for Diagnosing Plasma Density and Magnetic Field Profiles," accepted by *Plasma Phys. and Contr. Fusion*, UCRL-JC-127025. 97-SI-009.

Cohen, R. H., and D. D. Ryutov, "Sheath over a divertor plate with small-scale surface imperfections," *International Sherwood Fusion Theory Conference*, UCRL-JC-129678Abs. 98-LW-023.

Cohen, R. H., and D. D. Ryutov, "Sheath over a rough surface in a tilted magnetic field," *Physics of Plasmas* **5**, 2194, UCRL-JC-128506. 98-LW-023.

Cohen, R. H., E. B. Hooper, L. L. LoDestro, N. Mattor, L. D. Pearlstein, D. D. Ryutov, *Theoretical Issues in Spheromak Research*, UCRL-ID-127002. 97-SI-009.

Cohen, R. H., R. E. Cid, E. B. Hooper, et al., "Sheath over a finely-structured divertor plate," accepted by *J. Nucl. Mat.*, UCRL-JC-128903. 98-LW-023.

Colston, Jr., B.W., M. J. Everett, L. B. Da Silva, L. L. Otis, P. Stroeve, H. Nathel, "Imaging of hard and soft-tissue structure in the oral cavity by optical coherence tomography," *Appl. Optics* **37**, 3582, UCRL-JC-127487. 98-ERD-062.

Colvin, M. E, C. L. Janssen, E. T. Seidl, I. M. B. Nielsen, C. F. Melius, "Energies, resonance and UHF instabilities in polycyclic aromatic hydrocarbons and linear polyenes," *Chem. Phys. Lett.* **287**, 537, UCRL-JC-128594. 98-SI-008.

Colvin, M. E., E. T. Seidl, I. M. B. Nielsen, L. LeBui, F. T. Hatch, "Deprotonation and hydride shifts in nitrenium and iminium forms of aminoimidazole-azaarene mutagens," *Chemnico-Biological Interactions* **108**, 39–66. UCRL-JC-128579. 96-DI-010.

Colvin, M. E., F. T. Hatch, J. S. Felton, "Chemical and biological factors affecting mutagen potency," *Mutation Research* **400**, 479, UCRL-JC-130001. 98-SI-008.

Cox, L., A. Schach von Wittenau, P. Bergstrom, R. Mohan, B. Libby, Q. Wu, D. Lovelock, "Photon Beam Description in PEREGRINE for Monte Carlo Dose Calculations," *International Conference on Computers in Radiotherapy*, May 27–30, 1997, UCRL-JC-12673. 96-DI-006.

Cox, L., J. T. Bohm, M. Chadwick, P. Deluca, J. Siebers, "PEREGRINE Monte Carlo Dose Calculations for Radiotherapy using Clinically Realistic Neutron and Proton Beams," *International Conference on Nuclear Data for Science and Technology (NDST)*, May 19–24, 1997, UCRL-JC-127198. 96-DI-006.

Crespo López-Urrutia, J. R., P. Beiersdorfer, D. W. Savin, K. Widmann, "Precision Measurement of the Lifetime of the 1s2s $^3S_1$ Metastable Level in Heliumlike O^{6+}," *Phys. Rev. A* **58**, 238, UCRL-JC-129347. 97-ERD-103.

Critchlow, T., "Automatic Generation of Warehouse Mediators using an Ontology Engine," presentation, *5th International Workshop on Knowledge Rep. Meets Databases*, UCRL-MI-130883. 97-ERD-033.

Critchlow, T., "DataFoundry," presentation, *Conference on Information Technology Applications in Biomed*., UCRL-MI-130707. 97-ERD-033.

Critchlow, T., "Metadata-based Mediator Generation," presentation, *3rd International Conference on Cooperative Information Systems*, UCRL-MI-130234. 97-ERD-033.

Critchlow, T., K. Fidelis, M. Ganesh, R. Musick, T. Slezak, "Warehousing Techniques for Dynamic Environments," submitted to the *International Symposium on Molecular Biology*, UCRL-JC-129576. 97-ERD-033

Critchlow, T., M. Ganesh, C. Musick, "DataFoundry," *SuperComputing 97*, UCRL-TB-127593-Rev. 1. 97-ERD-033.

Critchlow, T., M. Ganesh, C. Musick, *The DataFoundry Website*, located at http://www.llnl.gov/casc/datafoundry/index.html, UCRL-MI-127680-Rev. 1. 97-ERD-033.

Critchlow, T., M. Ganesh, R. Musick, "Automatic generation of warehouse mediators using an ontology engine," *5th International Workshop on Knowledge Representation meets Databases*. UCRL-JC-129930-Rev. 1. 97-ERD-033.

Critchlow, T., M. Ganesh, R. Musick, "Metadata-based mediator generation," *3rd International Conference on Cooperative Information Systems*. UCRL-JC-130234. 97-ERD-033.

Critchlow, T., M. Ganesh, R. Musick, *DataFoundry Interface Page*, located at http://ihem.llnl.gov/datafoundry/html/access-home.html, UCRL-MI-127680-Rev. 1. 97-ERD-033.

Critchlow, T., M. Ganesh, R. Musick, *DataFoundry, Pre-proposal, Life Science Informatics Program*, UCRL-PROP-131341. 97-ERD-033.

Critchlow, T., and R. Musick, *Metadata '99 Web Pages*, located at http://www.llnl.gov/liv_comp/metadata/md99.html, UCRL-MI-131328. 97-ERD-033.

Cullen, J., and K. T. Bogen, *Historical U.S. residential fuel use and female lung cancer mortality*, UCRL-JC-131635. 97-ERD-050.

Cynn, H., and C. S. Yoo, "Equation of state of tantalum to 174 GPa," *Phys. Rev. B*, in print, UCRL-JC-130367. 98-ERD-059.

De Breuck, C., M., S. Brotherton, H. D. Tran, W. van Breugel, H. J. A. Röttgering, "Discovery of an Ultra-Steep Spectrum, Highly Polarized Red Quasar at $Z = 1.462$," *Astronom. J.* **116**, 13, UCRL-JC-129737. 98-ERI-005.

De Yoreo, J. J., C. Orme, H. Teng, P. M. Dove, "Physical controls on crystal growth during biomineralization," *Twelfth International Conference on Crystal Growth and the Tenth International Conference on Vapor Growth and Epitaxy*, July 1998, UCRL-JC-128976Abs. 97-LW-069.

De Yoreo, J. J., et al., "Atomic force microscopy studies of solution crystal growth morphology and dynamics," *American Chemical Society*, April 1997, UCRL-JC-125437. 97-LW-069.

De Yoreo, J. J., et al., "Atomic force microscopy studies of solution crystal growth morphology and dynamics," *Materials Research Society* **46**, Spring 1997, UCRL-JC-125437. 97-LW-069.

De Yoreo, J. J., et al., "Characterization of optical performance and defect structure of rapidly grown crystals of KDP and DKDP," *American Conference on Crystal Growth West*, UCRL-JC-130623Abs. 97-ERD-098.

De Yoreo, J. J., T. A. Land, C. Orme, J. D. Lee, "Investigating the surface morphology and growth dynamics of solution-based crystals using the AFM," *Gordon Research Conference, Thin Film and Crystal Growth Mechanisms*, UCRL-JC-129021Abs. 97-LW-069.

De Yoreo, J. J., T. A. Land, C. Orme, J. D. Lee, "Studying the surface morphology and growth dynamics of solution-based crystals using the atomic force microscope," *Romanian Conference on Advanced Materials '97*, UCRL-JC-127726Abs. 97-LW-069.

De Yoreo, J. J., T. A. Land, C. Orme, M. Mc Bride, J. T. Palmore, "Investigating the evolution of crystal growth morphology and kinetics from small to large molecules using in situ atomic force microscopy," *Seventh International Conference on the Crystallisation of Biological Macromolecules*, UCRL-JC-129226Abs. 97-LW-069.

Demos, S. G., et al., "Temperature and spectral investigation of bulk KDP below damage using 355nm laser irradiation," *Proc. SPIE 29th Annual Boulder Damage Conference* **3244**, 223, UCRL-JC-128357. 97-ERD-098.

Demos, S. G., M. Staggs, M. Yan, J. J. De Yoreo, H. B. Radousky, "Raman scattering investigation of KH2PO4 subsequent to high fluence laser irradiation," *Appl. Phys. Lett.* **72**, 2367, UCRL-JC-129340. 97-ERI-006.

Demos, S. G., M. Yan, M. Staggs, H. B. Woods, Z. L. Wu, H. B. Radousky, J. J. De Yoreo, "Temperature and spectral investigation of bulk KDP below damage using 355 nm laser irradiation," *SPIE* **3244**, 223, UCRL-JC-128357. 97-ERI-006.

Demos, S. G., M. Yan, M. Staggs, J. J. De Yoreo, H. B. Radousky, "Raman scattering investigation of KH2PO4 subsequent to high fluence laser irradiation," *Appl. Phys. Lett.* **72,** 2367, UCRL-JC-129340. 97-ERD-098.

Deri, R. J., S. Gemelos, et al., "Simple fabrication of WDM filters for byte-wide, multimode cable interconnects," *Integrated Photonics Research Conference*, Victoria, Canada, April 1998, Paper IThC4, UCRL-JC-129066. 98-ERD-057.

Diaz de la Rubia, T., "Defect Production in Metals and Covalent Semiconductors," *Nuc. Instru. and Meth. B.* **120**, 19–26, UCRL-JC-126216. 96-ERD-009.

Diaz de la Rubia, T., M. J. Caturla, E. A. Alonso, M. J. Fluss, J. M. Perlado, "Self Decay -Induced Damage Production and Microstructure Evolution in FCC Metals: An Atomic Scale Computer Simulation Approach," *J. Comp.-Aided Mat. Sci.*, December 1998, UCRL-JC-131322. 98-ERD-028.

Dinh, L. N., W. McLean II, M. A. Schildbach, M. Balooch, "Synthesis and Characterization of Si/Cs/O Nanocluster Thin Film with Negative Electron Affinity," submitted to *Phys. Rev. B*, UCRL-JC-130945. 98-LW-006.

Ditmire, T., K. Shigemori, B. A. Remington, K. Estabrook, R. A. Smith, "The production of strong blast waves through the intense irradiation of atomic clusters," accepted by *Astrophys. J. Supp.*, UCRL-JC-131534. 98-ERD-084.

Divine, K. K., J. L. Lewis, P. G. Grant, G. Bench, "Quantitative Particle Induced X-ray Emission Imaging of Rat Olfactory Epithelium applied to the Permeability of Rat Epithelium to Inhaled Aluminum," *Proc. 216 American Chemical Society Meeting* **1**, Toxi 66, UCRL-JC-130665. 98-ERI-004.

Dong, L.-M., S. Parkin, B. Rupp, "Novel mechanism for defective receptor binding of apolipoptotein E2 in type-III hyperlipopproteinemia," *Nature Structural Biology* **3**(8), 718, UCRL-JC-124738. 96-DI-010.

Dong, L-M., et al., “Novel mechanism for defective receptor binding of apolipoptotein E2,” *Protein Science* **5**, 163, UCRL-JC-124738. 96-DI-010.

Dosanjh, M. K., et al., “Isolation and characterization of RAD51C, a new human member of the RAD51 family of related genes, including two-hybrid interactions,” *Nucleic Acids Res*. **26**(5), 1179–84. URCL-JC-128751. 96-ERD-076.

Duffy, P. K. Caldeira, “Sensitivity of Simulated Salinities in a Three-dimensional Ocean General Circulation Model to Vertical Mixing of Destabilizing Surface Fluxes,” *Climate Dynamics*, in press, UCRL-JC-129901. 98-ERD-007

Duffy, P., and K. Caldeira, “Sensitivity of simulated CFC-11 distributions in a global ocean model to the treatment of salt rejected during sea-ice formation,” *Geophys. Res. Lett.* **25**, 1003, UCRL-JC-127709. 98-ERD-007.

Eastman, R. G., P. T. Springer, W. H. Goldstein, C. A. Iglesias, “Laboratory Measurement of Supernova Expansion Opacities,” *Harvard Space Science Workshop*, UCRL-JC-13556Abs. 97-ERD-108.

Elisseev, V. V., I. Ourdev, W. Rozmus, V. T. Tikhonchuk, C. E. Capjack, P. E. Young, “Ion wave response to intense laser beams in underdense plasmas,” *Phys. Plasmas*, in press, UCRL-JC-127447. 96-ERI-011.

Erlandson, A. C., et al., “Flashlamp-pumped Nd:glass amplifiers for the National Ignition Facility,” submitted to *Proc. 13th Topical Meeting on the Technology of Fusion Energy* (Embedded Topical Meeting, 1998 ANS Annual Meeting) held June 7–11, 1998, Nashville, Tennessee, UCRL-JC-902345. 97-ERD-133.

Erlandson, A. C., et al., *Physics Basis for Optical Performance of the NIF Amplifiers*, LLNL, January 11, 1999, UCRL-ID-132680. 97-ERD-133.

Erzberger, J. D. Barsky, O. Scharer, M. Colvin, D. Wilson, “Elements in abasic site recognition by the major human and Escherichia coli apurinic/apyrimidinic endonucleases,” *Nucleic Acids Res*. **26**, 2771–2778, UCRL-JC-130481. 97-ERD-002.

Erzberger, J. P., D. Barsky, O. D. Scharer, M. E. Colvin, D. M. Wilson, III, “Elements in abasic site recognition by the major human and Escherichia coli apurinic/apyrimidinic endonucleases, *Nucleic Acids Res.* **26**, 2771–2778, UCRL-JC-130481. 96-DI-010/98-SI-008.

Everett, M. J., K. Schoenenberger, B. W. Colston, Jr., L. B. Da Silva, “Birefringence characterization of biological tissue using optical coherence tomography,” *Optics Lett*. **23**, 1, UCRL-JC-128617. 98-ERD-062.

Falgout, R., “AMGe: A Theory for a New Generation AMG for Finite Element Discretizations,” conference presentation, UCRL-MI-130240. 97-ERD-114.

Falgout, R., “Scalable Linear Solvers,” *Supercomputing 97*, UCRL-TB-128636. 97-ERD-114.

Falgout, R., “Scalable Linear Solvers,” *Supercomputing 98*, UCRL-TB-128636-Rev. 1. 97-ERD-114.

Feit, M. D., A. M. Rubenchik, F. Y. Genin, S. Schwartz, L. M. Sheehan, “Extrapolation of damage test data to predict performance of large area NIF optics at 355 nm,” *Laser Induced Damage in Optical Materials: 1998*, UCRL-ID-131222. 98-ERD-063.

Feit, M., A. Rubenchik, B. Shore, “Unique aspects of laser energy deposition in the fs pulse regime,” *SPIE* **2672**, 36, UCRL-JC-123302. 97-LW-074.

Feit, M., A. Rubenchik, B-M. Kim, L. Da Silva, M. Perry, B. Stuart, “Physical characterization of ultrashort laser pulse drilling of biological tissue,” *Appl. Surf. Sci*. **127**, 869, UCRL-JC-127269. 97-LW-074.

Feit, M., L. Stuart, M. Perry, A. Rubenchik, “Ultrashort laser ablation of hard tissue,” *OSA Trends in Optics and Photonics* **17**, 173, UCRL-JC-129002. 97-LW-074.

Fernandez, A., M. R. Gibbons, M. A. Wall, C. Cerjan, “Magnetic Domain Structure and Magnetization Reversal in Sub-micron-Scale Co Dots,” to appear in *J. Magnetism and Magnetic Materials*, UCRL-JC-130117. 97-LW-037.

Fessenden, T. J., et al., “Intense Heavy Ion Beam Transport with Electric and Magnetic Quadrupoles,” *Fusion Engineering and Design* **32**, 267, UCRL-JC-127103. 96-ERD-048.

Fife, R. A., et al., “The Proton Radiography Concept,” *Proc. Third International Symposium on Development and Application of Semiconductor Tracking Detectors* (The Hiroshima Symposium) at Melbourne, December 9–12, 1997, to be published in *Nucl. Instru. Meth.*, LA-UR-98-1368. 97-ERD-058.

Fluss, M., T. Diaz de la Rubia, M. Caturla, M. Wall, and T. Felter, “Radiation Studies of High *Z*, Low Melting FCC Metals and Alloys,” accepted by *J. Nucl. Mat.*, UCRL-JC-903681. 98-ERD-028.

Fournier, K. F., et al., “Benchmarking Atomic Physics Models for MCF Plasma Physics Experiments,” *Rev. Sci. Instruments*, UCRL-JC-132593. 97-ERD-057.

Fournier, K., M. Cohen, M. May, W. Goldstein, *Radiative Cooling Rate and Charge State Distribution for Argon in a Low Density Plasma, Atomic Data and Nuclear Data Tables*, UCRL-JC-129529. 97-ERD-057.

Fournier, K., M. Cohen, W. Goldstein, “Dielectronic Recombination Rates in H-like Ar17+ to Ne-like Ar8+,” *Phys. Rev. A* **56**, 4715, UCRL-JC-127789. 97-ERD-057.

Fournier, K., M. May, D. Pacella, B. Gregory, M. Finkenthal, W. Finkenthal, “Calculated Radiative Power Losses from Mid- and High-Z Impurities in Tokamak Plasmas,” *Proc. AIP Conference* **443**, 73, UCRL-JC-130183. 97-ERD-057.

Fowler, T. K., D. D. Hua, E. B. Hooper, R. W. Moir, L. D. Pearlstein, “Wall-Confined High Beta Spheromak,” *Proc. US-Japan Workshop on Physics of High-Beta Fusion Plasmas*, **96**, UCRL-JC-130151. 97-SI-009.

Fowler, T. K., D. D. Hua, E. B. Hooper, R. W. Moir, L. D. Pearlstein, “Pulsed Spheromak Fusion Reactors,” submitted to *Comments on Plasma Physics and Controlled Fusion*, UCRL-JC-132109. 97-SI-009.

Fried, L. E., and W. M. Howard, “An accurate equation of state for the exponential-6 fluid,” *J. Chem. Phys*. **109**, 7348, UCRL-JC-129145. 97-ERD-101.

Fried, L. E., C. Wu, G. Fox, P. Pagoria, “High performance explosive molecules,” *Proc. Energetic Material Workshop*, Annapolis, MD, December 3–6, 1996, UCRL-JC-125713Abs. 97-ERD-101.

Friedman, A., and D. P. Grote, “3D Particle Simulation of Space-Charge-Dominated Beams,” *International Meeting on Open Problems in Charged Particle Transport*, Paris, France, June 17-21, 1996, UCRL-JC-123767. 96-ERD-048.

Friedman, A., et al., “Recirculating induction accelerators for inertial fusion: prospects and status,” *Fusion Engineering and Design* **32**, 235, UCRL-JC-121455. 96-ERD-048.

Froula, D., and P. Young, “Sonoluminescence for the Undergraduate Laboratory,” UCRL-JC-129336. 98-ERD-081.

Gaarde, M. B., F. Salin, E. Constant, P. Balcou, K. Schafer, K. C. Kulander, A. L’Huillier, “Spatio-temporal separation of high harmonic radiation into two quantum path components,” *Phys. Rev. A* **59**, UCRL-JC-131594. 98-LW-013.

Gaarde, M. B., P. Antoine, A. L’Huillier, K. J. Schafer, K. C. Kulander, “Macroscopic studies of short-pulse high-order harmonic generation using the time-dependent Schrödinger equation,” *Phys. Rev. A* **57**, 4553, UCRL-JC-129924. 98-LW-013.

Gavel, D. T., and H. W. Friedman, “Measurements of the Lick Observatory sodium laser guide star,” *Proc. SPIE* **3353**, 254–259, September 1998. UCRL-JC-233687. 97-ERD-037.

Genin, F. Y., J. H. Campbell, A. Salleo, “Nano-second rear surface laser drilling of fused silica in the IR and the UV,” *Gordon Research Conference on Laser Interactions with Materials*, UCRL-MI-130967. 98-ERD-063.

Gibbard, S. G., E. H. Levy, J. I. Lunine, “Lightning on Neptune,” submitted to *Icarus*, UCRL-JC-129368. 96-ERI-002.

Gibbard, S., B. Macintosh, D. Gavel, C. Max, I. de Pater, A. Ghez, E. Young, C. McKay, “Titan: High Resolution Speckel Images from the Keck Telescope,” accepted by *Icarus*, UCRL-JC-128848. 96-ERI-002.

Gibbard, S., B. Macintosh, D. Gavel, C. Max, I. de Pater, A. Ghez, E. Young, C. McKay, “Very High Resolution IR Imaging of Titan’s Surface and Atmosphere,” *Bull. Amer. Astronom. Soc.*, UCRL-126420Abs. 96-ERI-002.

Govindasamy, B., M. Wehner, C. R. Mechoso, P. B. Duffy, “The Influence of a Land The Influence of a Land Surface Scheme on Simulated Climate by LLNL/UCLA AGCM,” *Global and Planetary Change*, in press, UCRL-JC-130941. 98-ERD-007

Greenspan, E., E. Elias, W. E. Kastenberg, N. Stone, “Non-Proliferation Liquid Metal Cooled Reactors for Developing Countries,” a document prepared and issued by the U.C. Center for Nuclear and Toxic Waste Management, 97-ERD-068.

Greenspan, E., W. E. Kastenberg, N. Stone, N. W. Brown, K. Aoki, “Compact Long Fuel-Life Reactors for Developing Countries,” *ICENES Conference*, Tel Aviv, Israel, July 98, a document submitted by the U.C. Nuclear Engineering Department, 97-ERD-068.

Gruber, L., B. R. Beck, J. Steiger, D. Schneider, J. P. Holder, D. A. Church, “Highly Charged Ion Trapping and Cooling,” *15th International Conference on the Application of Accelerators in Research and Industry*, AIP Press, New York, UCRL-JC-132208. 96-ERD-052.

Gu, M. P. Beiersdorfer, G. Brown, S. Kahn, D. Liedahl, K. Reed, D. Savin, “Laboratory Measurements of Resonant Contributions to Fe XXIV Line Emission,” *Proc. First International Conference on Atomic and Molecular Data and Their Applications*, UCRL-JC-132214. 97-ERD-057.

Hagmann, C., D. Kinion, W. Stoeffl, K. van Bibber, et al., “A large scale search for dark matter axions,” *18th Texas Symposium on Relativistic Astrophysics*, December 15-20, 1996, Chicago, Illinois, published by World Scientific, UCRL-JC-129343. 96-LW-061.

Hagmann, C., D. Kinion, W. Stoeffl, K. van Bibber, et al., “First results from a second generation galactic axion experiment," *Nuc. Phys. B* **51B**, 209, UCRL-JC-124162. 96-LW-061.

Hagmann, C., D. Kinion, W. Stoeffl, K. van Bibber, et al., "Results from a high-sensitivity search for cosmic axions," *Phys. Rev. Lett*. **80**, 2043, UCRL-JC-129346. 96-LW-061.

Hamza, A. V., A. Barnes, T. Schenkel, D. H. Schneider, "Secondary Ion Coincidence in Highly Charged Ion Based Secondary Ion Mass Spectrometry for Process Characterization," *J. Vacuum Sci. and Tech*. **A17**, UCRL-JC-130627. 97-ERD-102.

Harrison, T. M., A. Yin, F. J. Ryerson, "Orographic Evolution of the Himalayan and Tibetan Plateau," *Tectonics and Climate Change* (in press), UCRL-JC-126356. 97-ERI-003.

Hart, J., et al., "The Telescope System of the MACHO Program," *Publications of the Astronomical Society* **108**, 220, UCRL-JC-192382. 96-ERD-044.

Hartmann-Siantar, C. P. et al., "Validation and Clinical Implementation of the PEREGRINE Monte Carlo Dose Calculation System for Photon Beam Therapy Planning," *American Association of Physicists in Medicine, 38th Annual Meeting and Exhibition*, Milwaukee, WI, July 1997, UCRL-JC-127791. 96-DI-006.

Hartmann-Siantar, C., "Validation and Clinical Implementation of the PEREGRINE Monte Carlo Dose Calculation System for Photon Beam Therapy," *1997 World Congress on Medical Physics and Biomedical Engineering*, Nice, France, September 14-19, 1997, UCRL-JC-127791. 96-DI-006.

Hartmann-Siantar, C., E. Moses, "The PEREGRINE program: using physics and computer simulation to improve radiation therapy for cancer," *Eur. J. Phys*. **19**, 1-9, UCRL-JC-131610. 96-DI-006.

Hartmann-Siantar, C., et al., "The LLNL PEREGRINE Project," *International Conference on Computers in Radiotherapy*, May 27–30, 1997, UCRL-JC-126732. 96-DI-006.

Hartmann-Siantar, C., P. M. Bergstrom, et al., "Application of the PEREGRINE Monte Carlo Dose Calculation System for Radiation Therapy," *1997 International Conference on Monte Carlo Methods* $[E=(MC)^2]$, Monte Carlo, September 20, 1997, UCRL-JC-127185. 96-DI-006.

Hatch, F. T., and M. E. Colvin, "Quantitative structure-activity (QSAR) relationships of mutagenic aromatic and heterocyclic amines," *Mutation Res.* **376**, 87–96. UCRL-JC-126577. 96-DI-010.

Hatch, F. T., M. E. Colvin, E. T. Seidl, "Structural and Quantum Chemical Factors Affecting Mutagenic Potency of Aminoimidazo-Azaarenes," *Environmental and Molecular Mutagenesis* **27**, 314–330. UCRL-JC-122482. 96-DI-010.

Hatchett, S. P., S. C. Wilks, M. D. Perry, "Modeling Laser Driven Radiography," *28th Annual Anomalous Absorption Conference*, Bar Harbor, UCRL-JC-902678. 97-ERD-127.

Henry, G., et al., "Observation of Photonuclear Excitation in High-Energy Density Laser Experiments," *Bull. Am. Phys. Soc*., UCRL-JC-903196. 97-ERD-127.

Herman, S., M. Perry, A. Rubenchik, L. DaSilva, M. Glinsky, M. Feit, D. Mathews, "Subpicosecond laser cutting of hard tissue," submitted to *R&D100 Awards*, UCRL-JC-233660. 97-LW-074.

Hibbard, R. L., R. B. Michie, M. D. Summers, L. W. Liou, "Development of a metrology instrument for mapping the crystallographic axis in large optics," *1998 OSA Technical Digest Series, Optical Fabrication and Testing* **12**, 71, UCRL-MI-131111. 98-ERD-066.

Hibbard, R. L., R. E. English Jr., J. J. De Yoreo, R. C. Montesanti, "Frequency converter design and manufacturing considerations for the National Ignition Facility," *1998 OSA Technical Digest Series, Optical Fabrication and Testing* **12**, 74, UCRL-MI-131110. 98-ERD-066.

Hilgenfeldt, S., D. Lohse, W. Moss, "Water-Temperature - Dependence of Single Bubble Sonoluminescence," *Phys. Rev. Lett*. **80**, 1332, UCRL-JC-131347. 98-ERD-081.

Hill, D. N., et al., "Plasma Diagnostics for the Sustained Spheromak Physics Experiment," accepted by *Rev. of Sci. Instr*., UCRL-JC-129686Abs. 97-SI-009.

Hollerbach, K., et al., "3-d finite element model development for joint biomechanics," *Sixth International Symposium on Computer Simulation in Biomechanics*, UCRL-JC-126796. 96-ERI-003.

Hollerbach, K., et al., "3-d, nonlinear finite element analysis of prosthetic joint implants for the thumb carpometacarpal joint," *16th Congress of the International Society of Biomechanics*, UCRL-JC-127346Abs. 96-ERI-003.

Hollerbach, K., et al., "A 3-d finite element model of the human index finger," *16th Congress of the International Society of Biomechanics*, UCRL-JC-127342Abs. 96-ERI-003.

Hollerbach, K., et al., "A computational tool for comparison of kinematic mechanisms and commonly used kinematic models," *Sixth International Symposium on Computer Simulation in Biomechanics*, UCRL-JC-126797. 96-ERI-003.

Hollerbach, K., et al., “Computational Biomechanics: Finite element analyses of human and prosthetic joints,” Videotape, UCRL-MI-126408-Rev. 1. 96-ERI-003.

Hollerbach, K., et al., “Errors in applying the screw deviation method to calculate motion produced by single degree of freedom mechanisms,” *16th Congress of the International Society of Biomechanics*, UCRL-JC-127341Abs. 96-ERI-003.

Holloway, F. W., *CORBA Performance Measurements and Predictions within the ICCS*, **1**, 1, NIF-4131. 98-ERD-065.

Holloway, F. W., *Evaluation of CORBA for Use in Distributed Control Systems*, **1**, 1, NIF-15963. 98-ERD-065.

Hölzer, G., E. Förster, D. Klöpfel, P. Beiersdorfer, G. V. Brown, J. Crespo López-Urrutia, K. Widmann, “Absolute Wavelength Measurement of the Lyman-__Transitions of Hydrogenic Mg^{11+},” *Phys. Rev. A* **57**, 945, UCRL-JC-127511. 97-ERD-103.

Hooper, E. B., “Coupled Spheromak-Helicity Injector in the Sustained Spheromak Physics Experiment,” *Proc. US-Japan Workshop on Physics of High-Beta Fusion Plasmas* **39**, UCRL-JC-130428. 97-SI-009.

Hooper, E. B., et al., “Sustained Spheromak Physics Experiment,” accepted by *Fusion 1998*, UCRL-JC-132034. 97-SI-009.

Hooper, E. B., et al., *The Spheromak Path to Fusion Energy*, UCRL-ID-130429. 97-SI-009.

Hooper, E. B., L. D. Pearlstein, R. H. Bulmer, “MHD Equilibria in a Spheromak Sustained by Coaxial Injection,” submitted to *Nuclear Fusion*, UCRL-JC-132023. 97-SI-009.

Hooper, E. B., R. H. Cohen, D. D. Ryutov, “Theory of Edge Plasma in Spheromak,” accepted by *J. Nucl. Mat. and Methods*, UCRL-JC-103767. 97-SI-009.

Hooper, E. B., *Sustained Spheromak Physics Experiment, SSPX*, UCRL-ID-126278. 97-SI-009.

Horn, J. M., T. C. Legler, A. M. Happel, “Optimization of TCE Degradation by Methylosinus Strains,” *Abstracts of the 97th General Meeting of the Amer. Soc. for* Microbiology, 1997, **Q102**, 472, UCRL-JC-132817Abs. 97-ERD-030.

Hornung, R., and S. Kohn, “Future Directions for AMR in ASCI and Other LLNL Simulation Projects,” UCRL-ID-128332. 97-ERD-114.

Howell, R. H., T. E. Cowan, J. H. Hartley, P. A. Sterne, “Positron Beam Lifetime Spectroscopy at Lawrence Livermore National Laboratory,” ed. J. Duggan, *Applications of Accelerators in Research and Industry ’96*, North Holland, Amsterdam, **392**, 451, UCRL-JC-124616. 96-ERD-034.

Howell, R. H., J. Jean, K. G. Lynn, J. Poate, W. Pickett, S. Y. Tong, R. West, *Applications and Advances of Positron Beam Spectroscopy*, UCRL-JC-130205. 96-ERD-034.

Howell, R. H., T. E. Cowan, J. Hartley, P. Sterne, B. Brown, “Positron Beam Lifetime Spectroscopy of Atomic Scale Defect Distributions in Bulk and Microscopic Volumes,” *J. Appl. Surf. Sci*. **116**, 7, UCRL-JC-123636. 96-ERD-034.

Howell, R. H., W. Stoeffl, A. Kumar, P. A. Sterne, T. E. Cowan, J. Hartley, “High Current Pulsed Positron Microprobe,” ed. J. Jean, *Proc. Eleventh International Conference on Positron Annihilation* **11**, 644, UCRL-JC-126767. 96-ERD-034.

Hua, D. D., E. B. Hooper, T. K. Fowler, *Modeling Electron Heat Transport During Magnetic Field Buildup in SSPX*, UCRL-ID-128656. 97-SI-009.

Huber, R. D., D. J. Chinn, G. H. Thomas, J. V. Candy, J. B. Spicer, “Model-Based Signal Processing for Laser Ultrasonic Signal Enhancement,” *Review of Progress in Quantitative Nondestructive Evaluation Conference* **22**, 757, UCRL-JC-124350. 97-ERD-083.

Hutcheon, I. D., A. J. R. Kent, R. J. Ryerson, “The Temperature of Formation of Carbonate Minerals in Martian Meteorite ALH84001: Constraints from Cation Diffusion,” *EOS (Transactions of the American Geophysical Union)*, in press, UCRL-JC-131679Abs. 98-ERD-042.

Hyde, R. A., *Eyeglass: 1. Very Large Aperture Fresnel Telescopes*, UCRL-JC-131624. 97-ERD-060.

Hyde, R. A., *Large Aperture Fresnel Telescopes*, UCRL-ID-131320. 97-ERD-060.

Johnson, M.D., M. J. Caturla, T. Diaz de la Rubia, “Diffusion in silicon in the presence of carbon and boron,” *J. Appl. Phys.* **84**, 1963. UCRL-JC-128774. 96-ERD-009.

Kahn, S., et al., “Laboratory X-Ray Spectroscopy Experiments in Support of NASA’s X-Ray Satellite Missions,” *Proc. NASA Workshop on Laboratory Space Science*, UCRL-JC-130129. 97-ERD-057.

Kettering, B. M., *ICCS Computer System Startup Simulation*, **1**, 1, NIF-4132. 98-ERD-065.

Kettering, B. M., *ICCS Status Monitor Simulation*, **1**, 1, NIF 4133. 98-ERD-065.

Key, M. H., et al., “Atomic and nuclear processes produced in ultra-high intensity laser irradiation of solid targets,” in *Atomic Processes in Plasmas*, E. Ocks and M. S. Pinzola, Eds., *Proc. AIP Conference* **443**, 283, UCRL-JC-903068. 97-ERD-127.

Key, M. H., et al., “Hot electron production and heating by hot electrons in fast ignitor research,” *Phys. of Plasmas*, **5**, 1966, UCRL-JC-232301. 98-ERD-079.

Kim, B-M., M. Feit, A. Rubenchik, B. Mammini, L. Da Silva, “Optical feedback signal for ultrashort laser pulse ablation of tissue,” *Appl. Surf. Sci*. **127**, 862, UCRL-JC-128614. 97-LW-074.

Kim, B-M., M. Feit, A. Rubenchik, D. Gold, B. Stuart, L. Da Silva, “Ultrashort pulse laser ablation of biological tissue,” *SPIE* **3254**, 203, UCRL-JC-128093. 97-LW-074.

Kim, B-M., M. Feit, A. Rubenchik, D. Gold, C. Darrow, J. Marion, “Plasma luminescence feedback control system for precise ultrashort pulse laser tissue ablation,” *SPIE* **3255**, 92, UCRL-JC-128095. 97-LW-074.

King, W. E., and A. J. Schwartz, “Experimental study of the optimization of the grain boundary character distribution in copper,” Invited presentation abstract, UCRL-JC-128752Abs. 98-ERD-080.

King, W. E., and A. J. Schwartz, “Toward Optimization of the Grain boundary Character Distribution in OFE Copper,” *Scripta Materialia*, **38**(3), 449-455, UCRL-JC-126560. 98-ERD-080.

Klöpfel, D., G. Hölzer, E. Förster, P. Beiersdörfer, “A Quartz Monolith for Absolute X-Ray Wavelength Measurements,” *Rev. of Sci. Instr.* **68**, 3669-3675, UCRL-JC-126463. 97-ERD-103.

Knapp, K., and E. Moses, “Analysis Tools for Evaluation and Validation of Dose Calculation Algorithms,” *Med. Phys*. **25**, A128, UCRL-MI-131470. 96-DI-006.

Koch, J. A., et al., “X-ray Emission Spectroscopy of Deeply Buried Tracer Layers as a Deep-Heating Diagnostic for Fast Ignitor Experiments, *28th Annual Anomalous Absorption Conference*, Bar Harbor, UCRL-JC-902649. 97-ERD-127.

Kohn, M. J., and J. W. Valley, “Effects of cation substitutions in garnet and pyroxene on equilibrium oxygen isotope fractionations,” *J. Metamorphic Geol*. **16**, 625–639, UCRL-JC-130556. 97-ERI-003.

Kohn, M. J., and J. W. Valley, “Oxygen isotope geochemistry of the amphiboles: Isotope effects of cation substitutions in minerals,” *Geochim. Cosmochim. Acta* **62**, 1947–1958, UCRL-JC-128107. 97-ERI-003.

Kohn, S., A. Cleary, S. Smith, S. Smolinski, “Language Interoperability Mechanisms for High-Performance Scientific Applications,” workshop presentation, UCRL-JC-131823. 97-ERD-114.

Kohn, S., J. Weare, E. Ong, S. Baden, “Hierarchical Basis Preconditioners in Three Dimensions,” *SIAM J. Sci. Comp*. **18**, 479–98, UCRL-JC-122279. 97-ERD-114.

Kohn, S., J. Weare, E. Ong, S. Baden, “Parallel Adaptive Mesh Refinement for Electronic Structure Calculations,” *Proc. 8th SIAM Conf. on Parallel Processing for Scientific Computing*, Minneapolis, MN, March 12-13, UCRL-JC-126043. 97-ERD-114.

Kohn, S., J. Weare, E. Ong, S. Baden, “Software Abstractions and Computational Issues in Parallel Structured Adaptive Mesh Methods for Electronic Structure Calculations,” *Proc. Workshop on Structured AMR Grid Methods*, Minneapolis, MN, March 12–13, UCRL-JC-127598. 97-ERD-114.

Kohn, S., and R. Hornung, “SAMRAI: Structured Adaptive Mesh Refinement Applications Infrastructure,” *Supercomputing 98*, UCRL-TB-128634-Rev. 1. 97-ERD-114.

Kohn, S., R. Hornung, X. Garaizar, “SAMRAI: Structured Adaptive Mesh Refinement Applications Infrastructure,” *Supercomputing 97*, UCRL-TB-128634. 97-ERD-114.

Krishnan, V. V., and M. Cosman, “An empirical relationship between rotational correlation time and solvent accessible surface area,” *J. Biomolecular NMR* **12**, 177–182, UCRL-JC-128521. 96-DI-010.

Krulewich, D., and H. Hauschildt, “Spatial Frequency Domain Error Budget,” *Proc. American Society for Precision Engineering 1998 Annual Meeting*, **18**, UCRL-JC-131681. 97-ERD-084.

Labaune, C., H. A. Baldis, B. S. Bauer, E. Schifano, A. Michard, “Effect of crossed beams irradiation on Parametric Instabilities,” *Particle and Laser Beams*, in press, UCRL-JC-130642. 96-ERI-011.

Labaune, C., H. A. Baldis, B. S. Bauer, V. T. Tikhonchuk, G. Laval, “Time-resolved measurements of secondary Langmuir waves produced by the Langmuir decay instability,” *Phys. Plasmas* **5**, 234–242, UCRL-JC-127432. 96-ERI-011.

Labaune, C., H. A. Baldis, N. Renard, E. Schifano, A. Michard, “Interplay between ion acoustic waves and electron plasma waves associated with stimulated Brillouin and Raman scattering,” *Phys. Plasmas* **4**, 423, UCRL-JC-127429. 96-ERI-011.

Labaune, C., H. A. Baldis, N. Renard, E. Schifano, A. Michard, “Location of Ion Acoustic Waves from Back and Side Brillouin Scattering,” *Phys. Rev. Lett*. **76**, 3727, UCRL-JC-123550. 96-ERI-011.

Labaune, C., H. A. Baldis, V. T. Tikhonchuk, “Interpretation of stimulated Brillouin scattering measurements based on the use of random phase plates," *Euro Phys. Lett.*, in press, UCRL-UR-121872. 96-ERI-011.

Ladd, A, J. Kinney, D. Haupt, S. Goldstein, "Finite-element modeling of trabecular bone: comparison with mechanical testing and determination of trabecular modulus," *J. of Orthopaedic Res.* **16**, 622–628, UCRL-JC-128344. 97-LW-016.

Lamont, A., *Analysis of Market Penetration Scenarios of Clean Coal Technologies in China using the LLNL China Energy Model*, UCRL-ID-131690. 97-ERD-048.

Larsen, S. C., J. Grieger, "Elastic modeling initiative: 3-D computational modeling," *Proc. Soc. Expl. Geophys. Conference* **68**, 1803–1806, UCRL-JC-130224. 98-LW-028.

Larsen, S. C., M. Antolik, D. Dreger, C. Stidham, B. Romanowicz, "3-D simulations of scenario earthquakes in the San Francisco Bay Area," *EOS Trans*. **78**, 437, UCRL-JC-128458. 98-LW-028.

Lasinski, B. F., A. B. Langdom, M. Tabak, M. H. Key, "PIC Simulations of Hole-Boring for Fast-Ignitor Applications," *28th Annual Anomalous Absorption Conference*, Bar Harbor, UCRL-JC-902888. 97-ERD-127.

Lasinski, B. F., A. B. Langdon, S. P. Hatchett, M. Key, M. Tabak, "PIC Simulations of Ultra Intense Laser Pulses Propagating through Overdense Plasma for Fast-Ignitor and Radiography Applications," *Phys. of Plasmas*, May 1999, UCRL-JC-902888. 97-ERD-127.

Lawrence, J. D., G. G. Preckshot, G. L. Johnson, "Direct Qualification of Digital Components," *American Nuclear Society International Topical Meeting on Safety of Operating Reactors*, UCRL-JC-130821. 98-ERD-032.

Liedahl, D. A., "Spectroscopy with the New Generation of X-Ray Observatories," *Physica Scripta*, UCRL-JC-132424. 97-ERD-057.

Liedahl, D. A., *The X-Ray Properties of Photoionized Plasmas and Transient Plasmas, X-Ray Spectroscopy in Astrophysics*, UCRL-JC-132453. 97-ERD-057.

Liedahl, D., A., et. al., "Synergistic Approach to Modeling X-Ray Spectra," *Proc. NASA Workshop on Laboratory Space Science*, UCRL-JC-131403. 97-ERD-057.

Lodestro, L. L., T. A. Casper, R. H. Cohen, et al., "Edge and coupled core/edge modeling in tokamaks," *Proc. 17th IAEA Fusion Energy Conference*, UCRL-JC-130155. 98-LW-023.

London, R. A., D. S. Bailey, P. A. Amendt, S. R. Visuri, V. C. Esch, "Scaling model for laser-produced bubbles in soft tissue," *Laser-Tissue Interaction IX*, Ed. S. L. Jacques, *SPIE* **3154**, 256, UCRL- JC-128034. 97-ERD-056.

London, R. A., M. E. Glinsky, G. B. Zimmerman, D. S. Bailey, D. C. Eder, S. L. Jacques, "Laser-Tissue Interaction Modeling with LATIS," *Appl. Optics* **36**, 9068, UCRL- JC-125974. 97-ERD-056.

Lund, S. M., et al., "Numerical Simulation of Intense-Beam Experiments at LLNL and LBNL," *Proc. 12th International Symposium on Heavy Ion Inertial Fusion*, September 22–27, 1997, UCRL-JC-128601. 96-ERD-048.

Lundstrom, C. C., H. F. Shaw, F. J. Ryerson, Q. Williams, J. Gill, "Crystal Chemical Control on Clinopyroxene-Melt Partitioning in the Di-Ab-An System: Implications for Elemental Fractionation in the Depleted Mantle," *Geochemica Cosmochemica Acta* **62**, 2849, UCRL-JC-131769. 96-ERI-005.

Manaa, M. R., and L. E. Fried, "DFT and *ab initio* study of the unimolecular decomposition of the lowest singlet and triplet states of nitromethane," accepted by *J. Phys. Chem.*, UCRL-JC-130489. 97-ERD-101.

Marcy, G. W., R. P. Butler, S. S. Vogt, D. Fischer, M. C. Liu, "Two New Planets in Eccentric Orbits," (observations made by university-based authors using the LLNL adaptive optics system at Lick Observatory), submitted to *Astrophys. J.*, 98-ERD-036.

Mattor, N. "Collisionless fluid closure theory: Lagrangian, Eulerian, and local forms," accepted by *Phys. Plasmas*, UCRL-JC-131127. 98-ERD-099.

Mattor, N., "Collisionless fluid closure theory and the phase velocity transform," *Phys. Plasmas* **5**, 1892 (1998), UCRL-JC-128925-Rev. 1. 98-ERD-099.

Mattor, N., "Local approximation for the phase velocity transform," accepted by *Phys. Plasmas*, UCRL-JC-131128. 98-ERD-099.

Mattor, N., and S. E. Parker, "Nonlinear Kinetic-Fluid Equations," *Phys. Rev. Lett.* **79**, 3419, UCRL-JC-128378. 98-ERD-099.

Matula, T., D. Hallaj, R. Cleveland, L. Crum, W. Moss, R. Roy, "The Acoustic Emissions from Single-Bubble Sonoluminescence," *J. Acoustic Soc. of America* **103**, 1377, UCRL-JC-131348. 98-ERD-081.

Max, C. E., B. A. Macintosh, S. S. Olivier, D. T. Gavel, H. W. Friedman "Observing techniques for astronomical laser guide star adaptive optics," *SPIE* **3353**, pp. 277–281, September 1998. UCRL-JC-233312. 97-ERD-037.

McAninch, J., et al., “Detection of 99Tc by accelerator mass spectrometry: preliminary investigations,” *Proc. 4th International Conference on Methods and Applications of Radio-Analytical Chemistry*, in press, UCRL-JC-127235. 97-ERI-007.

McConnell, I. R., B. Thomas, F. Farrahi, J. S. Albala, “Characterization of a novel RAD51 homolog, RAD51B,” *Genetics Society of Americ*a, Warrenton, VA, April 1998, UCRL-JC-130779Abs. 96-ERD-076.

McEachern, R., and C. Alford, “Evaluation of Boron-doped Beryllium as an Ablator for NIF Target Capsules,” accepted by *Fusion Tech.*, UCRL-JC-130530. 97-ERD-129.

McEachern, R., C. Alford, R. Cook, D. Makowiecki, R. Wallace, “Sputter-deposited Be Ablators for NIF Target Capsules,” *Fusion Tech.* **31**, 435, UCRL-JC-127112. 97-ERD-129.

McEachern, R., J. Matsuo, I. Yamada, “Cluster Ion Beam Polishing for Inertial Confinement Fusion Target Capsules,” *Proc. 12th International Conference on Ion Implantation Technology*, UCRL-JC-130683. 97-ERD-129.

Mcnab, Jr., W., and R. Ruiz, “Palladium-Catalyzed Reductive Dehalogenation of Dissolved Chlorinated Aliphatics Using Electrolytically Generated Hydrogen,” *Chemosphere* **37**(5), 925-936, UCRL-JC-127470. 96-ERD-059.

McNabb, D. P., et al., “Spectroscopy of 112Sn(n,xnyp) channels using GEANIE/WNR,” *Bull. Amer. Phys. Soc.* **43**, 1550, UCRL-JC-131734Abs. 98-LW-051.

Minniti, D., T. Vandehei, K. H. Cook, K. Griest, C. Alcock, “Detection of Lithium in a Main Sequence Bulge Star Using Keck I as a 15m Diameter Telescope,” *Astrophys. J. Lett.* **499**, L175, UCRL-JC-129181. 96-ERD-044.

Molvik, A., et al., “Recirculating Heavy Ion Accelerator Experiment,” *APS Div. of Plasma Phys Meeting*., Denver, November 11–15, 1996, UCRL- JC-121479. 96-ERD-048.

Moore, M. D., D. P. Schrag, M. Kashgarian, “Coral radiocarbon constraints on the source of the Indonesian throughflow,” *JGR Oceans* **102**, UCRL-JC-12359. 97-ERI-009.

Moult, J., J. T. Pederson, R. Judson, K. A. Fidelis, “Large-Scale Experiment to Assess Protein Structure Prediction Methods,” *PROTEINS: Structure, Function and Genetics* **23**, i-iv, UCRL-JC-121716. 96-DI-010.

Musick, R., “Data Management,” presentation, *U.C. Advisory Committee Review*, UCRL-MI-130361. 97-ERD-033.

Musick, R., “DataFoundry,” *DOE Annual Report*, UCRL-TB-127593. 97-ERD-033.

Musick, R., “Large Scale Data Mining Pilot Project in Human Genome,” *Workshop on Research & Development Opportunities in Federal Information Services*, UCRL-JC-127338. 97-ERD-033.

Musick, R., C. Miller, “Report on the Second IEEE Metadata Conference,” invited paper, *Sigmod Record*, UCRL-JC-129094. 97-ERD-033.

Musick, R., T. Critchlow, K. Fidelis, M. Ganesh, T. Slezak, *DataFoundry, Proposal, DOE MICS and OBER Program Offices*, UCRL-PROP-127593. 97-ERD-033.

Nellis, W. J., “Making Metallic Hydrogen,” accepted by *Scientific American*, UCRL-JC-126769. 97-ERD-055.

Nellis, W. J., “Metallic Hydrogen at High Pressures and Temperatures in Jupiter,” *Chem. Eur*. **3**, 1921, UCRL-JC-125039. 97-ERD-055.

Nellis, W. J., “Metallization of Fluid Hydrogen at 140 GPa (1.4 Mbar): Implications for Jupiter,” submitted to *Planetary and Space Sciences*, 1998, UCRL-JC-132004. 97-ERD-055.

Nellis, W. J., “Metallization of Fluid Hydrogen at 140 GPa (1.4 Mbar),” *Proc. 1997 Conferences on Strongly Coupled Coulomb Systems*, in press, UCRL-JC-126769. 97-ERD-055.

Nellis, W. J., “Metastable Solid Metallic Hydrogen,” accepted by *Phil. Mag. B*, 1998, UCRL-JC-132070. 97-ERD-055.

Nellis, W. J., A. A. Louis, N. W. Ashcroft, “Metallization of Fluid Hydrogen,” *Proc. Royal Society of London* **A356**, 119–138 (1998), UCRL-JC-126769. 97-ERD-055.

Nellis, W. J., A. C. Mitchell, “Molecular and Planetary Fluids at High Shock Pressures,” in *Shock Compression of Condensed Matter–97*, ed. S. C. Schmidt, D. P. Dandekar, and J. W. Forbes (American Institute of Physics, Woodbury, NY, 1998), conference proceedings, 13–19, UCRL-JC-128749. 97-ERD-055.

Nellis, W. J., S. T. Weir, A. C. Mitchell, “Electrical Conductivity and Metallization of Fluid Hydrogen in the Pressure Range 90-180 GPa (0.9-1.8 Mbar),” *The Review of High Pressure Science and Technology* **7**, 870, *Proc. 1997 International Conference AIRAPT-16 and HPCJ-38 on High Pressure Science and Technology*, UCRL-JC-126769. 97-ERD-055.

Nellis, W. J., S. T. Weir, A. C. Mitchell, “Minimum Metallic Conductivity of Fluid Hydrogen at 140 GPa (1.4 Mbar), accepted by *Phys. Rev. B.*, 1998, UCRL-JC-126769. 97-ERD-055.

Nellis, W. J., S. T. Weir, N.C. Holmes, M. Ross, A. C. Mitchell, “Hydrogen at High Pressures and Temperatures: Implications for Jupiter,” in *Properties of Earth and Planetary Materials at High Pressure and Temperature*, ed. M. H. Manghnani and T. Yagi (American Geophysical Union, Washington, 1998), 357–364, UCRL-JC-125039. 97-ERD-055.

Neroda, E., J. M. Brenan, C. C. Lundstrom, H. F. Shaw, F. J. Ryerson, D. L. Phinney, “Mineral-melt partitioning of B, Be, and Li: Implications for mantle melting,” *EOS* **77**, S281, UCRL-JC-125592. 96-ERI-005.

Nikkel, D., A. Brown, J. Casey, “Evolution of Anisotropic Yield Behavior,” *Eng. Res., Dev., and Tech.* **5**, 1, UCRL-JC-53868-97. 98-ERD-020.

Nitao, J. J., and W. E. Glassley, “Modeled porosity modification in the near-field environment due to coupled thermal-hydrological and geochemical processes,” *Scientific Basis for Nuclear Waste Management XX*, UCRL-JC-131163. 97-SI-017.

Olivier, S. S., et al., “First significant image improvement from a sodium-layer laser guide star adaptive optics system at Lick Observatory,” *SPIE*, 240–248, October 1997. UCRL-JC-231970. 97-ERD-037.

Oraevsky, A. L., et al., “Plasma mediated ablation of biological tissues with nanosecond to femtosecond laser pulses,” *IEEE Topics Quant. Electr.* **2**, 801, UCRL-JC-120215, 97-LW-074.

Orme, C, S. Orme, H. H. Teng, P. M. Dove, J. J. De Yoreo, “In situ AFM investigations of surface morphology and kinetics during growth of $CaCO_3$,” *Twelfth International Conference on Crystal Growth and the Tenth International Conference on Vapor Growth and Epitaxy*, July 1998, UCRL-JC-128978Abs. 97-LW-069.

Orme, C., H. H. Teng, P. A. Dove, J. J. De Yoreo, “In situ AFM investigations of surface morphology and kinetics during growth of $CaCO_3$,” *American Conference on Crystal Growth West*, June 1998, UCRL-JC-128978Abs-Rev 1. 97-LW-069.

Orme, C., H. Teng. P. Dove, J. J. De Yoreo, “In situ AFM investigations of surface morphology and kinetics during growth of $CaCO_3$,” *American Conference on Crystal Growth West*, June 1997, UCRL-JC-128978Abs. 97-LW-069.

Owens, T. J., and G. Zandt, “The implications of crustal property variations on models of Tibetan Plateau evolution,” *Nature* **387**, 37–43, UCRL-JC-126608. 97-ERI-003.

Pacella, D., et al., “Measurement of the Radiative Cooling Rate for Krypton and Argon and Their Profiles in the FTU Plasma,” *Proc. 25th European Conference on Controlled Fusion and Plasma Physics*, UCRL-JC-130884. 97-ERD-057.

Pagoria, P. F., A. R. Mitchell, R. D. Schmidt, L. E. Fried, “Synthesis and scale-up of new explosives,” UCRL-ID-125792. 97-ERD-101.

Park, H-S., et al, “Instrumentation of LOTIS: A Fully Automated Wide Field of View Telescope,” *SPIE Symposium on Astronomical Telescopes and Instrumentation* **658**, 3355, UCRL-JC-130017. 97-LW-019.

Park, H-S., et al., “New Constraints on Simultaneous Optical Emission From GRBs Measured by the LOTIS Experiment,” *Astrophys. J. Lett*. **490**, L21, UCRL-JC-128146. 97-LW-019.

Park, H-S., et al., “Real-time Optical Flux Limits from Gamma-Ray Bursts Measured by the GROCSE Experiment,” *Astrophys. J.* **490**, 99, UCRL-JC-126711. 97-LW-019.

Park, H-S., et al., “Super-LOTIS: A High Sensitive Optical Counterpart Search Experiment,” *Proc. AIP Conference, 4th Huntsville GRB Workshop* **428**, 842, UCRL-JC-128898. 97-LW-019.

Parkin, S., B. Rupp, H. Hope, “Atomic Resolution Structure of Concanavalin A at 120K,” *Acta Crystallographica*, in press, UCRL-JC-123947. 96-DI-010.

Parkin, S., B. Rupp, H. Hope, “The Structure of Bovine Pancreatic Trypsin Inhibitor (BPTI) at 125K: Definition of Carboxyl-Residues Gly-57 and Ala-58,” *Acta Crystallographica* **D52**, 18, UCRL-JC-119845. 96-DI-010.

Parkin, S., et al., “Comparison of Crystal Structure and Theory for 2-Amino-1-Methyl-6-Phenylimidazo[4,5]bypyridine,” *Chemical Research Toxicology* **9**, 574, UCRL-JC-122232. 96-DI-010.

Parkin, S., et al., “Comparison of Crystal Structure and Theory for 2-amino-1-methyl-6-phenylimidazo[4,5-b]pyridine, *Chem. Res. Toxicol*. **9**, 574–579, UCRL-JC-122232. 96-DI-010.

Pechik, I., et al., “Crystallographic, Molecular Modeling, and Biophysical Characterization of the Valine67 (E11)->Threonine Variant of Hemoglobin,” *Biochemistry* **35**, 1935, UCRL-JC-121981. 96-DI-010.

Perry, M. D., and G. Mourou, “Table-top Ultrahigh Intensity Lasers,” *Optics and Photonics News* **41**, UCRL-JC-252154. 98-ERD-079.

Perry, M. D., et al., “Petawatt Laser Pulses,” *Optics Lett.* **24**, 61, UCRL-JC-129760. 98-ERD-079.

Pham, A. Q., and R. S. Glass, “Oxygen Pumping Characteristics of Yttria-Stabilized-Zirconia,” *Electrochimica Acta* **43**, 2699, UCRL-JC-126553. 97-LW-009.

Phillips, T. W., et al., “Diagnosing hot electron production by short pulse, high intensity lasers using photonuclear reactions,” *Rev. Sci. Instru*., (in press), UCRL-JC-902975. 97-ERD-127.

Phillips, T. W., et al., “Diagnosing hot electron production by short pulse high intensity lasers using photonuclear reactions,” *Rev. Sci. Instr*. **70**, 1213, UCRL-JC-233922. 98-ERD-079.

Pinto, P. A., and R. G. Eastman, “The Physics of Type Ia Supernova Lightcurves: II Opacity and Diffusion,” accepted by *Astrophys. J*., UCRL-JC-132022-Pt. 2. 97-ERD-108.

Pinto, P. A., and R. G. Eastman, “The Physics of Type Ia Supernova Lightcurves: I Analytic Results,” accepted by *Astrophys. J*., UCRL-JC-132022-Pt. 1. 97-ERD-108.

Porter, G. D., R. E. Cid, R. H. Cohen, et al., “Experiments on penetration of a plasma with magnetized electrons across a magnetic field,” submitted to *Bull. Am. Phys. Soc*., UCRL-JC-131316Abs. 98-LW-023.

Post, R. F., “Mirror-Based Fusion, Some Possible New Directions,” accepted by *Fusion Technology*, UCRL-JC-130404. 98-FS-001.

Post, R. F., “Open Systems in the Quest for Fusion,” *Plasma Phys. Rep.* **23**, 756, UCRL-JC-127005. 98-FS-001.

Post, R. F., and D. D. Ryutov, “Ambient-Temperature Passive Magnetic Bearings: Theory and Design Equations,” *Proc. Sixth Int. Symposium on Magnetic Bearings* **1**, 109, UCRL-JC-129214. 98-ERD-035.

Putirka, K., “Clinopyroxene+liquid equilibrium to 100 kbar and 2450 K,” submitted to *Contrib. Min. Petrology*, UCRL-JC-131481. 96-ERI-005.

Putirka, K., “Empirical Constraints on melt productivity and the production of oceanic crust,” submitted to *Earth Planet Sci. Lett.*, UCRL-JC-131486. 96-ERI-005.

Putirka, K., “Melting depths and mantle heterogeneity beneath Hawaii and the East Pacific Rise: Constraints from Na/Ti and REE ratios,” *J. Geophys. Res*., in press, UCRL-JC-131482. 96-ERI-005.

Ratowsky, R. P., B. B. Afeyan, J. S. Kallman, M. D. Feit, “Propagation modeling for multimode photonics,” *Optoelectronics ‘99*, UCRL-JC-131253Abs. 98-ERD-019.

Ratowsky, R. P., S. Dijaili, J. S. Kallman, M. D. Feit, J. Walker, W. Goward, M. Lowry, “Modeling a distributed spatial filter low-noise semiconductor optical amplifier,” *Integrated Photonics Research* (conference),Victoria, BC, Canada, March 30-April 1, 1998, UCRL-JC-129108. 97-LW-014.

(Reynolds, J. G.) Science/Technologies Concentrates, “Crown Polymer Extracts Mercury from Water” an article about Hg removal in waste streams in *Chemical & Engineering News*, August 17, 1998, page 37. 97-ERD-015.

Rhee, M., H. M. Zbib, J. P. Hirth, H. Huang, T. Diaz de la Rubia, “Models for long/short range interactions and cross slip in 3D dislocation simulation of BCC single crystals,” *Sim. Mater. Sci. Eng.* **6**, 467, UCRL-JC -129126. 97-SI-010.

Roberts, C. C., S. A. Letts, M. D. Saculla, E. J. Hsieh, R. C. Cook, “Polyimide Films from Vapor Deposition: Toward High Strength NIF Capsules,” *Fusion Tech.*, March 1999, UCRL- JC-132194, 97-ERD-016.

Roberts, C. C., S. A. Letts, M. D. Saculla, R. C. Cook, *High Performance Polyimide Coating Technology*, UCRL-ID-129313. 97-ERD-016.

Rognlien, T., X. Xu, et al., “Parallelization of an Edge Plasma Transport Code via Domain Decomposition,” *Bull. Am. Phys. Soc.* **42**, 1584, UCRL-JC-127375Abs. 97-ERD-045.

Rosenberg, L., K. van Bibber, “Axion overview and the U.S. RF cavity axion search,” *Proc. Dark Matter in the Universe and its Detection*, November 26-28, 1996, Tokyo, published by Universal Academy Press, UCRL-JC-129345. 96-LW-061.

Röttgering, H. J., A., R. van Ojik, G. K. Miley, K. C. Chambers, W. J. M. van Breugel, S. de Koff, “Spectroscopy of Ultra-Steep-Spectrum Radio Sources: A Sample of $Z > 2$ Radio Galaxies,” *Astronomy and Astrophysics* **326**, 505, UCRL-JC-123261. 98-ERI-005.

Rozmus, W., S. Glenzer, K. Estabrook, H. A. Baldis, B. MacGowan, “Modeling of Thomson scattering spectra in high-*Z*, laser produced plasmas,” *Astrophys. J.*, in press, UCRL-JC-130646. 96-ERI-011.

Rubenchik, A., M. Feit, M. Perry, J. Larsen, “Numerical simulation of ultrashort laser pulse energy deposition and transport,” *App. Surf. Sci*. **127**, 171, UCRL-JC-127279. 97-LW-074.

Ruggiero, A. J., M. W. Bowers, R. A. Young, “Mini-AM DIAL System,” prepared for the *Proc. Conference on Lasers and Electro-Optics 1999*. UCRL-JC-132474. 97-ERD-006.

Rupp, B., D. Marshak, S. Parkin, “Crystallization and Preliminary X-ray Analysis of Two New Crystal Forms of

Calmodulin," *Acta Crystallographica* **D52**, 411, UCRL-JC-120363. 96-DI-010.

Rupp, B., et al., "Novel Mechanism for Defective Receptor Binding of Apolipoprotein E2 in Type-III Hyperlipoproteinemia," *Nature Structural Biology* **3**, 718, UCRL-JC-124738. 96-DI-010.

Ryerson, F. J., T. M. Harrison, A. Yin, M. Murphy, "The Gangdese and Renbu-Zedong Thrust Systems: Lateral Extent and Thrust History," *Tibet-Himalaya-Karakorum Workshop*, UCRL-JC-126611Abs. 97-ERI-003.

Salleo, A., R. R. Chinsio, J. H. Campbell, F. Genin, "Crack propagation in fused silica during UV and IR ns-laser illumination," *Laser-Induced Damage in Optical Materials: 1998*, UCRL-ID-131218. 98-ERD-063.

Samudrala, R., J. T. Pederson, H. Zhou, R. Luo, K. Fidelis, J. Moult, "Confronting the Problem of Interconnecting Structural Changes in the Comparative Modeling of Proteins," *PROTEINS: Structure, Function and Genetics* **23**, 327, UCRL-JC-121718. 96-DI-010.

Sangster, T. C., et al., "Status of Experiments Leading to a Small Recirculator," *Proc. 12th International Symposium on Heavy Ion Inertial Fusion*, September 22–27, 1997, UCRL-JC- 233095. 96-ERD-048.

Sangster, T. C., et al., "Status of Experiments Leading to a Small Recirculator," *12th International Symposium on Heavy Ion Inertial Fusion*, September 24-27, 1997, submitted to *Nuc. Instru. and Meth. in Phys. Res.*, UCRL-JC- 233095. 97-ERD-086.

Sangster, T. C., et al., "Status of the LLNL Experiments on Bending and Recirculation," *Particle Accelerator Conference 97*, May 12-16, 1997, Vancouver, Canada, UCRL- JC-126544. 96-ERD-048.

Savin, D. W., M. F. Gu, P. Beiersdorfer, "The effects of electron spiraling on the anisotropy and polarization of photon emission from on electron beam ion trap," *NIF Publication Series* **37**, 90, UCRL-JC-130148. 97-ERD-103.

Savin, D., B. Beck, P. Beiersdorfer, S. Kahn, G. Brown, M. Gu, D. Liedahl, J. Scofield, "Simulations of a Maxwellian Plasma Using an Electron Beam Ion Trap," *Physica Scripta*, UCRL-JC-131735. 97-ERD-057.

Schach von Wittenau, A, P. Bergstrom, L. Cox, R. Mohan, B. Libby, Q. Wu, D. Lovelock, "Treatment of Patient-Dependent Beam Modifiers in Photon Treatments by PEREGRINE for Monte Carlo Dose Calculations," *International Conference on Computers in Radiotherapy*, May 27–30, 1997, UCRL-JC-126730. 96-DI-006.

Schach von Wittenau, A., P. Bergstrom, W. Chandler, L. Cox, C Hartmann-Siantar, R. I. House, M. Mohan, "Accelerator-specific Photon Phase Space Description and Sampling Techniques in the PEREGRINE Monte Carlo Dose Calculation System," *Med. Phys*. **25**, A187, UCRL-MI-131469. 96-DI-006.

Schenkel, T., A. V. Barnes, A. V. Hamza, D. H. Schneider, J. C. Banks, B. L. Doyle, "Synergy of Electronic Excitations and Elastic Collision Spikes in Sputtering of Heavy Metal Oxides," *Phys. Rev. Lett*. **80**, 4325, UCRL-JC-129534. 97-ERD-102.

Schenkel, T., A. V. Barnes, M. A. Briere, A. Hamza, A. Schach von Wittenau, D. H. Schneider, "Emission of Secondary Particles from Metals and Insulators at Impact of Slow Highly Charged Ions," *Nuc. Instr. and Meth. in Phys. Res. B* **125**, 153, UCRL-JC-126721. 97-ERD-102.

Schenkel, T., A. V. Hamza, A. V. Barnes, D. H. Schneider, "Cluster Ion Emission upon Slow, Highly Charged Ion Impact," *European Physical Journal D - Clusters and Molecules* **1**, 297, UCRL-JC-127177. 97-ERD-102

Schenkel, T., A. V. Hamza, A. V. Barnes, D. H. Schneider, "Energy Loss of Slow Highly Charged Ions in Solids," *Phys. Rev. A* **56**, R1701, UCRL-JC-127784. 97-ERD-102.

Schenkel, T., A. V. Hamza, A. V. Barnes, D. H. Schneider, D. S. Walsh, B. L. Doyle, "Analysis of B-SiO_2 Films by Highly Charged Ion Based Time-of-Flight Secondary Mass Spectrometry and Elastic Recoil Detection," J. *Vacuum Sci. and Tech*. **A16**, 1384, UCRL-JC-128724. 97-ERD-102.

Schenkel, T., A. V. Hamza, A. V. Barnes, D. H. Schneider, J. C. Banks, B. L. Doyle, "Ablation of GaAs by Intense ultra-fast electronic excitation on a Nanometer Scale," *Phys. Rev. Lett*. **81**, 2590, UCRL-JC-130626. 97-ERD-102.

Schenkel, T., et al., "Electronic Desorption of Alkyl Monolayers from Silicon by Very Highly Charged Ions," *J. Vacuum Sci. and Tech*. **B16**, UCRL-JC-131064. 97-ERD-102.

Schenkel, T., M. A. Briere, A. V. Barnes, A. V. Hamza, K. Bethge, H. Schmidt-Böcking, D. H. Schneider, "Charge State Dependent Energy Loss of Slow Heavy Ions in Solids," *Phys. Rev. Lett*. **79**, 2030, UCRL-JC-127783. 97-ERD-102.

Schenkel, T., M. A. Briere, H. Schmidt-Böcking, K. Bethge, D. H. Schneider, "Electronic Sputtering of Thin Conductors by Neutralization of Slow Highly Charged Ions," *Phys. Rev. Lett*. **78**, 2481, UCRL-JC-125421. 97-ERD-102.

Schenkel, T., M. A. Briere, H. Schmidt-Böcking, K. Bethge, D. Schnieder, "Electronic Sputtering and Desorption Effects in TOF-SIMS Studies Using Slow Highly Charged Ions like

Au69+," *Materials Science Forum* **413**, 248-249, UCRL-JC-125358. 97-ERD-102.

Schmid, G., D. Beckedahl, J. Blair, J. Kammeraad, "HPGe Compton Suppression using Pulse Shape Analysis," accepted by *Nucl. Instr. and Meth., in Phys. Res.,* UCRL-JC-130495. 97-ERD-017.

Schoenenberger K., B. W. Colston, Jr., L. B. Da Silva, D. J. Maitland, M. J. Everett, "Mapping of birefringence and thermal damage in tissue by polarization-sensitive optical coherence tomography," *Appl. Optics* **37**, 6026, UCRL-JC-130145. 98-ERD-062.

Schwartz, A. J., and W. E. King, "The Potential Engineering of Grain boundaries through Thermomechanical Processing," *JOM* **50**(2), 50–55, UCRL-JC-129111. 98-ERD-080.

Schwartz, A. J., W. E. King, G. H. Campbell, J. S. Stolken, D. H. Lassila, "Orientation Imaging Microscopy Investigation of the Compression Deformation of a [011] Ta Single Crystal," *Proc. Society of Engineering Sciences Symposium on Mechanics of Materials*, Pullman, WA, 1998, UCRL-JC-131663. 97-SI-010.

Schwartz, A. J., W. E. King, M. Kumar, "Role of twinning in the optimization of the grain boundary character distribution," Invited paper abstract, UCRL-JC-131664Abs. 98-ERD-080.

Seidl, P., et al., "Heavy Ion Fusion Research at Berkeley and Livermore," *Fusion Energy 96 (IAEA)* **3**, 145, LBNL-39278. 96-ERD-048.

Sharp, W. M., A. Friedman, D. P. Grote, "Manipulation of High-Current Pulses for Heavy-Ion Fusion," *1996 Comp. Accel. Phys. Conference (CAP96)*, Williamsburg, VA, September 24–27, 1996, UCRL-JC-124486. 96-ERD-048.

Sharp, W. M., D. P. Grote, M. A. Hernandez, G. W. Kamin, "Steering Algorithms for a Small Recirculating Heavy Ion Accelerator," *12th InternationalSymposium on Heavy Ion Inertial Fusion*, September 24–27, 1997, submitted to *Nuc. Instru. and Meth. in Phys. Res. A*, UCRL-JC-232229. 97-ERD-086.

Shaw, H. F., J. M. Brenan, F. J. Ryerson, "Experimental constraints on element cycling at convergent margins," (Abstracts) *Geochemical Earth Reference Model Workshop*, Lyon, France, March 28–30, 1996, UCRL-JC-125595. 96-ERI-005.

Shaw, H., J. Brenan, F. Ryerson," Experimental constraints on the role of aqueous fluids in the origin of B/Be variations of arc magmas," (Abstracts) *GAC/MAC Conference*, May 19–21, 1997, Toronto, Canada, UCRL-JC-126372. 96-ERI-005.

Shlyaptseva, A. S., R. C. Mancini, P. Neill, P. Beiersdorfer, J. R. Crespo López-Urrutia, K. Widmann, "Polarization-dependent spectra of x-ray dielectronic satellite lines of Be-like Fe," *Phys. Rev. A* **57**, 888, UCRL-JC-128403. 97-ERD-103.

Shlyaptseva, A. S., R. C. Mancini, P. Neill, P. Beiersdorfer, *Polarization Properties of Dielectronic Satellite Lines in the K-shell X-ray Spectra of B-like Fe XXII*, UCRL-JC-131409. 97-ERD-103.

Skidmore, M. O., et al., Crystallization of the A-alpha Subunit of Protein Phosphatase 2A, *Protein Science* **5**, 1198, UCRL-JC-123402. 96-DI-010.

Soneda, N., and T. Diaz de la Rubia, "Defect production, annealing kinetics and damage evolution in alpha-Fe: An atomic scale computer simulation," *Philo. Mag. A* **78**, 995, UCRL-JC-126852. 98-ERD-090.

Springer, J. B., M. E. Colvin, O. M. Colvin, S. M. Ludeman, "Isophosporamide Mustard and Its Mechanism of Bisalkylation," *J. Org. Chem*. **63**, 7218, UCRL-JC-132588. 98-SI-008.

Springer, P. T., et al., "Laboratory Measurement of Opacity for Stellar Envelopes," *J. of Quant. Spectro. and Rad. Trans.* **58**, 927–935, UCRL-JC-127171. 97-ERD-108.

Springer, P. T., R. G. Eastman, P. A. Pinto, C. A. Iglesias, "Laboratory Measurement of Opacity for Stellar Envelopes," *Harvard Space Science Workshop*, UCRL-JC-127171. 97-ERD-108.

Stanford, S. A., P. R. Eisenhardt, M. E. Dickinson, "The Evolution of Early-Type Galaxies in Distant Clusters, The Evolution of Early-Type Galaxies in Distant Clusters," *Astrophys. J.* **492**, 461, UCRL-JC-126384. 98-ERI-005.

Staudigel, H., F. Albarede, H. Shaw, W. White, "The Geochemical Earth Reference Model (GERM)," *Chem. Geol*. **145**, 153, UCRL-JC-126054. 96-ERI-005.

Steiger, J., B. R. Beck, L. Gruber, D. A. Church, J. P. Holder, D. Schneider, "Coulomb Clusters in RETRAP," *Trapped Charged Particles and Fundamental Physics* **457**, AIP Press, New York, UCRL-JC-132209. 96-ERD-052.

Steiger, J., D. A. Church, G. Weinberg, B. Beck, J. McDonald, D. Schneider, "Observation of Sequential Electron Capture to Individual Highly Charged Th Ions," *Hyperfine Interactions* **108**, 115, UCRL-JC-122127. 96-ERD-052.

Stern, L., D. Hogenboom, W. Durham, S. Kirby, I. Chou, "Optical-Cell Evidence for Superheated Ice under Gas-

Hydrate-Forming Conditions," *J. Phys. Chem. B* **102**, 2627, UCRL-JC-132369. 98-ERD-008.

Stern, L., S. Kirby, W. Durham, "Polycrystalline Methane Hydrate: Synthesis from Superheated Ice, and Low-Temperature Mechanical Properties," *Energy & Fuels* **12**, 201, UCRL-JC-132370. 98-ERD-008.

Still, C. H., et al., "Extending Laser-Plasma Interaction Simulations with MPP-F3D," *Num. Sim. of Plasmas*, UCRL-JC-902897. 97-ERD-127.

Stoeffl, W., P. Asoka-Kumar, R. H. Howell, "The Positron Microprobe at LLNL," accepted by *J . Appl. Surf. Sci*., UCRL-JC-126768. 96-ERD-034.

Stuart, B., M. Perry, M. Feit, A. Rubenchik, L. DaSilva, "Femtosecond laser cutting and drilling of tissue," *SPIE BIOS Europe*, UCRL-JC-126546. 97-LW-074.

Stuart, B., M. Perry, M. Feit, L. DaSilva, A. Rubenchik, J. Neev, "Machining of biological materials, dielectrics and metals with femtosecond lasers," *OSA Topics in Optical Science* **9**, 94, UCRL-JC-125735, 97-LW-074.

Summers, J. S., D. Roe, P. D. Boyle, M. Colvin, B. R. Shaw, "Structural Studies of a Borane-Modified Phosphate Diester Linkage: Ab Initio Calculations on the Dimethylboranophosphate Anion and the Single-Crystal X-ray Structure of Its Diisopropylammonium Salt," *Inorgan. Chem.* **37**, 4158, UCRL-JC-132589. 98-SI-008.

Sutton, S. E., et al., "Thermal Recovery of the NIF Amplifiers," submitted to *Proc. Third International Conference on Solid State Laser Application to Inertial Confinement Fusion*, held June 7-12, 1998, Monterey, CA, SPIE proceedings series, Society of Photo-Optical Instrumentation Engineers, Bellingham, WA, UCRL-JC-234352. 97-ERD-133.

Svatos, M., et al., "Single Scatter Electron Monte Carlo," *1997 Joint International Conference on Mathematical Methods and Supercomputing for Nuclear Applications*, Saratoga, NY, UCRL-JC-127158. 96-DI-006.

Teng H. H., P. A. Dove, C. A. Orme, J. J. De Yoreo , "Thermodynamics of Calcite Growth: Baseline for Understanding Biomineral Formation," *Science* **282**, 724, UCRL-JC-132308. 97-LW-069.

Tittiranonda, P., S. Burastero, D. Rempel, "Risk Factors for Musculoskeletal Disorders Among Computer Users," *State of Art Reviews in Occupational Medicine* **14**(1) UCRL-JC-131928. 97-ERD-031.

Tompson, A. F. B., et al., "Analysis of Subsurface Contaminant Migration and Remediation using High Performance Computing," *Advances in Water Resources* **22**, 201–221, UCRL-JC-124650. 97-ERD-114.

Tompson, A. F. B., S. F. Carle, N. D. Rosenberg, R. M. Maxwell, "Analysis of Groundwater Migration from Artificial Recharge in a Large Urban Aquifer: A Simulation Perspective," submitted to *Water Resources Research*, UCRL-JC-129563. 97-ERD-035.

Träbert, E. P. Beiersdorfer, S. B. Utter, J. R. Crespo López-Urrutia, "Forbidden transitions in the visible spectra of an electron beam ion trap," *Physica Scripta* **58**, 599 (1998), UCRL-JC-129662. 98-LW-057.

Trakhanov, S., D. L. Kreimer, S. Parkin, G. F. Ames, B. Rupp, "Cadmium induced crystallization of proteins: II. Crystallization of the Salmonella typhimurium Histidine binding protein in complex with L-histidine, L-arginine or L-lysine," *Protein Science*, **7**, 600–604. UCRL-JC-128577. 96-DI-010.

Trakhanov, S., et al., "Crystal structure of a monoclonal 2E8 Fab antibody fragment specific to the low density lipoprotein receptor binding region of Apolipoprotein E refined at 1.9 Å," *Acta Cryst* **D54**, in press. UCRL-JC-130084. 96-DI-010.

Tran, H. D., M. H. Cohen, P. M. Ogle, R. W. Goodrich, S. D. Alighieri, "Scattered Radiation from Obscured Quasars in Distant Radio Galaxies," *Astrophys. J*. **500**, 660, UCRL-JC-128461. 98-ERI-005.

Utter, S. B., P. Beiersdorfer, J. R. Crespo López-Urrutia, E. Träbert, "Implementation of a Normal Incidence Spectrometer on an Electron Beam Ion Trap," *Rev. Sci. Instru*., in press, UCRL-JC-129794. 98-LW-057.

van Breugel, W. J., M., S. A. Stanford, H. Spinrad, D. Stern, J. R. Graham, "Morphological Evolution in High Redshift Radio Galaxies and the Formation of Giant Elliptical Galaxies," *Astrophys. J*. **502**, 614, UCRL-JC-128464. 98-ERI-005.

Van der Woerd, J., et al. "Holocene left-slip rate determined by cosmogenic surface dating on the Xidatan segment of the Kunlun Fault (Qinghai, China)," *Geology* **26**, 695–698, UCRL-JC-128338. 97-ERI-003.

Van der Woerd, J., et al., "Strain-Styles, Large-Scale Morphology and Post-Glacial Slip-Rates Along the Active Kunlun Fault," *EOS* **77**, F687, UCRL-JC-126614Abs. 97-ERI-003.

Van Vorhis, R. L. et al., "Joint coordinate system (JCS) application for different joint mechanisms: comparison of actual and JCS axes' rotations and translations," *16th Congress of* *the International Society of Biomechanics,*, UCRL-JC-127343Abs. 96-ERI-003.

Van Vorhis, R. L., et al., "Measurement of human wrist functional axes motions: preliminary validation of method," *16th Congress of the International Society of Biomechanics*, UCRL-JC-127345Abs. 96-ERI-003.

Van Vorhis, R., K. Hollerbach, A. Hollister, P. Tittiranonda, S. Burastero, *Kinematic Measurements about Wrist Functional Anatomic Axes: Validation of Mechanical Wrist Phantom for Ergonomic Motion Studies*, UCRL-JC-127345Abs. 97-ERD-031.

Venclovas, C., A. Zemla, K. Fidelis, J. Moult, "Numerical criteria for evaluating protein structures derived from comparative modeling," *Proteins: Structure, Function, and Genetics*, Supp. 1, 7–13. UCRL-JC-129139. 96-DI-010.

Visuri, S. R., R. A. London, L. B. Da Silva, "Stress Wave Focusing Transducers," *Trends in Optics and Photonics* **22**, 330–332, UCRL-JC-130697. 98-LW-030.

Vogel, J. S., "Accelerator mass spectrometry as a bioanalytical tool, *Proc. Isotopically Labeled Compounds* **6**, 11–20, UCRL-JC-128826. 97-ERI-007.

Vogel, J., and K. Turteltaub, "Accelerator mass spectrometry as a bioanalytical tool in nutritional research," *Advances in Experimental Biology and Medicine*, **445**, 397–410, UCRL-JC-128472. 97-ERI-007.

Walling, R., C. Hartmann-Siantar, N. Albright, D. Wieczorek, K. Knapp, L. Verhey, S. May, E. Moses, "Clinical Validation of the PEREGRINE Monte Carlo Dose Calculation Systems for Photon Beam Teletherapy," *Med. Phys.* **25**, A128, UCRL-MI-131467. 96-DI-006.

Wang, L., M. Yan, W. Siekhaus, L. Sheehan, J. De Yoreo, M. Kozlowski, J. Yang, U. Mohideen, "Defects and laser damage studies using near field scanning optical microscopy," *Boulder Optical Material Damage Conference'97*, UCRL-JC-128354. 97-ERD-013.

Wang, L., M. Yan, W. Siekhaus, S. Oberhelman, "Probing nanodefects in fused silica by near field scanning optical microscopy," *J. Appl. Phys.* **84**, 3016, UCRL-JC-130635. 97-ERD-013.

Wargelin, B., P. Beiersdorfer, D. Liedahl, S. Kahn, S. von Goeler, "Observation and Modeling of High-n Iron L-Shell Lines From Intermediate Ion Stages," *Astrophys. J.* **496**, 1031, UCRL-JC-128010. 97-ERD-057.

Wharton, K., et al, "Experimental Measurement of hot electrons generated by ultra-intense lasers," *Phys. Rev. Lett.* **81**, 822, UCRL-JC-903014. 98-ERD-079.

Widmann, K., et al., "Polarization-Specific Phase and Reflectivity Dynamics from Femtosecond Laser Pulse-Probe Experiments," UCRL-JC-132045Abs. 97-ERD-107.

Williams, G., H-S. Park, et al., "First Year Results from LOTIS," *Proc. AIP Conference, 4th Huntsville GRB Workshop* **428**, 837, UCRL-JC-128899. 97-LW-019.

Williams, R. V., W. D. Edwards, V. R. Gadgil, M. E. Colvin, E. T. Seidl, D. van der Helm, M. B. Hossain, "Pyramidalized Olefins: Ab Initio Study and X-ray Structure Determination of Bicyclo[2.2.2]octadienes," *J. Org. Chem.* **63**, 5268, UCRL-JC-132591. 98-SI-008.

Wilson, D., J. Carney, M. Coleman, A. Adamson, M. Christensen, J. Lamerdin, "HEX1: A new human nuclease family member with homology to Saccharomyces cerevisiae exonuclease I," *Nucleic Acids Res.* **26**, 3762–3768, UCRL-JC-130499. 97-ERD-002.

Wilson, M., D. Goerz, R. Speer, R. Moal, *Heavy Ion Fusion (HIF) Impulse Injector Design, Construction, and Checkout*, UCRL-ID-130764. 97-ERD-086.

Wittenbrink, C., et al., "Parallel and Distributed Volume Visualization," *SPIE Electronic Imaging*, UCRL-CR-126386. 96-ERI-003.

Woodruff, J. P., and P. J. Van Arsdall, "A Large Distributed Control System Using Ada in Fusion Research," *Proc. ACM SIGAda*, UCRL-JC-130569. 98-ERD-065.

Woodruff, J. P., and P. J. Van Arsdall, "A Large Distributed Control System Using Ada in Fusion Research," *Proc. ACM SIGAda*, 121–131, ISBN 1-58113-033-3, November 8, 1998, UCRL-JC-130569-Rev. 1. 98-ERD-065.

Woods, B. W., et al., "Investigation of damage in KDP using light scattering techniques," *Proc. SPIE 28th Annual Boulder Damage Conference* **2966**, 20, UCRL-JC-125368. 97-ERD-098.

Woodward, C. S., "A Newton-Krylov-Multigrid Solver for Variably Saturated Flow Problems," *Proc. Twelfth International Conference on Computational Methods in Water Resources* **2**, 609–616, UCRL-JC-129371. 97-ERD-035.

Wu, C. J., and L. E. Fried, "Ab initio study of RDX decomposition mechanisms," *J. Phys. Chem.* **101**, 8675, UCRL-JC-125718. 97-ERD-101.

Wu, C. J., and L. E. Fried, "First-principles study of high explosive decomposition energetics," *Proc. 11th International Symposium on Detonation*, UCRL-JC-127877. 97-ERD-101.

Wu, Z., M. D. Feit, J. D. Natoli, A. M. Rubenchik, L. M. Sheehan, M. Yan, "Single-beam photothermal microscopy-a new diagnostic tool for optical materials," *Laser Induced Damage in Optical Materials: 1998*, UCRL-ID-131212. 98-ERD-063.

Wu, Z., M. D. Feit, M. R. Kozlowski, A. M. Rubenchik, L. M. Sheehan, "Laser modulated scattering as a nondestructive evaluation tool for optical surfaces," *Laser Induced Damage in Optical Materials: 1998,* UCRL-ID-131211. 98-ERD-063.

Xu, X., R. Cohen, R., et al., "Turbulence Studies in Tokamak Boundary Plasmas with Realistic Geometry," *Proc. IAEA Conference on Fusion Energy*, paper, CN-69, THP2/03, UCRL-JC-130160. 97-ERD-045.

Yan, M., et al., "Impurity and laser-induced damage in the growth sectors of rapidly grown KDP crystals," *Proc. SPIE 28th Annual Boulder Damage Conference* **11**, 2996, UCRL-JC-126804. 97-ERD-098.

Yan, M., et al., "Impurity segregation and its effects on the optical properties of KH_2PO_4," *SPIE: Solid State Lasers for Application to ICF*, UCRL-JC-123594Abs-Rev. 2. 97-ERD-098.

Yan, M., L. Wang, W. Siekhaus, M. Kozlowski, "Defect Study in Fused silica using near field scanning optical microscopy," *SPIE* **3244**, 268, UCRL-JC-129506. 97-ERD-013.

Yan, M., L. Westin, R. A. Torres, J. J. De Yoreo, L. Carman, N. P. Zaitseva, "Molecular defects in KDP crystals," *International Conference on Crystal Growth*, UCRL-JC-129022Abs. 97-ERD-098.

Yan, M., P. Santiago, M. Staggs, J. J. De Yoreo, L. Carman, L., N. Zaitseva, "Optical properties of doped KDP crystals, *Bull. Amer. Phys. Soc*., **42**, 97, UCRL-JC-125972Abs. 97-ERD-098.

Yan, M., R. Torres, I. Hutcheon, J. J. De Yoreo, N. P. Zaitseva, Z. U. Rek, "Impurity segregation and its effects on the optical properties of KH_2PO_4," *American Conference on Crystal Growth West*, UCRL-JC-123594Abs. 97-ERD-098.

Yan, M., S. K. Oberhelman, W. J. Siekhaus, Z. Wu, L. M. Sheehan, M. R. Kozlowski, "Characterization of surface and sub-surface defects in optical materials using near field evanescent wave," *Laser Induced Damage in Optical Materials: 1998*, UCRL-ID-131225. 98-ERD-063.

Yan, M., S. Oberhelman, W. Siekhaus, M. Kozlowski, "Observation of Laser Field Enhancement and Damage using Near Field Evanescent Wave," *Boulder Optical Material Damage Conference'98*, UCRL-MI-131933. 97-ERD-013.

Yoo, C. S., H. Cynn, P. Soderlind, "Phase diagram of uranium at high pressures and temperatures," *Phys. Rev. B* **57**, 10359, UCRL-JC-12995498. 98-ERD-059.

Yoo, C. S., P. Soderlind, H. Cynn, "The phase diagram of cobalt at high pressure and temperature: the stability of g(fcc)-cobalt and new e'(dhcp)-cobalt," *J. Phys.: Condens. Matter* **10**, L311, UCRL-JC-128794. 98-ERD-059.

Zemla, A., C. Venclovas, A. Reinhardt, K. Fidelis, T. J. Hubbard, "Numerical criteria for the evaluation of ab initio predictions of protein structure," *J. Struct. Proteins,* Supp. 1, 140–150. UCRL-JC-129138. 96-DI-010.

Zemla, A., C. Venclovas, K. Fidelis, B. Rost, "A modified definition of Sov, a segment based measure for protein secondary structure prediction assessment," *J. Mol. Bio*, in press, UCRL-JC-129140. 96-DI-010.

Principal Investigators Index

Tracking Code Index